Delft University of Technology

Faculty of Aerospace Engineering
Department of Aerospace Structures and Materials

German Aerospace Center

Institute of Aeroelasticity
Department of Structural Dynamics and System Identification

Shape Sensing and Load Reconstruction for Static and Dynamic Applications

---

Master of Science Thesis

For obtaining the degree of Master of Science in Aerospace Engineering
at Delft University of Technology

Author:
Paolo Minigher

Supervisor:
Dr.-Ing. Saullo Giovani Pereira Castro (TU Delft)
Dipl.-Ing. Janto Gundlach (DLR)

July 25, 2022

TUDelft DLR

Contents

CONTENTS

List of Symbols

$A^{(e)}$	element cross section area
b	width
$\boldsymbol{b}$	generic input vector ($\boldsymbol{Ax} = \boldsymbol{b}$)
$\boldsymbol{B}$	strain-displacement matrix (iFEM)
c	measure of taper ratio / distance from neutral axis (Ko Theory)
$\boldsymbol{C}$	damping matrix
$C_1,\ C_2,\ C_3,\ C_4$	integration constants
$e_1,\ e_2,\ e_3$	section strains (beam element)
$\boldsymbol{e}_1,\ \boldsymbol{e}_2,\ \boldsymbol{e}_3$	unit vectors local reference system
$\boldsymbol{e}$	vector of membrane strain measures (iQS4) / vector of input errors
E	elastic modulus / strain energy
$\boldsymbol{f}^{(e)}$	element input vector (iFEM)
G	shear modulus
$\boldsymbol{g}$	vector of transverse shear strains (iQS4)
h	height
$\boldsymbol{h}$	impulse response function
$H_{ij}^{(k)}$	Hermite polynomial
$\boldsymbol{H}$	FRF matrix
$I_y^{(e)},\ I_z^{(e)}$	element second moment of area
$I_{y\omega},\ I_{z\omega}$	sectorial product of area
$\boldsymbol{J}_e$	element jacobian
J	torsional constant
$\boldsymbol{K}$	stiffness matrix
$\boldsymbol{K}^{(e)}$	element system matrix (iFEM)
$\boldsymbol{k}$	vector of curvatures (iQS4)
$L^{(e)}$	element length
$\boldsymbol{L}$	shape function matrix iQS4
$\boldsymbol{M}$	shape function matrix iQS4
$M_y,\ M_z$	internal moments from inverse beam elements
$\overline{M}_y,\ \overline{M}_z$	internal moments from actual loads
M_x	torsional moment
$M_x^{(+)}$	torsional moment at end node of beam element
$\overline{m}_x$	distributed torsional moment
M_{eq}	equivalent internal moment
$\boldsymbol{M}$	mass matrix
$\boldsymbol{N}$	shape function matrix / null space
N	normal force

P .... concentrated force

$\boldsymbol{p}$ .... vector containing pressure values

$\boldsymbol{P}$ .... input vector cross-sectional properties

$q_y,\ q_z$ .... distributed load

$Q_y,\ Q_z$ .... first moments of area

r .... taper ratio

$\boldsymbol{r}$ .... modal coordinates

$\boldsymbol{s}$ .... generic degrees of freedom for SEA element

$\boldsymbol{S}_\varepsilon$ .... sensitivity matrix of strain measurements

$\boldsymbol{S}$ .... sensitivity matrix of displacements

t .... thickness

$\boldsymbol{T}$ .... convolution matrix

u .... translational displacement along x

$\boldsymbol{u}^{(e)}$ .... element degrees of freedom vector

$\boldsymbol{u}_i$ .... left SVD vector

$\boldsymbol{v}_i$ .... right singular vector

v .... translational displacement along y

$V_y,\ V_z$ .... internal shear forces

$V_y^{(+)},\ V_z^{(+)}$ .... internal shear forces at end node of beam element

$x_1,\ x_2$ .... axial positions of axial strain measurements

x_3 .... axial positions of shear-sensitive strain gauge

$y_C,\ z_C$ .... centroid coordinates

$y_S,\ z_S$ .... shear center coordinates

w .... translational displacement along z / weighting function

$\boldsymbol{W}$ .... weighting function matrix

α .... regularization coefficient SEA / Tikhonov regularization coefficient

β .... regularization coefficient SEA for curvature

γ_{xy} .... shear strain

Γ .... warping constant

δ .... angle due to taper / angle central reference system

$\boldsymbol{\varepsilon}^\varepsilon$ .... vector of strain measurements

$\varepsilon_x,\ \varepsilon_y$ .... direct strain in (x,y) reference system

ε_1 .... axial strain in local $(1,2)$ reference system

η .... logarithm of residual (SEA/Tikhonov regularization) / sensitivity coefficient

θ_x .... rotation around x

θ_y .... rotation around y

θ_z .... rotation around z

$\kappa_x,\ \kappa_y$ .... curvatures

$\boldsymbol{\Lambda}$ .... diagonal matrix containing squared natural frequencies

μ .... mean of distribution

ν .... Poisson coefficient

ρ .... logarithm of residual (SEA/Tikhonov regularization) / density

$\boldsymbol{\rho}$ .... vector of control points values

σ_x .... direct stress

σ .... standard deviation

σ_i .... singular value

CONTENTS

τ_{bj}	basic shear stress on segment j
τ_{nb}	non-basic shear stress
τ_{12}^{ε}	experimental measured shear stress
$\tau_{12}^{y}, \tau_{12}^{z}, \tau_{12}^{t}$	shear stress due to unit internal forces V_y, V_z, M_x
$\mathbf{\Phi}$	mode shape matrix
$\phi_1, \phi_2, \phi_3, \phi_4$	dummy variables
$\mathbf{\Psi}$	strain mode shape matrix
$\Phi^{(e)}$	error functional (iFEM)
$\Phi_{\varepsilon}, \Phi_{\alpha}, \Phi_{\beta}$	residual terms SEA
Ω	area enclosed by cross-section
ω	warping function / circular frequency

List of Abbreviations

DFT   Discrete Fourier Transform

FEM   Finite Element Method

GFRP   Glass Fiber Reinforced Polymer

iFEM   inverse Finite Element Method

iQS4   inverse 4-node shell element

IDFT   Inverse Discrete Fourier Transform

MM   Modal Method

MC   Monte Carlo

MIMO   Multiple Input Multiple Output

PCE   Polynomial Chaos Expansion

SEA   Smoothing Element Analysis

SDOF   Single Degree of Freedom system

SVD   Singular Value Decomposition

Preface

This work has been carried out at the DLR Institute of Aeroelasiticty in Göttingen within the Structural Dynamics and System Identification Department, in fulfillment of the MSc thesis project at TU Delft.

The end result which is shown in the next pages is the product of several factors. Without the DLR department and facilities, the project would have not even started. So a big thank you goes to the Institute, for having accepted me as a student and for having invested time and resources into the project.

On a personal level, the gratitude goes especially to the supervisors of the thesis, Saullo Castro and Janto Gundlach, who are the ones most touched by the time investment mentioned before and from whom I have learnt more than I imagined. Their advice, questions and continuous support given throughout the work have shaped the project (and, in general, the overall experience) making it with no doubt much better, richer and enjoyable.

I want also to express gratitude to my family and everyone not directly involved into the thesis but who has given support and help during the studies.

It is hoped that the product of all these factors have resulted in a work useful to other researchers and engineers.

Paolo Minigher
Göttingen, July 2022

Abstract

The reconstruction of the elastic deformed shape of a structure from strain measurements is a field which has received considerable attention over the years. This work aims to suggest some improvements for wing-like structures trying to limit as much as possible the amount of strain measurements needed. In particular, a simple beam model is proposed based on the framework of the inverse Finite Element Method (iFEM). Then, the performances of iFEM using shell elements will be enhanced pre-extrapolating the strain field and the results will be compared with another shape sensing method, the so-called Modal Method (MM). In the final part of the work the external loads under the form of a pressure field are recovered using either the reconstructed displacements and directly the strain measurements. Static and dynamic analyses will be carried out, so recovering the load both in space and in time.

The results obtained show that the beam model developed allows to obtain a satisfactory bending reconstruction of the structure, while the twist is not always accurate. Computing the full displacement field with iFEM brings to a relatively good representation, even though not as satisfactory as the one delivered by the Modal Method. Finally, recovering the static external loads directly from the strain measurements seems to perform better compared to the reconstruction from the full displacement field, but it is significantly affected by noise and uncertainties. The dynamic load reconstruction is in general much more challenging and the results obtained often show a significant error compared to the reference solution.

Chapter 1

Introduction

The vehicle health management has become an important factor in Aerospace, with the aim to provide safer and more reliable structures. It is generally desired to accomplish the following objectives [8]:

- provide valuable information to adaptive control systems.

- detect and localize impact events and damage initialization.

- maximize performance and service life.

- provide real-time vehicle health information.

In this context *shape sensing* plays an important role. A real-time reconstruction of the deformed structural shape using in-situ strain measurements would provide valuable information in order to assess the full strain and stress fields, failure states and in general to improve the structural health monitoring of the structure. For this reason, this topic has attracted interest from many researchers over the years.

1.1   Overview of previous works for shape sensing analysis

Several methods have emerged with the aim to reconstruct the structural deformations from strain measurements. In Figure 1.1 the historical development of some approaches is briefly outlined. The aim is not to give a detailed historical overview with this picture, but mainly to give an idea of when the methods have started to appear and if papers have been continuously published over the years. Just some works are highlighted on the time line (which are deemed most important), with no intention to be complete.
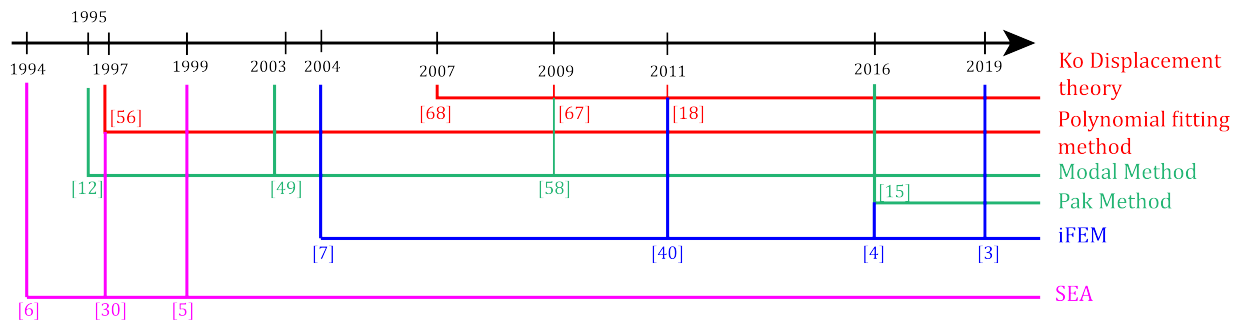

Figure 1.1: *Time-line of some shape sensing methods.*

1

In the following, some methods are briefly outlined in order to give a general overview of the shape sensing topic. In the scope of the thesis, the focus will be especially on the Modal Method (MM) and on the inverse Finite Element Method (iFEM).

Polynomial Fitting Method

The shape sensing method developed in [56] is based on a least-squares minimization algorithm applied to a continuous function describing the strain field.
In order to describe the method, consider the bending behaviour of a cantilever beam subjected to a tip force P. From the Euler-Bernoulli beam theory it is possible to write:

$$\varepsilon_x = -z\frac{\partial^2 w}{\partial x^2} \tag{1.1}$$

where w is the vertical displacement and z the vertical axis. The strain gauge positions are identified by the coordinates x_i along the axial x axis.
The axial strain ε_x can be expressed for example as a quadratic polynomial function:

$$\varepsilon_x(x) = a_1 + a_2 x + a_3 x^2 \tag{1.2}$$

Considering that m strain measurements have been done at the coordinates x_i $(i = 1 \cdots m)$, then the following error functional is defined:

$$\Phi\big(\varepsilon_x(x)\big) = \sum_{i=0}^{m} \big[\varepsilon_x(x_i) - \varepsilon_x^\varepsilon(x_i)\big]^2 \tag{1.3}$$

where $\varepsilon_x^\varepsilon(x_i)$ are the experimental strain measurements at x_i. It is important to note that depending on the degree of the polynomial chosen, a minimum m number of strain measurements is required. Then, following what can be seen for example in [47], the error Φ has a minimum if (since Φ is a sum of convex functions, hence convex itself):

$$\frac{\partial \Phi}{\partial a_j} = 0 \quad ; \quad j = \{1, 2, 3\} \tag{1.4}$$

This condition brings three linear equations from which the unknowns a_j can be determined. In this particular case the equations turn out to be the following ones:

$$\frac{\partial \Phi}{\partial a_1} = \frac{\partial}{\partial a_1} \sum_{i=1}^{m} \big(a_1 + a_2 x_i + a_3 x_i^2 - \varepsilon_x^\varepsilon(x_i)\big)^2$$

$$= \sum_{i=1}^{m} 2\big(a_1 + a_2 x_i + a_3 x_i^2 - \varepsilon_x^\varepsilon(x_i)\big) = 0 \tag{1.5}$$

$$\Rightarrow \quad (m+1)a_1 + \left(\sum_{i=1}^{m} x_i\right)a_2 + \left(\sum_{i=1}^{m} x_i^2\right)a_3 = \sum_{i=1}^{m} \varepsilon_x^\varepsilon(x_i)$$

$$\frac{\partial \Phi}{\partial a_2} = 0 \quad \Rightarrow \quad \left(\sum_{i=1}^{m} x_i\right)a_1 + \left(\sum_{i=1}^{m} x_i^2\right)a_2 + \left(\sum_{i=1}^{m} x_i^3\right)a_3 = \sum_{i=1}^{m} x_i \varepsilon_x^\varepsilon(x_i) \tag{1.6}$$

$$\frac{\partial \Phi}{\partial a_3} = 0 \quad \Rightarrow \quad \left(\sum_{i=1}^{m} x_i^2\right)a_1 + \left(\sum_{i=1}^{m} x_i^3\right)a_2 + \left(\sum_{i=1}^{m} x_i^4\right)a_3 = \sum_{i=1}^{m} x_i^2 \varepsilon_x^\varepsilon(x_i) \tag{1.7}$$

The equations can be conveniently written in matrix form defining the following quantities:

$$\boldsymbol{V} = \begin{bmatrix} 1 & x_0 & x_0^2 \\ \vdots & \vdots & \vdots \\ 1 & x_N & x_N^2 \end{bmatrix} \quad ; \quad \boldsymbol{a} = \begin{bmatrix} a_1 \\ a_2 \\ a_3 \end{bmatrix} \quad ; \quad \boldsymbol{f} = \begin{bmatrix} \varepsilon_x^\varepsilon(x_1) \\ \varepsilon_x^\varepsilon(x_2) \\ \varepsilon_x^\varepsilon(x_3) \end{bmatrix} \tag{1.8}$$

And so the equations, which are generally named *normal equations* in the least-squares minimization, can be written as:

$$\boldsymbol{V}^\top \boldsymbol{V} \boldsymbol{a} = \boldsymbol{V}^\top \boldsymbol{f} \tag{1.9}$$

From which the unknown coefficients are determined:

$$\boldsymbol{a} = (\boldsymbol{V}^\top \boldsymbol{V})^{-1} \boldsymbol{V}^\top \boldsymbol{f} \tag{1.10}$$

Once the strain field is known, recalling the Euler-Bernoulli relation 1.1 it is possible to write:

$$\frac{\partial^2 w}{\partial x^2} = -\frac{1}{z} \left(a_1 + a_2 x + a_3 x^2 \right) \tag{1.11}$$

Integrating twice the displacement $w(x)$ can be found:

$$\frac{\partial w}{\partial x} = -\frac{1}{z} \left(a_1 x + a_2 \frac{x^2}{2} + a_3 \frac{x^3}{3} \right) + C_1 \tag{1.12}$$

$$w(x) = -\frac{1}{z} \left(\frac{a_1}{2} x^2 + \frac{a_2}{6} x^3 + \frac{a_3}{12} x^4 \right) + C_1 x + C_2 \tag{1.13}$$

where C_1 and C_2 are integration constants. They can be found applying the boundary conditions and so the full displacement field is now know.

Ko Displacement Theory

The theory developed by W. L. Ko [68] is based on the Euler-Bernoulli beam theory and aims at computing slopes and deflections of wings in operating conditions. From the classical beam theory, it is well-known that:

$$\frac{\mathrm{d}^2 w}{\mathrm{d}x^2} = \frac{M(x)}{EI} \tag{1.14}$$

where w is the vertical displacement, x the axial coordinate, M the moment applied and EI the flexural stiffness. Considering a constant cross-section, then the so-called Navier equation holds:

$$\sigma_x(x) = \frac{M(x)c}{I} \tag{1.15}$$

with $\sigma_x(x)$ the axial stress measured at the top / bottom of the beam section and c the vertical distance of the measurement point from the beam neutral axis. So, substituting the constitutive relation $\sigma_x(x) = E\varepsilon_x(x)$ Eq.(1.14) can be rewritten as:

$$\frac{\mathrm{d}^2 w}{\mathrm{d}x^2} = \frac{\varepsilon_x(x)}{c} \tag{1.16}$$

This simple relation is the equation at the basis of the whole theory which basically integrates it twice to recover the deflection $w(x)$.

Consider now more specifically a clamped beam at $x = 0$ subjected to bending. The strains are measured at *equally spaced* stations at the top or bottom surface of the beam cross section. This assumption is quite important and has a fundamental role in the theory. For this reason, this method is especially suitable for strain measurements taken with optical fibres since they allow to have closely spaced measurements on the same sensing line. The situation is illustrated in Figure 1.2. As it is possible to see, each station located at x_i is positioned at a distance equal to Δl from the previous one. A total of m strain measurements is taken.
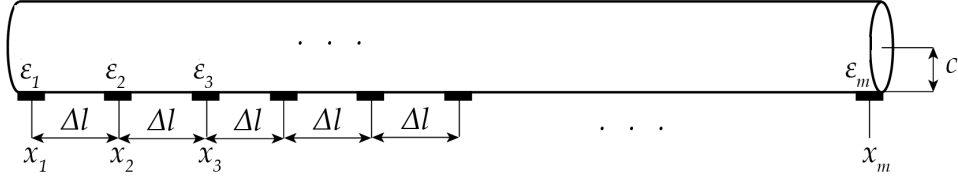
Figure 1.2: *Clamped beam model taken as reference for Ko Displacement theory* [68]

Between two measurement stations the axial strain $\varepsilon(x)$ is assumed to be linear. So:

$$\varepsilon(x) = \varepsilon_{i-1} - (\varepsilon_{i-1} - \varepsilon_i)\frac{x - x_{i-1}}{\Delta l} \quad ; \quad x_{i-1} < x < x_i \tag{1.17}$$

Therefore, the slope $\tan\theta$ can be estimated integrating the curvature. Since in the interval $x_{i-1} < x < x_i$ the beam segment is already inclined by the deflection at x_{i-1}, the slope in the interval is given by:
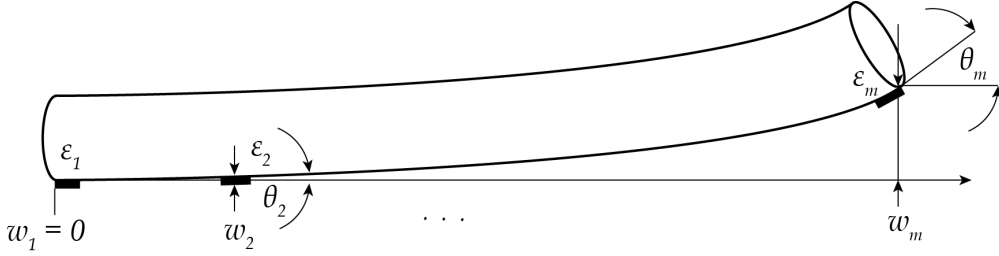
Figure 1.3: *Deflection of clamped beam for visualization of Ko Displacement theory procedure* [68]

$$\tan\theta(x) = \int_{x_{i-1}}^{x} \frac{\mathrm{d}^2 w}{\mathrm{d}x^2}\mathrm{d}x + \tan\theta_{i-1} = \int_{x_{i-1}}^{x} \frac{\varepsilon(x)}{c}\mathrm{d}x + \tan\theta_{i-1} \quad ; \quad x_{i-1} < x < x_i \tag{1.18}$$

See Figure 1.3 for a visualization. Now, substituting Eq.(1.17) and integrating it is possible to obtain:

$$
\begin{aligned}
\tan\theta(x) &= \frac{1}{c}\int_{x_{i-1}}^{x}\left[\varepsilon_{i-1} - (\varepsilon_{i-1} - \varepsilon_i)\frac{x - x_{i-1}}{\Delta l}\right]dx + \tan\theta_{i-1}\\
&= \frac{1}{c}\left[\varepsilon_{i-1}(x - x_{i-1}) - (\varepsilon_{i-1} - \varepsilon_i)\frac{(x - x_{i-1})^2}{2\Delta l}\right] + \tan\theta_{i-1}\\
\tan\theta_i &= \frac{1}{c}\left[\varepsilon_{i-1}(\Delta l) - (\varepsilon_{i-1} - \varepsilon_i)\frac{(\Delta l)^2}{2\Delta l}\right] + \tan\theta_{i-1} \quad \text{(at the strain station } x_i)\\
&= \frac{\Delta l}{2c}(\varepsilon_{i-1} + \varepsilon) + \tan\theta_{i-1}
\end{aligned}
\tag{1.19}
$$

where at the starting point $\tan\theta_1 = 0$ since the beam is clamped. At this point, also the deflection w_i at the measurement points can be obtained. Similarly as before:

$$
\begin{aligned}
w(x) &= \int_{x_{i-1}}^{x} \tan\theta(x)\,\mathrm{d}x + w_{i-1}\\
&= \int_{x_{i-1}}^{x}\int_{x_{i-1}}^{x} \frac{\varepsilon(x)}{c}\,\mathrm{d}x\mathrm{d}x + \int_{x_{i-1}}^{x} \tan\theta_{i-1}\,\mathrm{d}x + w_{i-1}
\end{aligned}
\tag{1.20}
$$

Carrying out the integrals and evaluating the deflection at $x = x_i$ the final expression results in:

$$w_i = \frac{(\Delta l)^2}{6c}\left(2\varepsilon_{i-1} + \varepsilon_i\right) + \Delta l \tan\theta_{i-1} + w_{i-1} \tag{1.21}$$

where again $w_1 = 0$. In this way the full deflection of the beam under bending can be evaluated.

Several studies have been published using this method, using both numerically extracted strains [68], [67] and experimental ones [18], [31]. In general, the deflections are accurately recovered, but the twist angle is much poorer because of its sensitivity to errors in bending.

Modal Method

The so-called Modal Method (MM) ([49], [12]) is based on a the idea of reconstructing the displacement field from a linear combination of mode shapes. Thanks to its relatively ease of use, it has been applied in several studies and in different applications which prove its usefulness. For example, in [58] and [33] the reconstruction of a plate deformation is carried out obtaining satisfactory results. Extensive studies have also been done on beams, both in terms of numerical and experimental analyses (see for example [29]). In [28] rotating beams are analysed (pointing to the monitoring of rotor blades) taking as input the strains from optical fibres.
It will be described in more detail at the beginning of Chapter 3 where it will be effectively put into practice.

The so-called Pak Method [15] can be seen as a particular application of the Modal Method, also taking advantage from the methods based on the direct integration of the strains. Therefore, it is generally referred to as an hybrid method.

Inverse Finite Element Method

The inverse Finite Element Method (iFEM), based on the initial work done in [7], faces the shape sensing problem from a different perspective compared to the techniques described in the previous chapters, even though it shares with them some features. It does not require any information about the material since only strain-displacement relations are used in the formulation. Furthermore, the same framework of FEM is used, so it is applicable to arbitrary topologies, making it a suitable choice of a wide range of applications.

In the following the method will be applied to beams (Chapter 2) and shells (Chapter 3). For each case the formulation of the method will be described in detail. Here, just a brief overview is given. Considering the formulation which is applicable to plates, a suitable error functional Φ is defined based on the difference with the experimental strains. The following form will be used:

$$\Phi(\boldsymbol{u}) = \underbrace{\|\boldsymbol{e}(\boldsymbol{u}) - \boldsymbol{e}^\varepsilon\|^2}_{\text{membrane}} + \underbrace{\|\boldsymbol{k}(\boldsymbol{u}) - \boldsymbol{k}^\varepsilon\|^2}_{\text{curvature}} + \underbrace{\|\boldsymbol{g}(\boldsymbol{u}) - \boldsymbol{g}^\varepsilon\|^2}_{\text{transverse shear}} \tag{1.22}$$

where $\boldsymbol{u}$ is the interpolated displacement field, $\boldsymbol{e}$ the membrane part of the strain, $\boldsymbol{k}$ the curvature and $\boldsymbol{g}$ the transverse shear strain. The superscript $\bullet^\varepsilon$ stands for an experimental strain. After having defined a suitable interpolation for the displacement field, the substitution in Eq.(1.22) and the minimization with respect to $\boldsymbol{u}$ will result in a system of linear equations with the form:

$$\boldsymbol{K}\boldsymbol{u} = \boldsymbol{f} \tag{1.23}$$

Applying the boundary conditions, the solution of the system will give the displacement field of the structure. An important point to highlight already now is that $\boldsymbol{K}$ depends just on the

inverse element formulation, while $\boldsymbol{f}$ on both the experimental strain measurements and on the interpolation chosen. So, $\boldsymbol{K}$ has to be computed only once and its inverse can be stored so that the displacement field can be updated almost continuously as the input strain measurements change over time.

Finally, in Figure 1.1 the so-called Smoothing Element Analysis (SEA) is also mentioned. It is not a proper shape sensing method, but it will be useful in this context since it will provide the full strain field as an input for iFEM. It will be described in detail in Chapter 3.

1.1.1   Methods of interest in the scope of the thesis

In the scope of the thesis it has been decided to focus solely on the Modal Method and on the inverse Finite Element Method.

Regarding the Modal Method, this is motivated by the following points:

- It can be easily applied to any structure provided the FE model is available.

- Since it exploits the structural mode shapes, it allows to retrieve the global deformation even if a very sparse set of measurements is available.

- Several studies assessed the method for different applications.

The inverse Finite Element Method, being based only on strain-displacement relations, offers the significant advantage of not requiring any constitutive property of the structure. So, a large part of the thesis will be devoted to study the performances of iFEM and to compare them w.r.t. the ones from MM.

1.2   Thesis outline

It this section it is briefly mentioned which are the motivations behind the research, which are the objectives that will be accomplished and how the work has been structured.

1.2.1   Motivations and objectives

As pointed out in the previous section, the reconstruction of the elastic deformed shape has received considerable attention. However, in many studies some common disadvantages have been identified which could harm the applicability of the methods for real-life applications. In particular:

- Several methods are applied only on relatively simple structures, while hardly used for more complex situations (as the so-called Polynomial Fitting Method mentioned before).

- Many studies, especially based on numerical strains extracted from FEM models, assume the presence of a considerable amount of strain data, hardly possible for real structures.

- Often, the strain gauge positions are optimized based on the external load applied, which however is in general unknown (otherwise there would be no need to retrieve the deformations from the strain data).

These possible drawbacks have motivated the research which will be explained in the next chapters with the primary aim to deliver useful models and studies which could be used for real applications. The main objective which motivates the research consists in limiting the amount of measurements needed to monitor the structure, so trying to recover the deformations (and

later the external loads) in case of sparse strain measurements.

In particular, the following research questions will be addressed:

(1) **Is it possible to develop a simple beam model which requires the minimum amount of input strain data, but which allows to obtain the deformations of relatively complex beam-like structures?**

(2) **How does iFEM perform in case of sparse strain measurements in comparison with the Modal Method? And which approach is advisable for the shape sensing monitoring of wing-like structures under real measurement conditions?**

(3) **Can the external loads be reconstructed both for static and dynamic applications from the deformed shape computed with the selected shape sensing scheme? And how do the results compare with the load reconstructed directly from the measured strains?**

To answer these questions the thesis has been structured as briefly summarized in Figure 1.4. The organization is explained in more detail in the next section.
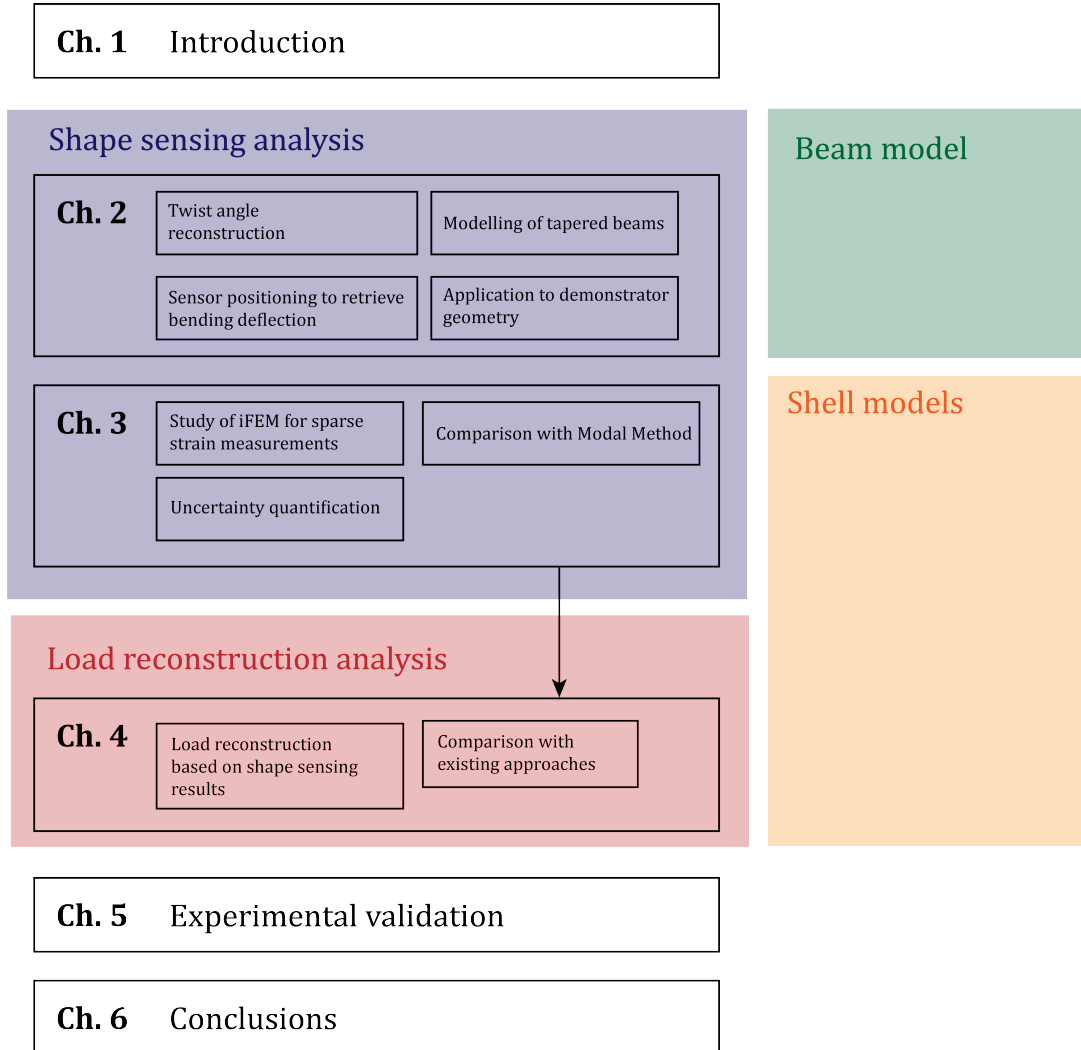

Figure 1.4: *Thesis structure.*

1.2.2 Thesis structure

The first part of the thesis, Chapter 2, is devoted to answer research question (1). Beam models have been commonly used for shape sensing purposes for wing applications (recall for example the so-called Ko Displacement Theory). Here however the aim is to develop a simple beam model based on the framework of the inverse Finite Element Method. Several works have been published in this context, applying the method both to the Euler-Bernoulli theory [48] and to the Timoshenko one [40]. Restricting to the Euler-Bernoulli case, so for relatively slender structures, some improvements will be suggested trying to limit as much as possible the number of measurements needed and to model relatively complex geometries.

Chapter 3 lies in the same field of the previous chapter, that is the shape reconstruction for wing-like structures, but employs methods which estimate the full displacement field. The focus will be especially on iFEM, trying to improve its performances in case of limited and sparse strain measurements. The results will be then compared with those from the Modal Method, both using exact strain data and noisy ones in order to understand how much uncertainty affects the final results. At the end of the chapter the results presented will help in answering research question (2).

Chapter 4 is focused on research question (3). Starting from the reconstructed deformed shape, the external loads under the form of a pressure field will be computed. The results will be then compared with a more common method which consists in computing the loads directly from the strain measurements. Both static and dynamic analyses will be carried out.

The final part of the thesis, Chapter 5, presents the experimental part of the thesis with the aim to assess the results obtained numerically with real-life data. Both the shape sensing part and the load reconstruction one will be considered.

Finally, in Chapter 6 some conclusions are drawn and recommendations for future work given.

In general, each chapter presents an introduction with a theoretical background explaining the methods and ideas used from literature. Then, some improvements are suggested together with some study cases. In particular:

Chapter 1: Introduction.

Chapter 2: Shape sensing with beam model.

- Theoretical background: iFEM with beam elements.
- Shape sensing for prismatic beams.
- Shape sensing for tapered beams.
- Application to ISTAR demonstrator wing (see Section 1.2.3).

Chapter 3: Shape sensing with shell models.

- Theoretical background: MM, iFEM with shell elements and SEA.
- Application of SEA with quadrilateral elements.
- Coupling SEA with iFEM.
- Comparison between iFEM and MM.
- Uncertainty quantification for shape sensing analysis.

Chapter 4: Load reconstruction.

- − Theoretical background: methods used in literature for load reconstruction in static applications.

- − Improvements of load reconstruction for static applications.

- − Uncertainty quantification for load reconstruction analysis.

- − Load reconstruction for dynamic applications.

Chapter 5: Experimental activity.

Chapter 6: Conclusions.

1.2.3 Study cases and assessment
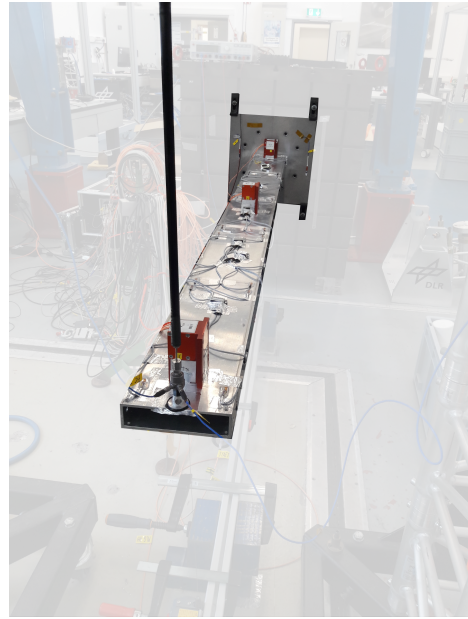

Figure 1.5: *ISTAR demonstrator.*

Figure 1.6: *Aluminum clamped beam.*

The focus of the thesis is on wing-like applications. The results and the methods outlined will be assessed with different study cases. In particular Chapter 2, Chapter 3 and Chapter 4 will be based on strain data coming just from numerical simulations while Chapter 5 on experimental ones. However, the study cases will be different.

For the numerical analyses, the main study case will be represented by the FE model of the wing of the ISTAR[1] demonstrator, illustrated in Figure 1.5. As it will described in more detail in Section 2.5, the wing is a rather simple load-carrying GFRP composite skin filled with foam. Even though it does not have the features of a real wing, it still offers some geometrical complexities which are worth to be analysed. On the other hand, Chapter 5, being based on experimental data, exploits the strain values coming from an aluminum beam clamped at its root (Figure 1.6).

An exception is Chapter 2 where a beam model is shown and the results are gradually assessed with strain data coming from relatively simple beam-like structures. However, also here the final goal is the application of the model to the geometry of the ISTAR demonstrator wing.

---

[1]Dassault Falcon 2000LX DLR research aircraft.

Chapter 2

Shape sensing with a beam model

In this chapter a simple beam model using the inverse Finite Element Method (iFEM) and the Euler-Bernoulli beam theory is described.

In particular, in Section 2.1 the basis of the method are briefly explained based on the work done in [48]. Then, using the so-called 0th order inverse beam element, some improvements are suggested, in particular:

- In the original formulation, the inverse Euler-Bernoulli beam element does not give any information about the torsional behavior of the beam. At the cost of an additional strain measurement it is possible to compute the twist rate on the domain of each inverse element and finally obtaining the twist angle starting from the beam root where no initial twist is assumed. This is described in Section 2.2.

- The simplicity of the inverse element used does not allow in principle to exactly match the deformed shape for load cases more complex than concentrated nodal forces. The common approach, derived from FEM, would be either to increase the element order or to increase the elements number. In the shape sensing context the first method implies higher orders for the shape functions which in turn implies a larger number of strain measurements. The second method brings to the same conclusion. It is considered undesired to increase the amount of measurements needed. Therefore, it has been decided to keep the simplicity of the so-called 0th order Euler-Bernoulli inverse element and to suggest some improvements which allow to recover the deformed shape of the beam under more complex loads. In this way, even though the deformed shape is not exactly recovered everywhere, it is still possible to obtain a good estimate of the deflections with no need to increase the amount of measurements. This framework is described in detail in Section 2.3.

The decision to keep using the simple 0th order Euler-Bernoulli inverse element comes also from the fact that it is desired to develop a beam model for tapered beams. In general, coming up with suitable shape functions in this context can be rather complex. Here instead the same philosophy of before is followed: the shape functions are not modified and a similar approach used for the prismatic beams will be applied. More details are given in Section 2.4, where both the bending and the twist reconstruction are discussed.

Finally, the ideas put forth in the previous sections have been applied to the shape reconstruction of the ISTAR demonstrator wing model. This is discussed in Section 2.5.

2.1 Theoretical background on Inverse Finite Element Method applied to Euler-Bernoulli beam theory

Several studies have been published on the applicability of iFEM for beams. For example, in [41] the method has been developed from the Timoshenko beam theory and in [25] for beams with variable cross-sections. However, in this study the focus will be just on the simple Euler-Bernoulli beam theory. How to couple it with iFEM is explained in [48] and this work will be briefly reviewed in the following paragraphs.

In the context of the Euler-Bernoulli beam theory, referring to Figure 2.1 the displacement field (u_x, u_y, u_z) can be written as:
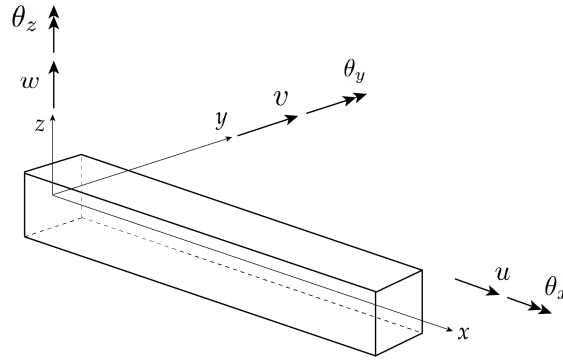

Figure 2.1: *Reference system and kinematic variables used for Euler-Bernoulli beam.*

$$\begin{cases} u_x = u(x) + z\theta_y(x) - y\theta_z(x) \\ u_y = v(x) \\ u_z = w(x) \end{cases} \tag{2.1}$$

So the kinematic variables involved are:

$$\boldsymbol{u} = \begin{bmatrix} u & v & w & \theta_x & \theta_y \end{bmatrix}^\top \tag{2.2}$$

The corresponding linear strain field is:

$$\begin{cases} \varepsilon_x = \dfrac{\mathrm{d}u}{\mathrm{d}x} + z\dfrac{\mathrm{d}\theta_y}{\mathrm{d}x} - y\dfrac{\mathrm{d}\theta_z}{\mathrm{d}x} \\ \gamma_{xz} = \dfrac{\mathrm{d}w}{\mathrm{d}x} + \theta_y = 0 \\ \gamma_{xy} = \dfrac{\mathrm{d}v}{\mathrm{d}x} - \theta_z = 0 \end{cases} \tag{2.3}$$

Where the last two equations come from the fact that the transverse shear strains are assumed to be null if the beam is slender enough. Therefore the axial strain becomes:

$$\begin{aligned} \varepsilon_x &= \frac{\mathrm{d}u}{\mathrm{d}x} - y\frac{\mathrm{d}^2v}{\mathrm{d}x^2} - z\frac{\mathrm{d}^2w}{\mathrm{d}x^2} \\ &= \varepsilon_{x0} + y\kappa_z + z\kappa_y \end{aligned} \tag{2.4}$$

where the following variables, called *section strains*, are defined:

$$\varepsilon_{x0} = \frac{\mathrm{d}u}{\mathrm{d}x} \quad ; \quad \kappa_y = \frac{\mathrm{d}\theta_y}{\mathrm{d}x} = -\frac{\mathrm{d}^2w}{\mathrm{d}x^2} \quad ; \quad \kappa_z = -\frac{\mathrm{d}\theta_z}{\mathrm{d}x} = -\frac{\mathrm{d}^2v}{\mathrm{d}x^2} \tag{2.5}$$

11

which can be grouped together in the following vector:

$$\boldsymbol{e} = \begin{bmatrix} \varepsilon_{x0} \\ \kappa_y \\ \kappa_z \end{bmatrix} = \begin{bmatrix} e_1 \\ e_2 \\ e_3 \end{bmatrix} \tag{2.6}$$

Finally, the last important fact to recall from the Euler-Bernoulli beam theory are the constitutive equations and the equilibrium ones. They are given below:

$$\begin{cases} N = EAe_1 \\ M_y = EI_ye_2 \\ M_z = EI_ze_3 \end{cases} \qquad \begin{cases} \dfrac{\mathrm{d}N}{\mathrm{d}x} = -q_x(x) \\ \dfrac{\mathrm{d}V_y}{\mathrm{d}x} = -q_y(x) \\ \dfrac{\mathrm{d}M_y}{\mathrm{d}x} = V_z \\ \dfrac{\mathrm{d}V_z}{\mathrm{d}x} = -q_z(z) \\ \dfrac{\mathrm{d}M_z}{\mathrm{d}x} = V_y \end{cases} \tag{2.7}$$

where N denotes the normal force per unit area, M_y and M_z the moment and V_y, V_z the shear force. At this point, the iFEM methodology can be applied. The first step consists in minimizing the error between measured and analytical strains. Considering a generic element (e), this is expressed with the following functional:

$$\Phi^{(e)} = \|\boldsymbol{e} - \boldsymbol{e}^\varepsilon\|^2 \tag{2.8}$$

where $\boldsymbol{e}^\varepsilon$ are the experimental section strains. The functional $\Phi^{(e)}$ will be characterized by three contributions (for each section strain) per element. So, following what has been done in [48], it can be written that:

$$\Phi^{(e)} = \boldsymbol{w} \cdot \begin{bmatrix} \Phi_1^{(e)} \\ \Phi_2^{(e)} \\ \Phi_3^{(e)} \end{bmatrix} = \boldsymbol{w} \cdot \begin{bmatrix} \dfrac{L^{(e)}}{n} \displaystyle\sum_{j=1}^{n} (e_1(x_j) - e_1^\varepsilon(x_j))^2 \\ \dfrac{L^{(e)}}{n} \displaystyle\sum_{j=1}^{n} (e_2(x_j) - e_2^\varepsilon(x_j))^2 \\ \dfrac{L^{(e)}}{n} \displaystyle\sum_{j=1}^{n} (e_3(x_j) - e_3^\varepsilon(x_j))^2 \end{bmatrix} \tag{2.9}$$

where "$\cdot$" stands for the internal product, n is the number of axial locations where the section strains are evaluated and the coordinate x is taken here in the element reference system, that is $0 \leq x \leq L^{(e)}$ (with $L^{(e)}$ the element length). Finally, the vector $\boldsymbol{w}$ must be introduced to assure dimensional consistency between the section strain measures. It can be expressed as [48]:

$$\boldsymbol{w} = \begin{bmatrix} 1 & \dfrac{I_x^{(e)}}{A^{(e)}} & \dfrac{I_y^{(e)}}{A^{(e)}} \end{bmatrix}^\top \tag{2.10}$$

with $I_x^{(e)}$, $I_y^{(e)}$ the element second moment of area and $A^{(e)}$ the cross-section area.

At this point, the procedure is similar to the direct FEM formulation. The kinematic variables $\boldsymbol{u}$ are interpolated with shape functions grouped in the matrix $\boldsymbol{N}$ which links $\boldsymbol{u}$ to the degrees of freedom of the element (e) given by $\boldsymbol{u}^{(e)}$. So it is possible to write:

$$\boldsymbol{u} = \boldsymbol{N}\boldsymbol{u}^{(e)} \tag{2.11}$$

Now, the element section strains can be computed from Eq.(2.5) and this results in the following expression:

$$e = Bu^{(e)} = \begin{bmatrix} B_1 \\ B_2 \\ B_3 \end{bmatrix} u^{(e)} \tag{2.12}$$

So, the functional $\Phi^{(e)}$ of the element becomes:

$$
\begin{aligned}
\Phi^{(e)} &= \frac{L^{(e)}}{n} \sum_{k=1}^{3} \sum_{j=1}^{n} w_k \big[e_k(x_j) - e_k^{\varepsilon}(x_j) \big]^2 \\
&= \frac{L^{(e)}}{n} \sum_{k=1}^{3} \sum_{j=1}^{n} w_k \big[u^{(e)\top} (B_k^{\top}(x_j) B_k(x_j)) u^{(e)} + \big(e_k^{\varepsilon}(x_j) \big)^2 - 2 e_k^{\varepsilon}(x_j) B_k(x_j) u^{(e)} \big]
\end{aligned}
\tag{2.13}
$$

where $k = \{1, 2, 3\}$ since there are three section strains. The previous expression can be rewritten as:

$$\frac{\Phi^{(e)}}{2} = \frac{1}{2} u^{(e)} K^{(e)} u^{(e)} - u^{(e)T} f^{(e)} + \frac{L^{(e)}}{n} \sum_{k=1}^{3} \sum_{j=1}^{n} w_k (e_k^{\varepsilon}(x_j))^2 \tag{2.14}$$

where the following quantities are defined:

$$K^{(e)} = \frac{L^{(e)}}{n} \sum_{k=1}^{3} w_k \sum_{j=1}^{n} \big[B_k^{\top}(x_j) B_k(x_j) \big] \tag{2.15}$$

$$f^{(e)} = \frac{L^{(e)}}{n} \sum_{k=1}^{3} w_k \sum_{j=1}^{n} B_k^{\top}(x_j) e_k^{\varepsilon}(x_j) \tag{2.16}$$

Minimizing the functional with respect to $u^{(e)}$ and equating to zero results in:

$$\frac{1}{2} \frac{\partial \Phi^{(e)}}{\partial u^{(e)}} = 0 \quad \Rightarrow \quad K^{(e)} u^{(e)} = f^{(e)} \tag{2.17}$$

All what has been done so far holds for a single element. Taking into account more elements, the usual assembly procedure can be carried out, eventually accounting for appropriate coordinate transformation, and finally obtaining a system as:

$$Ku = f \tag{2.18}$$

It is important to note that K is independent of the strain measurements, contrarily to f. Therefore, it is necessary to invert K only once to compute the degrees of freedom of the system, rendering the whole procedure extremely fast if the strain measurements change over time.

At this point, in order to explicitly build the inverse elements, the shape functions should be defined. From this choice the element formulation is determined and this will be done in the following sections.

0th Order inverse Euler-Bernoulli beam element

The first element which is developed is a two node inverse element which looks like the one depicted in Figure 2.2.
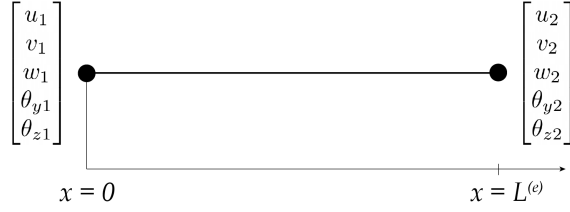
Figure 2.2: 0th Order inverse Euler-Bernoulli beam element

The formulation is guided by the Euler-Bernoulli beam equilibrium equations in case of just nodal forces (that is no distributed forces). It is possible to write[1]:

$$EA\frac{\mathrm{d}e_1}{\mathrm{d}x} = 0 \quad \Rightarrow \quad e_1 = \text{constant}$$
$$EI_y\frac{\mathrm{d}e_2}{\mathrm{d}x} = \text{constant} \quad \Rightarrow \quad e_2 = \text{linear} \qquad (2.19)$$
$$EI_z\frac{\mathrm{d}e_3}{\mathrm{d}x} = \text{constant} \quad \Rightarrow \quad e_3 = \text{linear}$$

So, recalling the relation between section strains and kinematic variables:

$$e_1 = \frac{\mathrm{d}u}{\mathrm{d}x} \quad ; \quad e_2 = -\frac{\mathrm{d}^2w}{\mathrm{d}x^2} \quad ; \quad e_3 = -\frac{\mathrm{d}^2v}{\mathrm{d}x^2} \qquad (2.20)$$

Now, u must have a linear interpolation, while v and w a cubic one. Since C^0 continuity must be ensured for the axial displacement, but C^1 for v and w, in [48] Hermite polynomials are used:

$$\begin{cases} u(x) = \sum_{i=1}^{2} H_{0i}^{(0)} u_i \\ v(x) = \sum_{i=1}^{2} H_{0i}^{(1)} v_i + H_{1i}^{(1)} \theta_{zi} \\ w(x) = \sum_{i=1}^{2} H_{0i}^{(1)} w_i - H_{1i}^{(1)} \theta_{yi} \end{cases} \qquad (2.21)$$

where the expressions of the polynomials used are (derivation in Appendix A):

$$H_{01}^{(0)}(x) = 1 - \frac{x}{L^{(e)}}$$
$$H_{02}^{(0)}(x) = \frac{x}{L^{(e)}}$$
$$H_{01}^{(1)}(x) = \frac{1}{(L^{(e)})^3}\left(2x^3 - 3L^{(e)}x^2 + (L^{(e)})^3\right)$$
$$H_{11}^{(1)}(x) = \frac{1}{(L^{(e)})^2}\left(x^3 - 2L^{(e)}x^2 + (L^{(e)})^2 x\right) \qquad (2.22)$$
$$H_{02}^{(1)}(x) = -\frac{1}{(L^{(e)})^3}\left(2x^3 - 3L^{(e)}x^2\right)$$
$$H_{12}^{(1)}(x) = \frac{1}{(L^{(e)})^2}\left(x^3 - L^{(e)}x^2\right)$$

So the section strains can now be explicitly expressed as:

$$e_1 = \frac{\mathrm{d}u}{\mathrm{d}x} = \frac{1}{(L^{(e)})^3}\left(-\frac{1}{L^{(e)}}u_1 - \frac{1}{L^{(e)}}u_2\right) \qquad (2.23)$$

---

[1]because from the equilibrium equations: $\dfrac{\mathrm{d}V_y}{\mathrm{d}x} = 0 \quad ; \quad \dfrac{\mathrm{d}V_z}{\mathrm{d}x} = 0$

$$
\begin{aligned}
e_2 &= -\frac{\mathrm{d}^2 w}{\mathrm{d}x^2} \\
&= -\left[\frac{1}{(L^{(e)})^3}(12x - 6L^{(e)})w_1 - \frac{1}{(L^{(e)})^2}(6x - 4L^{(e)})\theta_{y1}+ \right. \\
&\quad \left. - \frac{1}{(L^{(e)})^3}(12x - 6L^{(e)})w_2 + \frac{1}{(L^{(e)})^2}(6x - 2L^{(e)})\theta_{y2}\right]
\end{aligned}
\tag{2.24}
$$

$$
\begin{aligned}
e_3 &= -\frac{\mathrm{d}^2 v}{\mathrm{d}x^2} \\
&= -\frac{1}{(L^{(e)})^3}(12x - 6L^{(e)})v_1 - \frac{1}{(L^{(e)})^2}(6x - 4L^{(e)})\theta_{z1}+ \\
&\quad + \frac{1}{(L^{(e)})^3}(12x - 6L^{(e)})v_2 - \frac{1}{(L^{(e)})^2}(6x - 2L^{(e)})\theta_{z2}
\end{aligned}
\tag{2.25}
$$

And the strain-displacement matrix $\boldsymbol{B}$ for the 0th order element can be written:

$$
\boldsymbol{e} = \begin{bmatrix} e_1 \\ e_2 \\ e_3 \end{bmatrix} = \begin{bmatrix} \boldsymbol{B}_1 \\ \boldsymbol{B}_2 \\ \boldsymbol{B}_3 \end{bmatrix} \begin{bmatrix} u_1 & v_1 & w_1 & \theta_{y1} & \theta_{z1} & u_2 & v_2 & w_2 & \theta_{y2} & \theta_{z2} \end{bmatrix}^T
\tag{2.26}
$$

where:

$$
\boldsymbol{B}_1 = \begin{bmatrix} -\dfrac{1}{L^{(e)}} & 0 & 0 & 0 & 0 & \dfrac{1}{L^{(e)}} & 0 & 0 & 0 & 0 \end{bmatrix}
\tag{2.27}
$$

$$
\begin{aligned}
\boldsymbol{B}_2 = \left[0 \quad 0 \quad -\frac{1}{(L^{(e)})^3}(12x - 6L^{(e)}) \quad \frac{1}{(L^{(e)})^2}(6x - 4L^{(e)}) \quad 0 \right. \\
\left. 0 \quad 0 \quad \frac{1}{(L^{(e)})^3}(12x - 6L^{(e)}) \quad \frac{1}{(L^{(e)})^2}(6x - 2L^{(e)}) \quad 0 \right]
\end{aligned}
\tag{2.28}
$$

$$
\begin{aligned}
\boldsymbol{B}_3 = \left[0 \quad -\frac{1}{(L^{(e)})^3}(12x - 6L^{(e)}) \quad 0 \quad 0 \quad -\frac{1}{(L^{(e)})^2}(6x - 4L^{(e)}) \quad 0 \right. \\
\left. \frac{1}{(L^{(e)})^3}(12x - 6L^{(e)}) \quad 0 \quad 0 \quad -\frac{1}{(L^{(e)})^2}(6x - 2L^{(e)}) \right]
\end{aligned}
\tag{2.29}
$$

Since $\boldsymbol{B}$ is completely defined, the element matrix $\boldsymbol{K}^{(e)}$ is known. In order to compute $\boldsymbol{f}^{(e)}$ also the experimental section strains should be computed. It is known that e_1 is constant, e_2 and e_3 are linear. This can be expressed as:

$$
\begin{cases}
e_1(x) = e_{10} \\
e_2(x) = e_{20} + xe_{21} \\
e_3(x) = e_{30} + xe_{31}
\end{cases}
\tag{2.30}
$$

So for each strain measurement it can be written the following equation using Eq.(2.4):

$$
e_{10} + z_i(e_{20} + x_ie_{21}) + y_i(e_{30} + x_ie_{31}) = \varepsilon^{\varepsilon}_{xi}
\tag{2.31}
$$

where $\varepsilon^{\varepsilon}_x$ is the measurement taken from the ith strain gauge positioned at (x_i, y_i, z_i). From Eq.(2.30) it follows that at least five measurements per element are needed in at least two

positions because of the linearity of e_2 and e_3. So all the equations can be grouped in a linear system as follows:

$$
\begin{bmatrix}
1 & z_1 & z_1x_1 & y_1 & y_1z_1 \\
1 & z_2 & z_2x_2 & y_2 & y_2z_2 \\
1 & z_3 & z_3x_3 & y_3 & y_3z_3 \\
1 & z_4 & z_4x_4 & y_4 & y_4z_4 \\
1 & z_5 & z_5x_5 & y_5 & y_5z_5
\end{bmatrix}
\begin{bmatrix}
e_{10} \\
e_{20} \\
e_{21} \\
e_{30} \\
e_{31}
\end{bmatrix}
=
\begin{bmatrix}
\varepsilon_{z1}^{\varepsilon} \\
\varepsilon_{z2}^{\varepsilon} \\
\varepsilon_{z3}^{\varepsilon} \\
\varepsilon_{z4}^{\varepsilon} \\
\varepsilon_{z5}^{\varepsilon}
\end{bmatrix}
\tag{2.32}
$$

In order to assess the element formulation, a simple clamped beam has been modelled with a single 0th order element. The beam has a rectangular cross-section and the measurement points are shown in Figure 2.3a. The material is isotropic with $E = 73e3\,MPa$ and $\nu = 0.3$. A tip load P is acting on the free end.
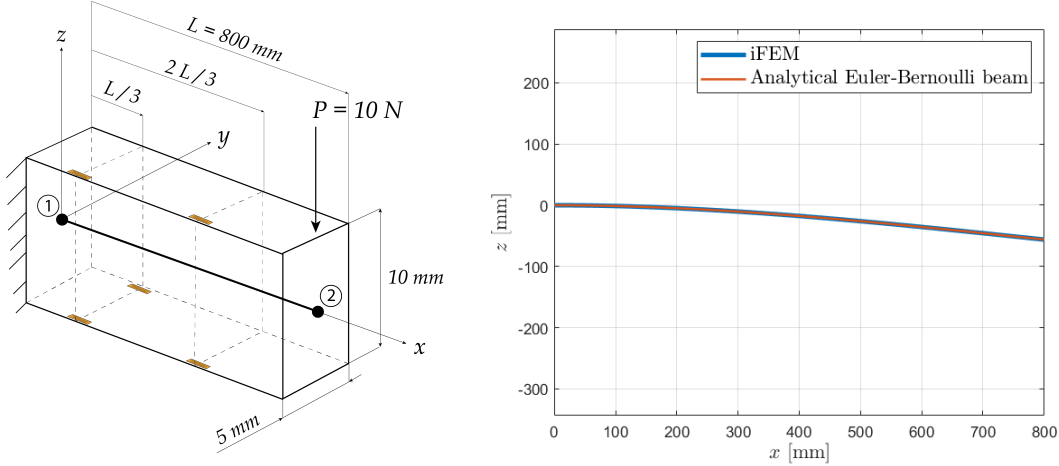
(a) *Strain gauge positions (not in scale).*

(b) *Vertical displacement and comparison between iFEM and analytical results.*

Figure 2.3: *Clamped Beam under tip load modelled with a single 0th order inverse element.*

Since the model is quite simple, the "experimental" strains have been computed analytically. Using the Euler-Bernoulli beam theory, the axial strain in this case is equal to (see Appendix B):

$$
\varepsilon_x^{\varepsilon}(x, z) = \frac{P(x - L)}{EI_y} z
\tag{2.33}
$$

Carrying out the simulation and plotting the deformed shape, the results of Figure 2.3b have been obtained, where the displacement $w(x)$ from the iFEM model has been interpolated with the corresponding shape functions between the two end nodes. As expected there is an exact correspondence since the inverse element has been developed exactly for this load case from the equilibrium beam equations.

Now the performance of the element is checked when the beam is subjected to a distributed load $q_z = 0.1$ N/mm. The same strain gauge distribution is kept and the analytical strain is given by (see Appendix B for the derivation):
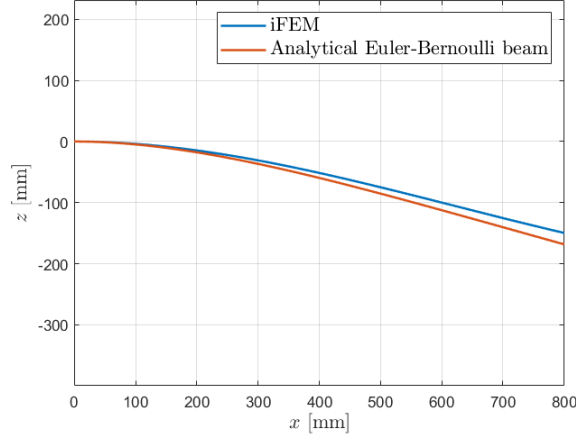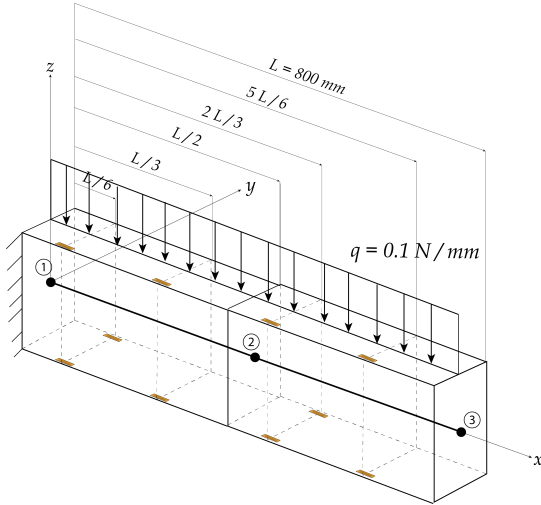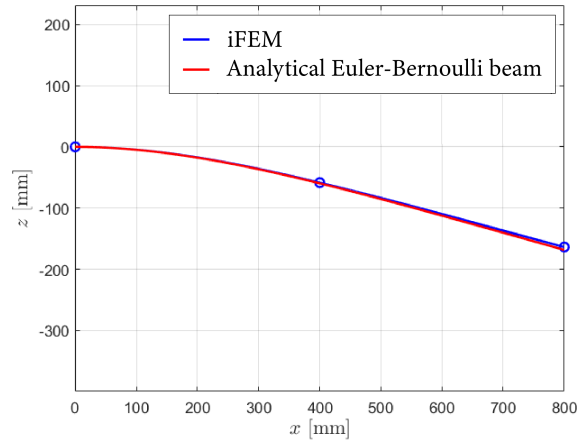
Figure 2.4: *Vertical displacement of clamped beam under distributed load modelled with a single 0th order inverse element.*

$$\varepsilon_x^\varepsilon(x,z) = \frac{q_z}{EI_y}\left(\frac{x^2}{2} - Lx + \frac{L^2}{2}\right)z \tag{2.34}$$

Repeating the same steps as before, the results in Figure 2.4 have been obtained. Now, as expected, an error is present which could be reduced increasing the number of inverse elements. For example, two inverse elements can be used as illustrated in Figure 2.5a. In this way the results reported in Figure 2.5b have been obtained and a more correct solution is now achieved.



(a) *Strain gauges positions.*

(b) *Vertical displacement and comparison between iFEM and analytical results.*

Figure 2.5: *Clamped Beam under distributed load modelled with two 0th order inverse elements.*

1st Order inverse Euler-Bernoulli beam element

If in the equilibrium equations distributed constant forces q_y and q_z are now considered, a new element can be obtained on the same lines of the one developed in the previous section. The element is sketched in Figure 2.6. Carrying out similar substitutions as before, it is possible to obtain that e_1 must again be constant, while e_2 and e_3 should be quadratic. At the same time, the element must be C^1 continuous and if the Hermite polynomials are used the following can be obtained:
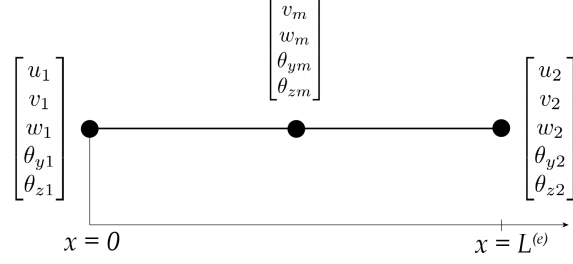
Figure 2.6: 1st *Order inverse Euler-Bernoulli beam element*

$$
\begin{cases}
u(x) = \sum_{i=1,2} H_{0i}^{(0)} u_i \\
v(x) = \sum_{i=1,m,2} H_{0i}^{(1)} v_i + H_{1i}^{(1)} \theta_{zi} \\
w(x) = \sum_{i=1,m,2} H_{0i}^{(1)} w_i - H_{1i}^{(1)} \theta_{yi}
\end{cases}
\tag{2.35}
$$

where this time $H_{0i}^{(1)}$ are fifth order polynomials since the element has three nodes. This means that $v(x)$ and $w(x)$ are interpolated with a fifth order polynomial and therefore that e_2 and e_3 are of order three (and not two) as it should from the equilibrium equations. This problem can be solved writing down explicitly the section strains e_2 and e_3 as:

$$
e_2 = -\frac{\mathrm{d}^2 w}{\mathrm{d}x^2} = -\sum_{i=1,m,2} \frac{\mathrm{d}^2 H_{0i}^{(1)}}{\mathrm{d}z^2} w_i - \frac{\mathrm{d}^2 H_{1i}^{(1)}}{\mathrm{d}z^2} \theta_{yi}
\tag{2.36}
$$

$$
e_3 = -\frac{\mathrm{d}^2 v}{\mathrm{d}x^2} = \sum_{i=1,m,2} \frac{\mathrm{d}^2 H_{0i}^{(1)}}{\mathrm{d}z^2} v_i + \frac{\mathrm{d}^2 H_{1i}^{(1)}}{\mathrm{d}z^2} \theta_{zi}
\tag{2.37}
$$

where the expressions of the cubic Hermite polynomials are given in Appendix A. For example, for e_2 this results in:

$$
\begin{aligned}
e_2 = -\Bigg[&\left(-\frac{46}{(L^{(e)})^2} + \frac{396}{(L^{(e)})^3}x - \frac{816}{(L^{(e)})^4}x^2 + \frac{480}{(L^{(e)})^5}x^3 \right) w_1 + \\
&+ \left(\frac{32}{(L^{(e)})^2} - \frac{192}{(L^{(e)})^3}x + \frac{192}{(L^{(e)})^4}x^2 \right) w_m + \\
&+ \left(\frac{14}{L_e^2} - \frac{204}{L_e^3}x + \frac{624}{(L^{(e)})^4}x^2 - \frac{480}{(L^{(e)})^5}x^3 \right) w_2 + \\
&+ \left(-\frac{12}{(L^{(e)})} + \frac{78}{(L^{(e)})^2}x - \frac{144}{(L^{(e)})^3}x^2 + \frac{80}{(L^{(e)})^4}x^3 \right) \theta_{y1} + \\
&+ \left(-\frac{16}{(L^{(e)})} + \frac{192}{(L^{(e)})^2}x - \frac{480}{(L^{(e)})^3}x^2 + \frac{320}{(L^{(e)})^4}x^3 \right) \theta_{ym} + \\
&+ \left(-\frac{2}{(L^{(e)})} + \frac{30}{(L^{(e)})^2}x - \frac{96}{(L^{(e)})^3}x^2 + \frac{80}{(L^{(e)})^4}x^3 \right) \theta_{y2} \Bigg]
\end{aligned}
\tag{2.38}
$$

At this point all the cubic terms of e_2 and e_3 can be set equal to zero. This results in the following equation:

$$
\frac{480}{(L^{(e)})^5}w_1 - \frac{480}{(L^{(e)})^5}w_2 + \frac{80}{(L^{(e)})^4}\theta_{y1} + \frac{320}{(L^{(e)})^4}\theta_{ym} + \frac{80}{(L^{(e)})^4}\theta_{y2} = 0
\tag{2.39}
$$

Similarly for e_3:

$$\frac{480}{(L^{(e)})^5}v_1 - \frac{480}{(L^{(e)})^5}v_2 + \frac{80}{(L^{(e)})^4}\theta_{z1} + \frac{320}{(L^{(e)})^4}\theta_{zm} + \frac{80}{(L^{(e)})^4}\theta_{z2} = 0 \qquad (2.40)$$

Now, the variables θ_{ym} and θ_{zm} can be obtained from the previous two equations and substituted in the original interpolation. This eventually results in the final interpolation of v and w, which is of fourth order.

Now, again the strain-displacement matrix $\boldsymbol{B}$ can be computed and so $\boldsymbol{K}^{(e)}$ and $\boldsymbol{f}^{(e)}$ can be in turn be obtained.

As a final note, the procedure to compute the experimental section strains is analogous as before. However, now due to the higher order of the element at least seven strain measurement are needed in at least three axial locations (because e_2 and e_3 are quadratic).

2.2 Inverse Euler-Bernoulli element with torsional sensitivity

In this section the iFEM beam model described in Section 2.1 is extended introducing the possibility to take into account the torsion of the beam. Even though the framework used is the one of iFEM, the twist reconstruction is simply based on an analytical computation of the twist rate with the applied torsion moment. From iFEM the internal shear force over the beam is obtained which in turn allows to compute the actual shear stress induced by torsional forces and so finally the twist rate. Therefore, the torsional deformation reconstruction is just indirectly based on iFEM, but still the deformation is recovered step-wise on each element. In this way, rather complex shapes could be obtained. The details of the method are explained in Section 2.2.1. It follows the brief description of the development of a code to compute the properties of general-shaped cross-sections (Section 2.2.2) and some simple applications with the aim to give more insight into the results which can possibly be obtained (Section 2.2.3, Section 2.2.4 and Section 2.2.5).

2.2.1 Algorithm to recover both bending and torsional deformations

The inverse Euler-Bernoulli beam element developed in [48] has relatively limited capabilities since it is able to recover just the bending behaviour of the beam, with no information about its torsion. The difficulty does not lie in the element formulation, since it is relatively easy to add the torsional degree of freedom. Consider the 0th order element, whose formulation comes from the applications of just nodal forces (no distributed forces), then from the equilibrium equations:

$$
\begin{aligned}
e_1 &= \text{constant} &&\Rightarrow& u &= \text{linear} \\
e_2 &= \text{linear} &&\Rightarrow& \theta_y &= \text{quadratic} &&\Rightarrow& w &= \text{cubic} \\
e_3 &= \text{linear} &&\Rightarrow& \theta_z &= \text{quadratic} &&\Rightarrow& v &= \text{cubic} \\
e_6 &= \mathrm{d}\theta_x/\mathrm{d}x = \text{constant} &&\Rightarrow& \theta_x &= \text{linear}
\end{aligned}
\tag{2.41}
$$

from which is follows that a simple linear interpolation for the torsional degrees of freedom θ_x is sufficient, and so:

$$
\begin{cases}
u(x) = \displaystyle\sum_{i=1}^{2} H_{0i}^{(0)} u_i \\[2mm]
v(x) = \displaystyle\sum_{i=1}^{2} H_{0i}^{(1)} v_i + H_{1i}^{(1)} \theta_{zi} \\[2mm]
w(x) = \displaystyle\sum_{i=1}^{2} H_{0i}^{(1)} w_i - H_{1i}^{(1)} \theta_{yi} \\[2mm]
\theta_x(x) = \displaystyle\sum_{i=1}^{2} L_i^{(1)} \theta_{xi}
\end{cases}
\tag{2.42}
$$

with $H_{ij}^{(N)}$ cubic Hermite polynomials and $L_i^{(1)}$ linear Lagrange polynomials.

The problem consists in relating the measured strains to the shear strains generated by torsion. In general, measuring the shear strain at a certain location, the value obtained comes both from torsional loads and shear loads. So there is the need to *uncouple* the two contributions, retaining just the effect due to torsion. It is possible to do that keeping the same iFEM formulation for the *bending* behavior, but at the same time adding to the shape sensing study a few steps needed to recover the torsional deformation. In the following, the 0th order element is considered, so only nodal forces are present in the element formulation. The methods proceeds along the following lines:

1. First, the bending deflection can be computed with iFEM. This requires five axial strain measurements per element in at least two different axial locations.

2. From the element formulation used, only concentrated nodal forces are acting on the element. Therefore, a *constant* internal shear force is present along the element itself. This can be computed from the equilibrium equations as:

$$V_y = \frac{\mathrm{d}M_y}{\mathrm{d}x} = \frac{\mathrm{d}}{\mathrm{d}x}\left(-EI_z\frac{\mathrm{d}^2 v}{\mathrm{d}x^2}\right)$$
$$V_z = \frac{\mathrm{d}M_z}{\mathrm{d}x} = \frac{\mathrm{d}}{\mathrm{d}x}\left(-EI_y\frac{\mathrm{d}^2 w}{\mathrm{d}x^2}\right)$$
(2.43)

Knowing the interpolation used for $v(x)$ and $w(x)$ (Eq.(2.42)), it is possible to obtain:

$$V_y = -6EI_z\frac{2v_1 - 2v_2 + L^{(e)}\theta_{z1} + L^{(e)}\theta_{z2}}{(L^{(e)})^3}$$
$$V_z = 6EI_y\frac{2w_2 - 2w_1 + L^{(e)}\theta_{y1} + L^{(e)}\theta_{y2}}{(L^{(e)})^3}$$
(2.44)

3. Now, *assuming* that V_y and V_z are acting on the *shear center* of the beam cross-section, it is possible to compute the shear stress due to these loads. The shear stress developed by a *unit* V_z or V_y will be denoted respectively with τ_{12}^z and τ_{12}^y. This can be achieved basically in two different ways:

   - for simple cross-sections, the shear stress can be computed analytically using well-known methods, as in [63].
   - if a Finite Element model is available, then the shear stress can be retrieved from a simple linear static analysis of the beam modeled with shell elements and whose cross-section has been extruded for a sufficient length such that the Euler-Bernoulli beam theory assumptions are satisfied.

   In a similar manner, in this step it is also important to compute (either analytically or numerically) the shear stress developed by a pure *unit* torsional moment applied at the end of the beam. This shear stress will be named τ_{12}^t.

4. Consider the presence of an additional strain gauge over the inverse beam element, oriented with angle β w.r.t. the beam axis (Figure 2.7). Since its purpose will be to measure the twist angle of the beam, it will be referred in the following as *shear-sensitive strain gauge*. At the same location where this strain gauge is positioned, the axial strain ε_x can be retrieved knowing the section strains (from iFEM) developed in the beam element, and so the shear strain γ can be obtained as (see for example [14] for the tensor rotation transformation):
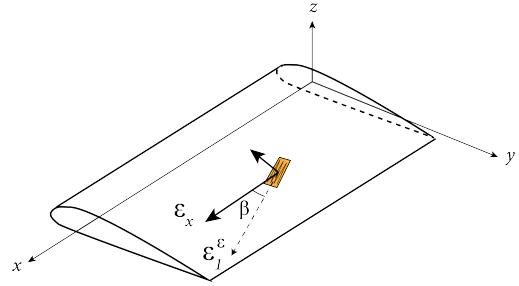

Figure 2.7: *Shear-sensitive strain gauge positioned on beam element.*

$$\varepsilon_1^\varepsilon = \varepsilon_x \cos^2\beta - \nu\varepsilon_x \sin^2\beta + \gamma\cos\beta\sin\beta$$
(2.45)
$$\Rightarrow \quad \gamma = \frac{\varepsilon_1^\varepsilon - \varepsilon_x\cos^2\beta + \nu\varepsilon_x\sin^2\beta}{\cos\beta\sin\beta}$$

where ε_x can be computed as:

$$\varepsilon_x = e_1^\varepsilon(x) + z e_2^\varepsilon(x) + y e_3^\varepsilon(x)$$

and $\varepsilon_1^\varepsilon$ is the measured strain by the gauge. Knowing the shear modulus G of the material, this results in the shear stress where the strain gauge is positioned: $\tau_{12}^\varepsilon = G\gamma$.

5. At this point it is possible to compare the shear stress τ_{12}^z, τ_{12}^y computed at point (3) with τ_{12}^ε. The difference must be due to shear stresses attributed to torsion and so the torsional moment can be derived simply as:

$$M_x = \frac{\tau_{12}^\varepsilon - (V_z \tau_{12}^z + V_y \tau_{12}^y)}{\tau_{12}^t} \tag{2.46}$$

This enables to compute the twist angle $\theta_x(x)$ along the beam element length:

$$\theta_x(x) = \theta_{x0} + \int_0^x \frac{M_x}{GJ}\,\mathrm{d}x$$

with $\theta_x(x=0) = \theta_{x0}$ the torsion angle at the first node of the element and GJ the torsional stiffness. Obviously, for the element directly connected to the root $\theta_{x0} = 0$.

The first important fact to outline is that the torsional deformation obtained in this way will be linear, that is the twist angle varies linearly along the beam length, since τ_{12}^t was computed applying a concentrated torsional moment at the beam end. So for a general loading condition if more precise results are needed the number of inverse elements should be increased. This of course brings to increase the number of strain measurements: for each element 6 gauges are needed: 5 for the iFEM formulation along the beam axis to retrieve the bending deformation and 1 for the torsional sensitivity oriented with angle β w.r.t the axis.

As pointed out before, it is necessary to know which are the shear stresses along the beam cross-section due to shear forces V_y and V_z applied on the shear center and due to a unit torsional couple M_x. Therefore:

- The position of the shear center is required. For a general cross-section shape (such as an airfoil), its position must be computed. Furthermore, also other cross-section properties (I_y, I_z) are needed in order to retrieve the internal shear forces (Eq.(2.44)). Therefore, a code to compute all the relevant properties for generally shaped cross-sections has been developed. It will be briefly described in Section 2.2.2.

- As already mentioned, the shear stresses τ_{12}^y, τ_{12}^z and τ_{12}^t can be computed analytically if for example the beam cross-section is thin-walled. In this way, a very quick result can be obtained. However, for more complex cross-sections, the analytical computations might be cumbersome. An easy workaround consists in simply simulating with FEM a three-dimensional long enough beam (to be in accordance with the Euler-Bernoulli assumptions), applying a unit load at the tip shear center, and in exporting the shear stress at the gauge location over the cross-section. This operation needs to be done just once, so it does not represent a computational burden. Furthermore, the same model can be used to apply a unit torsion moment at the tip of the beam and again in retrieving the shear stress at the gauge location.

The work-flow just outlined is visually depicted in Figure 2.8 where the highlighted box off-line stands for the tasks which need to be done only once and which do not depend on the strain measurements that are instead an input for the on-line part.
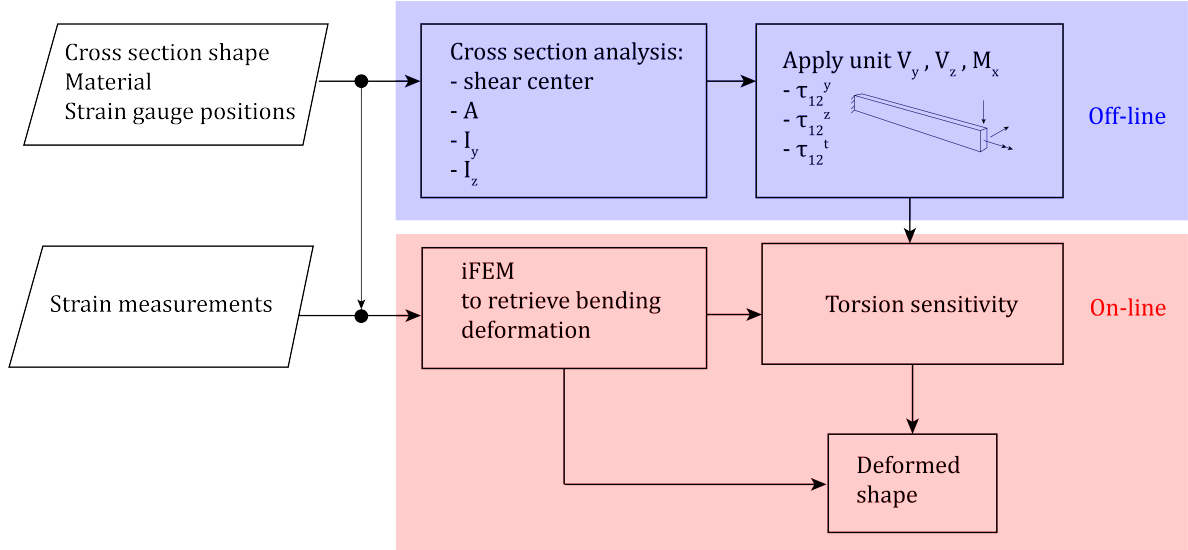
Figure 2.8: *Work-flow to follow in order to retrieve both the bending and the torsional deformation from the beam model.*

In order to assess the results which can be obtained with this framework, some simple simulations have been carried out. First, the shear stresses are retrieved analytically for a simple rectangular thin-walled cross-section (Section 2.2.3). Then, for an open L cross-section they are directly imported from a FEM simulation (Section 2.2.4). Finally, a beam with a thin-walled airfoil cross-section will be analyzed in Section 2.2.5.

2.2.2 Computation of cross-sectional properties

A crucial step in the method outlined consists in knowing the beam cross-sectional properties and in particular the position of the shear center in order to retrieve the torsional deformations. For simple cross-sections this task can be easily carried out by hand. However, for more complex shapes a more general solution is needed. Here, a Finite Element based solution has been developed using some results from [66]. As input it is needed the discretization of the cross-section and the elements connectivity, while as output the properties retrieved are the cross-section area, first moments of area, centroid position, second moments of area, torsional constant and shear center position (computed according to two different definitions).

Cross-section area

It can be simply computed sweeping through all the elements and summing the individual element areas $A^{(e)}$ as:

$$A = \sum_e A^{(e)} = \sum_e \int_{-1}^{1} \int_{-1}^{1} |\boldsymbol{J}_e| \, \mathrm{d}\xi \mathrm{d}\eta \qquad (2.47)$$

with $\boldsymbol{J}_e$ the element Jacobian and $(\xi, \eta) \in [-1, 1]$ the natural coordinates.

First moments of area

From their definitions it follows that they can be computed as:

$$
\begin{aligned}
Q_y &= \iint_A z\,\mathrm{d}A = \sum_e \int_{-1}^{1}\int_{-1}^{1} \boldsymbol{N}\boldsymbol{z}^{(e)}|\boldsymbol{J}_e|\,\mathrm{d}\xi\mathrm{d}\eta \\
Q_z &= \iint_A y\,\mathrm{d}A = \sum_e \int_{-1}^{1}\int_{-1}^{1} \boldsymbol{N}\boldsymbol{y}^{(e)}|\boldsymbol{J}_e|\,\mathrm{d}\xi\mathrm{d}\eta
\end{aligned}
\tag{2.48}
$$

with $\boldsymbol{N}$ the vector containing the shape functions and $\boldsymbol{y}^{(e)}$, $\boldsymbol{z}^{(e)}$ element nodal coordinates.

Centroid position

The centroid position can be directly computed from the first moments of area:

$$
y_C = \frac{Q_z}{A} \quad ; \quad z_C = \frac{Q_y}{A}
\tag{2.49}
$$

Second moments of area

Similarly as for the first moments of area, in this case:

$$
\begin{aligned}
I_y &= \iint_A z^2\,\mathrm{d}A = \sum_e \int_{-1}^{1}\int_{-1}^{1} (\boldsymbol{N}\boldsymbol{z}^{(e)})^2|\boldsymbol{J}_e|\,\mathrm{d}\xi\mathrm{d}\eta \\
I_z &= \iint_A y^2\,\mathrm{d}A = \sum_e \int_{-1}^{1}\int_{-1}^{1} (\boldsymbol{N}\boldsymbol{y}^{(e)})^2|\boldsymbol{J}_e|\,\mathrm{d}\xi\mathrm{d}\eta \\
I_{yz} &= \iint_A yz\,\mathrm{d}A = \sum_e \int_{-1}^{1}\int_{-1}^{1} \boldsymbol{N}\boldsymbol{y}^{(e)}\boldsymbol{N}\boldsymbol{z}^{(e)}|\boldsymbol{J}_e|\,\mathrm{d}\xi\mathrm{d}\eta
\end{aligned}
\tag{2.50}
$$

These values can be easily referred to the centroidal reference system as:

$$
\begin{aligned}
I_{yC} &= I_y - z_C^2 A \\
I_{zC} &= I_z - y_C^2 A \\
I_{yzC} &= I_{yz} - y_C z_C A
\end{aligned}
\tag{2.51}
$$

Torsional constant

It is possible to demonstrate [66] that the torsional constant J of the cross-section can be computed as:

$$
J = \iint_A \left[\left(\frac{\partial \omega}{\partial z} + y\right) y - \left(\frac{\partial \omega}{\partial y} - z\right) z \right] \mathrm{d}A
\tag{2.52}
$$

with $\omega(y, z)$ the so-called *warping function* which defines the axial displacement field under pure torsion. Therefore, there is the need to compute the warping function over the cross-section. Jumping directly to the final steps, it is possible to derive from the Principle of Virtual Work that $\omega(y, z)$ must satisfy:

$$
\iint_A \left[\left(\frac{\partial}{\partial y}\delta\omega\frac{\partial \omega}{\partial y} + \frac{\partial}{\partial z}\delta\omega\frac{\partial \omega}{\partial z}\right) - \left(\frac{\partial}{\partial y}\delta\omega z - \frac{\partial}{\partial z}\delta\omega\, y\right) \right] \mathrm{d}A = 0
\tag{2.53}
$$

Interpolating the warping function over the element domain as:

$$
\omega(y, z) = \boldsymbol{N}\boldsymbol{\omega}^{(e)}
\tag{2.54}
$$

and substituting into Eq.(2.53) it is possible to obtain:

$$\boldsymbol{K}_{\omega}^{(e)}\boldsymbol{\omega}^{(e)} = \boldsymbol{P}^{(e)} \tag{2.55}$$

where:

$$\boldsymbol{K}_{\omega}^{(e)} = \iint_{A^{(e)}} \left(\frac{\partial \boldsymbol{N}^{\top}}{\partial y} \frac{\partial \boldsymbol{N}}{\partial y} + \frac{\partial \boldsymbol{N}^{\top}}{\partial z} \frac{\partial \boldsymbol{N}}{\partial z} \right) dA^{(e)} \quad ; \quad \boldsymbol{P}^{(e)} = \iint_{A^{(e)}} \left(z \frac{\partial \boldsymbol{N}^{\top}}{\partial y} - y \frac{\partial \boldsymbol{N}^{\top}}{\partial z} \right) dA^{(e)}$$

Assembling over all the cross-section elements and solving the corresponding linear system:

$$\boldsymbol{K}_{\omega}\boldsymbol{\omega} = \boldsymbol{P}$$

allows to retrieve the warping function distribution. At this point, substituting into Eq.(2.52) it is possible to obtain the torsional constant as (see again [66] for all the steps):

$$J = I_y + I_z - \boldsymbol{\omega}^{\top}\boldsymbol{P} \tag{2.56}$$

Shear center position

The position of the shear center has been implemented using two different approaches as explained in the following.

A common method to compute the shear center consists in the so-called Trefftz definition. According to this approach, the shear center can be obtained uncoupling the strain energy due to transverse shear and torsional stresses. Considering a beam subjected to torsion and shear loads, then the total strain energy stored is:

$$U = \frac{1}{2E} \iint_A \left(\int_0^L \sigma_x^2 dx \right) dA + \frac{L}{2G} \iint_A \left[(t_{xy} + \tau_{xy})^2 + (t_{xz} + \tau_{xz})^2 \right] dA \tag{2.57}$$

where L is the beam length, E, G the elastic and shear moduli, t_{xy}, t_{xz} are the torsional shear stresses, while τ_{xy}, τ_{xz} are the transverse shear stresses. As it is possible to see, in the second integral torsion and shear are uncoupled if the following holds:

$$\iint_A \left(t_{xy}\tau_{xy} + t_{xz}\tau_{xz} \right) dA = 0 \tag{2.58}$$

which represents the definition of torsion-free flexure according to Trefftz. At this point, expressing the torsional shear stresses with the warping function $\omega(y, z)$ and using the equilibrium equations it is possible to derive the position (y_S, z_S) of the shear center [66]:

$$\begin{cases} y_S = \dfrac{I_{yz}I_{y\omega} - I_z I_{z\omega}}{I_y I_z - I_{yz}^2} \\ z_S = \dfrac{I_y I_{y\omega} - I_{yz}I_{z\omega}}{I_y I_z - I_{yz}^2} \end{cases} \tag{2.59}$$

where the so-called sectorial products of area are defined as:

$$I_{y\omega} = \iint_A y\,\omega(y, z)dA \quad ; \quad I_{z\omega} = \iint_A z\,\omega(y, z)dA \tag{2.60}$$

Knowing the warping function from the previous point, it is easily possible to compute these integrals and therefore to obtain the shear center position.

A completely different approach to compute the shear center position consists in directly solving the elasticity equations. Since the procedure is relatively lengthy, just the main steps

and expressions will be shown, without going into details (refer to [66] for a more in-depth derivation). In particular, considering for example a beam subjected to a tip load V_z acting on the shear center, then no torsion is present and the shear stress τ_{xz}, τ_{xy} expressions are chosen to automatically satisfy the compatibility equations as:

$$\tau_{xy} = \frac{V_z}{\Delta}\left(\frac{\partial \Phi}{\partial y} - h_y\right) \quad ; \quad \tau_{xz} = \frac{V_z}{\Delta}\left(\frac{\partial \Phi}{\partial z} - h_z\right) \tag{2.61}$$

where:

$$\Delta = 2(1+\nu)\left(I_y I_z - I_{yz}^2\right) \quad ; \quad h_y = v\left(I_z yz + I_{yz}\frac{y^2 - z^2}{2}\right) \quad ; \quad h_z = -v\left(I_{yz}yz + I_z\frac{y^2 - z^2}{2}\right)$$

substituting into the equilibrium equations the function $\Phi = \Phi(y, z)$ needs to satisfy:

$$\nabla^2 \Phi = 2\left(I_{yz}y - I_z z\right) \tag{2.62}$$

The boundary conditions for $\Phi(y, z)$ can be obtained from the fact that the stress normal to the cross-section boundary must be null. In this way the function $\Phi(y, z)$ is fully defined. Applying for example the Galerkin method, the weak form of the problem can be obtained which can be solved within the Finite Element framework leading to the usual linear system of equations:

$$\boldsymbol{K}_\Phi^{(e)} \boldsymbol{\Phi}^{(e)} = \boldsymbol{p}_z^{(e)} \tag{2.63}$$

Once $\Phi(y, z)$ is known, the shear center position y_S can be obtained imposing that the shear stress distribution must be equivalent to the couple $y_S V_z$, that is:

$$y_S V_z = \iint_A \left(\tau_{xz}y - \tau_{xy}z\right) dA \tag{2.64}$$

from which y_S can be obtained.
A completely analogous procedure holds also for the computation of z_S. In this case, the shear stresses are expressed in function of $\Psi = \Psi(y, z)$ which is obtained from:

$$\boldsymbol{K}_\Psi^{(e)} \boldsymbol{\Psi}^{(e)} = \boldsymbol{p}_y^{(e)} \tag{2.65}$$

and again the shear center position z_S is obtained from the corresponding counterpart of Eq.(2.64).

Assessment of cross-section properties for C-section

(a) *Warping function $\omega(y, z)$.*

(b) *Shear center position according to Trefftz.*
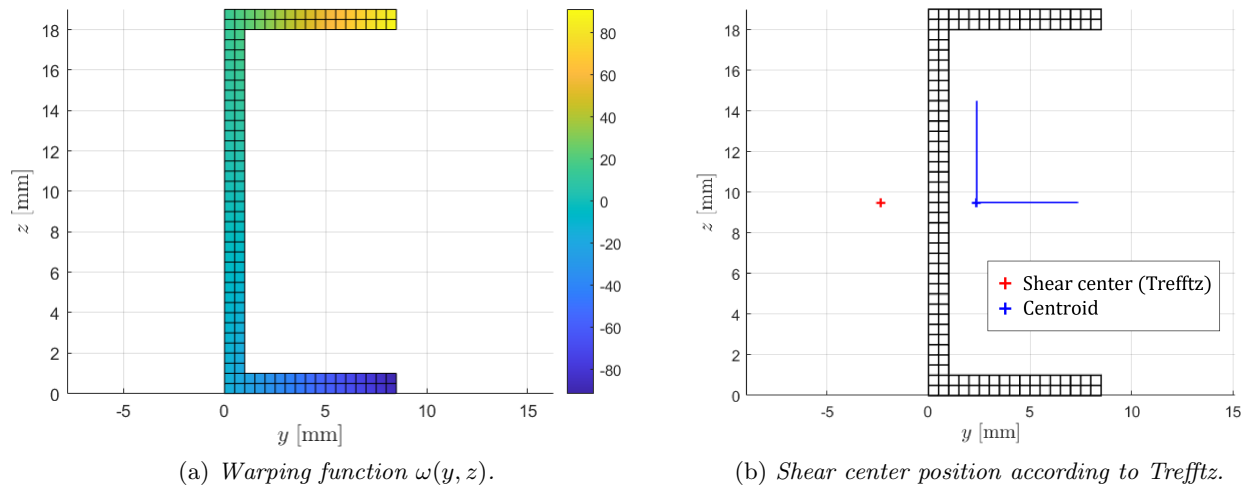
Figure 2.9: *C-section.*

As an example, the computed cross-sectional properties have been compared with numerical study from [66] for a channel section as illustrated in Figure 2.9.

The comparison is reported in Table 2.1 just for some properties of interest, in particular the shear center position (computed both with the Trefftz definition and the elasticity-based solution) and the torsional constant. The results closely agree with the ones obtained from [66].

	In-house code	[66]
y_S(Trefftz) wrt centroid	-4.742	-4.742
z_S(Trefftz) wrt centroid	0	0
y_S(Elasticity) wrt centroid	-4.742	-4.742
z_S(Elasticity) wrt centroid	0	0
J	11.290	11.288

Table 2.1: *Comparison of some cross-section properties of interest (units as from* [66] *).*

2.2.3 Application to thin-walled box beam

A simple cantilever beam with rectangular thin-walled cross-section will be considered here. For now, a single inverse beam element will be used and so a total of six strain gauges is needed. The geometry and the strain locations are shown in Figure 2.10.

(a) *Beam geometry and strain gauges positions.*

(b) *Beam cross-section and reference system.*
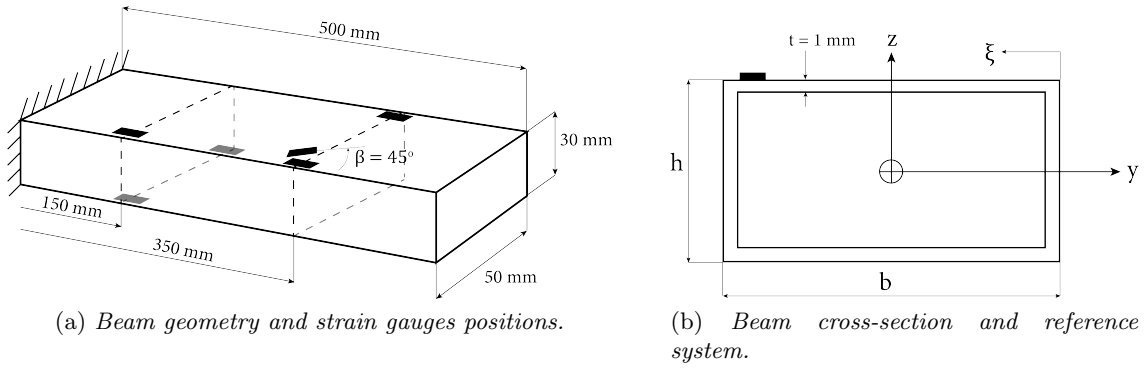
Figure 2.10: *Box thin-walled beam.*

The cross-section is relatively simple and the shear center position is defined from symmetry. Only shear forces along z (V_z) will be considered and the corresponding shear stress can be obtained analytically with the common techniques used for thin-walled structures [63]. In particular, the shear-sensitive gauge orientation β is positioned as in Figure 2.10b and so the value of the shear stress is needed in that position. It is possible to derive (see Appendix C) that in the upper panel the shear stress is given by:

$$\tau_{12}^z(\xi) = \frac{V_z t}{I_y}\left(-\frac{h}{2}\xi + \frac{hb}{4}\right) \tag{2.66}$$

with $\xi \in [0,b]$ the coordinate shown in Figure 2.10b, t the thickness, h and b the cross-section dimensions and I_y the second moment of area around y.

Since in this case the cross-section is simply a closed mono-cell thin-walled one, the torsion angle rate is given by:

$$\frac{\mathrm{d}\theta_x}{\mathrm{d}x} = \frac{\tau_{12}^z - \tau_{12}^\varepsilon}{4G\Omega t(h+b)}$$

with Ω the enclosed area by the cross section and G the shear modulus.

Three different load cases have been simulated, taking the input strain measurements from the corresponding FE model.

(a) *Load case: beam under bending and torsion.*

(b) *Reconstructed deformed shape.*

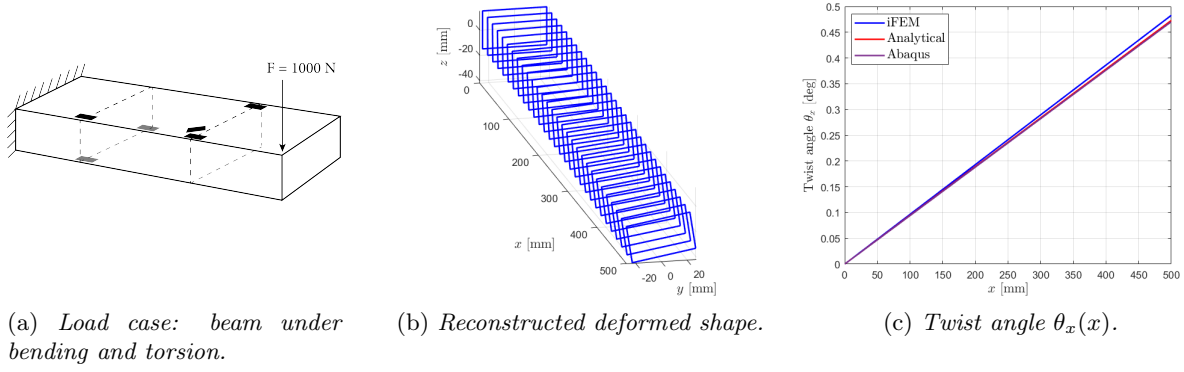(c) *Twist angle $\theta_x(x)$.*

Figure 2.11: *Thin-walled box beam under tip load.*

A concentrated load has been applied on a free corner of the beam, as in Figure 2.11a. In Figure 2.11b the obtained deformed shape is shown, while in Figure 2.11c the twist angle $\theta_x(x)$ along the span has been plotted, comparing the results obtained from the reconstructed shape (iFEM), from the analytical formula and from the FEM simulation (`Abaqus`). The analytical results are obtained simply integrating $\dot{\theta}_x = M_x/GJ$.

In the second load case study, a pure torque is applied at the beam end, as in Figure 2.12a. In general the deformed shape is well recovered. Also in this case a comparison with FEM and analytical results has been carried out, leading to Figure 2.12c for the twist angle reconstruction. The error which is possible to see comes mainly from the the iFEM results. The translational displacements should be null (since just torsion is applied), however this is not exactly achieved and a (small) shear force is identified. This in turn affects the computation of the shear stress due to torsion and therefore the twist angle reconstruction.

(a) *Load case: beam under torsion.*

(b) *Reconstructed deformed shape.*

(c) *Twist angle $\theta_x(x)$.*
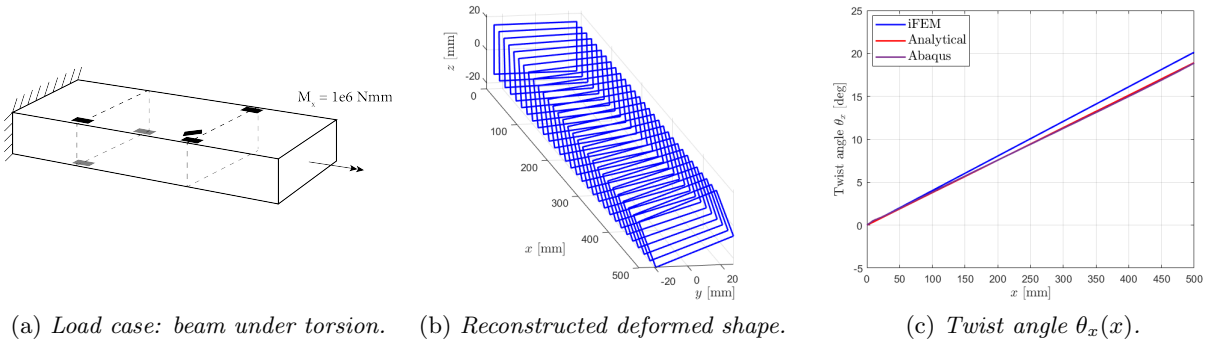
Figure 2.12: *Thin-walled box beam under tip torsional moment.*

A final simulation has been done with a more complex load case and using two inverse elements, as shown in Figure 2.13a. A concentrated load is acting on the middle of the beam with an offset w.r.t the cross-section center, so that a torsional load is induced. At the same time, at the tip two other concentrated forces are acting: a force pointing upwards and a torque. Also in this case the twist angle has been computed along the beam span. Since concentrated forces are acting at the extremities of the inverse beam elements used, the twist angle is approximately step-wise linear and this is well captured by the shape reconstruction, as shown in Figure 2.13c.

(a) *Load case: beam under mid-span and tip forces.* (b) *Reconstructed deformed shape.* (c) *Twist angle $\theta_x(x)$.*
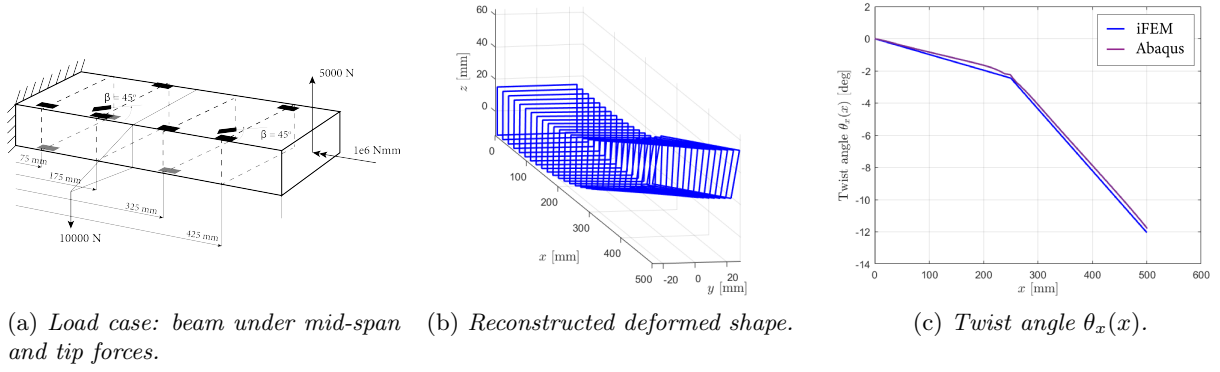
Figure 2.13: *Thin-walled box beam under multiple concentrated forces.*

2.2.4 Application to thin-walled L-beam

In this subsection another beam with an L cross-section is considered and the same approach outlined before is used. Here, however, the shear stresses τ_{12}^y, τ_{12}^z, τ_{12}^t are directly taken from a FEM simulation applying unit loads, and no analytical result is used. The aim is to study a section where centroid and shear center do not coincide as previously. Furthermore, the fact that it is an open section brings about some consequences which should be considered.

Consider the beam as shown in Figure 2.14a. Just one inverse element will be used, so six strain gauges are sufficient. Their positions are shown again in Figure 2.14a and a concentrated load has been applied at the tip as illustrated. The cross-section dimensions are given in Figure 2.14b. The central axes have been drawn and also the shear center position.

(a) *Load case and strain gauges positions.* (b) *Cross-section geometry.*
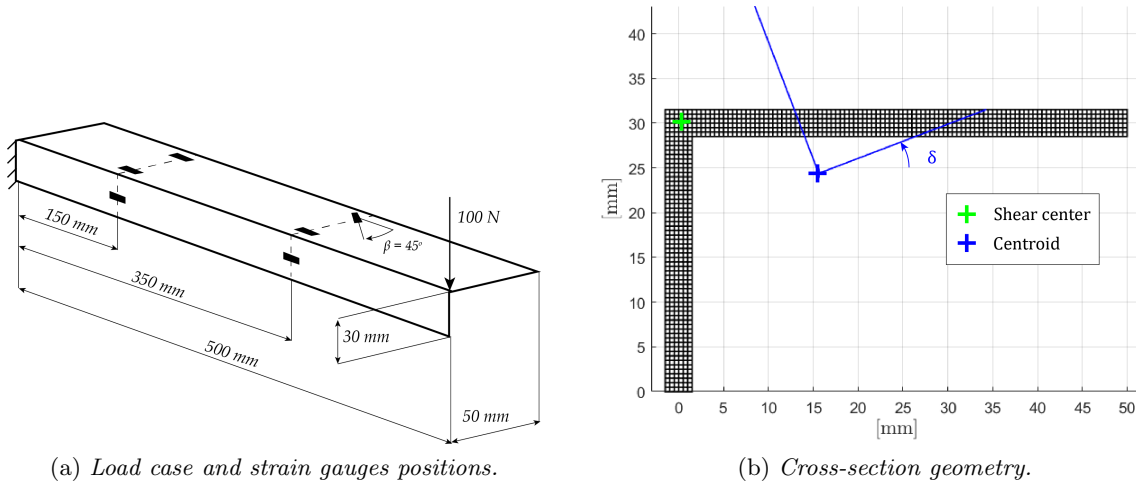
Figure 2.14: *L-beam.*

Since the cross-section is thin-walled, it is known that the shear center coincides with the corner of the section. The load is applied on the shear center and therefore no rotation of the cross-section is expected.

First, a simulation using the central reference system has been carried out. The only care should be taken in this case is to put the strain gauge positions in the correct reference system. Considering that their positions are given in the reference system shown by the cartesian axes

of Figure 2.14b, then the following simple transformation holds:

$$\begin{bmatrix} \bar{y} \\ \bar{z} \end{bmatrix} = \begin{bmatrix} \cos\delta & \sin\delta \\ -\sin\delta & \cos\delta \end{bmatrix} \left(\begin{bmatrix} y \\ z \end{bmatrix} - \begin{bmatrix} y_C \\ z_C \end{bmatrix} \right) \tag{2.67}$$

where δ is the angle created as in Figure 2.14b, the overbar represents quantities in the central reference system and y_C, z_C are the centroid coordinates. With this slight precaution, the same method outlined before holds also in this case.

If a centroidal but non-principal reference system is used, for example without rotating the reference system, the computation of the shear forces V_y, V_z is different. It is possible to demonstrate that for a general reference system the moments M_y and M_z are given by [70]:

$$M_y = EQ_y e_1 + EI_y e_2 + EI_{yz} e_3 \quad ; \quad M_z = EQ_z e_1 + EI_{yz} e_2 + EI_z e_3 \tag{2.68}$$

Now, for a centroidal reference system the first moments of area are null $Q_y = Q_z = 0$ and so using as usual the 0th order inverse element it is possible to derive:

$$V_y = \frac{\mathrm{d}M_y}{\mathrm{d}x}$$
$$= -6E \frac{2I_z v_1 - 2I_z v_2 + 2I_{yz} w_1 - 2I_{yz} w_2 - I_{yz} L^{(e)} \theta_{y1} - I_{yz} L^{(e)} \theta_{y2} + I_z L^{(e)} \theta_{z1} + I_z L^{(e)} \theta_{z2}}{(L^{(e)})^3}$$

$$V_z = \frac{\mathrm{d}M_z}{\mathrm{d}x}$$
$$= -6E \frac{2I_{yz} v_1 - 2I_{yz} v_2 + 2I_y w_1 - 2I_y w_2 - I_y L^{(e)} \theta_{y1} - I_y L^{(e)} \theta_{y2} + I_{yz} L^{(e)} \theta_{z1} + I_{yz} L^{(e)} \theta_{z2}}{(L^{(e)})^3}$$

$$\tag{2.69}$$

The equivalence of the results using the two reference systems has been carried out comparing the outcomes for the load case of Figure 2.14. As it is possible to see in Table 2.2, the nodal displacements given by iFEM do not change if the reference system is principal or not. Furthermore, in both cases an almost null twist is obtained (as it should since the load is applied on the shear center, Figure 2.15).

	v_2	w_2
FEM	$-4.738\,mm$	$1.517\,mm$
Central	$-4.7176\,mm$	$1.5032\,mm$
Centroidal	$-4.7176\,mm$	$1.5032\,mm$

Table 2.2: *End nodal displacements.*

If however the load is applied away from the shear center, torsion occurs and also this time the behaviour is well captured by the model as shown in Figure 2.16, where central axes have been used. However near the beam root the simple model based on the de Saint-Venant torsion theory is not capable to capture the non-linearity occurring there. This can be explained considering the constrained warping of the cross-section and will be briefly considered in Section 2.3.2.

A final note has to be done in case the torsional stiffness of the beam is relatively low. The thickness of the L cross-section has been decreased up to 0.5 mm and this drastically reduces J (Figure 2.17a). The concentrated load has been applied on the shear center and repeating the simulation a much different twist is found. Even if still close to zero, the error has increased considerably due to the small differences in the bending reconstruction coming from iFEM (blue line Figure 2.17b). Furthermore, there is a large sensitivity on input errors. For example, it is shown a simple case which might actually occur in a numerical study. That is, the strain gauge positions have been considered coincident to the nodal positions (at the mid-plane of the panels) even if the strain is extracted at top / bottom of the element, so there should be an offset of half

the thickness. If this small quantity (in this case 0.25 mm) is neglected, then the twist which is obtained is quite erroneous (red line Figure 2.17b) giving an idea of how much this type of section if sensitive because of the low torsional stiffness GJ.
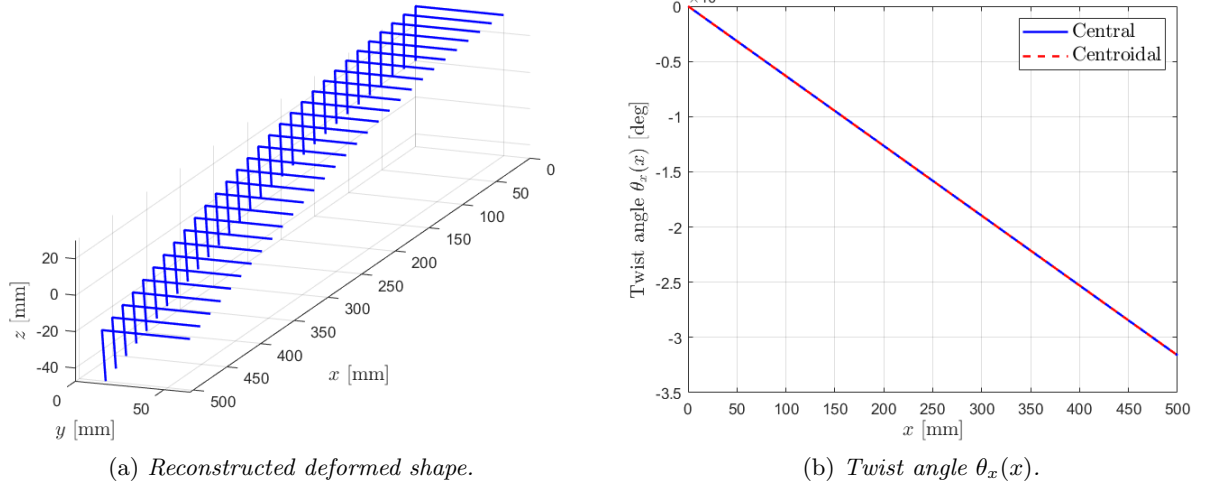

(a) *Reconstructed deformed shape.*

(b) *Twist angle $\theta_x(x)$.*

Figure 2.15: *Shape reconstruction of L-beam under concentrated load on the tip corner.*

(a) *Load case.*

(b) *Twist angle $\theta_x(x)$.*
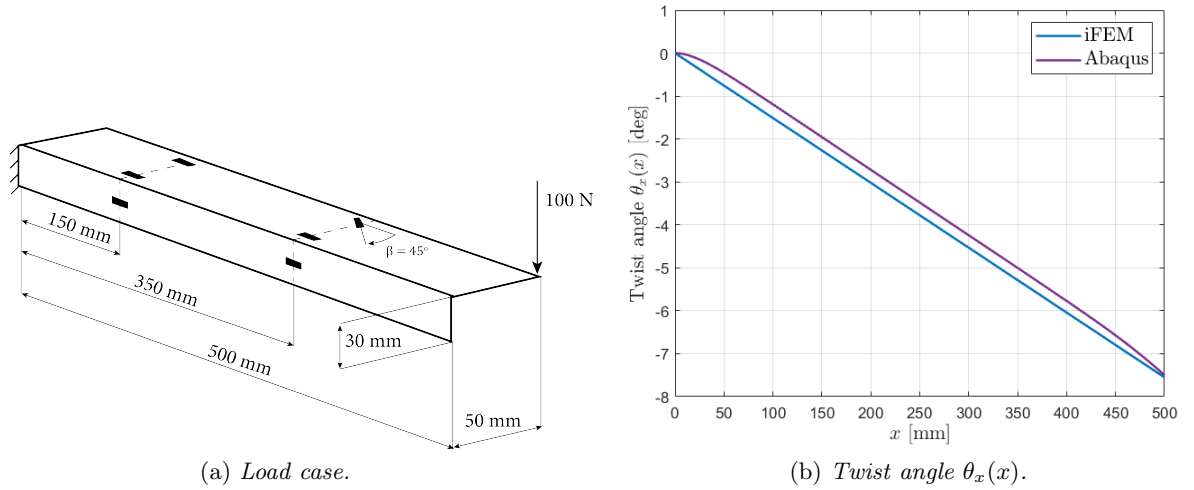
Figure 2.16: *L-beam under bending and torsion.*

(a) *Cross-section geometry.*

(b) *Twist angle $\theta_x(x)$.*
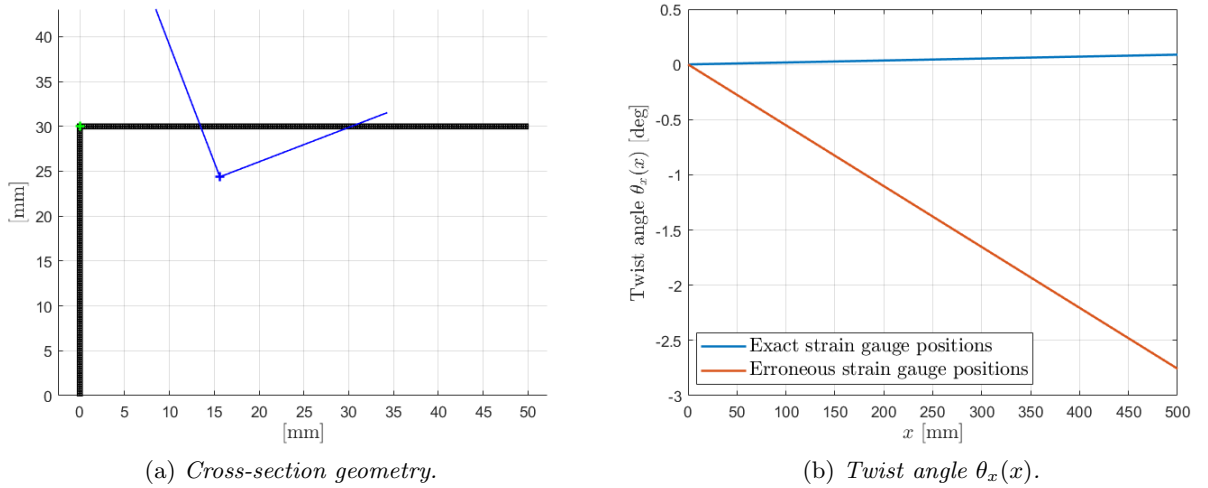
Figure 2.17: *L-beam with law torsional stiffness.*

31

2.2.5 Application to thin-walled airfoil beam

In this section the theory developed so far is applied to a prismatic beam with thin-walled airfoil cross-section. The airfoil studied is shown in Figure 2.18: it has been discretized with quadrilateral quadratic elements and in Table 2.3 some properties of the cross-section have been listed.
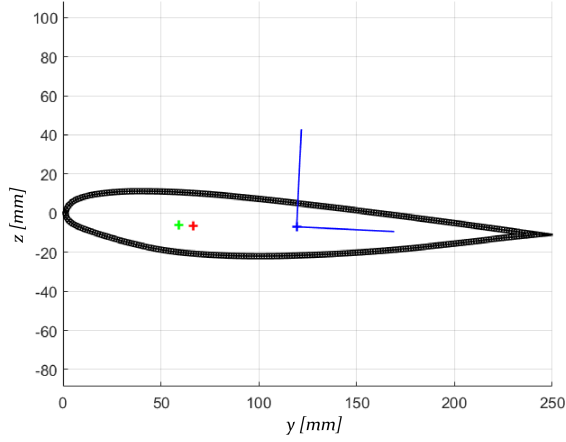
Figure 2.18: *Aifoil cross-section.*

Chord	$250\,\text{mm}$
Wall thickness	$2.5\,\text{mm}$
y_C	$119.3\,\text{mm}$
z_C	$-7.031\,\text{mm}$
y_S (Trefftz)	$66.48\,\text{mm}$
z_S (Trefftz)	$-6.438\,\text{mm}$
y_S (Elasticity)	$59.03\,\text{mm}$
z_S (Elasticity)	$-6.08\,\text{mm}$
I_y	$1.5442e5\,\text{mm}^4$
I_z	$6.1370e6\,\text{mm}^4$
δ	$-0.0484\,\text{rad}$
J	$5.1214e5\,\text{mm}^4$
E, ν	$70e3\,\text{MPa}, 0.3$

Table 2.3: *Cross-section properties.*

The wing is shown in Figure 2.19 together with the strain gauge positions. For the moment a single inverse element will be used, and so five strain gauges plus one to measure the twist are sufficient. The details of the FE model from which the strains will be extracted are reported in Appendix M.
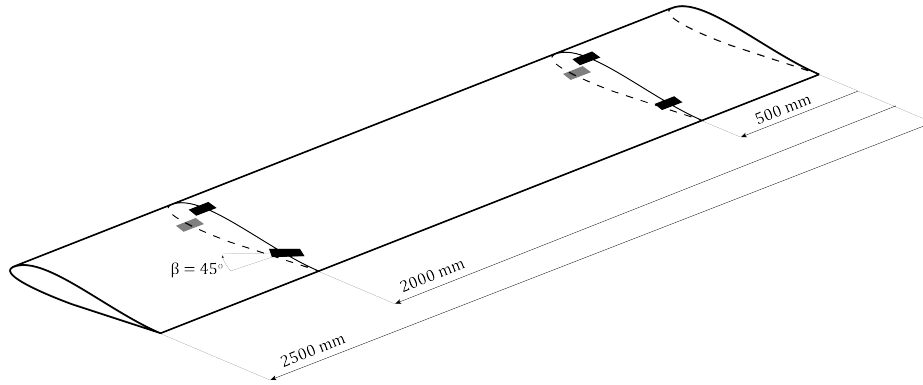
Figure 2.19: *Wing discretized with a single inverse element and strain gauge positions.*

As it is possible to see from Figure 2.18, the Trefftz definition of shear center and the elasticity solution give slightly different results. So, before proceeding it has been decided to choose the most accurate answer between the two. The wing model has been built in `Abaqus` simply from the extrusion of the cross-section of Figure 2.18 and a concentrated load has been applied on the two shear center positions as shown in Figure 2.20a. Then, from the leading edge and trailing edge vertical displacements the twist angle has been obtained. It is reported in Figure 2.20b along the wing span. The elasticity solution seems to give results overall closer to zero (which is the expected answer since the load is applied on the shear center) and therefore it is deemed more accurate and it will be only one considered in the following.

At this point the three-dimensional wing model is used to extract the shear stresses where the strain gauge oriented with angle β is positioned. So, a unit load is applied on the shear center (respectively V_y, V_z and M_x) and the shear stresses are recorded as reported in Table 2.4.

	Shear stress
τ_{12}^y	$-9.931\,10^{-4}\,\mathrm{MPa/N}$
τ_{12}^z	$4.634\,10^{-3}\,\mathrm{MPa/N}$
τ_{12}^t	$4.585\,10^{-5}\,\mathrm{MPa/Nmm}$

Table 2.4: *Shear stresses given by unit loads.*
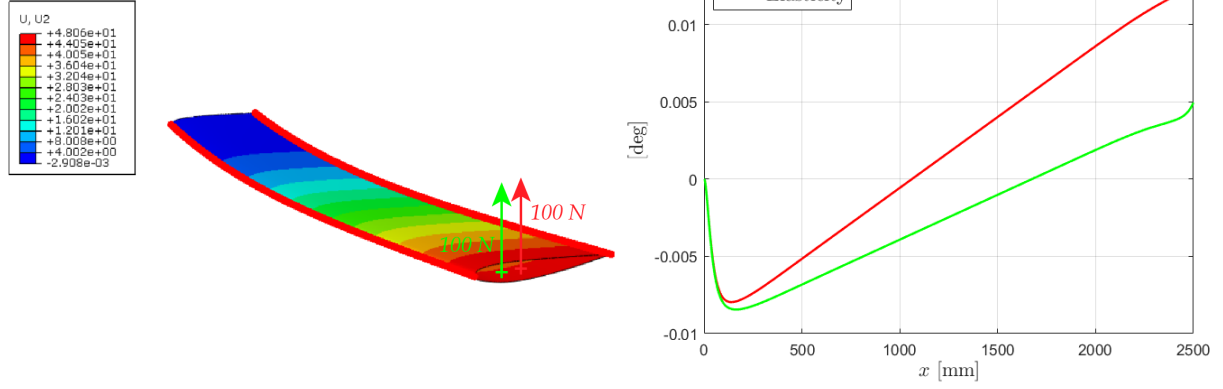
(a) *Application of concentrated loads at beam tip.*

(b) *Twist angle obtained applying the load on the two possible positions for the shear center.*

Figure 2.20: *Study of the accuracy of the shear center position for the two results obtained respectively by the Trefftz definition and by the elasticity-based solution.*

Note that the values of the shear stress found theoretically depend only on the position on the cross-section, and not on the span position. However, in order to avoid the presence of edge effects, values at the middle of the span should preferably be used. At this point everything is known and some simulations can be carried out.
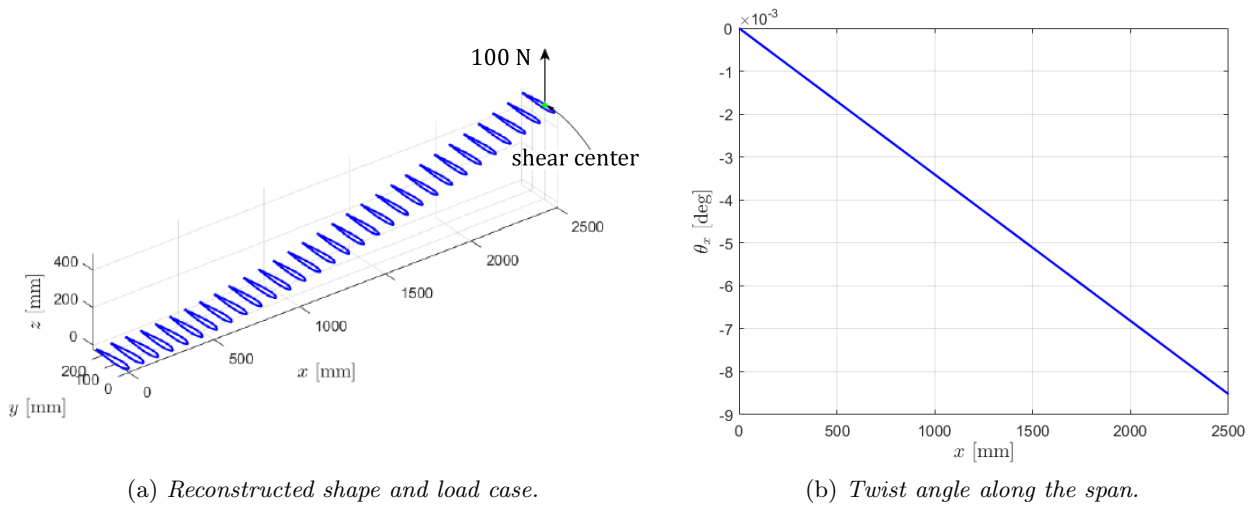
(a) *Reconstructed shape and load case.*

(b) *Twist angle along the span.*

Figure 2.21: *Wing with tip force applied on the shear center.*

First, in order to assess the results, a force in the shear center has been applied as shown in Figure 2.21a. As expected, the twist angle is close to zero (the error has the same order of

magnitude of the one shown in Figure 2.20b).

Next, again a concentrated tip force has been applied, but this time on the leading edge as in Figure 2.22. Plotting the twist angle along the span, there is a relatively good agreement between FEM results and the reconstructed ones (Figure 2.22b). Also the bending deformation (from iFEM) closely matches the reference one.

(a) *Reconstructed shape and load case.*

(b) *Twist angle along the span.*
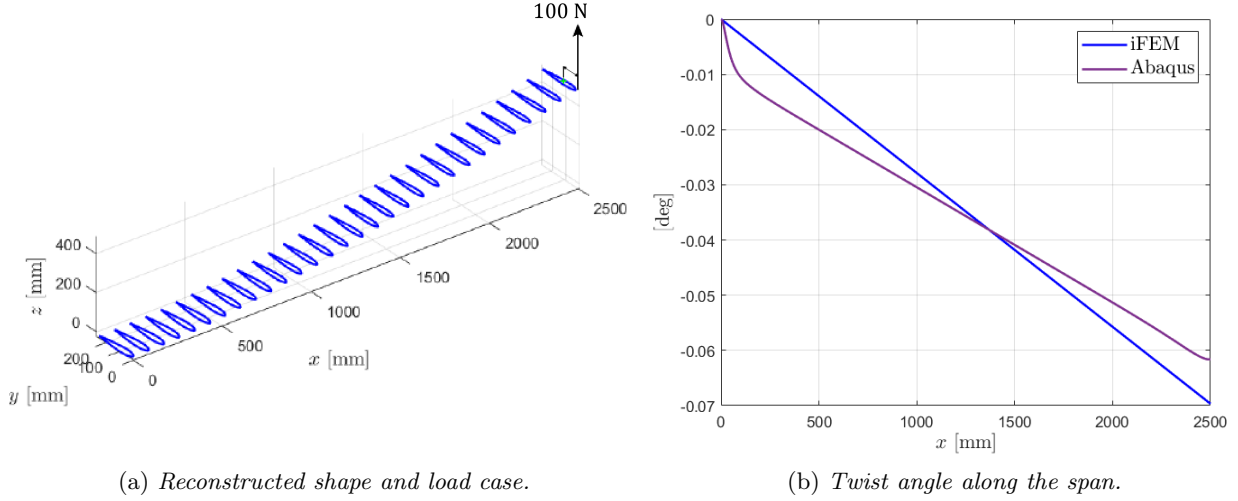
Figure 2.22: *Wing with tip force applied on the leading edge.*

From Figure 2.22b the twist recorded from the direct FEM simulation is not exactly linear, especially near the wing root. This effect is mainly to be attributed to the low torsion in comparison to the shear force applied which makes the expected solution less close w.r.t. the de Saint-Venant torsion theory. For higher torques the twist rate becomes closer and closer to a constant value. For example, in Figure 2.23 some results are presented: using the same shear force (100 N) applied on the tip shear center, different values of torque M_x have been used (respectively 10^6 Nmm, 10^4 Nmm, 10^2 Nmm). For larger values of torque the expected linear twist is obtained, while for lower values this type of solution is completely lost.

(a) $M_x = 10^6$ Nmm

(b) $M_x = 10^4$ Nmm

(c) $M_x = 10^2$ Nmm
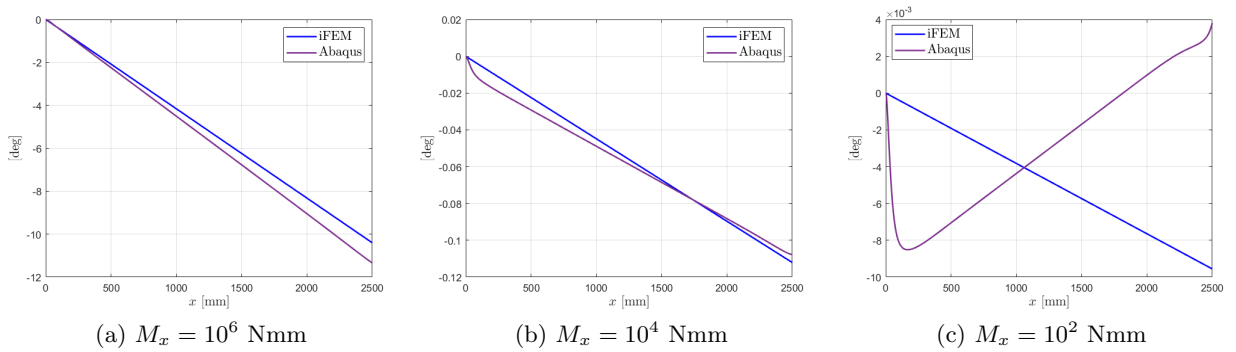
Figure 2.23: *Twist angle reconstruction using different torques applied at the beam tip.*

2.3 Improvements in the bending and twist reconstruction for 0th order Euler-Bernoulli inverse elements

In this section some improvements of the shape sensing framework are presented. The simulations will again be carried out with the 0th order inverse beam element and it will be suggested a way to obtain satisfactory reconstructed shapes in case of distributed loads without increasing the element order / number of elements. The details are given in Section 2.3.1. It follows a brief discussion on how to take into account restrained warping for the twist reconstruction (Section 2.3.2) and finally in Section 2.3.3 it is computed the deformation of a prismatic clamped beam with airfoil profile under a relatively complex pressure field from FE strain measurements.

2.3.1 Tuning strain gauge positions for bending and twist reconstruction

From the applications studied in the previous sections it might be concluded that with the shape sensing framework defined it is possible to get quite satisfactory results, simplifying a 3D structure with a much simpler beam model. However, it must be recalled that the inverse element formulation used so far gives exact answers only when nodal forces are applied (that is with no distributed forces). If this is not the case, the 0th order iFEM formulation would give just an approximation of the displacement field. In order to increase the accuracy two ways can be followed along the same lines of what happens for the direct FE formulation:
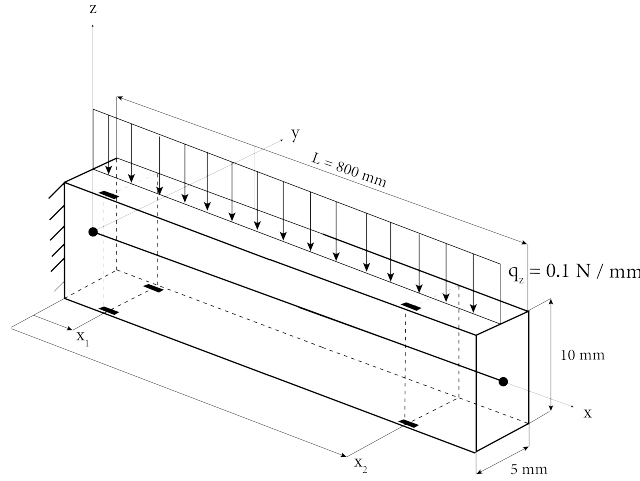
Figure 2.24: *Beam discretized with a single inverse element (5 strain gauges for bending reconstruction) under a constant distributed load.*

(a) $x_1 = 0$, $x_2 = L$ (b) $x_1 = L/3$, $x_2 = L$ (c) $x_1 = L/3$, $x_2 = L/2$
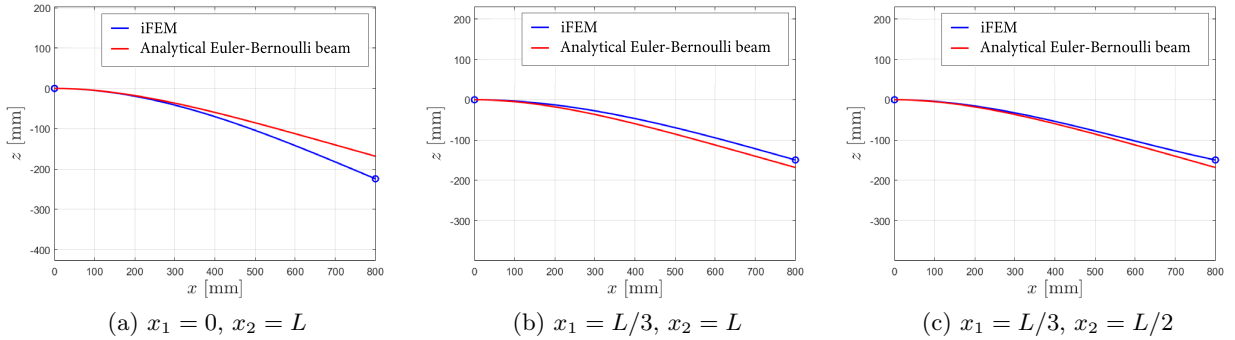
Figure 2.25: *Bending deflection reconstruction using different values for the strain gauges axial positions x_1 and x_2.*

- "h-refinement": either increasing the number of 0th order inverse elements. This occurs at the cost of five strain gauges per element (not counting the one used for the torsion sensitivity).

- "p-refinement": or increasing the order of the element, using the so called 1st order beam inverse element, specifically developed for the case of (constant) distributed loads applied on the element. The inverse Euler-Bernoulli beam element developed in [48] needs seven strain measurements in at least three different locations for each element (again, not counting the strain gauge used for torsion sensitivity).

In this shape sensing context however, a third factor can exploited, that is the strain gauge positions. Until now, no particular reasoning has been used to decide on the locations of the strain gauges. In fact, always concentrated nodal forces have been used, and so the axial position was not crucial since the axial strain varies linearly along the span. For more complex load cases this is no more true (basically because the strain might be no more linear). As it will be clear from the next paragraphs, choosing the right positions can lead to more accurate results.
Just to intuitively show the importance of the axial sensor positions, consider the Euler-Bernoulli beam shown in Figure 2.24. A single 0th order inverse element has been used and so five strain gauges (in this discussion the twist is not important and will not be considered). However, a constant distributed load has been applied. It is possible to plot the deformed shape reconstruction using different axial strain gauge positions x_1 and x_2. Some results are shown in Figure 2.25.
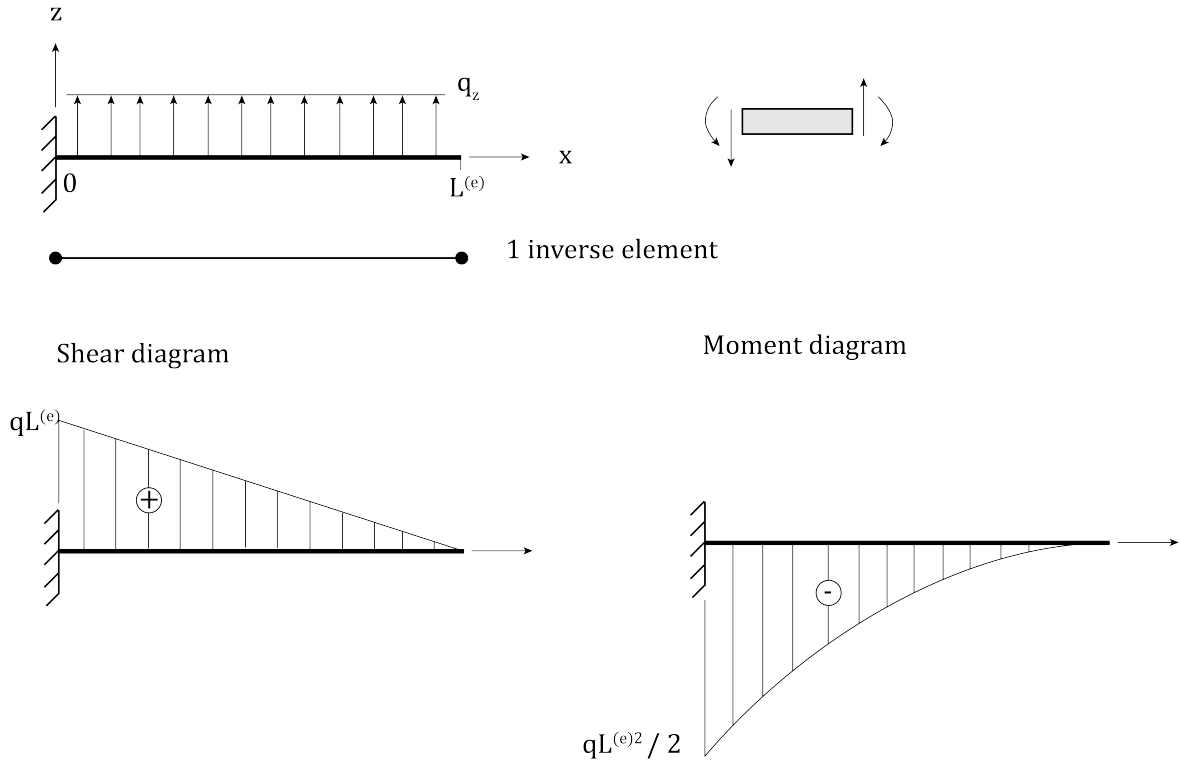
Figure 2.26: *Clamped beam modeled as a single inverse element under constant distributed load, together with the well known diagrams for the internal shear force and the internal moment.*

As it is possible to see, the results change quite significantly depending on the values used for x_1 and x_2. It follows naturally the question: is it possible to find a combination of x_1 and x_2 such that there is good reconstruction of the deformed shape? In other words, is it possible to

recover the displacement under a distributed load using a 0th order element?

Of course, a perfect correspondence is not possible, since higher order shape functions should be used instead of the Hermite cubic ones employed for the 0th order element. However, it is possible to find a sensor configuration such that the resulting *linear* strain distribution gives the same maximum deformation for the distributed load case. The maximum deformation is, in most cases, at the beam element tip and so there is the need to match this value.

Consider a clamped beam under the distributed load q_z as in Figure 2.26. For now, the beam will be modeled with a single inverse element and $x \in [0, L^{(e)}]$ with $L^{(e)}$ the element length.

The internal shear force and internal moment diagrams can be easily computed and are given by:

$$V_z(x) = q_z(L - x) \tag{2.70}$$

$$\overline{M}_y(x) = -\frac{q_z}{2}x^2 + q_z L^{(e)} x - \frac{q_z L^{(e)2}}{2} \tag{2.71}$$

Now, from the constitutive equations and using the Euler-Bernoulli assumptions in pure bending:

$$-\frac{\mathrm{d}^2 w}{\mathrm{d}x^2} = \frac{M_y(x)}{EI} \quad ; \quad \varepsilon_x(x) = \frac{M_y(x)}{EI}z \tag{2.72}$$

In other words, the axial strain for a fixed value z has the same shape of the bending moment $M_y(x)$ and the displacement can be simply obtained by:

$$w(x) = -\iint \frac{M_y(x)}{EI}\mathrm{d}x\mathrm{d}x \tag{2.73}$$

Consider now two axial strain measurements along the beam span at x_1 and x_2. Since the strain distribution is the same of the moment one, consider that directly the moment $M_y(x)$ is measured as in Figure 2.27 at the sampling locations x_1 and x_2. Using a 0th order inverse beam element effectively means that $M_y(x)$ is taken as a linear function since nodal forces produce a linear-varying strain along the element.
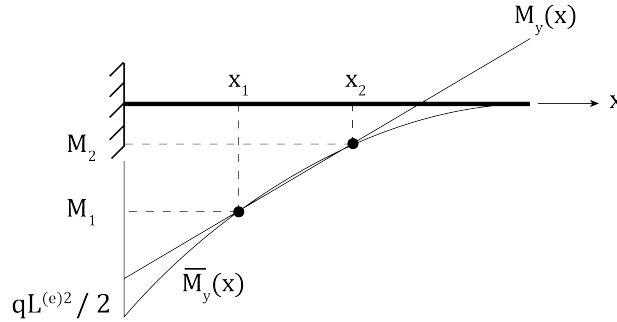
Figure 2.27: *Internal moment distribution over the element span:* $\overline{M}_y(x)$ *(true one) and* $M_y(x)$ *(sampled one).*

The linear moment $M_y(x)$ along the element is:

$$M_y(x) = \frac{M_2 - M_1}{x_2 - x_1}x - x_1\left(\frac{M_2 - M_1}{x_2 - x_1}\right) + M_1 \tag{2.74}$$

where:

$$M_1 = \overline{M}_y(x_1) = -\frac{q_z}{2}x_1^2 + q_z L^{(e)} x_1 - \frac{q_z L^{(e)2}}{2}$$
$$M_2 = \overline{M}_y(x_2) = -\frac{q_z}{2}x_2^2 + q_z L^{(e)} x_2 - \frac{q_z L^{(e)2}}{2} \tag{2.75}$$

Therefore:

$$M_y(x) = \left(-\frac{q_z}{2}(x_1 + x_2) + q_z L^{(e)}\right)x - x_1\left(-\frac{q_z}{2}(x_1 + x_2) + q_z L^{(e)}\right) +$$
$$- \frac{q_z}{2}x_1^2 + q_z L^{(e)}x_1 - \frac{q_z L^{(e)2}}{2} \tag{2.76}$$

It is desired that the displacement w at $x = L^{(e)}$ given by $M_y(x)$ is the same of the one $\overline{w}$ produced by $\overline{M}_y(x)$, so the following condition should hold:

$$\underbrace{-\frac{1}{EI_y}\iint_0^{L^{(e)}} M_y(x)\mathrm{d}x\mathrm{d}x}_{w(x = L^{(e)})} = \underbrace{-\frac{1}{EI_y}\iint_0^{L^{(e)}} \overline{M}_y(x)\mathrm{d}x\mathrm{d}x}_{\overline{w}(x = L^{(e)})} \tag{2.77}$$

The integral of the right hand side is given by:

$$\iint \overline{M}_y(x)\mathrm{d}x\mathrm{d}x = -\frac{q_z}{24}x^4 + \frac{q_z L^{(e)}}{6}x^3 - \frac{q_z L^{(e)}}{4}x^2 + C_1 x + C_2 \tag{2.78}$$

The integral of the left hand side is given by:

$$\iint M_y(x)\mathrm{d}x\mathrm{d}x = \left(-\frac{q_z}{2}(x_1 + x_2) + q_z L^{(e)}\right)\frac{x^3}{6} - x_1\left(-\frac{q_z}{2}(x_1 + x_2) + q_z L^{(e)}\right)\frac{x^2}{2} +$$
$$+ \left(-\frac{q_z}{2}x_1^2 + q_z L^{(e)}x_1 - \frac{q_z L^{(e)2}}{2}\right)\frac{x^2}{2} + C_3 x + C_4 \tag{2.79}$$

Now, regarding the integration constants C_1, C_2, C_3, C_4, the following conditions at $x = 0$ can be set to identify them:

$$\begin{cases} w(0) = \overline{w}(0) & \Rightarrow \quad C_2 = C_4 \\ \left.\dfrac{\mathrm{d}w}{\mathrm{d}x}\right|_{x=0} = \left.\dfrac{\mathrm{d}\overline{w}}{\mathrm{d}x}\right|_{x=0} & \Rightarrow \quad C_1 = C_3 \end{cases} \tag{2.80}$$

The same deflection at $x = L^{(e)}$ can be required in order to obtain a relation between x_1 and x_2:

$$w(L^{(e)}) = \overline{w}(L^{(e)}) \quad \Rightarrow \tag{2.81}$$

$$\Rightarrow \quad -\frac{q_z L^{(e)4}}{24} + \frac{q_z L^{(e)4}}{6} = -\frac{q_z L^{(e)3}}{12}x_1 - -\frac{q_z L^{(e)3}}{12}x_2 + \frac{q_z L^{(e)2}}{4}x_1 x_2 + \frac{q_z L^{(e)4}}{6}$$

$$\Rightarrow \quad x_2 = \frac{L^{(e)}(L^{(e)} - 2x_1)}{2(L^{(e)} - 3x_1)} \tag{2.82}$$

From Eq.(2.82) therefore, choosing x_1, it is possible to obtain the span position x_2 for which the linear inverse element is able to recover the exact tip displacement under a uniform constant distributed load. It might be important to note that x_1 cannot be chosen completely arbitrarily since $x_2 \leq L^{(e)}$, that is x_2 must lie inside the element domain. As a consequence:

$$\frac{L^{(e)}(L^{(e)} - 2x_1)}{2(L^{(e)} - 3x_1)} \leq L^{(e)} \quad \Rightarrow \quad \frac{2}{3}x_1 \leq \frac{L^{(e)}}{3} - \frac{L^{(e)}}{6} \quad \Rightarrow \quad x_1 \leq \frac{L^{(e)}}{4} \tag{2.83}$$

So the first span position must be at most at a quarter of the element length. Using this approach, for the previous study case (Figure 2.24) with for example $x_1 = L^{(e)}/4$ and $x_2 = L^{(e)}$ the deformed shape of Figure 2.28 is obtained.
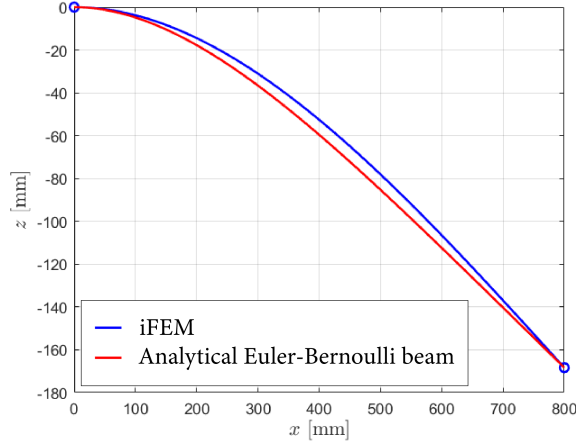
Figure 2.28: *Bending deflection of clamped beam under uniform load: comparison between analytical results and iFEM with "optimal" sensor positions.*

Now also the exact internal shear force variation along the element can be recovered (see shear diagram of Figure 2.26). Using the 0th order inverse element formulation a constant internal shear force would be obtained from the equilibrium equations (recall Eq.(2.44)). The value obtained is the derivative of $M_y(x)$ and so, using Eq.(2.76):

$$V_z = \frac{\mathrm{d}M_y}{\mathrm{d}x} = -\frac{q_z}{2}(x_1 + x_2) + q_z L^{(e)} \quad \Rightarrow \quad q_z = \frac{V_z}{L^{(e)} - \dfrac{x_1 + x_2}{2}} \tag{2.84}$$

where it is important to note that V_z is known (computed from Eq.(2.44)) and so the value of q_z can be directly obtained. This means that the exact internal shear force distribution can be known for every span position x as:

$$V_z(x) = q_z L^{(e)} \left(1 - \frac{x}{L^{(e)}}\right) \tag{2.85}$$
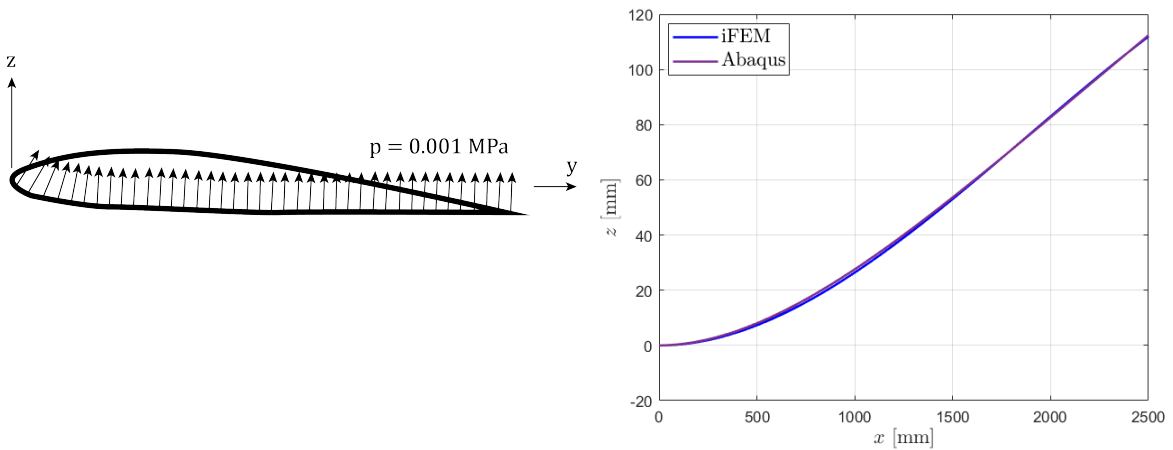
(a) *Pressure distribution on wing section.*

(b) *Deformed shape reconstruction: comparison between iFEM and direct FEM results (Abaqus).*

Figure 2.29: *Clamped thin-walled wing subjected to uniform pressure.*

In order to show some results with this method, consider again the wing studied in Section 2.2.5. Now the strain gauge axial positions are chosen according to Eq.(2.82). In particular,

$x_1 = 400\,\text{mm}$ and $x_2 = 1634.6\,\text{mm}$. With this sensor configuration, the wing has been subjected to a uniform pressure applied on the bottom skin as shown in Figure 2.29a. Applying iFEM the bending deformation closely matches the reference one (Figure 2.29b).

Improvements can be seen also for the torsional behavior. Considering again the wing under constant pressure (Figure 2.29a), as usual the reference twist angle has been computed from the FEM simulation comparing leading edge and trailing edge displacements. If a constant internal shear force is used, as it comes from the 0th order inverse element, then completely wrong results are obtained (Figure 2.31a). This can intuitively be explained looking at the internal shear force diagram (Figure 2.30): the (constant) internal shear force obtained is much higher than the real one. As a consequence the shear stress due to torsion is wrongly assumed to be smaller leading to a very small twist rate.
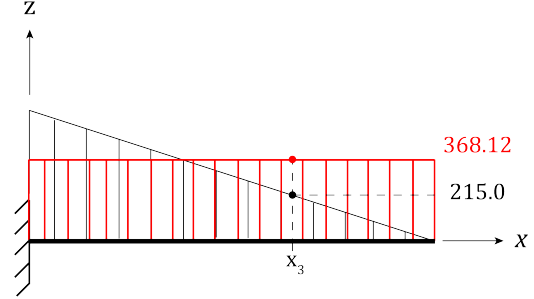
Figure 2.30: *Comparison of internal shear force distribution along the beam span between constant and linear case. The shear-sensitive strain gauge is positioned at x_3.*

If however the internal shear force is recovered using Eq.(2.85), then better results are obtained as illustrated in Figure 2.31b. Since the torsion angle is approximated linearly, a large influence is also dictated by the position of the shear-sensitive strain gauge. This aspect will be covered in a later paragraph.
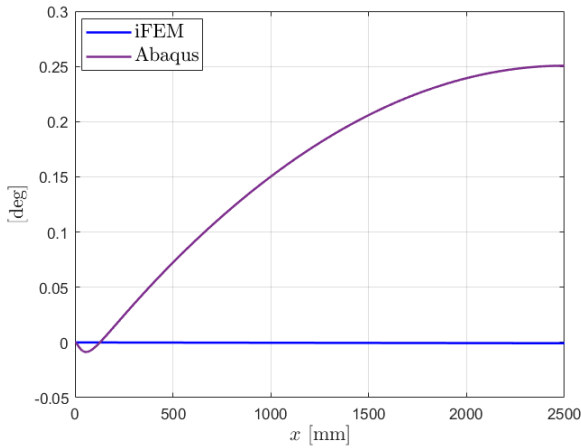
(a) *Using the constant internal shear force.*
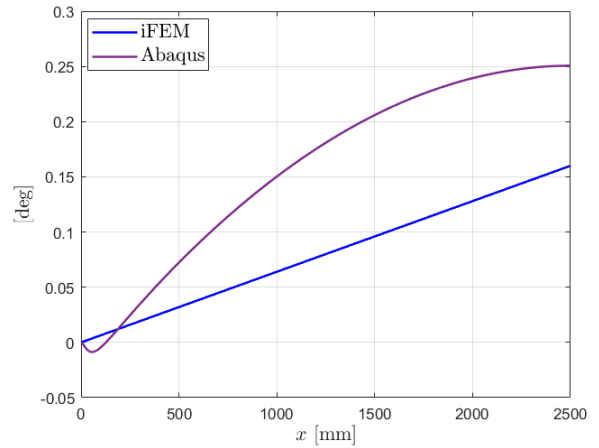
(b) *Using the recovered linear distribution for the internal shear force.*

Figure 2.31: *Twist angle reconstruction for wing under constant pressure.*

So far, a single inverse element has always been considered in simulating the wing. Of course, more elements can be used. The procedure to retrieve a linear shear distribution from a constant one described before for a single element can be extended to more than one element with only slight changes (Figure 2.32).
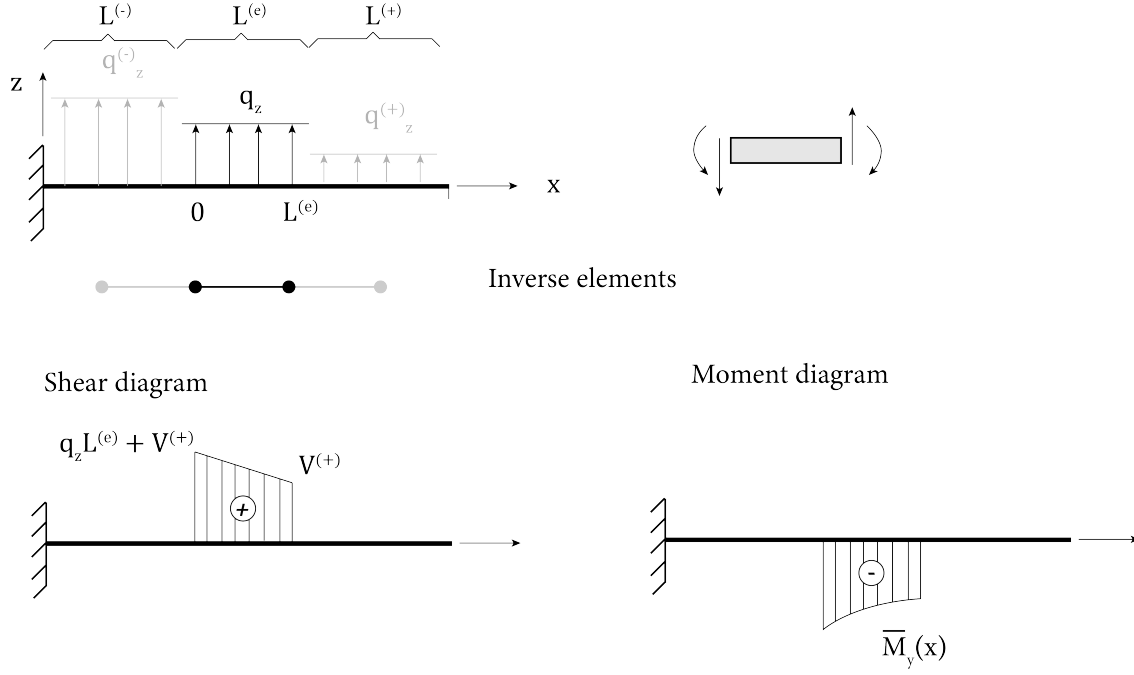
Figure 2.32: *Clamped beam modeled with multiple inverse elements under piece-wise constant distributed loads, together with the well-known diagrams for the internal shear force and the internal moment.*

On the right and left hand side of the inverse element taken into consideration the presence of other elements is assumed, each one with its *constant* load distribution. So, it is possible to think that on the right of the element there is a constant load $q_z^{(+)}$ and on the left $q_z^{(-)}$ (if more than three elements are present, then $q_z^{(+)}$ and $q_z^{(-)}$ can be seen as the average values of the the elements respectively on the right and left side). Then, the internal shear force distribution on the element is:

$$V_z(x) = -q_z x + q_z L^{(e)} + V_z^{(+)} \tag{2.86}$$

with $V_z^{(+)} = q_z^{(+)} L^{(+)}$. And the moment distribution is:

$$\overline{M}_y(x) = -\frac{q_z}{2} x^2 + (q_z L^{(e)} + V_z^{(+)})x + \overline{M}(0) \tag{2.87}$$

with:

$$\overline{M}(0) = -\frac{q_z L^{(e)2}}{2} - V_z^{(+)} L^{(e)} - V_z^{(+)} \frac{L^{(+)}}{2} \tag{2.88}$$

And from $\overline{M}_y(x)$ the moment $M_y(x)$ can be computed as before. Now the integrals of the moments become:

$$\iint \overline{M}_y(x) \mathrm{d}x \mathrm{d}x = -\frac{q_z}{24} x^4 + (q_z L^{(e)} + V^{(+)}) \frac{x^3}{6} + \overline{M}_y(0) \frac{x^2}{2} + C_1 x + C_2 \tag{2.89}$$

$$\iint M_y(x) \mathrm{d}x \mathrm{d}x = \left(-\frac{q_z}{2}(x_1 + x_2) + q_z L^{(e)} + V_z^{(+)} \right) \frac{x^3}{6} - x_1 \left(-\frac{q_z}{2}(x_1 + x_2) + q_z L^{(e)} + V_z^{(+)} \right) \frac{x^2}{2} +$$
$$+ \left(-\frac{q_z}{2} x_1^2 + q_z L^{(e)} x_1 + V_z^{(+)} x_1 \right) \frac{x^2}{2} + \overline{M}_y(0) \frac{x^2}{2} + C_3 x + C_4 \tag{2.90}$$

Evaluating Eq.(2.89) and Eq.(2.90) at $x = L^{(e)}$ and equating them, it is possible to obtain that all the terms related to $V_z^{(+)}$ can be simplified and the same relation between x_1 and x_2 can be

found as in Eq.(2.82). The difference now consists in the computation of q_z:

$$V_z = \frac{\mathrm{d}M_y}{\mathrm{d}x} = -\frac{q_z}{2}(x_1 + x_2) + q_z L^{(e)} + V_z^{(+)} \quad \Rightarrow \quad q_z = \frac{V_z - V_z^{(+)}}{L^{(e)} - \dfrac{x_1 + x_2}{2}} \tag{2.91}$$

From which the internal shear force distribution over the element can be known using Eq.(2.86). It is important to note that $V_z^{(+)}$ is not known for every element, but just for the last one (the one with a free end) since in this case $V_z^{(+)} = 0$. So, the computation should proceed "backwards", from the tip element to the root one. In this way, from a piecewise constant shear distribution it is possible to retrieve a piecewise linear shear distribution (see Figure 2.33 for an intuitive representation).
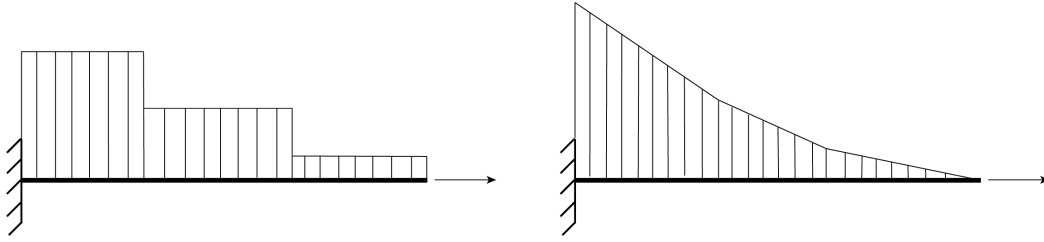
Figure 2.33: *The outlined workflow allows using 0th order inverse elements not to obtain a step-wise constant internal shear force (left), but a step-wise linear one (right).*

In order to give a small example, the same wing and loading condition (uniform pressure) as before are studied here using two inverse elements. This example will be used to highlight the importance of the position of the shear-sensitive strain gauges used for the torsion sensitivity. In particular, three different positions have been chosen for these strain gauges as illustrated in Figure 2.34:

- At the position $x_3 = x_1 = 200\,\mathrm{mm}$, that is coincident with the position of the first set of the gauges used for the bending reconstruction with iFEM.

- In the middle of the each element: $x_3 = L^{(e)}/2$.

- At the position $x_3 = x_2 = 817.3\,\mathrm{mm}$, that is coincident with the position of the second set of the gauges used for the bending reconstruction with iFEM.
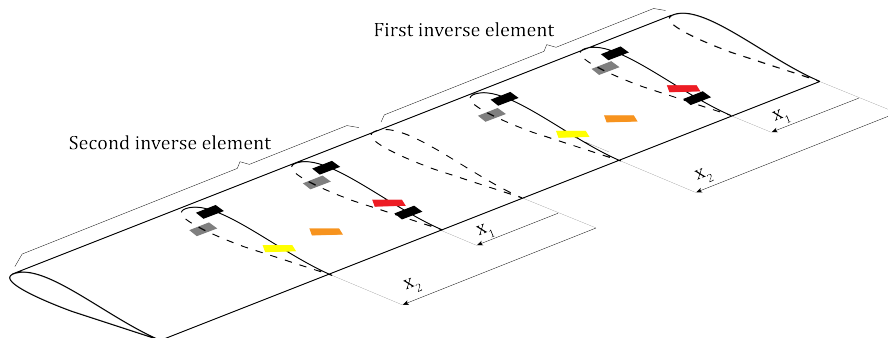
Figure 2.34: *Wing discretized with two inverse elements, each one with strain gauges at axial position x_1 and x_2. The shear-sensitive strain gauges are positioned at x_3.*

Carrying out the shape sensing study for the uniform pressure load case, the twist angle can be computed using the piece-wise linear distribution of the shear force as explained before. In this way the results of Figure 2.35 can be obtained.

(a) $x_3 = x_1$ (b) $x_3 = L^{(e)}/2$ (c) $x_3 = x_2$
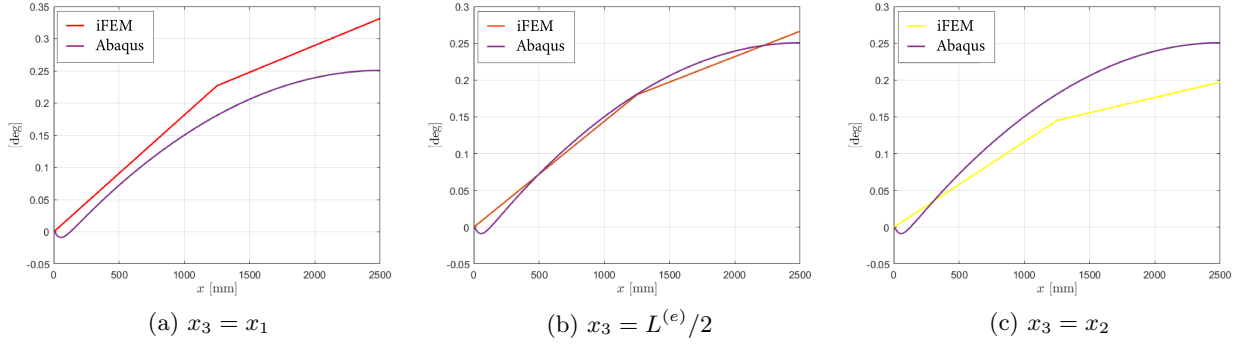
Figure 2.35: *Twist angle reconstruction for strain-sensitive strain gauges positioned at three different axial positions.*

As expected, the results change depending on the gauge positions and using a gauge at the middle of the element brings the most consistent results given the fact that an "average" twist rate is used. This statement can actually be easily verified assuming that the beam follows the de Saint-Venant torsion theory. Considering a constant distributed load, the torsion moment along the element span is linear, as in Figure 2.36 and given by:

$$\overline{M}_x(x) = (L^{(e)} - x)\overline{m}_x \tag{2.92}$$

with $\overline{m}_x$ the distributed torsional moment.
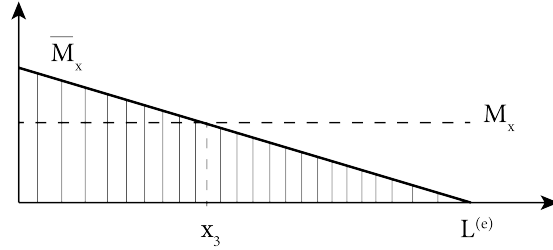
Figure 2.36: *Internal torsional moment for a beam loaded by a constant distributed load and free end.*

The measured value of M_x implies that the moment distribution is assumed constant, since τ_{12}^t is computed under this assumption (Eq.(2.46)). Furthermore, it can be seen as sampling $\overline{M}_x(x)$ at $x = x_3$ (Figure 2.36). Therefore $M_x = (L^{(e)} - x_3)\overline{m}_x$, with $\overline{m}_x$ the unknown distributed torsional moment. The tip torsion angle given by the two distributions is equal if:

$$\int_0^{L^{(e)}} \frac{M_x}{GJ}\mathrm{d}x = \int_0^{L^{(e)}} \frac{\overline{M}_x}{GJ}\mathrm{d}x \quad \Rightarrow \quad x_3 = \frac{L^{(e)}}{2} \tag{2.93}$$

Furthermore, if directly the quadratic twist angle distribution is needed to be recovered, then it is possible to see that:

$$\overline{m}_x = \frac{M_x}{L^{(e)} - x_3} \tag{2.94}$$

43

and so the twist angle $\theta_x(x)$ can be computed along the element span as:

$$
\begin{cases}
-GJ\dfrac{\mathrm{d}^2\theta_x}{\mathrm{d}x^2} = \overline{m}_x \\[2ex]
\theta_x(0) = 0 \quad \text{(zero initial twist)} \\[2ex]
\dfrac{\mathrm{d}\theta_x}{\mathrm{d}x}\bigg|_{x_3} = \dfrac{M_x}{GJ} \quad \text{(de Saint-Venant torsional moment)}
\end{cases}
\tag{2.95}
$$

$$
\Rightarrow \quad \theta_x(x) = -\frac{\overline{m}_x}{GJ}\frac{x^2}{2} + \frac{L^{(e)}\overline{m}_x}{GJ}x
\tag{2.96}
$$

Now, for an element not connected to the free end (that is $\overline{M}_x(L^{(e)}) \neq 0$), then:

$$
\overline{M}_x(x) = (L^{(e)} - x)\overline{m}_x + M^{(+)}
\tag{2.97}
$$

with $M^{(+)}$ the internal torsion moment at the right element end. It follows that:

$$
\overline{m}_x = \frac{M_x - M^{(+)}}{L^{(+)} - x_3}
\tag{2.98}
$$

and so the twist rate along the element can be computed as:

$$
\frac{\mathrm{d}\theta_x}{\mathrm{d}x} = -\frac{\overline{m}_x}{GJ}x + \frac{M^{(+)} + L^{(e)}\overline{m}_x}{GJ}
\tag{2.99}
$$

from which the twist angle can be derived.

This procedure can be followed for the previous study case of the wing subjected to a distributed pressure analysed with two inverse elements, giving a smoother behaviour as shown in Figure 2.37.
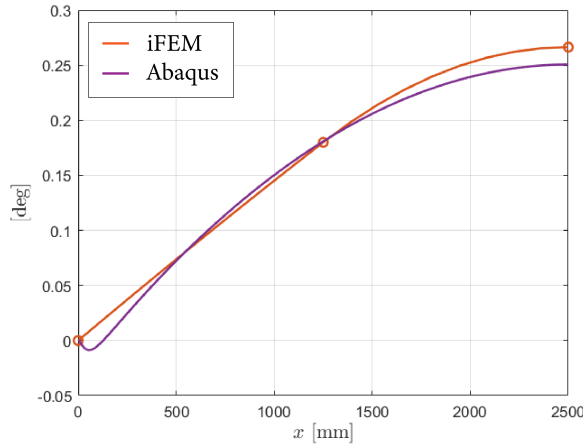
Figure 2.37: *Twist angle reconstruction using a quadratic polynomial for the twist angle for each inverse element.*

Still, the reference and reconstructed twist distribution do not exactly match. This can be mainly attributed to the fact that, since the torsion applied is relatively small, shear effects are important and the de Saint-Venant torsion theory gives just an approximation. However, it can be seen that this effect decreases significantly when torsion becomes more important (and so also the twist angle increases in magnitude). For example, using the same wing as before and

the same sensor configuration (two inverse elements with shear-sensitive strain gauges in the middle of the elements), a distributed pure torsion moment has been applied as shown in Figure 2.38a leading to a far better agreement in the twist angle plot of Figure 2.38b.

(a) *Wing geometry and loading condition.*

(b) *Twist angle reconstruction.*
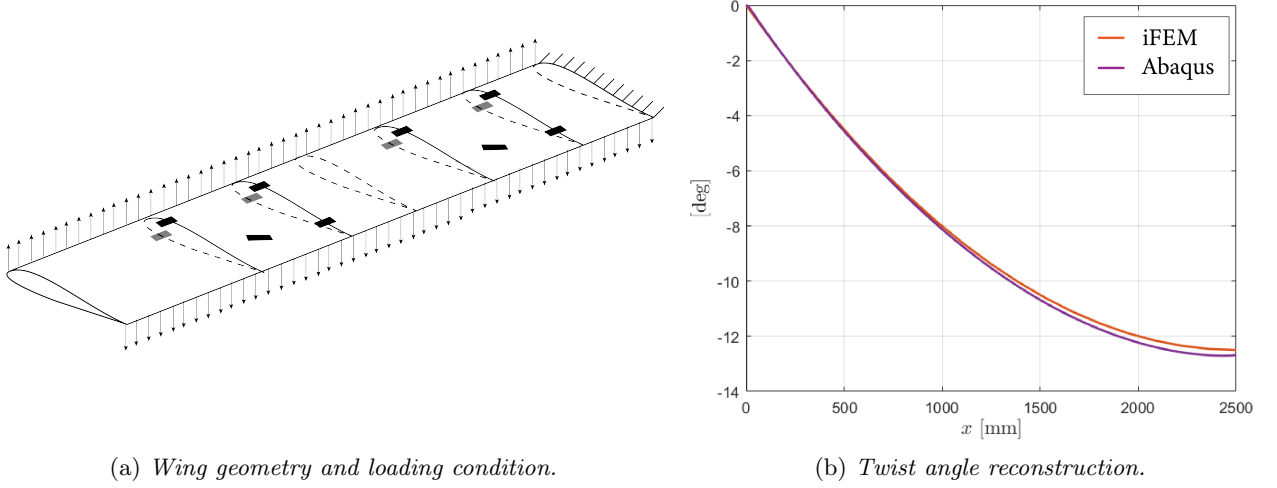
Figure 2.38: *Pure torsional load applied to the wing and corresponding twist angle reconstruction.*

2.3.2 Twist reconstruction with constrained warping

In the twist reconstruction so far the de Saint-Venant assumptions have always been taken for granted. However, if for example the beam root can be considered as completely constrained such that $\mathrm{d}\theta_x/\mathrm{d}x = 0$, it would be beneficial to take that into account. Furthermore, since the twist is reconstructed "sequentially" for each inverse element, it is advantageous to have a very good reconstruction especially near the root in order to avoid the propagation of the errors.

As it is demonstrated in [66] and [43], taking into account warping the governing equation describing the twist angle becomes:

$$E\Gamma\frac{\mathrm{d}^4\theta_x}{\mathrm{d}x^4} - GJ\frac{\mathrm{d}^2\theta_x}{\mathrm{d}x^2} = \overline{m}_x \tag{2.100}$$

where the additional term containing the fourth derivative of the twist angle θ_x is due to warping and Γ is the so-called warping constant.

In order to obtain the twist θ_x an estimate of the warping constant Γ is needed. Here, the focus will be just on thin-walled *closed* mono-cell cross-sections, since this is the case mostly analysed so far. It is assumed that the shear strain due to warping is zero and that it is all due to the Saint Venant shear strain. Under this assumption, for thin-walled sections it is possible to define the warping function as [43]:

$$\omega_P(s) = \int_0^s \left(p_P(s) - \frac{1}{t(s)}\frac{2\Omega}{\oint \frac{\mathrm{d}s}{t(s)}} \right) \mathrm{d}s \tag{2.101}$$

where $p_P(s)$ is the distance from a pole P, and therefore it depends on its location, Ω is the enclosed area, $t(s)$ the thickness and finally s the curvilinear coordinate on the profile. The warping constant is defined as:

$$\Gamma = \iint_A \omega_S^2 \,\mathrm{d}A \tag{2.102}$$

45

where the warping function is evaluated w.r.t. the shear center S. How to compute Γ is very well detailed in [43] and so here it will be just described which are the steps which have to be taken in order to compute it, without giving many justifications:

1. Compute the centroid position of the section and the centroidal second moments of area as:

$$I_z = \iint_A y^2 \, \mathrm{d}A \quad ; \quad I_y = \iint_A z^2 \, \mathrm{d}A \quad ; \quad I_{yz} = \iint_A yz \, \mathrm{d}A$$

   where, y, z are the centroidal section coordinates.

2. Compute the warping function as in Eq.(2.101) using as pole the centroid, and starting from any point on the cross section (where $\omega_C(s = 0) = 0$).

3. Normalize the warping function such that $\oint \omega_C \mathrm{d}A = 0$. This can be obtained by subtracting from $\omega_C(s)$ its "average" value:

$$\omega_C \leftarrow \omega_C - \frac{\oint p_C \omega_C \, \mathrm{d}s}{A} \tag{2.103}$$

4. Compute the so-called sectorial products of area as:

$$I_{\omega_C y} = \iint_A \omega_C z \, \mathrm{d}A$$

$$I_{\omega_C \omega_C} = \iint_A \omega_C^2 \, \mathrm{d}A$$

$$I_{\omega_C z} = \iint_A \omega_C y \, \mathrm{d}A$$

5. Compute the shear center location using the Trefftz definition:

$$y_S = \frac{I_{yz} I_{y\omega} - I_z I_{z\omega}}{I_y I_z - I_{yz}^2}$$

$$z_S = \frac{I_y I_{y\omega} - I_{yz} I_{z\omega}}{I_y I_z - I_{yz}^2} \tag{2.104}$$

6. Finally, the warping constant can be computed as:

$$\Gamma = I_{\omega_C \omega_C} + z_S I_{\omega_C y} - y_S I_{\omega_C z} \tag{2.105}$$

At this point it is also possible to obtain the warping function w.r.t. the shear center S. This can be done from $\omega_C(s)$ using a simple transformation equation as proved in [43]:

$$\omega_S(s) = \omega_C(s) + z_S y - y_S z \tag{2.106}$$

Using as example the airfoil cross section previously introduced, then the values of $\omega_S(s)$ are visually reported in Figure 2.39 and it is possible to obtain that $\Gamma = 7.4984e + 08 \, \mathrm{mm}^2$.
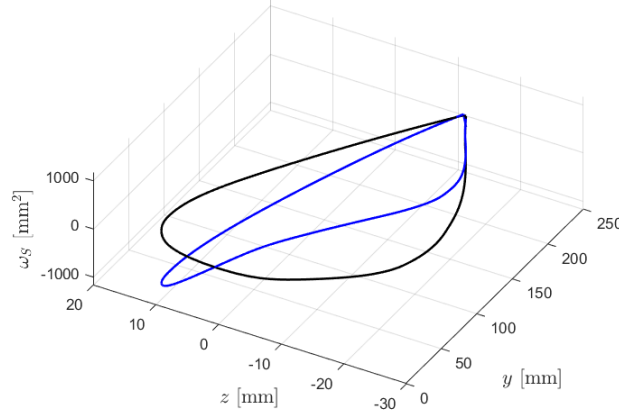
Figure 2.39: *Warping function $\omega_S(s)$ (blue line) displayed over the airfoil profile (black line).*

Now the twist angle can be recovered solving Eq.(2.100). As it is possible to see, four conditions must be known in order to obtain $\theta_x(x)$. Consider a cantilever beam under a distributed moment $\overline{m}_x$ as in Figure 2.40, it is desired to reconstruct the twist in $x \in [0, L^{(e)}]$. Then it is possible to say:
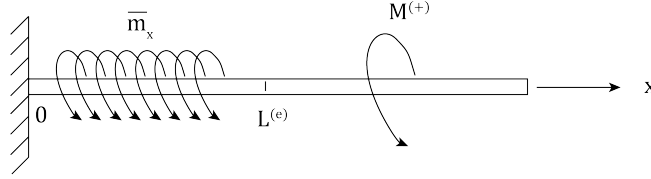
Figure 2.40: *Cantilever beam under distributed torsional moment.*

- Since the root is restrained:

$$\theta_x(x=0) = 0 \quad ; \quad \left.\frac{\mathrm{d}\theta_x}{\mathrm{d}x}\right|_{x=0} = 0 \tag{2.107}$$

- The torsional moment at $x = L^{(e)}$ must be in equilibrium with the moment applied for $x > L^{(e)}$, which here is called $M^{(+)}$. It is possible to demonstrate that in case of restrained warping the total torsional moment is given by two contributions: the de Saint-Venant part and a warping torsion moment:

$$M(x) = GJ\frac{\mathrm{d}\theta_x}{\mathrm{d}x} - E\Gamma\frac{\mathrm{d}^3\theta_x}{\mathrm{d}x^3} \tag{2.108}$$

so this condition states that:

$$M(L^{(e)}) = GJ\left.\frac{\mathrm{d}\theta_x}{\mathrm{d}x}\right|_{x=L^{(e)}} - E\Gamma\left.\frac{\mathrm{d}^3\theta_x}{\mathrm{d}x^3}\right|_{x=L^{(e)}} = M^{(+)} \tag{2.109}$$

- Finally, it is possible to say that at $x = L^{(e)}$ the influence of the restrained warping at the root is negligible. This means that the so-called bimoment at the tip is null:

$$-E\Gamma\left.\frac{\mathrm{d}^2\theta_x}{\mathrm{d}x^2}\right|_{x=L^{(e)}} = 0 \tag{2.110}$$

Now, every condition which can be applied to $\theta_x(x)$ has been stated and Eq.(2.100) can be solved. Note that the equation cannot be solved as a initial value problem, since two conditions are set at $x = 0$ and the remaining ones at $x = L^{(e)}$. The equation has been solved in MATLAB with the built-in function `bvp4c` which solves boundary value problems with finite difference methods. In order to do so, the equation must be first rewritten as a system of first order ODE. This can be done defining the following variables:

$$\phi_1 = \theta_x \quad ; \quad \phi_2 = \frac{\mathrm{d}\theta_x}{\mathrm{d}x} \quad ; \quad \phi_3 = \frac{\mathrm{d}^2\theta_x}{\mathrm{d}x^2} \quad ; \quad \phi_4 = \frac{\mathrm{d}^3\theta_x}{\mathrm{d}x^3} \tag{2.111}$$

The system of first order ODE to be solved and the corresponding boundary conditions are:

$$\begin{cases} \dfrac{\mathrm{d}\phi_1}{\mathrm{d}x} = \phi_2 \\[2mm] \dfrac{\mathrm{d}\phi_2}{\mathrm{d}x} = \phi_3 \\[2mm] \dfrac{\mathrm{d}\phi_3}{\mathrm{d}x} = \phi_4 \\[2mm] E\Gamma\dfrac{\mathrm{d}\phi_4}{\mathrm{d}x} - GJ\phi_3 = \overline{m}_x \end{cases} \qquad \begin{cases} \phi_1(0) = 0 \\[2mm] \phi_2(0) = 0 \\[2mm] E\Gamma\phi_3(L^{(e)}) = 0 \\[2mm] -E\Gamma\phi_4(L^{(e)}) + GJ\phi_2(L^{(e)}) = M^{(+)} \end{cases} \tag{2.112}$$

The snippet of MATLAB code which solves the problem is reported below for completeness.

```matlab
% Notes:
% E, Gamma, J - properties
% L - length
% Mplus - torsional moment at x = L

% System ODE
dphidx = @(x,phi) [phi(2); phi(3); phi(4); (m+G*J*phi(3)) / (E*Gamma)];
% Boundary conditions
res = @(phia,yphi) [phia(1); phia(2);
                    -E*Gamma*phib(4)+G*J*phib(2) - Mplus; % equilibrium
                    -E*Gamma*phib(3)]; % null bimoment at the tip
guess = @(x) [x 0 0 0]; % initial guess
xmesh = linspace(0,L,50); solinit = bvpinit(xmesh,guess); sol = bvp4c(dydx,res,solinit);
```

Generally, a situation similar to the one in Figure 2.41 is expected: the twist angle should be lower if the root section is restrained, therefore the beam is effectively stiffer.
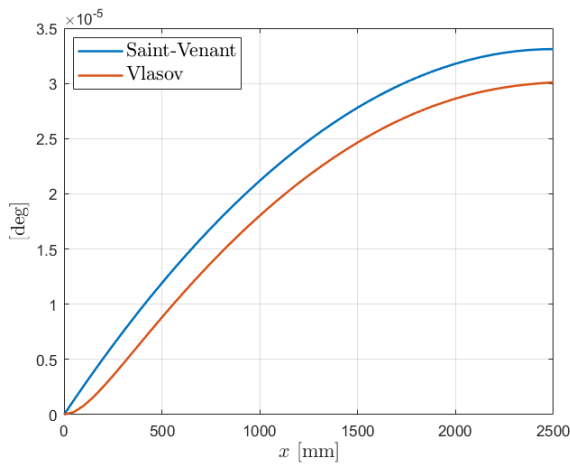
Figure 2.41: *Comparison of twist angle evolution between de Saint-Venant theory and the restrained warping case (sometimes named after Vlasov) with null initial twist rate.*
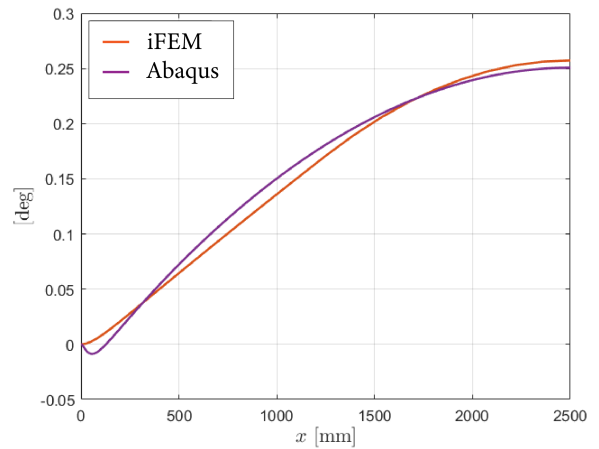
Figure 2.42: *Twist angle reconstruction under the restrained warping assumptions and comparison with the reference* `Abaqus` *results.*

This method can be followed for the previous example of Figure 2.37. The restrained warping solution has been applied to the first element, while for the second one the already used de Saint-Venant solution has been kept. In this way, the twist variation of Figure 2.42 has been obtained.

2.3.3 Application to a more complex load case

Finally, some results are given using the wing model of the previous section, but applying a more complex load case.
In particular, a pressure on the bottom skin of the wing has been applied with parabolic span distribution and linear along the chord, as in Figure 2.43.
Several simulations have been carried out:
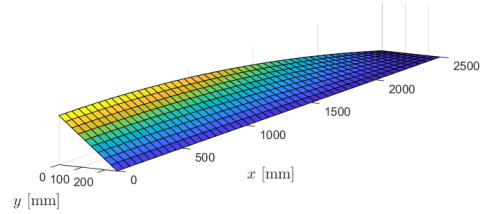
Figure 2.43: *Pressure distribution.*

- Using two equilength inverse elements (Figure 2.45a-c).

- Using a shorter element near the root (Figure 2.45d-f). In this case the twist angle is largely affected by the shear distribution near the wing root, which is very different from the one predicted from the de Saint-Venant theory.

- Using a longer element near the tip (Figure 2.45g-i).

- Using ten equilength inverse elements (Figure 2.45j-l).

Even using a larger number of inverse elements the twist near the root is not exactly recovered and this ruins the twist distribution all over the wing span. A possible improvement consists in simply not sampling the shear strain near the wing root.
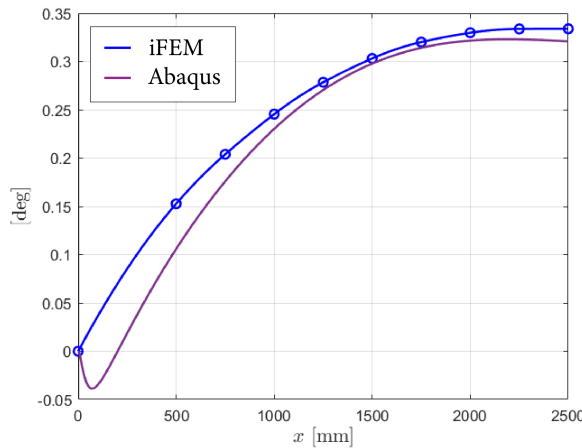
Figure 2.44: *Twist reconstruction without taking measurements near the beam root.*

For example in Figure 2.44 the first shear strain measurement has been neglected, taking into consideration just the one of the second inverse element. In this way a more accurate representation is obtained. However, it is important to underline that, as mentioned before, this occurs for a low amount of torsion and so for twist angles very low in magnitude (so with arguable importance in the reconstruction).

(a) *Deflection along z.*

(b) *Deflection along y.*

(c) *Twist angle.*

(d) *Deflection along z.*

(e) *Deflection along y.*

(f) *Twist angle.*

(g) *Deflection along z.*

(h) *Deflection along y.*

(i) *Twist angle.*

(j) *Deflection along z.*

(k) *Deflection along y.*
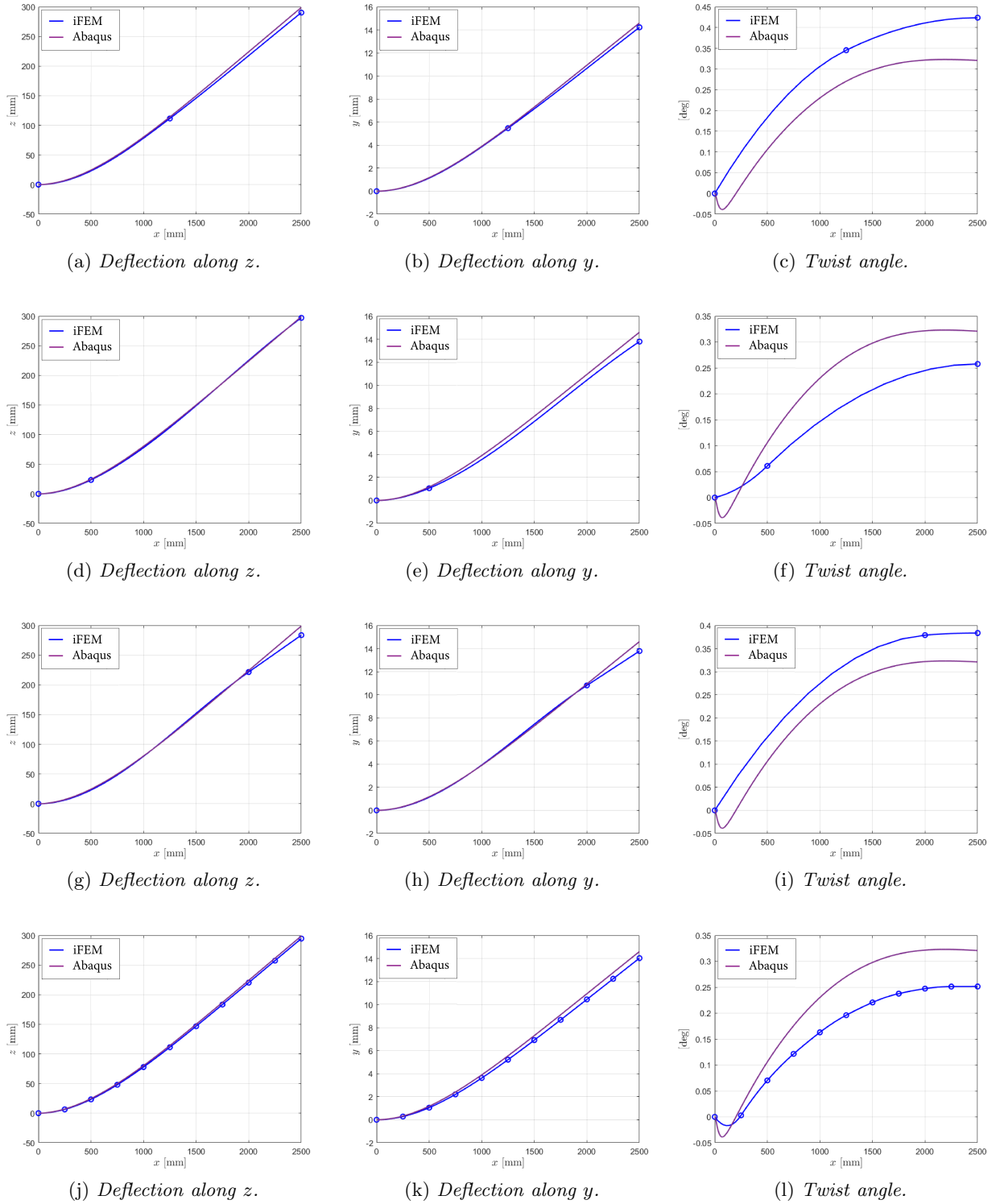
(l) *Twist angle.*

Figure 2.45: *Bending and twist reconstruction using different element numbers and sizes.*

2.4 Shape sensing for tapered beams

In this section the deflection and twist angle reconstruction for tapered beams is discussed. The main idea consists in applying a similar method to the one used for prismatic beams. The different geometry however will oblige to estimate the applied loads. This will become evident in Section 2.4.1 where the bending reconstruction is discussed, followed by an example applied to a thin-walled tapered wing (Section 2.4.2). Even if the application shown is about a rather simple structure, that is a monocell wing, the method is general and more complex cross-sections can be used without incurring in difficulties.
On the contrary, the twist reconstruction for tapered beams of Section 2.4.3 is focused just on thin-walled monocell structures. It is suggested a simple interpretation in order to compute the shear stress on tapered beams and just the monocell-case is discussed. For more complex sections considerations analogous to prismatic beams could be done, but this has not been analysed here. Finally, in Section 2.4.4 some applications are discussed for the twist reconstruction of tapered thin-walled wings.

2.4.1 Development of a model from the prismatic beam case for bending reconstruction

In this section the previous methods are extended for the case of tapered beams. Just a particular case which is deemed most important will be taken into consideration. That is, the cross-section is assumed to be scaled uniformly such that the overall shape remains the same. This is applicable especially to wings since in this way the airfoil profile is maintained.
Consider a tapered beam with rectangular cross-section as in Figure 2.46: the base $b(x)$ and the height $h(x)$ both vary linearly, while the thickness t remains constant along x. Let the taper ratio be r, then:

$$r = \frac{b(L^{(e)})}{b(0)} = \frac{h(L^{(e)})}{h(0)} \tag{2.113}$$

And the cross-section dimensions along x can be expressed as:

$$
\begin{aligned}
h(x) &= h_0 + \frac{h(L^{(e)}) - h(0)}{L^{(e)}}x \\
&= h_0\left(1 + \frac{r-1}{L^{(e)}}x\right)
\end{aligned}
\quad ; \quad
\begin{aligned}
b(x) &= b_0 + \frac{b(L^{(e)}) - b(0)}{L^{(e)}}x \\
&= b_0\left(1 + \frac{r-1}{L^{(e)}}x\right)
\end{aligned}
\tag{2.114}
$$
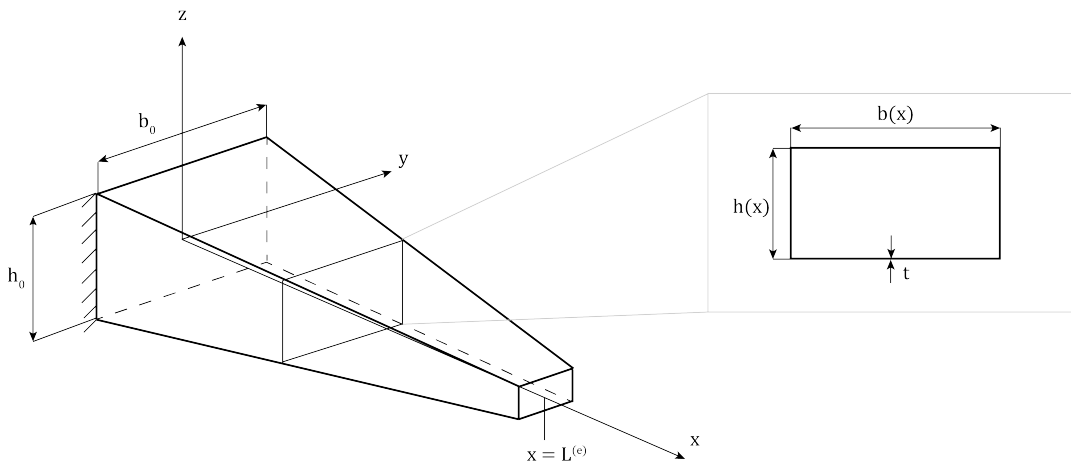
Figure 2.46: *Prismatic thin-walled mono-cell beam with rectangular cross-section.*

And so for example the cross-section area in function of x is given by:

$$
\begin{aligned}
A(x) &= 2t\big(h(x) + b(x)\big) \\
&= 2t\left[h_0 + b_0 + h_0\left(1 + \frac{r-1}{L^{(e)}}x\right) + b_0\left(1 + \frac{r-1}{L^{(e)}}x\right)\right] \\
&= A_0\left(1 + \frac{r-1}{L^{(e)}}x\right)
\end{aligned}
\tag{2.115}
$$

And similarly for the area moment of inertia:

$$
\begin{aligned}
I_y(x) &= 2\frac{1}{12}th(x)^3 + 2\left[\frac{b(x)t^3}{12} + b(x)t\frac{h(x)^2}{2}\right] \\
&= \left(\frac{t}{6}h_0^3 + \frac{t}{2}b_0h_0^2\right)\left(1 + \frac{r-1}{L^{(e)}}\right)^3 + \frac{t^3}{6}b_0\left(1 + \frac{r-1}{L^{(e)}}x\right) \\
&\approx I_{y0}\left(1 + \frac{r-1}{L^{(e)}}\right)^3
\end{aligned}
\tag{2.116}
$$

$$
I_z(x) = I_{z0}\left(1 + \frac{r-1}{L^{(e)}}\right)^3
\tag{2.117}
$$

In the following the factor $(r-1)/L^{(e)}$ will be named c and so the previous relations can be summarized as:

$$
\begin{cases}
A(x) = A_0(1 + cx) \\
I_y(x) = I_{y0}(1 + cx)^3 \\
I_z(x) = I_{z0}(1 + cx)^3
\end{cases}
\tag{2.118}
$$

The Euler-Bernoulli inverse beam element used in the previous sections strictly holds only for prismatic beams since it was developed starting from the equilibrium equations in the case when the cross-section properties do not depend on x. Therefore, there would be the need to develop suitable shape functions for the case of tapered beams. This task has been initially faced in [25]. However, finding adequate shape functions is not trivial and adds up several problems. Here, a different approach has been taken along the lines of the ones previously introduced. That is, the inverse Euler-Bernoulli beam is not modified, but the sensor positions are chosen with the aim to recover the tip displacement of the tapered beam case for each inverse element.

Consider the tapered beam of Figure 2.47 subjected to a tip load P, modeled with just a single inverse element (so 5 strain gauges in total in two axial positions x_1 and x_2 for bending reconstruction).
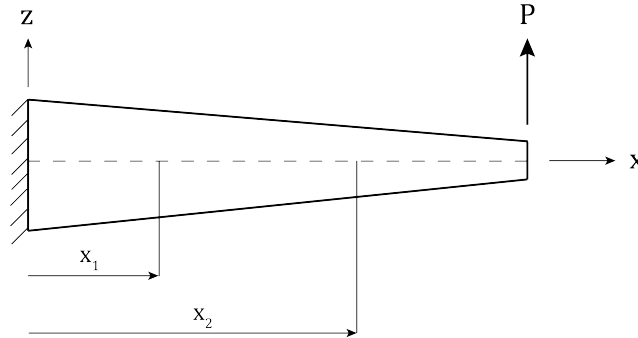
Figure 2.47: *Tapered beam under tip load modelled with a single inverse element (sensors positioned at x_1 and x_2).*

The deflection of the beam $w(x)$, using the Euler-Bernoulli assumptions, can be expressed as:

$$w(x) = -\iint \frac{M_y(x)}{EI_y(x)}\mathrm{d}x\mathrm{d}x = -\iint \frac{P(x - L^{(e)})}{EI_{y0}(1 + cx)^3}\mathrm{d}x\mathrm{d}x = -\frac{1}{EI_{y0}}\iint \frac{P(x - L^{(e)})}{(1 + cx)^3}\mathrm{d}x\mathrm{d}x \tag{2.119}$$

Following the intuition given in [21], the quantity:

$$M_{eq}(x) = \frac{P(x - L^{(e)})}{(1 + cx)^3} \tag{2.120}$$

can be seen as the equivalent internal moment of a *prismatic* beam with constant bending stiffness EI_{y0} such that the same elastic line of the tapered beam is recovered. And now, similarly to what it has been done before, the same tip displacement is required:

$$\underbrace{-\frac{1}{EI_{y0}}\iint_0^{L^{(e)}} M_{eq}(x)\mathrm{d}x\mathrm{d}x}_{w(L^{(e)})} = \underbrace{-\frac{1}{EI_{y0}}\iint_0^{L^{(e)}} M_y(x)\mathrm{d}x\mathrm{d}x}_{\overline{w}(L^{(e)})} \tag{2.121}$$

where $M_y(x)$ is the internal moment linearly distributed coming from the inverse Euler-Bernoulli beam used:

$$M_y(x) = \left(\frac{M_{eq2} - M_{eq1}}{x_2 - x_1}\right)(x - x_1) + M_{eq1} \tag{2.122}$$

where:

$$M_{eq1} = \frac{P(x_1 - L^{(e)})}{(1 + cx_1)^3}$$
$$M_{eq2} = \frac{P(x_2 - L^{(e)})}{(1 + cx_2)^3} \tag{2.123}$$

At this point the integrations of the internal moments can be carried out and give:

$$\iint M_{eq}(x)\mathrm{d}x\mathrm{d}x = P\left(\frac{1}{2}\frac{L^{(e)}}{c^2(cx + 1)} + \frac{1}{2c^3(cx + 1)} + \frac{\ln(cx + 1)}{c^3} + C_1 x + C_2\right) \tag{2.124}$$

$$\iint M_y\mathrm{d}x\mathrm{d}x = \left(\frac{M_{eq2} - M_{eq1}}{x_2 - x_1}\right)\left(\frac{x^3}{6} - x_1\frac{x^2}{2}\right) + M_{eq1}\frac{x^2}{2} + C_3 x + C_4$$
$$= P\left[\left(\frac{\widetilde{M}_{eq2} - \widetilde{M}_{eq1}}{x_2 - x_1}\right)\left(\frac{x^3}{6} - x_1\frac{x^2}{2}\right) + \widetilde{M}_{eq1}\frac{x^2}{2} + C_3 x + C_4\right] \tag{2.125}$$

where the quantities $\widetilde{M}_{eq1}$ and $\widetilde{M}_{eq2}$ are simply defined as:

$$\widetilde{M}_{eq1} = \frac{M_{eq1}}{P} = \frac{x_1 - L^{(e)}}{(1 + cx_1)^3}$$
$$\widetilde{M}_{eq2} = \frac{M_{eq2}}{P} = \frac{x_2 - L^{(e)}}{(1 + cx_2)^3}$$

The relations between the integrations constants C_1, C_2, C_3, C_4 can be found from the boundary conditions:

$$\left.\frac{\mathrm{d}w}{\mathrm{d}x}\right|_{x=0} = \left.\frac{\mathrm{d}\overline{w}}{\mathrm{d}x}\right|_{x=0}$$
$$\Rightarrow \quad C_3 = C_1 - \frac{1}{2}\frac{L^{(e)}c + 1}{c^2} + \frac{1}{c^2} \tag{2.126}$$

$$w(0) = \overline{w}(0) \quad \Rightarrow \quad C_4 = C_2 + \frac{1}{2}\frac{L^{(e)}}{c^2} + \frac{1}{2c^3} \tag{2.127}$$

So Eq.(2.121) becomes:

$$
\frac{1}{2}\frac{L^{(e)}}{c^2(cL^{(e)}+1)} + \frac{1}{2c^3(cL^{(e)}+1)} + \frac{\ln(cL^{(e)}+1)}{c^3} =
$$

$$
= \left(\frac{\widetilde{M}_{eq2} - \widetilde{M}_{eq1}}{x_2 - x_1}\right)\left(\frac{L^{(e)3}}{6} - x_1\frac{L^{(e)2}}{2}\right) + \widetilde{M}_{eq1}\frac{L^{(e)2}}{2} + \left(-\frac{1}{2}\frac{L^{(e)}c+1}{c^2} + \frac{1}{c^2}\right)L^{(e)} + \qquad (2.128)
$$

$$
+ \left(\frac{1}{2}\frac{L^{(e)}}{c^2} + \frac{1}{2c^3}\right)
$$

which is a function of only x_1 and x_2. One variable cannot be expressed explicitly in function of the other one in this case, so the equation has to be solved numerically, setting for example x_1 and retrieving x_2. As it is possible to see in Figure 2.48, in general the solution is not unique. Note also that the graph of Figure 2.48 is symmetric w.r.t. the bisector, that is (x_1, x_2) and (x_2, x_1) are both solutions, as it should.
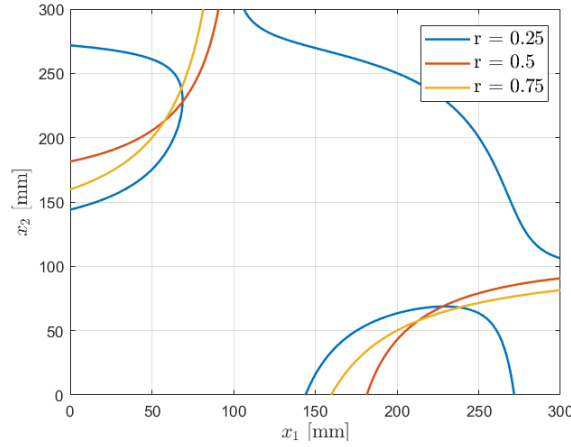
Figure 2.48: *Set of all possible solutions (x_1, x_2) for different taper ratios r.*

The suitability of the choice of x_1 and x_2 has been assessed for a tapered beam with rectangular thin-walled cross-section under tip load P. First, directly the analytical solution has been used to extract the "experimental" strains. In this case, using the Euler-Bernoulli assumptions, the deflection is given by:

$$
\begin{aligned}
w(x) &= -\iint \frac{P(x - L^{(e)})}{EI_{y0}(1 + cx)^3}\,\mathrm{d}x\mathrm{d}x \\
&= -\frac{P}{EI_{y0}}\left[\frac{1}{2}\frac{L^{(e)}}{c^2(cx+1)} + \frac{1}{2c^3(cx+1)} + \frac{\ln(cx+1)}{c^3} + C_1 x + C_2\right]
\end{aligned}
\qquad (2.129)
$$

where the integration constants are given by:

$$
\begin{aligned}
\left.\frac{\mathrm{d}w}{\mathrm{d}x}\right|_{x=0} = 0 &\quad\Rightarrow\quad C_1 = \frac{1}{2}\frac{L^{(e)}c+1}{c^2} - \frac{1}{c^2} \\
w(0) = 0 &\quad\Rightarrow\quad C_2 = -\frac{1}{2}\frac{L^{(e)}}{c^2} - \frac{1}{2c^3}
\end{aligned}
\qquad (2.130)
$$

Using this solution, the axial strain ε_x can be computed and used as input for the iFEM simulation. The properties of the beam are reported in Table 2.5, together with the two axial positions of the sensors x_1 and x_2. As shown in Figure 2.49 the tip displacement is correctly recovered, in the sense that the same tip displacement is reached, as it should.

h_0	$30\,\mathrm{mm}$
b_0	$50\,\mathrm{mm}$
t	$1\,\mathrm{mm}$
r	0.25
$L^{(e)}$	$300\,\mathrm{mm}$
P	$1e4\,\mathrm{N}$
E	$70e3\,\mathrm{MPa}$
ν	0.3
x_1	$120\,\mathrm{mm}$
x_2	$282.7\,\mathrm{mm}$

Table 2.5: *Properties of tapered beam with rectangular cross-section.*
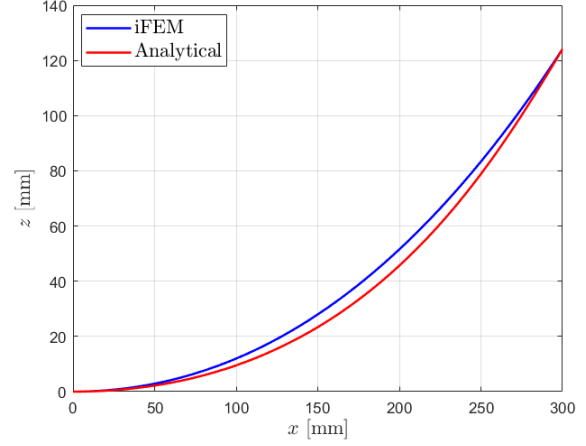
Figure 2.49: *Deflection of tapered beam under tip load: comparison between analytical solution and reconstructed one.*

In a second simulation, the strain measurements have been taken from the FEM model of the tapered beam (Figure 2.50a), so the exact strains from the Euler-Bernoulli beam model are not used anymore. The details of the FE model are reported in Appendix M. The results are shown in Figure 2.50b. The FEM solution gives a larger deflection compared to the analytical one and, since the strains have been taken from the FEM model, the iFEM shape reconstruction does not agree as before to the analytical deflection. The differences between Euler-Bernoulli model and FEM results should be attributed both to transverse shear effects and to the fact that the beam is not so slender. In any case, it is deemed the deflection is relatively well recovered.
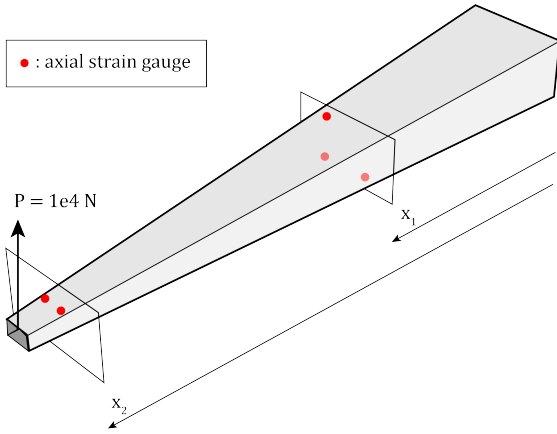
(a) *Tapered box beam: geometry and load.*
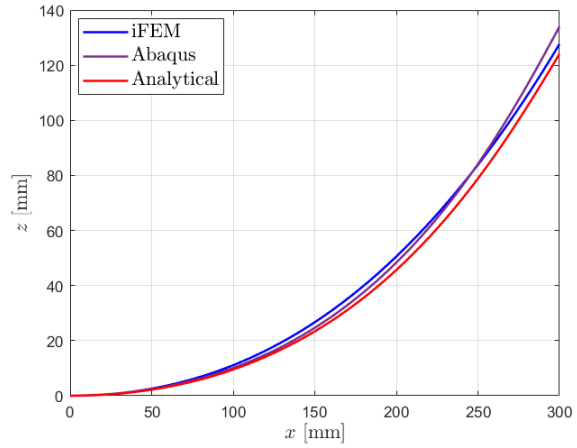
(b) *Deflection reconstruction of tapered beam using as input the FEM strains.*

Figure 2.50: *Tapered beam under tip load using FEM model.*

So far it has been used only one inverse element. In other words, the element tip was free and so the internal moment is simply given by $M_y(x) = P(x - L^{(e)})$. At this point, it is useful to extend the model presented when more than one element are used in order to get more accurate results under complex loads.
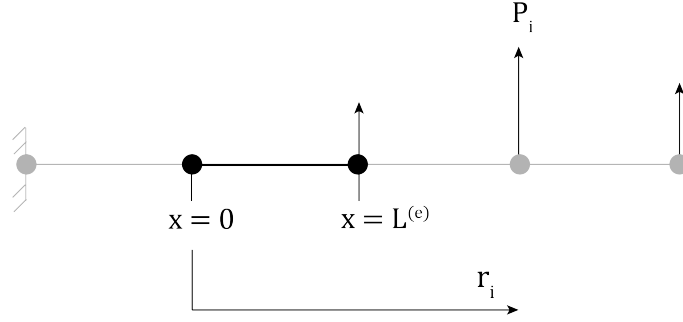
Figure 2.51: *Tapered beam discretized using multiple inverse elements and with concentrated nodal forces.*

For the moment just the presence of concentrated nodal forces is studied. Consider the tapered beam as in Figure 2.51, discretized with several inverse elements. The internal moment of the highlighted element can be obtained from :

$$M_y(x) = -x \sum_i P_i + \sum_i P_i r_i \tag{2.131}$$

with P_i the nodal forces and r_i the corresponding distances. So, the equivalent internal moment becomes:

$$M_{eq}(x) = \frac{-x \sum_i P_i + \sum_i P_i r_i}{(1 + cx)^3} \tag{2.132}$$

which can be used in Eq.(2.121), that is:

$$-\frac{1}{EI_{y0}} \iint_0^{L^{(e)}} M_{eq}(x)\mathrm{d}x\mathrm{d}x = -\frac{1}{EI_{y0}} \iint_0^{L^{(e)}} M_y(x)\mathrm{d}x\mathrm{d}x \tag{2.133}$$

where:

$$M_y(x) = \left(\frac{M_{eq2} - M_{eq1}}{x_2 - x_1} \right)(x - x_1) + M_{eq1}$$

$$M_{eq1} = \frac{-x_1 \sum_i P_i + \sum_i P_i r_i}{(1 + cx_1)^3}$$

$$M_{eq2} = \frac{-x_2 \sum_i P_i + \sum_i P_i r_i}{(1 + cx_2)^3}$$

So Eq.(2.133) now becomes:

$$\begin{aligned}
\frac{1}{2}\frac{\sum_i P_i r_i}{c^2(cL^{(e)} + 1)} + \frac{1}{2}\frac{\sum_i P_i}{c^3(cL^{(e)} + 1)} + \frac{\sum_i P_i \ln(cL^{(e)} + 1)}{c^3} + C_1 L^{(e)} + C_2 = \\
= \left(\frac{M_{eq2} - M_{eq1}}{x_2 - x_1} \right)\left(\frac{L^{(e)3}}{6} - x_1\frac{L^{(e)2}}{2} \right) + M_{eq1}\frac{L^{(e)2}}{2} + C_3 L^{(e)} + C_4
\end{aligned} \tag{2.134}$$

And the relations between the integration constants can be obtained as before:

$$\begin{aligned}
\frac{\mathrm{d}w}{\mathrm{d}x}\bigg|_{x=0} &= \frac{\mathrm{d}\overline{w}}{\mathrm{d}x}\bigg|_{x=0} \\
\Rightarrow \quad C_3 &= C_1 - \frac{1}{2}\frac{c \sum_i P_i r_i + \sum_i P_i}{c^2} + \frac{\sum_i P_i}{c^2}
\end{aligned} \tag{2.135}$$

$$w(0) = \bar{w}(0)$$

$$\Rightarrow \quad C_4 = C_2 + \frac{1}{2}\frac{\sum_i P_i r_i}{c^2} + \frac{1}{2}\frac{\sum_i P_i}{c^3} \tag{2.136}$$

So Eq.(2.134) finally becomes:

$$\frac{1}{2}\frac{\sum_i P_i r_i}{c^2(cL^{(e)}+1)} + \frac{1}{2}\frac{\sum_i P_i}{c^3(cL^{(e)}+1)} + \frac{\sum_i P_i \ln(cL^{(e)}+1)}{c^3} =$$

$$= \left(\frac{M_{eq2}-M_{eq1}}{x_2-x_1}\right)\left(\frac{L^{(e)3}}{6} - x_1\frac{L^{(e)2}}{2}\right) + M_{eq1}\frac{L^{(e)2}}{2} + \left[-\frac{1}{2}\frac{c\sum_i P_i r_i + \sum_i P_i}{c^2} + \frac{\sum_i P_i}{c^2}\right]L^{(e)} +$$

$$+ \left[\frac{1}{2}\frac{\sum_i P_i r_i}{c^2} + \frac{1}{2}\frac{\sum_i P_i}{c^3}\right] \tag{2.137}$$

As it is possible to see, the terms related to P_i do not simplify, so the final solution depends on the loads P_i which are, of course, *unknown*.

In order to face this problem, the following algorithm could be followed:

1. Install strain gauges with initial guess of x_1 and x_2.

2. Measure the experimental strains.

3. Interpolate the strain measurements over the beam.

4. Compute $\sum_i P_i$ and $\sum_i P_i r_i$.

5. Compute the new values of x_1 and x_2 from Eq.(2.137).

6. From the strain interpolation done at step (3), sample the new values of the axial strains at the new positions x_1 and x_2.

7. Carry out iFEM to retrieve the deformed shape.

Let's consider first point (3), that is the strain interpolation. For the load case which is considered now (only nodal forces), the axial strain within each element is given by:

$$\varepsilon_x(x,z) = \frac{-x\sum_i P_i + \sum_i P_i r_i}{EI_{y0}(1+cx)^3}z = \frac{A+Bx}{(1+cx)^3}z \tag{2.138}$$

with A and B coefficients to be determined:

$$A = \frac{\sum_i P_i r_i}{EI_{y0}} \quad ; \quad B = -\frac{\sum_i P_i}{EI_{y0}} \tag{2.139}$$

Since on each element two different axial measurements are done, A and B can be easily computed:

$$\begin{cases} \varepsilon_{x1}^\varepsilon = \dfrac{A+Bx_1}{(1+cx_1)^3}z_1 \\ \varepsilon_{x2}^\varepsilon = \dfrac{A+Bx_2}{(1+cx_2)^3}z_2 \end{cases} \Rightarrow \begin{cases} B = \dfrac{1}{x_2-x_1}\left[\dfrac{\varepsilon_{x2}^\varepsilon}{z_2}(1+cx_2)^3 - \dfrac{\varepsilon_{x1}^\varepsilon}{z_1}(1+cx_1)^3\right] \\ A = \dfrac{\varepsilon_{x1}}{z_1}(1+cx_1)^3 - Bx_1 \end{cases} \tag{2.140}$$

It is clear how to deal with point (4), that is the computation of $\sum_i P_i$ and $\sum_i P_i r_i$. From Eq.(2.139) it follows that:

$$\sum_i P_i r_i = AEI_{y0} \quad ; \quad \sum_i P_i = -BEI_{y0} \tag{2.141}$$

And so now all the steps outlined before can be done.

As an example, consider the same tapered beam with rectangular cross-section as before. This time, two concentrated loads are present (Figure 2.5a), one at the tip equal to $5e3$ N and one at the middle of the span equal to $1e4$ N. Two inverse elements have been used, each one 150 mm long, with the axial sensor positions x_1 and x_2 as in Table 2.6 (recall that x_1, x_2 are both expressed in the local element reference system such that $x \in [0, L^{(e)}]$). The measured strains have been interpolated as explained before giving place to Figure 2.52b.

Initial	x_1	x_2
First element	100 mm	110 mm
Second element	100 mm	110 mm
Updated	x_1	x_2
First element	100 mm	23.5451 mm
Second element	31.4125 mm	110 mm

Table 2.6: *Strain gauge positions for initial and updated configuration.*
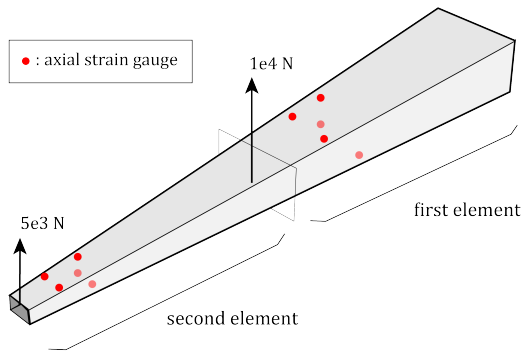
(a) *Tapered box beam: geometry and load.*
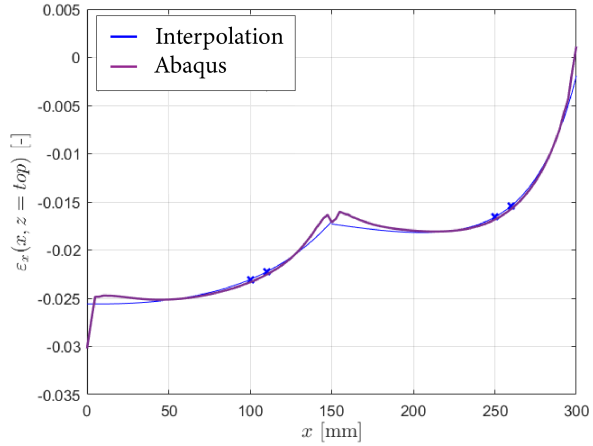
(b) *Interpolation of axial strain at the top surface of the tapered beam. Measurement points highlighted by* ×*.*

Figure 2.52: *Deflection reconstruction for tapered beam under two concentrated loads.*

From the estimated values of A and B, the new span positions x_1 and x_2 have been computed (see Table 2.6) and subsequently the axial strains have been obtained from the interpolation carried out before. The results from iFEM are shown in Figure 2.53, both using the initial strain gauge positions (Figure 2.53a) and the updated ones (Figure 2.53b).
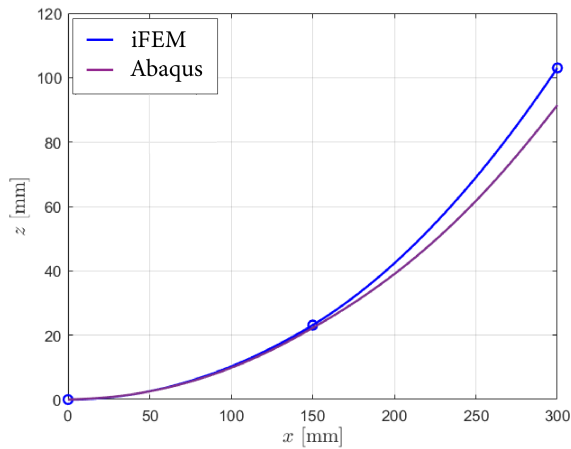
(a) *Deflection along z with initial strain gauge positions.*
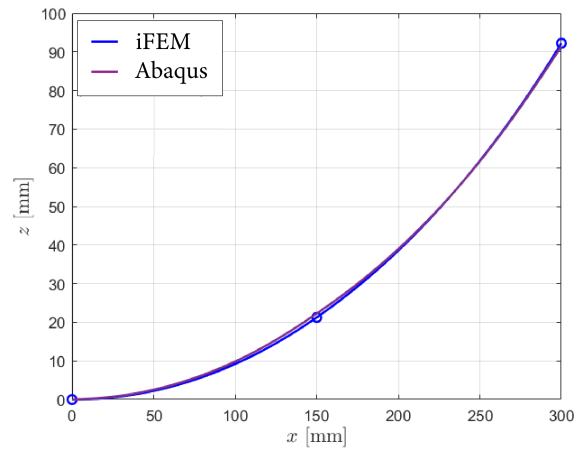
(b) *Deflection along z with updated strain gauge positions.*

Figure 2.53: *Deflection reconstruction of tapered beam under two concentrated fores.*

It is important to remark that, even though so far just concentrated forces have been considered, the formulation is the same also in presence of concentrated moments at the nodes. In this case the internal moment of the highlighted element in Figure 2.54 becomes:

$$M_y(x) = -x \sum_i P_i + \sum_i (P_i r_i + M_i) \tag{2.142}$$

and so it is necessary to make the substitution $\sum_i P_i r_i \leftarrow \sum_i (P_i r_i + M_i)$ in all the previous steps. However, this does not change anything in the method.
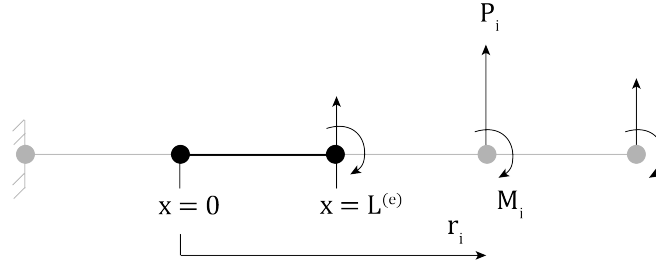
Figure 2.54: *Tapered beam discretized using multiple inverse elements with concentrated nodal forces and moments.*

So far just the bending in one direction has been discussed. When the nodal forces act in two different directions, then there is the need to distinguish between $M_y(x)$ and $M_z(x)$ (Figure 2.55a). Analogously as before, the internal moment for every element can be written as:

$$M_y(x) = -x \sum_i P_{yi} + \sum_i P_{yi} r_i \tag{2.143}$$

$$M_z(x) = -x \sum_i P_{zi} + \sum_i P_{zi} r_i \tag{2.144}$$

Since in general $M_y(x)$ and $M_z(x)$ are different, also the optimal values of x_1 and x_2 will not coincide, so the two cases have to be properly distinguished but the procedure to follow is the same as the one outlined before. The main difference now consists in the interpolation of the strain field.

(a) *Discretization with multiple inverse elements.*

(b) *Tapered box beam: geometry and load.*
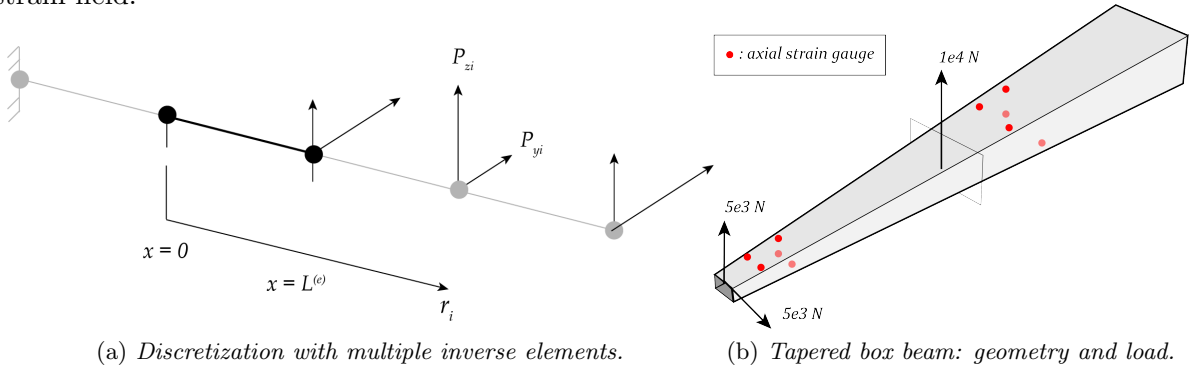
Figure 2.55: *Tapered beam under concentrated loads acting in two different planes.*

Since the axial strain can be written as:

$$\varepsilon_x(x, y, z) = \frac{N}{EA(x)} - y \frac{M_z(x)}{EI_z(x)} + z \frac{M_y(x)}{EI_y(x)} \tag{2.145}$$

and since $M_y(x)$ and $M_z(x)$ are both linear, ε_x can be expressed as:

$$\varepsilon_x(x, y, z) = \frac{\varepsilon_{10}}{(1 + cx)} + y\frac{\varepsilon_{20} + \varepsilon_{21}x}{(1 + cx)^3} + z\frac{\varepsilon_{30} + \varepsilon_{31}x}{(1 + cx)^3} \qquad (2.146)$$

where the constants ε_{10}, ε_{20}, ε_{21}, ε_{30} and ε_{31} can be determined from the strain measurements done over the element solving the corresponding linear system (five strain measurements, five unknowns). From this solution, the terms $\sum_i P_{yi}$, $\sum_i P_{yi}r_i$, $\sum_i P_{zi}$, $\sum_i P_{zi}r_i$ can be determined as:

$$\sum_i P_{zi}r_i = EI_{z0}\varepsilon_{20} \quad ; \quad \sum_i P_{zi} = -EI_{z0}\varepsilon_{21} \quad ; \quad \sum_i P_{yi}r_i = EI_{y0}\varepsilon_{30} \quad ; \quad \sum_i P_{yi} = -EI_{y0}\varepsilon_{31}$$
$$(2.147)$$

As an example, to the previous tapered beam a tip load of $5e3$ N along the the y axis has been applied, together with the previous loads along z (Figure 2.55b). The reconstructed displacement along the y axis is shown in Figure 2.56: compared to the direct application of iFEM to the extracted strains (Figure 2.56a) there is a slight improvement (Figure 2.56b).
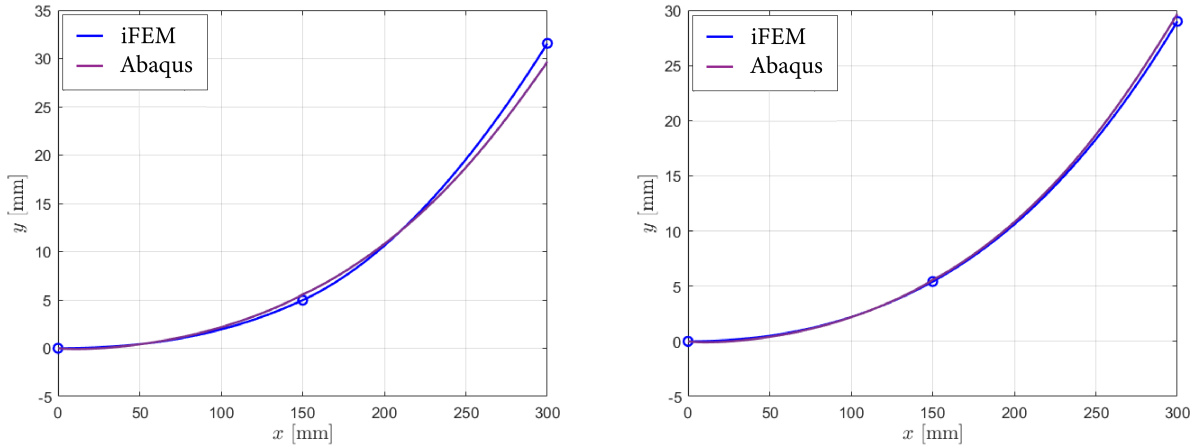
(a) *Deflection along y with initial strain gauge positions.* (b) *Deflection along y with updated strain gauge positions.*

Figure 2.56: *Deflection of tapered beam under concentrated forces acting in two planes.*

Before proceeding, another way to estimate the applied loads to feed Eq.(2.137) is explained. Consider that, using the measured strain values, iFEM is carried out and so a deformed shape is retrieved. At this point from the displacements obtained the external loads can be estimated. A simple way to do that consists in building an sensitivity matrix from the analytical displacements (see Appendix F) and from this obtain the applied loads. Since the solution is based on the deformed shape obtained with the direct application of iFEM from the strain measurements, the estimated loads in general will not be very accurate. But in any case an estimate can be obtained. This will be the method which will be used later on for the case of distributed loads. It might be argued however why there is the need to carry out iFEM if the loads can be retrieved. In other words, since the loads are estimated, a direct FEM simulation on the model would directly give the deformed shape of the beam. The problem with this approach is that in general the loads, especially for more complex cases, are not very accurate. So estimating the displacements from a direct simulation using them as an input might not deliver satisfactory results. On the contrary, it was observed that Eq.(2.137) is not heavily influenced by the terms $\sum_i P_i r_i$ and $\sum_i P_i$. The equation actually depends just upon the quantity $\sum_i P_i r_i / \sum_i P_i$ which represents a "weighted average" of the applied loads on the beam. So, even a "rough" estimate would be enough in this context.

Now, the effect of *distributed* loads has to be studied. On the tapered beam with rectangular cross-section a constant distributed load has been applied as in Figure 2.57. Using the same sensor configuration of Figure 2.52, the solution developed for concentrated nodal loads can be used. However, as it is possible to see from Figure 2.58 the results obtained are not more accurate compared to the ones from the simple application of iFEM. This is due to the fact that the solution developed so far has been derived just from cases in which concentrated forces are applied.
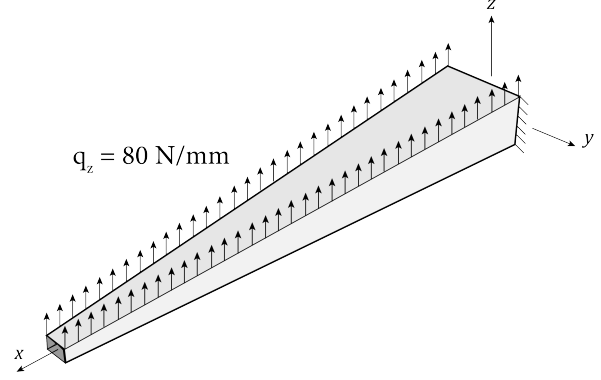
Figure 2.57: *Tapered beam under constant distributed load $q_z = 80$ N/mm.*
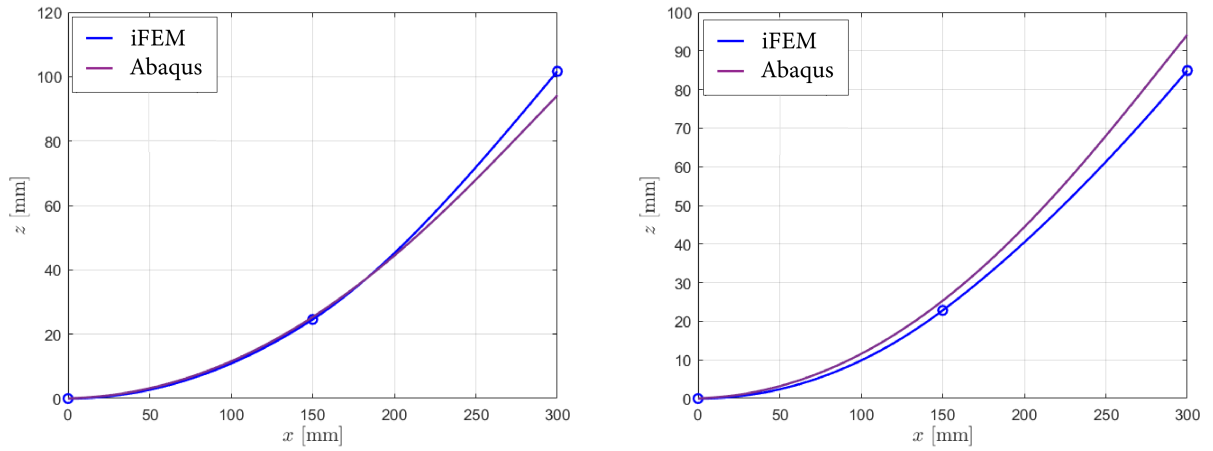
(a) *Deflection along z with initial strain gauge positions.* (b) *Deflection along z with updated strain gauge positions.*

Figure 2.58: *Deflection of tapered beam under constant distributed load using the solution for concentrated forces.*

Therefore, a solution developed for the case of distributed loads seems to be needed. Considering for the moment a single inverse element, the solution can be developed along the same lines of the one described before. The details are reported in Appendix D.
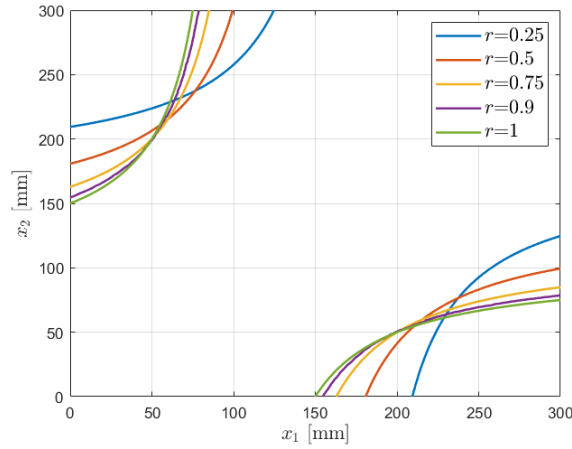
Figure 2.59: *Solutions (x_1, x_2) for a single inverse element under constant distributed load.*

Even though the relation between x_1 and x_2 depends on the taper ratio r, the results soon

converge to the prismatic solution given by Eq.(2.82), as for example in shown in Figure 2.59 (for $r = 1$). This means that the prismatic solution can lead to acceptable results if the taper ratio is not too low. Similar results would also hold for the case of more inverse elements. Using two inverse elements and the prismatic solution (with $x_1 = 30\,\text{mm}$ and $x_2 = 112.5\,\text{mm}$) brings the deflection reconstruction shown in Figure 2.60 which is deemed sufficiently accurate for a wide range of applications.
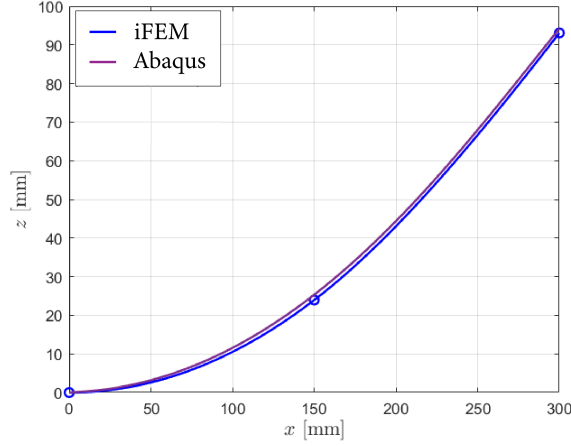
Figure 2.60: *Deflection reconstruction under constant distributed load for tapered beam using the prismatic solution.*

However, a specific solution can be developed also for this case. This is not only motivated by an improvement of the shape reconstruction (which apparently is small, if any), but also by the estimation of the distributed load acting on the beam, as it will be clear in the next paragraphs. So, consider the tapered beam discretized with several elements and subjected to a step-wise constant distributed load as in Figure 2.61.
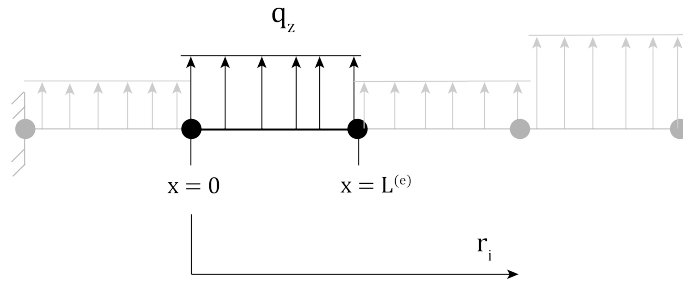
Figure 2.61: *Tapered beam discretized by multiple inverse elements under step-wise constant load.*

The internal shear force and moment over the element domain are given by:

$$V_z(x) = q_z(L^{(e)} - x) + \sum_{i+1} q_{zi} L_i^{(e)} \tag{2.148}$$

$$\overline{M}_y(x) = q_z \left(L^{(e)} x - \frac{x^2}{2} \right) + \left(\sum_{i+1} q_{zi} L_i^{(e)} \right) x - \sum_i q_{zi} L_i^{(e)} r_i$$

note that the summation signs start from different values: one from the element itself (i) and the other from the next one ($i + 1$). Furthermore, the variable r_i stands for the arm of the moment, which for a constant distributed load is simply the midpoint of each element. The equivalent internal moment of the beam is simply given by:

$$\overline{M}_{eq}(x) = \frac{\overline{M}_y(x)}{(1 + cx)^3} = \frac{1}{(1 + cx)^3} \left[q_z \left(L^{(e)}x - \frac{x^2}{2} \right) + \left(\sum_{i+1} q_{zi} L_i^{(e)} \right) x - \sum_i q_{zi} L_i^{(e)} r_i \right] \quad (2.149)$$

and the usual procedure to come up with an equation relating x_1 with x_2 can be followed. The expressions are too long to be reported here (see Appendix E) and must be handled with a code (MATLAB symbolic toolbox). Here it is important to underline that the final equation depends on the variables q_z, $\sum_{i+1} q_{zi} L_i^{(e)}$ and $\sum_i q_{zi} L_i^{(e)} r_i$ and so they need to be estimated in order to compute x_2 in function of x_1 or vice-versa. In other words, an estimate of the distributed loads q_{zi} is needed. Furthermore, also interpolating the axial strain field is necessary and a similar procedure as before could be followed. However here a different method is employed which is deemed to be more consistent and able to deliver more accurate results. Since the internal moment is quadratic, in theory seven strain measurements over the element would be needed:

$$\varepsilon_x(x, y, z) = \frac{\varepsilon_{10}}{(1 + cx)} + z\frac{\varepsilon_{20} + x\varepsilon_{21} + x^2\varepsilon_{22}}{(1 + cx)^3} + y\frac{\varepsilon_{30} + x\varepsilon_{31} + x^2\varepsilon_{32}}{(1 + cx)^3} \quad (2.150)$$

A first simplification can be done considering that the beam is experiencing mainly bending, so the first term can be neglected reducing the unknowns to six. Furthermore, it is also known that the beam tip is free and so the strain must be zero there. So it is possible to write that:

$$\varepsilon_x(L^{(e)}, y, z) = z\frac{\varepsilon_{20} + L^{(e)}\varepsilon_{21} + L^{(e)2}\varepsilon_{22}}{(1 + cL^{(e)})^3} + y\frac{\varepsilon_{30} + L^{(e)}\varepsilon_{31} + L^{(e)2}\varepsilon_{32}}{(1 + cL^{(e)})^3} = 0 \quad ; \quad \forall y, z \quad (2.151)$$

which holds $\forall y, z$ over the cross-section. Therefore the following equations need to be satisfied:

$$\begin{cases} \varepsilon_{20} + L^{(e)}\varepsilon_{21} + L^{(e)2}\varepsilon_{22} = 0 \\ \varepsilon_{30} + L^{(e)}\varepsilon_{31} + L^{(e)2}\varepsilon_{32} = 0 \end{cases} \quad (2.152)$$

So a total of seven equations (and six unknowns) has been derived, which can be solved with least-squares. For all the internal elements additional equations can be obtained simply setting the continuity of the strain between the elements. So, at each interface:

$$z\frac{\varepsilon_{20} + L^{(e)}\varepsilon_{21} + L^{(e)2}\varepsilon_{22}}{(1 + cL^{(e)})^3} + y\frac{\varepsilon_{30} + L^{(e)}\varepsilon_{31} + L^{(e)2}\varepsilon_{32}}{(1 + cL^{(e)})^3} = z\varepsilon_{20}^{(+)} + y\varepsilon_{30}^{(+)} \quad (2.153)$$

$$\Rightarrow \quad z \left(\frac{\varepsilon_{20} + L^{(e)}\varepsilon_{21} + L^{(e)2}\varepsilon_{22}}{(1 + cL^{(e)})^3} - \varepsilon_{20}^{(+)} \right) + y \left(\frac{\varepsilon_{30} + L^{(e)}\varepsilon_{31} + L^{(e)2}\varepsilon_{32}}{(1 + cL^{(e)})^3} - \varepsilon_{30}^{(+)} \right) = 0$$

which again holds for every y, z on the cross section, so:

$$\begin{cases} \dfrac{\varepsilon_{20} + L^{(e)}\varepsilon_{21} + L^{(e)2}\varepsilon_{22}}{(1 + cL^{(e)})^3} = \varepsilon_{20}^{(+)} \\ \dfrac{\varepsilon_{30} + L^{(e)}\varepsilon_{31} + L^{(e)2}\varepsilon_{32}}{(1 + cL^{(e)})^3} = \varepsilon_{30}^{(+)} \end{cases} \quad (2.154)$$

where the superscript $(+)$ stands for the quantities belonging to the next element. Note that this means the axial strain needs to be interpolated starting from the tip of the beam, and going backwards till the root.
Once this is done, as said before the load terms needed could be derived as for the concentrated

nodal forces case. However, it must be realized that the interpolation might be affected by errors, giving inaccurate results. So, it has been decided to retrieve the distributed loads q_{zi} using a common technique for load recovery. The procedure can be explained with the following steps:

1. Apply a unit distributed load q_{zi} on each element separately and measure the nodal deflection w_i for each node.

2. Build the sensitivity matrix $\boldsymbol{A}$ which is defined such that:

$$\boldsymbol{w} = \boldsymbol{A}\boldsymbol{q}_z \quad ; \quad \boldsymbol{w} = \begin{bmatrix} w_1 \\ w_2 \\ \vdots \end{bmatrix} \quad ; \quad \boldsymbol{q}_z = \begin{bmatrix} q_{z1} \\ q_{z2} \\ \vdots \end{bmatrix} \quad ; \quad \boldsymbol{A} = \begin{bmatrix} \dfrac{\partial w_1}{\partial q_{z1}} & \dfrac{\partial w_1}{\partial q_{z2}} & \cdots \\ \dfrac{\partial w_2}{\partial q_{z1}} & \dfrac{\partial w_2}{\partial q_{z2}} & \cdots \\ \vdots & \vdots & \vdots \end{bmatrix} \tag{2.155}$$

3. Solve the linear system of Eq.(2.155). Since the matrix $\boldsymbol{A}$ is square, the system is determined and can be solved with common techniques.

For our case, the application of the load q_{zi} on each element (point 1) can be done analytically giving a very fast computation of the sensitivity matrix $\boldsymbol{A}$. The analytical solution needed for this part is reported in Appendix G. This method is deemed to be consistent since all the procedure developed aims to recover the deflection at the nodes of the inverse elements, while no condition is set over the beam domain. And in the load reconstruction just these values are used, so theoretically allowing to retrieve a more accurate load q_{zi}. This is also particularly important for the twist angle reconstruction as will be explained later. Once this is done, the new values of x_1 and x_2 can be obtained. So, taking advantage from the strain interpolation available from before, the strain can be sampled at x_1 and x_2 and iFEM can be carried out to retrieve the deformed shape.
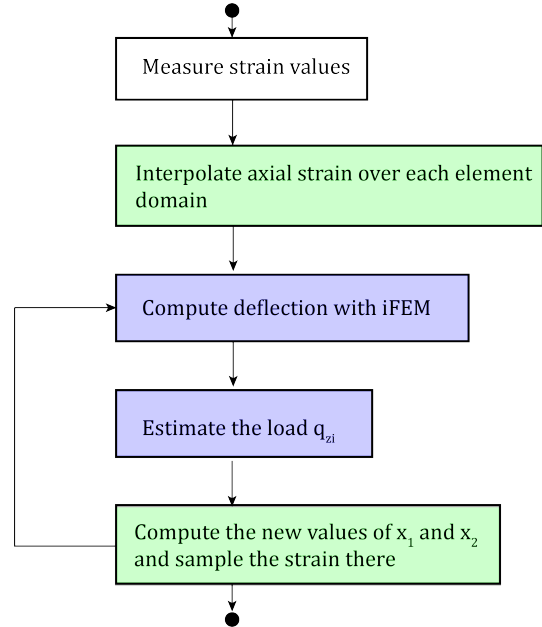
Figure 2.62: *Step-wise constant load reconstruction for tapered beams.*

This will in turn give new deflections which can be used to estimate again the load q_{zi}, repeating the whole procedure. The algorithm is illustrated in Figure 2.62, where the tasks which are related to each other by the corresponding outputs have been color-coded.

Before illustrating some examples, it is important to underline the fact that, similarly to the previous cases, there are in general multiple solutions of x_1 and x_2 which can be used. A suitable choice can be done considering that, in general, the extrapolation of the strain becomes less accurate far away from the measurement points. So, it is desired to obtain the new values of x_1 and x_2 as close as possible to the original positions where the strain gauges are actually installed. Intuitively, given the solution curves displayed in Figure 2.63 and the initial position (x_{10}, x_{20}), the solution highlighted (x_1, x_2) is desired.
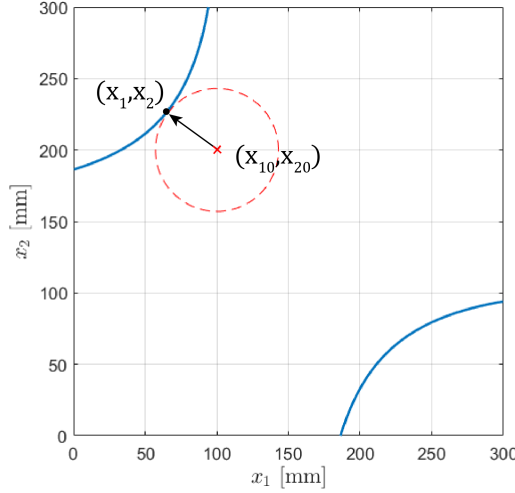
Figure 2.63: *Optimal solution for (x_1, x_2) given the initial position (x_{10}, x_{20}).*

This problem can be solved numerically looking for the minimum value of:

$$\min_{(x_1,x_2)} \left\{ f(x_1, x_2) + \sqrt{(x_1 - x_{10})^2 + (x_2 - x_{20})^2} \right\} \quad \text{s.t.} \quad 0 \le x_1, x_2 \le L^{(e)} \tag{2.156}$$

where $f(x_1, x_2)$ is the expression relating x_1 and x_2.

The method has first been checked using the analytical solution for the usual tapered beam with rectangular cross-section under a constant distributed load equal to $q_z = 100$ N/mm. Two inverse elements have been used both with $(x_{10}, x_{20}) = (50, 100)$ mm. The deformed shape of the first and second iterations are shown in Figure 2.64 and the corresponding estimates of the distributed load are:

$$\text{Iteration 1}: \begin{bmatrix} q_{z1} \\ q_{z2} \end{bmatrix} = \begin{bmatrix} 77.33 \\ 104.00 \end{bmatrix} \quad ; \quad \text{Iteration 2}: \begin{bmatrix} q_{z1} \\ q_{z2} \end{bmatrix} = \begin{bmatrix} 95.18 \\ 100.04 \end{bmatrix} \quad ; \quad \text{Reference}: \begin{bmatrix} q_{z1} \\ q_{z2} \end{bmatrix} = \begin{bmatrix} 100 \\ 100 \end{bmatrix}$$

After the second iteration the results remain practically the same. This fact has been observed also in later simulations, so generally just two evaluations with iFEM have been done. In any case, comparing Figure 2.64a and Figure 2.64b the shape reconstruction is slightly improved. As mentioned before, the shape sensing deformation does not gain a considerable improvement, but a more accurate estimate of the distributed load is recovered.
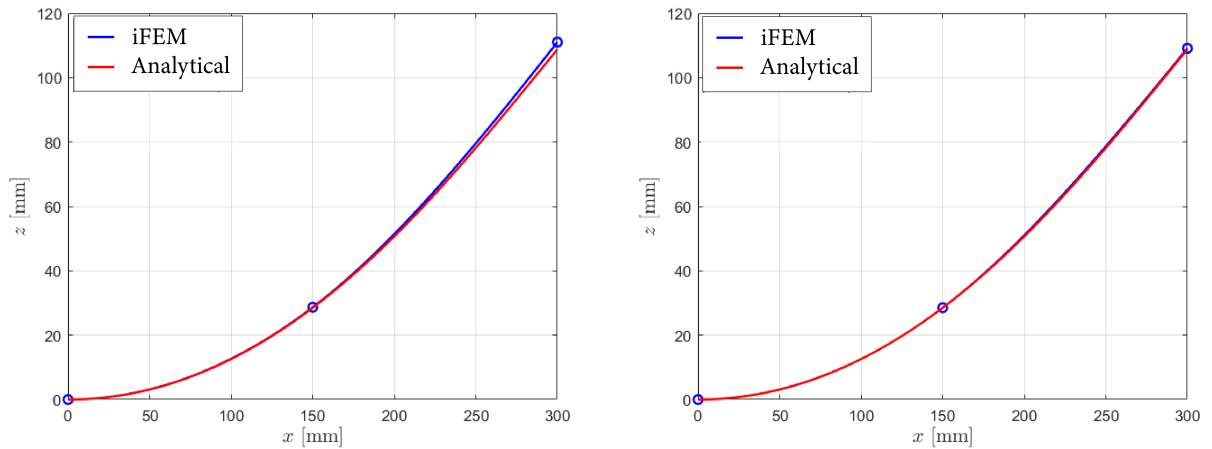
(a) *Deflection along z with initial strain gauge positions.* (b) *Deflection along z with updated strain gauge positions.*

Figure 2.64: *Delflection reconstruction of tapered beam under constant load $q_z = 100\,N/mm$ using analytical input strains.*

Now the FEM model of the beam of Figure 2.57 has again been considered and the strains have been directly extracted from there. The results for this case are shown below and in Figure 2.65:

$$\text{Iteration 1}: \begin{bmatrix} q_{z1} \\ q_{z2} \end{bmatrix} = \begin{bmatrix} 42.07 \\ 92.78 \end{bmatrix} \quad ; \quad \text{Iteration 2}: \begin{bmatrix} q_{z1} \\ q_{z2} \end{bmatrix} = \begin{bmatrix} 58.49 \\ 89.37 \end{bmatrix} \quad ; \quad \text{Reference}: \begin{bmatrix} q_{z1} \\ q_{z2} \end{bmatrix} = \begin{bmatrix} 80 \\ 80 \end{bmatrix}$$
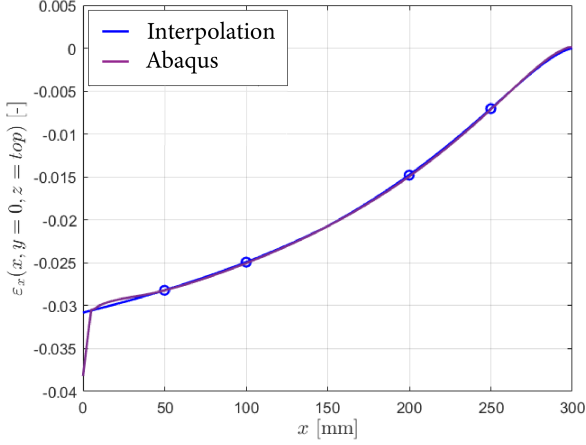
(a) *Interpolation of axial strain over upper surface.*
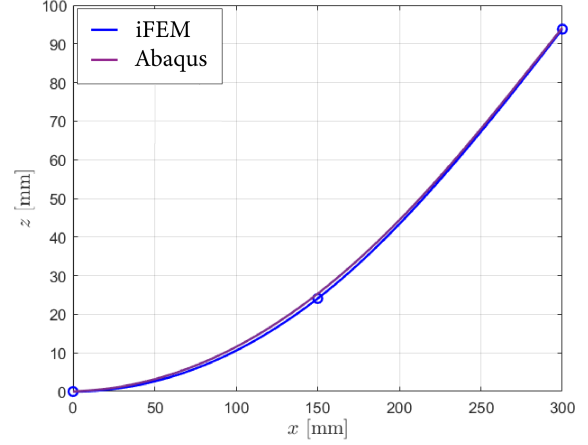
(b) *Final deflection reconstruction.*

Figure 2.65: *Tapered beam deflection reconstruction using strain data from FEM.*

Now, especially for the first element the distributed load is not well obtained. Even though this does not seem to affect the shape reconstruction, this might be due to the fact that near the root the strain field does not resemble exactly the one given by the Euler-Bernoulli theory. If the simulation is carried out with a single inverse element this effect cannot be clearly seen since the element spans the whole beam length. The shape reconstructions of the first and second iterations are shown in Figure 2.66 where the load goes from $q_{z1} = 93.44$ N/mm to $q_{z1} = 85.33$ N/mm, closer to the exact solution.
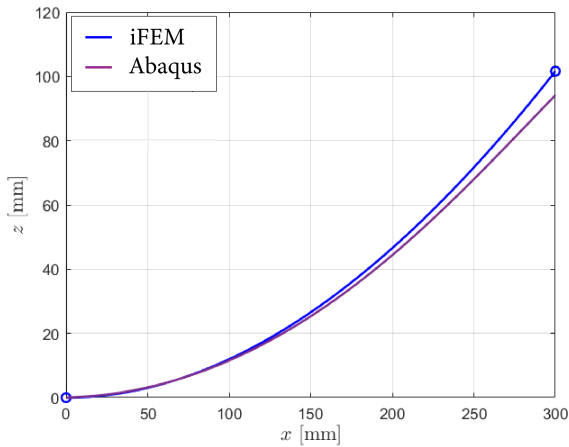
(a) *Deflection along z using initial strain gauge positions.* (b) *Deflection along z using updated strain gauge positions.*
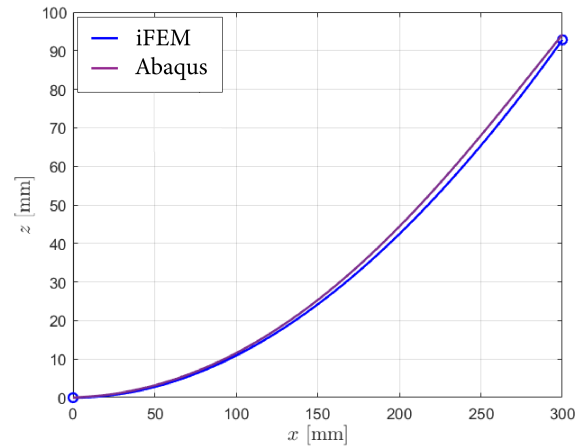
Figure 2.66: *Tapered beam deflection reconstruction using a single inverse element.*

The methods just developed can of course be applied also to more complex load cases. For example, keeping the usual box beam, a parabolic load has been applied to the FEM model as in Figure 2.67.

Carrying out several analyses, increasing each time the number of elements used, the results of Figure 2.68 have been obtained. Already with 2 inverse elements there is a good reconstruction of the deflection and increasing the number of elements (and so strain gauges) there is no significant improvement.
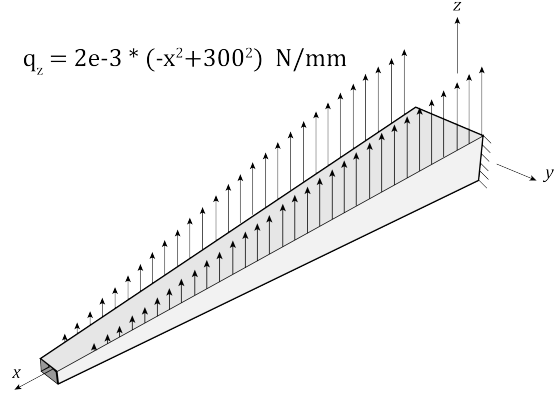
Figure 2.67: *Tapered beam under $q_z(x) = 2(-x^2 + 300^2)$ mN/mm.*
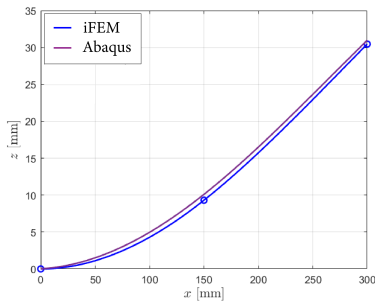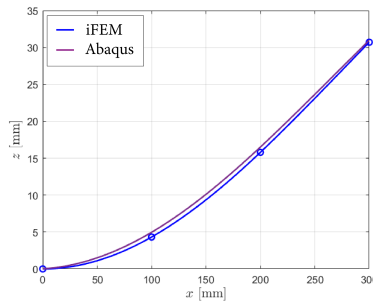
(a) *2 inverse elements.*   (b) *3 inverse elements.*   (c) *6 inverse elements.*
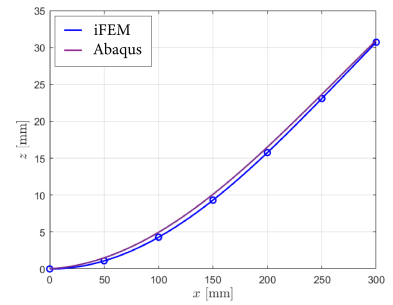
Figure 2.68: *Deflection reconstruction for tapered beam under parabolic distributed load.*

2.4.2 Application of bending reconstruction to tapered wing

The methods used so far for tapered beams have been applied to a simple wing in order to assess the results. As study case, the same airfoil as before has been used for a tapered thin-walled wing whose specifications are reported in Figure 2.69. Some details of the FE model from which the strains are extracted are reported in Appendix M.
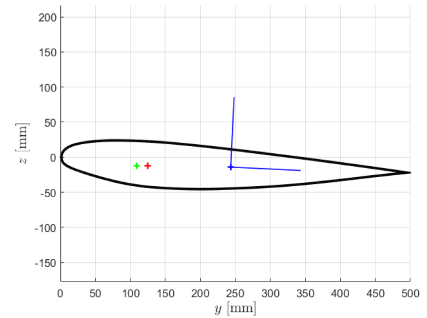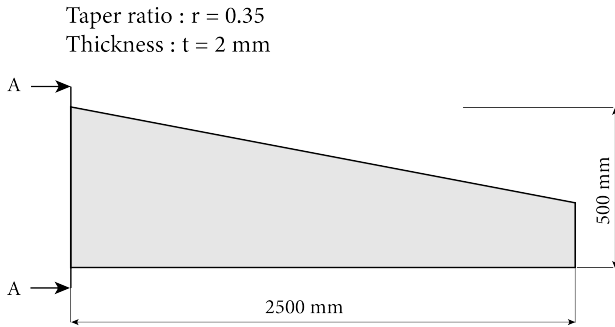
Figure 2.69: *Tapered thin-walled monocell wing.*

The taper ratio used is equal to 0.35 and the thickness is constant along the span. First, a simple tip load equal to $P = 5e3$ N has been applied. Just a single inverse element has been used (Figure 2.70). The results obtained with the methodology outlined before bring accurate results which agree well with the deflections obtained from the FEM model (Figure 2.71). Notice that the load has been applied along the z axis, which is not exactly parallel to a principal direction of the cross-section. Therefore, there will be a deflection along both the z and the y axes.
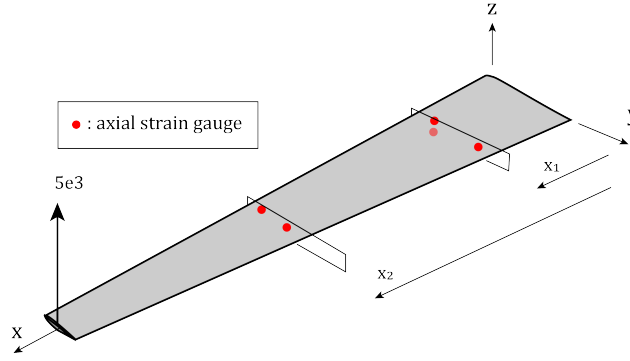
Figure 2.70: *Load case and sensor positions for tip load using a single inverse element.*

(a) *Deflection along z.*
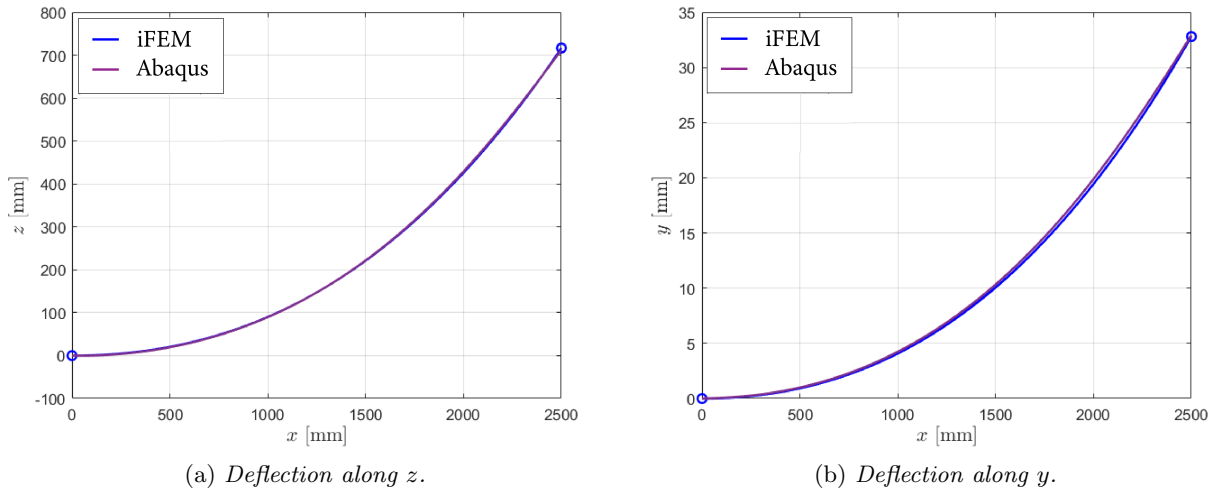
(b) *Deflection along y.*

Figure 2.71: *Deflection reconstruction for tapered wing under tip load.*

It is important to note that, in general, the optimal locations for x_1 and x_2 are not the same for the deflections along the two principal directions. So, two different simulations should be carried out, for each principal direction.

Next, a constant pressure of 0.01 MPa on the bottom skin has been applied (Figure 2.72). Two inverse elements have been used, delivering the results shown in Figure 2.73. The deflection along y seems to be not exactly well recovered. This might be due to the fact that the wing in this direction is not slender enough for the Euler-Bernoulli beam theory.
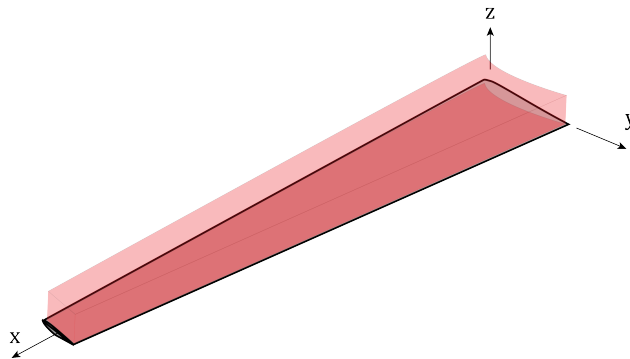
Figure 2.72: *Tapered wing under uniform pressure: $p = 0.01$ MPa.*

(a) *Deflection along z.* (b) *Deflection along y.*
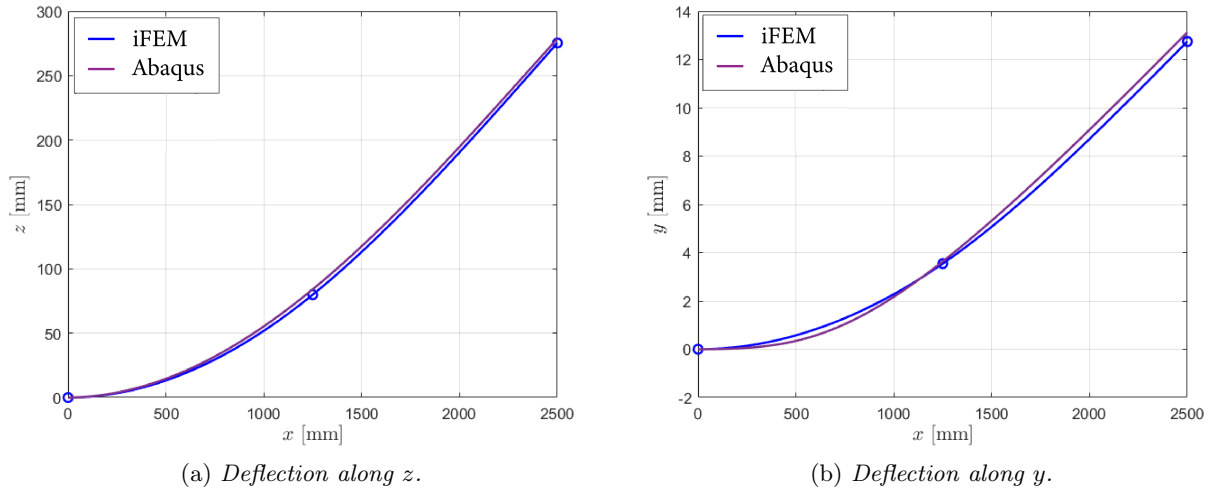
Figure 2.73: *Deflection reconstruction for tapered wing under constant pressure load.*

If the constant pressure distribution is substituted by a parabolic one (Figure 2.74), then the recovered deflection is in general worse, as in Figure 2.75. It is still possible to see the same trend as before, even if there is a larger error between FEM solution and the reconstructed displacement.
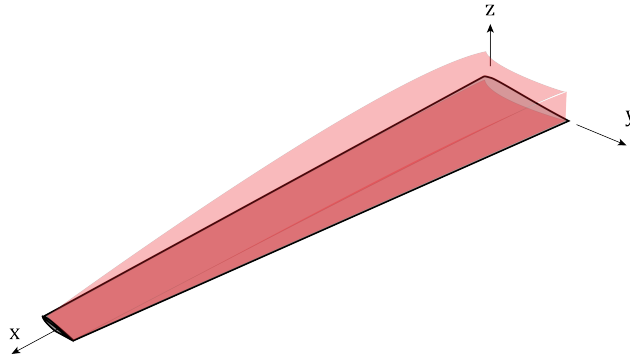
Figure 2.74: *Tapered wing under parabolic pressure:* $p(x, y) = (-x^2 + 2500^2)10^{-8}$ MPa.

(a) *Deflection along z.* (b) *Deflection along y.*
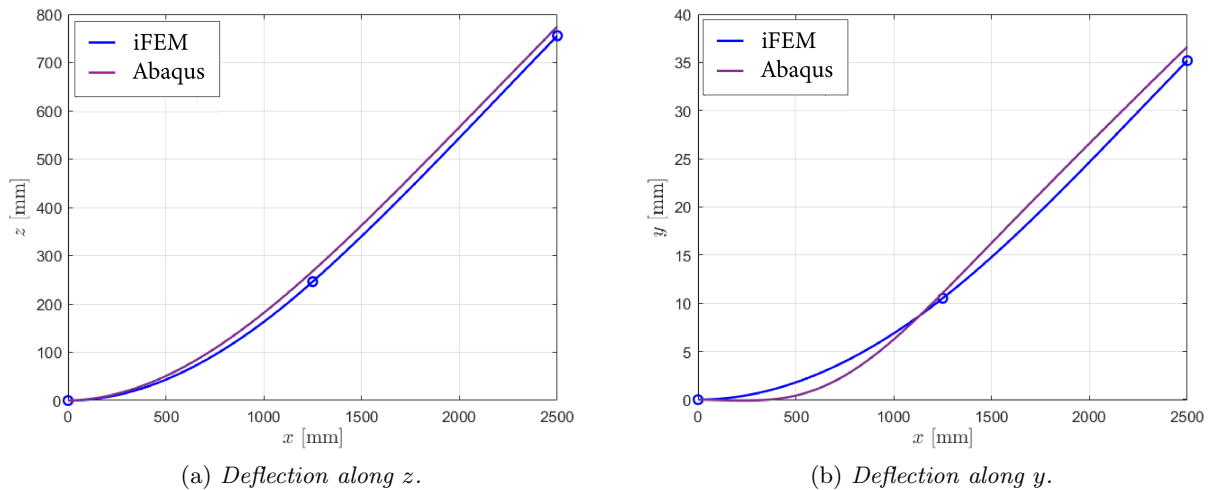
Figure 2.75: *Deflection reconstruction under parabolic pressure load using 2 inverse elements.*

An improvement can be obtained increasing the number of elements, even though still the deflection along y is not well described, possibly because of the reasons pointed out before. In Figure 2.76 four inverse elements have been used, leading to a good agreement for the deflection along z.

(a) *Deflection along z.*   (b) *Deflection along y.*
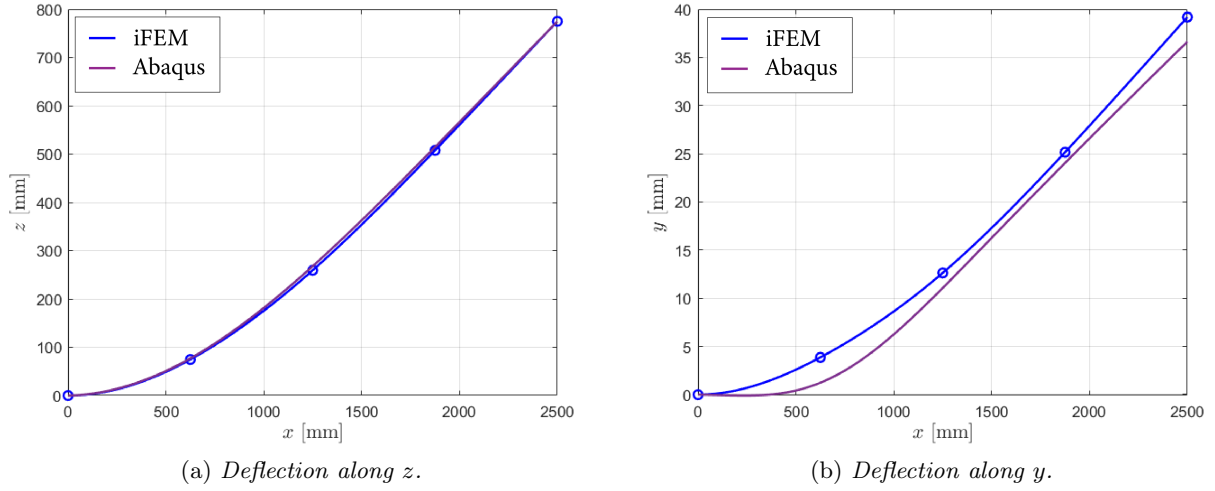
Figure 2.76: *Deflection reconstruction for tapered wing under parabolic pressure load using 4 inverse elements*

2.4.3 Twist reconstruction for tapered beams

Once the bending deformation has been recovered for a tapered beam, it might also be interesting to reconstruct the twist angle variation along the span, in case torsional forces are acting on the structure. As before, also in this case the approach used will consist in trying to decouple the measured shear stress in a contribution due to shear forces and a contribution due to pure torsion. From the latter, the twist angle can be derived.

There is the need then to obtain the distribution of the shear stress along the beam span under shear forces. The problem turns out to be more complicated compared to the prismatic case. Several studies have been carried out for tapered beams with rectangular cross-sections. For example, [24] gives a good and simple overview of the problem. In [46], an extended version of the Jourawski formula is derived and a similar task is also carried out in [34]. The issues of this particular problem come mainly from the fact that the shear stress distribution is highly influenced by the taper which couples the stress distribution with the internal moment of the beam. In order to intuitively explain this effect, consider a tapered beam with rectangular cross section subjected to a tip load, as in Figure 2.77. The axial equilibrium of the highlighted stress element results in:

$$\tau b = b \int_A^B \sigma \mathrm{d}z - b \int_C^D (\sigma + \mathrm{d}\sigma) \mathrm{d}z \tag{2.157}$$

with b the beam width. Now, for a prismatic beam the two integrals are carried out over the same area and therefore the σ term disappears. This is not the case for a tapered beam and this causes the shear stress distribution to be dependent on the internal moment $M_y(x)$.
Following the procedure just described, a solution for a tapered rectangular beam can be derived and this has been widely studied in open literature.
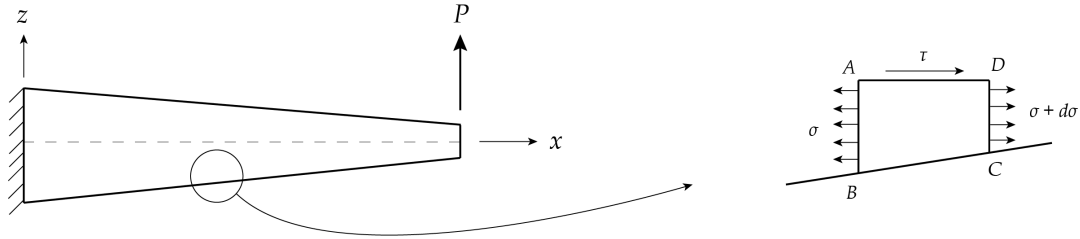

Figure 2.77: *Axial equilibrium for stress element of tapered beam.*

Here, the focus has been restricted just on thin-walled structures which greatly simplifies the problem. In order to conceive a solution, consider how the shear stress is usually computed for prismatic beams. In particular, looking at a stress element (Figure 2.78), the axial equilibrium gives:

$$\left(\sigma_x + \frac{\partial \sigma_x}{\partial x}\delta x\right)\delta s - \sigma_x \delta s + \left(\tau + \frac{\partial \tau}{\partial s}\delta s\right)\delta x - \tau \delta x = 0 \tag{2.158}$$

which neglecting higher order terms simply reduces to:

$$\frac{\partial \tau}{\partial s} + \frac{\partial \sigma_x}{\partial x} = 0 \tag{2.159}$$

The differential equation can be easily solved knowing the distribution of the internal moment. Now, since the direct stress σ_x is influenced by the taper (due to the variation of the second moment of area), a simple way to consider that is to account for it in the expression of σ_x.
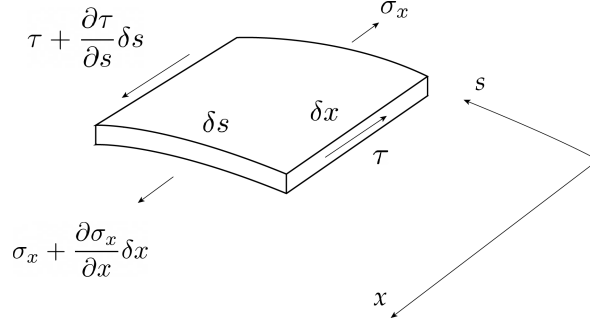
Figure 2.78: *Axial equilibrium for prismatic beams.*

Consider the clamped beam of before with tip load equal to P and that the second moment of area varies with a cubic polynomial. Then:

$$\sigma_x = \frac{M_y(x)}{I_y(x)} z(x) = \frac{P(L-x)}{I_{y0}(1+cx)^3} z(x) \tag{2.160}$$

Note also the coordinate $z(x)$ is dependent on x due to the taper. Since the hope is to apply the method to relatively complex thin-walled cross-sections such as airfoils, there is the need to express $z(x)$ and its derivative in a simple way. In order to do that, it is possible to discretize the cross-section in small segments (Figure 2.79). Considering the j segment, it can be expressed with a parametric expression $\gamma_j(t)$ as follows:

$$\gamma_j(t) = \big(y_1 + t(y_2 - y_1), z_1 + t(z_2 - z_1)\big) \quad ; \quad t \in [0,1] \tag{2.161}$$
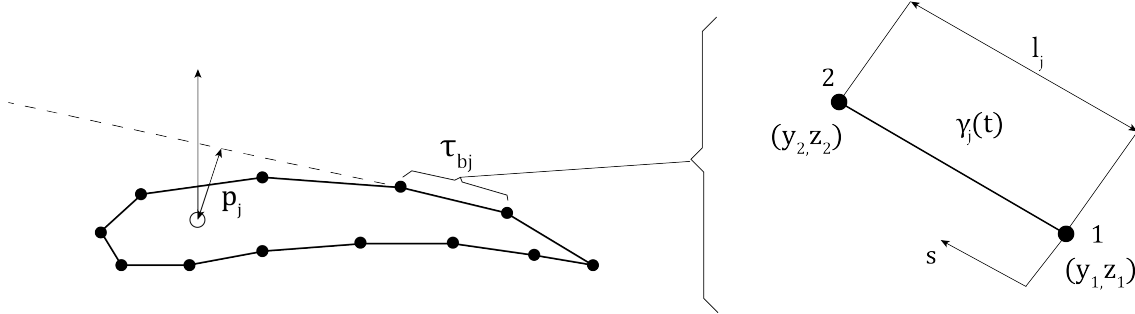
Figure 2.79: *Generic thin-walled cross-section discretized in several segments.*

where $s = t\, l_j$ and the nodal coordinates are function of x as:

$$z_1(x) = z_{10}(1 + cx) \quad ; \quad z_2(x) = z_{20}(1 + cx)$$

$$y_1(x) = y_{10}(1 + cx) \quad ; \quad y_2(x) = y_{20}(1 + cx)$$

where (y_{10}, z_{10}) and (y_{20}, z_{20}) are the corresponding coordinates at the root. So, coming back to our case, the variable $z(x)$ can be written as:

$$z(x) = z_1(x) + t\big(z_2(x) + z_1(x)\big) \tag{2.162}$$

And so the derivative of σ_x w.r.t. x in Eq.(2.159) becomes:

$$
\begin{aligned}
\frac{\partial \sigma_x}{\partial x} &= \frac{\partial}{\partial x}\left(\frac{M_y(x)}{I_y(x)}z(x)\right) \\
&= \frac{\partial}{\partial x}\left[\frac{P(L-x)}{I_{y0}(1+cx)^3}\big[z_1(x)+t(z_2(x)+z_1(x))\big]\right] \\
&= \frac{-P(3Lc-2cx+1)}{I_{y0}(1+cx)^4}[z_1+t(z_2-z_1)] + \frac{P(L-x)}{I_{y0}(1+cx)^3}c[z_{10}+t(z_{20}-z_{10})]
\end{aligned}
\tag{2.163}
$$

Using this expression, the value of τ can be obtained from simple integration. Note that:

- The integration should be performed over s. Expressing the integral in t:

$$
\tau = \int_0^s -\frac{\partial \sigma_x}{\partial x}\mathrm{d}s = l_j \int_0^t -\frac{\partial \sigma_x}{\partial x}\mathrm{d}t
\tag{2.164}
$$

- The integration can be started anywhere on the cross-section, but the initial value of τ is in general unknown (for a simple open cross-section the situation is different and will be considered later). The usual approach followed for prismatic beams is to set $\tau = 0$ where the integration starts, as if the closed cross-section were "cut" there. From the integration the so-called "basic" shear stress is obtained (τ_b). Then, a constant shear flow is added (non-basic shear stress τ_{nb}) such that the resulting stress distribution gives an equivalent (torsional) moment to the one applied on the cross section. Taking the moment center to coincide with the line of action of the applied load, it is possible to obtain that [63]:

$$
\tau_{nb} = -\frac{1}{2\Omega}\oint p\tau_b \mathrm{d}s = -\frac{1}{2\Omega}\sum_j p_i \int_0^{l_j}\tau_{bj}(s)\mathrm{d}s
\tag{2.165}
$$

where Ω is the enclosed area by the cross-section, p is the arm defined in Figure 2.79 and the integral $\oint$ can be computed from the sum performed on each segment j.

The approach just outlined can be applied to a simple thin-walled beam with rectangular cross-section, shown in Figure 2.80. A concentrated load is acting at the tip and the taper ratio used is $r = 0.5$.
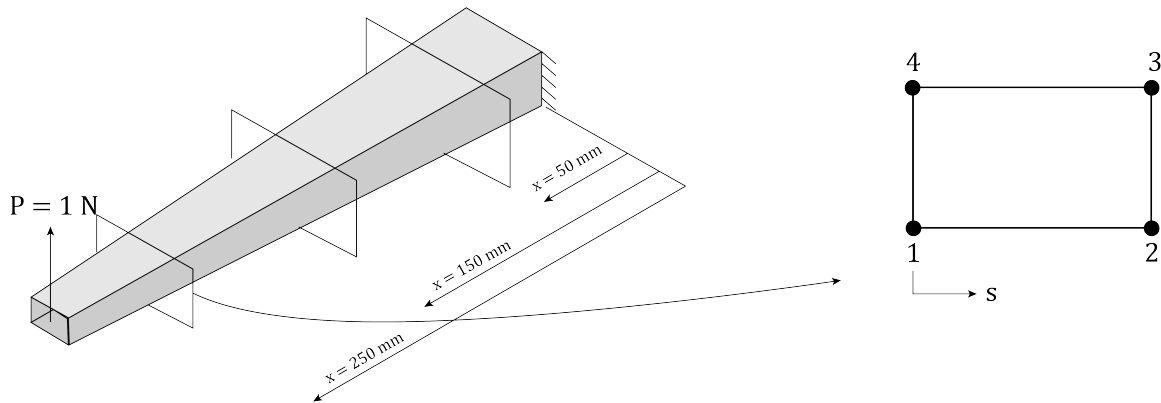

Figure 2.80: *Tapered box beam.*

The shear stress distribution has been computed over three different cross-sections (Figure 2.81), respectively at $x = 250\,\text{mm}$, $x = 150\,\text{mm}$ and $x = 50\,\text{mm}$ in order to show its evolution along the span. The shear stress is plotted along the profile following the ordering of Figure 2.80. Several points have to be pointed out, such as:

- Towards the tip, the solution obtained resembles the reference one: the shear stress is linear in the upper and lower panels, and parabolic in the webs.

- Proceeding along the root, the shear stress distribution in the webs deeply changes, resulting in a change of convexity as illustrated in Figure 2.81c.

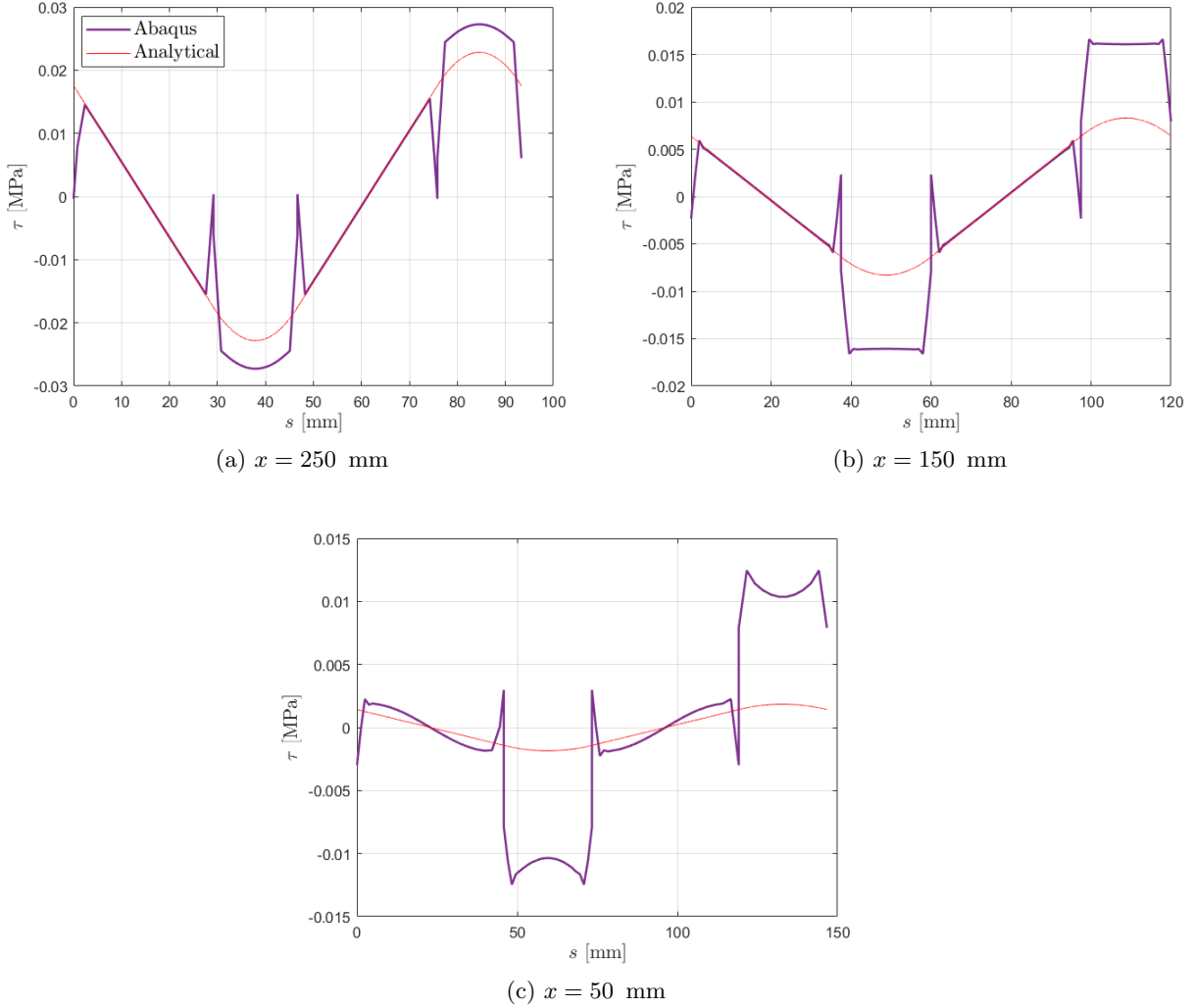- At the corners of the cross-section, the shear stress distribution seems discontinuous.

(a) $x = 250$ mm

(b) $x = 150$ mm

(c) $x = 50$ mm

Figure 2.81: *Shear stress distribution for tapered box beam at three different cross-sections.*

Let us start from the last point, that is the discontinuity observed in the distribution. This effect is related to the fact that the beam is tapered and can be explained from a simple equilibrium along the axial direction. Looking closely at a corner of the cross section, the situation shown in Figure 2.82 occurs.

From the equilibrium along x it is possible to write:
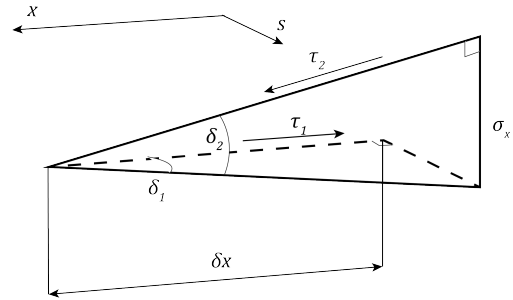
Figure 2.82: *Axial equilibrium at a corner of the tapered box beam.*

$$\tau_1 \delta x - \tau_2 \delta x - \sigma_x \delta x \tan \delta_1 - \sigma_x \delta x \tan \delta_2 = 0 \quad \Rightarrow \quad \tau_2 = \tau_1 + \sigma_x(\tan \delta_1 + \tan \delta_2) \qquad (2.166)$$

therefore, there is a discontinuity in τ given by the term $\sigma_x(\tan \delta_1 + \tan \delta_2)$, which as expected becomes null for the prismatic case since $\delta_1 = \delta_2 = 0$.

From Figure 2.81 it is also clear that the solution of Eq.(2.159), even though considers the presence of tapering (through σ_x), is not enough and apparently is not able to take into account some factors. It is interesting to observe that along the upper and lower panels the solution obtained is relatively accurate, while most of the error occurs in the webs. It is possible to think then that Eq.(2.159) should contain an additional term which is null in the upper and lower panels and appears when the integration is carried out along the webs. Following this intuition, consider an infinitesimal element belonging to a tapered beam. Due to taper, it can be drawn as in Figure 2.83.
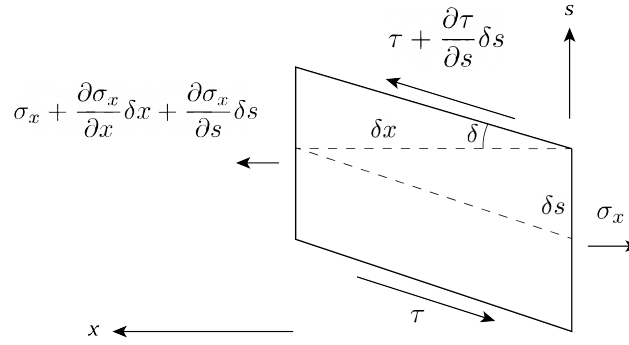
Figure 2.83: *Axial equilibrium for stress element of tapered beam.*

From axial equilibrium, it is possible to write:

$$-\sigma_x \delta s + \left(\sigma_x + \frac{\partial \sigma_x}{\partial x}\delta x + \frac{\partial \sigma_x}{\partial s}\delta s\right)\delta s + \left(\tau + \frac{\partial \tau}{\partial s}\delta s\right)\delta x \cos \delta - \tau \cos \theta \delta x = 0 \qquad (2.167)$$

$$\Rightarrow \quad \frac{\partial \sigma_x}{\partial x} + \frac{\partial \tau}{\partial s}\cos \theta + \frac{\partial \sigma_x}{\partial s}\frac{\delta s}{\delta x} = 0$$

Now, the term $\delta s/\delta x$ can be seen as the corresponding derivative and related to the tapering angle δ, so $\delta s/\delta x = \tan \delta$ and so Eq.(2.167) becomes:

$$\frac{\partial \sigma_x}{\partial x} + \frac{\partial \tau}{\partial s}\cos \delta + \frac{\partial \sigma_x}{\partial s}\tan \delta = 0$$

solving the equation by simple integration, it is possible to obtain the shear stress τ. For closed cross-sections this will be however just the so-called basic shear stress, since it will not satisfy the equivalence of the moments on the cross-section. As pointed out before, a constant shear stress has to be added. For tapered beams however it is important to realize that the situation is slightly different compared to the prismatic case. Considering for example Figure 2.84, it is clear that in the moment equivalence a role is played also by the direct stress σ_x.
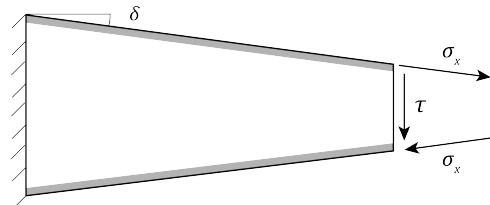

Figure 2.84: *Stress distribution at generic cross-section of tapered beam.*

75

Taking the moment center to coincide with the line of action of the applied loads, it is possible to modify Eq.(2.165) as:

$$\oint p\tau_b \mathrm{d}s + 2\Omega\tau_{nb} + \oint p\sigma_x(\boldsymbol{l}\cdot\boldsymbol{u})\mathrm{d}s = 0 \tag{2.168}$$

$$\Rightarrow \quad \tau_{nb} = -\frac{1}{2\Omega}\left(\oint p\tau_b\mathrm{d}s + \oint p\sigma_x(\boldsymbol{l}\cdot\boldsymbol{u})\mathrm{d}s\right)$$

with $\boldsymbol{l}$ the tangent vector to the cross-section profile and $\boldsymbol{u}$ the direction along which σ_x is acting.

The shear stress distribution which can be obtained in this way has been tested first on a rather simple case, that is a thin-walled tapered strip subjected to a tip force. In Figure 2.85 the strip is shown and, from the FEM simulation, it is possible to qualitatively see the distribution of the shear stress along the span.
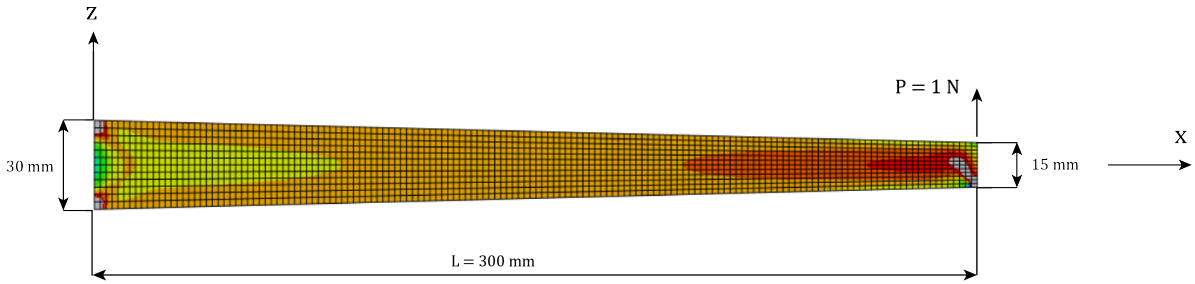
Figure 2.85: *Shear stress distribution for a tapered strip under tip load.*

Since in this case the cross-section is open, no additional shear stress has to be added (τ_{nb}). However, it is important to understand that the shear at the upper and lower edges is not zero, even though the edge is free. Similarly to the case of the rectangular cross section, this is simply caused by the taper angle, as shown in Figure 2.86. Therefore, the initial value to be given to τ is $\sigma_x(x,z)\tan\delta$.
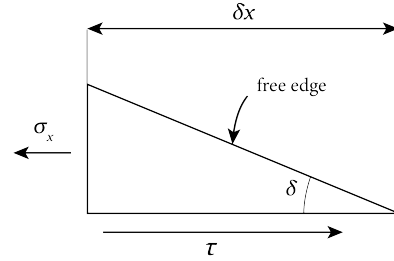

Figure 2.86: *Axial equilibrium for an edge stress element of the tapered strip.*

Now the shear stress can be computed. In order to do that, the cross-section has been divided into small segments even though it consists just of a straight line. This is advantageous because the angle δ depends on s and, for sufficiently small segment lengths l_j, it can be considered to be constant $\delta(s)\approx\delta_j$, rendering the integrations simpler to carry out. So, the stress on the j segment can be written as:

$$\begin{aligned}
\tau_{bj} &= \frac{1}{\cos\delta_j}\int_0^s -\frac{\partial\sigma_x}{\partial x} - \tan\delta_j\frac{\partial\sigma_x}{\partial s}\,\mathrm{d}s \\
&= \frac{l_j}{\cos\delta_j}\int_0^t -\frac{\partial\sigma_x}{\partial x} - \tan\delta_j\frac{\partial\sigma_x}{\partial s}\,\mathrm{d}t
\end{aligned} \tag{2.169}$$

For tip loads the direct stress σ_x is:

$$\sigma_x = \frac{M_y(x)}{I_y(x)}z(x) = \frac{P(L-x)}{I_{y0}(1+cx)^3}\big[z_1(x)+t\big(z_2(x)-z_1(x)\big)\big] \tag{2.170}$$

76

And so Eq.(2.169) becomes:

$$
\begin{aligned}
\tau_{bj} =& \frac{l_j}{\cos \delta_j} \int_0^t \frac{P(3Lc - 2cx + 1)}{I_{y0}(1+cx)^4}\big[z_1(x) + t\big(z_2(x) - z_1(x)\big)\big] - \frac{P(L-x)}{I_{y0}(1+cx)^3}c\big[z_{10} + t\big(z_{20} - z_{10}\big)\big]+ \\
& - \frac{\tan \delta_j}{l_i}\frac{P(L-x)}{I_{y0}(1+cx)^3}\big(z_2(x) - z_1(x)\big)\,\mathrm{d}t \\
=& \frac{l_j}{\cos \delta_j}\bigg[\frac{P(3Lc - 2cx + 1)}{I_{y0}(1+cx)^4}\big[z_1(x)t + \frac{t^2}{2}\big(z_2(x) - z_1(x)\big)\big] - \frac{P(L-x)}{I_{y0}(1+cx)^3}c\big[z_{10}t + \frac{t^2}{2}\big(z_{20} - z_{10}\big)\big]+ \\
& - \frac{\tan \delta_j}{l_j}\frac{P(L-x)}{I_{y0}(1+cx)^3}\big(z_2(x) - z_1(x)\big)t\bigg] + \tau_{bj,0}
\end{aligned}
$$

$$(2.171)$$

with $\tau_{bj,0}$ the shear stress for $t = 0$. The shear stress distribution has been computed in Figure 2.87 at two different span positions, bringing to a good correlation with the FEM reference solution.

(a) $x = 250$ mm

(b) $x = 50$ mm
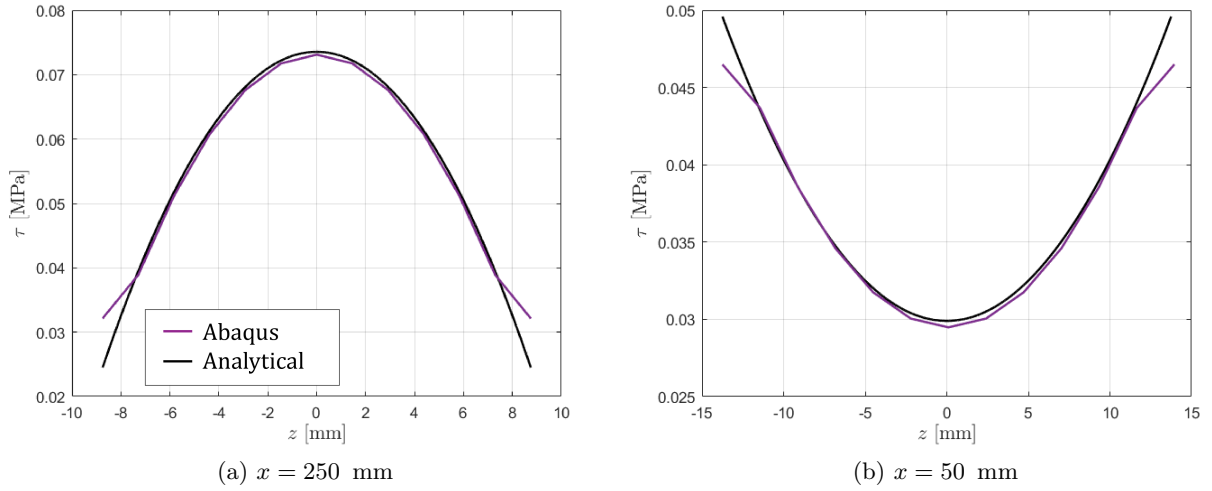
Figure 2.87: *Shear stress distribution for the tapered strip at two different x positions.*

Now the method can be applied also to the box tapered beam introduced before (Figure 2.80). Contrarily to the tapered strip, this beam is more complicated to study because, being closed, there is the need to take into account the non-basic shear stress τ_{nb}. Eq.(2.168) has to be evaluated, substituting the expression of the basic shear stress (Eq.(2.171)) it is possible to obtain:

$$
\begin{aligned}
\tau_{nb} =& -\frac{1}{2\Omega}\bigg[\sum_j l_j p_j \int_0^1 \tau_{bj}\,\mathrm{d}t + \oint \sigma_x(\boldsymbol{l}\cdot\boldsymbol{u})p\,\mathrm{d}s\bigg] \\
=& -\frac{1}{2\Omega}\bigg[\sum_j l_j p_j\bigg[\frac{l_j}{\cos \delta_j}\bigg[\frac{P(3Lc - 2cx + 1)}{I_{y0}(1+cx)^4}\bigg(\frac{z_1}{2} + \frac{1}{6}(z_2 - z_1)\bigg) + \\
& - \frac{P(L-x)}{I_{y0}(1+cx)^3}c\bigg(z_{10}\frac{1}{2} + \frac{1}{6}(z_{20} - z_{10})\bigg) - \frac{\tan \delta_j}{l_j}\frac{P(L-x)}{I_{y0}(1+cx)^3}(z_2 - z_1)\frac{1}{2}\bigg] + \tau_{bj,0}\bigg]+ \\
& + \oint \sigma_x(\boldsymbol{l}\cdot\boldsymbol{u})p\,\mathrm{d}s\bigg]
\end{aligned}
$$

$$(2.172)$$

Using this method, the shear stress has been computed on the rectangular cross-sections shown before and obtaining the results of Figure 2.88. As it is possible to see, there is a significant improvement compared to the previous solutions and a good correspondence with the FEM reference solution.

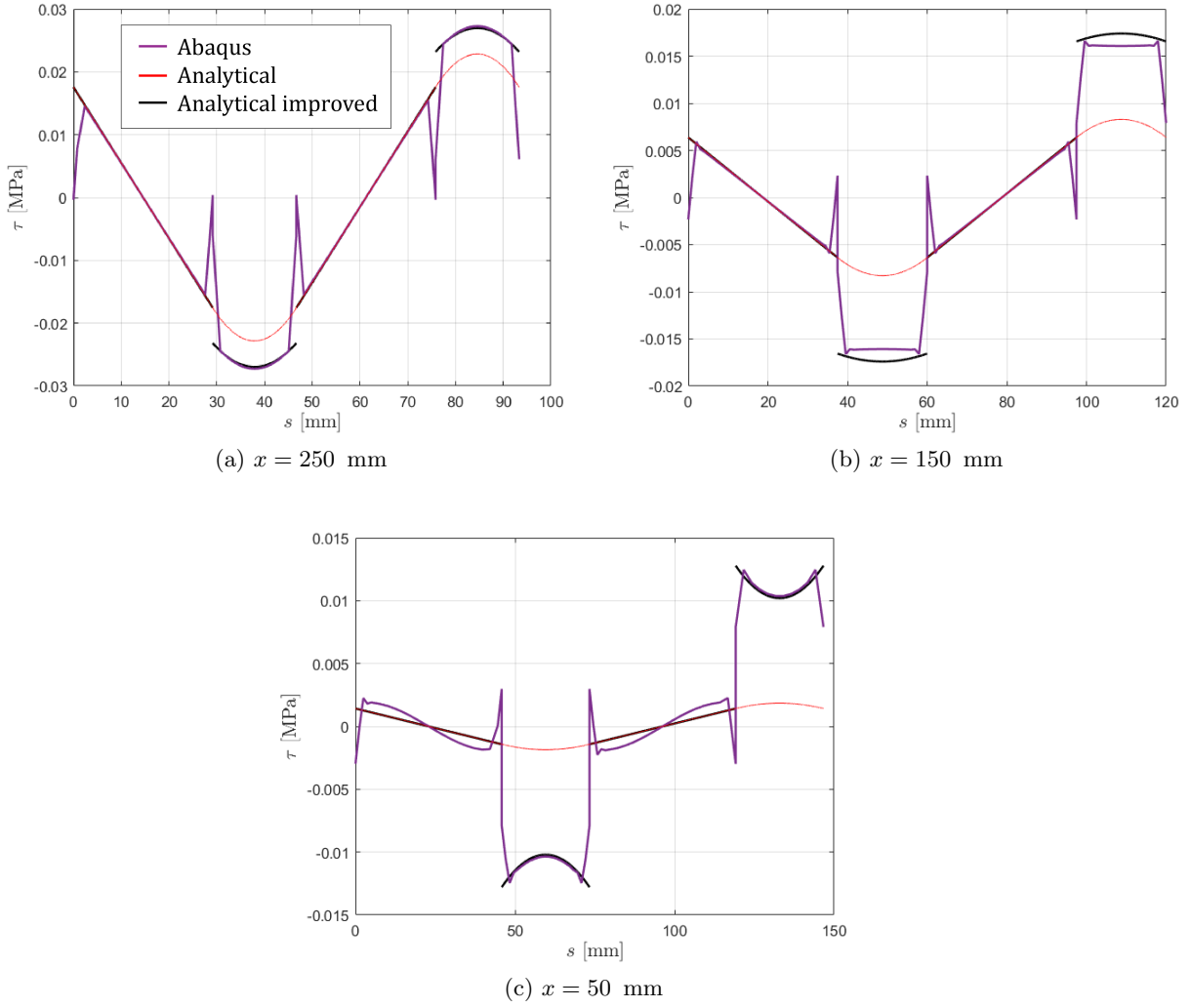(a) $x = 250$ mm

(b) $x = 150$ mm

(c) $x = 50$ mm

Figure 2.88: *Shear stress distribution for tapered box beam using the analytical method introduced.*

To further explore the results which can be obtained with this method, consider again the tapered thin-walled wing of Figure 2.69. This case, being much more complicated compared to the previous one, allows to assess the method for a relatively complex cross-section. The results, shown as usual at three different span positions, are illustrated in Figure 2.89. In general there is a good correspondence, apart near the root. However, this is expected since there the highest bending moments are induced. In any case, the general behaviour has still been captured.

It has been also observed that the results depend greatly on the point where the tapered beam is converging. For the wing used in Figure 2.89 this was lying on the leading edge. In Appendix H it has been slightly moved, but leading to significant changes in the shear stress distribution.
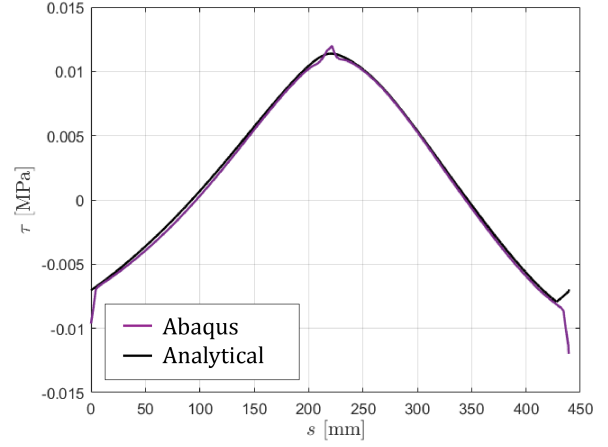
The method developed so far can also be easily extended to a more general internal moment distribution. Consider for example that the beam has been discretized in elements and that the internal moment $M_y(x)$ can be written as (as in Eq.(2.148)):

$$M_y(x) = q_z \left(L^{(e)} x - \frac{x^2}{2} \right) + \left(\sum_{i+1} q_{zi} L_i^{(e)} \right) x - \sum_i q_{zi} L_i^{(e)} r_i \qquad (2.173)$$
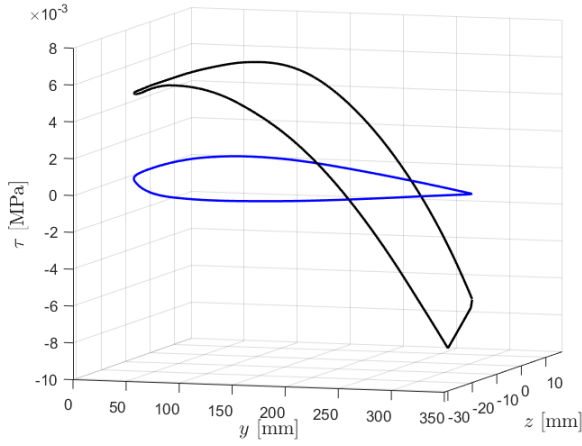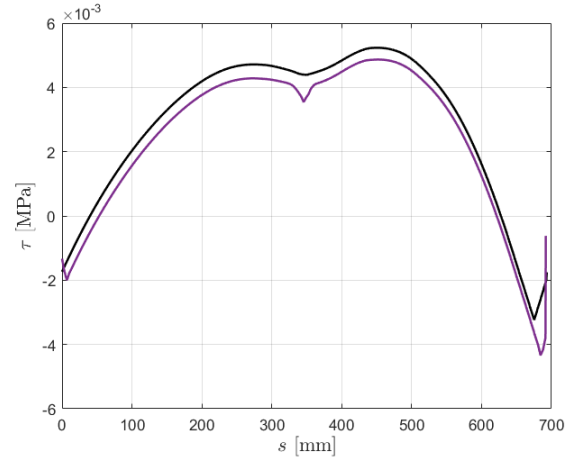
then it is possible to derive that:
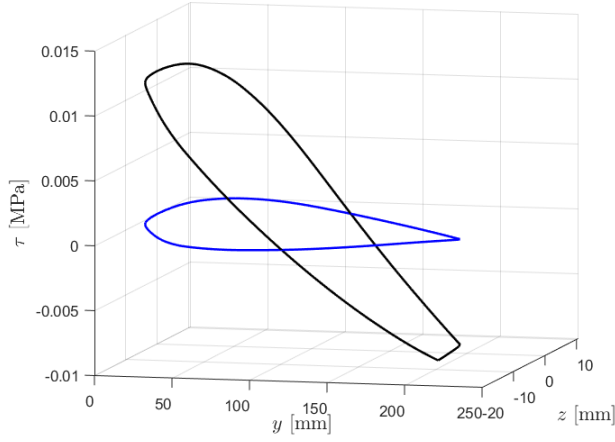
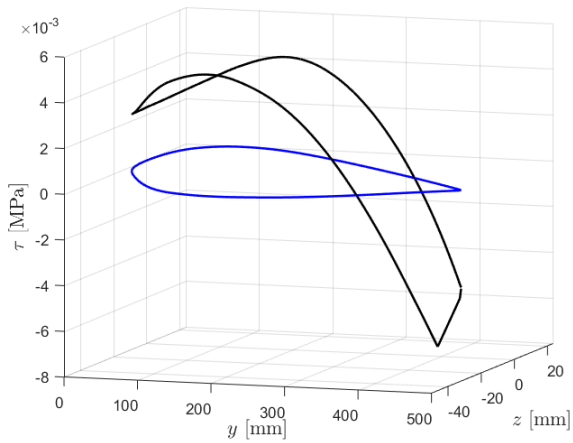(a) *Shear stress over airfoil profile at $x = 2200$ mm.*

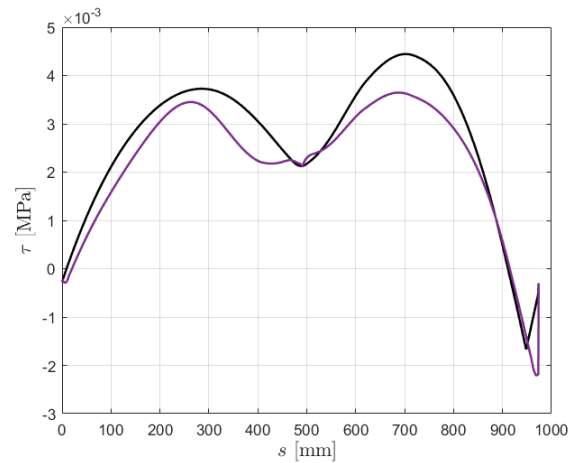(b) *Shear stress along airfoil profile at $x = 2200$ mm.*

(c) *Shear stress over airfoil profile at $x = 1250$ mm.*

(d) *Shear stress along airfoil profile at $x = 1250$ mm.*

(e) *Shear stress over airfoil profile at $x = 200$ mm.*

(f) *Shear stress along airfoil profile at $x = 200$ mm.*

Figure 2.89: *Shear stress distribution for the tapered wing at three different cross-sections.*

$$\frac{\partial \sigma_x}{\partial x} = -\frac{3}{2} \frac{c\left(2L^{(e)}q_z x - q_z x^2 + 2\left(\sum_{i+1} q_{zi}L_i^{(e)}\right)x - 2\sum_i q_{zi}L_i^{(e)}r_i\right)}{I_{y0}(1+cx)^4}\left[z_1 + t(z_2 - z_1)\right] +$$

$$+ \frac{1}{I_{y0}(1+cx)^3}\left[q_z\left(L^{(e)}x - \frac{x^2}{2}\right) + \left(\sum_{i+1} q_{zi}L_i^{(e)}\right)x - \sum_i q_{zi}L_i^{(e)}r_i\right]c\left[z_{10} + t(z_{20} - z_{10})\right]$$

$$\frac{\partial \sigma_x}{\partial s} = \frac{1}{l_j}\frac{\partial \sigma_x}{\partial t} = \frac{1}{l_j}\frac{1}{I_{y0}(1+cx)^3}\left[q_z\left(L^{(e)}x - \frac{x^2}{2}\right) + \left(\sum_{i+1} q_{zi}L_i^{(e)}\right)x - \sum_i q_{zi}L_i^{(e)}r_i\right](z_2 - z_1) \tag{2.174}$$

$$\tag{2.175}$$

and so the basic shear stress of the j segment becomes:

$$\tau_{bj} = \frac{l_j}{\cos \delta_j}\int_0^t\left[-\frac{\partial \sigma_x}{\partial x} - \tan\delta_j\frac{\partial \sigma_x}{\partial s}\right]\mathrm{d}t$$

$$= -\frac{l_j}{\cos \delta_j}\left[-\frac{3}{2}\frac{c\left(2L^{(e)}q_z x - q_z x^2 + 2\sum_{i+1} q_{zi}L_i^{(e)}x - 2\sum_i q_{zi}L_i^{(e)}r_i\right)}{I_{y0}(1+cx)^4}\left(z_1 t + \frac{t^2}{2}(z_1 - z_1)\right) +\right.$$

$$+ \frac{1}{I_{y0}(1+cx)^3}\left[q_z\left(L^{(e)}x - \frac{x^2}{2}\right) + \sum_{i+1} q_{zi}L_i^{(e)}x - \sum_i q_{zi}L_i^{(e)}r_i\right]c\left(z_{10}t + \frac{t^2}{2}(z_{20} - z_{10})\right) +$$

$$\left. + \frac{\tan\delta_j}{l}\frac{1}{I_{y0}(1+cx)^3}\left[q_z\left(L^{(e)}x - \frac{x^2}{2}\right) + \sum_{i+1} q_{zi}L_i^{(e)}x - \sum_i q_{zi}L_i^{(e)}r_i\right](z_2 - z_1)t\right] + \tau_{bj,0} \tag{2.176}$$
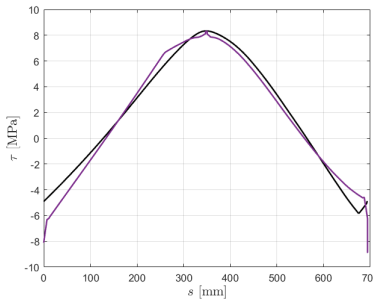
Eq.(2.176) can be integrated to obtain the non-basic shear stress using Eq.(2.168).
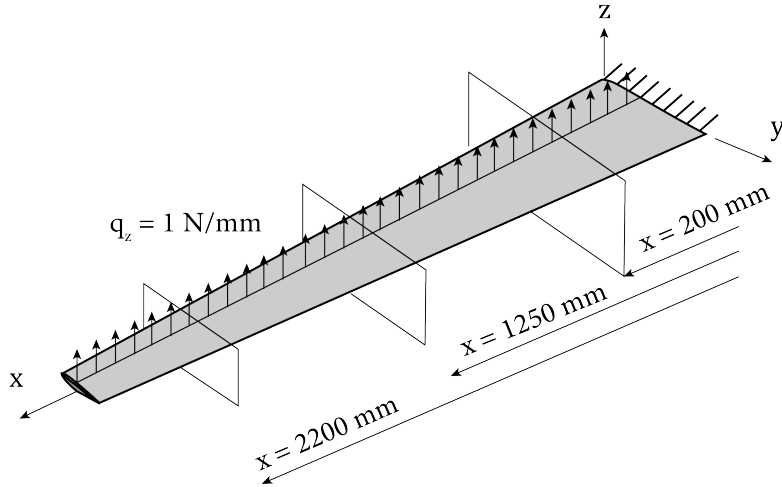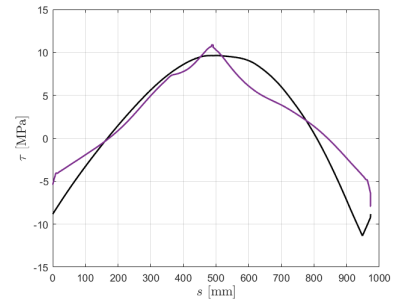

(a) *Tapered wing under constant distributed load.*
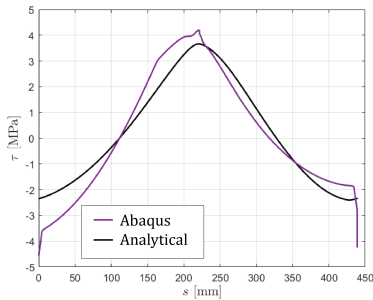
(b) *Shear stress at $x = 2200$ mm.* (c) *Shear stress at $x = 1250$ mm.* (d) *Shear stress at $x = 200$ mm.*

Figure 2.90: *Shear stress distribution for the tapered wing.*

Using the same wing as before, a constant distributed load $q_z = 1$ N/mm has been applied, as in Figure 2.90a, and the corresponding results are displayed in Figure 2.90b-d. For this load case, a worse correlation with the reference FEM results is observed. Apart from the approximate method used, this is also due to the fact that in the FEM model the load has been applied directly on the skin with a set of concentrated nodal forces which approximate the distributed load.

Having at disposal an estimate of the shear stress distribution over the section induced by shear forces, it is possible to derive the angle of twist of the beam along its span. Similarly as before (Section 2.2.1), the main idea consists in comparing the experimental shear stress with the analytical one given by just shear forces. The difference will be due to torsional forces from which the angle of twist can be derived.

First of all, it is important to know the shear stress due to a unit torsional moment at the position where the shear-sensitive strain gauge is positioned (τ_{12}^t). This can be done either analytically or numerically with FEM, for example using as model a simple extrusion of the cross-section. For tapered beams however in theory this should be done for every section where a shear-sensitive strain gauge is positioned. It would be convenient to know which relation occurs between the shear stresses due to torsion at different sections for tapered beams. In other words, looking at Figure 2.91, the problem consists in finding how $\tilde{\tau}_{12}^t$ is related to τ_{12}^t.
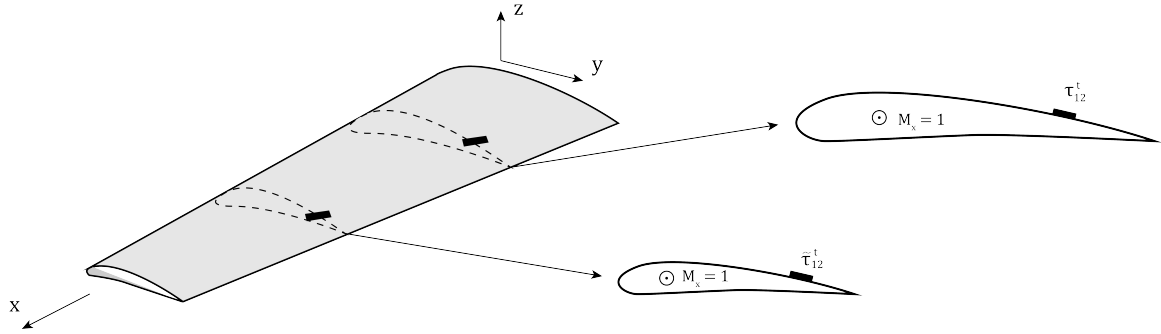

Figure 2.91: *Tapered wing with shear-sensitive strain gauges at two different cross-sections.*

Considering that between the two sections the linear dimensions are reduced by a factor r, then it is possible to write:

$$\mathrm{d}\tilde{A} = r^2 \mathrm{d}A \quad ; \quad \tilde{y} = ry \quad ; \quad \tilde{z} = rz \tag{2.177}$$

where the sign $\tilde{\bullet}$ refers to the section where $\tilde{\tau}_{12}^t$ is present. Since the sections are homologous, the shear stresses will have the same distribution given by the generic function $f(y,z)$. So it is possible to write:

$$\begin{aligned}
\tau_{xz} &= T_{xz} f(y,z) \\
\tau_{yz} &= T_{yz} f(y,z) \\
\tilde{\tau}_{xz} &= \alpha T_{xz} f(\tilde{y}, \tilde{z}) \\
\tilde{\tau}_{yz} &= \alpha T_{yz} f(\tilde{y}, \tilde{z})
\end{aligned} \tag{2.178}$$

where T_{ij} stands for the magnitude of the shear stress and the factor α is the unknown factor of proportionality. Since both sections are under a unit torsional moment M_x:

$$M_x = \iint_A \left(\tau_{xz} y - \tau_{xy} z \right) \mathrm{d}A = \iint_{\tilde{A}} \left(\tilde{\tau}_{xz} \tilde{y} - \tilde{\tau}_{xy} \tilde{z} \right) \mathrm{d}\tilde{A} \tag{2.179}$$

and substituting Eq.(2.177) and Eq.(2.178) it is possible to obtain that $\alpha = 1/r^3$. Now, if the skin thickness is considered to be constant along the span, then $d\tilde{A} = r\,dA$ and as a consequence $\alpha = 1/r^2$.

Before proceeding, it is also useful to know how the torsional constant $J = J(x)$ changes along the tapered beam span. Considering as usual that the linear dimensions change linearly and that the thickness remains constant, for thin-walled cross-sections the following holds:

$$J(x) = 4\Omega^2 \left/ \oint \frac{ds}{t} \right. \tag{2.180}$$

Using the usual notation:

$$\Omega(x) = \Omega_0(1 + cx)^2 \quad ; \quad \oint ds(x) = \oint ds \bigg|_{x=0} (1 + cx)$$

and therefore it is possible to write that:

$$J(x) = J_0(1 + cx)^3 \tag{2.181}$$

At this point, we can start the discussion assessing first the twist angle reconstruction in presence of tip concentrated loads. Consider a tapered beam which has been discretized in several elements, in each of them a shear-sensitive strain gauge is present and the torsional moment is constant along the element span (Figure 2.92). Assuming that the torsional moment M_x has been recovered comparing the experimental shear stress and the one computed analytically due to only shear forces, the twist angle θ_x is given by:
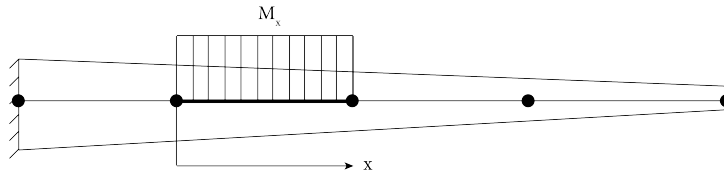

Figure 2.92: *Tapered wing with step-wise constant torsional moment M_x.*

$$\frac{d\theta_x}{dx} = \frac{M_x}{GJ(x)} \quad \Rightarrow \quad \theta_x(x) = \frac{M_x}{GJ_0} \int_0^x \frac{1}{(1 + cx)^3} dx \tag{2.182}$$

$$\theta_x(x) = \frac{M_x}{GJ_0 c} \left[-\frac{1}{2(1 + cx)^2} + \frac{1}{2} \right] + C$$

where the constant of integration can be computed imposing continuity with the previous element:

$$\theta_x(0) = \theta_{x0} \quad \Rightarrow \quad C = \frac{1}{2} + \frac{\theta_{x0}GJ_0 c}{M_x} \tag{2.183}$$

In order to show some results, consider again the thin-walled tapered beam with rectangular cross-section, loaded as shown in Figure 2.93a and discretized with a single inverse element. The beam is loaded by concentrated forces and moments at the tip and the twist angle has been reconstructed installing the shear-sensitive strain gauges respectively at $x = 50\,\text{mm}$, $x = 150\,\text{mm}$ and $x = 250\,\text{mm}$. In all cases a good reconstruction is possible. However, it is important to underline that the shear stress due to the tip force is much smaller compared to the one coming from the torsional moment applied. Therefore, small inaccuracies in the computation of the shear stress due to shear forces have a negligible effect. For lower values of the torsional moment in general a worse correlation is expected.
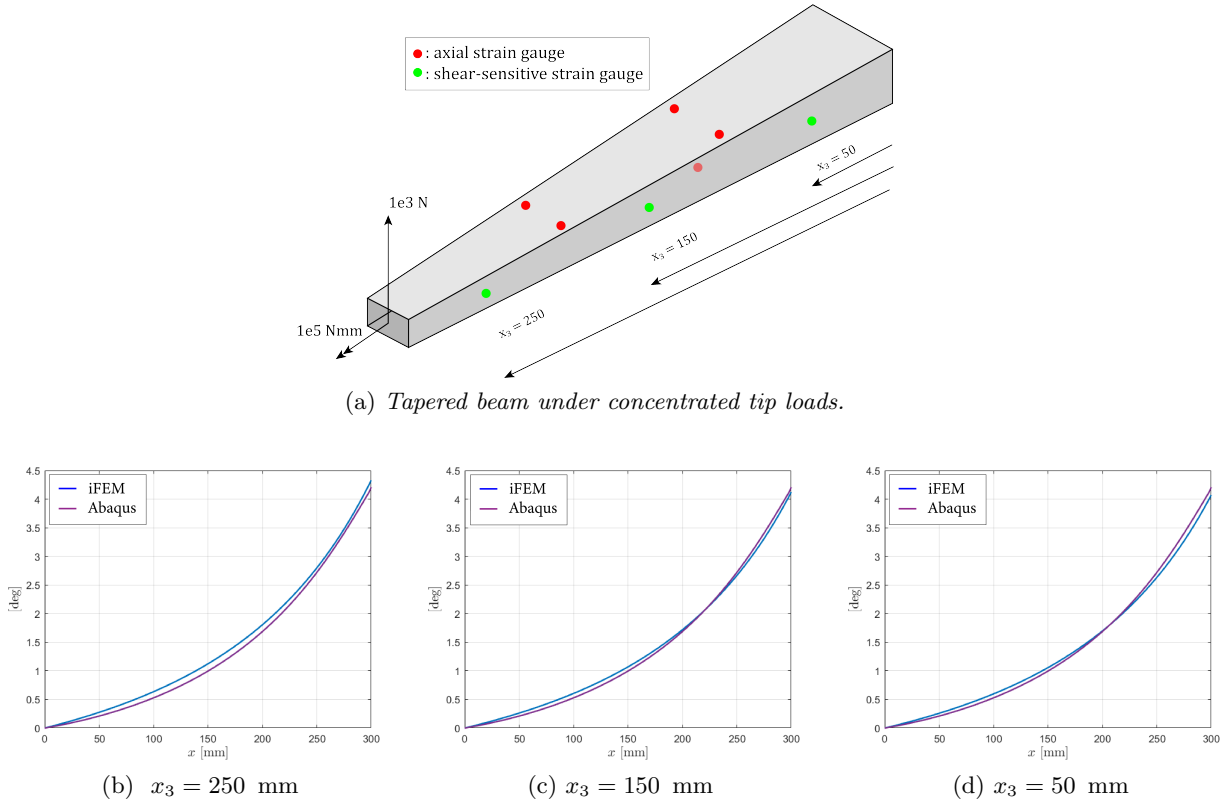
(a) *Tapered beam under concentrated tip loads.*

(b) $x_3 = 250$ mm (c) $x_3 = 150$ mm (d) $x_3 = 50$ mm

Figure 2.93: *Twist angle reconstruction for tapered box beam under concentrated fores at the tip using different positions x_3 for the shear-sensitive strain gauge.*

2.4.4 Application of twist reconstruction to tapered wing

Consider now the usual tapered wing, loaded at the tip as in Figure 2.94. Also in this case, three different positions of the shear-sensitive strain gauges have been tested. They are located at 1/4 of the local chord length (from the trailing edge), while along the wing span at $x = 200$ mm, $x = 1250$ mm and $x = 2200$ mm.
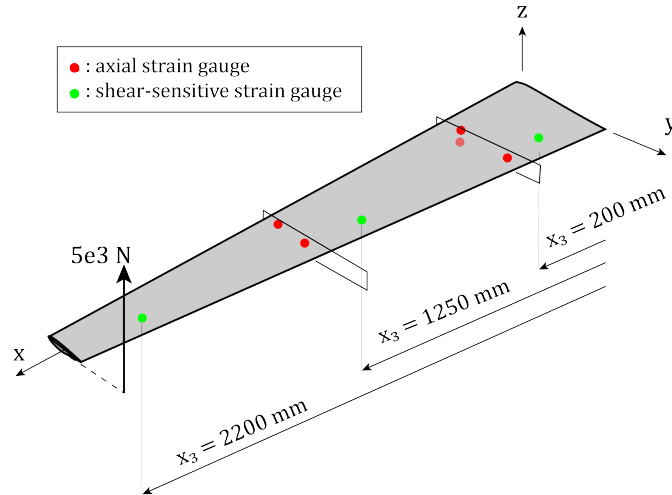

Figure 2.94: *Tapered wing under tip load with off-set from shear center.*

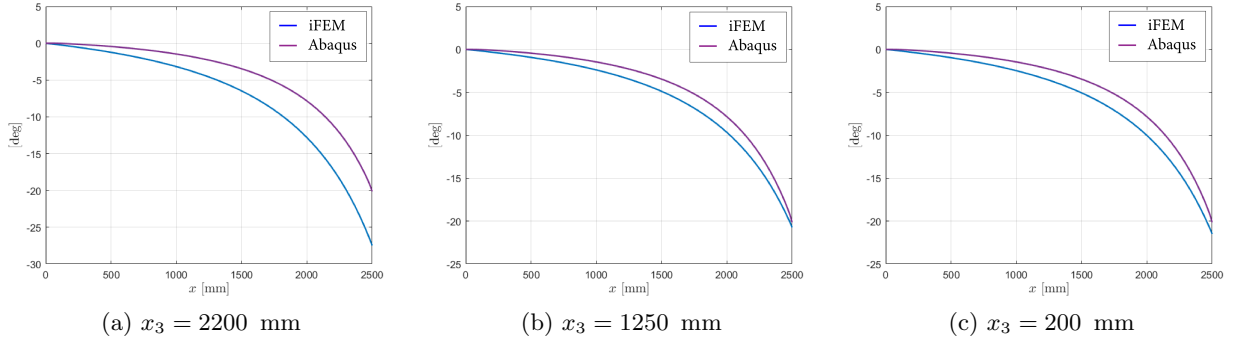(a) $x_3 = 2200$ mm   (b) $x_3 = 1250$ mm   (c) $x_3 = 200$ mm

Figure 2.95: *Twist angle reconstruction of tapered wing under tip load using three different positions for the shear-sensitive strain gauges.*

Looking at the results of Figure 2.95, it might be surprising to see that for the case $x_3 = 2200$ mm the error in the twist reconstruction is larger compared to sampling the strain at $x_3 = 1250$ mm. The shear stress is actually better reconstructed from the analytical model at $x_3 = 2200$ mm than at $x_3 = 1250$ mm, as it is clear from Figure 2.96.

These results can be explained looking at the strain field where the shear-sensitive strain gauges have been positioned. In Table 2.7 the axial (ε_x) and in-plane transversal (ε_2) strain at each location has been extracted from the FEM model. From beam theory the in-plane transversal strain ε_2 should be given by $-\nu\varepsilon_x$. However, due to the load introduction, at $x_3 = 2200$ mm a large difference is present w.r.t. this value, as it is possible to see. This highlights the unsuitability to use the experimental strain sampled there to recover the shear strain, and in turn to recover the twist angle.

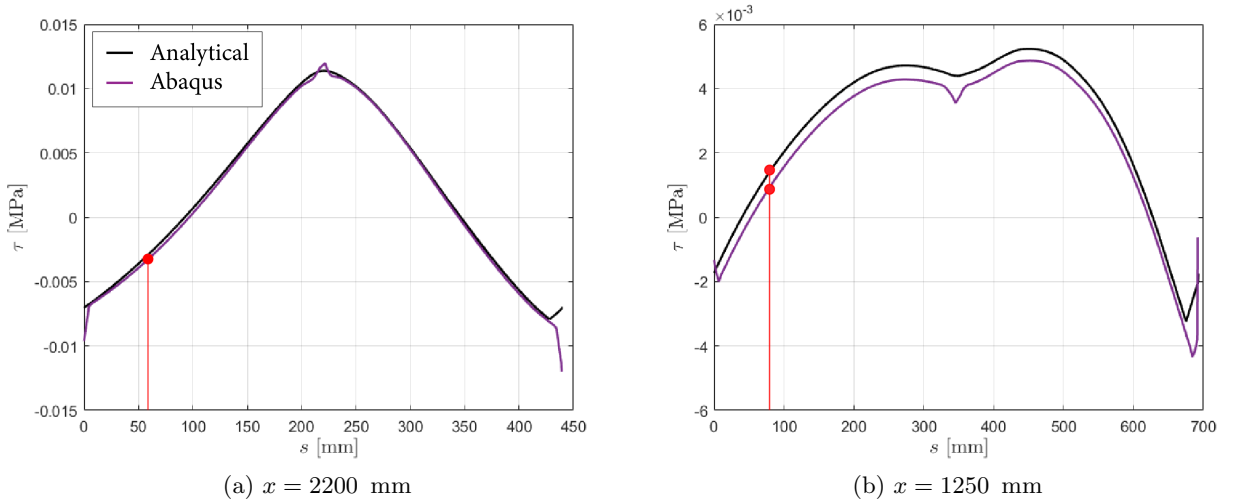(a) $x = 2200$ mm   (b) $x = 1250$ mm

Figure 2.96: *Comparison of analytical and reference shear stress distribution at two different cross-sections. The red line shows the position on the airfoil where the strain is measured.*

Axial position	ε_x	ε_2	$-\nu\varepsilon_x$	$|\varepsilon_2 + \nu\varepsilon_x|/\varepsilon_2$
$x = 2200$ mm	$-2.44e-3$	$1.27e-3$	$7.32e-4$	42%
$x = 1250$ mm	$-3.05e-3$	$1.08e-3$	$9.156e-4$	15%
$x = 200$ mm	$-2.55e-3$	$8.69e-4$	$7.66e-4$	12%

Table 2.7: *Axial and transversal strain at the locations where the shear-sensitive strain gauges have been positioned.*

Now consider a more general scenario, that is in case of constant distributed loads. Similarly to what was done for prismatic beams, the torsional moment along the beam span can be expressed as:

$$M_x(x) = (L^{(e)} - x)\overline{m}_x + M_x^{(+)} \tag{2.184}$$

with $M_x^{(+)}$ the torsional moment at the beam element end. Assuming that M_x has been computed at $x = x_3$, then:

$$\overline{m}_x = \frac{M_x^\varepsilon - M_x^{(+)}}{L^{(e)} - x_3} \tag{2.185}$$

with M_x^ε the measured value, and so the twist angle along the beam span can be obtained as usual:

$$
\begin{aligned}
\theta_x(x) &= \int_0^x \frac{M_x(x)}{GJ(x)} \mathrm{d}x \\
&= \int_0^x \frac{(L^{(e)} - x)\overline{m}_x + M_x^{(+)}}{GJ_0(1 + cx)^3} \mathrm{d}x \\
&= -\frac{1}{2} \frac{L^{(e)} c \overline{m}_x - 2c\overline{m}_x x + M_x^{(+)} c - \overline{m}_x}{GJ_0 c^2 (1 + cx)^2} + C
\end{aligned}
\tag{2.186}
$$

where the integration constant C is determined from $\theta_x(0) = \theta_{x0}$.

As an example, the usual tapered wing has been subjected to a constant distributed load with an offset from the shear center. In this case, four inverse elements have been considered and in the middle of each one a shear-sensitive strain gauge has been positioned at the mid-chord on the upper skin (Figure 2.97). Three different load cases have been considered:

1. Load case 1: A constant distributed load of 1 N/mm applied at 70% of the chord on the bottom skin. The load, in the FE model, has been applied with a set of concentrated nodal forces (Figure 2.98a).

2. Load case 2: A constant distributed load of 1 N/mm applied at the trailing edge (Figure 2.98b).

3. Load case 3: Two sets of constant distributed loads, respectively of 1 N/mm on the trailing edge and 0.5 N/mm on the leading edge (Figure 2.98c).
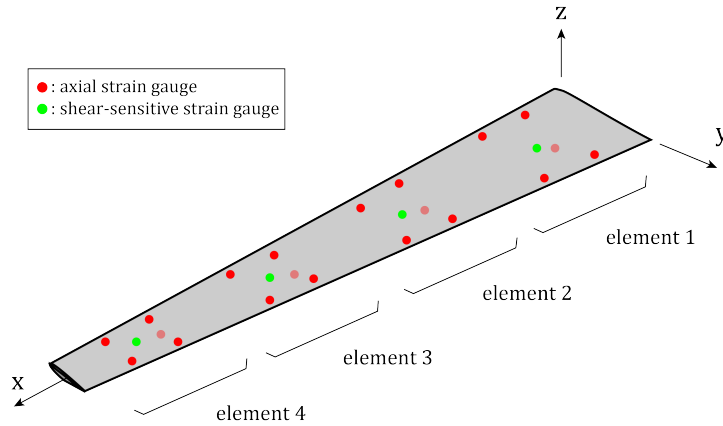

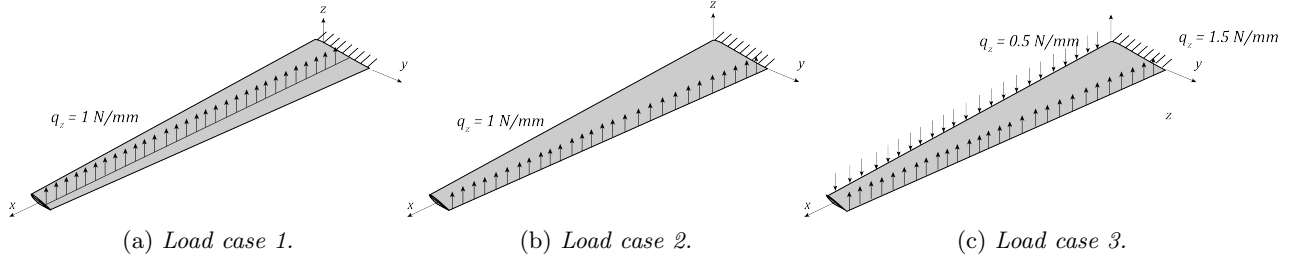Figure 2.97: *Tapered wing discretized with four inverse elements.*

(a) *Load case 1.* (b) *Load case 2.* (c) *Load case 3.*

Figure 2.98: *Load cases: the same bending moment is applied, but the torsional moment changes among the configurations.*

(a) *Twist for load case 1.* (b) *Twist for load case 2.* (c) *Twist for load case 3.*
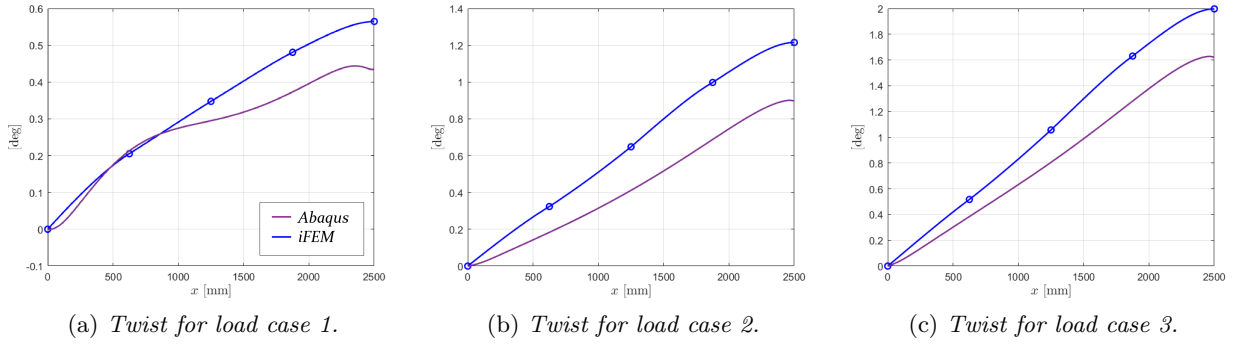
Figure 2.99: *Twist angle reconstruction for tapered wing under constant distributed load.*

In this way, the overall torsional moment applied is increased, but the applied bending moment remains the same. The results are shown in Figure 2.99 where the twist angle has been plotted. In general it is possible to observe a not negligible error in all cases, but with some improvements of the performance increasing the torsion applied to the wing. Considering Figure 2.98b as the reference, the sources of error can be classified follows:

1. From the iFEM analysis, the magnitude of the distributed loads is derived from the bending deflection (Figure 2.100). In this case $q_z = 1$ N/mm, but due to the not prefect reconstruction (and the simple Euler-Bernoulli beam theory to model the wing) the load is only approximately recovered, obtaining over the elements the following:

$$q_z = \begin{bmatrix} \text{element \#1: } 0.27 \\ \text{element \#2: } 1.12 \\ \text{element \#3: } 0.85 \\ \text{element \#4: } 1.13 \end{bmatrix} \text{ N/mm}$$
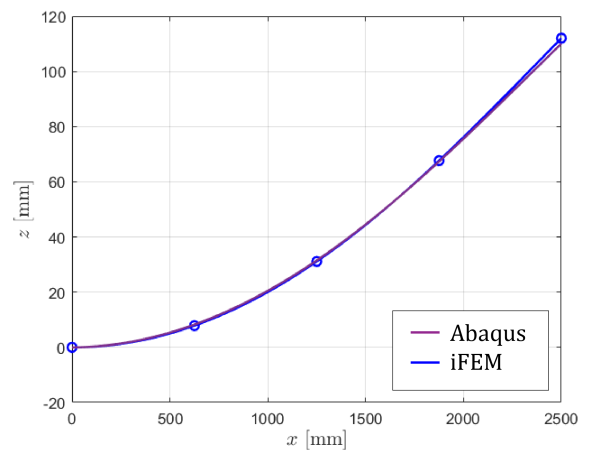

Figure 2.100: *Bending reconstruction.*

2. The strain over the wing follows only approximately the beam theory assumptions. Looking at the axial and in-plane transversal strains of the FEM model at the shear-sensitive gauge locations, it is possible to obtain Table 2.8.

86

	ε_x	ε_2	$-\nu\varepsilon_x$	$|\varepsilon_2 + \nu\varepsilon_x|/\varepsilon_2$
#4 element	$-1.03e-4$	$3.39e-5$	$3.08e-5$	9%
#3 element	$-4.48e-4$	$1.46e-4$	$1.34e-4$	8%
#2 element	$-7.46e-4$	$2.43e-4$	$2.24e-4$	8%
#1 element	$-9.51e-4$	$3.33e-4$	$2.85e-4$	14%

Table 2.8: *Axial and in-plane transversal strain at the locations where the shear-sensitive strain gauges have been positioned.*

In general a relatively close correspondence between ε_2 and $-\nu\varepsilon_x$ is present, so this source of error is not expected to play a major role.

3. The axial strain is interpolated over the shear-sensitive strain gauges in order to obtain the shear strain at those positions.

4. The shear stress due to the shear forces has been computed analytically as explained before. The solutions however contain errors (see Figure 2.90).

The weight on the final solution of points (1), (3) and (4) can be assessed using as input for the twist angle reconstruction directly the FEM results. In other words, both the shear stress due to shear forces and the actual shear stress have been extracted from FEM. The results following this approach are shown with a cyan line in Figure 2.101, together with the ones previously obtained.
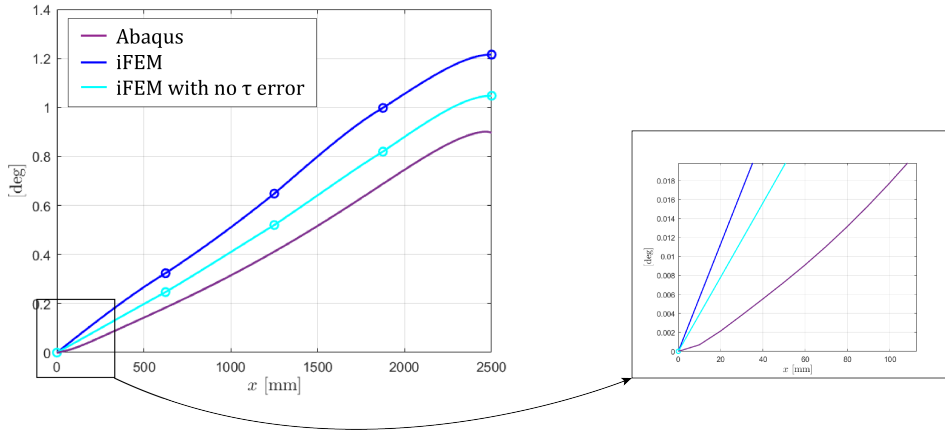

Figure 2.101: *Twist reconstruction for load case 2 using the exact shear stress values.*

As it is possible to see, the situation has improved but still a not negligible error is present. This is deemed to be due to the fact that the simple de Saint-Venant assumptions have been used, but at the wing root the section seems to be stiffer. Therefore, a possible better approximation would take this into account by setting $\mathrm{d}\theta_x/\mathrm{d}x|_{x=0} = 0$. However, this would mean extending the restrained warping theory to tapered beams and it has not been studied here.

2.5 Development of a beam model for the ISTAR demonstrator wing

In this section the model of the ISTAR wing demonstrator is described in detail (Section 2.5.1). Furthermore, is derived the beam model used to retrieve the bending deformations of the wing and it will be assessed using different load cases, in particular a simple tip load (Section 2.5.2), a constant pressure load (Section 2.5.3) and a parabolic pressure load (Section 2.5.4). Just the bending reconstruction will be considered since from Section 2.4.4 it was observed that the twist reconstruction can lead to quite approximate results. Therefore, it has been decided not to investigate the twist reconstruction for this more complex study case.

2.5.1 Model specifications and simplifications

(a) *Top view.*

(b) *Isometric view.*
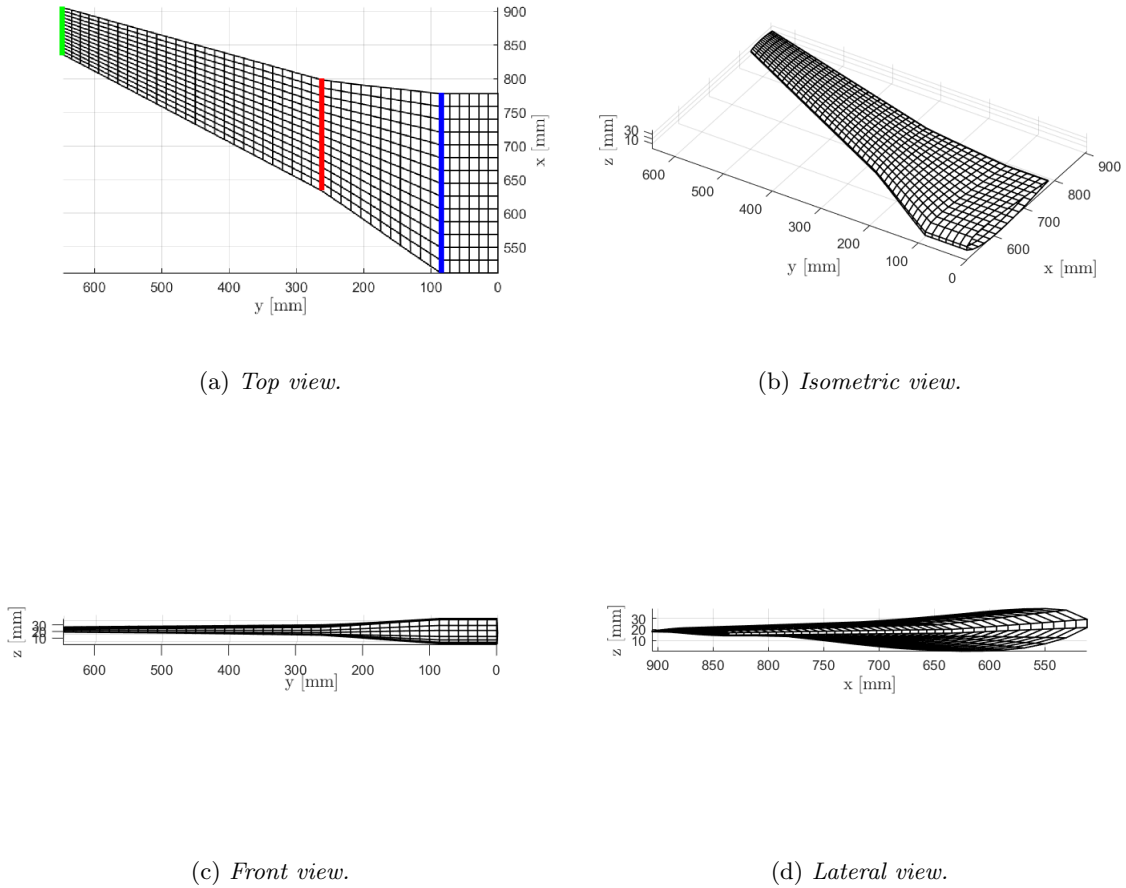
(c) *Front view.*

(d) *Lateral view.*

Figure 2.102: *ISTAR demonstrator wing FE mesh.*

The wing FE mesh is represented in Figure 2.102 using different views for clearness. The geometry of the wing is rather complex, not only because it is swept and tapered at the same time, but also because its profile is changing along the wing span. In particular, in Figure 2.102a three sections have been highlighted. The corresponding wing profiles used are represented in Figure 2.103 using the same chord length.
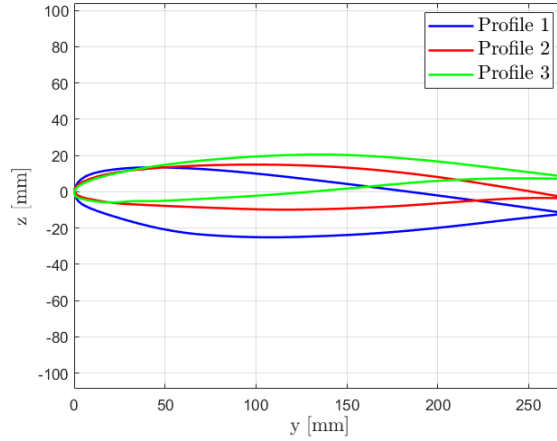
Figure 2.103: *Airfoils used for the ISTAR demonstrator wing.*

The wing has been manufactured with a fiber-glass composite layup which makes the skin of the wing. Below this rather thin skin, some layers of foam, separated by layers of fabric, have been inserted. An overview of the layup is shown in Figure 2.104, while in Table 2.9 more details are given. Note that the fabric plies in Table 2.9 have been considered as two different plies with perpendicular orientation and half the thickness.
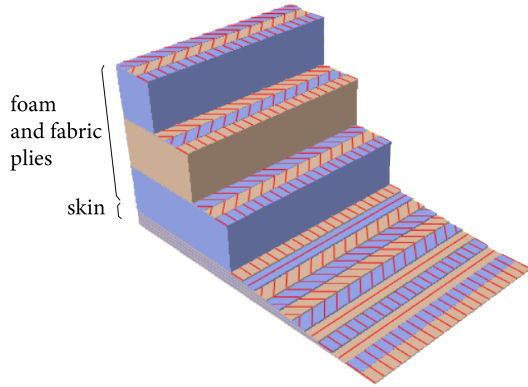
Figure 2.104: *Layup of demonstrator skin.*

#ply	Thickness	Orientation
1	$3.5e-5\,\mathrm{m}$	$0°$
2, 3	$8.525e-6\,\mathrm{m}$	$0°/90°$
4, 5	$5.456e-5\,\mathrm{m}$	$0°/90°$
6, 7	$5.456e-5\,\mathrm{m}$	$-45°/45°$
8, 9	$5.456e-5\,\mathrm{m}$	$45°/-45°$
10, 11	$5.456e-5\,\mathrm{m}$	$90°/0°$
12 (foam)	$0.0015\,\mathrm{m}$	$0°$
13, 14	$1.67e-5\,m$	$-45°/45°$
15 (foam)	$0.0015\,\mathrm{m}$	$0°$
16, 17	$1.67e-5\,\mathrm{m}$	$-45°/45°$
18 (foam)	$0.0015\,\mathrm{m}$	$0°$
19, 20	$1.67e-5\,\mathrm{m}$	$-45°/45°$

Table 2.9: *Ply sequence.*

The material properties of the plies are reported in Table 2.10 and the plies orientation w.r.t the wing is displayed in Figure 2.105.

	E_1	E_2	ν_{12}	G_{12}	G_{13}	G_{23}
fiber-glass ply	$41.75\,\mathrm{GPa}$	$12.94\,\mathrm{GPa}$	0.26	$4.96\,\mathrm{GPa}$	$4.13\,\mathrm{GPa}$	$4.13\,\mathrm{GPa}$
foam	$0.092\,\mathrm{GPa}$	$00926\,\mathrm{GPa}$	0.4	$0.029\,\mathrm{GPa}$	$0.024\,\mathrm{GPa}$	$0.024\,\mathrm{GPa}$

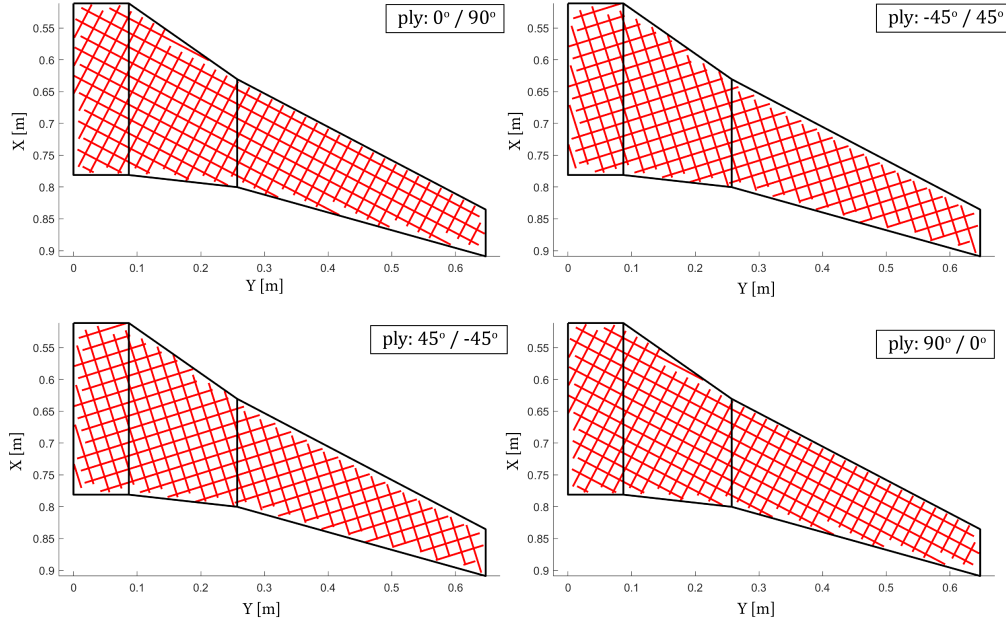Table 2.10: *Material properties of fiber-glass plies.*

89

Figure 2.105: *Ply orientations with respect to the wing geometry.*

In order to build a beam model for the wing, some simplifications have to be introduced. First, the wing model at the root is characterized by a straight part, after which the wing is swept backwards. This part is actually below the fuselage itself and effectively will not be modeled. Regarding the sweep angle, a constant angle has been extracted from the model locating the position at the quarter chord at the root and at the tip. A value of $\psi = 26.08°$ will be used.

Since the wing profile is changing along the span, the wing axis has been divided into two parts, connecting the corresponding centroids of the sections. In order to do so, the centroid should be computed for a section perpendicular to the beam axis, which is considered to be inclined by the sweep angle ψ. It would be incorrect to take as centroid the one of the cross section in the (x, z) plane of Figure 2.102a due to the sweep angle. After having computed the centroid position in the cross-section plane, it has been projected over the (x, z) plane. This is illustrated in Figure 2.106.
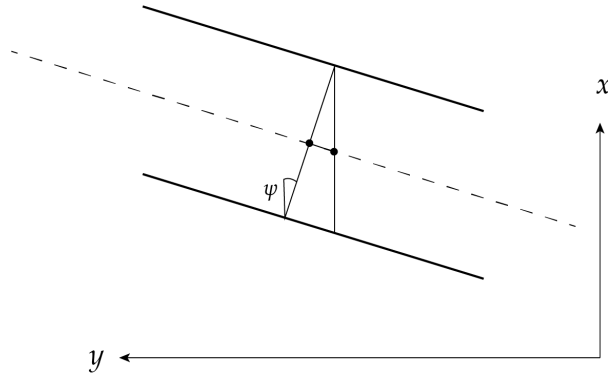

Figure 2.106: *Cross-section to be analyzed considering the sweep angle ψ.*

This has been repeated for the three sections highlighted in Figure 2.102a. Regarding the

computation of the centroid itself, the cross-section has been discretized in FE, computing all the section properties with the in-house code briefly described in Section 2.2.2. Since the material changes significantly between the outer part and the inner part of the skin, it has been decided to take this into account by using the so-called *modulus-weighted properties* [66]. That is, the cross-section has been divided into two parts, with two different elastic moduli. These have been computed from the equivalent elastic moduli of the two layups (Figure 2.107) as explained in Appendix I.
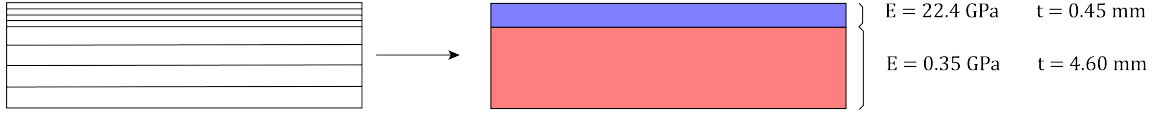

Figure 2.107: *Cross-section of the layup and equivalent elastic moduli.*

At this point, since the wing cross-section is not homogeneous, its properties have been computed with a modulus-weighted differential area:

$$\mathrm{d}\tilde{A} = \frac{E}{E_r}\mathrm{d}A$$

where E is the elastic modulus of the part of the cross-section with area $\mathrm{d}A$ and E_r is a the reference elastic modulus, which in this case is the one of the skin ($E_r = 22.4$ GPa). In this way, for example, the centroid position given by:

$$y_C = \frac{\iint_{\tilde{A}} y\,\mathrm{d}\tilde{A}}{\tilde{A}} \quad ; \quad z_C = \frac{\iint_{\tilde{A}} z\,\mathrm{d}\tilde{A}}{\tilde{A}}$$

does not depend on the ratio E/E_r, but other properties, such as the area moments of inertia do. The three cross-sections identified before and the corresponding centroids and shear center positions are represented in Figure 2.108.

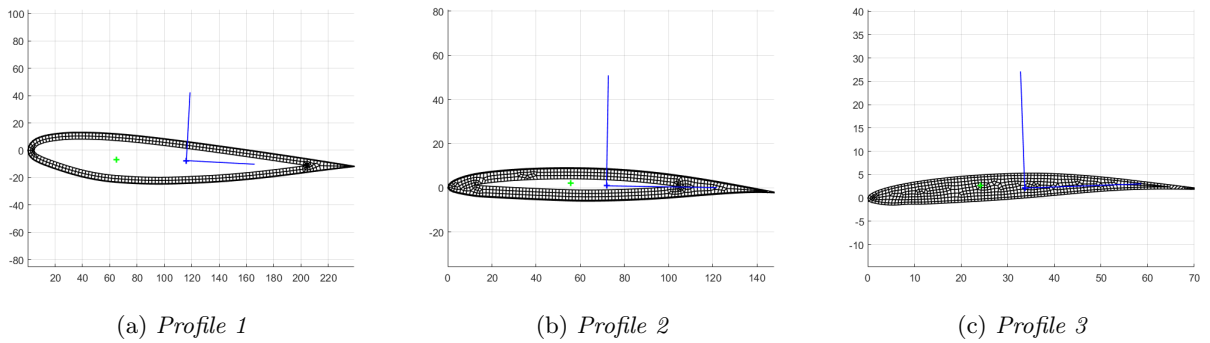(a) *Profile 1*   (b) *Profile 2*   (c) *Profile 3*

Figure 2.108: *Cross-sections of demonstrator ISTAR wing.*

At each cross-section the corresponding centroid location has been identified, allowing to retrieve the centroidal beam axis (Figure 2.109). It is important to know its position since the strain measurements must be referred to that. It is easy to relate the strain gauge positions in the global reference system ($Oxyz$) to the ones in the centroidal reference system.
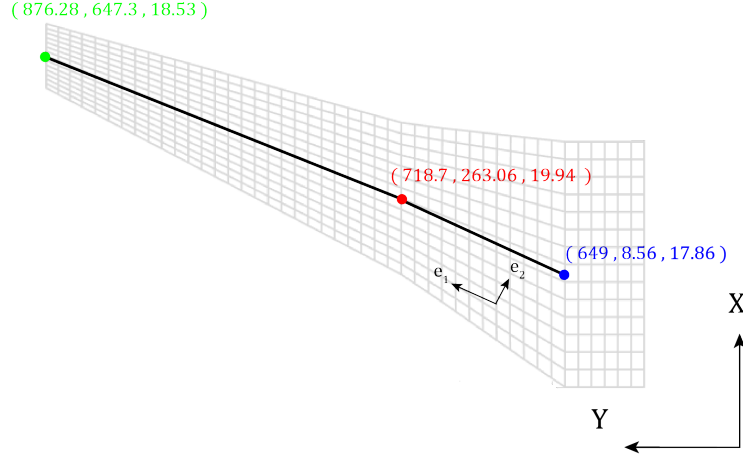
Figure 2.109: *Identified centroidal beam axis of the demonstrator ISTAR wing.*

This can be defined by three unit vectors $\boldsymbol{e}_1$, $\boldsymbol{e}_2$ and $\boldsymbol{e}_3$ which for this application are defined as follows:

- $\boldsymbol{e}_1$ along beam axis.

- Let $\boldsymbol{t} = [-1\,0\,0]^\top$, then:

$$\boldsymbol{e}_3 = \frac{\boldsymbol{t} \times \boldsymbol{e}_1}{\|\boldsymbol{t} \times \boldsymbol{e}_1\|}$$

- Finally:

$$\boldsymbol{e}_2 = \frac{\boldsymbol{e}_3 \times \boldsymbol{e}_2}{\|\boldsymbol{e}_3 \times \boldsymbol{e}_2\|}$$

Given the strain gauge positions $\boldsymbol{X}$ in the global reference system, the corresponding one $\boldsymbol{x}$ in the local beam reference system is simply given by:

$$\begin{aligned} \boldsymbol{x} &= \begin{bmatrix} \boldsymbol{e}_1 \, \boldsymbol{e}_2 \, \boldsymbol{e}_3 \end{bmatrix} \big(\boldsymbol{X} - \boldsymbol{X}_0 \big) \\ &= \boldsymbol{R} \big(\boldsymbol{X} - \boldsymbol{X}_0 \big) \end{aligned} \tag{2.187}$$

with $\boldsymbol{X}_0$ the first node of the beam element in the global reference system and $\boldsymbol{R} = \begin{bmatrix} \boldsymbol{e}_1 \, \boldsymbol{e}_2 \, \boldsymbol{e}_3 \end{bmatrix}$ the rotation matrix.

Looking at Figure 2.109, it is possible to find that the two centroidal axes which have been identified are not exactly aligned. Therefore, it is necessary to relate the local inverse beam degrees of freedom to some global ones in order to retrieve the displacements. The problem which arises at this point is that the inverse beam elements used so far do not have any torsional degree of freedom. However, it is necessary to have three rotations in the global reference system in order to correctly relate the local degrees of freedom with the global ones. The problem can be solved introducing in the inverse Euler-Bernoulli element the θ_x rotation, but adding just zeros in the corresponding entries of the strain-displacement matrices. So, the $\boldsymbol{B}$ matrix simply becomes (compare to Eq.(2.26)):

$$\boldsymbol{B} = \begin{bmatrix} \boldsymbol{B}_1 \\ \boldsymbol{B}_2 \\ \boldsymbol{B}_3 \end{bmatrix} \tag{2.188}$$

$$\boldsymbol{B}_1 = \begin{bmatrix} -\dfrac{1}{L^{(e)}} & 0 & 0 & 0 & 0 & 0 & \dfrac{1}{L^{(e)}} & 0 & 0 & 0 & 0 & 0 \end{bmatrix} \tag{2.189}$$

$$\boldsymbol{B}_2 = \begin{bmatrix} 0 & 0 & -\dfrac{1}{(L^{(e)})^3}(12x - 6L^{(e)}) & 0 & \dfrac{1}{(L^{(e)})^2}(6x - 4L^{(e)}) & 0 \\[2mm] & & 0 & 0 & \dfrac{1}{(L^{(e)})^3}(12x - 6L^{(e)}) & 0 & \dfrac{1}{(L^{(e)})^2}(6x - 2L^{(e)}) & 0 \end{bmatrix} \tag{2.190}$$

$$\boldsymbol{B}_3 = \begin{bmatrix} 0 & -\dfrac{1}{(L^{(e)})^3}(12x - 6L^{(e)}) & 0 & 0 & 0 & -\dfrac{1}{(L^{(e)})^2}(6x - 4L^{(e)}) & 0 \\[2mm] \dfrac{1}{(L^{(e)})^3}(12x - 6L^{(e)}) & 0 & 0 & 0 & -\dfrac{1}{(L^{(e)})^2}(6x - 2L^{(e)}) \end{bmatrix} \tag{2.191}$$

Now the element $\boldsymbol{K}^{(e)}$ matrix and load vector $\boldsymbol{f}^{(e)}$ can be put in the global reference system as:

$$\boldsymbol{K}^{(e)} = \boldsymbol{T}^\top \boldsymbol{k}^{(e)} \boldsymbol{T} \tag{2.192}$$

$$\boldsymbol{F}^{(e)} = \boldsymbol{T}^\top \boldsymbol{f}^{(e)} \tag{2.193}$$

and assembled with the usual procedure. Taking into account the boundary conditions, the system $\boldsymbol{KU} = \boldsymbol{F}$ needs to be solved. To these equations it is necessary to add the constraint that the torsion angle in the local beam reference system must be null. So, for each node the following equation can be written:

$$\theta_x = 0 \quad \Rightarrow \quad R_{11}\Theta_x + R_{12}\Theta_y + R_{13}\Theta_z = 0 \tag{2.194}$$

with Θ_x, Θ_y, Θ_z the degrees of freedom in the global reference system. Adding these equations to the system $\boldsymbol{KU} = \boldsymbol{F}$ an overdetermined linear system is obtained which can be solved with least-squares.

Using this approach, the wing has been divided into two inverse beam elements, thus requiring 10 axial strain gauges in total. The nodal positions are the ones illustrated in Figure 2.109. Due to the geometry of the wing, the taper is *not* constant. Furthermore, also the airfoil shape changes along the beam axis and so it would not be optimal to simply say as before that the linear dimensions change along the span by the factor $(1 + cx)$ with $c = (r - 1)/L^{(e)}$ (with r the taper ratio). As a consequence, it has been decided to compute the value of c directly from the moments of area of the cross-sections at the nodal positions:

$$\tilde{A}(x) = \tilde{A}_0(1 + c_A x) \quad ; \quad \tilde{I}_z(x) = \tilde{I}_{z0}(1 + c_{I_z}x)^3 \quad ; \quad \tilde{I}_z(x) = \tilde{I}_{z0}(1 + c_{I_z}x)^3 \tag{2.195}$$

with $\tilde{A}$, $\tilde{I}_y$, $\tilde{I}_z$ the modulus weighted cross-sectional properties. And so:

$$\tilde{A}(x = L^{(e)}) = \tilde{A}_f = \tilde{A}_0(1 + c_A L^{(e)})^3 \quad \Rightarrow \quad c_A = \frac{1}{L^{(e)}}\left(\sqrt[3]{\frac{\tilde{A}_f}{\tilde{A}_0}} - 1\right) \tag{2.196}$$

$$\tilde{I}_y(x = L^{(e)}) = \tilde{I}_{yf} = \tilde{I}_{y0}(1 + c_{I_y} L^{(e)})^3 \quad \Rightarrow \quad c_{I_y} = \frac{1}{L^{(e)}}\left(\sqrt[3]{\frac{\tilde{I}_{yf}}{\tilde{I}_{y0}}} - 1\right) \tag{2.197}$$

$$\tilde{I}_z(x = L^{(e)}) = \tilde{I}_{zf} = \tilde{I}_{z0}(1 + c_{I_z} L^{(e)})^3 \quad \Rightarrow \quad c_{I_z} = \frac{1}{L^{(e)}}\left(\sqrt[3]{\frac{\tilde{I}_{zf}}{\tilde{I}_{z0}}} - 1\right) \tag{2.198}$$

Now all the properties of the wing have been defined and the shape sensing analysis can be carried out.

The strain gauge positions have been defined directly from the FEM wing model. In particualr, two different configurations will be taken into consideration as in Figure 2.110.

(a) *Strain gauge configuration 1.*

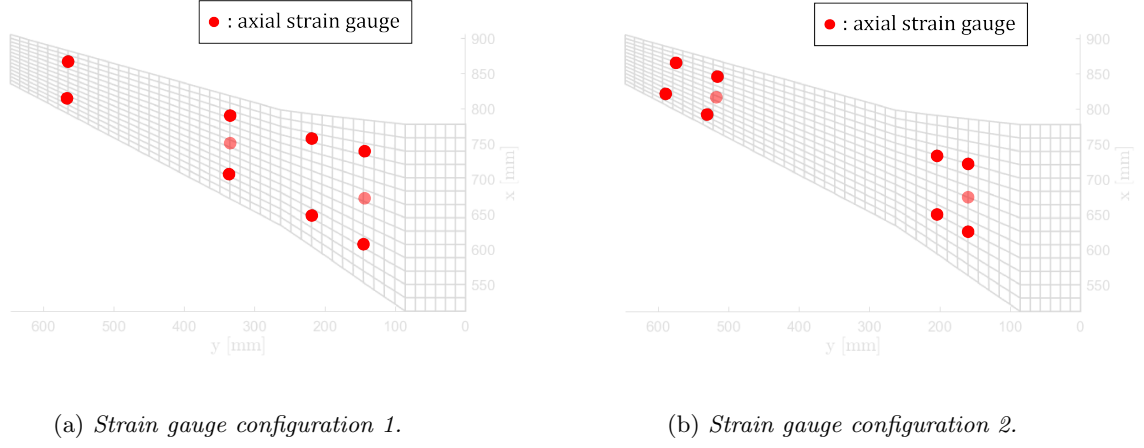(b) *Strain gauge configuration 2.*

Figure 2.110: *Strain gauge positions for ISTAR demonstrator wing.*

Furthermore, three different load cases will be studied (Figure 2.111): a concentrated tip load (Figure 2.111a), a constant pressure (Figure 2.111b) and a parabolic-varying (along the span) pressure field (Figure 2.11˙ˉ˙

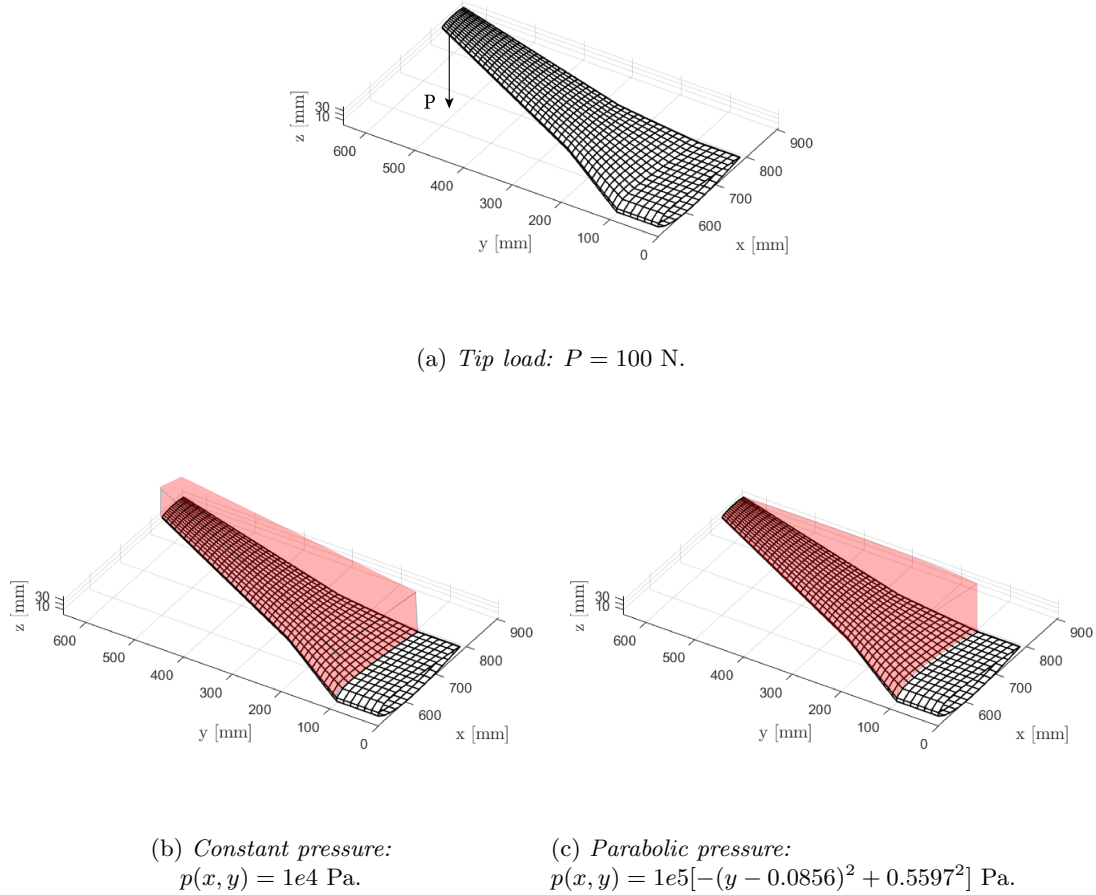

(a) *Tip load: $P = 100$ N.*

(b) *Constant pressure:*
$p(x,y) = 1e4$ Pa.

(c) *Parabolic pressure:*
$p(x,y) = 1e5[-(y - 0.0856)^2 + 0.5597^2]$ Pa.

Figure 2.111: *Load cases applied on the ISTAR demonstrator wing.*

2.5.2 Tip load

The wing tip has been subjected to a concentrated load and the strain gauge positions used are shown in Figure 2.110a. In Figure 2.112 the deflection reconstruction along z is reported for the first two iterations. The first one consists simply in applying iFEM with the original strain gauge positions, while for the second one the strain has been sampled at the locations found from Figure 2.112b and 2.112c. As it is possible to see, the two solutions give similar answers, and the same holds if further iterations are carried out.
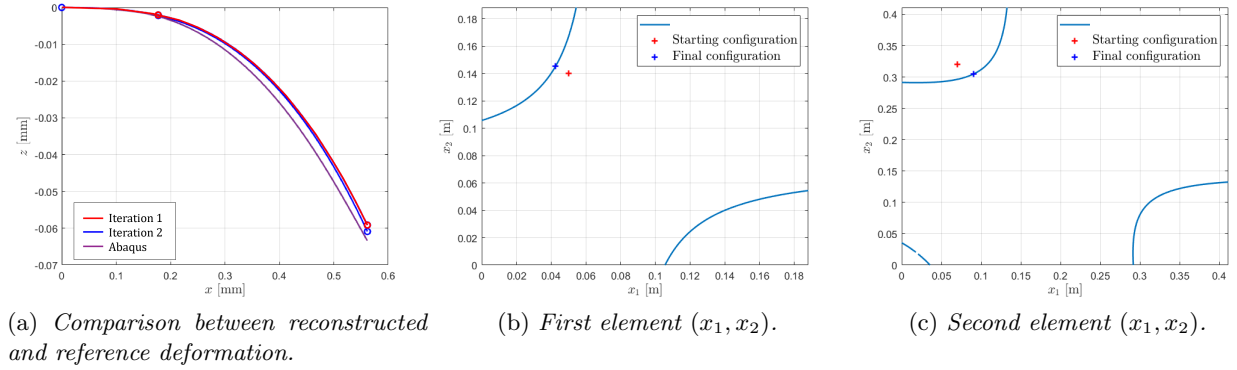

(a) *Comparison between reconstructed and reference deformation.*

(b) *First element (x_1, x_2).*

(c) *Second element (x_1, x_2).*

Figure 2.112: *Deflection reconstruction under tip load using strain configuration 1.*

This however is not always the case. For example, if the strain gauges are moved as in Figure 2.110b, then the second iteration brings a considerable improvement as it is possible to see in Figure 2.113.
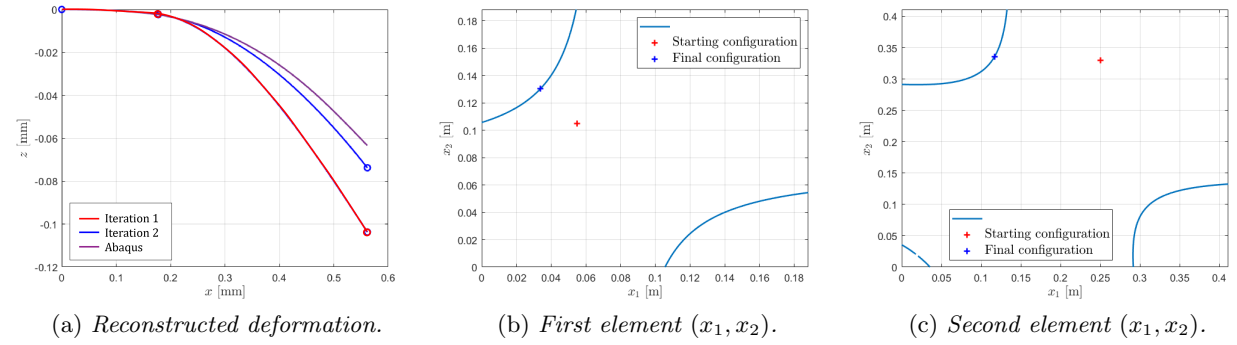

(a) *Reconstructed deformation.*

(b) *First element (x_1, x_2).*

(c) *Second element (x_1, x_2).*

Figure 2.113: *Deflection reconstruction under tip load using strain configuration 2.*

2.5.3 Constant pressure

The wing has been subjected to a constant pressure on the bottom skin equal to 10 MPa. The strain gauge positions used are the ones of Figure 2.110a. In Figure 2.114 the obtained results are shown, while in Figure 2.115 a tri-dimensional representation is given.
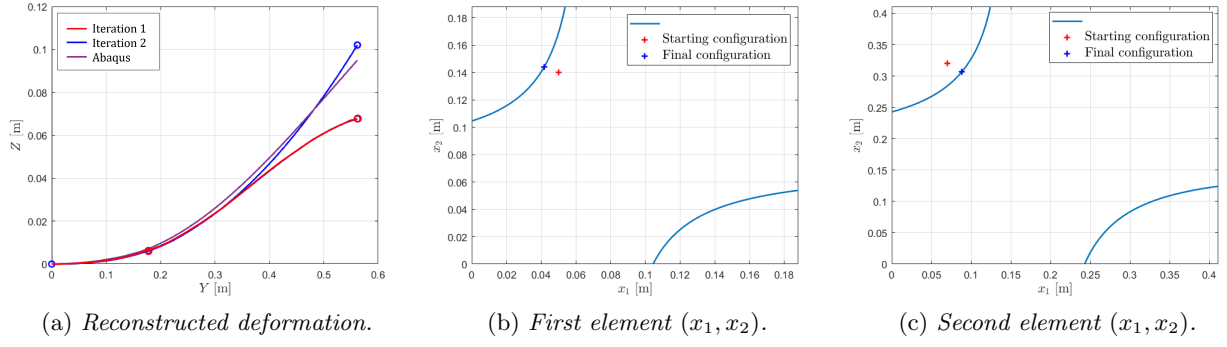
(a) *Reconstructed deformation.* (b) *First element (x_1, x_2).* (c) *Second element (x_1, x_2).*

Figure 2.114: *Deflection reconstruction under constant pressure.*

(a) *Top view.*

(b) *Isometric view.*

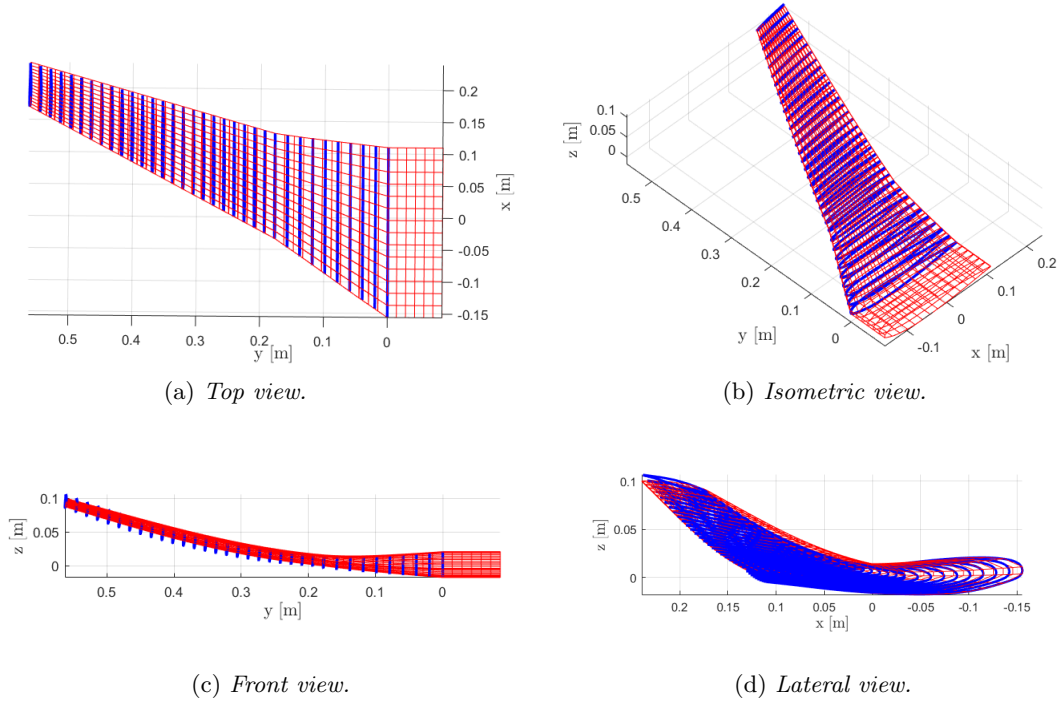(c) *Front view.*

(d) *Lateral view.*

Figure 2.115: *Reconstructed deflection (blue line) and reference deformed shape (red mesh) for constant pressure case.*

2.5.4 Parabolic pressure

Finally, the wing has been subjected to a parabolic pressure distribution applied on the bottom skin, again with strain gauge positions of Figure 2.110a. The results are reported in Figure 2.116, while in Figure 2.117 a tri-dimensional representation is given. Similar results to the ones obtained for the constant pressure case can be observed.
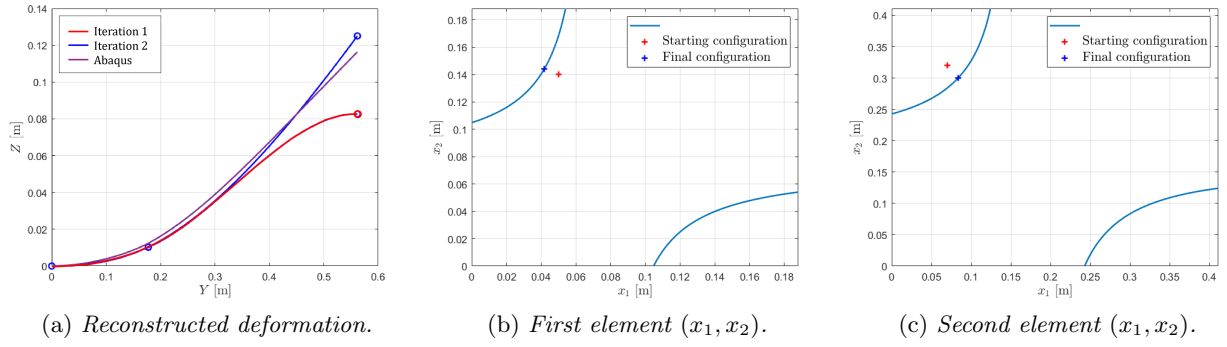
96

(a) *Reconstructed deformation.*　　(b) *First element (x_1, x_2).*　　(c) *Second element (x_1, x_2).*

Figure 2.116: *Deflection reconstruction under parabolic pressure.*

(a) *Top view.*

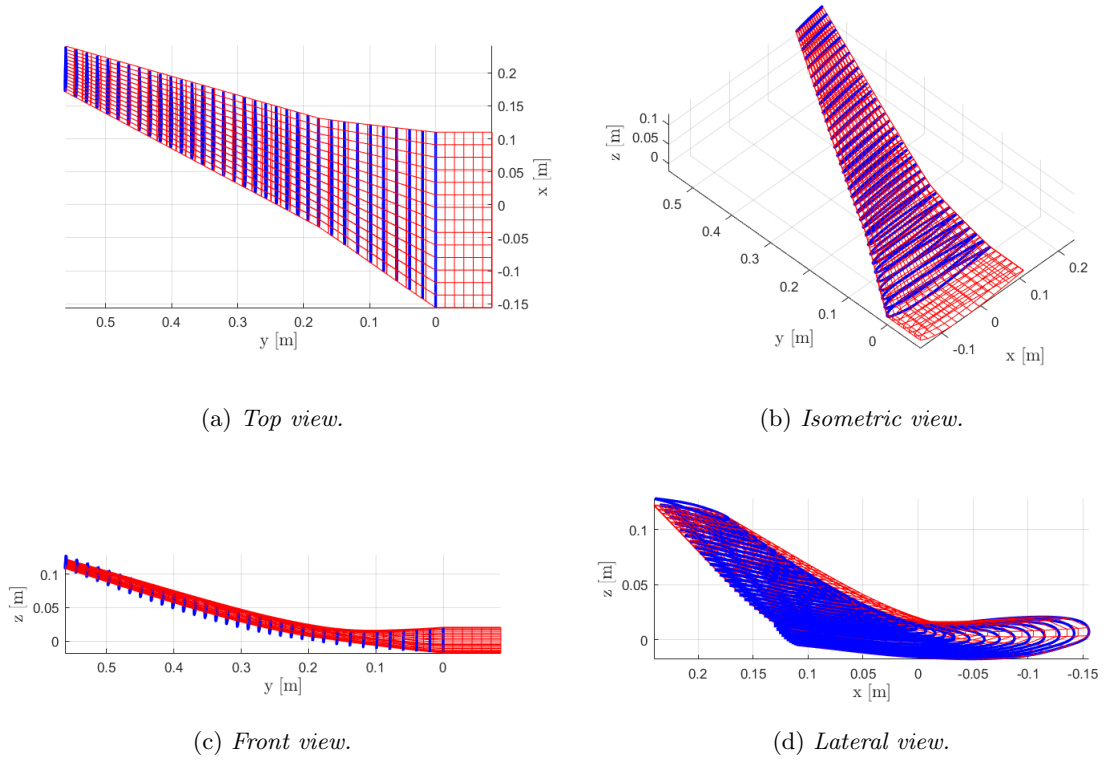(b) *Isometric view.*

(c) *Front view.*

(d) *Lateral view.*

Figure 2.117: *Reconstructed deflection (blue line) and reference deformed shape (red mesh) for parabolic pressure case.*

97

2.6 Summary of the chapter

In this chapter the shape sensing problem has been studied with a beam model. Using the framework of iFEM and in particular the so-called 0th order element (so assuming a linear moment variation inside the element domain) some improvements are suggested. In particular, the twist can be estimated with an additional strain measurement, computing the shear strain and deriving just the component due to torsion. Furthermore, in order to limit the amount of strain measurements needed, it is suggested to measure the axial strain in appropriate axial locations such that an overall good bending reconstruction can be achieved also under complex load cases.

These ideas have then been applied to tapered beams which however require an estimate of the applied loads in order to choose the axial positions for the strain measurements. Two methods have been proposed, either from the interpolation of the axial strain or from an iterative solution of the system deriving the load as a superposition of step-wise constant distributed loads. Regarding the twist reconstruction, an analytical method to compute the shear stress in thin-walled monocell tapered beams is suggested. This can be used to uncouple the measured shear stress from the shear force contribution and so deriving the twist rate.

Overall, this approach seems to give a satisfactory bending representation of the beam, while the twist suffers from errors occurring especially near the beam root since they propagate linearly till the tip.

Chapter 3

Shape sensing with shell models

The aim of this chapter is studying the shape reconstruction from strain measurements using two- and three-dimensional models such that there is a recovery of the entire displacement field. In order to do so, two methods will be taken into consideration: the Modal Method (MM) and the inverse Finite Element Method (iFEM). The chapter is structured as follows:

- In Section 4.1 the methods which will be used are briefly described.

- Section 3.2 is focused on pre-extrapolating the strain measurements in order to obtain an estimate of the strain field over the whole structural domain. This will be a fundamental step in the shape sensing analysis with iFEM.

- Section 3.3 represents the central part of the chapter. It aims at studying in-depth the results obtained with iFEM and to compare them with the ones from MM.

- Finally, Section 3.4 completes the previous section studying how uncertainty in the strain measurements and model errors can affect the shape sensing study. The focus is again on comparing iFEM with MM.

Contrarily to Chapter 1, now the applications will be almost exclusively based on the ISTAR demonstrator wing, using the strain measurements of the FEM model to feed the shape sensing methods. In order to study a broader range of cases, similarly as done for the beam model, three load cases will be analyzed, that is:

- A concentrated tip load.

- A constant pressure field applied on the bottom skin.

- A parabolic-varying along the span pressure field, again applied on the bottom skin.

For the exact field distributions refer to Figure 2.111. It is deemed that in this way a more in-depth study can be done, giving more confidence in the results obtained and in the conclusions which will be drawn.

3.1 Theoretical background

The aim of this section is to give some theoretical background which will be used in the following studies.

In Section 3.1.1 a common shape sensing method is presented under the name of Modal Method. It is simply based on reconstructing the deformed shape of the structure as a combination of mode shapes. It has been widely used in open literature for several applications and in the following it will be used also in the scope of the thesis.

In Section 3.1.2 the inverse Finite Element Method (iFEM) developed to describe two- and three- dimensional structures will be reviewed. In particular, the focus will be just on the four-node element (called iQS4). Even though this is a common formulation used in literature which was proved to give good and reliable results, it is not the only one. Other elements have been developed, for example a three-node plate element (iMIN3) [7] and an eight-node shell element (iCS8) [3]. However, they will not be described here.
One of the assumptions behind the inverse quadrilateral element used is the simple First Order Shear Deformation theory. Therefore, the applicability is restricted to rather thin structures, where transverse shear effects are negligible. If this is not the case, other theories should be applied. For example, an inverse formulation of the so-called Zig-Zag theory for thick composites and sandwich has recently been developed [45].

In Section 3.1.3 the so-called Smoothing Element Analysis (SEA) is reviewed. Since for real applications having a relatively dense set of strain measurements might be unfeasible, it is important to be able to give an estimate of the strain over the structure also where no gauge is present. In this way inverse elements without any physical strain gauge could be instrumented. Since their measure would be fictitious though, a lower weight should be used so that they would weight less in the minimization of the error functional with the actual strain measurements. This procedure is commonly referred to as strain pre-extrapolation. In this context SEA is used to interpolate the strain field over the structural domain with the aim to improve the shape sensing capability of iFEM.

3.1.1 Modal Method

It is known that the modal coordinates $\boldsymbol{r}$ can be related to the actual degrees of freedom of the system $\boldsymbol{u}$ as:

$$\boldsymbol{u} = \boldsymbol{\Phi r} \tag{3.1}$$

where $\boldsymbol{\Phi}$ is the mode shape matrix. Analogously, for the strains a similar relation holds:

$$\boldsymbol{\varepsilon} = \boldsymbol{\Psi r} \tag{3.2}$$

where $\boldsymbol{\Psi}$ is the so-called matrix of strain modes which contains the strains for each corresponding deformation mode. Since from experimental measurements the strain values can be obtained, it is necessary to relate $\boldsymbol{\varepsilon}$ (vector containing the experimental strains) with $\boldsymbol{u}$. At first sight, this might be done simply seeing that $\boldsymbol{r} = \boldsymbol{\Psi}^{-1}\boldsymbol{\varepsilon}$ and therefore:

$$\underbrace{\boldsymbol{u}}_{N \times 1} = \underbrace{\boldsymbol{\Phi}}_{N \times p} \underbrace{\boldsymbol{\Psi}^{-1}}_{m \times p} \underbrace{\boldsymbol{\varepsilon}}_{m \times 1} \tag{3.3}$$

where the dimension of each component is highlighted: N is the number of degrees of freedom of the system, p the number of mode shapes considered and m the number of strain measures taken. As it is possible to see, in order to compute $\boldsymbol{u}$ it is required that the matrices used are square, or in other words that the number of strain measures m equals the number of modes used p.

However, this is not always the case. Therefore, Eq.(3.2) can be solved using the pseudo-inverse matrix as [49]

$$\boldsymbol{r} = \left(\boldsymbol{\Psi}^T\boldsymbol{\Psi}\right)^{-1}\boldsymbol{\Psi}^T\boldsymbol{\varepsilon} \tag{3.4}$$

And so substituting in Eq.(3.1) it is possible to obtain:

$$\boldsymbol{u} = \underbrace{\boldsymbol{\Phi}\left(\boldsymbol{\Psi}^T\boldsymbol{\Psi}\right)^{-1}\boldsymbol{\Psi}^T}_{\textbf{DST}}\boldsymbol{\varepsilon} \tag{3.5}$$

which gives the value of all the degrees of freedom in which the structure has been discretized. The matrix which relates $\boldsymbol{u}$ with $\boldsymbol{r}$ is commonly referred to as **DST**, the displacement-strain transformation matrix.

Several applications have been studied with this method, bringing in general satisfactory results. The main drawback consists in the fact that the mode shapes have to be known in advance. Since these are generally computed with FEM, the material and geometrical properties of the structure have to be precisely known. Alternatively, experimental mode shapes could also be used.

3.1.2 Inverse Finite Element Method with shell elements

From the First Order Shear Deformation theory the following relations for the kinematic variables hold:

$$\begin{cases} u_x(x,y) = u + z\theta_y \\ u_y(x,y) = v - z\theta_x \\ u_z(x,y) = w \end{cases} \tag{3.6}$$

where u and v are the mid-plane displacements, θ_x and θ_y the rotations about the x and y axes and w the out-of-plane displacement (constant across the thickness). The in-plane strains can be computed as:

$$\varepsilon_x = \frac{\partial u_x}{\partial x} = \underbrace{\frac{\partial u}{\partial x}}_{\varepsilon_{x0}} + z\underbrace{\frac{\partial \theta_y}{\partial x}}_{\kappa_{x0}}$$

$$\varepsilon_y = \frac{\partial u_y}{\partial y} = \underbrace{\frac{\partial v}{\partial y}}_{\varepsilon_{y0}} - z\underbrace{\frac{\partial \theta_x}{\partial y}}_{\kappa_{y0}} \tag{3.7}$$

$$\gamma_{xy} = \frac{\partial u_x}{\partial y} + \frac{\partial u_y}{\partial x} = \underbrace{\frac{\partial u}{\partial y} + \frac{\partial v}{\partial x}}_{\gamma_{xy0}} + z\underbrace{\left(\frac{\partial \theta_x}{\partial x} - \frac{\partial \theta_y}{\partial y}\right)}_{\kappa_{xy0}}$$

which can be written as:

$$\begin{bmatrix} \varepsilon_x \\ \varepsilon_y \\ \gamma_{xy} \end{bmatrix} = \begin{bmatrix} \varepsilon_{x0} \\ \varepsilon_{y0} \\ \gamma_{xy0} \end{bmatrix} + z\begin{bmatrix} \kappa_{x0} \\ \kappa_{y0} \\ \gamma_{xy0} \end{bmatrix} \tag{3.8}$$

$$= \boldsymbol{e}(\boldsymbol{u}) + z\boldsymbol{k}(\boldsymbol{u})$$

where $\boldsymbol{e}$ represents the membrane strain measures, $\boldsymbol{k}$ the curvatures and $\boldsymbol{u} = \begin{bmatrix} u & v & w & \theta_x & \theta_y \end{bmatrix}^\top$ the kinematic variables. Similarly, also the transverse shear strain can be expressed as:

$$\boldsymbol{g}(\boldsymbol{u}) = \begin{bmatrix} \gamma_{xz} \\ \gamma_{yz} \end{bmatrix} = \begin{bmatrix} \dfrac{\partial w}{\partial x} + \theta_y \\ \dfrac{\partial w}{\partial y} - \theta_x \end{bmatrix} \tag{3.9}$$

It is possible to obtain experimentally the values of the strain measures $\boldsymbol{e}$ and $\boldsymbol{k}$. Imagine that on both sides of the shell a strain rosette has been installed as in Figure 3.1.
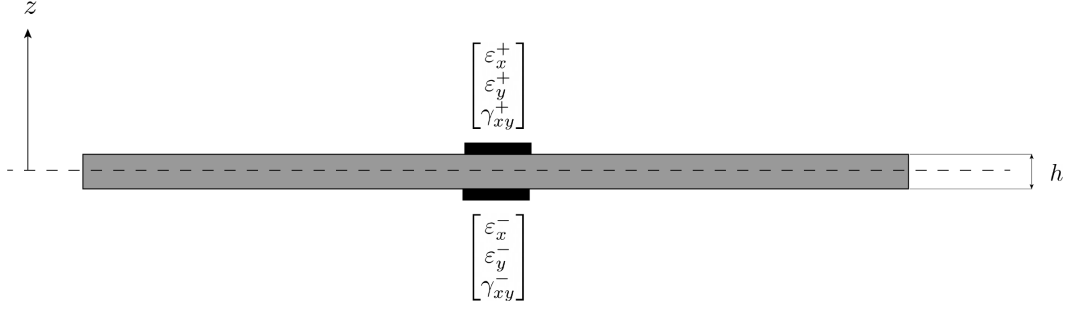

Figure 3.1: *Strain rosettes installed on both sides of a plate in order to measure membrane strains and curvatures.*

Then, taking for example just the ε_x strain measurement, it is possible to write:

$$\begin{cases} \varepsilon_x^+ = \varepsilon_{x0} + \dfrac{h}{2}\kappa_{x0} \\[2mm] \varepsilon_x^- = \varepsilon_{x0} - \dfrac{h}{2}\kappa_{x0} \end{cases} \tag{3.10}$$

where $+$ stands for example for the measurement of the top of the plate and $-$ for the one on the bottom. Summing the two equations the membrane strain measurement can be easily computed:

$$\varepsilon_{x0} = \frac{1}{2}\left(\varepsilon_x^+ + \varepsilon_x^-\right) \tag{3.11}$$

Subtracting the two equations:

$$\kappa_{x0} = \frac{1}{h}\left(\varepsilon_x^+ - \varepsilon_x^-\right) \tag{3.12}$$

Repeating the procedure for the other components it is possible to finally obtain the experimental values for the membrane strain measures and curvature:

$$\begin{aligned} \boldsymbol{e}^\varepsilon &= \begin{bmatrix} \varepsilon_{x0}^\varepsilon \\ \varepsilon_{y0}^\varepsilon \\ \gamma_{xy0}^\varepsilon \end{bmatrix} = \frac{1}{2}\left(\begin{bmatrix} \varepsilon_{xx}^+ \\ \varepsilon_{yy}^+ \\ \gamma_{xy}^+ \end{bmatrix} + \begin{bmatrix} \varepsilon_{xx}^- \\ \varepsilon_{yy}^- \\ \gamma_{xy}^- \end{bmatrix}\right) \\[4mm] \boldsymbol{k}^\varepsilon &= \begin{bmatrix} \kappa_{x0}^\varepsilon \\ \kappa_{y0}^\varepsilon \\ \kappa_{xy0}^\varepsilon \end{bmatrix} = \frac{1}{h}\left(\begin{bmatrix} \varepsilon_{xx}^+ \\ \varepsilon_{yy}^+ \\ \gamma_{xy}^+ \end{bmatrix} - \begin{bmatrix} \varepsilon_{xx}^- \\ \varepsilon_{yy}^- \\ \gamma_{xy}^- \end{bmatrix}\right) \end{aligned} \tag{3.13}$$

At this point, iFEM can be applied. The error functional to be minimized for the element (e) is expressed as:

$$\Phi^{(e)}(\boldsymbol{u}^{(e)}) = w_e\|\boldsymbol{e}(\boldsymbol{u}^{(e)}) - \boldsymbol{e}^\varepsilon\|^2 + w_k\|\boldsymbol{k}(\boldsymbol{u}^{(e)}) - \boldsymbol{k}^\varepsilon\|^2 + w_g\|\boldsymbol{g}(\boldsymbol{u}^{(e)}) - \boldsymbol{g}^\varepsilon\|^2 \tag{3.14}$$

where $\boldsymbol{u}^{(e)}$ are the element degrees of freedom, w_e, w_k and w_g are scalar weight whose role is described below and the norms are expressed as:

$$\left\|\boldsymbol{e}(\boldsymbol{u}^{(e)}) - \boldsymbol{e}^\varepsilon\right\|^2 = \frac{1}{n^{(e)}}\iint_{A^{(e)}} \sum_{i=1}^{n^{(e)}} \left[\boldsymbol{e}(\boldsymbol{u}^{(e)})_i - \boldsymbol{e}_i^\varepsilon\right]^2 dxdy$$

$$\left\|\boldsymbol{k}(\boldsymbol{u}^{(e)}) - \boldsymbol{k}^\varepsilon\right\|^2 = \frac{h^2}{n^{(e)}}\iint_{A^{(e)}} \sum_{i=1}^{n^{(e)}} \left[\boldsymbol{k}(\boldsymbol{u}^{(e)})_i - \boldsymbol{k}_i^\varepsilon\right]^2 dxdy \tag{3.15}$$

$$\left\|\boldsymbol{g}(\boldsymbol{u}^{(e)}) - \boldsymbol{g}^\varepsilon\right\|^2 = \frac{1}{n^{(e)}}\iint_{A^{(e)}} \sum_{i=1}^{n^{(e)}} \left[\boldsymbol{g}(\boldsymbol{u}^{(e)})_i - \boldsymbol{g}_i^\varepsilon\right]^2 dxdy$$

where $n^{(e)}$ is the number of strain measurements done on the element (e) domain. Note that the norm related to $\boldsymbol{k}$ has been multiplied by the thickness h for dimensional consistency. Before proceeding it is important to point out that it is not always possible to obtain experimental measures for every inverse element. This is already clear thinking about the transverse shear strain measurement $\boldsymbol{g}^\varepsilon$ which cannot be measured directly. In these cases there is the need to maintain the connectivity between the elements and this is done modifying the definition of the error functional and acting on the weights w_e, w_k and w_g. When no strain measurement is present on an element, so that $\boldsymbol{e}^\varepsilon$ or $\boldsymbol{k}^\varepsilon$ or $\boldsymbol{g}^\varepsilon$ is missing, the norm definition becomes:

$$\left\| \boldsymbol{e}(\boldsymbol{u}^{(e)}) \right\|^2 = \iint_{A^{(e)}} \boldsymbol{e}(\boldsymbol{u}^{(e)})^2 dx dy$$

$$\left\| \boldsymbol{k}(\boldsymbol{u}^{(e)}) \right\|^2 = h^2 \iint_{A^{(e)}} \boldsymbol{k}(\boldsymbol{u}^{(e)})^2 dx dy \qquad (3.16)$$

$$\left\| \boldsymbol{g}(\boldsymbol{u}^{(e)}) \right\|^2 = \iint_{A^{(e)}} \boldsymbol{g}(\boldsymbol{u}^{(e)})^2 dx dy$$

and the corresponding weights assume relatively small values ($\approx 10^{-5}$ from literature). Intuitively this means that the minimization done with iFEM is very little affected by these components so that just the errors created from the actual experimental measurements are minimized. At the same time, in this way not only there is the possibility to neglect the transverse shear component (which is the case for thin shells), but also to define so-called *strainless* elements where no strain measurement is done and which allow to estimate the displacement field also where no instrumented element is present.

Now, the displacement field needs to be interpolated using suitable shape functions. A four-node inverse element has been developed in [4], called iQS4. It was built with a drilling rotation degree of freedom which allows to model also complex shell structures. Therefore, for each node 6 degrees of freedom are present (3 translations and 3 rotations). The kinematic variables are interpolated in the following way:

$$u(x,y) = \sum_{i=1}^{4} N_i u_i + \sum_{i=1}^{4} L_i \theta_{zi} \quad ; \quad v(x,y) = \sum_{i=1}^{4} N_i v_i + \sum_{i=1}^{4} M_i \theta_{zi} \qquad (3.17)$$

$$w(x,y) = \sum_{i=1}^{4} N_i w_i - \sum_{i=1}^{4} L_i \theta_{xi} - \sum_{i=1}^{4} M_i \theta_{yi}$$

$$\theta_x(x,y) = \sum_{i=1}^{4} N_i \theta_{xi} \quad ; \quad \theta_y(x,y) = \sum_{i=1}^{4} N_i \theta_{yi} \qquad (3.18)$$

where N_i ($i = \{1,2,3,4\}$) are linear Lagrangian shape functions and L_i, M_i are developed to take into consideration the interaction of in-plane translations with the drilling degree of freedom (see Eq.(3.17)) and at the same time to have a so-called anisotropic interpolation in Eq.(3.18) (see discussion below and [4] for the detailed expressions of the shape functions). In Appendix J some background information about anisotropic interpolation has been reported.

The in-plane displacements $u(x,y)$ and $v(x,y)$ in Eq.(3.17) are interpolated following [55], while the out-of-plane displacement in Eq.(3.18) w and the rotations θ_x, θ_y take advantage from the anisotropic interpolations. For the four-node quadrilateral element this has been developed in [10]. The deflection w is interpolated biquadratically and the rotations bilinearly resulting in the element in Figure 3.2. To achieve a simpler four-node configuration, the mid-edge w_i degrees of freedom are then condensed imposing that the transverse shear must the continuous and constant along each edge, that is:
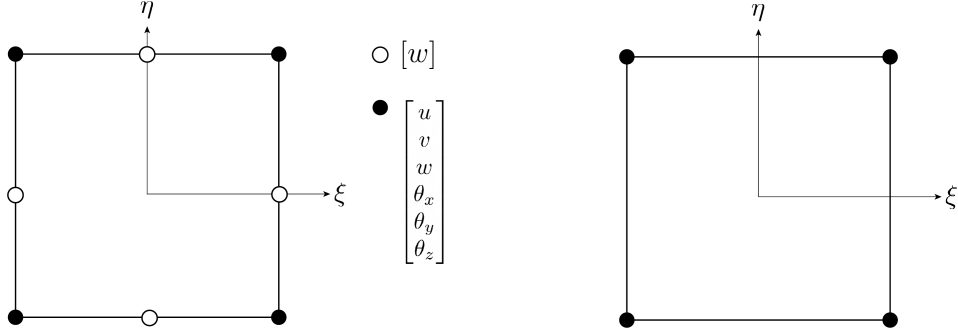
Figure 3.2: *iQS4 before and after condensation* [10].

$$\frac{\partial \gamma_{sz}}{\partial s} = \frac{\partial}{\partial s}\left(\frac{\partial w}{\partial s} + \theta_n\right) = 0 \quad \text{with} \quad s = \{\xi, \eta\} \quad ; \quad n = \{\eta, \xi\} \tag{3.19}$$

This will result in four equations which can give the expressions of the mid-edge w_i degrees of freedom in function of the others. So, a four-node element can be developed in this way. The shape functions used in the interpolation are illustrated in Figure 3.3.
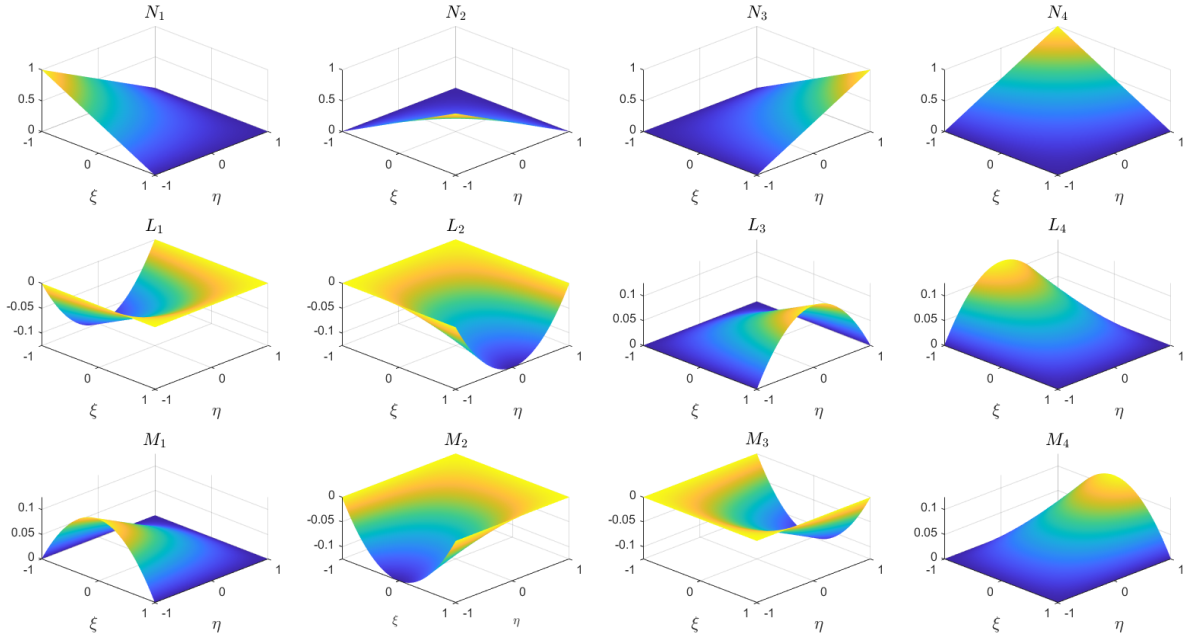
Figure 3.3: *Shape functions used for iQS4.*

The interpolation of the kinematic variables chosen can be used in the strain-displacement relations to get:

$$\begin{bmatrix} \varepsilon_x \\ \varepsilon_y \\ \gamma_{xy} \end{bmatrix} = \boldsymbol{e}(\boldsymbol{u}^{(e)}) + z\boldsymbol{k}(\boldsymbol{u}^{(e)}) = \boldsymbol{B}_m \boldsymbol{u}^{(e)} + z\boldsymbol{B}_b \boldsymbol{u}^{(e)} \tag{3.20}$$

$$\begin{bmatrix} \gamma_{xz} \\ \gamma_{yz} \end{bmatrix} = \boldsymbol{g}(\boldsymbol{u}^{(e)}) = \boldsymbol{B}_s \boldsymbol{u}^{(e)} \tag{3.21}$$

where the element degrees of freedom vector $\boldsymbol{u}^{(e)}$ is built as $\boldsymbol{u}^{(e)} = \begin{bmatrix} \boldsymbol{u}_1^{(e)} \, \boldsymbol{u}_2^{(e)} \, \boldsymbol{u}_3^{(e)} \, \boldsymbol{u}_4^{(e)} \end{bmatrix}^\top$ with $\boldsymbol{u}_i^{(e)} = \begin{bmatrix} u_i \, v_i \, w_i \, \theta_{xi} \, \theta_{yi} \end{bmatrix}^\top$ the nodal degrees of freedom. The explicit expressions of the

strain-displacement matrices $\boldsymbol{B}_m$, $\boldsymbol{B}_b$ and $\boldsymbol{B}_s$ can be obtained from [4].

Once the strain-displacement matrices have been defined, similarly to what has been done for the beam inverse elements, the expressions of the strain measures in function of the nodal degrees of freedom can be substituted in the error functional and the resulting relation has to be minimized with respect to $\boldsymbol{u}^{(e)}$:

$$\frac{\partial \Phi^{(e)}(\boldsymbol{u}^e)}{\partial \boldsymbol{u}^{(e)}} = 0 \quad \Rightarrow \quad \boldsymbol{K}^{(e)} \boldsymbol{u}^{(e)} = \boldsymbol{f}^{(e)} \tag{3.22}$$

where:

$$\boldsymbol{K}^{(e)} = \frac{1}{A^{(e)}} \iint_{A^{(e)}} \left[w_e (\boldsymbol{B}_m)^\top \boldsymbol{B}_m + w_k h^2 (\boldsymbol{B}_b)^\top \boldsymbol{B}_b + w_g (\boldsymbol{B}_s)^\top \boldsymbol{B}_s \right] \mathrm{d}A^{(e)} \tag{3.23}$$

$$\boldsymbol{f}^{(e)} = \frac{1}{A^{(e)}} \iint_{A^{(e)}} \left[w_e (\boldsymbol{B}_m)^\top \boldsymbol{e}^\varepsilon + w_k h^2 (\boldsymbol{B}_b)^\top \boldsymbol{k}^\varepsilon + w_g (\boldsymbol{B}_s)^\top \boldsymbol{g}^\varepsilon \right] \mathrm{d}A^{(e)} \tag{3.24}$$

Some important notes are listed below:

- The error functional $\Phi^{(e)}$ has been introduced as it was described in the original formulation, that is, rewriting the expression for convenience:

$$\Phi^{(e)}(\boldsymbol{u}) = w_e \| \boldsymbol{e}(\boldsymbol{u}) - \boldsymbol{e}^\varepsilon \|^2 + w_k \| \boldsymbol{k}(\boldsymbol{u}) - \boldsymbol{k}^\varepsilon \|^2 + w_g \| \boldsymbol{g}(\boldsymbol{u}) - \boldsymbol{g}^\varepsilon \|^2$$

And as it is possible to see different weights are assigned to respectively membrane, curvature and transverse shear part. In some cases it might be more useful to further distinguish between the different components of the strain measures. For example, it might be possible that the membrane strain is measured only in one direction (say ε_{x0}), and so there would be the need to give a lower weight to ε_{y0} and γ_{xy0}. So, introducing a single vector $\bar{\boldsymbol{e}}$ which contains all the strain measures:

$$\bar{\boldsymbol{e}} = \begin{bmatrix} \varepsilon_{x0} & \varepsilon_{y0} & \gamma_{xy0} & \kappa_{x0} & \kappa_{y0} & \kappa_{xy0} & \gamma_{xz} & \gamma_{yz} \end{bmatrix}^\top \tag{3.25}$$

It is possible to define a more "flexible" definition of the error functional as:

$$\Phi^{(e)} = \sum_{k=1}^{8} w_k \iint_{A^{(e)}} \left(\bar{e}_k(\boldsymbol{u}^{(e)}) - \bar{e}_k^\varepsilon \right)^2 dx dy \tag{3.26}$$

From which the expressions of $\boldsymbol{K}^{(e)}$ and $\boldsymbol{f}^{(e)}$ become:

$$\begin{aligned} \boldsymbol{K}^{(e)} &= \frac{1}{A^{(e)}} \iint_{A^{(e)}} \sum_{k=1}^{8} w_k \boldsymbol{B}_k^\top \boldsymbol{B}_k \, dx dy \\ \boldsymbol{f}^{(e)} &= \frac{1}{A^{(e)}} \iint_{A^{(e)}} \sum_{k=1}^{8} w_k \boldsymbol{B}_k^\top \bar{e}_k^\varepsilon \, dx dy \end{aligned} \tag{3.27}$$

where $\boldsymbol{B}_k$ ($k = \{1, ..., 8\}$) is a row of the matrix $\begin{bmatrix} \boldsymbol{B}_m & \boldsymbol{B}_b & \boldsymbol{B}_s \end{bmatrix}^\top$ defined by Eq.(3.20) and Eq.(3.21).

- The integrals of Eq.(3.27) are computed numerically with Gauss quadrature and in general it is common to place a single strain gauge sensor in the centroid of the element. It has been observed (see for example [37] and [36]) that penalizing the Gauss points where no strain

measurement is taken results in more accurate results. So the expressions of $\boldsymbol{K}^{(e)}$ and $\boldsymbol{f}^{(e)}$ become:

$$
\begin{aligned}
\boldsymbol{K}^{(e)} &= \frac{1}{A^{(e)}} \sum_{k=1}^{8} \sum_{i=1}^{n^{(g)} \times n^{(g)}} w_k \chi_i \boldsymbol{B}_k^\top \boldsymbol{B}_k \, dx dy \\
\boldsymbol{f}^{(e)} &= \frac{1}{A^{(e)}} \sum_{k=1}^{8} \sum_{i=1}^{n^{(g)} \times n^{(g)}} w_k \chi_i \boldsymbol{B}_k^\top \bar{e}_k^\varepsilon \, dx dy
\end{aligned}
\tag{3.28}
$$

where $n^{(g)}$ is the number of Gauss points used and $\chi_i = 1$ if the Gauss point is centroidal (that is coincident with the strain gauge), otherwise $\chi_i = 10^{-4}$ [36].

- So far it was assumed that the element local reference system coincided with the global one. If this is not the case, for example in three dimensional problems, a suitable rotation has to be carried out as explained for example in [32]. For the case of a four-node element, the element local reference system can be defined by the following vectors:

$$
\boldsymbol{n} = \frac{\boldsymbol{X}_{31} \times \boldsymbol{X}_{42}}{\|\boldsymbol{X}_{31} \times \boldsymbol{X}_{42}\|} \quad ; \quad \boldsymbol{p} = \frac{\boldsymbol{X}_{31} + \boldsymbol{X}_{42}}{\|\boldsymbol{X}_{31} + \boldsymbol{X}_{42}\|} \quad ; \quad \boldsymbol{l} = \boldsymbol{p} \times \boldsymbol{n} \tag{3.29}
$$

where $\boldsymbol{X}_{ij} = \boldsymbol{X}_i - \boldsymbol{X}_j$ and $\boldsymbol{x}_i$ is the nodal position in the global reference system. Then the transformation matrix $\boldsymbol{\tau} = \begin{bmatrix} \boldsymbol{l} & \boldsymbol{p} & \boldsymbol{n} \end{bmatrix}^\top$ can be used to build the following:

$$
\boldsymbol{T}^{(e)} = \begin{bmatrix}
\boldsymbol{\tau} & 0 & 0 & 0 & 0 & 0 & 0 & 0 \\
0 & \boldsymbol{\tau} & 0 & 0 & 0 & 0 & 0 & 0 \\
0 & 0 & \boldsymbol{\tau} & 0 & 0 & 0 & 0 & 0 \\
0 & 0 & 0 & \boldsymbol{\tau} & 0 & 0 & 0 & 0 \\
0 & 0 & 0 & 0 & \boldsymbol{\tau} & 0 & 0 & 0 \\
0 & 0 & 0 & 0 & 0 & \boldsymbol{\tau} & 0 & 0 \\
0 & 0 & 0 & 0 & 0 & 0 & \boldsymbol{\tau} & 0 \\
0 & 0 & 0 & 0 & 0 & 0 & 0 & \boldsymbol{\tau}
\end{bmatrix}
\tag{3.30}
$$

which enables the rotation of the iFEM matrices similarly as in the direct FEM formulation:

$$
\boldsymbol{K}^{(E)} = (\boldsymbol{T}^{(e)})^\top \boldsymbol{K}^{(e)} \boldsymbol{T}^{(e)} \quad ; \quad \boldsymbol{f}^{(E)} = (\boldsymbol{T}^{(e)})^\top \boldsymbol{f}^{(e)} \tag{3.31}
$$

where the superscript (E) stands for the element formulation in the global reference system.

In order to give more insight into the performance of the method, consider a simple cantilever plate under uniform pressure. Distributing the sensors all along the bottom edge, the results in Figure 3.4 have been obtained.
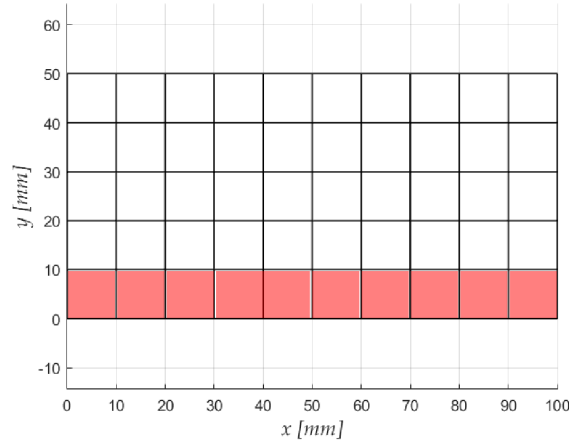
Figure 3.4: *Instrumented elements over clamped plate.*
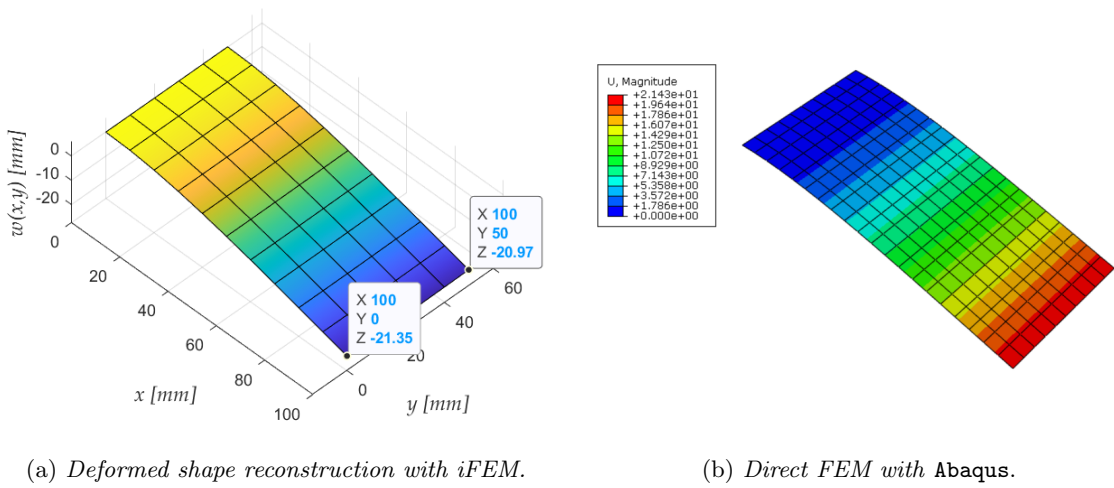
(a) *Deformed shape reconstruction with iFEM.*

(b) *Direct FEM with* `Abaqus`.

Figure 3.5: *Comparison of the results between iFEM and direct FEM.*

Overall, a good correspondence if found. The strainless elements help in defining the displacement field also where no strain gauge is placed. A bit of accuracy is lost away from the strain measurement points, but overall it is quite negligible for this load case. It is useful to assess how the results vary if the gauge configuration is changed. In Figure 3.6 the case already analyzed is plotted as a reference, while in Figure 3.7 the number of strain measurements is decreased. As it is possible to see, the results are *very* dependent on the sensor positions. This has been observed for example in [54] where several configurations are studied and in general it is given the advice to have continuous patterns of sensors over the plate.

A possible remedy to this issue is given for example in [19] where some solutions are developed. So far the *strainless* elements did not have any influence on the error minimization and their only usefulness was to extend the knowledge of the displacement field also where no sensor is present. A better technique consists in giving to these elements an estimate of one or more strain measurements. Since these fictitious strain measurements are just estimates, a lower weight will be given to them. But this will help in obtaining a better reconstruction of the displacement field. This need leads to the technique explained in the next section.

(a) *Instrumented elements.*

(b) *Deflection along bottom edge.*
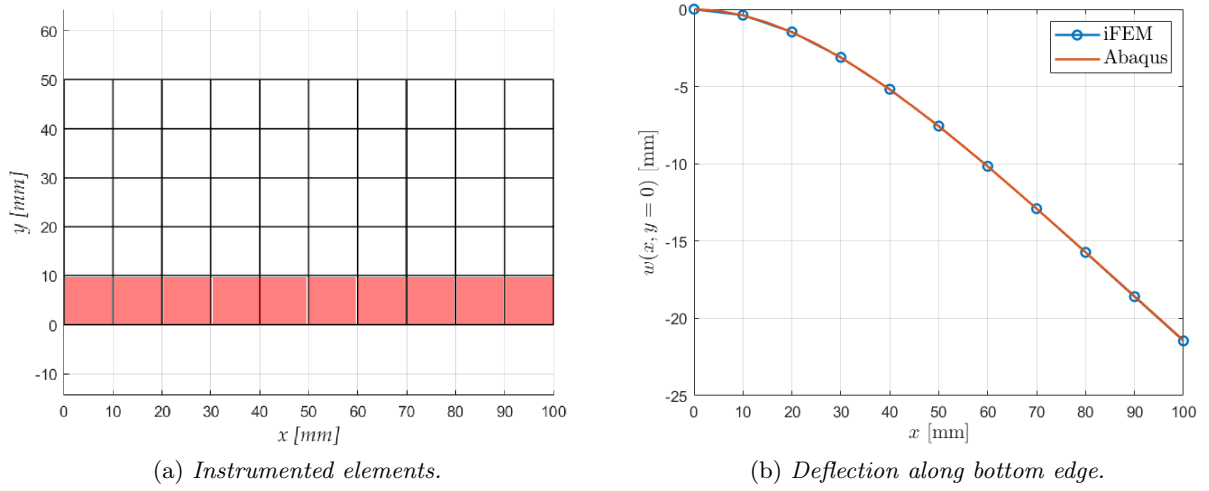
Figure 3.6: *Reference solution continuously instrumenting the whole bottom edge.*

(a) *Instrumented elements.*

(b) *Deflection along bottom edge.*
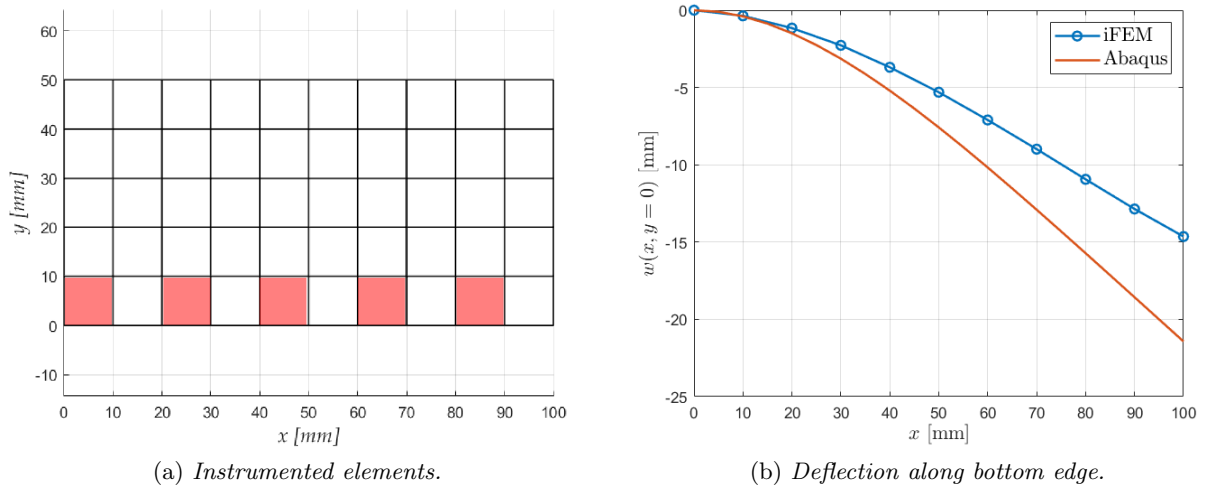
Figure 3.7: *iFEM results and comparison with direct FEM.*

3.1.3 Smoothing Element Analysis

As the name itself suggests, the Smoothing Element Analysis (SEA) is a technique used in order to smoothen discrete data over a certain domain. Initially, the method was mainly devised in order to recover C^1 continuous stresses from direct FEM simulation so that a posteriori error estimates were possible. However, the input of the method is not confined to stress alone, but it might any scalar field which needs to be interpolated over a domain. The main advantage of this method (compared to other smoothing techniques, such as polynomial fitting) is that it uses the same framework of FEM so that SEA becomes extremely versatile and applicable to geometries of any form. The interest in this method has given light to several works which explore SEA, such as [5], [11], [30], [6].

The procedure followed resembles under several points of view the iFEM. Also here the aim is

to minimize an error functional which for the element (e) is expressed as:

$$
\Phi^{(e)} = \overbrace{\frac{1}{N}\sum_{i=1}^{n^{(e)}}\left[\varepsilon_i^\varepsilon - \varepsilon(\boldsymbol{x}_i)\right]^2}^{(1)} + \overbrace{\alpha \iint_{A^{(e)}}\left[\left(\frac{\partial\varepsilon}{\partial x}-\theta_x\right)^2 + \left(\frac{\partial\varepsilon}{\partial y}-\theta_y\right)^2\right]\mathrm{d}A^{(e)}}^{(2)} +
$$
$$
+ \underbrace{\beta A^{(e)}\iint_{A^{(e)}}\left[\left(\frac{\partial\theta_x}{\partial x}\right)^2 + \left(\frac{\partial\theta_y}{\partial y}\right)^2 + \frac{1}{2}\left(\frac{\partial\theta_x}{\partial y}+\frac{\partial\theta_y}{\partial x}\right)^2\right]\mathrm{d}A^{(e)}}_{(3)}
$$

$$(3.32)$$

Three terms build up the functional $\Phi^{(e)}$:

(1) The first term represents the squared error between the smoothed field $\varepsilon(\boldsymbol{x})$ (computed at the sampled point i) and the sampled field $\varepsilon_i^\varepsilon$ (which is our case will be the strain experimental value taken from a strain gauge). The variable N represents the total input strains and is introduced simply as a normalization parameter, while $n^{(e)}$ is the number of strain measurements inside the element domain.

(2) The second term represents a penalty factor whose weight is tuned by the scalar parameter α. In this term $\partial\varepsilon/\partial x$, $\partial\varepsilon/\partial y$ represent the derivatives of the strain field with respect to the Cartesian reference system used, while θ_x, θ_y are independent variables corresponding to the derivatives of the smoothed field (function of the nodal degrees of freedom). As it is possible to see, for large values of α a C^1 field is obtained since:

$$
\theta_x \to \frac{\partial\varepsilon}{\partial x} \quad ; \quad \theta_y \to \frac{\partial\varepsilon}{\partial y}
$$

(3) The third term has been introduced just in later works and represents a regularization term. It contains the derivatives of θ_x, θ_y, that is the curvatures of the smoothed field. Therefore, this term imposes a constraint on the curvature of the field whose severity is governed by the magnitude of β. For example, as stated in [11], if the sampled data $\varepsilon_i^\varepsilon$ are affected by a substantial error, then larger values should be used to further smoothen the field. As reported in [19], its influence is however much less important than the one of α and, from literature, a value equal to 10^{-4} will generally be used in the following.

After having defined the functional to be minimized, the framework of FEA can be set up to find a proper solution. The maximum derivative appearing in $\Phi^{(e)}$ is of order one, therefore a C^0 continuous shape functions can be used to interpolate ε, θ_x and θ_y. An important observation consists in realizing that this functional has a similar expression to the one used for shear deformable beams and plates. For example, for a shear deformable beam of length L the strain energy U can be written in function the deflection w and rotation θ as [64]:

$$
U(w,\theta) = \frac{1}{2}\frac{Eh^3}{12}\left[\int_0^L\left(\frac{\mathrm{d}\theta}{\mathrm{d}x}\right)^2\mathrm{d}x + \kappa\frac{12G}{Eh^2}\int_0^L\left(\frac{\mathrm{d}w}{\mathrm{d}x}-\theta\right)^2\mathrm{d}x\right]
$$

$$(3.33)$$

where the second term has the same structure of (2) in Eq.(3.32) highlighted above. Therefore, it has been decided to use also in this case anisotropic shape functions which limit the effect of *locking*. In particular, for SEA a three node element has been developed and the same shape functions of the three-node inverse element (iMIN3) have been used. They are reported here for

convenience:

$$\varepsilon(\xi, \eta) = \sum_{i=1}^{3} L_i(\xi, \eta) s_i + \sum_{i=1}^{3} (Q_i \theta_{xi} + R_i \theta_{yi})$$

$$\theta_x(\xi, \eta) = \sum_{i=1}^{3} L_i(\xi, \eta) \theta_{xi} \tag{3.34}$$

$$\theta_y(\xi, \eta) = \sum_{i=1}^{3} L_i(\xi, \eta) \theta_{yi}$$

where:

$$L_1 = 1 - \xi - \eta \quad ; \quad L_2 = \xi \quad ; \quad L_3 = \eta$$

$$Q_i = \frac{L_i}{2} (a_j L_k - a_k L_j) \quad ; \quad R_i = \frac{L_i}{2} (b_k L_j - b_j L_k)$$

$$\text{with:} \quad a_i = x_k - x_j \quad ; \quad b_i = y_j - y_k$$

$$i = \{1, 2, 3\} \quad ; \quad j = \{2, 3, 1\} \quad ; \quad k = \{3, 1, 2\}$$

The element outlook is presented in Figure 3.8 where as it is possible to see three degrees of freedom per node are used. It is important to highlight that the variable ε used here can be an arbitrary scalar field. This also means that different interpolations have to be carried out for the different components of the strain field (such as ε_x, ε_y and γ_{xy}) since the SEA holds for just one component.
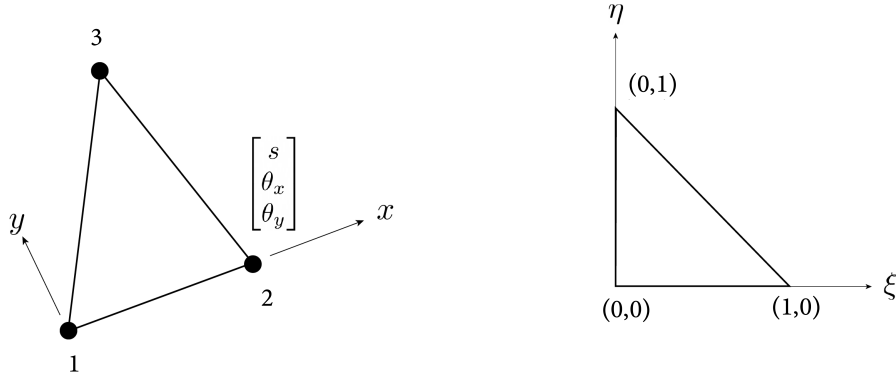
Figure 3.8: *SEA 3-node element in local reference system and parent domain.*

In the following, the element degrees of freedom will be referred to with the following vectors:

$$\boldsymbol{s} = \begin{bmatrix} s_1 \\ s_2 \\ s_3 \end{bmatrix} \quad ; \quad \boldsymbol{s}_x = \begin{bmatrix} \theta_{x1} \\ \theta_{x2} \\ \theta_{x3} \end{bmatrix} \quad ; \quad \boldsymbol{s}_y = \begin{bmatrix} \theta_{y1} \\ \theta_{y2} \\ \theta_{y3} \end{bmatrix} \quad ; \quad \boldsymbol{u}^{(e)} = \begin{bmatrix} \boldsymbol{s} \\ \boldsymbol{s}_x \\ \boldsymbol{s}_y \end{bmatrix}$$

$$\boldsymbol{L} = \begin{bmatrix} L_1 & L_2 & L_3 \end{bmatrix} \quad ; \quad \boldsymbol{Q} = \begin{bmatrix} Q_1 & Q_2 & Q_3 \end{bmatrix} \quad ; \quad \boldsymbol{R} = \begin{bmatrix} R_1 & R_2 & R_3 \end{bmatrix}$$

And so the interpolation of the variables involved in the formulation can be written as:

$$\varepsilon = \boldsymbol{L} \boldsymbol{s} + \boldsymbol{Q} \boldsymbol{s}_x + \boldsymbol{R} \boldsymbol{s}_y$$

$$\theta_x = \boldsymbol{P} \boldsymbol{s}_x \tag{3.35}$$

$$\theta_y = \boldsymbol{L} \boldsymbol{s}_y$$

The element matrices coming from the minimization of the functional can be obtained from each term separately:

(1) Consider the first term:

$$\Phi_\varepsilon = \frac{1}{N} \sum_{i=1}^{n^{(e)}} \left[\varepsilon_i^\varepsilon - \varepsilon(\boldsymbol{u}^{(e)}) \right]^2$$

$$= \frac{1}{N} \sum_{i=1}^{n^{(e)}} \left[\varepsilon_i^\varepsilon - \underbrace{\begin{bmatrix} \boldsymbol{L}(\boldsymbol{x}_i) & \boldsymbol{Q}(\boldsymbol{x}_i) & \boldsymbol{R}(\boldsymbol{x}_i) \end{bmatrix}}_{\boldsymbol{N}} \boldsymbol{u}^{(e)} \right]^2 \quad (3.36)$$

$$= \frac{1}{N} \sum_{i=1}^{n^{(e)}} \left[(\varepsilon_i^\varepsilon)^2 + (\boldsymbol{u}^{(e)})^\top \boldsymbol{N}^\top \boldsymbol{N} \boldsymbol{u}^{(e)} - 2\varepsilon_i^\varepsilon \boldsymbol{N} \boldsymbol{u}^{(e)} \right]$$

which can be rewritten as:

$$\frac{\Phi_\varepsilon}{2} = \frac{1}{2} (\boldsymbol{u}^{(e)})^\top \boldsymbol{K}_\varepsilon \boldsymbol{u}^{(e)} - \boldsymbol{f}_\varepsilon + \frac{1}{2N} \sum_{i=1}^{n^{(e)}} (\varepsilon_i^\varepsilon)^2 \quad (3.37)$$

where:

$$\boldsymbol{K}_\varepsilon = \frac{1}{N} \sum_{i=1}^{n^{(e)}} \boldsymbol{N}^\top \boldsymbol{N} \quad ; \quad \boldsymbol{f}_\varepsilon = \frac{1}{N} \sum_{i=1}^{n^{(e)}} \varepsilon_i^\varepsilon \boldsymbol{N} \quad (3.38)$$

And finally, minimizing:

$$\frac{\partial \Phi_\varepsilon}{\partial \boldsymbol{u}^{(e)}} = 0 \quad \Rightarrow \quad \boldsymbol{K}_\varepsilon \boldsymbol{u}^{(e)} = \boldsymbol{f}_\varepsilon \quad (3.39)$$

(2) Consider the second term:

$$\Phi_\alpha = \alpha \iint_{A^{(e)}} \left[\left(\frac{\partial \varepsilon}{\partial x} - \theta_x \right)^2 + \left(\frac{\partial \varepsilon}{\partial y} - \theta_y \right)^2 \right] dA^{(e)}$$

$$= \alpha \iint_{A^{(e)}} \left[\underbrace{\begin{bmatrix} \frac{\partial \boldsymbol{L}}{\partial x} & \left(\frac{\partial \boldsymbol{Q}}{\partial x} - \boldsymbol{L} \right) & \frac{\partial \boldsymbol{R}}{\partial x} \end{bmatrix}}_{\boldsymbol{B}_1} \boldsymbol{u}^{(e)} \right]^2 + \left[\underbrace{\begin{bmatrix} \frac{\partial \boldsymbol{L}}{\partial y} & \frac{\partial \boldsymbol{Q}}{\partial y} & \left(\frac{\partial \boldsymbol{R}}{\partial y} - \boldsymbol{L} \right) \end{bmatrix}}_{\boldsymbol{B}_2} \boldsymbol{u}^{(e)} \right]^2 dA^{(e)} \quad (3.40)$$

$$= \alpha \iint_{A^{(e)}} (\boldsymbol{u}^{(e)})^\top \boldsymbol{B}_1^\top \boldsymbol{B}_1 \boldsymbol{u}^{(e)} dA^{(e)} + \alpha \iint_{A^{(e)}} (\boldsymbol{u}^{(e)})^\top \boldsymbol{B}_2^\top \boldsymbol{B}_2 \boldsymbol{u}^{(e)} dA^{(e)}$$

and minimizing analogously as before:

$$\boldsymbol{K}_\alpha \boldsymbol{u}^{(e)} = \boldsymbol{0} \quad (3.41)$$

where:

$$\boldsymbol{K}_\alpha = \alpha \iint_{A^{(e)}} \begin{bmatrix} \boldsymbol{B}_1 & \boldsymbol{B}_2 \end{bmatrix} \begin{bmatrix} \boldsymbol{B}_1 \\ \boldsymbol{B}_2 \end{bmatrix} dA^{(e)} \quad (3.42)$$

(3) Consider the third term:

$$\Phi_\beta = \beta A^{(e)} \iint_{A^{(e)}} \left[\left(\frac{\partial \theta_x}{\partial x} \right)^2 + \left(\frac{\partial \theta_y}{\partial y} \right)^2 + \frac{1}{2} \left(\frac{\partial \theta_x}{\partial y} + \frac{\partial \theta_y}{\partial x} \right)^2 \right] dA^{(e)}$$

$$= \beta A^{(e)} \iint_{A^{(e)}} \left[\left(\frac{\partial \boldsymbol{L}}{\partial x} \boldsymbol{s}_x \right)^2 + \left(\frac{\partial \boldsymbol{L}}{\partial y} \boldsymbol{s}_y \right)^2 + \frac{1}{2} \left(\frac{\partial \boldsymbol{L}}{\partial y} \boldsymbol{s}_y + \frac{\partial \boldsymbol{L}}{\partial x} \boldsymbol{s}_y \right)^2 \right] dA^{(e)}$$

$$= \beta A^{(e)} \iint_{A^{(e)}} \left[\boldsymbol{s}_x^T \left(\frac{\partial \boldsymbol{L}}{\partial x} \right)^\top \left(\frac{\partial \boldsymbol{L}}{\partial x} \right) \boldsymbol{s}_x + \boldsymbol{s}_y^\top \left(\frac{\partial \boldsymbol{L}}{\partial y} \right)^\top \left(\frac{\partial \boldsymbol{L}}{\partial y} \right) \boldsymbol{s}_y + \right. \quad (3.43)$$

$$\left. + \frac{1}{2} \left[\left(\frac{\partial \boldsymbol{L}}{\partial y} \boldsymbol{s}_y \right)^2 + \left(\frac{\partial \boldsymbol{L}}{\partial x} \boldsymbol{s}_y \right)^2 + 2 \frac{\partial \boldsymbol{L}}{\partial y} \boldsymbol{s}_x \frac{\partial \boldsymbol{L}}{\partial x} \boldsymbol{s}_y \right] dA^{(e)}$$

Now, minimizing with respect to the degrees of freedom:

$$\frac{\partial \Phi_\beta}{\partial \boldsymbol{s}} = 0 \tag{3.44}$$

is identically null.

$$
\begin{aligned}
\frac{\partial \Phi_\beta}{\partial \boldsymbol{s}_x} &= \beta A^{(e)} \iint_{A^{(e)}} \left[2\left(\frac{\partial \boldsymbol{L}^\top}{\partial x} \frac{\partial \boldsymbol{L}}{\partial x} \right) \boldsymbol{s}_x + \left(\frac{\partial \boldsymbol{L}^\top}{\partial y} \frac{\partial \boldsymbol{L}}{\partial y} \right) \boldsymbol{s}_x + \frac{\partial \boldsymbol{L}^\top}{\partial y} \frac{\partial \boldsymbol{L}}{\partial x} \boldsymbol{s}_y \right] \mathrm{d}A^{(e)} \\
&= \beta A^{(e)} \iint_{A^{(e)}} \left[\boldsymbol{0} \quad \frac{\partial \boldsymbol{L}^\top}{\partial x} \frac{\partial \boldsymbol{L}}{\partial x} + \frac{1}{2} \frac{\partial \boldsymbol{L}^\top}{\partial y} \frac{\partial \boldsymbol{L}}{\partial y} \quad \frac{1}{2} \frac{\partial \boldsymbol{L}^\top}{\partial y} \frac{\partial \boldsymbol{L}}{\partial x} \right] \boldsymbol{u}^{(e)} \mathrm{d}A^{(e)} = 0
\end{aligned}
\tag{3.45}
$$

Analogously:

$$\frac{\partial \Phi_\beta}{\partial \boldsymbol{s}_y} = \beta A^{(e)} \iint_{A^{(e)}} \left[\boldsymbol{0} \quad \frac{1}{2}\frac{\partial \boldsymbol{L}}{\partial y} \quad \frac{\partial \boldsymbol{L}^\top}{\partial y} \frac{\partial \boldsymbol{L}}{\partial y} \quad \frac{1}{2}\frac{\partial \boldsymbol{L}^\top}{\partial x} \frac{\partial \boldsymbol{L}}{\partial x} \right] \boldsymbol{u}^{(e)} \mathrm{d}A^{(e)} = 0 \tag{3.46}$$

And so summing up:

$$\beta A^{(e)} \iint_{A^{(e)}} \begin{bmatrix} \boldsymbol{0} & \boldsymbol{0} & \boldsymbol{0} \\ \boldsymbol{0} & \frac{\partial \boldsymbol{L}^\top}{\partial x} \frac{\partial \boldsymbol{L}}{\partial x} + \frac{1}{2} \frac{\partial \boldsymbol{L}^\top}{\partial y} \frac{\partial \boldsymbol{L}}{\partial y} & \frac{1}{2} \frac{\partial \boldsymbol{L}^T}{\partial y} \frac{\partial \boldsymbol{L}}{\partial x} \\ \boldsymbol{0} & \frac{1}{2}\frac{\partial \boldsymbol{L}}{\partial y} & \frac{\partial \boldsymbol{L}^\top}{\partial y} \frac{\partial \boldsymbol{L}}{\partial y} \quad \frac{1}{2} \frac{\partial \boldsymbol{L}^\top}{\partial x} \frac{\partial \boldsymbol{L}}{\partial x} \end{bmatrix} \mathrm{d}A^{(e)} \boldsymbol{u}^{(e)} = \boldsymbol{0} \tag{3.47}$$

From which it is possible to define:

$$\boldsymbol{K}_\beta = \beta A^{(e)} \iint_{A^{(e)}} \begin{bmatrix} \boldsymbol{0} & \boldsymbol{0} & \boldsymbol{0} \\ \boldsymbol{0} & \frac{\partial \boldsymbol{L}^\top}{\partial x} \frac{\partial \boldsymbol{L}}{\partial x} + \frac{1}{2} \frac{\partial \boldsymbol{L}^\top}{\partial y} \frac{\partial \boldsymbol{L}}{\partial y} & \frac{1}{2} \frac{\partial \boldsymbol{L}^\top}{\partial y} \frac{\partial \boldsymbol{L}}{\partial x} \\ \boldsymbol{0} & \frac{1}{2}\frac{\partial \boldsymbol{L}}{\partial y} & \frac{\partial \boldsymbol{L}^\top}{\partial y} \frac{\partial \boldsymbol{L}}{\partial y} \quad \frac{1}{2} \frac{\partial \boldsymbol{L}^\top}{\partial x} \frac{\partial \boldsymbol{L}}{\partial x} \end{bmatrix} \mathrm{d}A^{(e)} \tag{3.48}$$

In literature the argument of the integral in Eq.(3.48) is usually written as:

$$\begin{bmatrix} \boldsymbol{0} & \boldsymbol{0} & \boldsymbol{0} \\ \boldsymbol{0} & \frac{\partial \boldsymbol{L}^\top}{\partial x} \frac{\partial \boldsymbol{L}}{\partial x} + \frac{1}{2} \frac{\partial \boldsymbol{L}^\top}{\partial y} \frac{\partial \boldsymbol{L}}{\partial y} & \frac{1}{2} \frac{\partial \boldsymbol{L}^T}{\partial y} \frac{\partial \boldsymbol{L}}{\partial x} \\ \boldsymbol{0} & \frac{1}{2}\frac{\partial \boldsymbol{L}}{\partial y} & \frac{\partial \boldsymbol{L}^\top}{\partial y} \frac{\partial \boldsymbol{L}}{\partial y} \quad \frac{1}{2} \frac{\partial \boldsymbol{L}^T}{\partial x} \frac{\partial \boldsymbol{L}}{\partial x} \end{bmatrix} = \begin{bmatrix} \boldsymbol{0} & \boldsymbol{0} & \boldsymbol{0} \\ \frac{\partial \boldsymbol{L}}{\partial x} & \boldsymbol{0} & \frac{\partial \boldsymbol{L}}{\partial y} \\ \boldsymbol{0} & \frac{\partial \boldsymbol{L}}{\partial y} & \frac{\partial \boldsymbol{L}}{\partial x} \end{bmatrix}^\top \begin{bmatrix} 1 & 0 & 0 \\ 0 & 1 & 0 \\ 0 & 0 & \frac{1}{2} \end{bmatrix} \begin{bmatrix} \boldsymbol{0} & \boldsymbol{0} & \boldsymbol{0} \\ \frac{\partial \boldsymbol{L}}{\partial x} & \boldsymbol{0} & \frac{\partial \boldsymbol{L}}{\partial y} \\ \boldsymbol{0} & \frac{\partial \boldsymbol{L}}{\partial y} & \frac{\partial \boldsymbol{L}}{\partial x} \end{bmatrix} \tag{3.49}$$
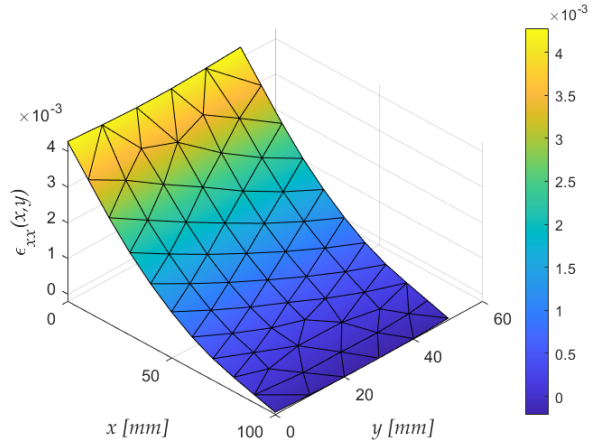
Finally, the relation which determines the element degrees of freedom is obtained summing the contributions of the three terms derived above:

$$(\boldsymbol{K}_\varepsilon + \boldsymbol{K}_\alpha + \boldsymbol{K}_\beta) \boldsymbol{u}^{(e)} = \boldsymbol{f}_\varepsilon \tag{3.50}$$
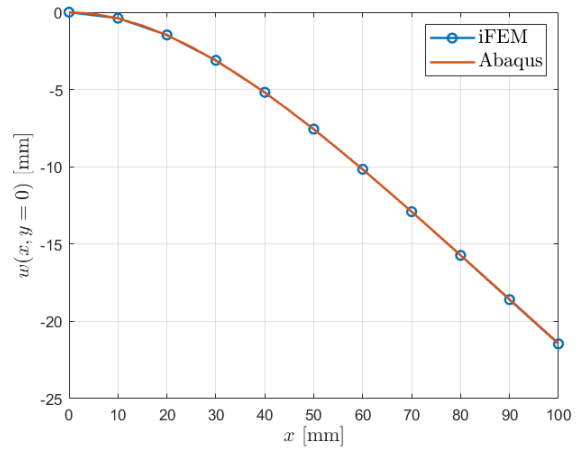
which can be assembled following the usual rules of the standard FEM. It is important to highlight though that a set of boundary conditions is *not* mandatory in this case.
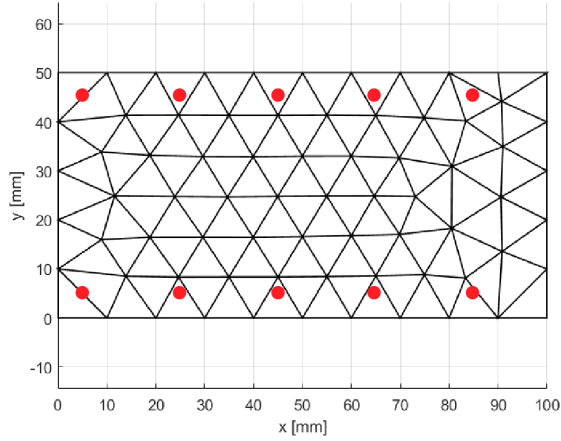
(a) *Strain gauge positions.*

(b) *Strain field $\varepsilon_x(x, y)$ pre-extrapolation with SEA.*
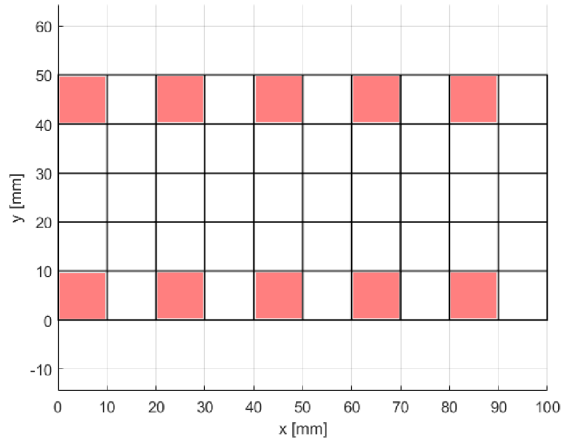
(c) *Instrumented elements.*

(d) *Deflection along bottom edge.*

Figure 3.9: *iFEM results and comparison with direct FEM.*

Pre-extrapolating the strain field before applying iFEM is in general beneficial to obtain better estimations of the deformed shape. Considering again the clamped plate of Section 3.1.2, the strain measurements have first been used as input for SEA. In this case, both the upper and lower side of the plate have been instrumented since otherwise the SEA system of equations becomes very ill-conditioned. Using the results of SEA as input of iFEM together with the actual strain measurements leads to a considerable improvement in the determination of the deformed shape (Figure 3.9).

3.2 Strain pre-extrapolation on ISTAR demonstrator wing

Considering that on the wing a few strain measurements are taken, in order to apply iFEM it is necessary first to pre-extrapolate the strain field all over the structural domain. It is possible to see that, if this preliminary operation is not carried out, the iFEM results are quite poor.
The problem so consists in fitting a strain field consistent with the strain measurements. Note that, since in general are required three strain components (ε_x, ε_y and γ_{xy}), three different fits are needed. For simple domains a polynomial interpolation could be used. However, for relatively complex shapes such as a wing this might bring several issues concerning the parametrization of the wing surface. It is possible to overcome this problem using SEA, and this will be the approach used in the following. In particular, in Section 3.2.2 the strain pre-extrapolation is carried out using the three-node element available in literature and described in Section 4.1. Due to some difficulties, SEA with a quadrilateral element will be developed (Section 3.2.2) and it is suggested a method to choose suitable parameters for the interpolation.

The case study for all the following analyses will be the FE model of the ISTAR demonstrator wing. It has been decided to use a rather sparse sensor configuration, but at the same time to measure the strain homogeneously over all the skin. So 20 different positions have been chosen as in Figure 3.10 at which the strain field is measured. It has been observed that especially iFEM requires an estimate of the full strain field and not just a component. Therefore, at the measurement locations it is as if a strain rosette has been installed, so measuring the three components of the strain field. The detailed positions of the virtual strain rosettes are reported in Appendix M.

(a) *Isometric view.* (b) *Top view.*
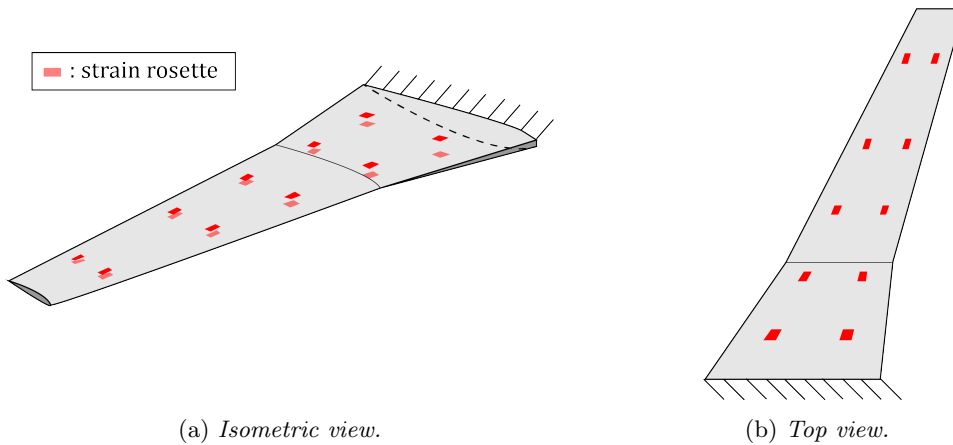
Figure 3.10: *Strain rosette positions used to recover the deformed shape of the ISTAR demonstrator wing.*

3.2.1 Strain pre-extrapolation with SEA 3-node elements

Since the three-node SEA elements described in Section 3.1.3 have been developed mainly for two-dimensional problems, there is the need to add a "drilling" degree of freedom in order to allow a proper rotation to the global reference system. In direct FEM this can be accomplished in several ways, for example [44]:

- Inserting an arbitrary stiffness coefficient k_{θ_z} such that in local coordinates the following equation holds: $k_{\theta_z}\theta_{zi} = 0$. This leads to a well-behaved system without occurring in ill-conditioning problems.

- A more consistent approach consists in adding to the element total potential energy Π a contribution due to the drilling part as:

$$\Pi \leftarrow \Pi + \int_{A^{(e)}} \alpha E (\overline{\theta}_z - \theta_z)^2 \mathrm{d}A^{(e)}$$

with $\overline{\theta}_z$ the mean out-of-plane element rotation and α a scalar coefficient to tune.

In the framework of SEA however the second option would be hardly possible to implement since the functional to be minimized does not represent a total potential energy, but is based on a penalized discrete least-squares variational principle with the experimental measurements. Therefore, it has been decided to simply add a fictitious drilling stiffness to each element. The effect of this choice will be analysed in the following. The element $\boldsymbol{K}^{(e)}$ matrix therefore for the triangular element looks like the one in Figure 3.11, where the variable $\boldsymbol{s} = \begin{bmatrix} s_1 & s_2 & s_2 \end{bmatrix}^{\top}$ stands for the generic scalar field to be smoothed, $\boldsymbol{\theta}_x$, $\boldsymbol{\theta}_y$ for the gradients of the field and finally $\boldsymbol{\theta}_z$ for the additional drilling degrees of freedom.
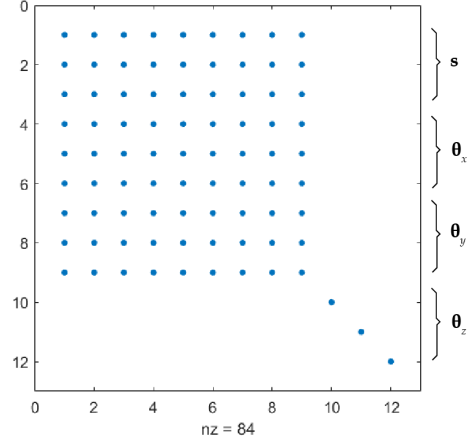
Figure 3.11: *Element $\boldsymbol{K}^{(e)}$ matrix.*

As in direct FEM, this matrix should be properly defined in the global reference system with a transformation matrix $\boldsymbol{T}$ as: $\boldsymbol{T}^{\top} \boldsymbol{K}^{(e)} \boldsymbol{T}$.

Before looking at some results, it is important to discuss the influence of the parameter α in SEA. The functional to be minimized can be written as:

$$\Phi^{(e)} = \Phi_\varepsilon + \alpha \Phi_\alpha + \beta \Phi_\beta \tag{3.51}$$

where Φ_ε depends on the strain measurements and Φ_α, Φ_β are the *regularization* terms. In general Φ_β is introduced just to obtain a well-conditioned system, but has a negligible influence compared to the other terms and so it will be neglected in the following discussion. A major role is played instead by Φ_α and the corresponding parameter α. For convenience the expressions of Φ_ε and Φ_α are reported below:

$$\Phi_\varepsilon = \frac{1}{N} \sum_{i=1}^{n^{(e)}} [\varepsilon_i^\varepsilon - \varepsilon(\boldsymbol{x}_i)]^2$$

$$\Phi_\alpha = \iint_{A^{(e)}} \left[\left(\frac{\partial \varepsilon}{\partial x} - \theta_x \right)^2 + \left(\frac{\partial \varepsilon}{\partial y} - \theta_y \right)^2 \right] \mathrm{d}A^{(e)} \tag{3.52}$$

As it is possible to see, for low values of α, $\Phi^{(e)}$ mainly depends on Φ_ε and so the functional is dominated by this term. This means that the resulting field to be smoothed $\varepsilon(\boldsymbol{x})$ will be very close to the strain measurements $\varepsilon_i^\varepsilon$ nearby $\boldsymbol{x}_i$, while the rest of the domain hardly plays any role, leading to a quite discontinuous field. For larger values of α the regularization term becomes more important and in the limit $\alpha \rightarrow +\infty$ a C^1 continuous field is obtained. At the same time, in general this will result also in a larger deviation from $\varepsilon_i^\varepsilon$ at $\boldsymbol{x}_i$.

It is therefore necessary to tune the parameter α such that a good compromise between the two terms Φ_ε and Φ_α is reached. Here, a simple method sometimes followed in the solution

of least-squares problems will be applied [16]. That is, the residual Φ_ε is plotted over Φ_α in a log-log plot. This will result in a curve which generally presents a distinct corner. For this point the parameter α is chosen. The method is intuitive and simple to implement, but heuristic. Therefore the choice of the regularization parameter α will be checked computing the error w.r.t. the reference strain field.

Using triangular SEA elements several simulations have been carried out applying a simple tip load to the wing. With suitable parameters, a relatively good approximation of the strain field can be found. For example, in Figure 3.12 it is shown ε_x over the wing surface using $k_{\theta_z} = 1e-4$, $\alpha = 1e-2$ and $\beta = 1e-4$ (as stated before, β has a lower impact compared to α and in the following the value $1e-4$ will be used).
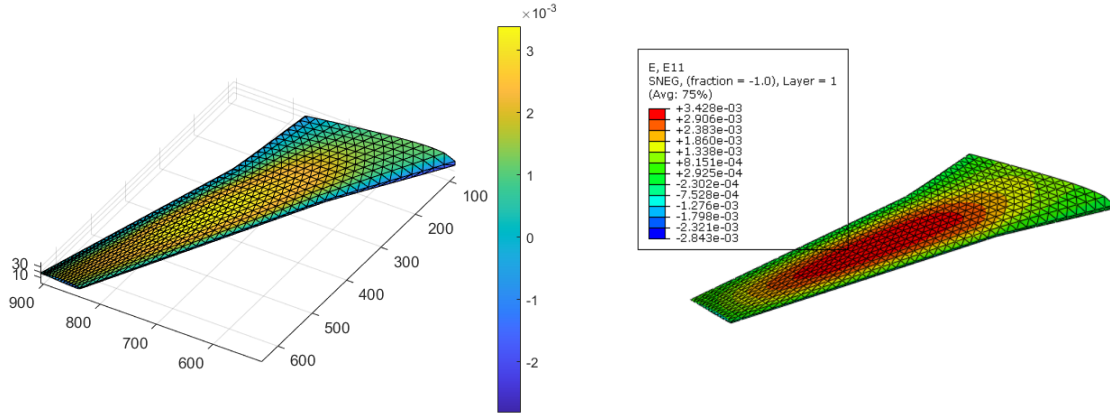
(a) *Interpolated ε_x field over wing skin.*　　(b) *Reference ε_x field from direct FEM.*

Figure 3.12: *SEA with three-node elements.*

However, the results seem to be very dependent on α and k_{θ_z} in a not well defined way. For example, using $k_{\theta_z} = 1e-8$ in Figure 3.13a the residuals are plotted for different values of α and the corresponding L2-norm error of the strain field in Figure 3.13b.
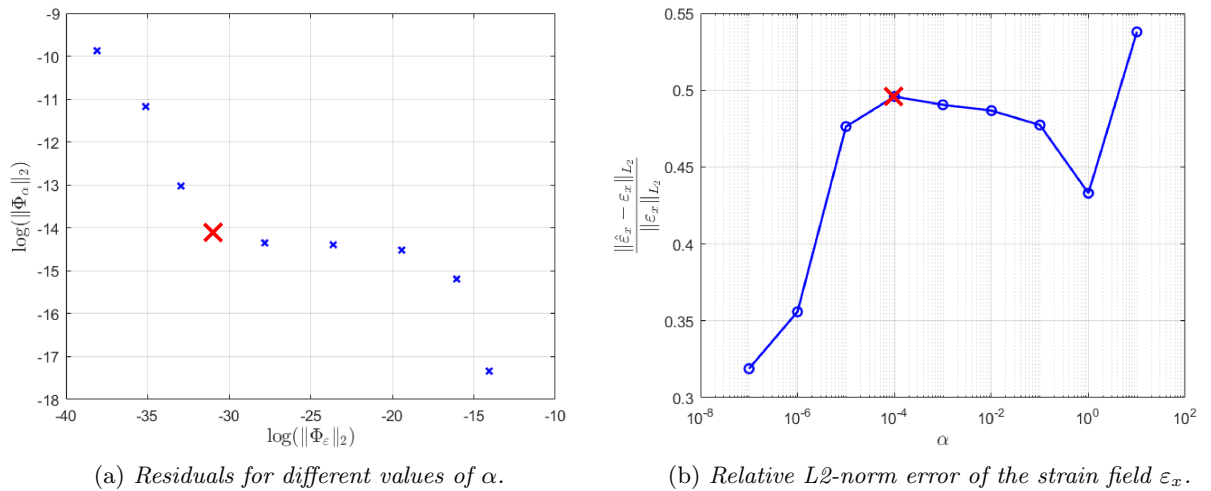
(a) *Residuals for different values of α.*　　(b) *Relative L2-norm error of the strain field ε_x.*

Figure 3.13: *Example of difficulty in choosing the regularization parameter α.*

As it is possible to see, the corner of the curve ($\times$) of the residuals does not correspond to a

minimum in the error of the strain field. Furthermore, using different values for k_{θ_z} the results seem to largely depend on this parameter. This is illustrated in Figure 3.14.

(a) *Residuals for different values of α and k_{θ_z}.*

(b) *Relative L2-norm error of the strain field ε_x.*
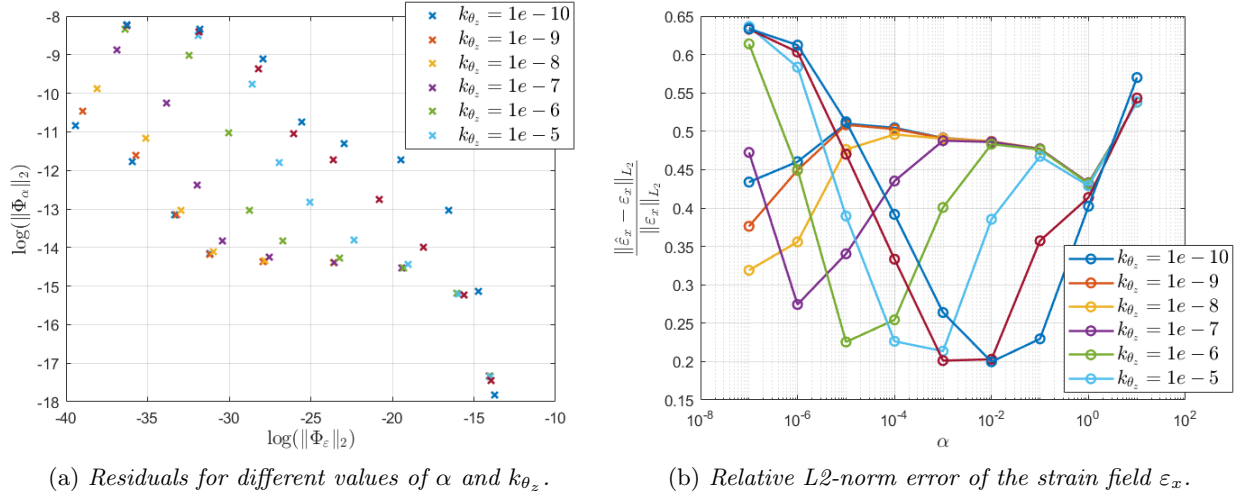
Figure 3.14: *Dependence of the results in function of the drilling stiffness k_{θ_z}.*

Therefore, it seems that using three-node SEA elements is hardly possible to identify an optimal configuration for the parameters in order to obtain a consistent strain field from the strain measurements. A different situation occurs using quadrilateral elements as it will described in the next section.

3.2.2   Strain pre-extrapolation with SEA 4-node elements

In this section the SEA has been applied using quadrilateral elements. The study case that will be analyzed is again the wing instrumented as before. In order to use quadrilateral elements the functional to be minimized has been slightly modified compared to the one used in literature because of the different element formulation:

$$
\begin{aligned}
\Phi^{(e)} = &\frac{1}{N} \sum_{i=1}^{n^{(e)}} \left[\varepsilon_i^\varepsilon - \varepsilon(\boldsymbol{x}_i) \right]^2 + \alpha \iint_{A^{(e)}} \left[\left(\frac{\partial \varepsilon}{\partial x} {\color{red}+} \theta_y \right)^2 + \left(\frac{\partial \varepsilon}{\partial y} - \theta_x \right)^2 \right] \mathrm{d}A^{(e)} + \\
&+ \beta A^{(e)} \iint_{A^{(e)}} \left[\left(\frac{\partial \theta_x}{\partial y} \right)^2 + \left(\frac{\partial \theta_y}{\partial x} \right)^2 + \frac{1}{2} \left(\frac{\partial \theta_x}{\partial y} + \frac{\partial \theta_y}{\partial x} \right)^2 \right] \mathrm{d}A^{(e)}
\end{aligned}
\tag{3.53}
$$

The shape functions of the iQS4 element have been used and the following analogy can be done between the displacement field and the scalar field ε to be interpolated:

$$
\begin{aligned}
w &\leftrightarrow \varepsilon \\
\gamma_{xz} &\leftrightarrow \frac{\partial \varepsilon}{\partial x} + \theta_y \\
\gamma_{yz} &\leftrightarrow \frac{\partial \varepsilon}{\partial y} - \theta_x
\end{aligned}
$$

Following what it has been done in iFEM, the interpolation used in reported below:

$$
\begin{aligned}
\varepsilon &= \boldsymbol{N}\boldsymbol{s} - \boldsymbol{L}\boldsymbol{s}_x - \boldsymbol{M}\boldsymbol{s}_y \\
\theta_x &= \boldsymbol{N}\boldsymbol{s}_x \\
\theta_y &= \boldsymbol{N}\boldsymbol{s}_y
\end{aligned}
\tag{3.54}
$$

with $\boldsymbol{N}$, $\boldsymbol{L}$, $\boldsymbol{M}$ the corresponding shape function matrices of the iQS4 element. And now the element matrices can be derived along the same lines of the procedure outlined in Section 3.1.3:

- For the first term:

$$
\begin{aligned}
\Phi_\varepsilon &= \frac{1}{N}\sum_i \left[\varepsilon_i^\varepsilon - \varepsilon(\boldsymbol{u}^{(e)})\right]^2 \\
&= \frac{1}{N}\sum_i \left[\varepsilon_i^\varepsilon - \underbrace{\begin{bmatrix}\boldsymbol{N} & -\boldsymbol{L} & -\boldsymbol{M}\end{bmatrix}}_{\widetilde{\boldsymbol{N}}}\boldsymbol{u}^{(e)}\right]^2 \\
&= \frac{1}{N}\sum_i \left[(\varepsilon_i^\varepsilon)^2 + \boldsymbol{u}^{(e)\top}\widetilde{\boldsymbol{N}}^\top\widetilde{\boldsymbol{N}}\boldsymbol{u}^{(e)} - 2\varepsilon_i^\varepsilon\widetilde{\boldsymbol{N}}\boldsymbol{u}^{(e)}\right]
\end{aligned}
\tag{3.55}
$$

And minimizing w.r.t. $\boldsymbol{u}^{(e)}$ is is possible to obtain:

$$
\boldsymbol{K}_\varepsilon\boldsymbol{u}^{(e)} = \boldsymbol{f}_\varepsilon
\tag{3.56}
$$

where:

$$
\boldsymbol{K}_\varepsilon = \frac{1}{N}\sum_i \widetilde{\boldsymbol{N}}^\top\tilde{\boldsymbol{N}} \quad ; \quad \boldsymbol{f}_\varepsilon = \frac{1}{N}\sum_i \varepsilon_i^\varepsilon\widetilde{\boldsymbol{N}}
\tag{3.57}
$$

- For the second term:

$$
\begin{aligned}
\Phi_\alpha &= \iint_{A^{(e)}} \left[\left(\frac{\partial\varepsilon}{\partial x} + \theta_y\right)^2 + \left(\frac{\partial\varepsilon}{\partial y} - \theta_x\right)^2\right] \mathrm{d}A^{(e)} \\
&= \iint_{A^{(e)}} \left[\underbrace{\begin{bmatrix}\frac{\partial\boldsymbol{N}}{\partial x} & -\frac{\partial\boldsymbol{L}}{\partial x} & \left(-\frac{\partial\boldsymbol{M}}{\partial x} + \boldsymbol{N}\right)\end{bmatrix}}_{\boldsymbol{B}_1}\boldsymbol{u}^{(e)}\right]^2 + \left[\underbrace{\begin{bmatrix}\frac{\partial\boldsymbol{N}}{\partial x} & \left(-\frac{\partial\boldsymbol{L}}{\partial x} - \boldsymbol{N}\right) & -\frac{\partial\boldsymbol{M}}{\partial x}\end{bmatrix}}_{\boldsymbol{B}_2}\boldsymbol{u}^{(e)}\right]^2 \mathrm{d}A^{(e)}
\end{aligned}
\tag{3.58}
$$

And carrying out the same steps as before it is possible to obtain:

$$
\boldsymbol{K}_\alpha\boldsymbol{u}^{(e)} = \boldsymbol{0}
\tag{3.59}
$$

with:

$$
\boldsymbol{K}_\alpha = \iint_{A^{(e)}} \left(\boldsymbol{B}_1^\top\boldsymbol{B}_1 + \boldsymbol{B}_2^\top\boldsymbol{B}_2\right) \mathrm{d}A^{(e)}
\tag{3.60}
$$

- Finally, for the last term:

$$
\begin{aligned}
\Phi_\beta &= \iint_{A^{(e)}} \left[\left(\frac{\partial\theta_x}{\partial y}\right)^2 + \left(\frac{\partial\theta_y}{\partial x}\right)^2 + \frac{1}{2}\left(\frac{\partial\theta_x}{\partial y} + \frac{\partial\theta_y}{\partial x}\right)^2\right] \mathrm{d}A^{(e)} \\
&= \iint_{A^{(e)}} \left[\left(\frac{\partial\boldsymbol{N}}{\partial y}\theta_x\right)^2 + \left(\frac{\partial\boldsymbol{N}}{\partial x}\theta_y\right)^2 + \frac{1}{2}\left(\frac{\partial\boldsymbol{N}}{\partial y}\theta_x + \frac{\partial\boldsymbol{N}}{\partial x}\theta_y\right)^2\right] \mathrm{d}A^{(e)} \\
&= \iint_{A^{(e)}} \left[\theta_x^\top\left(\frac{\partial\boldsymbol{N}}{\partial y}\right)^\top\frac{\partial\boldsymbol{N}}{\partial y}\theta_x + \theta_y^T\left(\frac{\partial\boldsymbol{N}}{\partial x}\right)^T\frac{\partial\boldsymbol{N}}{\partial x}\theta_y + \right. \\
&\quad \left. + \frac{1}{2}\left(\left(\frac{\partial\boldsymbol{N}}{\partial y}\theta_x\right)^2 + \left(\frac{\partial\boldsymbol{N}}{\partial x}\theta_y\right)^2 + 2\frac{\partial\boldsymbol{N}}{\partial y}\theta_x\frac{\partial\boldsymbol{N}}{\partial x}\theta_y\right)\right]
\end{aligned}
\tag{3.61}
$$

$$
\frac{\partial\Phi_\beta}{\partial\boldsymbol{s}} = \boldsymbol{0}
\tag{3.62}
$$

$$\frac{\partial \Phi_\beta}{\partial \boldsymbol{s}_x} = \iint_{A^{(e)}} \left[2 \left(\frac{\partial \boldsymbol{N}^\top}{\partial y} \frac{\partial \boldsymbol{N}}{\partial y} \right) \theta_x + \left(\frac{\partial \boldsymbol{N}^\top}{\partial y} \frac{\partial \boldsymbol{N}}{\partial y} \right) \theta_x + \frac{\partial \boldsymbol{N}^\top}{\partial y} \frac{\partial \boldsymbol{N}}{\partial x} \theta_y \right] \mathrm{d}A^{(e)}$$
$$\iint_{A^{(e)}} \left[0 \quad \left(\frac{\partial \boldsymbol{N}^\top}{\partial y} \frac{\partial \boldsymbol{N}}{\partial y} + \frac{1}{2} \frac{\partial \boldsymbol{N}^\top}{\partial y} \frac{\partial \boldsymbol{N}}{\partial y} \right) \quad \frac{1}{2} \frac{\partial \boldsymbol{N}^\top}{\partial y} \frac{\partial \boldsymbol{N}}{\partial x} \right] \boldsymbol{u}^{(e)} \, \mathrm{d}A^{(e)}$$
(3.63)

$$\frac{\partial \Phi_\beta}{\partial \boldsymbol{s}_y} = \iint_{A^{(e)}} \left[2 \left(\frac{\partial \boldsymbol{N}^\top}{\partial x} \frac{\partial \boldsymbol{N}}{\partial x} \right) \theta_y + \left(\frac{\partial \boldsymbol{N}^\top}{\partial x} \frac{\partial \boldsymbol{N}}{\partial x} \right) \theta_y + \frac{\partial \boldsymbol{N}^\top}{\partial y} \frac{\partial \boldsymbol{N}}{\partial x} \theta_x \right] \mathrm{d}A^{(e)}$$
$$\iint_{A^{(e)}} \left[0 \quad \frac{1}{2} \frac{\partial \boldsymbol{N}^T}{\partial y} \frac{\partial \boldsymbol{N}}{\partial x} \quad \left(\frac{\partial \boldsymbol{N}^\top}{\partial x} \frac{\partial \boldsymbol{N}}{\partial x} + \frac{1}{2} \frac{\partial \boldsymbol{N}^\top}{\partial x} \frac{\partial \boldsymbol{N}}{\partial x} \right) \right] \boldsymbol{u}^{(e)} \, \mathrm{d}A^{(e)}$$
(3.64)

And so:

$$\boldsymbol{K}_\beta \boldsymbol{u}^{(e)} = \boldsymbol{0} \tag{3.65}$$

with:

$$\boldsymbol{K}_\beta = \iint_{A^{(e)}} \begin{bmatrix} \boldsymbol{0} & \boldsymbol{0} & \boldsymbol{0} \\ \boldsymbol{0} & \frac{3}{2} \frac{\partial \boldsymbol{N}^\top}{\partial y} \frac{\partial \boldsymbol{N}}{\partial y} & \frac{1}{2} \frac{\partial \boldsymbol{N}^T}{\partial y} \frac{\partial \boldsymbol{N}}{\partial x} \\ \boldsymbol{0} & \frac{1}{2} \frac{\partial \boldsymbol{N}^\top}{\partial y} \frac{\partial \boldsymbol{N}}{\partial y} & \frac{3}{2} \frac{\partial \boldsymbol{N}^\top}{\partial x} \frac{\partial \boldsymbol{N}}{\partial x} \end{bmatrix} \mathrm{d}A^{(e)} \tag{3.66}$$

As before, also in this case it is necessary to add the degree of freedom θ_z for shell structures with a corresponding drilling stiffness k_{θ_z}.

Using this type of element the wing has been analysed, applying as before a tip load. Smoothing the axial strain field ε_x gives, for various values of α, the results presented in Figure 3.19.

This time it is possible to see that indeed a value close to the optimum can be found at the corner of the residual curve. This point has been identified from the maximum curvature of the curve. In Figure 3.18 the sampled residual curve has been plotted together with the corresponding relative L2-norm error for each strain component (ε_x, ε_y and γ_{xy}) for the tip load case. The highlighted points represent the locations of the highest curvature. As it is possible to see from the plot of the relative L2-norm error, they are very close to the actual optimum point. The correspondent values are reported in Table 3.1.

		α	L2-norm error
ε_x	Sampled	0.032	0.21
	Max curvature	0.034	0.21
ε_y	Sampled	0.1	0.30
	Max curvature	0.03	0.3
γ_{xy}	Sampled	0.1	0.47
	Max curvature	0.01	0.49

Table 3.1: *Error of interpolated strain field using optimal values for α, either from the sampled values and from the maximum curvature of the residual curve.*

Regarding the sensitivity on the choice for k_{θ_z}, this time a far lower dependence on this parameter can be seen. For example, in the case of ε_x for the tip load case the graphs of Figure 3.15 can be obtained. There is an almost perfect overlap for the different values of k_{θ_z} apart from very low values of α, which in any case are far away from the corner of the residual curve.
For completeness, some results are presented in Figure 3.16 and Figure 3.17 below for two other load cases, that is a constant pressure applied on the bottom skin and a parabolic one. Again, just the results for the axial strain ε_x are shown. Regarding the dependence on k_{θ_z} it is basically possible to observe a situation similar to the previous case. Furthermore, again the lower error values are located towards the corner of the residual curve, which therefore can be used to identify a suitable value for α. Plots analogous to Figure 3.18 for the constant and parabolic pressure cases are reported in Appendix K for completeness.
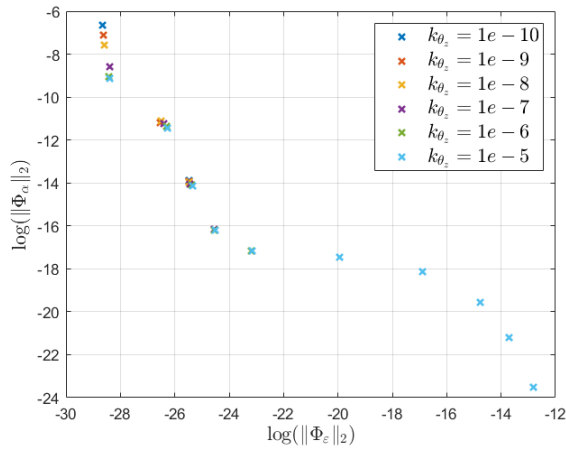
(a) *Residuals of ε_x.*
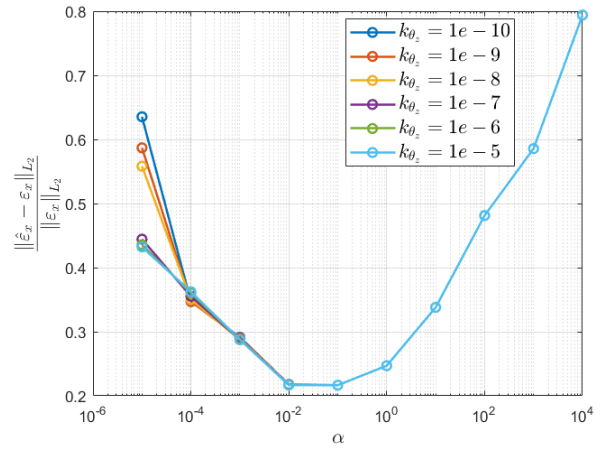
(b) *Relative L2-norm error for ε_x.*

Figure 3.15: *Dependence of the results on k_{θ_z} for tip load case.*
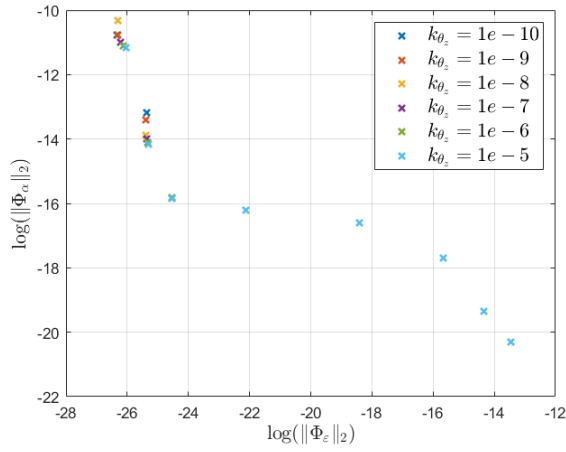
(a) *Residuals of ε_x.*
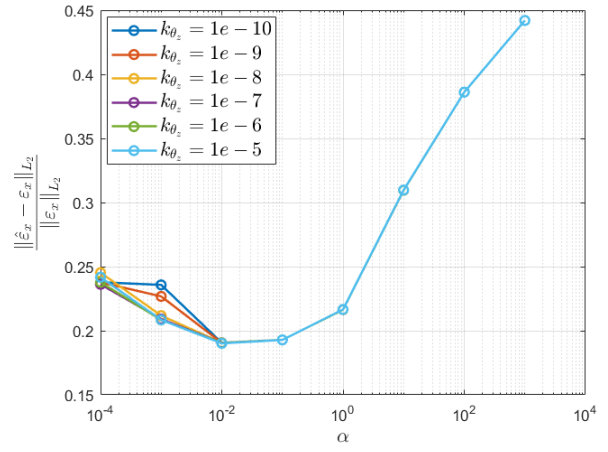
(b) *Relative L2-norm error for ε_x.*

Figure 3.16: *Dependence of the results on k_{θ_z} for constant pressure load case.*
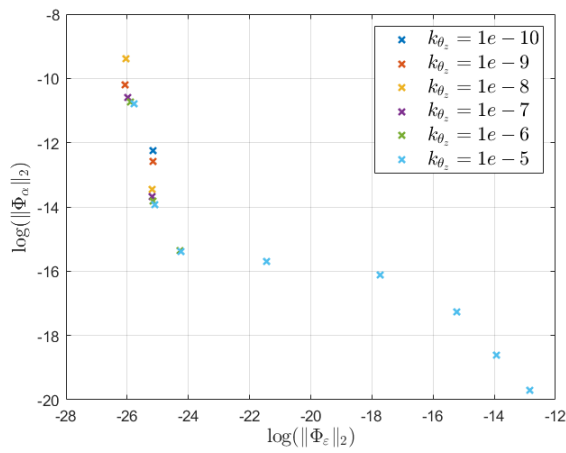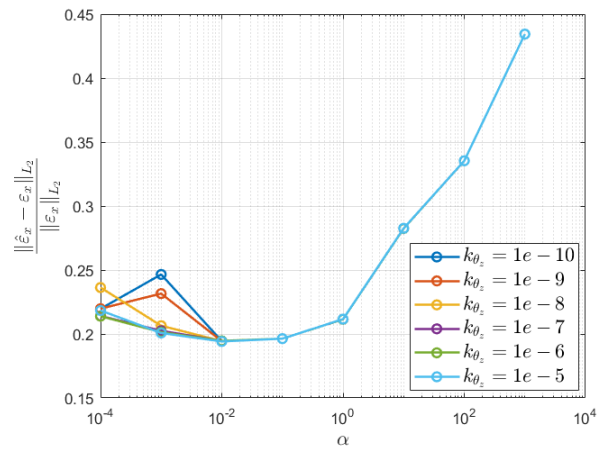
(a) *Residuals of ε_x.*

(b) *Relative L2-norm error for ε_x.*

Figure 3.17: *Dependence of the results on k_{θ_z} for parabolic pressure load case.*
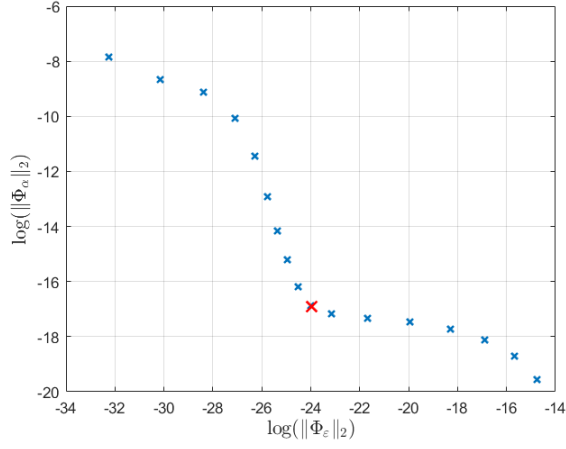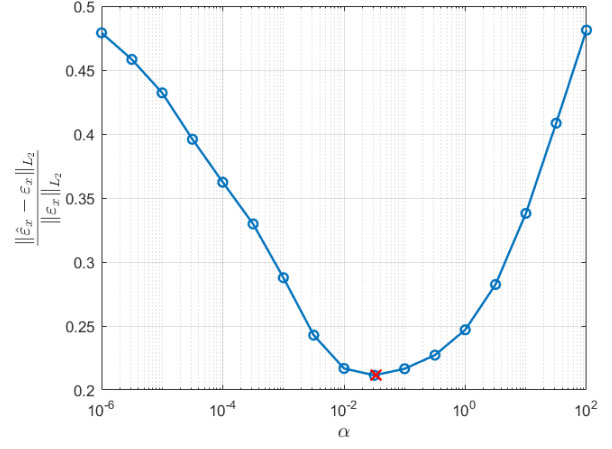
(a) *Residuals of ε_x for different values of α.*

(b) *Relative L2-norm error of ε_x strain field.*
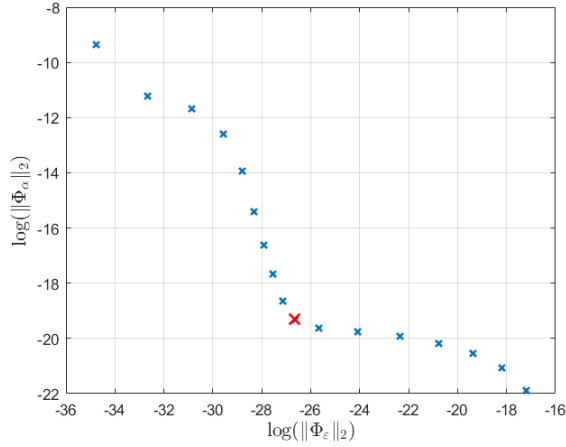
(c) *Residuals of ε_y for different values of α.*
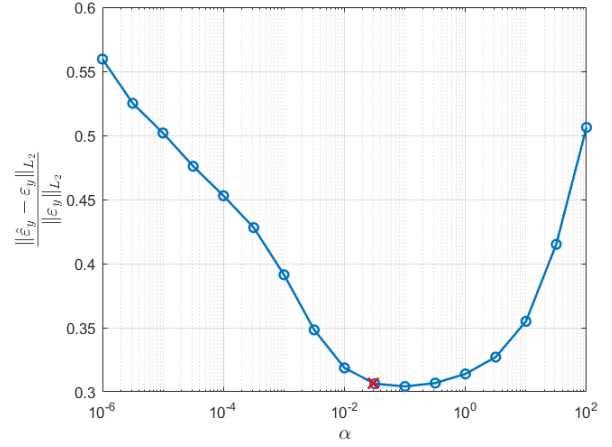
(d) *Relative L2-norm error of ε_y strain field.*
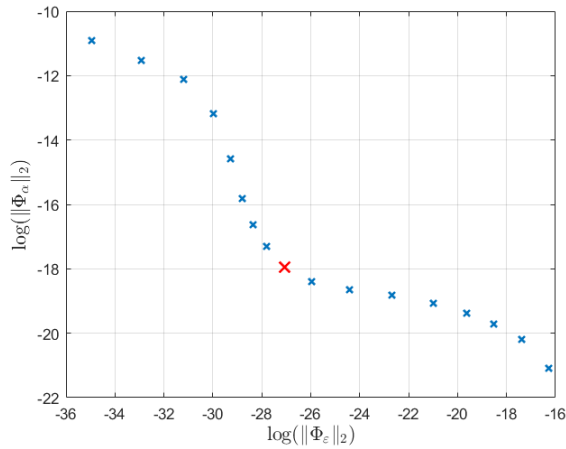
(e) *Residuals of γ_{xy} for different values of α.*
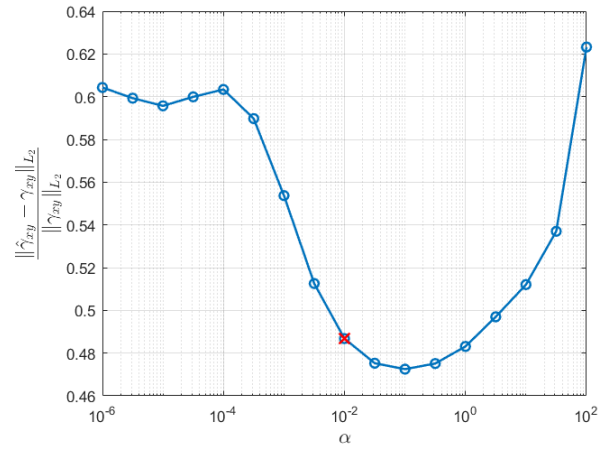
(f) *Relative L2-norm error of γ_{xy} strain field.*

Figure 3.18: *Interpolation of strain field with SEA for the tip load case.*

(a) $\alpha = 1e - 6$

(b) $\alpha = 1e - 5$

(c) $\alpha = 1e - 4$

(d) $\alpha = 1e - 3$

(e) $\alpha = 1e - 2$

(f) $\alpha = 1e - 1$

(g) $\alpha = 1$

(h) $\alpha = 1e + 1$

(i) $\alpha = 1e + 2$

(j) $\alpha = 1e + 3$

(k) $\alpha = 1e + 4$

(l) $\alpha = 1e + 5$
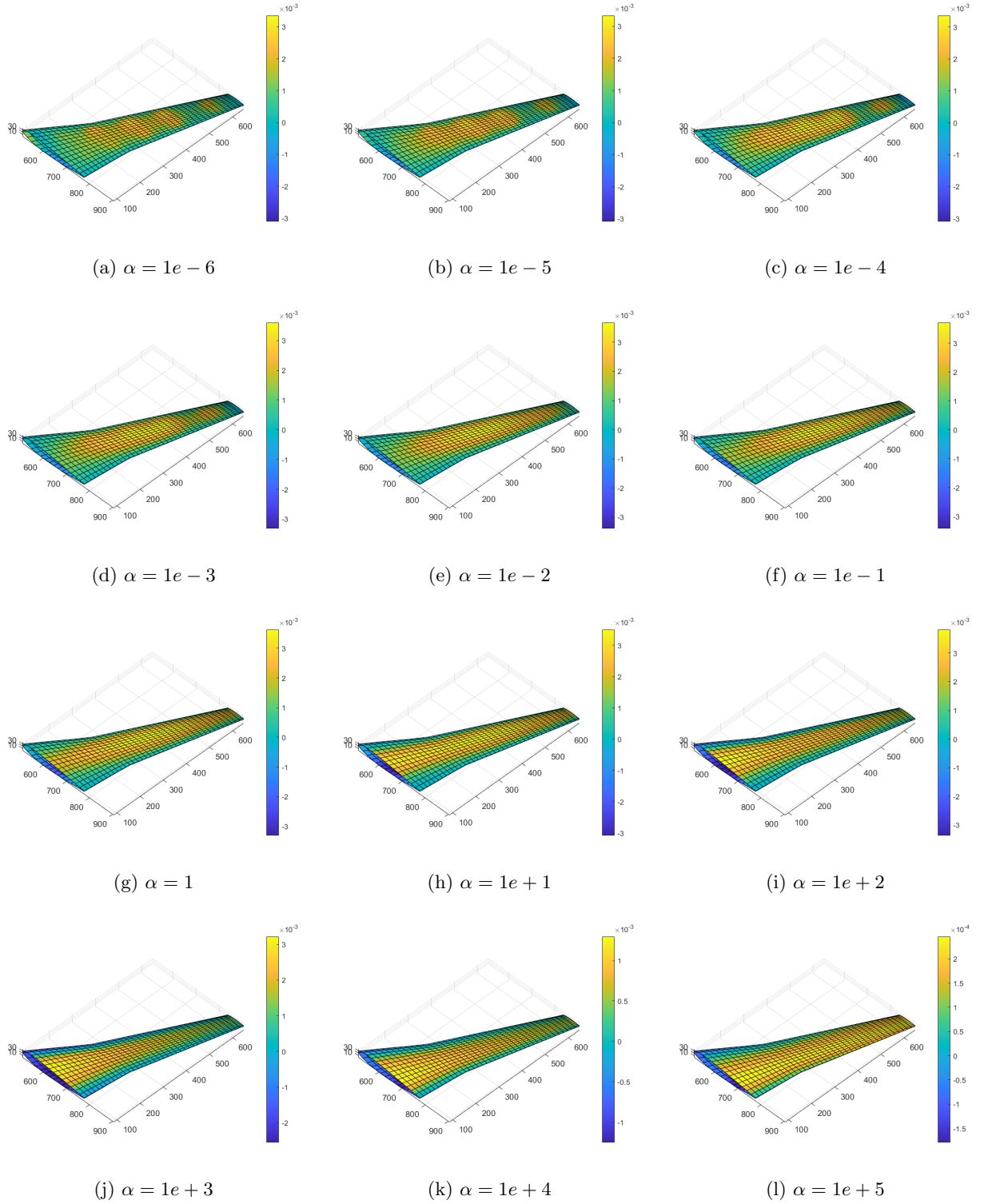
Figure 3.19: *Interpolated strain field ε_x for different values of α.*

It is possible to develop a simple algorithm in order to find the corner of the residual curve, similarly to what it has been done in [53]. Suppose that some points have been sampled using different values of α and that the corner is inside the identified range (from the minimum to the maximum value of α used). Furthermore, let $\eta = \log(\Phi_\varepsilon)$ and $\rho = \log(\Phi_\alpha)$. Then it is possible to follow the algorithm below:

1. Interpolate with cubic splines the points (η_i, α_i) and (ρ_i, α_i) such that the expressions of $\rho = \rho(\alpha)$ and $\eta = \eta(\alpha)$ are available.

2. Compute the maximum curvature of the interpolated residual curve from:

$$\kappa(\alpha) = \frac{\rho' \eta'' - \rho'' \eta'}{\left((\rho')^2 + (\eta')^2\right)^{3/2}} \quad \text{with} \quad \bullet' = \mathrm{d}/\mathrm{d}\alpha$$

3. Use the value of α found for the maximum curvature point to evaluate the residuals ρ and η at that point.

4. Repeat from (1) until convergence.

As an example, for the case of a tip load and considering the measurement of γ_{xy}, the algorithm has been started with 4 initial guesses. From these, convergence is reached after 5 iterations as shown in Figure 3.20. Compared to Figure 3.18e, with a far smaller number of evaluations it is possible to obtain a good estimate of α.
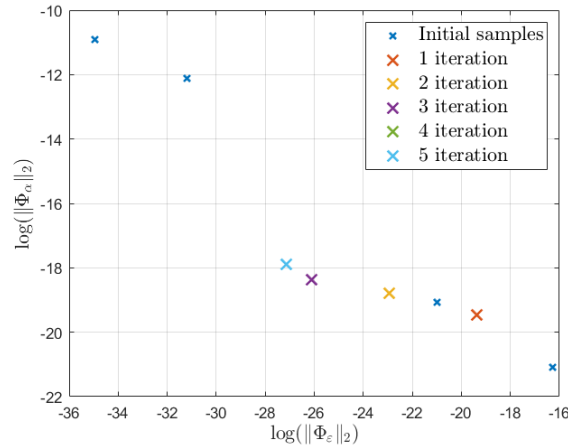
(a) *Iterations on the residual curve.*
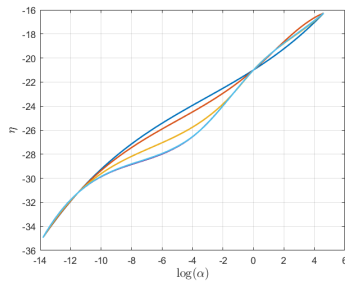
(b) *Interpolation of $\eta = \eta(\alpha)$ for the different iterations.*
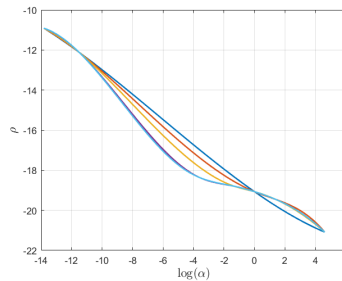
(c) *Interpolation of $\rho = \rho(\alpha)$ for the different iterations.*
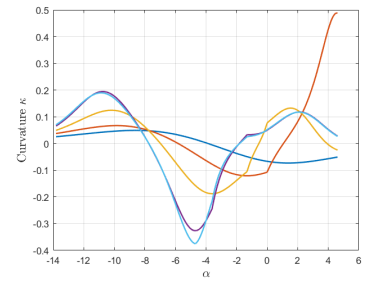
(d) *Curvature $\kappa = \kappa(\alpha)$ for the different iterations.*

Figure 3.20: *Example of the applicability of the algorithm to retrieve a suitable value of α in a few iterations.*

3.3 Shape sensing for ISTAR demonstrator wing

In this section the aim is to retrieve the three-dimensional deformed shape for the ISTAR demonstrator wing. The strain sensor configuration used will be the one shown in Section 3.2, so it is as if 20 strain rosettes have been applied on the outer surface of the wing skin. Furthermore, in order to assess the results in a broader context, similarly as before three different load cases will be considered: a concentrated tip load, a constant pressure filed applied on the bottom skin and a parabolic one.

In Section 3.3.1 iFEM is applied taking advantage from the preliminary strain pre-extrapolation carried out as explained before in Section 3.2. Then, the results will be compared with the ones obtained from the beam model (Section 3.3.2) and with the ones coming from the Modal Method (Section 3.3.3).

3.3.1 Application of SEA and iFEM

In this section the results obtained from SEA will used as an input for iFEM in order to reconstruct the wing deflection. Before proceeding, two points are highlighted:

- Only the strains on the upper surface are measured. Therefore, since no information of the curvature of the shell is known, it is assumed that the inverse shell elements are subjected mainly to membrane strains. This is consistent with the fact that the wing is a beam-like structure and is a common assumption also done in other studies in this context (see for example [37]).

- The strain is measured according to the material reference system, as if the strain rosettes are aligned with the direction of the outer ply. Therefore, it is necessary to rotate the measured strain in the local element reference system. The element local reference system has been defined as follows:

(a) *Local element reference systems.*

(b) *Material reference system in which the strain is measured.*
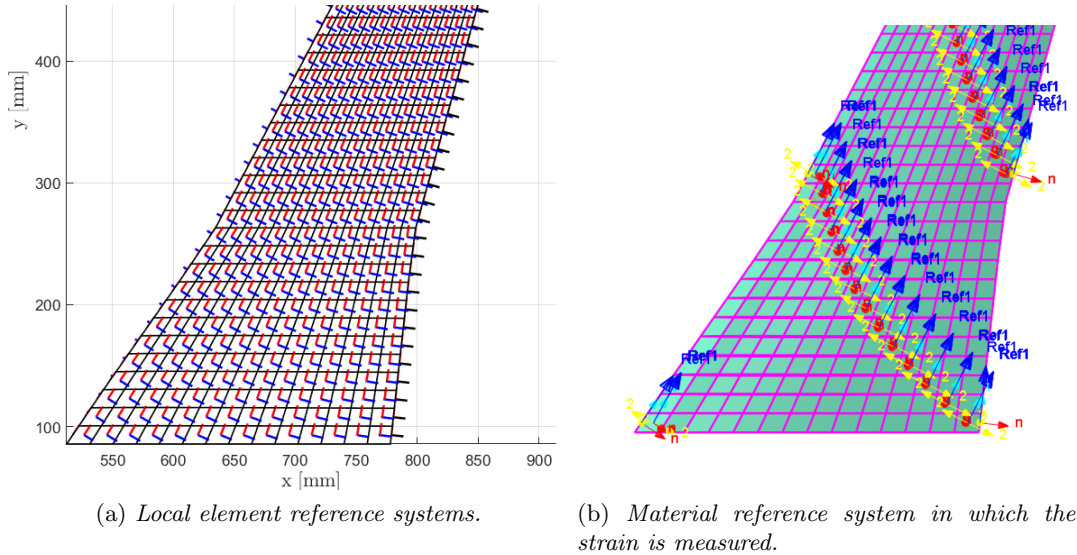
Figure 3.21: *Need to refer the measured strain in the element reference system.*

$$\boldsymbol{n} = \frac{\boldsymbol{X}_{31} \times \boldsymbol{X}_{42}}{\|\boldsymbol{X}_{31} \times \boldsymbol{X}_{42}\|} \quad ; \quad \boldsymbol{e}_1 = \frac{\boldsymbol{X}_{31} + \boldsymbol{X}_{24}}{\|\boldsymbol{X}_{31} + \boldsymbol{X}_{24}\|} \quad ; \quad \boldsymbol{e}_2 = -\boldsymbol{e}_1 \times \boldsymbol{n}$$

(color-coded w.r.t. Figure 3.21a) where $\boldsymbol{X}_{ij} = \boldsymbol{X}_i - \boldsymbol{X}_j$, with $\boldsymbol{X}_i$, $\boldsymbol{X}_j$ the nodal positions in the global reference system. So the transformation matrix is $\boldsymbol{T} = \begin{bmatrix} \boldsymbol{e}_1 & \boldsymbol{e}_2 & \boldsymbol{n} \end{bmatrix}^\top$

In Figure 3.21 the element reference system and the one from which the strain is extracted are shown, and the two differ especially near the wing root. Therefore, the measured strain needs to be rotated in the element reference system in the usual way:

$$
\begin{bmatrix} \varepsilon_x \\ \varepsilon_y \\ \gamma_{xy} \end{bmatrix} = \begin{bmatrix} \cos^2\theta & \sin^2\theta & \sin\theta\cos\theta \\ \sin^2\theta & \cos^2\theta & -\sin\theta\cos\theta \\ -2\sin\theta\cos\theta & 2\sin\theta\cos\theta & \cos^2\theta - \sin^2\theta \end{bmatrix} \begin{bmatrix} \varepsilon_x^\varepsilon \\ \varepsilon_y^\varepsilon \\ \gamma_{xy}^\varepsilon \end{bmatrix} \tag{3.67}
$$

with $\begin{bmatrix} \varepsilon_x^\varepsilon & \varepsilon_y^\varepsilon & \gamma_{xy}^\varepsilon \end{bmatrix}^\top$ the measured strains, $\begin{bmatrix} \varepsilon_x & \varepsilon_y & \gamma_{xy} \end{bmatrix}^\top$ the ones in the local element reference system and θ the angle between the two reference systems.

In order to assess the iFEM model, first the full strain field from the direct FEM analysis will be used as input. This is of course a limit case (in the sense that it would not be feasible to obtain strain measurements for every inverse element), but it is useful to check the model and understand which is the "maximum" accuracy which could be reached if every element were instrumented. This has been done for all the three load cases, obtaining the results of Table 3.2.

Load case	$\dfrac{\lVert \hat{w} - w \rVert_{L_2}}{\lVert w \rVert_{L_2}}$
Tip load	0.0195
Constant pressure	0.0166
Parabolic pressure	0.014

Table 3.2: *Relative L2-norm error of the vertical displacement field w.r.t. the reference solution for three different load cases.*

The error shown in Table 3.2 comes mainly from two sources: the discretization in inverse elements and the element formulation. Regarding the second point, it is important to recall that the elements used (iQS4) are based on the simple First Order Shear Deformation theory. The wing is made from a stiff outer skin, but also the inner presence of the foam material has some influence. However, due to the very low elastic modulus of the foam, the usage of iQS4 elements seems to be a suitable choice also for this study case.

In general, a good reconstruction of the deflection is obtained. For example, for the tip load case the reconstructed geometry is shown in Figure 3.22 together with the reference solution from the direct FEM simulation.

(a) *Front view.*

(b) *Isometric view.*
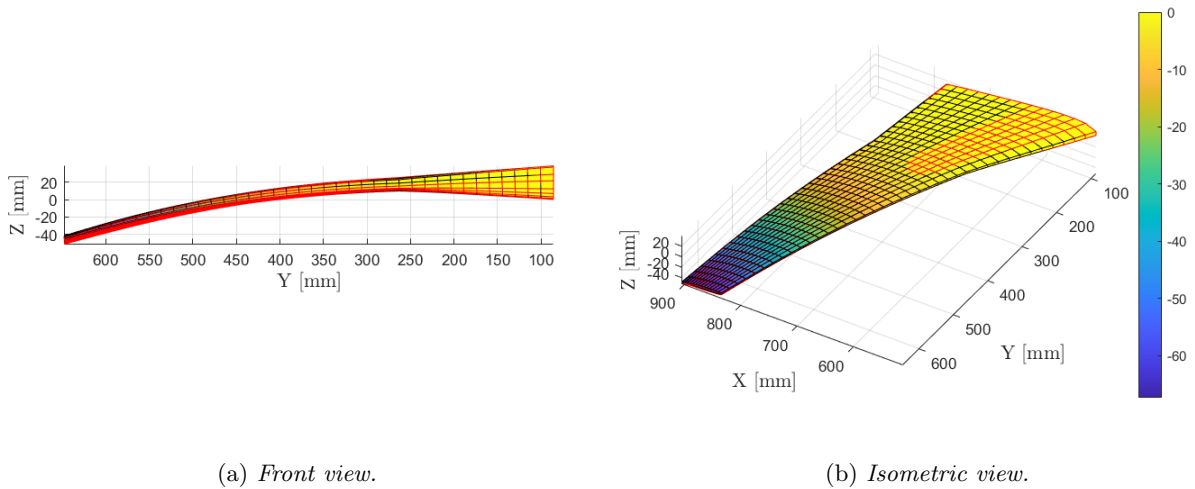
Figure 3.22: *Comparison of reconstructed and reference (red mesh) deflection for tip load case using the full strain field as input for iFEM.*

Next, the strain measurements have been limited to the configuration shown in Figure 3.10. Directly applying iFEM (setting as usually done in literature a weight of $1e-5$ to the strainless elements), a poor reconstruction of the deflection is obtained as shown in Figure 3.23 where the reference deflection extracted from the direct FEM simulation is also plotted. The deformed shape is in general much stiffer compared to the true, similarly as also observed before for the simple clamped plate of Section 3.7.

(a) *Front view.*

(b) *Isometric view.*
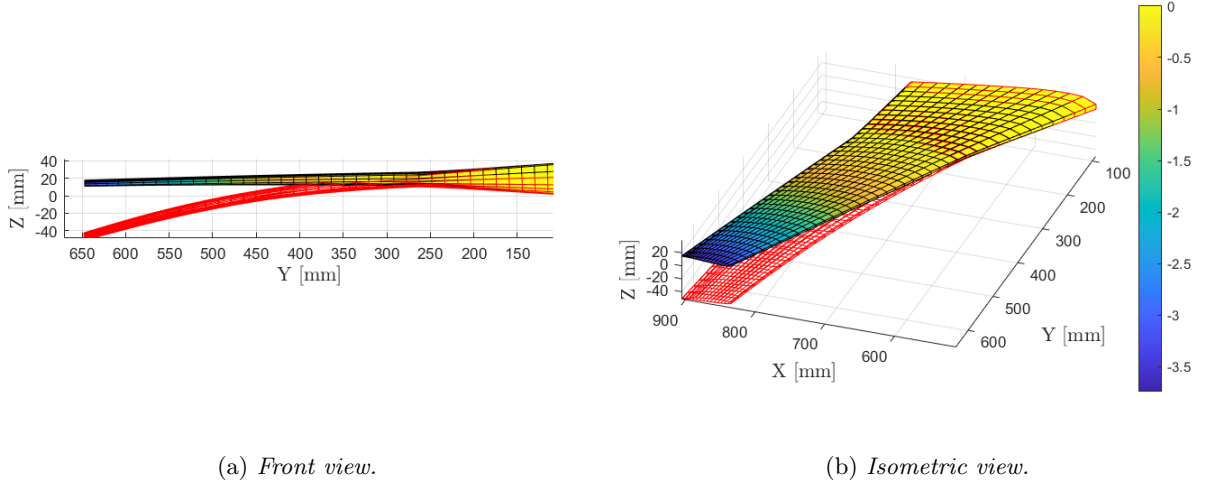
Figure 3.23: *Comparison of reconstructed and reference (red mesh) deflection for tip load case with the direct application of iFEM using a sparse configuration for the strain sensors.*

Therefore, there is the need to pre-extrapolate the strain field before applying iFEM. Using for SEA the optimal values of α found from Table 3.1 the results of Figure 3.24 have been obtained. In particular, a relative L2-norm error of 0.096 can be computed w.r.t the reference displacement along z.

(a) *Front view.*

(b) *Isometric view.*
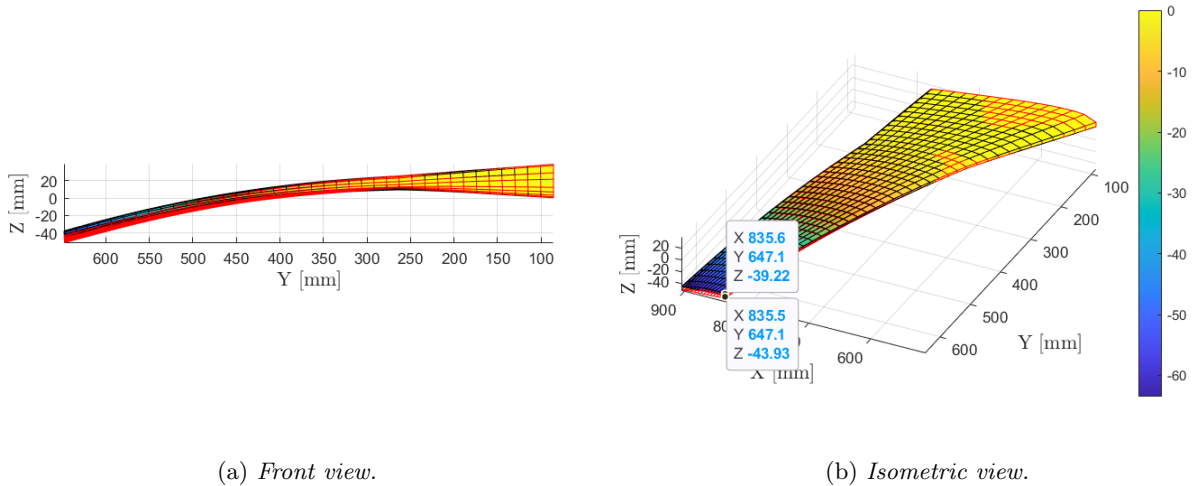
Figure 3.24: *Comparison of reconstructed and reference (red mesh) deflection for tip load case pre-extrapolating the strain field with SEA before applying iFEM.*

After these preliminary results, the influence of two important parameters need to be assessed on the final solution, that is the weight given to the strainless elements in the functional minimization and how the displacement reconstruction is affected by the preliminary SEA analysis (so, in other words, what is the influence of α on the final results).

Influence of weight given to strainless elements

It is often found in literature the statement that inverse elements without strain measurements should be given a lower weight in the minimization of the error functional. This in general brings about better results since it is given higher "importance" to the minimization of the error of the actual strain measurements. However, considering that the strainless elements are fictitiously instrumented by SEA, the strain measures given as input to the inverse elements are in general approximations of the true strain field and therefore it is useful to understand how the choice of the weights affects the final results.

Consider the graphs of Figure 3.25 where the error of the reconstructed displacement field is plotted versus the weight given to the strainless elements. Decreasing the weight at first there is an improvement in the overall solution. However, at some point the error starts to rise again. This can be explained in the following way. Initially, the error decreases because the minimization of the functional allows to match the "real" strain measurements. At some point, however, it has been observed that very low weights used for strainless elements result in a bad-conditioned linear system which reduces the accuracy and causes the error to rise. In any case, the range which can be used for the weights of the strainless elements is apparently quite broad and is consistent with what usually suggested in literature ($\approx 10^{-5}$). As a final note, from Figure 3.25 no particular difference can be spotted from the three different load cases presented. In the following, in general a weight of 10^{-4} will be used.
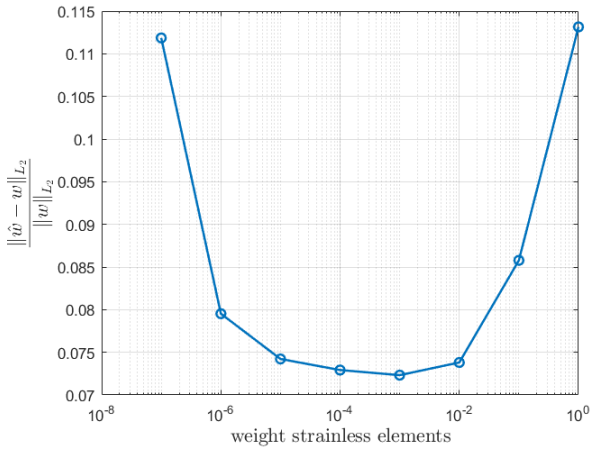
(a) *Relative L2-norm error for tip load case.*
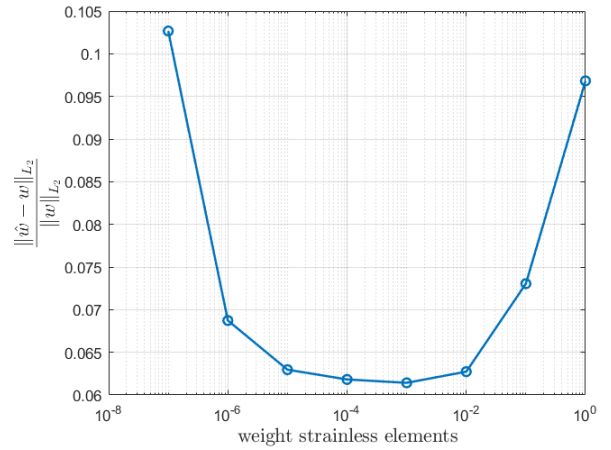
(b) *Relative L2-norm error for constant pressure load case.*
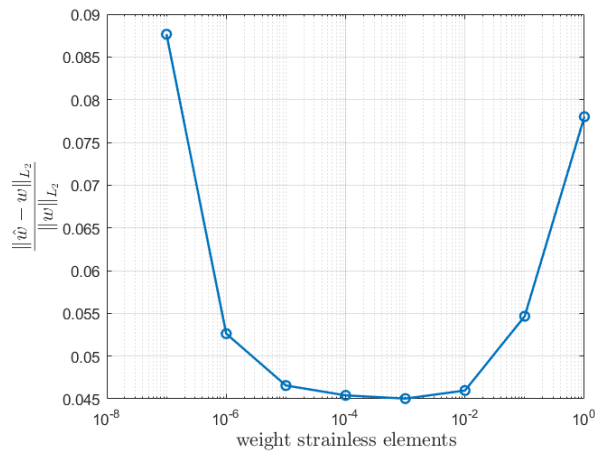
(c) *Relative L2-norm error for parabolic pressure load case.*

Figure 3.25: *Influence of the weights given to strainless element on the final shape reconstruction for three different load cases.*

Influence of SEA α coefficient on iFEM

It is also important to assess how the choice of the regularization parameter α influences the iFEM reconstruction of the displacement field. Therefore, a few parametric studies have been carried out as illustrated in Figure 3.26 where, as before, the three load cases have been analyzed. For each one the identified optimum values of α_{opt} from SEA have been replaced by the quantity $c\,\alpha_{\text{opt}}$, with the coefficient c displayed on the x axis.

(a) *Relative L2-norm error for tip load case.*

(b) *Relative L2-norm error for constant pressure load case.*

(c) *Relative L2-norm error for parabolic pressure load case.*
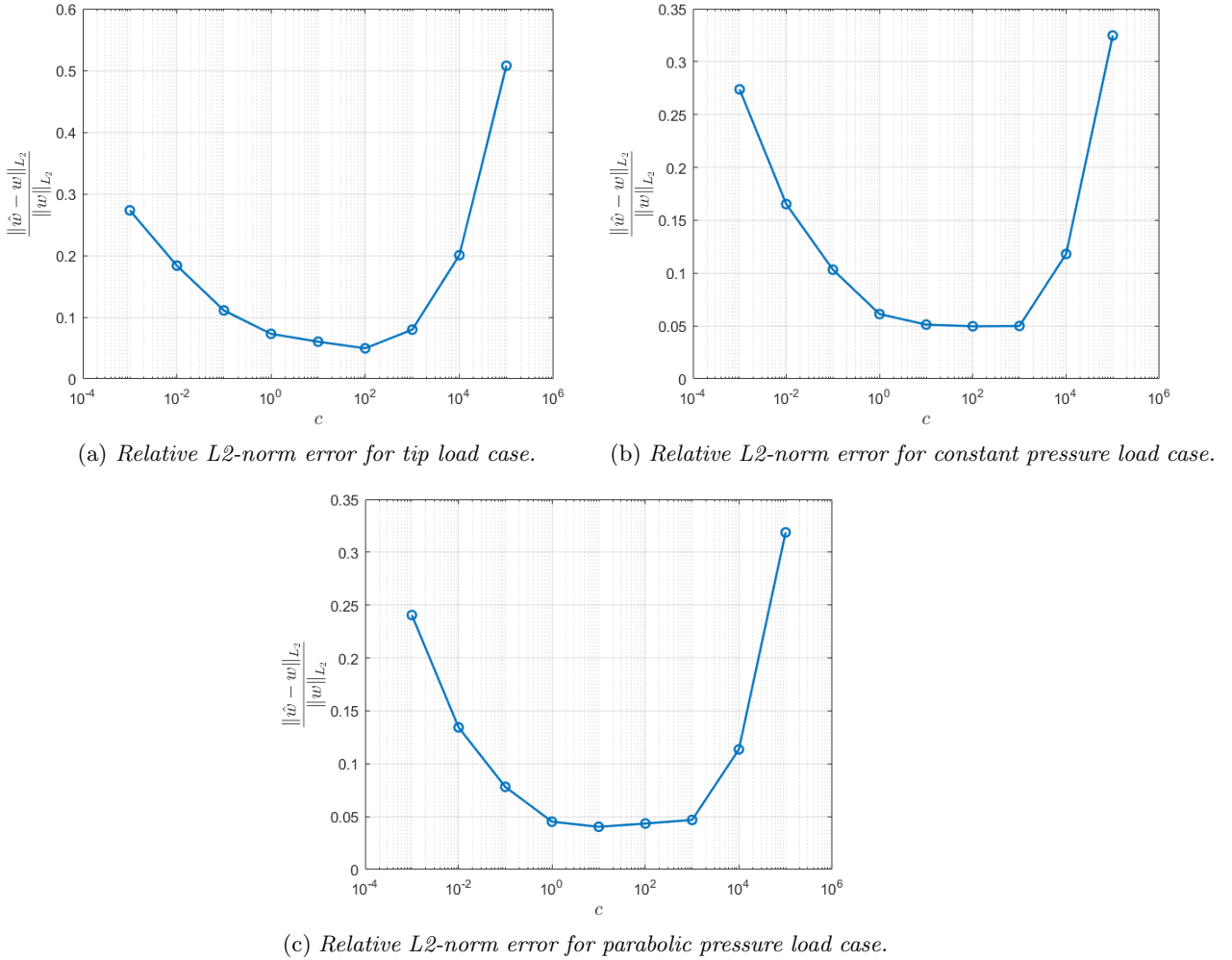
Figure 3.26: *Influence of the SEA regularization coefficient α on the final shape reconstruction for three different load cases.*

The plots show a relatively flat region towards the minimum, meaning that, at least in that region, the results are quite insensitive on the choice of α. This is especially true for the range higher than the identified optimum values of α ($1 < c < 10^3$).

3.3.2 Comparison with beam model

It is interesting to compare the performance of the wing shell model just developed with the beam model previously studied. This can give insight on how the algorithm performs in case of a very sparse strain gauge configuration as the one used for the beam model.

Therefore, the SEA analysis and the subsequent iFEM one has been repeated using as input strains the ones from the beam model of Figure 2.110a. Again, the usual three different load cases have been studied and the results are reported in Figure 3.27 (tip load), Figure 3.28 (constant pressure) and Figure 3.29 (parabolic pressure). The wing shell model results to be quite

inaccurate compared to the beam one. This implies that the very sparse strain measurements used are simply not sufficient for iFEM which would require more information to recover a better deformed shape.

(a) *iFEM.*
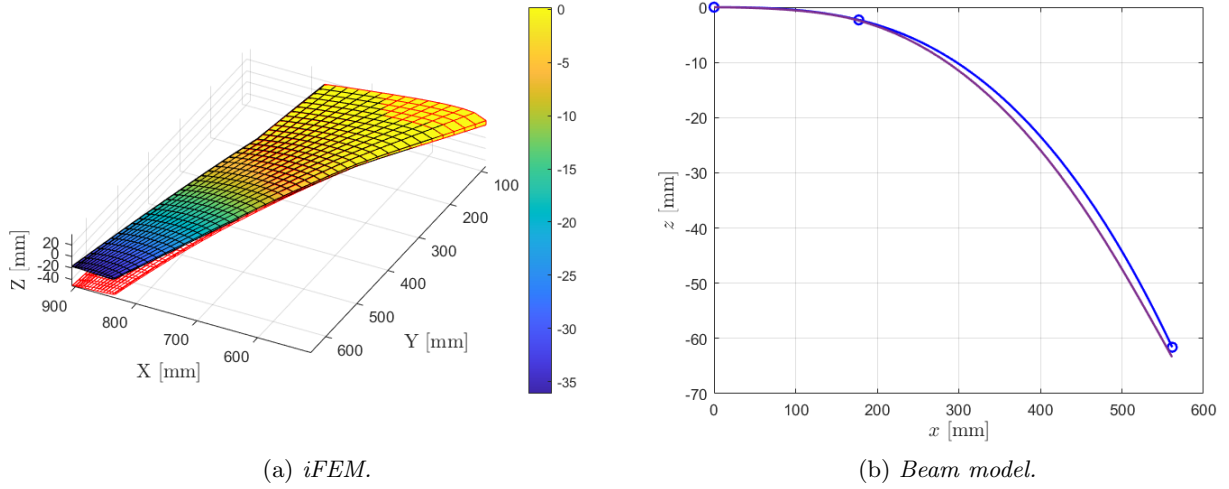
(b) *Beam model.*

Figure 3.27: *Comparison between iFEM and beam model for the wing under tip load.*

(a) *iFEM.*
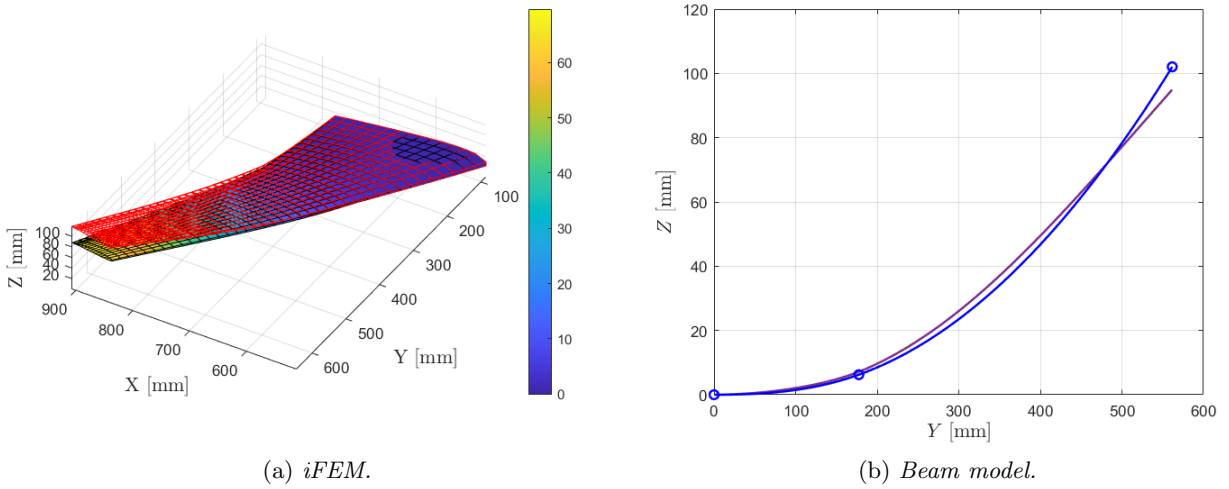
(b) *Beam model.*

Figure 3.28: *Comparison between iFEM and beam model for the wing under constant pressure.*

(a) *iFEM.*
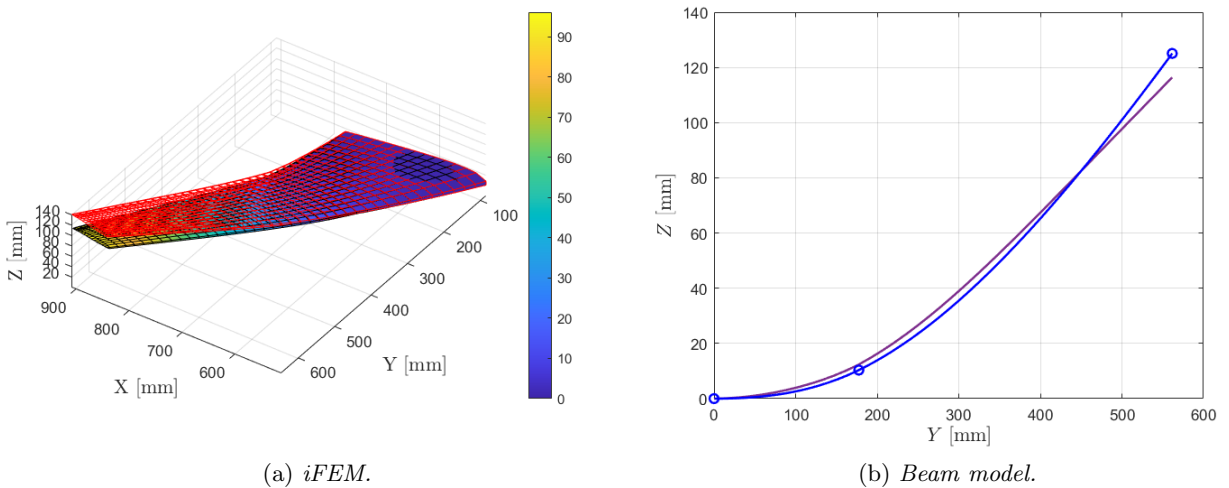
(b) *Beam model.*

Figure 3.29: *Comparison between iFEM and beam model for the wing under parabolic pressure.*

3.3.3 Comparison with Modal Method

In this section the results from iFEM of Section 3.3.1 will be compared to the ones obtained from the so-called Modal Method. In the implementation of the Modal Method, the first six modes of the model have been considered. They are reported in Figure 3.30 for completeness. From the seventh onwards, the modes become more and more shell-related and have been neglected in the shape reconstruction.

(a) $f_n = 38.68\,\mathrm{Hz}$ (b) $f_n = 139.03\,\mathrm{Hz}$ (c) $f_n = 272.28\,\mathrm{Hz}$

(d) $f_n = 285.78\,\mathrm{Hz}$ (e) $f_n = 311.82\,\mathrm{Hz}$ (f) $f_n = 430.25\,\mathrm{Hz}$
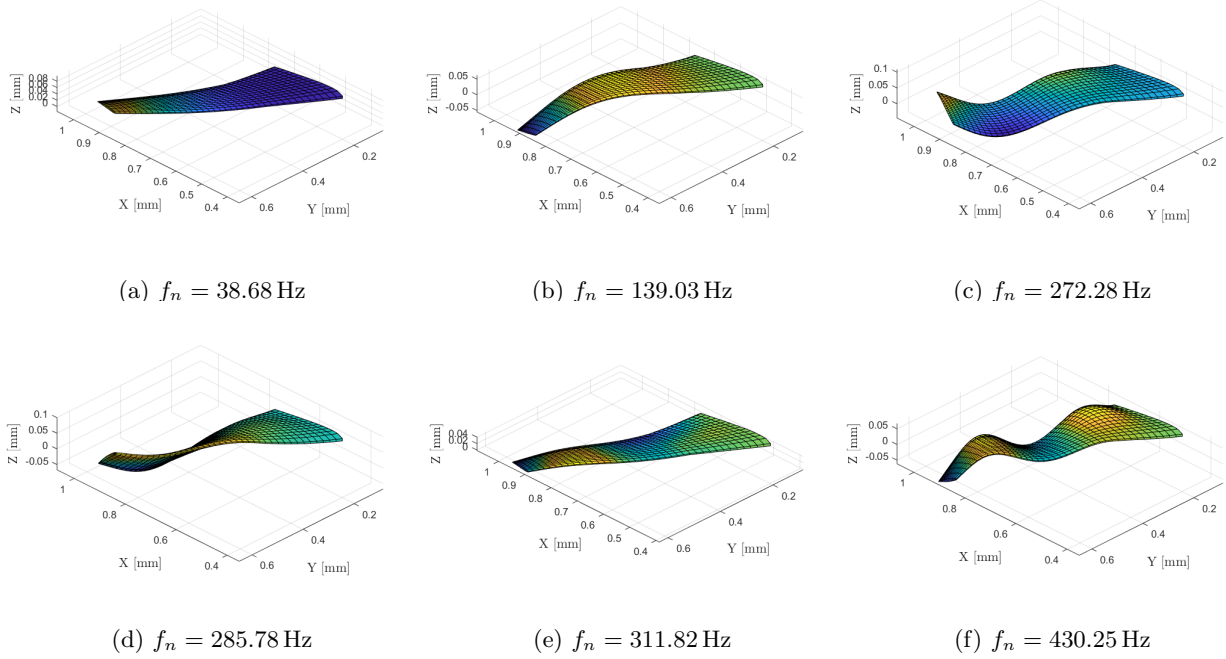
Figure 3.30: *First six modes of the wing and corresponding natural frequencies f_n.*

Since the deformation of the wing will be mainly bending-related, the first few modes will have the highest importance in reconstructing the displacement field. However, it was also seen that mode 6 slightly contributes to the shape sensing analysis. A quantitative method to assess the number of modes needed in the shape sensing analysis was proposed by [49] using a reference static deformed shape $\boldsymbol{U}$. Knowing that in general $\boldsymbol{U} = \boldsymbol{\Phi} \boldsymbol{r}$ with $\boldsymbol{r}$ the modal coordinates and Φ the mode shape matrix, then:

$$\boldsymbol{r} = \left(\boldsymbol{\Phi}^\top \boldsymbol{\Phi} \right)^{-1} \boldsymbol{\Phi}^\top \boldsymbol{U} \tag{3.68}$$

which are the modal coordinates that can best represent, in a least-square sense, the static deformed shape. Now, the strain energy of the i mode shape is given by:

$$E_r = \frac{1}{2} \left(\boldsymbol{\Phi}_i r_i \right)^\top \boldsymbol{K} \left(\boldsymbol{\Phi}_i r_i \right) = \frac{1}{2} r_i^T \boldsymbol{\Phi}_i^\top \boldsymbol{K} \left(\boldsymbol{\Phi}_i r_i \right) \tag{3.69}$$

with r_i the ith modal coordinate and $\boldsymbol{\Phi}_i$ the ith mode shape. Comparing E_r to the strain energy due to the static deformation given by:

$$E = \frac{1}{2} \boldsymbol{U}^\top \boldsymbol{K} \boldsymbol{U} \tag{3.70}$$

it is possible to assess the weight of each mode in the final shape sensing result. Of course, in general $\boldsymbol{U}$ is not known (otherwise there would be no reason to carry out the shape sensing study) and just an estimate should be used. In the following however the reference deformed shape from FEM will be directly used for $\boldsymbol{U}$. For the three load cases, in Figure 3.31 is shown both the modal selection study and the relative L2-norm error of the vertical displacement field w in function of the number of modes used.
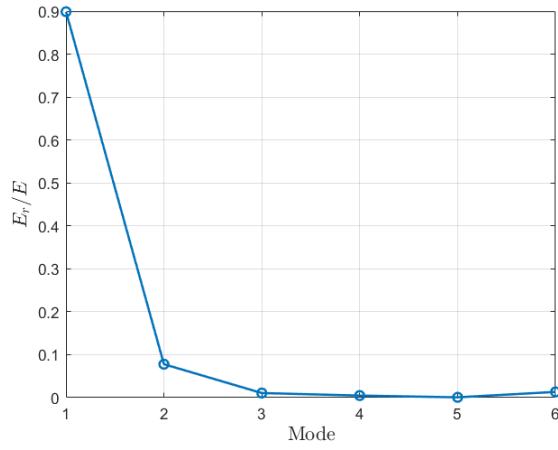
(a) *Mode strain energy for tip load case.*
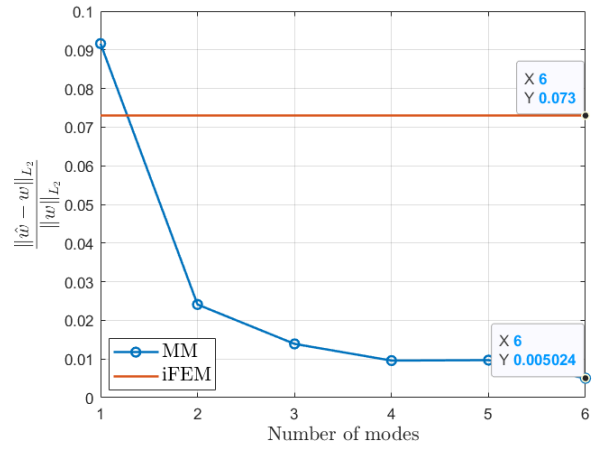
(b) *Shape sensing error for tip load case.*
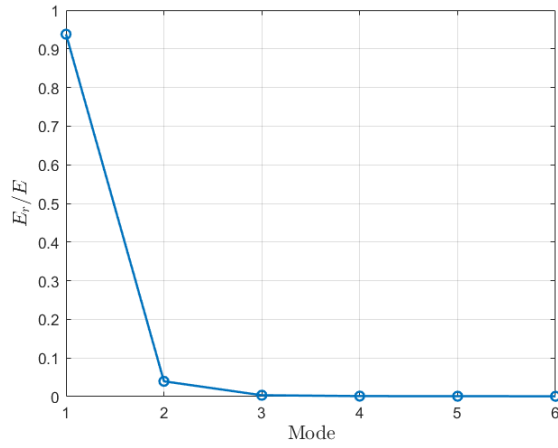
(c) *Mode strain energy for constant pressure load case.*
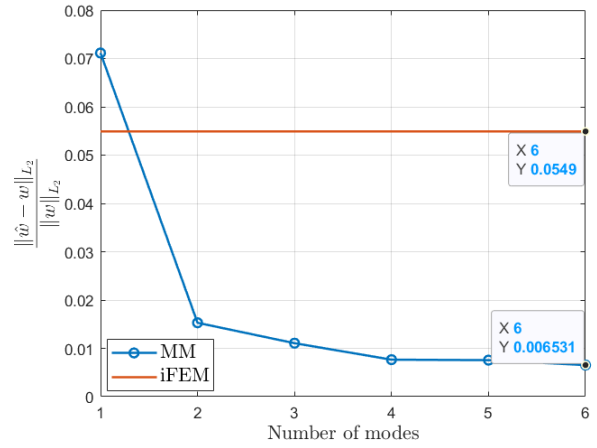
(d) *Shape sensing error for constant pressure load case.*
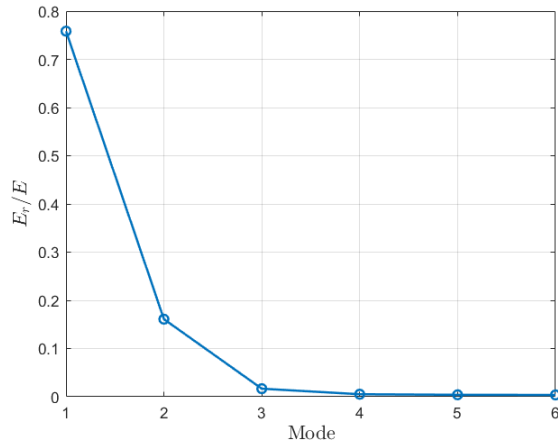
(e) *Mode strain energy for parabolic pressure load case.*
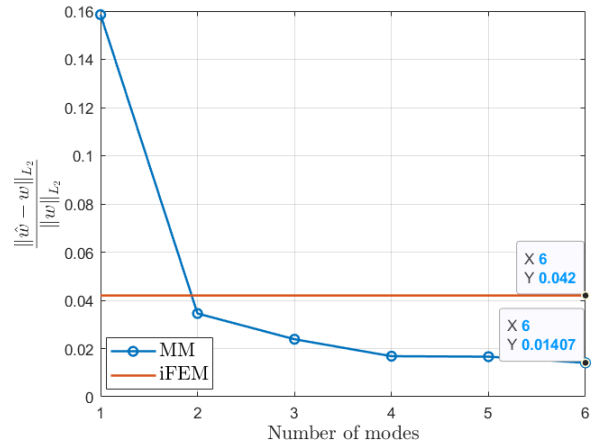
(f) *Shape sensing error for parabolic pressure load case.*

Figure 3.31: *Shape sensing with Modal Method for three different load case and comparison with iFEM.*

As it is possible to see, in general the Modal Method performs better compared to iFEM even if the reconstruction seems to be quite case sensitive. However, so far no uncertainties have been introduced in the system. This important topic will be addressed in the next section again comparing how iFEM performs w.r.t. the Modal Method.

3.4 Uncertainty quantification and Reliability-based shape reconstruction

In this section some simulations have been carried out with the aim to assess the influence of uncertainties on the shape sensing analysis. Assuming a Gaussian probability density function of the input variables, a Monte Carlo (MC) Simulation is carried out: each input variable is randomly sampled and iteratively computing the output it is possible to obtain the resulting distribution.

In this specific case the output of the simulation is represented by the L2-error norm of the reconstructed displacement w. The input variables on the other hand depend on the shape sensing scheme used. Since iFEM is solely based on strain-displacement relations, it will be affected just by measurements errors, while the Modal Method also by the uncertainties in the material properties of the structure, because the mode shapes are needed. In the following these two types of uncertainties will be studied separately, respectively in Section 3.4.1 (measurement uncertainty) and in Section 3.4.2 (material uncertainty). A similar study can be found in [38] where also iFEM and MM are compared to each other.

Beside the "brute force" Monte Carlo analysis, also other means have been taken into account in order to quantify uncertainty. For example, the so-called Polynomial Chaos Expansion (PCE) is a well-known method based on expressing the random variable of interest as a sum of orthonormal polynomials whose coefficients have to be determined appropriately sampling the model. Without explaining here the details (which can be found for example in [42] and [20]), in general this method has the significant advantage to allow retrieving the distribution of the quantity of interest with a limited number of evaluations. However, the number of samples required increases dramatically with the number of input random variables (sometimes referred to as the *curse of dimensionality*). In our case, with 20 strain rosettes, there are 60 random variables to be taken into account. From the simulations carried out, it has been seen that in this context PCE does not offer significant advantages on the computational side compared to the MC with Latin Hypercube Sampling. For example, Figure 3.32 displays a typical output which has been observed, where the mean and standard deviation of the shape sensing error is plotted versus the number of evaluations of the model. Being the results quite similar, it has been decided to simply carry out the MC simulation.
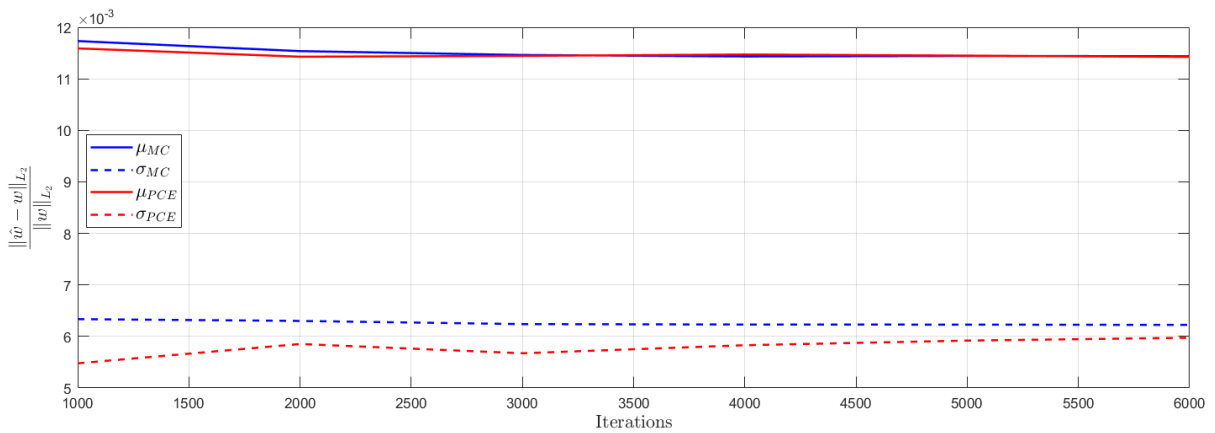
Figure 3.32: *Comparison of mean μ and standard deviation σ of relative error between Monte Carlo Simulation with Latin Hypercube Sampling (MC) and Polynomial Chaos Expansion (PCE).*

As a final note, the study of the performance of PCE, the sampling of the model and the sensitivity analysis later reported have been done through UQLab, a MATLAB toolbox for uncertainty quantification [57].

3.4.1   Measurement uncertainty

The strain measurements are assumed to be affected by an error normally distributed, with mean μ the deterministic measurement value. Two simulations have been carried out increasing the variance from $5\%\mu$ to $10\%\mu$, so the so-called Coefficient of Variation (CoV$= \sigma/\mu$) is respectively 0.05 and 0.1.

Tip load
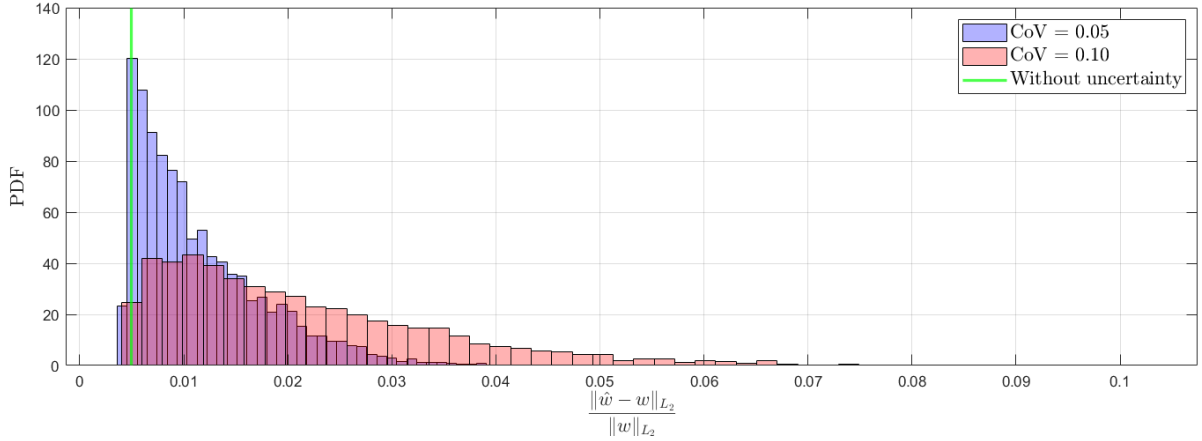
Figure 3.33: *Probability density function of relative L2-norm error of vertical displacement estimated with Monte Carlo Simulation from Modal Method with tip load.*
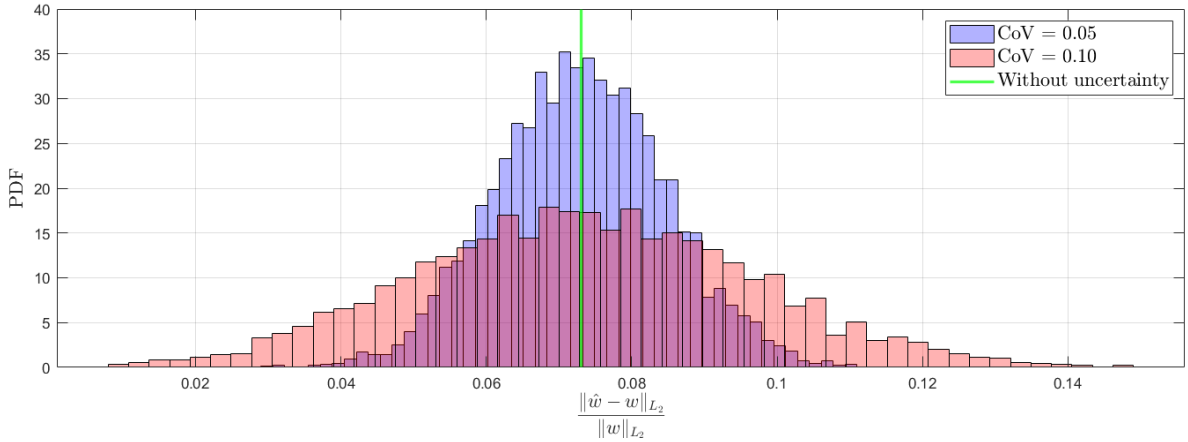
Figure 3.34: *Probability density function of relative L2-norm error of vertical displacement estimated with Monte Carlo Simulation from iFEM with tip load.*

		μ	σ	σ/μ	$(\mu - \text{exact})/\text{exact}$
CoV $= 0.05$	iFEM	0.073	0.01	0.137	-0.001
	MM	0.011	0.006	0.54	1.30
CoV $= 0.1$	iFEM	0.073	0.02	0.27	0
	MM	0.022	0.013	0.65	3

Table 3.3: *Comparison of Modal Method and iFEM for tip load case.*

The results of iFEM show a lower CoV w.r.t. the Modal Method one. Furthermore, the mean value of the resulting distribution μ almost coincides with the value unaffected by errors (exact). On the other hand, the Modal Method is relatively more affected by the input errors, but it is still able to deliver the best results in absolute value.

Constant pressure
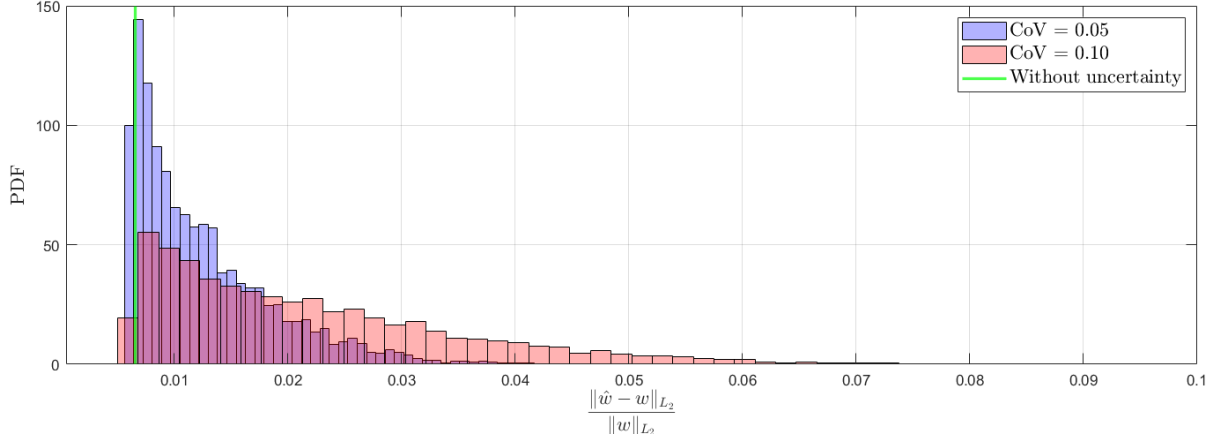
Figure 3.35: *Probability density function of relative L2-norm error of vertical displacement estimated with Monte Carlo Simulation from Modal Method with constant pressure load.*
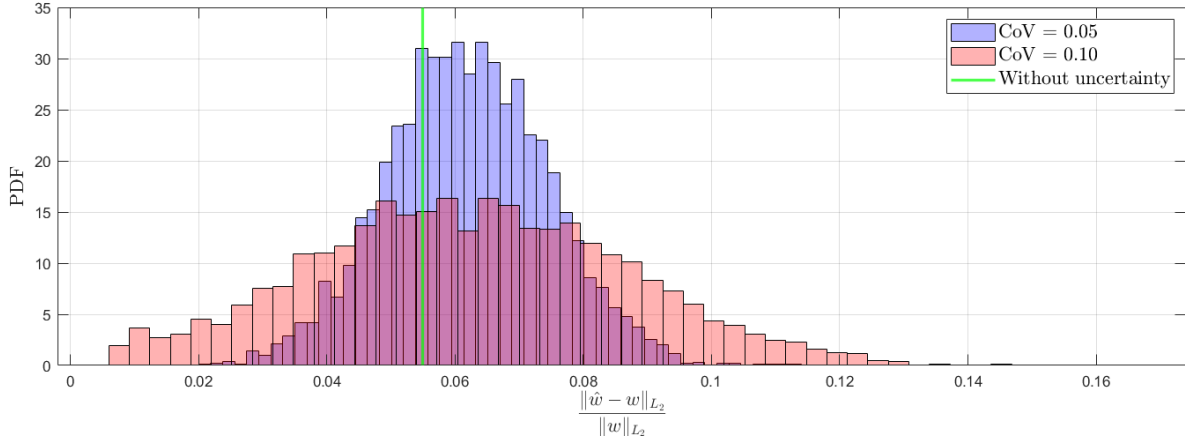
Figure 3.36: *Probability density function of relative L2-norm error of vertical displacement estimated with Monte Carlo Simulation from iFEM with constant pressure load.*

		μ	σ	σ/μ	$(\mu - \text{exact})/\text{exact}$
CoV = 0.05	iFEM	0.062	0.012	0.2	0.13
	MM	0.012	0.006	0.6	1.0
CoV = 0.1	iFEM	0.062	0.022	0.4	0.13
	MM	0.021	0.013	0.65	2.2

Table 3.4: *Comparison of Modal Method and iFEM for constant pressure load case.*

Also for the constant pressure load case similar features to the ones highlighted before can be observed. The Modal Method still performs better and is more affected by the input errors. Differently from before however, the mean of the distribution of the error from iFEM tends to be slightly higher compared to the value without input noise. This is basically due to the fact that the distribution approaches zero, but since the error cannot take negative values, the mean must move to higher values.

Parabolic pressure
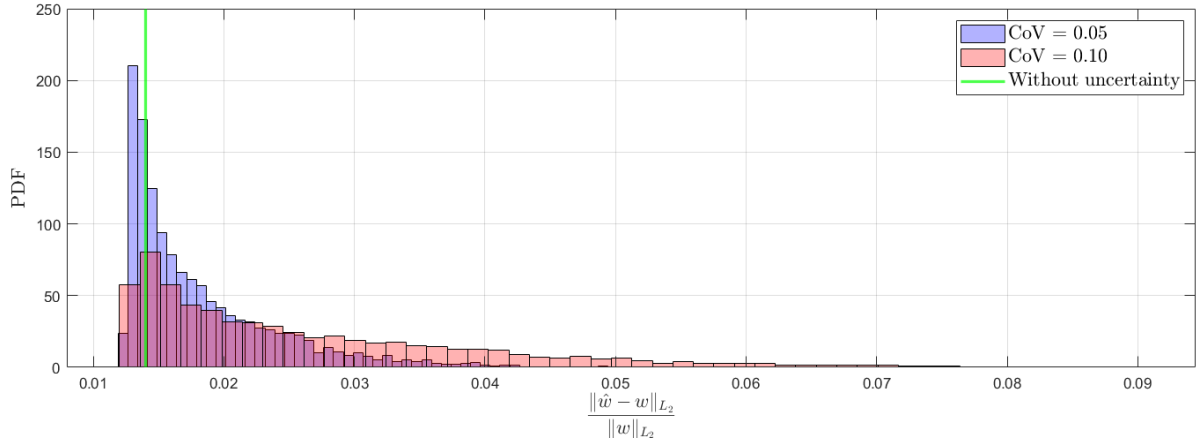
Figure 3.37: *Probability density function of relative L2-norm error of vertical displacement estimated with Monte Carlo Simulation from Modal Method with parabolic pressure load.*
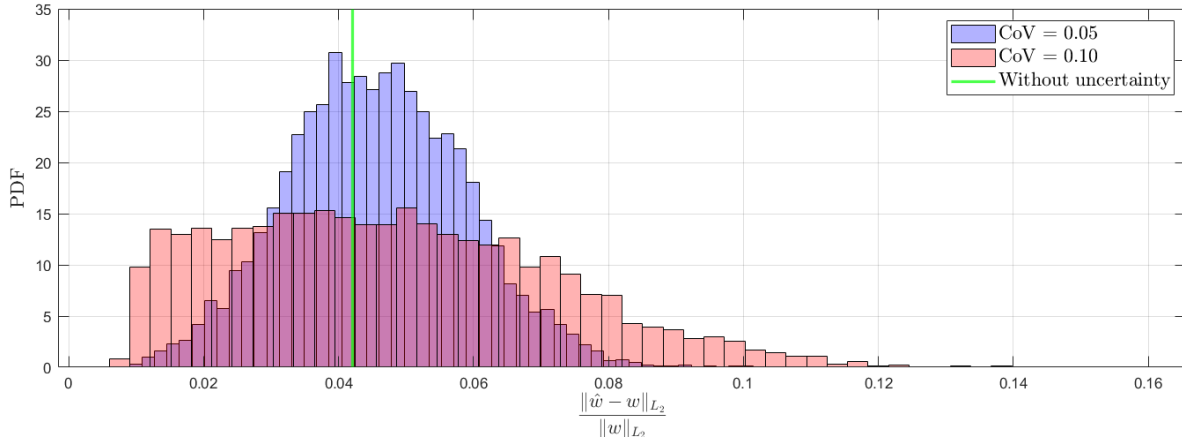
Figure 3.38: *Probability density function of relative L2-norm error of vertical displacement estimated with Monte Carlo Simulation from iFEM with parabolic pressure load.*

		μ	σ	σ/μ	$(\mu - \text{exact})/\text{exact}$
CoV = 0.05	iFEM	0.046	0.013	0.28	0
	MM	0.018	0.00578	0.31	0.28
CoV = 0.1	iFEM	0.048	0.023	0.5	0.05
	MM	0.026	0.013	0.51	0.83

Table 3.5: *Comparison of Modal Method and iFEM for parabolic pressure load case.*

Again, similar comments might be done in this case as before. Now however iFEM seems to perform better since the difference from the error given by the Modal Method is in general reduced.

Sensitivity analysis

Finally, a sensitivity study has been carried out in order to assess the dependence of the displacement reconstruction w.r.t. the strain measurement positions. The study has been carried out through UQLab using the so-called *perturbation method* [23]. In summary, the variance due to the contribution of each input random variable X_i is estimated from a first-order expansion of the model as: $\sigma^2(X_i) = \left(\left. \dfrac{\partial \|\hat{w} - w\|_{L_2})/\|w\|_{L_2}}{\partial X_i} \right|_\mu \right)^2 \sigma_i^2$ and so a sensitivity index η_i can be built dividing by the total variance: $\eta_i = \dfrac{\sigma^2(X_i)}{\sum_i \sigma^2(X_i)}$

Using this approach, for each load case the sensitivity indices have been computed and the comparison between iFEM and MM is shown in Figure 3.40. The results shown are related only to the axial strain measurements ε_x since it was seen that the sensitivity indices of the other strain components are negligible in comparison. Furthermore, they have been grouped into five different sections, depending on the span position (Figure 3.39).
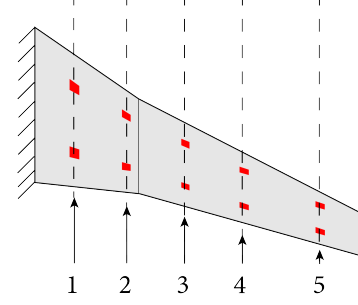
Figure 3.39: *Section numbering.*
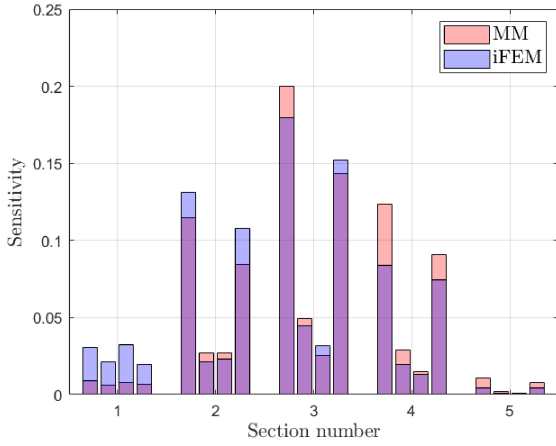
(a) *Sensitivity for tip load case.*
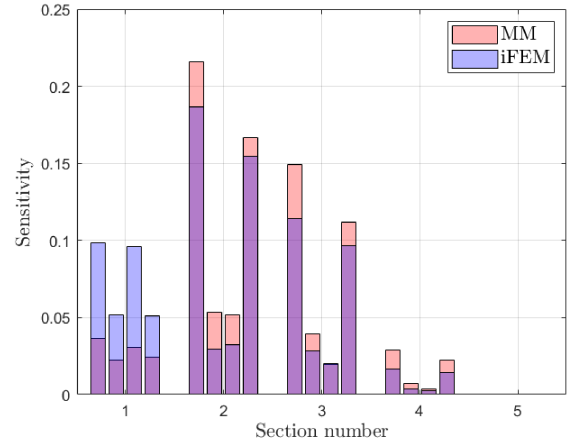
(b) *Sensitivity for constant pressure load case.*
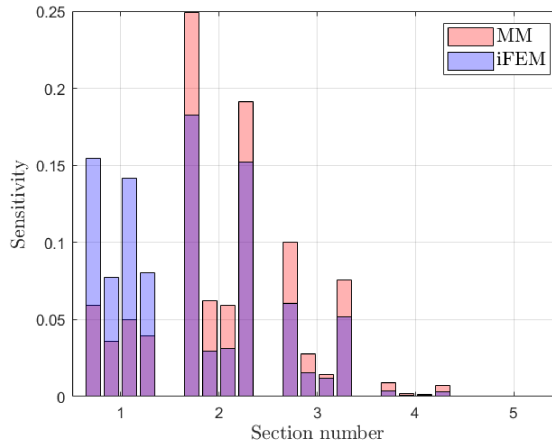
(c) *Sensitivity for parabolic pressure load case.*

Figure 3.40: *Sensitivity analysis for measurement uncertainty.*

In general, it is possible to say that the Modal Method shows an higher sensitivity due to the strain input noise (as also was seen before), apart for the measurements near the root where iFEM seems to be more sensitive.

3.4.2 Material uncertainty

Since iFEM is based just on strain-displacement relations, it is unaffected by any uncertainty on the material properties. This is not the case for the Modal Method and therefore in this section this aspect in analysed. In other words, the aim is to see how much the uncertainly on the material affects the MM results and whether in this context a larger or lower error compared to iFEM is obtained.

In order to assess the uncertainty on these parameters, they have been given a normal distribution with mean value the reference value and variance respectively 5-10%μ. The stochastic material which can be created in this way is then used as an input for MM carrying out a Monte Carlo Simulation. The work-flow is briefly summarized in Figure 3.41. First the stochastic material is created starting from the reference values of the deterministic one. Then, the mass $\boldsymbol{M}$ and stiffness $\boldsymbol{K}$ matrices are computed based on this input. This has been done externally with the help of the FEM package `Abaqus`. How to obtain the structural matrices directly from the commercial package used is briefly reported in Appendix L.

At this point, the mode shapes and strain mode shapes can be obtained and so the final displacement can be retrieved. This procedure is repeated iteratively in order to estimate the final PDF of the shape sensing error.
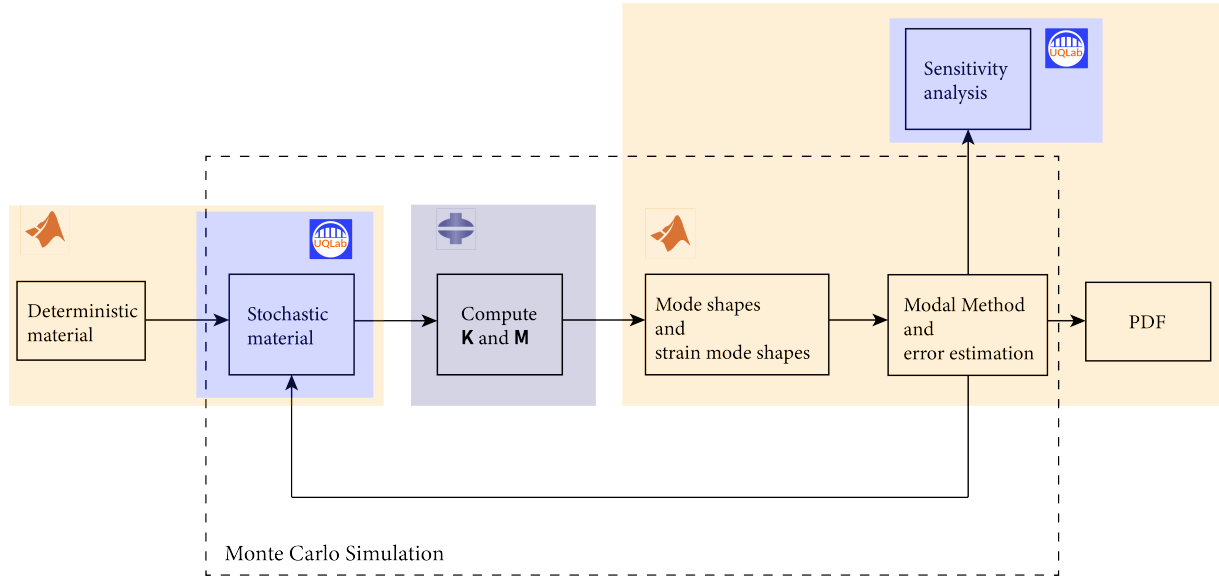
Figure 3.41: *Work-flow to assess how material uncertainty affects the results of MM.*

The variables used to create the stochastic material are shown in Table 3.6. Here, t is the ply thickness, ρ the material density and θ the ply angle.

	μ	σ
$E_1, E_2, \nu_{12}, G_{12}, G_{13}, G_{23}, \rho, t$	nominal	$(0.05\mu)\,k$
θ (ply angle)	nominal	$2° \, k$

Table 3.6: *Stochastic material parameters.*

Furthermore, $k = \{1, 2\}$ so that two different iterations are done increasing the uncertainty level.
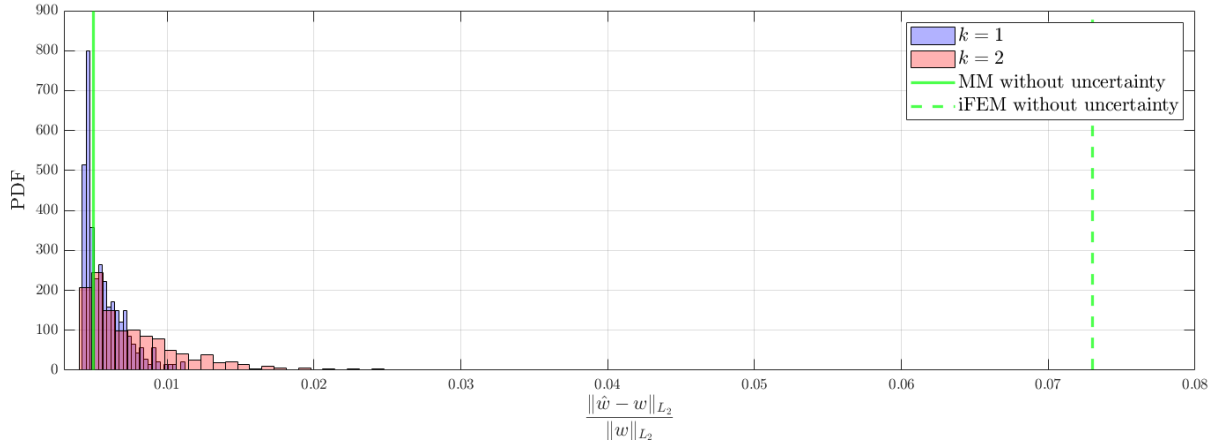
Figure 3.42: *Probability density function of relative L2-norm error of vertical displacement estimated with Monte Carlo Simulation for Modal Method with tip load.*
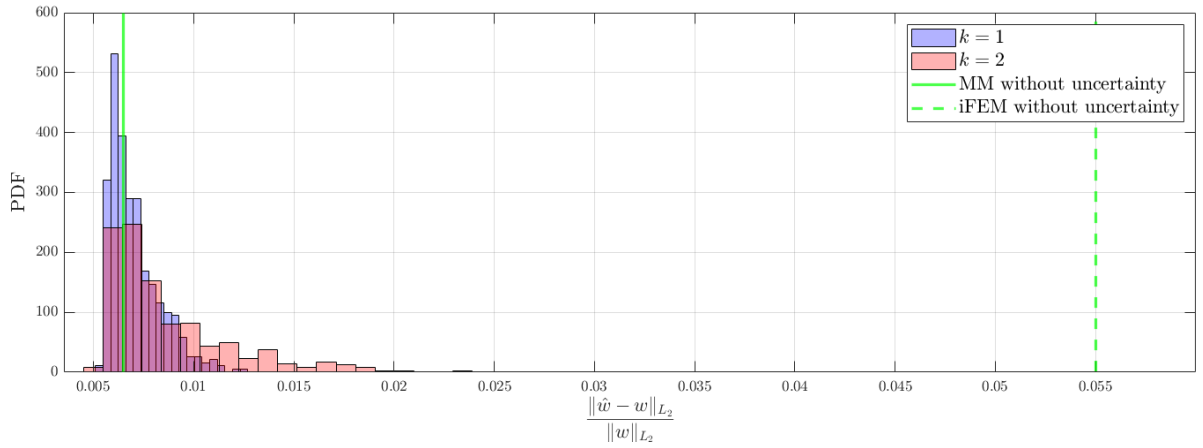
Figure 3.43: *Probability density function of relative L2-norm error of vertical displacement estimated with Monte Carlo Simulation for Modal Method with constant pressure load.*
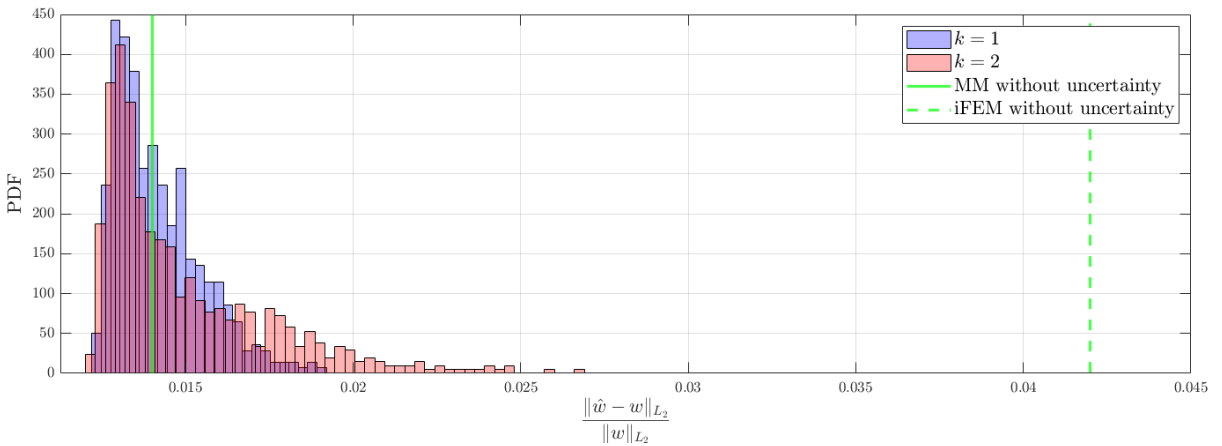
Figure 3.44: *Probability density function of relative L2-norm error of vertical displacement estimated with Monte Carlo Simulation for Modal Method with parabolic pressure load.*

The results are shown in Figure 3.42, Figure 3.43 and Figure 3.44 for each load case. The Modal Method appears to be relatively sturdy to this type of uncertainty with the mean value of the resulting distribution never approaching the error obtained with iFEM.

The effect of the uncertainty which has been introduced in this section can be also assessed looking at the distribution of the eigenfrequencies of the wing. From Figure 3.45 they result to be quite spread around the nominal value. This means that, even if the estimate of the eigenfrequencies of the system is not good, still the displacement reconstruction is satisfactory.
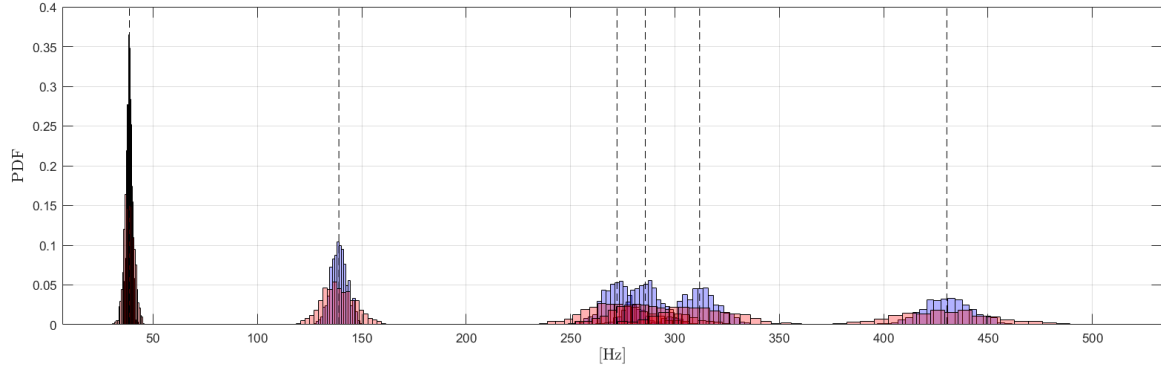
Figure 3.45: *Distribution of natural frequencies under the uncertainty of the material properties.*

Finally, similarly as before, a sensitivity analysis has been carried out looking for the properties that most affect the results. From Figure 3.46 it is the thickness of the plies which has the highest influence on the final displacement reconstruction.
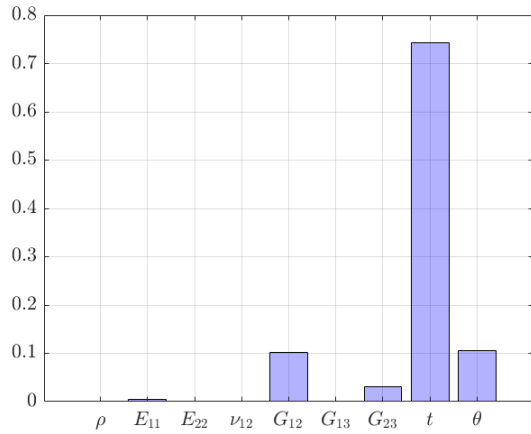
(a) *Sensitivity for tip load.*
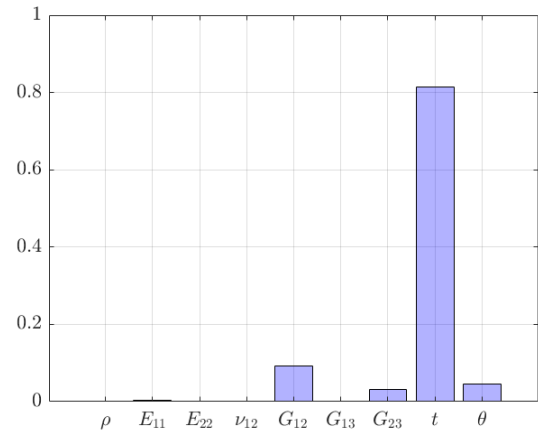
(b) *Sensitivity for constant pressure load.*
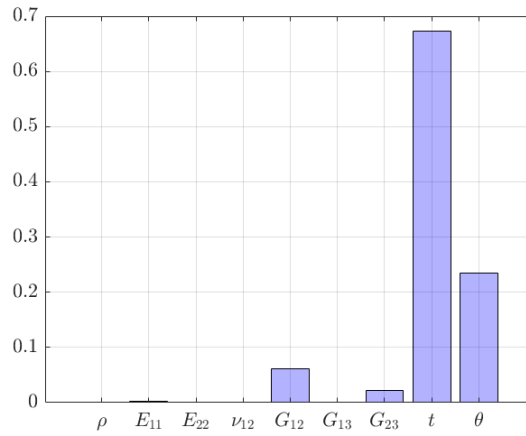
(c) *Sensitivity for parabolic pressure load.*

Figure 3.46: *Sensitivity analysis for material uncertainty.*

3.5   Summary of the chapter

The full displacement field of the deformation has been retrieved using two common shape sensing methods, that is iFEM and MM. Using the demonstrator ISTAR wing as main study case, the performances of the methods have been assessed in case of a rather sparse strain gauge configuration. In particular, iFEM has been improved with a preliminary strain pre-extrapolation using SEA with a newly developed 4-node element. This allows in general to obtain a better reconstruction, but worse compared to the one delivered by MM. The results have been confirmed also through an uncertainty quantification study, that is introducing noise and uncertainty both in the measurements and in the system.

Chapter 4

Load reconstruction

This chapter is focused on the external load reconstruction. In particular, the load will be expressed as a pressure field whose distribution will be be retrieved both in space and time.

The common approach used in literature consists in retrieving the external loads directly from the strain measurements, choosing the superposition of forces which allows to obtain the same measured strains (Figure 4.1). These methods will be referred to as "sensitivity matrix methods". Once the loads are recovered, it is easily possible to find the resulting deformed shape from a direct FEM analysis. Here, a different approach will be studied, trying to apply similar methods starting from the displacement field obtained from the shape sensing study (either MM or iFEM).
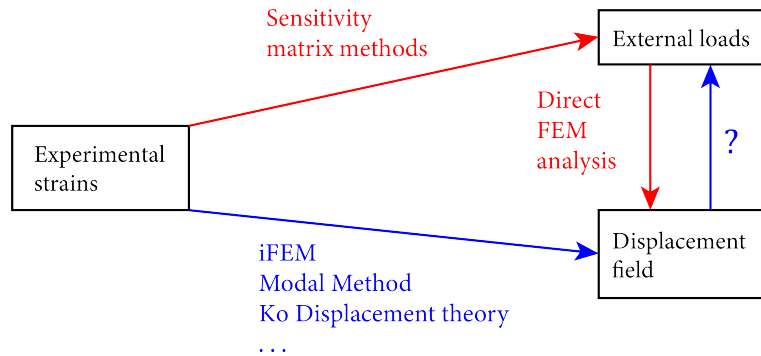
Figure 4.1: *Relations between experimental strains, external loads and displacement field.*

There are significant differences between the two approaches:

- In general the number of strain measurements is lower compared to the number of variables used to describe the external load. This implies that the linear system used to retrieve the load is under-determined, that is with infinite possible solutions.

- On the contrary, having at disposal the full displacement field from the shape sensing analysis leads in general to an over-determined system.

- In computing the load from the strain values only measurement errors will affect the results. On the other hand, using the displacement field on the final reconstruction will weight also the error coming from the shape sensing study.

Therefore the aim of this chapter is investigate the performances of the two approaches. It is structured as follows:

- In Section 4.1 some brief notes are presented about classical approaches used in literature for load reconstruction. Furthermore, the basis of regularization tools are explained in order to cope with ill-conditioned systems.

- In Section 4.2 the external pressure field is reconstructed for static cases, using both the displacement field (from MM and iFEM) and the strain measurements. Furthermore, the effect of measurements errors on the final reconstruction will be assessed.

- Finally Section 4.3 is focused on the dynamic load reconstruction. Three different methods will be applied, both in time and frequency domain.

The methods explained will be applied to the ISTAR demonstrator wing instrumented as in Figure 3.10. For the static analysis three different load cases will be studied: a constant pressure field, a parabolic one (along the span) and "parabolic-linear" (that is, parabolic-varying along the span and linearly along the chord). They are all applied on the bottom skin and as a reference are reported in Figure 4.2.

(a) *Constant pressure field:*
$p(x, y) = 10^4$ Pa.

(b) *Parabolic pressure field:*
$p(x, y) = [-(y - 0.0856)^2 + 0.5597^2]10^5$ Pa.

(c) *Parabolic-linear pressure field:*
$p(x, y) = [(y - 0.0856)^2 + 0.5597^2](1.318x - 0.3y - 1)10^6$ Pa.
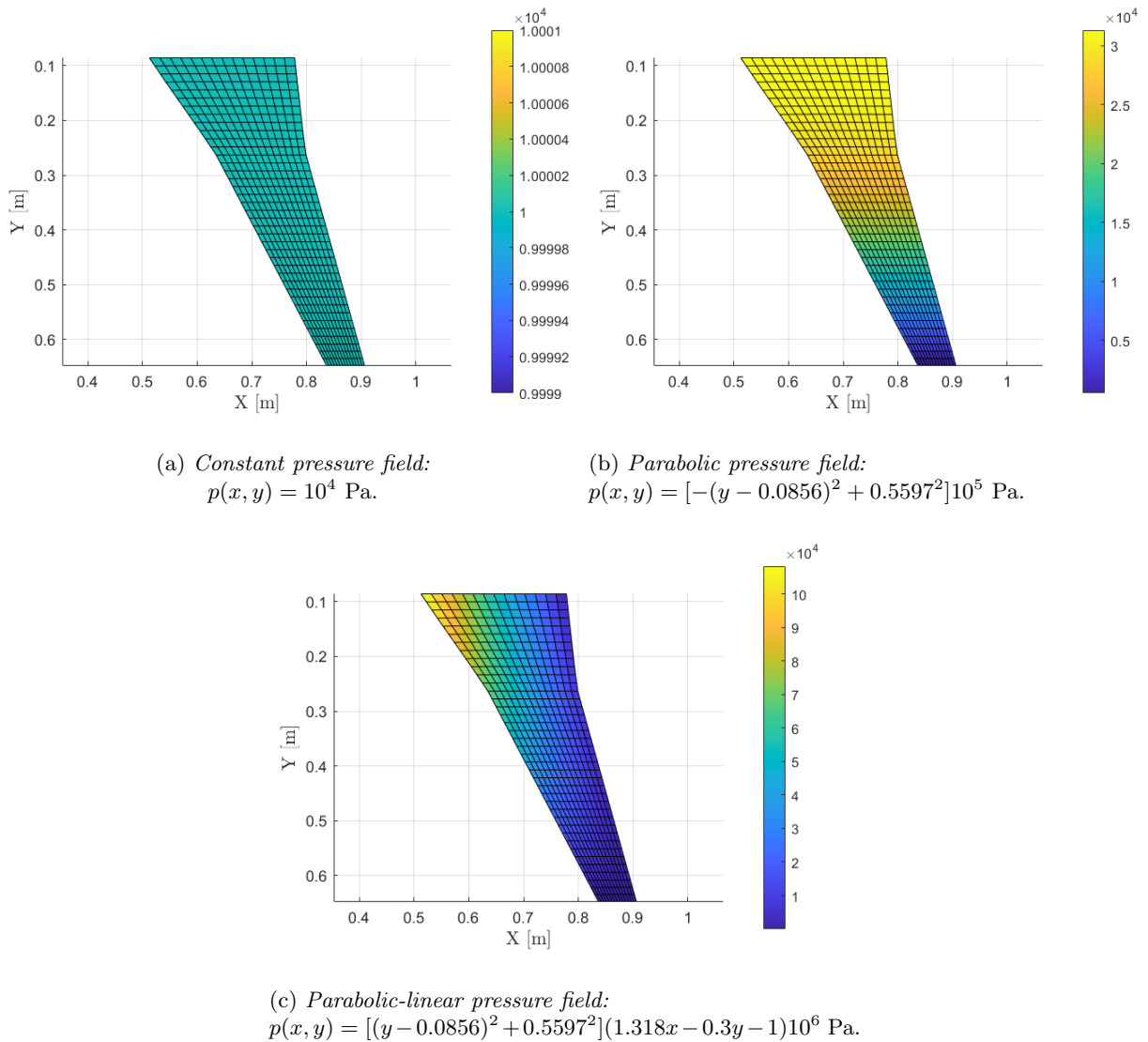
Figure 4.2: *Reference pressure field distributions.*

For the dynamic study it will be considered the parabolic and parabolic-linear load cases. Both pressure fields will constantly maintain their shape in space and only their magnitude will change in time.

4.1 Theoretical background

This brief section aims at giving the required background needed for the following studies. In particular, in Section 4.1.1 some difficulties in the load reconstruction are highlighted and the common methods based on a linear superposition of elementary loads are presented. Next, in Section 4.1.2 the regularization of ill-posed system is briefly touched. In particular, the focus will be on the well-known Tikhonov regularization which will become an important tool in the upcoming load reconstruction.

4.1.1 Difficulties in load reconstruction and sensitivity matrix methods

Having at disposal the full displacement field from the shape sensing study, at first sight it is possible to recover the external loads directly from the multiplication of the stiffness matrix of the system and the displacement vector. Sorting the degrees of freedom in the ones where external forces can be applied ($\boldsymbol{u}_u$) and the ones where reaction forces take place ($\boldsymbol{u}_k$), then:

$$\begin{bmatrix} \boldsymbol{K}_{uu} & \boldsymbol{K}_{uk} \\ \boldsymbol{K}_{ku} & \boldsymbol{K}_{kk} \end{bmatrix} \begin{bmatrix} \boldsymbol{u}_u \\ \boldsymbol{u}_k \end{bmatrix} = \begin{bmatrix} \boldsymbol{f}_u \\ \boldsymbol{f}_k \end{bmatrix} \tag{4.1}$$

assuming that $\boldsymbol{u}_k = \boldsymbol{0}$, it simply follows that:

$$\boldsymbol{K}_{uu}\boldsymbol{u}_u = \boldsymbol{f}_u \tag{4.2}$$

However, it was observed that the reconstructed load is quite poor even when the errors affecting $\boldsymbol{u}_u$ are negligibly small. A few attempts are reported below trying to improve the results following this line of thinking.

It is possible to help the load recovery analysis dividing the degrees of freedom vector $\boldsymbol{u}_u$ between a part where external forces are known to be applied ($\boldsymbol{u}_a$) and a part where it is known that external forces are not applied ($\boldsymbol{u}_n$). So Eq.(4.2) can be rewritten as:

$$\begin{bmatrix} \boldsymbol{K}_{uua} & \boldsymbol{K}_{uuan} \\ \boldsymbol{K}_{uuna} & \boldsymbol{K}_{uunn} \end{bmatrix} \begin{bmatrix} \boldsymbol{u}_a \\ \boldsymbol{u}_n \end{bmatrix} = \begin{bmatrix} \boldsymbol{f}_a \\ \boldsymbol{0} \end{bmatrix} \tag{4.3}$$

From the second equation it follows that $\begin{bmatrix} \boldsymbol{u}_a & \boldsymbol{u}_n \end{bmatrix}^\top$ belongs to the null space of the matrix $\begin{bmatrix} \boldsymbol{K}_{uuna} & \boldsymbol{K}_{uunn} \end{bmatrix}$ so that is is possible to write:

$$\boldsymbol{N}\boldsymbol{c} = \begin{bmatrix} \boldsymbol{u}_a \\ \boldsymbol{u}_n \end{bmatrix}$$

with $\boldsymbol{N}$ the null space and $\boldsymbol{c}$ an unknown coefficient vector which can be computed in a least-squares sense as:

$$\boldsymbol{c} = (\boldsymbol{N}^\top \boldsymbol{N})^{-1} \boldsymbol{N}^\top \begin{bmatrix} \boldsymbol{u}_a \\ \boldsymbol{u}_n \end{bmatrix} \tag{4.4}$$

At this point, the displacement vector $\boldsymbol{u}_u$ can be expressed in modal coordinates as:

$$\boldsymbol{u}_u = \boldsymbol{\Phi}\boldsymbol{r} \tag{4.5}$$

with $\boldsymbol{\Phi}$ the mode shape matrix. Therefore it is possible to obtain:

$$\boldsymbol{r} = \boldsymbol{\Phi}^\dagger \boldsymbol{N}\boldsymbol{c} \tag{4.6}$$

from which $\boldsymbol{u}_u$ can be computed using 4.5. Now, substituting in Eq.(4.3) it is possible to obtain the external loads as:

$$\boldsymbol{f}_a = \begin{bmatrix} \boldsymbol{K}_{uuaa} & \boldsymbol{K}_{uuan} \end{bmatrix} \boldsymbol{u}_a \qquad (4.7)$$

using the new value for $\boldsymbol{u}_u$. Following this approach the external pressure on the bottom skin of the ISTAR demonstrator wing was computed. A constant pressure of $1e4$ MPa has been applied but, as it is possible to see in Figure 4.3, the results are not satisfactory, leading to a field completely different from the applied constant one.
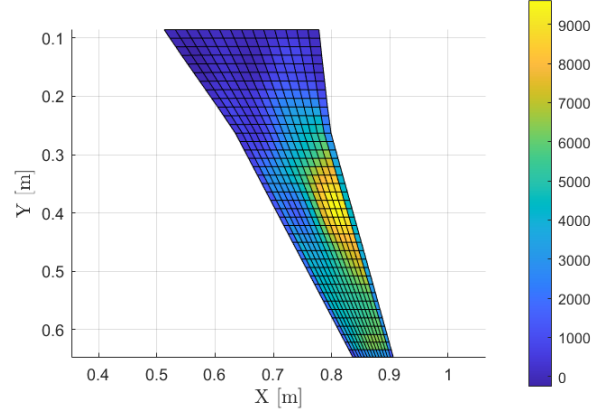
Figure 4.3: *Erroneous external pressure reconstruction.*

Another possible way to recover the external loads consists in applying the so-called Partial Modal Matrix Method developed in [26]. After having computed the modal coordinates as $\boldsymbol{r} = \boldsymbol{\Phi}^\dagger \boldsymbol{u}$, the load is simply recovered as:

$$\boldsymbol{\Lambda}\boldsymbol{r} = \boldsymbol{\Phi}^\top \boldsymbol{F}$$

$$\Rightarrow \quad \boldsymbol{F} = (\boldsymbol{\Phi}^\top)^\dagger \boldsymbol{\Lambda}\boldsymbol{r}$$

with $\boldsymbol{\Lambda}$ defined as:

$$\boldsymbol{\Lambda} = \begin{bmatrix} (\omega_n^{(1)})^2 & & \\ & \ddots & \\ & & (\omega_n^{(N)})^2 \end{bmatrix}$$
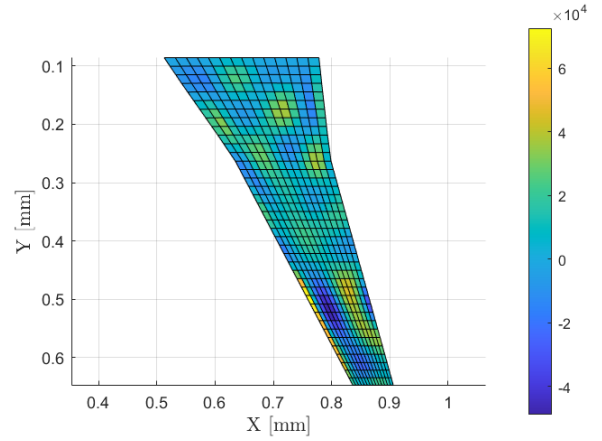
Figure 4.4: *Another erroneous external pressure reconstruction.*

This approach was applied on the same study case as before, obtaining the equally unsatisfactory results of Figure 4.4.

Methods which have gained more success in literature are based on reconstructing the external load as a linear superposition of elementary load cases [59]. Therefore, the load identification is based no more directly on the equation of motion. For example, let the measured strains be collected in the vector $\boldsymbol{\varepsilon}^\varepsilon$. Then, the contribution of the load F_i to $\boldsymbol{\varepsilon}^\varepsilon$ is:

$$\boldsymbol{\varepsilon}^{\varepsilon\,(i)} = \boldsymbol{\alpha}_i F_i$$

with $\boldsymbol{\alpha}_i$ is a vector of influence coefficients which provide the strains at the gauge locations for unit load F_i. In other words:

$$\boldsymbol{\alpha}_i = \begin{bmatrix} \dfrac{\partial \varepsilon_1^{\varepsilon(i)}}{\partial F_i} & \dfrac{\partial \varepsilon_2^{\varepsilon(i)}}{\partial F_i} & \cdots \end{bmatrix}^\top$$

Then, assuming linear superposition holds:

$$\boldsymbol{\varepsilon}^\varepsilon = \sum_i \boldsymbol{\varepsilon}^{\varepsilon\,(i)} = \begin{bmatrix} \boldsymbol{\alpha}_1 & \dots & \boldsymbol{\alpha}_N \end{bmatrix} \boldsymbol{F} \tag{4.8}$$

The unknown vector of applied loads $\boldsymbol{F}$ can be obtained minimizing the squared norm between experimental strains and analytical ones:

$$\|\boldsymbol{\varepsilon}^\varepsilon - \boldsymbol{\alpha} \boldsymbol{F}\|^2 = \sum_{i=1}^m \left(\varepsilon_i^\varepsilon - \sum_{j=1}^n \alpha_{ij} F_j \right)^2 \tag{4.9}$$

where n is the number of loads considered and m the strain measurements taken. Using least-squares:

$$\boldsymbol{F} = (\boldsymbol{\alpha}^\top \boldsymbol{\alpha})^{-1} \boldsymbol{\alpha}^\top \boldsymbol{\varepsilon}^\varepsilon \tag{4.10}$$

and in this way an approximation of the external loads acting on then structure is obtained. Several studies with the method just outlined have been carried out. For example, in [1] and [2] a wing and a composite spar are simulated and the load is reconstructed with a finite set of both concentrated and distributed forces.

Following a similar line of reasoning, in [39] based on the method proposed in [61] the goal is to reproduce to pressure distribution acting, for example, on a lifting surface. In order to do so, the surface where the pressure distribution is applied is discretized in FE. Applying a unit load on each element and recording the corresponding strains, it is possible to build a sensitivity matrix and to relate measured strains with applied pressure as:

$$\boldsymbol{\varepsilon}^\varepsilon = \boldsymbol{S}_\varepsilon \boldsymbol{p} \tag{4.11}$$

with $\boldsymbol{S}_\varepsilon$ a matrix basically containing the sensitivity of the strain measurements on the pressure variations, that is:

$$\begin{bmatrix} \varepsilon_1^\varepsilon \\ \vdots \\ \varepsilon_n^\varepsilon \end{bmatrix} = \begin{bmatrix} \dfrac{\partial \varepsilon_1^\varepsilon}{\partial p_1} & \cdots & \dfrac{\partial \varepsilon_n^\varepsilon}{\partial p_n} \\ \vdots & \cdots & \vdots \\ \dfrac{\partial \varepsilon_1^\varepsilon}{\partial p_1} & \cdots & \dfrac{\partial \varepsilon_n^\varepsilon}{\partial p_n} \end{bmatrix} \begin{bmatrix} p_1 \\ \vdots \\ p_n \end{bmatrix} \tag{4.12}$$

The matrix $\boldsymbol{S}_\varepsilon$ can be easily computed iteratively solving FE simulations of the model under consideration. Applying a unit pressure load $p_i = 1$ at the ith element and recording the strain measurements, it is possible to build $\boldsymbol{S}_\varepsilon$ column by column. After this operation is completed, the whole external applied pressure can be computed from the pseudo-inverse:

$$\boldsymbol{p} = \boldsymbol{S}^\dagger \boldsymbol{\varepsilon}^\varepsilon \tag{4.13}$$

This is in summary the approach followed in [39]. In the following, the load reconstruction will be based on a similar method.

4.1.2 Regularization of ill-posed problems

The load reconstruction usually leads a bad-conditioned over-determined system of equations. If it is directly solved with least-squares generally the results are quite poor. This is basically due to the high condition number of the system matrix. As a consequence, even small variations in the input vector cause large differences in the final output. Therefore in this section a few techniques used to face this problem will be reviewed . All the methods outlined are usually referred to as *regularization* methods. This topic is covered in detail in [51].

Consider the ill-posed problem whose discrete version is expressed in the general form:

$$\boldsymbol{A}\,\boldsymbol{x} = \boldsymbol{b} \tag{4.14}$$

with $\boldsymbol{A} \in \mathbb{R}^{m \times n}$. Most of the regularization methods available, at least in their simplest form, take advantage from the Singular Value Decomposition (SVD) of $\boldsymbol{A}$ which is expressed as:

$$\boldsymbol{A} = \sum_{i=1}^{n} \boldsymbol{u}_i\,\sigma_i\,\boldsymbol{v}_i^{\top} \tag{4.15}$$

it is easily possible to obtain the following standard relations:

$$\boldsymbol{b} = \sum_{i=1}^{n} (\boldsymbol{u}_i^{\top}\boldsymbol{b})\boldsymbol{u}_i \tag{4.16}$$

$$\boldsymbol{x} = \sum_{i=1}^{n} \frac{\boldsymbol{u}_i^{\top}\boldsymbol{b}}{\sigma_i}\boldsymbol{v}_i \tag{4.17}$$

Considering that the input vector $\boldsymbol{b}$ is affected by a certain level of error, the terms of Eq.(4.17) most affected by the noise will be the ones corresponding to the smallest singular values. Therefore, the main idea in many regularization methods is to recover the solution using just certain components of the SVD, while neglecting or putting less weight to others.

The simplest approach consists in the so-called Truncated SVD which approximates the solution $\boldsymbol{x}$ truncating the summation of Eq.(4.17) until the kth component in order to discard the terms related to the smallest singular values:

$$\boldsymbol{x} = \sum_{i=1}^{k} \frac{\boldsymbol{u}_i^{\top}\boldsymbol{b}}{\sigma_i}\boldsymbol{v}_i \tag{4.18}$$

The method which however has been among the most successful is the so-called Tikhonov regularization based on computing the solution to the initial problem Eq.(4.14) as:

$$\min_{\boldsymbol{x}} \left\{ \|\boldsymbol{A}\boldsymbol{x} - \boldsymbol{b}\|_2^2 + \alpha^2\|\boldsymbol{x}\|_2^2 \right\} \tag{4.19}$$

where:

- The term $\|\boldsymbol{A}\boldsymbol{x} - \boldsymbol{b}\|_2^2$ controls how well the solution $\boldsymbol{x}$ predicts the (noisy) data $\boldsymbol{b}$.

- The term $\|\boldsymbol{x}\|_2^2$ controls the norm of the solution avoiding that $\boldsymbol{x}$ becomes noisy due to the error which affects $\boldsymbol{b}$.

- Finally, the scalar coefficient α, also called *regularization parameter*, controls the balance between the previous two terms: for smaller values more weight is given to fit the noisy data, on the other hand for higher values more weight is given to the minimization of the solution norm.

Eq.(4.19) can be recast as a linear least-squares problem as:

$$\min_{\boldsymbol{x}} \left\| \begin{bmatrix} \boldsymbol{A} \\ \boldsymbol{I}\alpha \end{bmatrix} \boldsymbol{x} - \begin{bmatrix} \boldsymbol{b} \\ \boldsymbol{0} \end{bmatrix} \right\|_2 \tag{4.20}$$

whose solution is:

$$\boldsymbol{x} = (\boldsymbol{A}^{\top}\boldsymbol{A} + \alpha^2\boldsymbol{I})^{-1}\boldsymbol{A}^{\top}\boldsymbol{b} \tag{4.21}$$

Substituting the SVD of matrix $\boldsymbol{A}$ it is possible to compute after a few steps [51]:

$$x = \sum_{i=1}^{n} \frac{\sigma_i^2}{\sigma_i^2 + \alpha^2} \frac{\boldsymbol{u}_i^\top \boldsymbol{b}}{\sigma_i} \boldsymbol{v}_i \qquad (4.22)$$

Comparing to Eq.(4.17) it is clear presence of the additional factor which acts as a filter for the SVD components related to the smallest singular values (Figure 4.5).
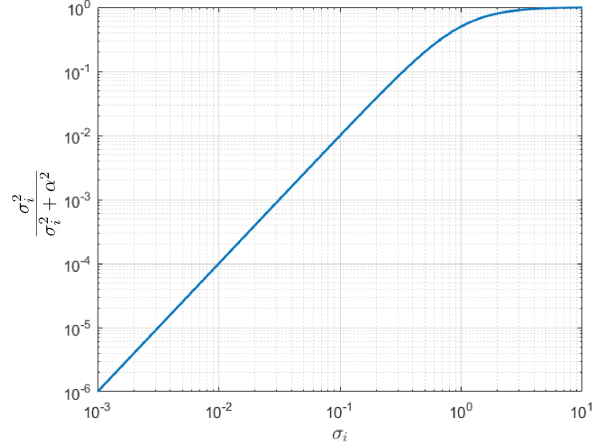
Figure 4.5: *Filter factor for Tikhonov regularization.*

Now, the question is how to choose a suitable regularization parameter α in order to suppress the noisy components but to retain the ones important to reconstruct the solution.

Several techniques have been proposed (again, see for example [51]) but the only one which will be considered in the following is based on the so-called L-curve criterion ([50], [53]). This method has been applied successfully in several contexts, it easy to implement, computationally inexpensive and does not require any knowledge of error affecting the problem. On other hand, it is an heuristic criterion and it does not always work as expected. The main idea behind is to find a good balance between the two norms of Eq.(4.19). Let:

$$\begin{aligned} x(\alpha) &= \|\boldsymbol{A}\boldsymbol{x} - \boldsymbol{b}\|_2^2 \\ y(\alpha) &= \|\boldsymbol{x}\|_2^2 \end{aligned} \qquad (4.23)$$

It is possible to write the solution norm as:

$$y(\alpha) = \sum_i \left(\frac{\sigma_i^2}{\sigma_i^2 + \alpha^2} \frac{\boldsymbol{u}_i^\top \boldsymbol{b}}{\sigma_i} \right)^2 = \sum_i \frac{\sigma_i^2 (\boldsymbol{u}_i^\top \boldsymbol{b})^2}{(\sigma_i^2 + \alpha^2)^2} \qquad (4.24)$$

While the norm of the residual can be expressed as:

$$\begin{aligned} x(\alpha) &= \sum_i \left[\left(1 - \frac{\sigma_i^2}{\sigma_i^2 + \alpha^2} \right) \boldsymbol{u}_i^\top \boldsymbol{b} \right]^2 + \|r_\perp\|_2^2 = \sum_i \left[\left(\frac{\alpha^2}{\sigma_i^2 + \alpha^2} \right) \boldsymbol{u}_i^\top \boldsymbol{b} \right]^2 + \|r_\perp\|_2^2 \\ &= \sum_i \frac{\alpha^4 (\boldsymbol{u}_i \boldsymbol{b})^2}{(\sigma_i^2 + \alpha^2)^2} + \|r_\perp\|_2^2 \end{aligned} \qquad (4.25)$$

with $\|r_\perp\|_2 = \|\boldsymbol{b} - \boldsymbol{U}^\top \boldsymbol{b}\|_2$ the norm of the components of $\boldsymbol{b}$ which lie outside from the column space of $\boldsymbol{A}$.

It is easily possible to compute that [50]:

$$\frac{\mathrm{d}x}{\mathrm{d}\alpha} = 4\alpha^3 \sum_i \frac{(\boldsymbol{u}_i^\top \boldsymbol{b})^2 \sigma_i^2}{(\sigma_i^2 + \alpha^2)^2} \quad ; \quad \frac{\mathrm{d}y}{\mathrm{d}\alpha} = -4\alpha \sum_i \frac{\sigma_i^2 (\boldsymbol{u}_I^\top \boldsymbol{b})^2}{(\sigma_i^2 + \alpha^2)^3} \qquad (4.26)$$

$$\frac{\mathrm{d}y}{\mathrm{d}\alpha} = \frac{\mathrm{d}y}{\mathrm{d}x} \frac{\mathrm{d}x}{\mathrm{d}\alpha} \quad \Rightarrow \quad \frac{\mathrm{d}y}{\mathrm{d}x} = \frac{\mathrm{d}y}{\mathrm{d}\alpha} \left(\frac{\mathrm{d}x}{\mathrm{d}\alpha} \right)^{-1} \qquad (4.27)$$

And so:

$$\frac{\mathrm{d}y}{\mathrm{d}x} = -\frac{1}{\alpha^2} \qquad (4.28)$$

which means that plotting y over x a strictly decaying function is obtained. The curve is of interest because it shows how the regularized solution changes as α changes. Plotting the curve in loglog scale, because of the large range of values covered by the norms, it is usually possible to identify two distinct parts: for low values of α the curve is almost vertical, while for higher values it is almost horizontal. In the first case the solution is dominated by the errors coming from the noise (under-regularized solution). In the second one on the contrary the solution is called over-regularized and it does not predict well the data $\boldsymbol{b}$. In between these two regions it usually possible to find a corner which represents a good compromise between the minimization of the two norms. Therefore, α can be chosen for example as the point of maximum curvature of the curve. As it is possible to see, the criterion is heuristic but seems to work for a broad range of problems. A visual representation of the L-curve and its different regions is shown in Figure 4.6.
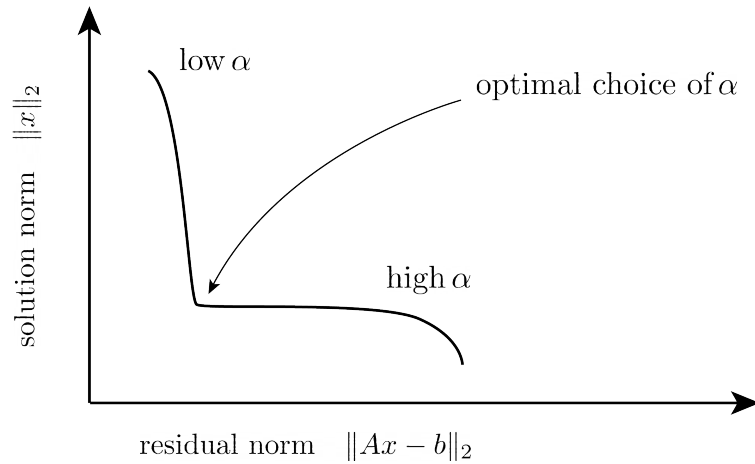
Figure 4.6: *Representation of a the usual shape of the so-called L-curve.*

Two points which are important to mention have to be highlighted:

- In general, there is no guarantee that a distinct corner is present. This depends on the problem and on the type of error affecting the data.

- Also, there is no guarantee that the corner is unique, rendering the choice of α sometimes ambiguous. This problem will be encountered in the following sections and a few possible solutions will be suggested.

As a final note, the implementation of the regularization in MATLAB has been done also with help of the pre-existing toolbox (Regularization Tools) described in detail in [52].

4.2 Static analysis

In this section the load reconstruction will be limited to studying static cases. First, in Section 4.2.1 it is suggested how to improve the load reconstruction based on a preliminary interpolation of the load. Then, in Section 4.2.2 a few approaches are described in order to choose a suitable value of the regularization parameter. Finally, in Section 4.2.3 it is studied the effect of measurement errors on the final load reconstruction. The load will be computed both from the reconstructed displacement field and from the strain measurements

4.2.1 Pressure reconstruction using measured strains and recovered displacements

Section 4.1.1 was concluded briefly stating how to recover the pressure field from the measured strains using the sensitivity matrix S_ε. However Eq.(4.13) deserves a few comments. The system which needs to be solved is in general under-determined, meaning that the number of strain measurements is lower compared to the number of variables used to describe the pressure distribution. Therefore, solving the system with the pseudo-inverse matrix $S^\dagger$ certainly delivers the minimum norm solution, but there is no guarantee that this solution, among all the others, is the one which best represents the load. For example, the pressure distribution has been reconstructed using this method for three different load cases and the results are presented in Figure 4.7.
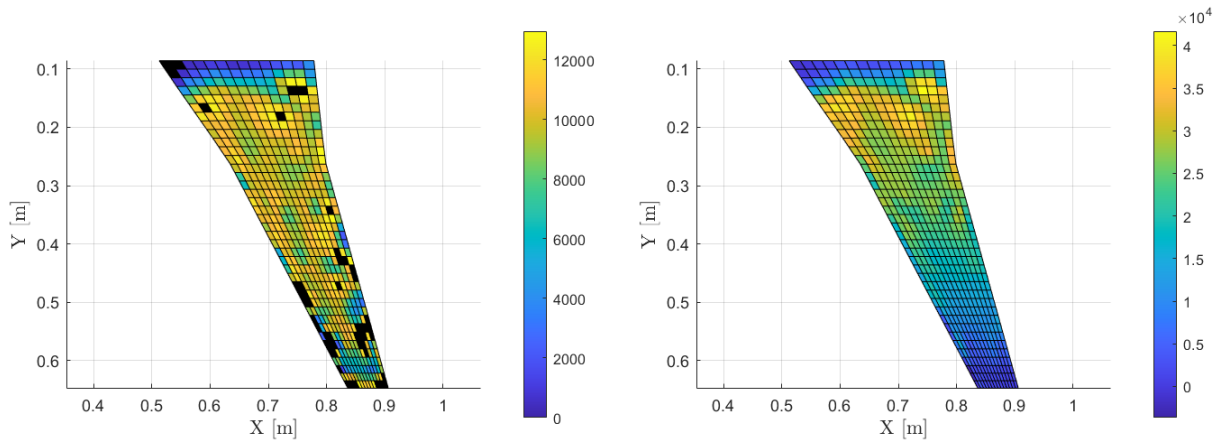
(a) *Constant pressure (pressure on black elements is out-of-range).*

(b) *Parabolic pressure.*
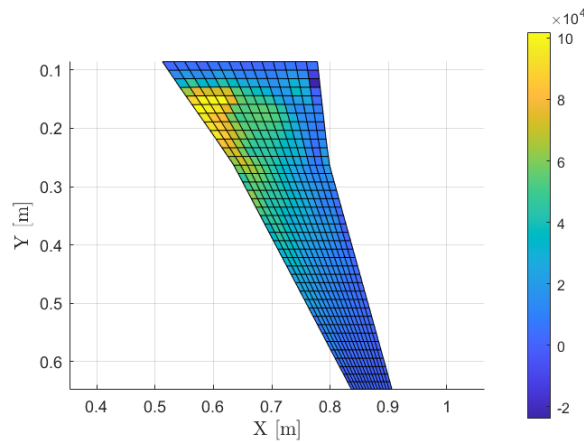
(c) *Parabolic-linear pressure.*

Figure 4.7: *Load reconstruction using strain measurements from the pseudo-inverse.*

The load is approximately recovered, even though it is far from being a good representation of the exact one. It is possible to improve the reconstruction adding an intermediate step and transforming the system from being under-determined to be over-constrained. This can be done interpolating the load and so expressing it with a limited number of variables. In particular, it has been chosen to express the load $\boldsymbol{p}$ with a certain distribution of control points using the so-called *inverse distance weighting* [65]. These basically act as interpolation points such that the pressure value at a certain position $\boldsymbol{x}$ can be expressed as:

$$p(\boldsymbol{x}) = \frac{\sum_i w_i(\boldsymbol{x})\rho_i}{\sum_i w_i(\boldsymbol{x})} \qquad (4.29)$$

with ρ_i the value of the ith control point and $w_i(\boldsymbol{x})$ a weighting function monotonously decreasing away from the control point. In the following, a function of the form:

$$w_i(\boldsymbol{x}) = e^{-\left(\frac{r(\boldsymbol{x})}{\lambda}\right)^2} \qquad (4.30)$$

will be used, with r the distance from the control point and λ a scalar coefficient. This has a similar meaning of the so-called *shape factor* for radial basis functions [17].
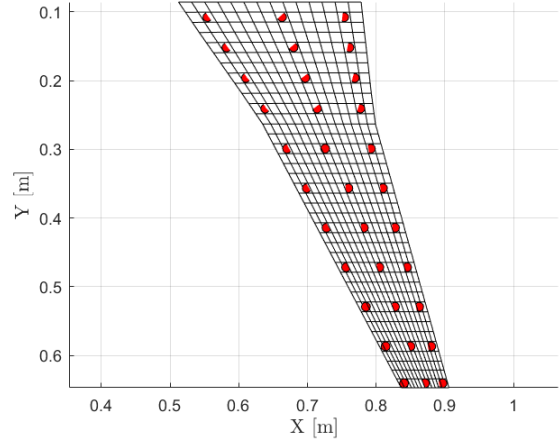
Figure 4.8: *Control point locations.*

The locations of the control points placed on the wing skin is displayed in Figure 4.8. As a consequence, it is possible to write that:

$$\boldsymbol{p} = \begin{bmatrix} \dfrac{w_1(r_1)}{\sum_i w_i(r_1)} & \cdots & \dfrac{w_n(r_m)}{\sum_i w_i(r_1)} \\ \vdots & \cdots & \vdots \\ \dfrac{w_1(r_1)}{\sum_i w_i(r_n)} & \cdots & \dfrac{w_n(r_m)}{\sum_i w_i(r_n)} \end{bmatrix} \begin{bmatrix} \rho_1 \\ \vdots \\ \rho_m \end{bmatrix} = \boldsymbol{W}\boldsymbol{\rho} \qquad (4.31)$$

And so substituting in Eq.(4.11):

$$\boldsymbol{\varepsilon}^\varepsilon = \boldsymbol{S}_\varepsilon \boldsymbol{W}\boldsymbol{\rho} \qquad (4.32)$$

Now, the system is overconstrained and could be solved with least-squares. However, it is possible to observe that often after the interpolation the condition number of the matrix $\boldsymbol{S}_\varepsilon \boldsymbol{W}$ increases dramatically. As a consequence, it is useful (and sometimes necessary) to apply a regularization scheme to the system in order to retrieve $\boldsymbol{\rho}$. Using the Tikhonov regularization together with the L-curve criterion, the results of Figure 4.9 have been obtained which show a very good load reconstruction.

Before proceeding it is instructive to think about the role of regularization in this context. As briefly mentioned in Section 4.1.2, all the framework of regularization is built in order to minimize the effect of input noise and errors on the ill-posed system. However, at the moment apparently no error has been added to the strain measurements so it would be questionable why it is necessary to regularize the system. The reason is that introducing the interpolation scheme with $\boldsymbol{W}$ we are effectively modifying the system such that:

$$\boldsymbol{\varepsilon}^\varepsilon = \boldsymbol{\varepsilon}^\varepsilon_{exact} + \boldsymbol{e}$$
$$\boldsymbol{S}_\varepsilon \boldsymbol{W}\boldsymbol{\rho} = \boldsymbol{\varepsilon}^\varepsilon_{exact} + \boldsymbol{e}$$

with $\boldsymbol{\varepsilon}^\varepsilon_{exact}$ the strain measurements for example defined as $\min_{\boldsymbol{\rho}} \|\boldsymbol{p}_{exact} - \boldsymbol{W}\boldsymbol{\rho}\|_2$ and $\boldsymbol{e}$ the strain mismatch w.r.t. the measured values for the best combination of $\boldsymbol{\rho}$. Introducing the interpolation scheme is equivalent to solving an ill-conditioned over-determined linear system with a certain "noise" $\boldsymbol{e}$. This motivates in the following the use of the L-curve to recover the load from the strain even when the exact strain measurements are used as input.

(a) *Constant pressure.*

(b) *Parabolic pressure.*

(c) *Parabolic-linear pressure.*

(d) *Typical L-curve used to choose the regularization parameter.*
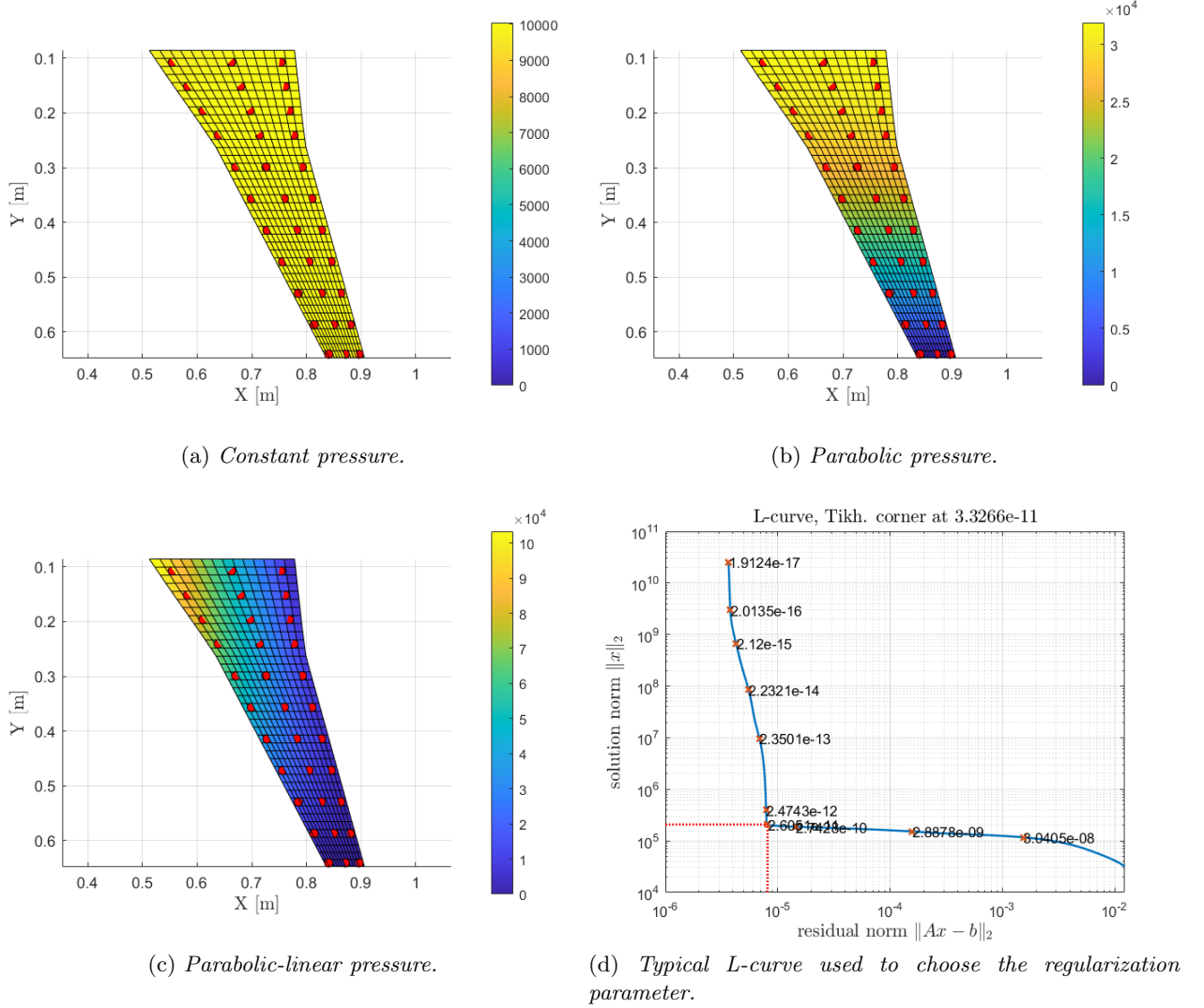
Figure 4.9: *Load reconstruction using strain measurements with pressure interpolation.*

A completely analogous procedure can be applied using as input not the strain measurements, but the recovered displacement field from the shape sensing analysis. So Eq.(4.32) now simply becomes:

$$\boldsymbol{u} = \boldsymbol{S}\boldsymbol{W}\boldsymbol{\rho} \tag{4.33}$$

where the matrix $\boldsymbol{S}$ contains the derivatives of the displacements w.r.t. the pressure load and is again obtained iteratively solving the FE model. Using both the displacement field from MM and from iFEM the pressure load has been recovered for the three load cases. The results are summarized in Table 4.1 and compared with the ones obtained before from the strain measurements.

Pressure distribution:		Constant	Parabolic	Parabolic-linear
MM	shape sensing error	0.05%	0.12%	0.23%
	pressure error	4.1%	2.3%	7.8%
iFEM	shape sensing error	6.18%	4.54%	3.5%
	pressure error	9.1%	20.9%	18.0%
From strain	pressure error	0.78%	0.42%	0.49%

Table 4.1: *Relative L2-norm error of reconstructed pressure field for three different load cases using either strain measurements and displacements as input.*

A few comments can be done as follows:

- The pressure reconstruction from the strain measurements performs better compared to the other methods.

- Despite the relatively large errors of the displacement field, iFEM is still able to give a reasonable estimate of the pressure field.

- Reconstructing the load from the diplacement field, it has been observed that sometimes it is not clear how to choose the optimal regularization parameter.

Regarding the last point, an example is illustrated in Figure 4.10. The L-curve does not show a unique corner and more than one solution could be identified. Heuristically, this would mean that there are more than one configurations which can give a good compromise between the minimization of the residual and solution norm. For the cases analysed this indeed happens especially reconstructing the load from iFEM whose displacement field has the largest error compared to the actual one. As a consequence several pressure fields are identified. In Section 4.2.2 some possible solutions to this problem are suggested.
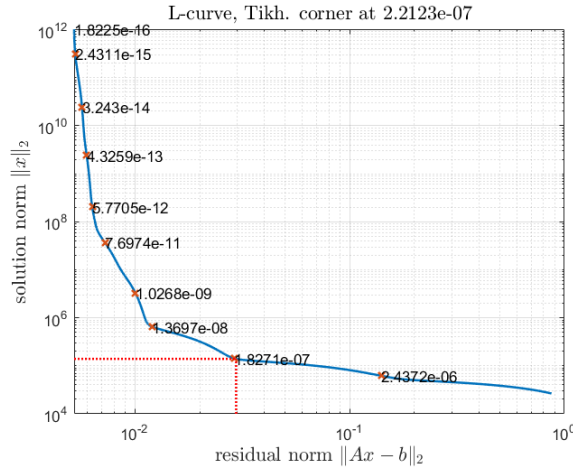
Figure 4.10: *Example of L-curve with not well defined corner using iFEM for parabolic-linear pressure distribution.*

Another important aspect which needs to be assessed is the performance of the method in case the pressure field domain covers the whole wing surface, as it is in usual flight conditions. So far, the external load was applied only on the bottom skin. Now, a pressure distribution is applied also on the top skin. This represents a far more challenging situation given the fact that there might be several different pressure distributions which cause nearly the same deformation but which act differently on the top and bottom skin surface. Two cases have been studied. In

the first one (Figure 4.11), a parabolic pressure has been applied on the bottom skin, while a constant one on the top skin. In the second one (Figure 4.12), two identical pressure distributions have been applied on the top and bottom skin (parabolically varying along the span and linearly along the chord), but with one double in magnitude compared to the other.

(a) *Upper skin.*
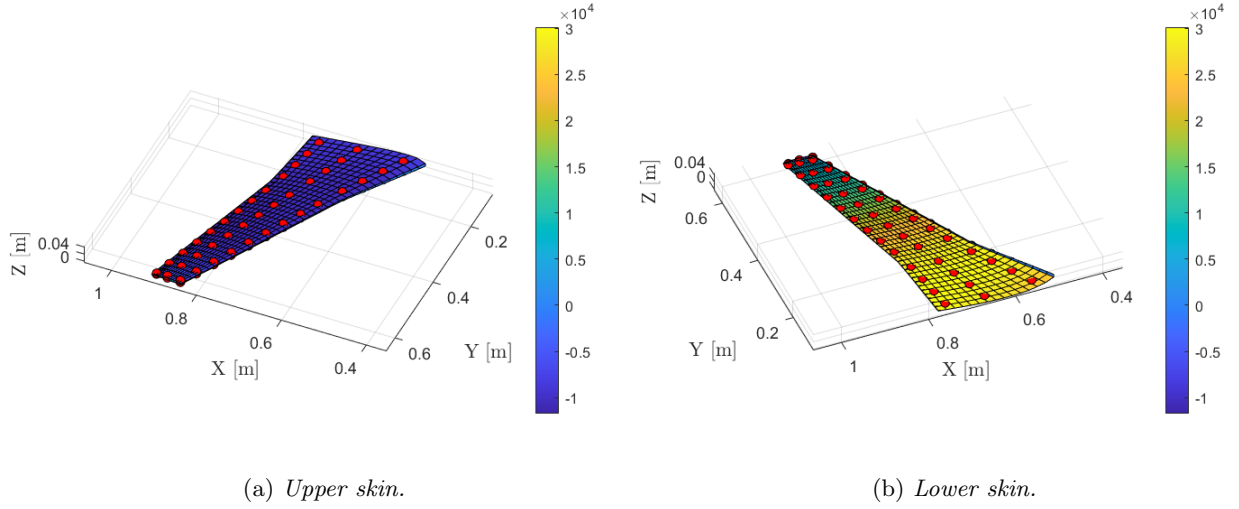
(b) *Lower skin.*

Figure 4.11: *Reconstructed pressure field from MM: constant (upper skin) and parabolic (lower skin)*

(a) *Upper skin.*
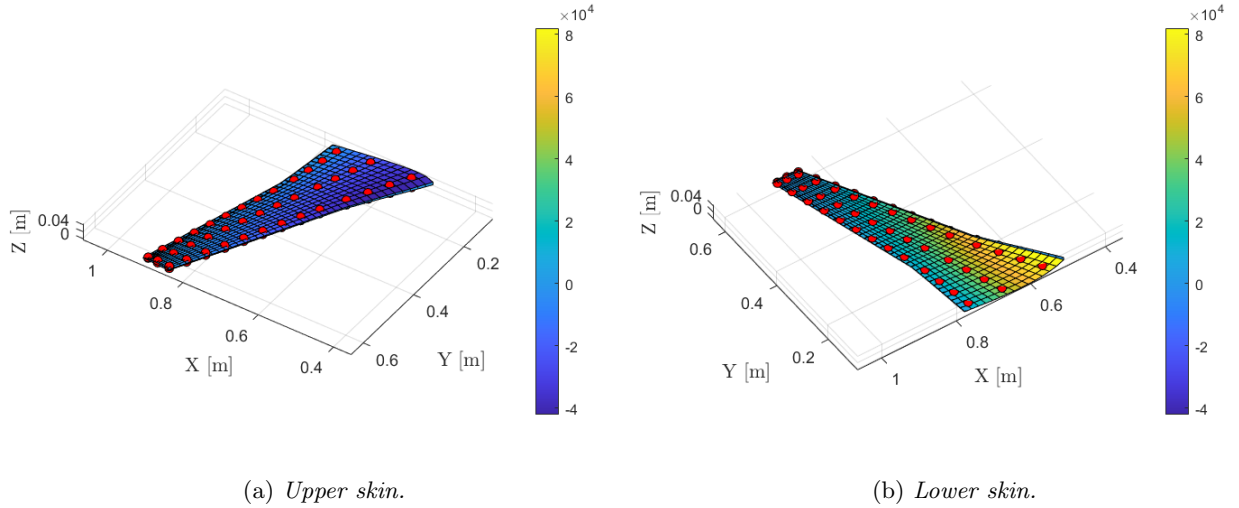
(b) *Lower skin.*

Figure 4.12: *Reconstructed pressure field from MM: parabolic and linear on both upper and lower skin, but with different magnitudes.*

Pressure:		Parabolic / Constant	Parabolic linear / Parabolic - linear
MM	shape sensing error	0.04%	0.08%
	pressure error	7.8%	10.7%
iFEM	shape sensing error	5.4%	3.7%
	pressure error	14.2%	21.9%
From strain	pressure error	3.89%	0.77%

Table 4.2: *Relative L2-norm error of reconstructed pressure field for two different load cases using either strain measurements and displacements as input.*

Quantitatively, the results obtained from both recovered displacements and measured strains are shown in Table 4.2. Similarly as before, even if iFEM perform worse, relative-wise it seems to deliver sturdier results given the error coming from the shape sensing analysis.

As a final study for this section, it is reported a brief analysis done in order to understand the influence of the shape factor λ in the interpolation of the pressure field. It is a measure of the influence of each control point and the decrement of the radial functions used depends on λ which defines the magnitude of the corresponding radius of influence. The effect of this parameter has been studied for the parabolic-linear pressure case introduced before. In general, the idea is to avoid too low values since this would lead to a situation similar to the one shown in Figure 4.13a. Changing λ iteratively, the L2-norm error of the resulting pressure field has been plotted in Figure 4.13b. Apart from relatively small values, the result seem to be quite independent on the choice of the parameter.

(a) *Pressure reconstruction for low values of α.*   (b) *Relative L2-norm pressure field error in function of α.*
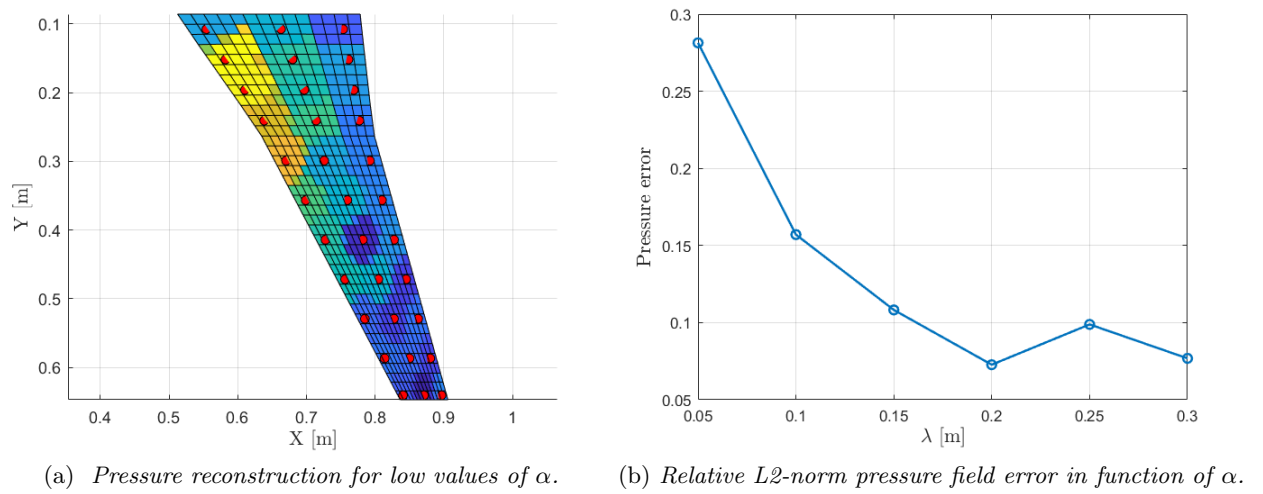
Figure 4.13: *Study on the influence of α on the final pressure reconstruction.*

However, it is important to note that this is heavily dependent on the distribution of the load applied. For the one considered until now, the pressure distribution is relatively smooth and there are not high gradients in the pressure field. A different situation of course occurs if this is not the case. As an example, a constant pressure distribution has been applied as shown in Figure 4.14a. For a relatively small value of $\lambda = 0.05$ m the discontinuity in the pressure field is approximately captured (Figure 4.14b), while it is completely lost using $\lambda = 0.5$ m (Figure 4.14c).

(a) *Pressure application region.* (b) *Pressure reconstruction with low λ.* (c) *Pressure reconstruction with high λ.*
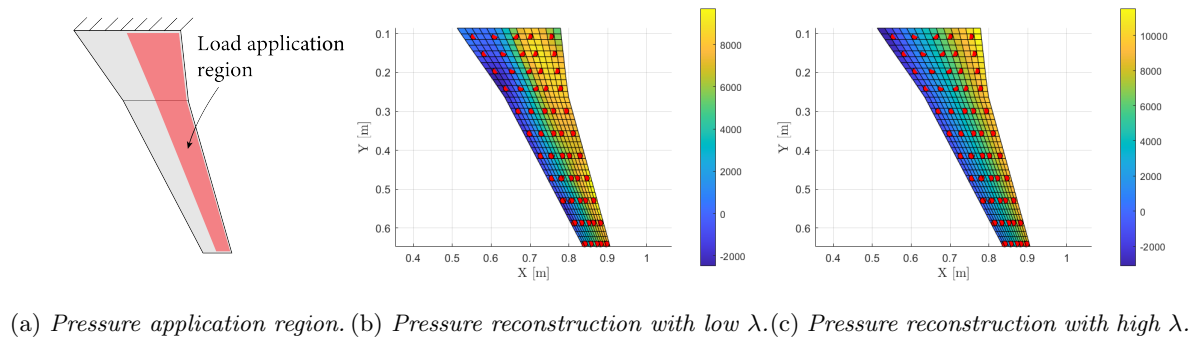
Figure 4.14: *Effect of the choice of λ for an highly discontinuous pressure field.*

From this small set of simulations, it is possible to state that if the pressure field is relatively smooth, then the shape factor should be chosen to be at least more than the average distance between control points. If, on the other hand it is important to capture steep gradients in the field, then a small value of λ would yield better results.

4.2.2 Choice of the regularization parameter using the L-curve criterion

It was observed in Figure 4.10 that the L-curve criterion might give more than one option in choosing a suitable regularization parameter. Therefore, in this section some suggestions are presented in order to either limit the choice to a smaller set or to identify a unique parameter.

Comparison of experimental and recovered strain measurements

The reconstructed pressure load can be used in a direct FEM analysis to compute the corresponding pressure field. This in turn allows to obtain the strain field and so to compare these values with the experimental measurements. For example, in Figure 4.15 several values of the regularization parameter α have been used to build a curve representing the error w.r.t. the strain measurements (Figure 4.15a). Correspondingly, in Figure 4.15b the error of the pressure field is plotted. The minimum value of 4.15a indeed corresponds to a minimum in Figure 4.15b, so giving the possibility to identify a suitable regularization parameter. However, the method has several disadvantages:

- The range covered by α is quite large and carrying out these types of simulations for a sufficient number of cases might be computationally expensive.

- For low values of the regularization parameter α the error w.r.t. the strain measurements levels off. This happens because the identified pressure field matches very well the input data, but the resulting identified load is under-regularized. So, the minimum of the strain error curve might not correspond to a minimum error of the pressure field.

(a) *Error curve w.r.t strain measurements.*   (b) *Error of pressure field.*
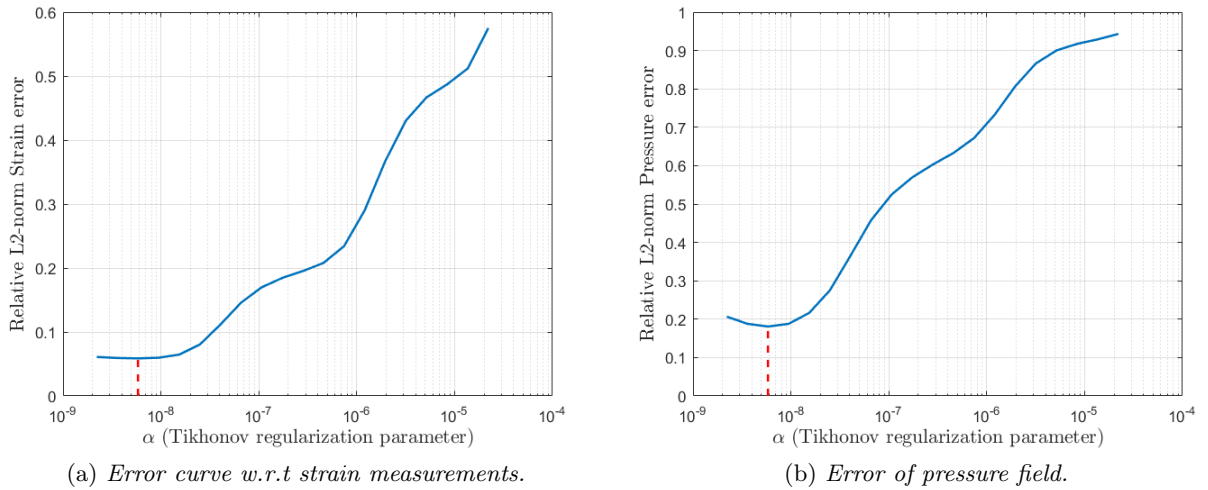
Figure 4.15: *Strain and pressure error in function of the regularization parameter.*
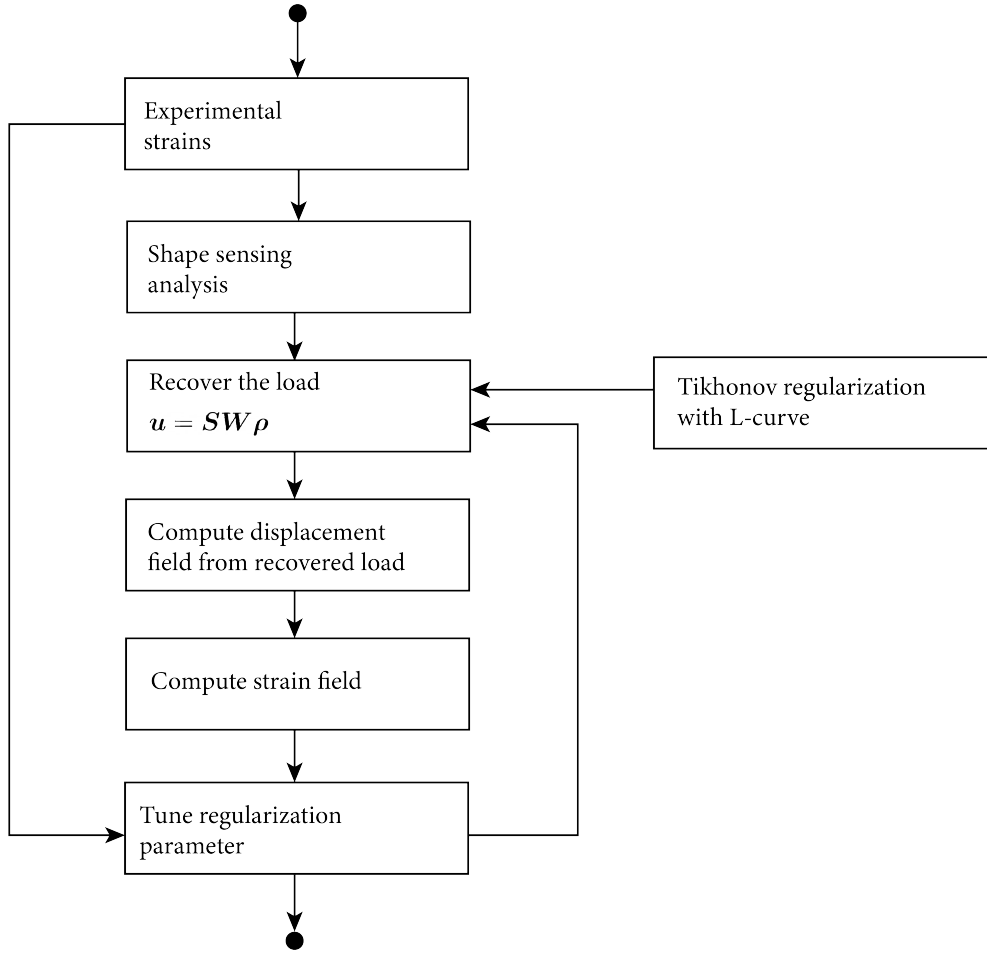
Figure 4.16: *Algorithm to find a suitable regularization parameter.*

Therefore, a better choice might consist in the following algorithm (Figure 4.16):

1. Identify all the possible corners on the L-curve, which become the candidates for the regularization parameter choice. These can be easily found looking for the local maxima of the curvature of the L-curve. For the example of Figure 4.10, it is shown in Figure 4.17.
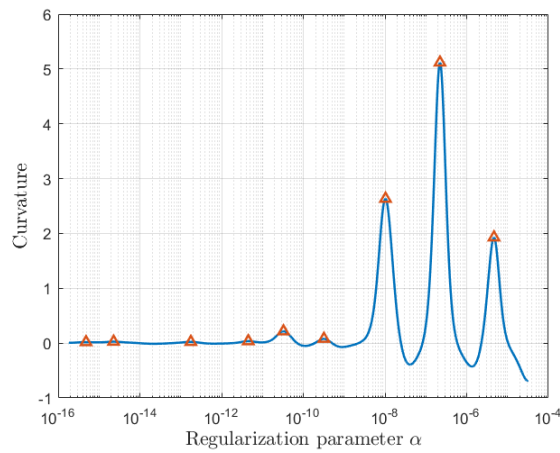
Figure 4.17: *Curvature of the L-curve. The local maxima correspond to the identified corners.*

2. For each value found from the previous point, recover the load and in turn the displacement field.

3. Compute the corresponding strain field and the error w.r.t. the strain measurements, for example as:

$$\frac{\sum_i \varepsilon_i - \varepsilon_i^\varepsilon}{\sum_i \varepsilon_i^\varepsilon}$$

with $\varepsilon_i^\varepsilon$ the experiential stain measurements and ε_i the recovered ones.

4. Plotting the strain error together with the L-curve, it is possible to identify the region where the strain error starts to increase. The corner closest to this point should represent a good regularization parameter choice. The obtained situation is represented in Figure 4.18, where also the error of the reconstructed pressure field is shown.
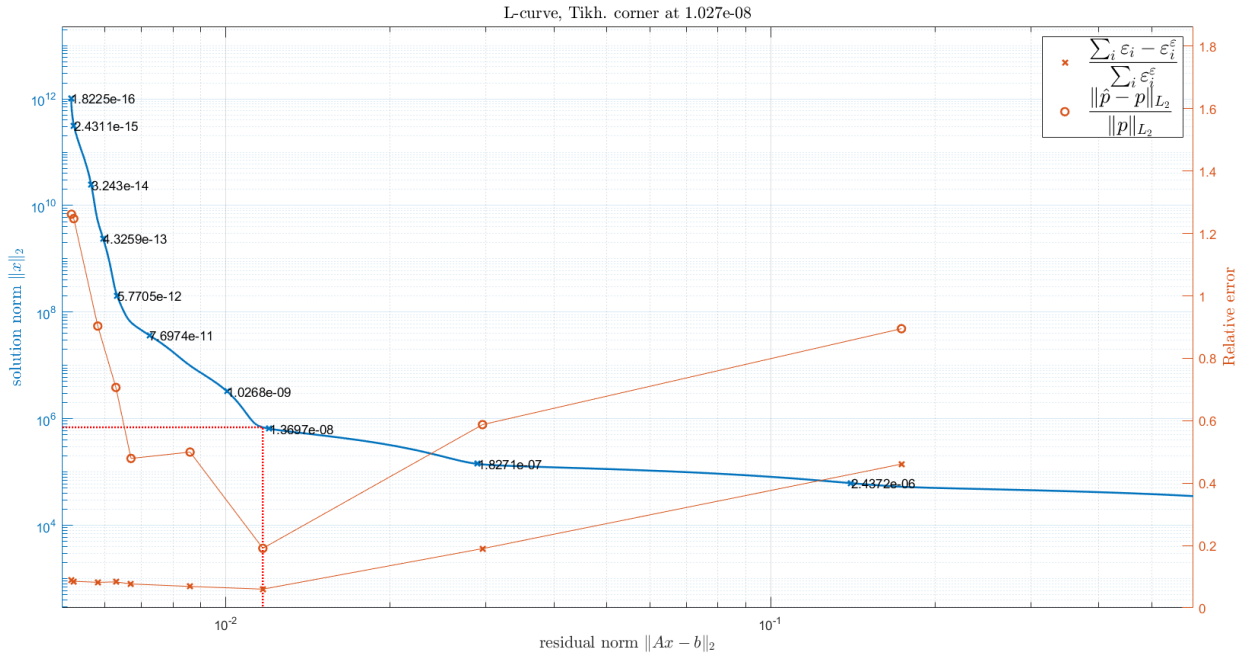
Figure 4.18: *Identification of the optimal corner of the L-curve.*

Interpolation with polynomial expansion

Another approach consists in realizing that the building blocks of the L-curve are as many as the singular values of the system. It is clear that the L-curve can be thought as the sum of the components corresponding to all the singular values. For example, in Figure 4.19 it has been plotted adding iteratively all the terms of the sum which built up the expressions of $x(\alpha)$ and $y(\alpha)$. As it is possible to see, the first singular values build the horizontal branch of the curve, while the smallest ones the vertical branch.

In general, lowering the dimensionality of the column space of the system matrix $\boldsymbol{A}$ will lead to fewer possible corners on the L-curve. This could make it easier to identify a suitable choice for the regularization parameter. In this context, using the inverse distance weighting as interpolation scheme would not be a good idea anymore: a very few number of control points would not provide a good interpolation over the whole domain. Instead, it might be beneficial to opt for a polynomial interpolation of low degree.
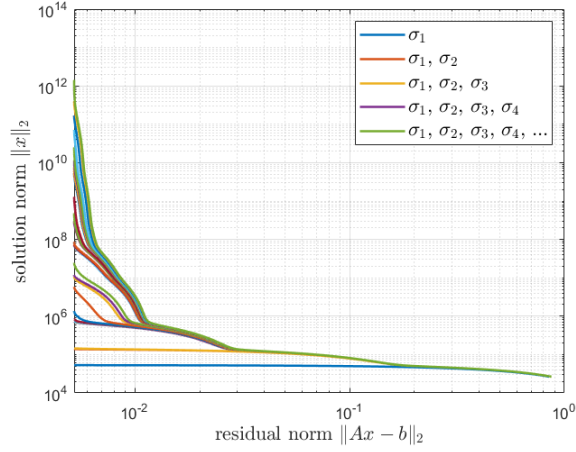
Figure 4.19: *L-curve built adding sequentially the components of the SVD.*
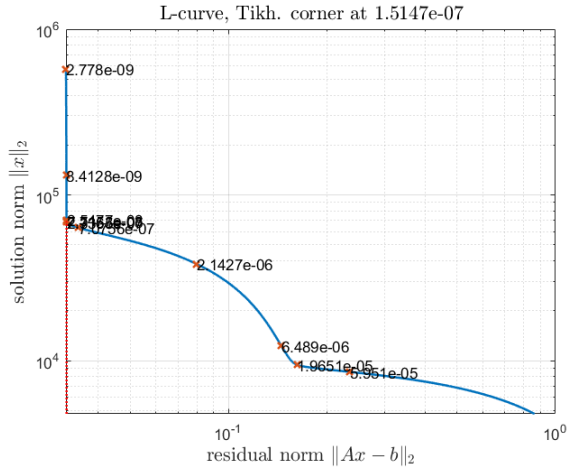
(a) *First corner of the L-curve.*
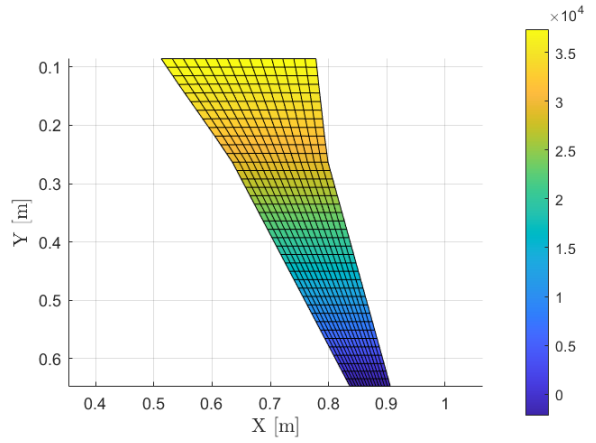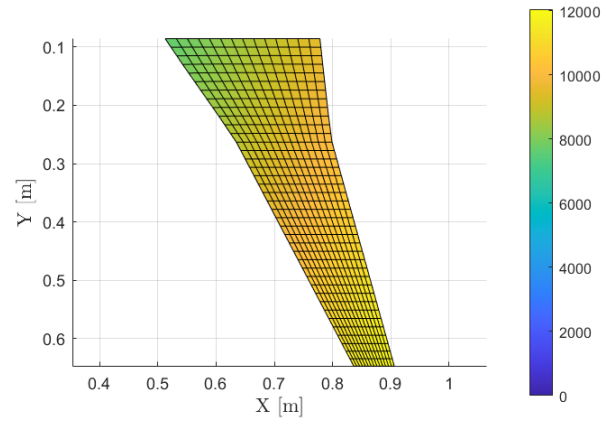
(b) *Resulting pressure field.*

Figure 4.20: *Pressure reconstruction using the first corner of the L-curve.*
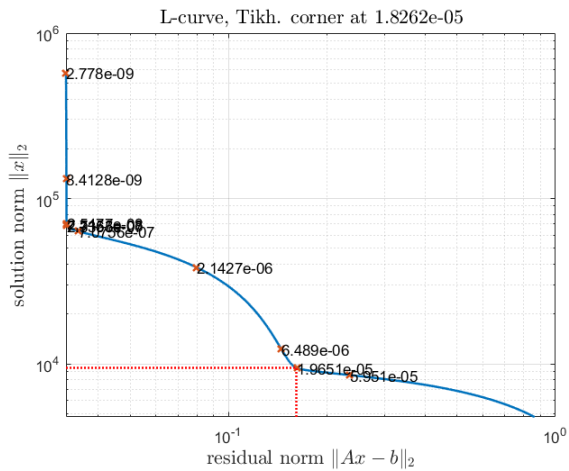
(a) *First corner of the L-curve.*
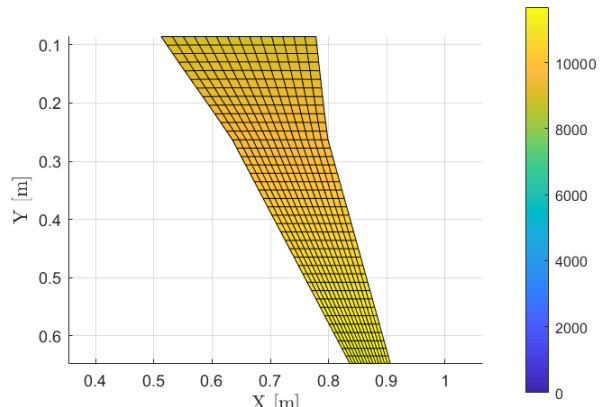
(b) *Resulting pressure field.*

Figure 4.21: *Pressure reconstruction using the first corner of the L-curve.*

For example, it is possible to interpolate the pressure field along the span with:

$$\boldsymbol{u} = \boldsymbol{S}\boldsymbol{W}\boldsymbol{\rho} \quad ; \quad \boldsymbol{W} = \begin{bmatrix} y_1^3 & y_1^2 & y_1 & 1 \\ y_2^3 & y_2^2 & y_2 & 1 \\ \vdots & \vdots & \vdots & \vdots \\ y_N^3 & y_N^2 & y_N & 1 \end{bmatrix} \tag{4.34}$$

In this way the matrix $\boldsymbol{A} = \boldsymbol{S}\boldsymbol{W}$ has at most rank equal to 4 and this should help in lowering the number of corners in the L-curve.

Using again the displacement field from iFEM and this interpolation scheme, as it is possible to see from Figure 4.20 and Figure 4.21 the L-curve presents just 2 corners. Even though the problem now again consists in choosing the right regularization parameter between the two choices, compared to before the situation has improved. Now, just two solutions have to be compared and the user can easily find out which is the most likely solution given the large difference between the two. This method will be also used later for the dynamic studies.

So far, the pressure field has been interpolated just along the span (Eq.(4.34)), even though the actual pressure applied pressure field changes also along the chord (parabolic-linear pressure case). Introducing a quadratic interpolation along the chord with:

$$\boldsymbol{W} = \begin{bmatrix} y_1^3 & y_1^2 & y_1 & x_1^2 & x_1 & 1 \\ y_2^3 & y_2^2 & y_2 & x_2^2 & x_2 & 1 \\ \vdots & \vdots & \vdots & \vdots & \vdots & \vdots \\ y_N^3 & y_N^2 & y_N & x_N^2 & x_N & 1 \end{bmatrix} \tag{4.35}$$

also in this case two possible candidates can be observed from the visual inspection of the L-curve (Figure 4.22a and Figure 4.23a). The corresponding pressure fields are shown in Figure 4.22b and Figure 4.23b. Similarly as before, the two identified solutions are very different and only the first one is closer to the true pressure field.

(a) *First corner of the L-curve.*

(b) *Resulting pressure field.*
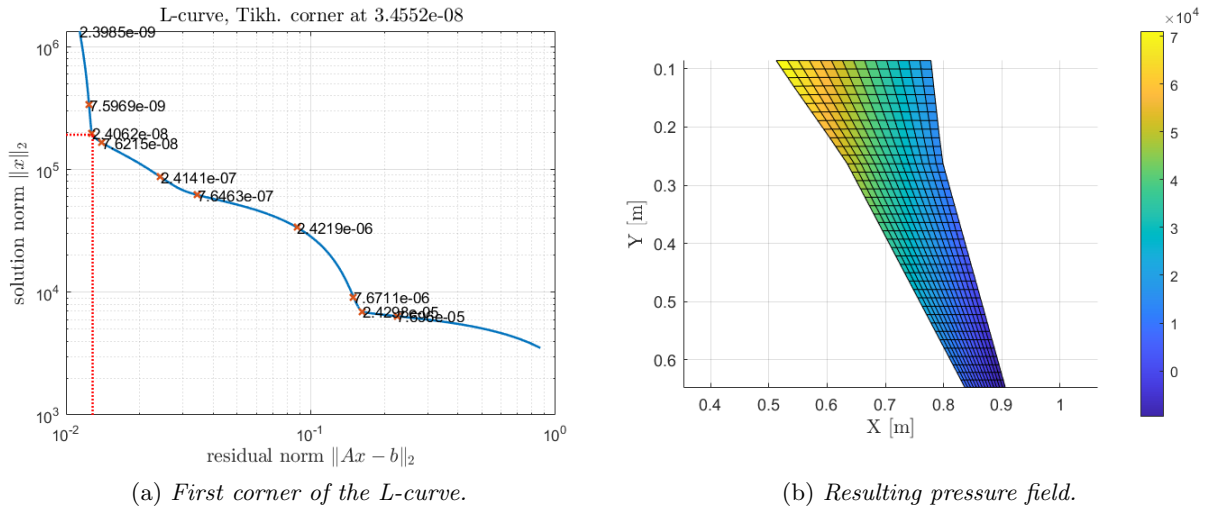
Figure 4.22: *Pressure reconstruction using the first corner of the L-curve.*
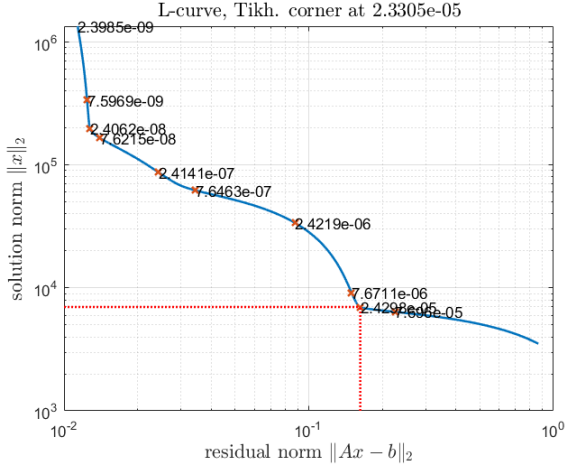
(a) *First corner of the L-curve.*

(b) *Resulting pressure field.*

Figure 4.23: *Pressure reconstruction using the first corner of the L-curve.*

Least squares with constraints

Another way to avoid ending up in the uncertainty of choosing a suitable regularization parameter consists in directly avoiding the regularization framework and in solving the least-squares problem. As was pointed out before however, in general this would not lead to meaningful results. Therefore, it is necessary to add further constraints to the problem, so basically solving a constrained linear least-squares problem. The prior knowledge of the load might be quite limited, but it is reasonable to assume that the pressure field has the same sign over all the structural domain under consideration. In other words, the problem becomes:

$$\min_{\boldsymbol{\rho}} \|\boldsymbol{u} - \boldsymbol{SW}\boldsymbol{\rho}\|_2^2 \quad \text{subject to} \quad \rho_i > 0 \tag{4.36}$$

These problems have been studied in several applications. For example, in [13] two approaches have been considered:

- Again apply Tikhonov regularization and choose the lowest regularization parameter for which the condition $\rho_i > 0$ is satisfied.

- Directly solve the least squares problem and enforce the non-negativity condition with the algorithm developed in [16].

The first approach can often lead to over-regularized solution and furthermore there is no guarantee that the regularization parameter found in this way gives a good compromise between the residual norm and the norm of the solution vector. Therefore, the second choice has been studied here. The algorithm mentioned has already been implemented in the MATLAB optimization toolbox in the function `lsqnonneg`.

For the study case under consideration, the results have been reported in Figure 4.24, together with the reference pressure field for visual comparison (Figure 4.24c)

(a) *Solution from least-squares.* (b) *Solution from constrained least-squares.* (c) *Reference pressure field.*
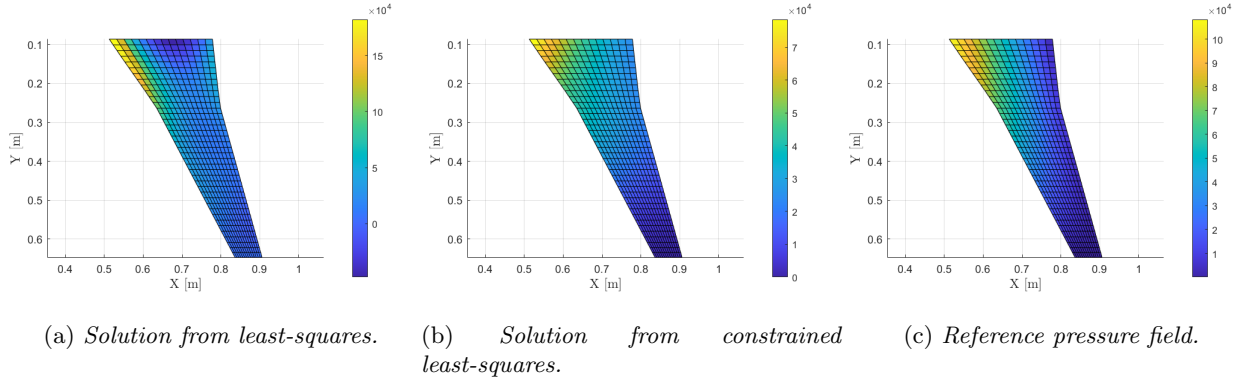
Figure 4.24: *Comparison of reconstructed pressure field using least-squares and constrained least-squares.*

The solution computed from `lsqnonneg` gives an error equal to 0.31, higher compared to the one obtained before, but it is still capable to convey the main features of the reference pressure field. There is a clear improvement compared to the simple least squares solution (Figure 4.24a), having a relative error of 0.64 and furthermore the main advantage of this approach is that there is no parameter to tune as in the regularization methods.

4.2.3 Measurement errors

In all the simulations of the previous sections the exact strain values were used. Since this is not the case for real applications, it is useful other than interesting to analyze the results when the strain measurements are affected by errors. To each strain measurement it will be given a normal distribution whose mean μ is the noise-less value and with variance $0.025\,\mu$ and $0.05\,\mu$ (so with respectively coefficient of variations $CoV = 0.025$ and $CoV = 0.05$). These values will be used for a Monte Carlo simulation and the load will be reconstructed both from the full displacement field (from the shape sensing study) and directly from the strain measurements as explained before. The three usual load cases are discussed and the results are reported in summary in Table 4.3 (constant pressure), Table 4.4 (parabolic pressure) and Table 4.5 (parabolic-linear pressure). In general, the following comments can be done:

- The best results are again obtained recovering the pressure field directly from the strain. However, this is also the approach which is most affected by the input noise looking at how much the mean of the error increases w.r.t. the noiseless value.

- Looking at the mean of the error distribution, the results from the MM are in general better compared to the ones from iFEM, except for the constant load case. However, they are also much more spread (higher CoV) compared to iFEM which gives more stable results.

	CoV =	0.025			CoV =	0.05		
	μ	σ	σ/μ	$(\mu - \text{exact})/\text{exact}$	μ	σ	σ/μ	$(\mu - \text{exact})/\text{exact}$
MM	0.096	0.060	0.63	1.34	0.152	0.096	0.63	2.7
iFEM	0.091	0.022	0.24	0	0.098	0.044	0.45	0.077
From strain	0.042	0.019	0.45	4.38	0.079	0.037	0.47	9.13

Table 4.3: *Distribution of the pressure field error retrieving the external load from the displacements and from the strains for constant pressure load case.*

	CoV =	0.025			CoV =	0.05		
	μ	σ	σ/μ	$(\mu - \text{exact})/\text{exact}$	μ	σ	σ/μ	$(\mu - \text{exact})/\text{exact}$
MM	0.115	0.045	0.39	4.0	0.1434	0.059	0.41	5.21
iFEM	0.200	0.014	0.07	−0.04	0.202	0.029	0.14	−0.03
From strain	0.047	0.021	0.45	9.95	0.090	0.022	0.24	20.97

Table 4.4: *Distribution of the pressure field error retrieving the external load from the displacements and from the strains for parabolic pressure load case.*

	CoV =	0.025			CoV =	0.05		
	μ	σ	σ/μ	$(\mu - \text{exact})/\text{exact}$	μ	σ	σ/μ	$(\mu - \text{exact})/\text{exact}$
MM	0.097	0.053	0.55	3.22	0.167	0.104	0.622	6.26
iFEM	0.189	0.0166	0.088	0.05	0.186	0.032	0.17	0.03
From strain	0.038	0.016	0.42	6.76	0.055	0.024	0.44	10.31

Table 4.5: *Distribution of the pressure field error retrieving the external load from the displacements and from the strains for parabolic - linear pressure load case.*

Constant pressure
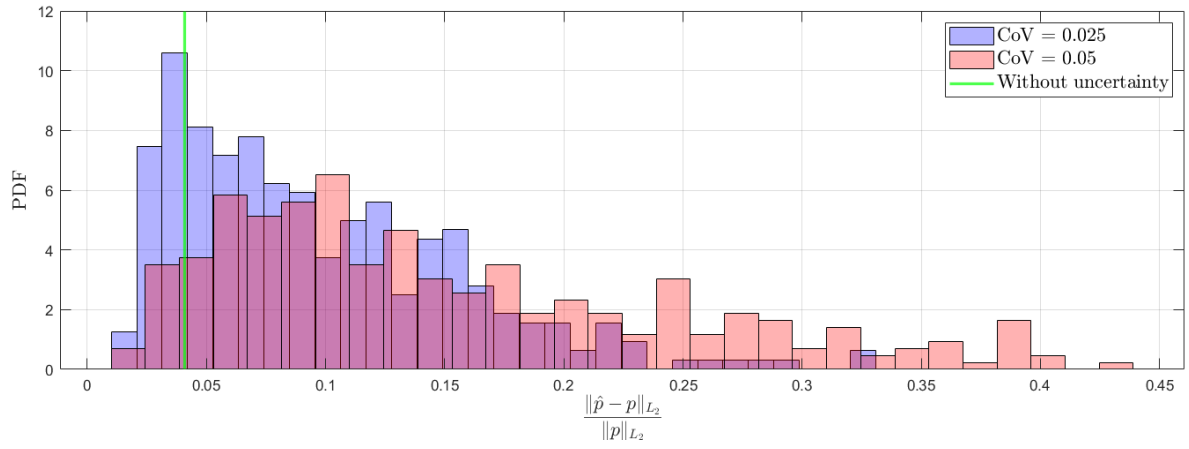
Figure 4.25: *Probability density function of relative L2-norm error of pressure field using MM for constant pressure load.*
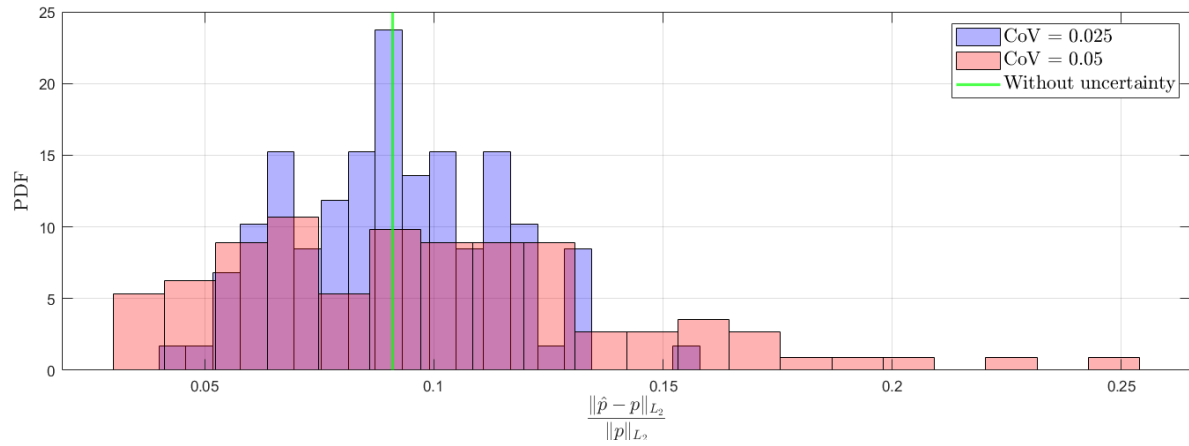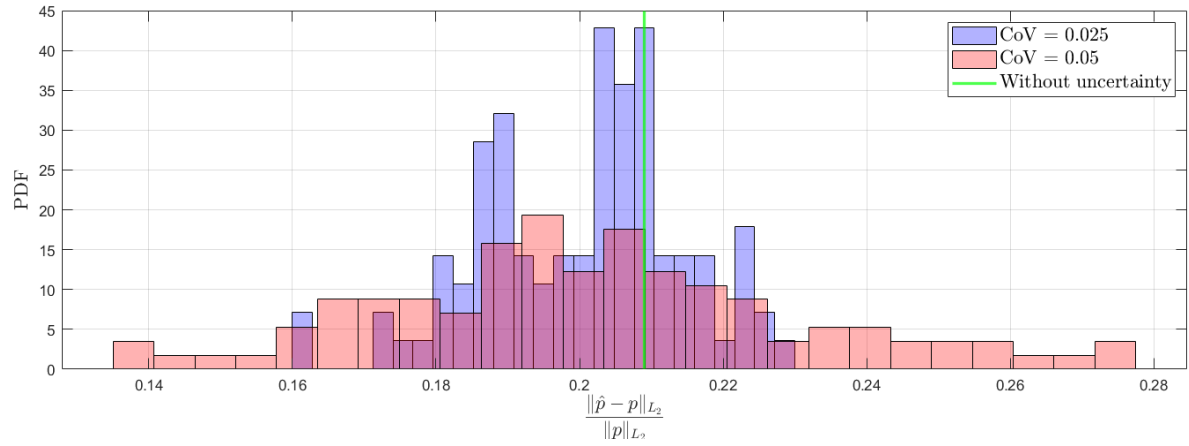

Figure 4.26: *Probability density function of relative L2-norm error of pressure field using iFEM for constant pressure load.*
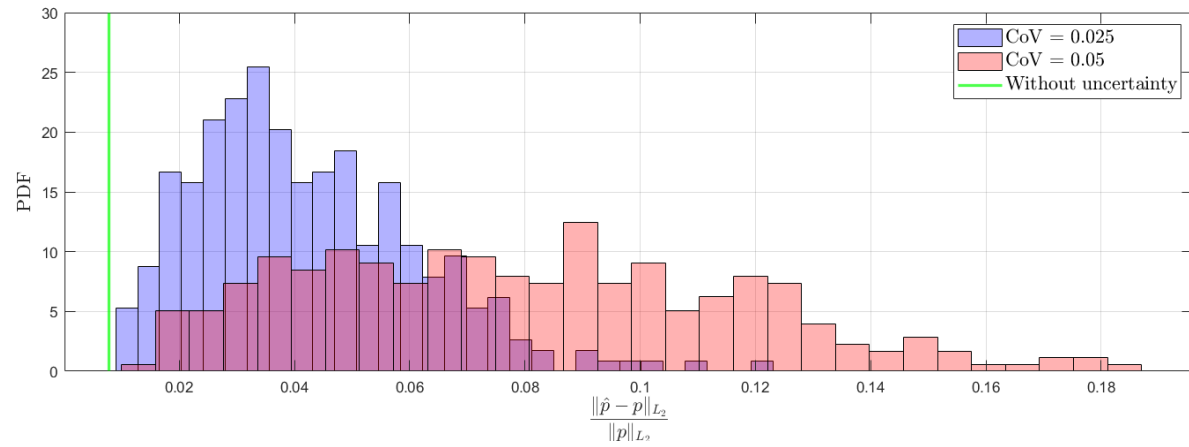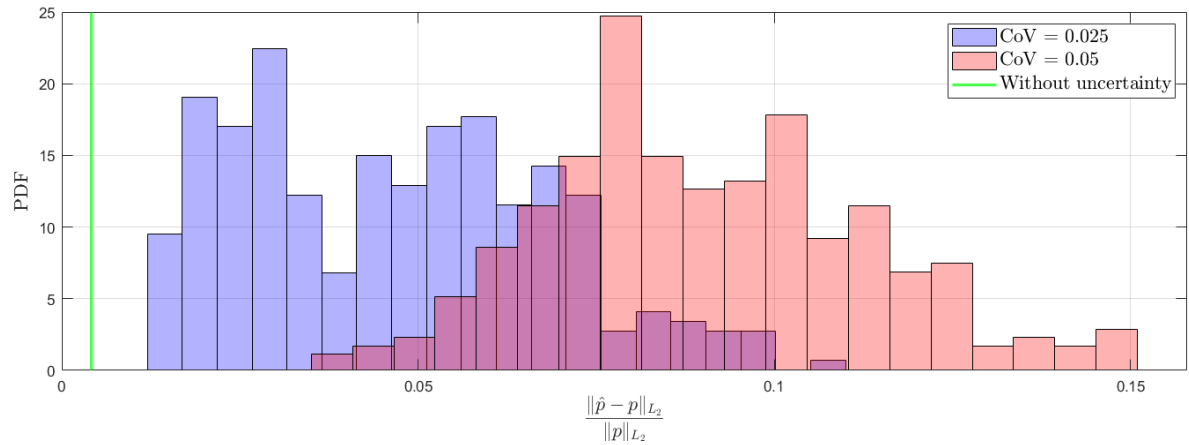

Figure 4.27: *Probability density function of relative L2-norm error of pressure field using directly the strain measurements for constant pressure load.*
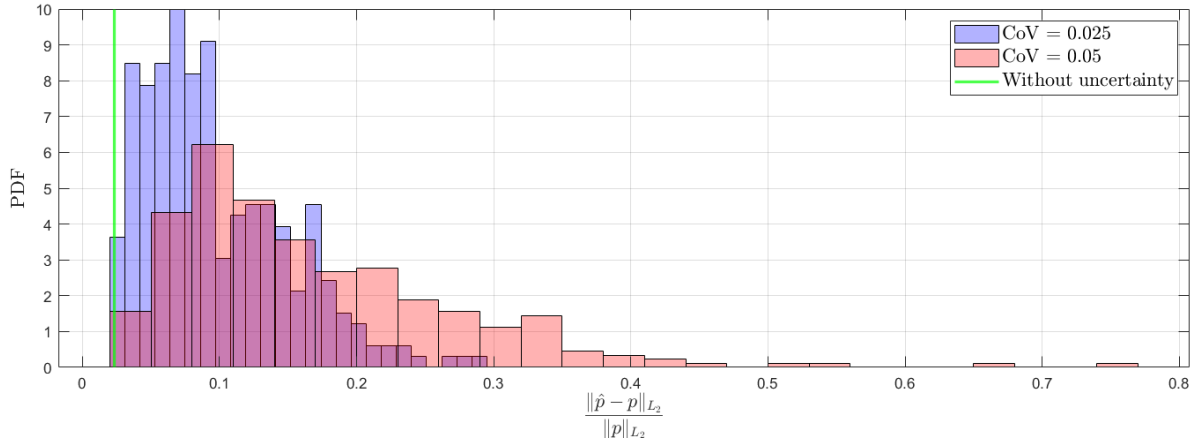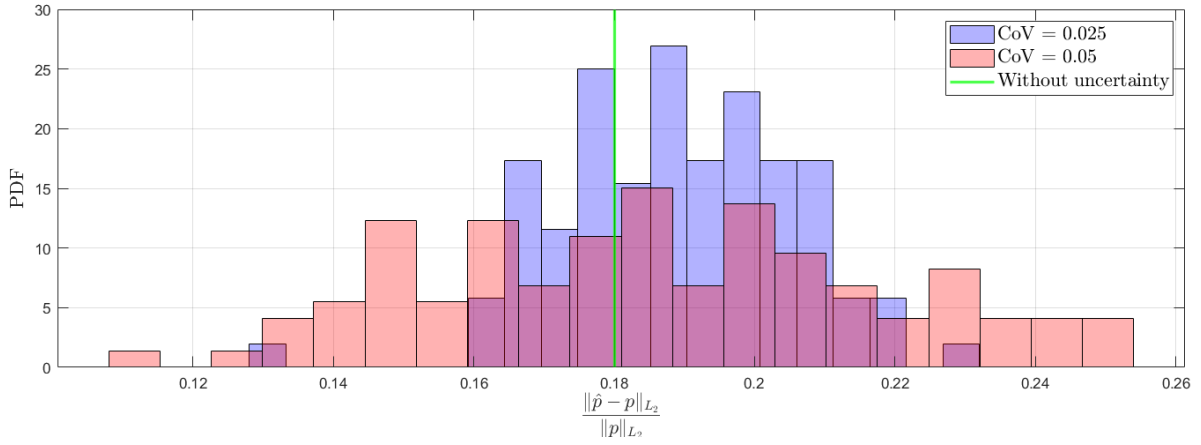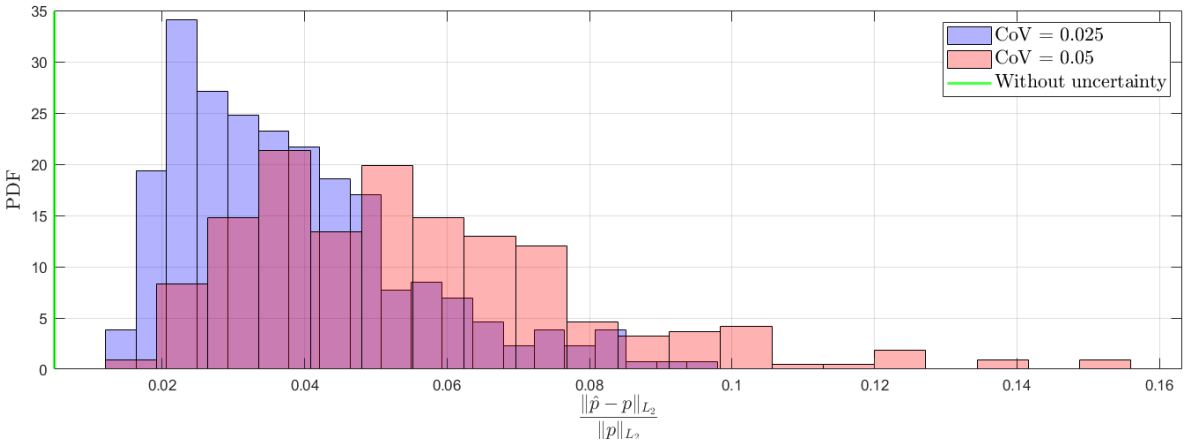
Parabolic pressure
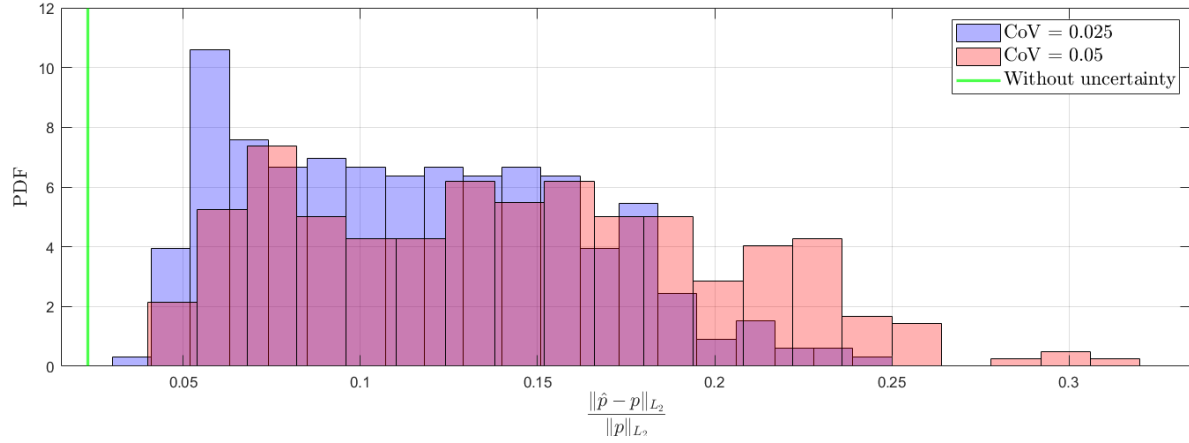
Figure 4.28: *Probability density function of relative L2-norm error of pressure field using MM for parabolic pressure load.*

Figure 4.29: *Probability density function of relative L2-norm error of pressure field using iFEM for parabolic pressure load.*

Figure 4.30: *Probability density function of relative L2-norm error of pressure field using directly the strain measurements for constant pressure load.*

Parabolic - linear pressure

Figure 4.31: *Probability density function of relative L2-norm error of pressure field using MM for parabolic - linear pressure load.*

Figure 4.32: *Probability density function of relative L2-norm error of pressure field using iFEM for parabolic - linear pressure load.*

Figure 4.33: *Probability density function of relative L2-norm error of pressure field using directly the strain measurements for parabolic - linear pressure load.*

4.3 Dynamic analysis

In this section the external dynamic loads applied on the ISTAR demonstrator wing will be reconstructed. The results of this type of analyses have been assessed with two load cases. In both a pressure field has been applied just on the bottom skin with a relatively steep step in time as in Figure 4.34. For the first case a parabolic pressure field has been used, while for the second one a parabolic-linear (as before).
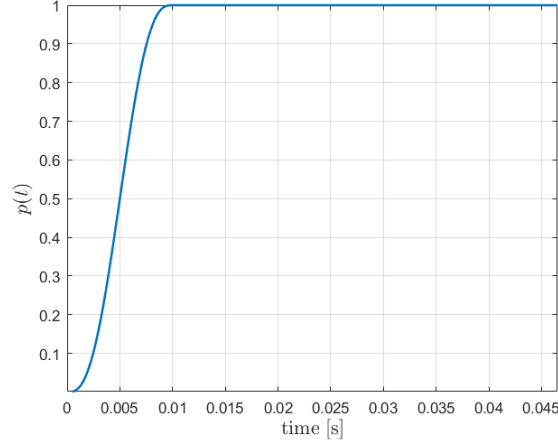
Figure 4.34: *Time-dependency of applied load.*

The pressure field will be reconstructed with different methods. In Section 4.3.1 the static solution is extended to take into account inertia forces. In Section 4.3.2 a more consistent method is used based on deconvolution. Finally, in Section 4.3.3 the load is reconstructed first in frequency domain and then expressed in time domain.

In all cases, the studies have been carried out recovering the pressure field both from the displacements and from the strain measurements.

4.3.1 Correction of inertia forces

In order to reconstruct the elastic deformed shape in time, the same procedure described in the Chapter 3 can be used either for iFEM or the Modal Method since these methods are time independent.

For the load recovery part some modifications need to be introduced compared to the static case. The sensitivity matrix which is computed iteratively solving the FEM model is derived from simple static analyses. For non-stationary cases also the inertia forces should be taken into account in order to correctly obtain the external forces acting on the structure. This can be done realizing that the force vector computed from the sensitivity matrix approach $\widetilde{\boldsymbol{F}}$ for dynamic cases is equal to:

$$\widetilde{\boldsymbol{F}} = \boldsymbol{F} - \boldsymbol{M}\ddot{\boldsymbol{x}} = \boldsymbol{K}\boldsymbol{x}$$

with $\boldsymbol{F}$ the actual load vector due to external forces (the damping has been neglected in the previous equation). The acceleration vector $\ddot{\boldsymbol{x}}$ can be computed from the shape sensing analysis using finite differences as:

$$\ddot{\boldsymbol{x}}(t_i) = \frac{\boldsymbol{x}(t_{i+1}) - 2\boldsymbol{x}(t_i) + \boldsymbol{x}(t_{i-1})}{\Delta t^2}$$

and so the actual load vector due to external forces can be derived from:

$$\boldsymbol{F} = \widetilde{\boldsymbol{F}} + \boldsymbol{M}\ddot{\boldsymbol{x}} \tag{4.37}$$

The main steps to carry out are reported below in more details:

1. First, the pressure field $\boldsymbol{W\rho}$ recovered from the sensitivity matrix approach must be converted to the corresponding load vector. This can be easily carried out as usually done in FEM. That is, expressing the kinematic variables in function of the element degrees of freedom $\boldsymbol{u}^{(e)}$ with the shape function matrix $\boldsymbol{N}$ as:

$$\boldsymbol{u} = \boldsymbol{N}\boldsymbol{u}^{(e)}$$

then:

$$\boldsymbol{f}^{(e)} = \iint_{A^{(e)}} \boldsymbol{N}^\top \boldsymbol{p} \, \mathrm{d}A^{(e)}$$

where:

$$\boldsymbol{u} = \begin{bmatrix} u \\ v \\ w \\ \theta_x \\ \theta_y \\ \theta_z \end{bmatrix} \quad ; \quad \boldsymbol{p} = \begin{bmatrix} 0 \\ 0 \\ p^{(e)} \\ 0 \\ 0 \\ 0 \end{bmatrix}$$

2. The correction of the inertia forces must be introduced adding the term $\boldsymbol{M\ddot{x}}$ to the load vector. This in general is just an approximation (see comments below).

3. Now, it is necessary to recover the pressure field starting from $\boldsymbol{F}$. This is a step which introduces a certain error in the final results. The following strategy has been used. For each element, the corresponding degrees of freedom of the load vector $\boldsymbol{F}$ are extracted. Considering only the translational degrees of freedom (because we are interested in recovering the pressure field which acts only in these dof), a rotation to the local element reference system needs to be carried out. Now the out-of-plane degrees of freedom should be considered and it is assumed that the nodal forces of each node equally contribute to the element pressure (Figure 4.35). As a consequence, the total out-of-plane force acting on the element is simply the sum of forces found at each node divided by 4 times the element area (since each node is shared by 4 elements). Of course, for elements on the boundary small modifications need to be introduced. Dividing by the element area, the (constant) pressure on the element can be recovered.
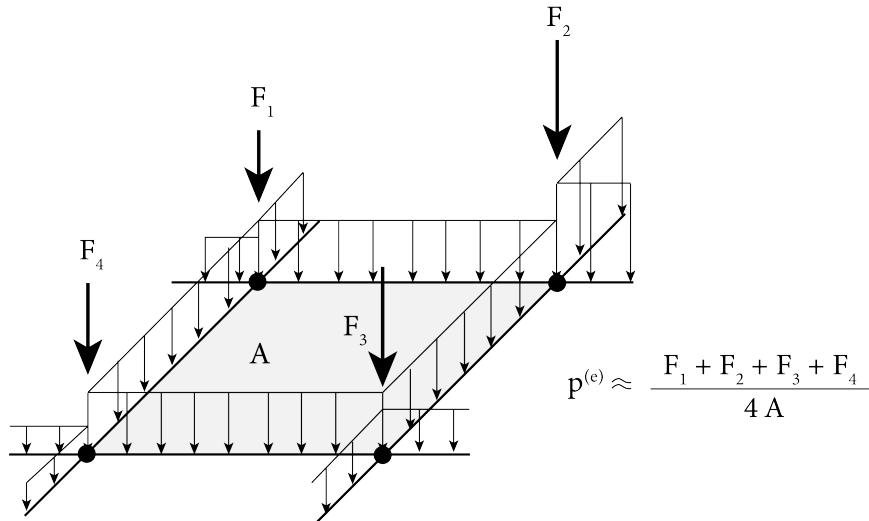
Figure 4.35: *Pressure field reconstruction from load vector.*

As a first example, the parabolic pressure field has been applied. The results have been computed from both MM and iFEM and are reported respectively in Figure 4.36 and Figure 4.37. Note

that, contrarily from before, in this case the L2-norm of the absolute error has been plotted, and not the corresponding relative quantity. This because if either the displacement w or the reference pressure field p become zero, the relative error is not a good indicator anymore.
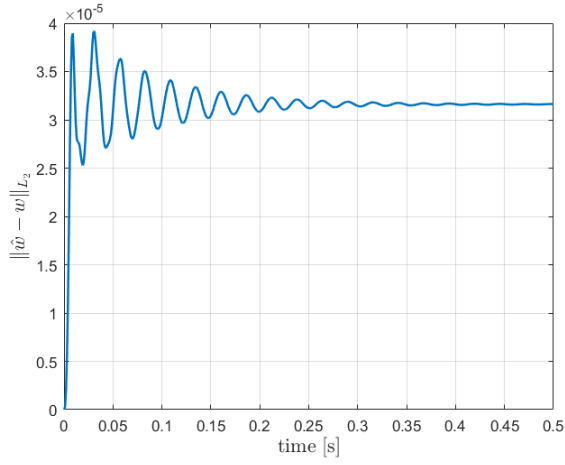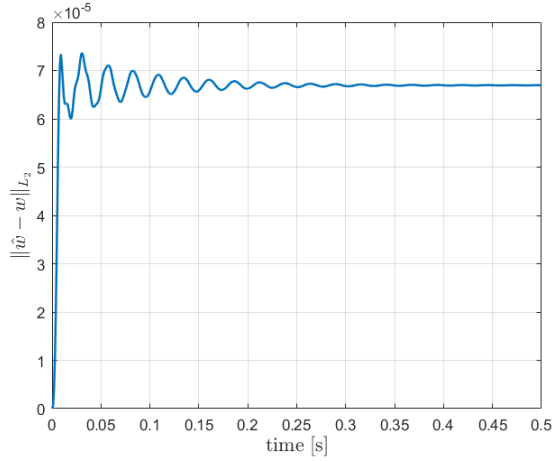

(a) *Error of reconstructed displacement over time.*
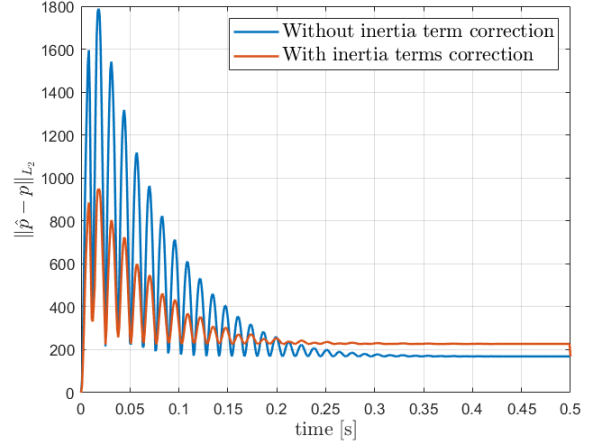
(b) *Error of reconstructed pressure field over time.*

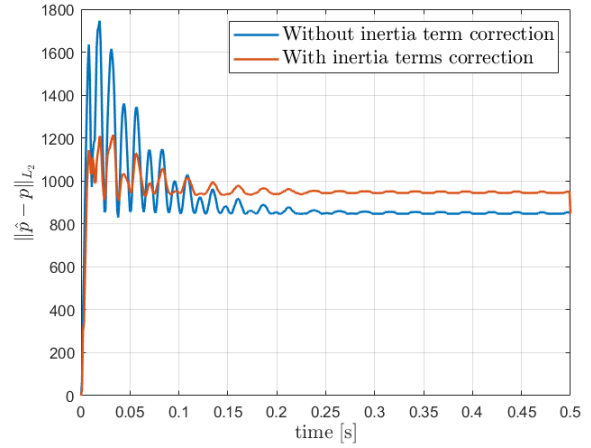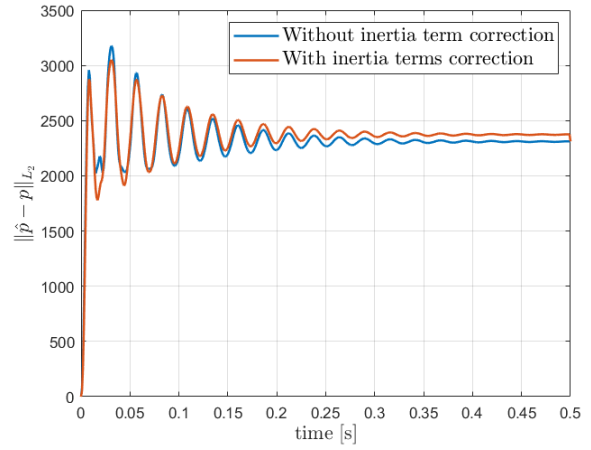Figure 4.36: *Parabolic time-varying pressure reconstruction from MM.*
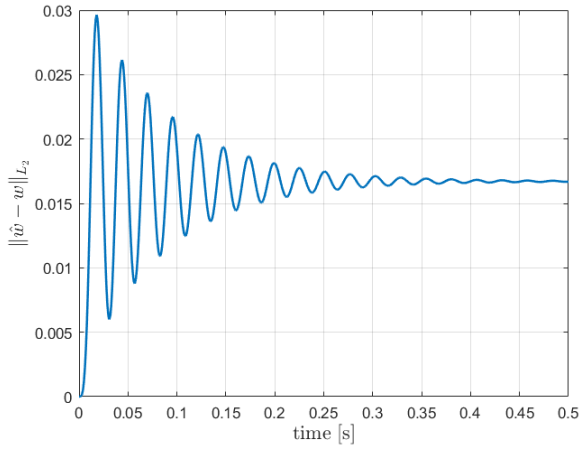
(a) *Error of reconstructed displacement over time.*
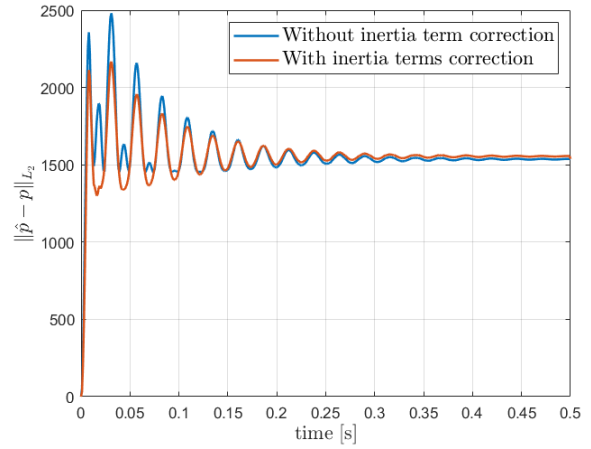
(b) *Error of reconstructed pressure field over time.*

Figure 4.37: *Parabolic time-varying pressure reconstruction from iFEM.*

For the second load case, it has been applied a pressure field parabolically varying along the span and linearly along the chord. The results are shown in Figure 4.38 and Figure 4.39.

As it is possible to see, the error of the resulting pressure field changes during the simulation time. This is due to two reasons:

- The error of the recovered displacement field is not constant. Since it is used as an input for the load sensing study, it affects the final results.

- The inertia forces play a role. They have been corrected as explained before, but in doing so some approximations are introduced.

(a) *Error of reconstructed displacement over time.* (b) *Error of reconstructed pressure field over time.*

Figure 4.38: *Parabolic-linear time-varying pressure reconstruction from MM.*
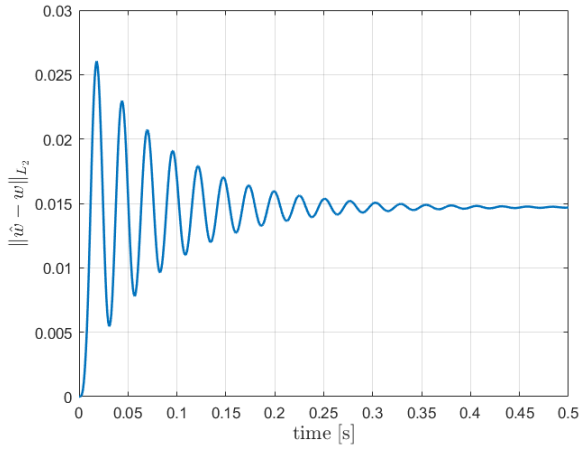
(a) *Error of reconstructed displacement over time.* (b) *Error of reconstructed pressure field over time.*

Figure 4.39: *Parabolic-linear time-varying pressure reconstruction from iFEM.*

Regarding the second point, it is important to realize that the method used is an approximation. In general, the term $\boldsymbol{M\ddot{x}}$ brings to a fully populated vector even if the load is applied only on a certain region of the structural domain (the bottom skin in this case). So, the reconstructed load vector $\boldsymbol{F}$ contains non-null components also where a force is not applied. These components have been neglected in the previous results.

As a final note, the discussion so far was focused on the load reconstruction from the displacement field with the shape sensing study (either MM or iFEM). Computing the load directly from the strain measurements gives results completely analogous to the ones from the MM.

4.3.2 Deconvolution

It is possible to recover the external load for dynamic cases recalling that the response of a linear system can in general be computed with the convolution integral as:

$$\boldsymbol{x}(t) = \int_0^t \boldsymbol{h}(t - \tau)\boldsymbol{f}(\tau)\,\mathrm{d}\tau \tag{4.38}$$

169

with $\boldsymbol{h}$ the impulse response function. This is an approach often used in literature (see for example [22]). Since the displacements $\boldsymbol{x}(t)$ are assumed to be known from the shape sensing study, the aim is to recover the force $\boldsymbol{f}(t)$. Furthermore, it is assumed that the system is fully known, so the impulse response function $\boldsymbol{h}(t)$ can also be computed. By discretizing the convolution integral it is possible to write Eq.(4.38) as [35]:

$$
\begin{bmatrix} \boldsymbol{x}_1 \\ \boldsymbol{x}_2 \\ \vdots \\ \boldsymbol{x}_N \end{bmatrix} = \underbrace{\begin{bmatrix} \boldsymbol{T}_1 & & & \boldsymbol{0} \\ \boldsymbol{T}_2 & \boldsymbol{T}_1 & & \\ \vdots & \vdots & \ddots & \\ \boldsymbol{T}_N & \boldsymbol{T}_{N-1} & \cdots & \boldsymbol{T}_1 \end{bmatrix}}_{\boldsymbol{T}} \begin{bmatrix} \boldsymbol{f}_0 \\ \boldsymbol{f}_1 \\ \vdots \\ \boldsymbol{f}_{N-1} \end{bmatrix}
\tag{4.39}
$$

where the subscripts are referred to the corresponding time step and the matrices $\boldsymbol{T}_k$ are given by:

$$
\boldsymbol{T}_k = \begin{bmatrix} h_{11}(k) & \cdots & h_{1n}(k) \\ \vdots & \vdots & \vdots \\ h_{m1}(k) & \cdots & h_{mn}(k) \end{bmatrix}
\tag{4.40}
$$

where m is the number of measured displacements and n the number of applied forces on the system. Since $\boldsymbol{T}$ is in general rectangular, it is possible to retrieve the force vector by least-squares as:

$$
\boldsymbol{F} = \left(\boldsymbol{T}^\top \boldsymbol{T} \right)^{-1} \boldsymbol{T}^\top \boldsymbol{T}
$$

However, given the high condition number of $\boldsymbol{T}$, this method is usually not advisable. Instead, it is necessary to first regularize the system. In the following, generally the Tikhonov regularization will be used.

Given the fact that the matrix $\boldsymbol{T}$ must contain the system impulse response for each time step, it is possible to understand that it becomes quickly difficult to simulate relatively long simulation times, especially for large systems since the matrix dimensions increase dramatically. Therefore, it might be a good idea to split the whole simulation in smaller intervals and to recover the force in each of them independently. In this way much quicker computations can be achieved. It is important to note however that the intervals should be "chained" together. Looking at Eq.(4.39), the index of the displacement goes from 1 to N, while for the force from 0 to $N-1$. So the intervals should share a time step as illustrated in Figure 4.40.
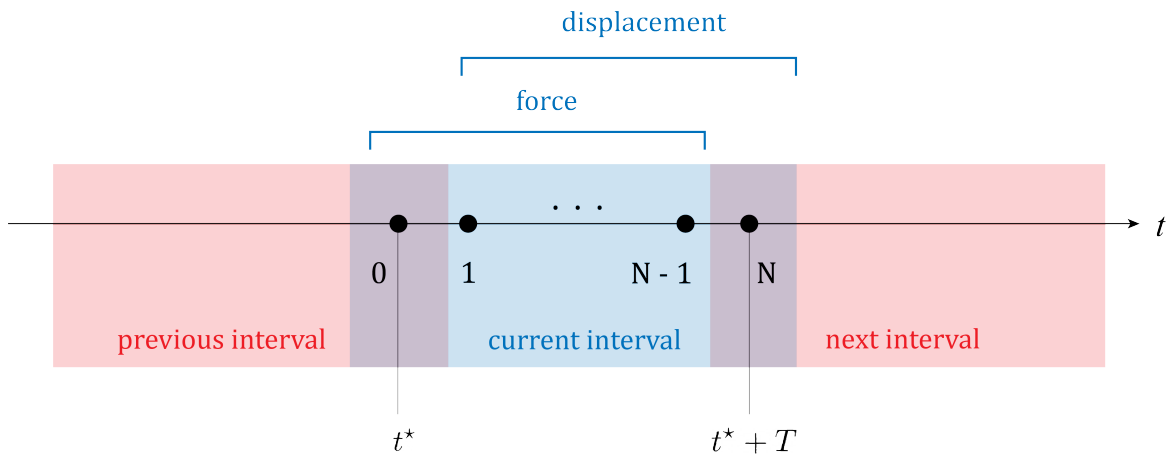
Figure 4.40: *Force reconstruction by deconvolution in shorter time intervals.*

In order to illustrate some features of the proposed approach, consider a simple single degree of freedom system. The system is excited by a simple force, linear in the first part and constant afterwards. The system response in plotted in Figure 4.41.
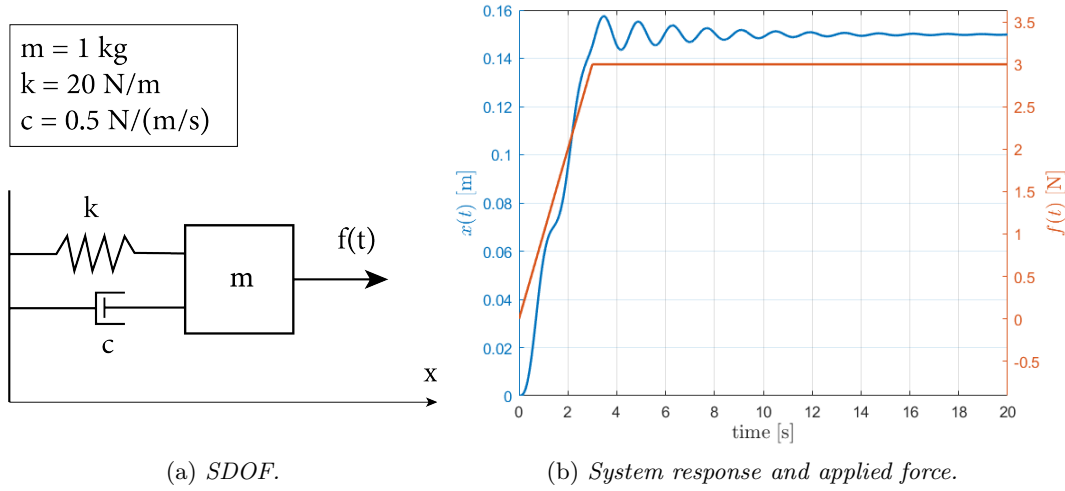

(a) *SDOF.*

(b) *System response and applied force.*

Figure 4.41: *Simulation of a SDOF system.*

Now, consider that $x(t)$ is known. For this simple case, the actual response will be used, but later the results coming from the preliminary shape sensing analysis will become the input. The simulation time as been divided into 10 intervals. Consider the temporal response in $[t^\star, t^\star + T]$, then it is possible to write:

$$x(t) = \int_0^{t^\star} h(t - \tau)f(\tau)\,\mathrm{d}t + \int_{t^\star}^{t^\star + T} h(t - t^\star - \tau)f(\tau)\,\mathrm{d}t \tag{4.41}$$

We are interested just in the second integral, which contains the force $f(t)$ we are looking. At first sight it might be necessary to evaluate also the first convolution integral. This approach however does not help in making the solution more computationally efficient. It is therefore important to realize that this integral corresponds to just the free response of the system, with initial conditions the ones reached at $t = t^\star$. Since the displacement is assumed to be known, it is easy to compute the system free response which will be called $x^\star(t)$ (in the following the free response is computed from modal analysis). As a consequence now it is necessary to solve:

$$x(t) - x^\star(t) = \int_{t^\star}^{t^\star + T} h(t - \tau)f(\tau)\,\mathrm{d}t \tag{4.42}$$

where the free response for this single degree of freedom system is simply given by:

$$x^\star(t) = Ae^{-\zeta\omega_n t}\sin(\omega_d t + \phi) \tag{4.43}$$

with A and ϕ depending on initial displacement and velocity. Eq.(4.42) can be recast in matrix form as:

$$\begin{bmatrix} x_1 - x_1^\star \\ x_2 - x_2^\star \\ \vdots \\ x_N - x_N^\star \end{bmatrix} = \begin{bmatrix} h_1 & & & 0 \\ h_2 & h_1 & & \\ \vdots & \vdots & \ddots & \\ h_N & h_{N-1} & \cdots & h_1 \end{bmatrix} \begin{bmatrix} f_0 \\ f_1 \\ \vdots \\ f_{N-1} \end{bmatrix} \tag{4.44}$$

Solving for $f(t)$ the results of Figure 4.42a have been obtained.

171
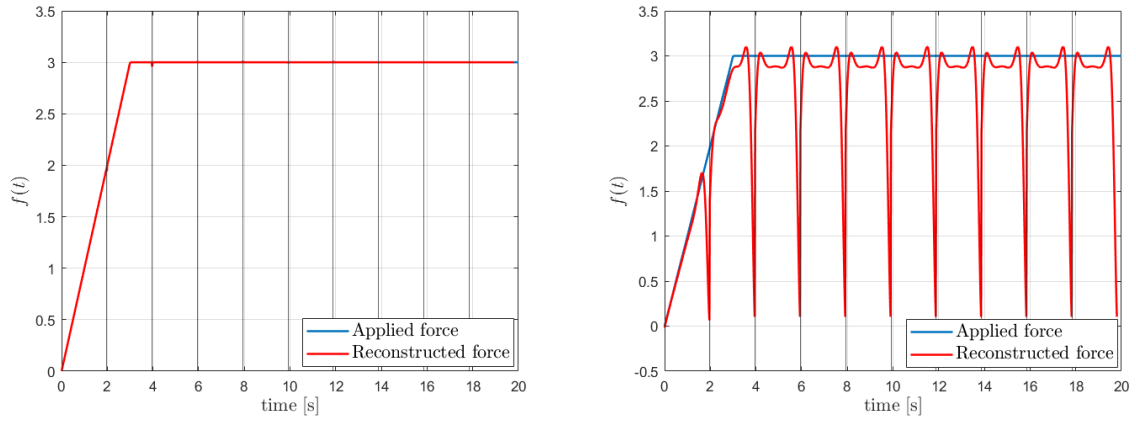
(a) *Force reconstruction for SDOF system without regularization.*

(b) *Force reconstruction for SDOF system with regularization.*

Figure 4.42: *Simulation of a SDOF system.*

It is important to understand what happens when the system of Eq.(4.44) is regularized. So far, no noise or any sort of error was introduced. So no regularization was necessary. However, in general this is a fundamental step since allows to obtain a much more stable solution when the input (that is, the displacement) is affected by some error. For the moment, the system is regularized but no error is introduced. This is done in order to understand how the regularization affects the force reconstruction. The Tikhonov regularization has been applied with $\alpha = 1e-2$. Then, it is possible to obtain the results of Figure 4.42b. The reconstructed force is largely affected the introduction of the regularization, especially at the ends of each time interval in which the simulation has been divided. This effect can be explained realizing that, because of the regularization, the smaller singular values are damped out. These components are also the ones which contribute most to the loads reconstruction at the ends of the intervals. It is possible to see this simply solving the system using the Truncated SVD instead of the Tikhonov regularization. This renders the situation more clear since in this way just some components of the SVD decomposition are used, while using the Tikhonov regularization actually all components have a certain weight, even though the higher ones are filtered out. In Figure 4.43 some cases of load reconstruction are presented, using different values for the truncation parameter of the TSVD. As expected, increasing the truncation parameter k the load reconstruction becomes better and better, even though the error at the ends of the intervals takes longer to drop compared to the one in the middle of the intervals.

(a) $k = 10$

(b) $k = 50$

(c) $k = 90$
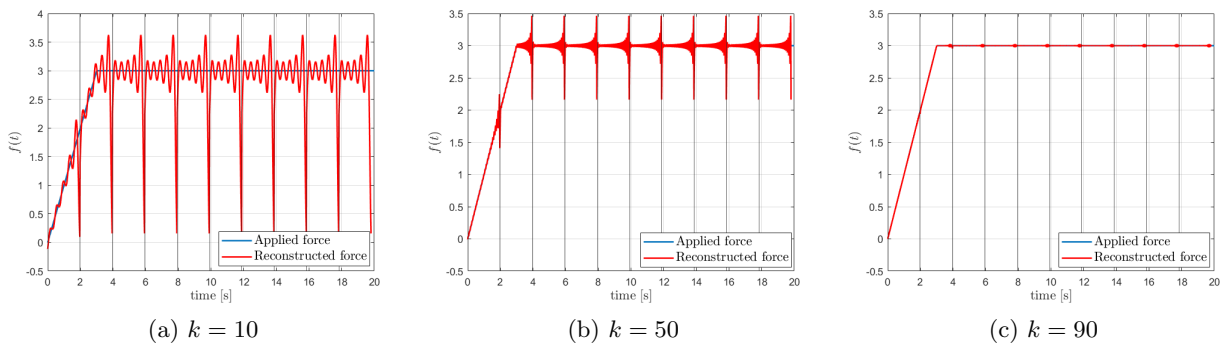
Figure 4.43: *Force reconstruction using TSVD for different truncation levels k.*

A possible approach to solve this problem consists in applying the load reconstruction two times

in parallel. The only difference being that between the two simulations the windows used for the intervals are shifted. This is illustrated in Figure 4.44a and Figure 4.44b, while the final results are in Figure 4.44c.

(a) *Load reconstruction with first time window.*

(b) *Load reconstruction with first time window.*

(c) *Final load reconstruction.*
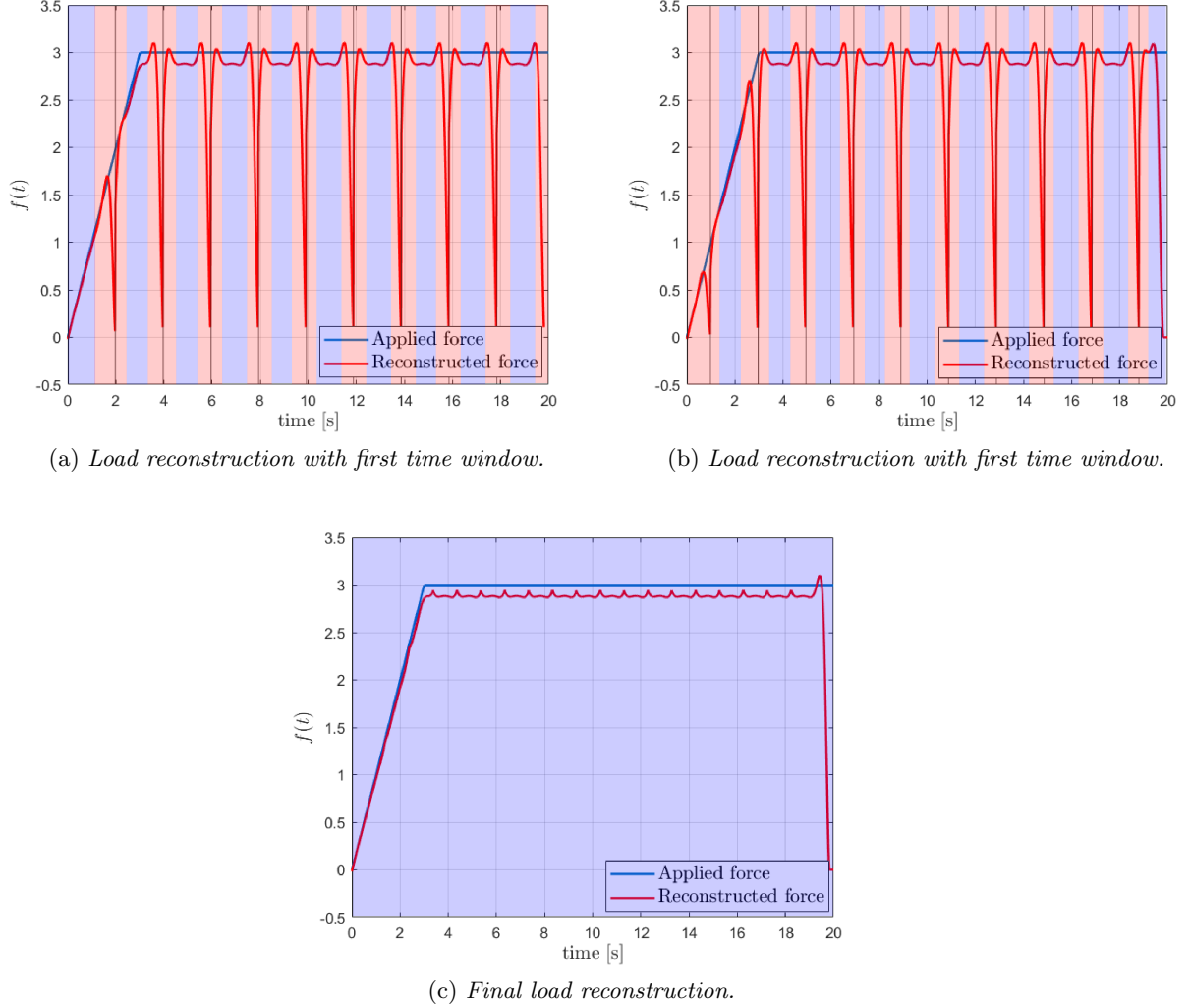
Figure 4.44: *Load reconstruction for SDOF system correcting for regularization errors.*

The same procedure, with limited modifications, can also be applied to multi-degrees of freedom systems. The main difference here consists in the fact that the force is again interpolated in space with the use of the control points as for the static case. Therefore, the deconvolution system becomes:

$$
\begin{bmatrix} \boldsymbol{x}_1 \\ \boldsymbol{x}_2 \\ \vdots \\ \boldsymbol{x}_N \end{bmatrix} = \begin{bmatrix} \boldsymbol{T}_1 & & & \boldsymbol{0} \\ \boldsymbol{T}_2 & \boldsymbol{T}_1 & & \\ \vdots & \vdots & \ddots & \\ \boldsymbol{T}_N & \boldsymbol{T}_{N-1} & \cdots & \boldsymbol{T}_1 \end{bmatrix} \begin{bmatrix} \boldsymbol{W} & & & \\ & \boldsymbol{W} & & \\ & & \ddots & \\ & & & \boldsymbol{W} \end{bmatrix} \begin{bmatrix} \boldsymbol{\rho}_0 \\ \boldsymbol{\rho}_1 \\ \vdots \\ \boldsymbol{\rho}_{N-1} \end{bmatrix} \tag{4.45}
$$

Considering again the ISTAR wing demonstrator, here just the load case with parabolic pressure along the span (and constant along the chord) will be studied. Furthermore, only two intervals will be used to illustrate some results. Using the Modal Method for the shape sensing part, which delivers a very good approximation of the displacement field (compare to Figure 4.36a), the error of the resulting pressure field over time is shown in Figure 4.45 for the two time windows used and for the final result merging the previous ones.

(a) *Pressure error with first time window.*

(b) *Pressure error with second time window.*

(c) *Final pressure error over time.*

(d) *L-curve and regularization parameter choice.*
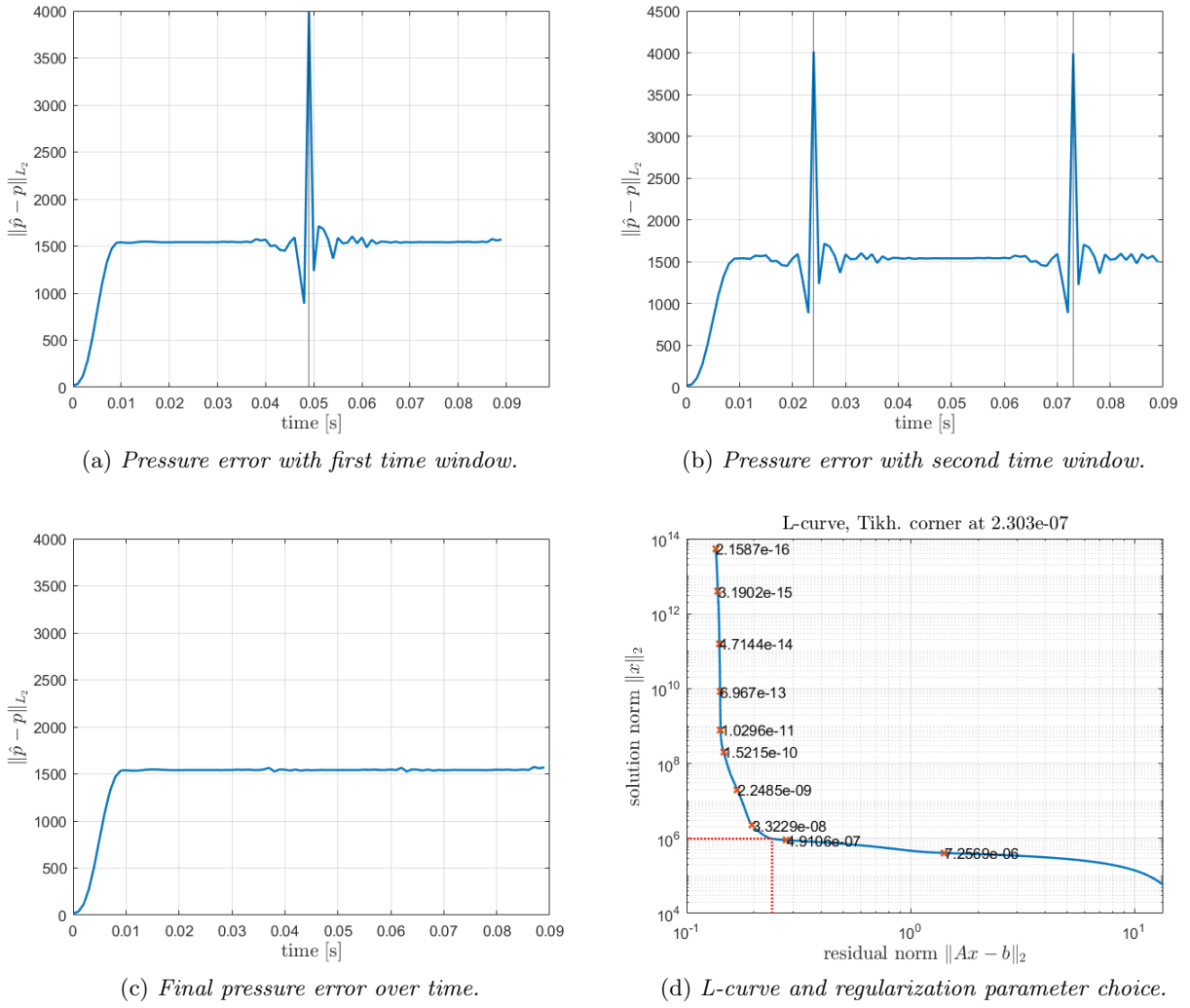
Figure 4.45: *Load reconstruction for ISTAR wing under parabolic pressure load from MM shape sensing results.*
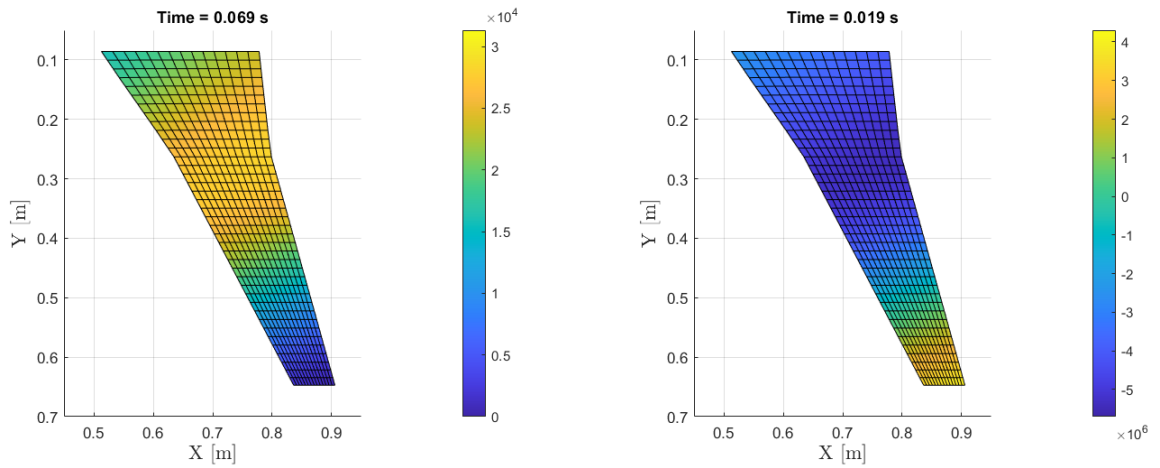
(a) *Steady-state pressure field reconstruction using MM.* (b) *Steady-state pressure field reconstruction using iFEM.*

Figure 4.46: *Deconvolution from shape sensing results.*

Compared to Figure 4.36b, now the error is much more stable, without the oscillations which appeared before. However, it is also clear that in magnitude it is much larger. This is due to

the fact that near the root the pressure field is not well reconstructed, as it is possible to see in Figure 4.46a.

The situation is even worse using the shape sensing results from iFEM (Figure 4.46b) where the parabolic distribution of the pressure is mostly lost. Furthermore, in Figure 4.45d it is shown the corresponding L-curve (which is almost the same for both the intervals): the corner in not precisely well defined and this brings some uncertainty in the choice of a suitable regularization parameter. Iteratively retrieving the load for different regularization parameters taken around the corner, it has been seen that this affects quite significantly the load reconstruction.

From this small set of simulations a few conclusions can be drawn:

- Dividing the simulation in smaller time intervals seems to be an efficient way to recover the load, without the need to carry out the deconvolution on the whole time domain in a single step.

- The deconvolution allows to correctly take into consideration the inertia forces, in a way much more consistent compared to the one used in the previous Section 4.3.1. However the results are acceptable only if the displacement field is really accurate, as for example using MM for this particular study case.

- If the error coming from the shape sensing study is larger, as it is happening for iFEM in this study case, the resulting pressure field can be very different from the real one and completely erroneous.

- Some uncertainty in the choice of the regularization parameter has been observed. This will be even more significant in the experimental results presented in Chapter 5.

The difficulties related to the last point can be seen as due to the fact that quite a few control points have been placed on the wing surface. This means that there is a (relatively) large number of free variables on which the pressure field depends. Following the same reasoning which has motivated Section 4.2.2, it is possible to think to reduce the number of independent variables. So, instead of applying the so-called *inverse distance weighting*, now it has been decided to represent the load as a simple polynomial expansion of order N in the form:

$$p(y) = \begin{bmatrix} y^N & y^{N-1} & \cdots & y & 1 \end{bmatrix} \begin{bmatrix} a_N \\ a_{N-1} \\ \vdots \\ a_1 \\ a_0 \end{bmatrix} \tag{4.46}$$

Introducing the dependence just on the wing span coordinate (y axis in this case), the weighting matrix becomes:

$$\boldsymbol{W} = \begin{bmatrix} y_1^N & y_1^{N-1} & \cdots & y_1 & 1 \\ y_2^N & y_2^{N-1} & \cdots & y_2 & 1 \\ \vdots & \vdots & \vdots & \vdots & \vdots \\ y_n^N & y_n^{N-1} & \cdots & y_n & 1 \end{bmatrix} \tag{4.47}$$

with n is the number of applied forces on the system. This new weighting matrix should be now substituted in the discrete form of the convolution integral (Eq.(4.45)), reported here again for convenienece:

$$\begin{bmatrix} \boldsymbol{x}_1 \\ \boldsymbol{x}_2 \\ \vdots \\ \boldsymbol{x}_N \end{bmatrix} = \begin{bmatrix} \boldsymbol{T}_1 & & & \boldsymbol{0} \\ \boldsymbol{T}_2 & \boldsymbol{T}_1 & & \\ \vdots & \vdots & \ddots & \\ \boldsymbol{T}_N & \boldsymbol{T}_{N-1} & \cdots & \boldsymbol{T}_1 \end{bmatrix} \begin{bmatrix} \boldsymbol{W} & & & \\ & \boldsymbol{W} & & \\ & & \ddots & \\ & & & \boldsymbol{W} \end{bmatrix} \begin{bmatrix} \boldsymbol{a}_0 \\ \boldsymbol{a}_1 \\ \vdots \\ \boldsymbol{a}_{N-1} \end{bmatrix} \tag{4.48}$$

In this way at each time step the pressure field is uniquely defined by just $N + 1$ free variables. Considering again the wing under the parabolic pressure load and using a quadratic polynomial (so $N = 2$), the new L-curve which can be obtained is represented in Figure 4.47a. Compared to before, now the possible values of the regularization parameter are much more well defined by the points of maximum curvature. On the other hand, it is also clear that two choices would be possible. In order to pick the right one, a general knowledge of the load is required. In any case, once the right corner is identified, the corresponding range for the regularization parameter can be set so automating the process and discarding the wrong corner of the L-curve without any user intervention. In this case, the solution we are looking for is the one in the corner highlighted in Figure 4.47a.
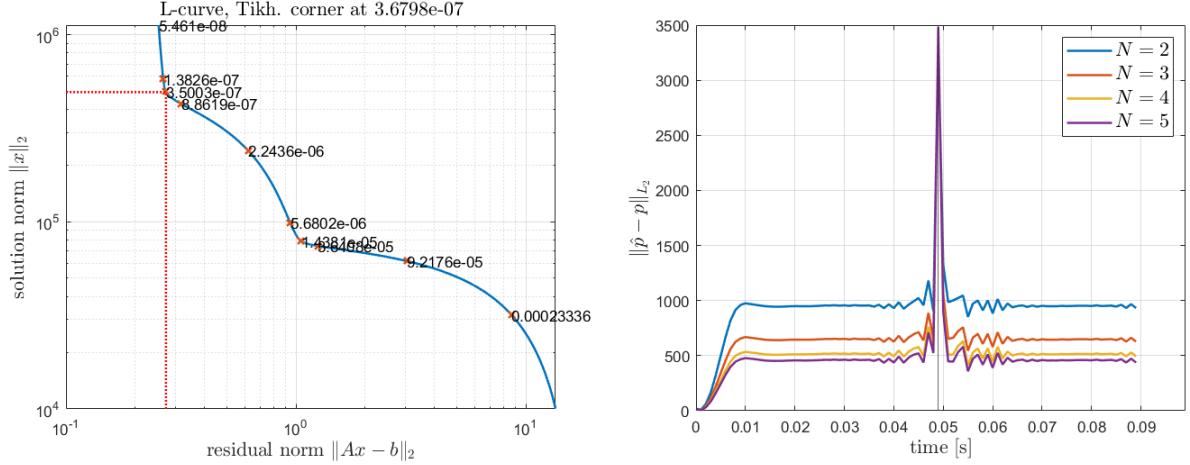
(a) *L-curve using a quadratic polynomial interpolation.* (b) *Error of pressure field for different orders of polynomial interpolation.*

Figure 4.47: *Deconvolution from shape sensing results using low order polynomial interpolations. Note that the error occurring at the ends of the intervals has not been corrected.*

Consider again just two intervals, without getting rid of the solution near the edges since this would involve just repeating the simulation on a different window, which would not add anything to the discussion. In Figure 4.47b the error of the resulting pressure field is shown: increasing the polynomial order N a better representation of the pressure field can be obtained. However, as it is possible to guess, this also brings to a similar problem encountered before employing the control points. For example, using $N = 10$ the L-curve becomes as in Figure 4.48: the choice of a good regularization parameter becomes more difficult and uncertain.

So far the load reconstruction with deconvolution has been obtained from the full displacement field of the shape sensing study. Using directly the strain measurements $\boldsymbol{\varepsilon}^{\varepsilon}$ a completely similar procedure can be followed, so Eq.(4.45) becomes:

$$\begin{bmatrix} \boldsymbol{\varepsilon}_1 \\ \boldsymbol{\varepsilon}_2 \\ \vdots \\ \boldsymbol{\varepsilon}_N \end{bmatrix} = \begin{bmatrix} \boldsymbol{T}_1 & & & \boldsymbol{0} \\ \boldsymbol{T}_2 & \boldsymbol{T}_1 & & \\ \vdots & \vdots & \ddots & \\ \boldsymbol{T}_N & \boldsymbol{T}_{N-1} & \cdots & \boldsymbol{T}_1 \end{bmatrix} \begin{bmatrix} \boldsymbol{W} & & & \\ & \boldsymbol{W} & & \\ & & \ddots & \\ & & & \boldsymbol{W} \end{bmatrix} \begin{bmatrix} \boldsymbol{\rho}_0 \\ \boldsymbol{\rho}_1 \\ \vdots \\ \boldsymbol{\rho}_{N-1} \end{bmatrix} \tag{4.49}$$
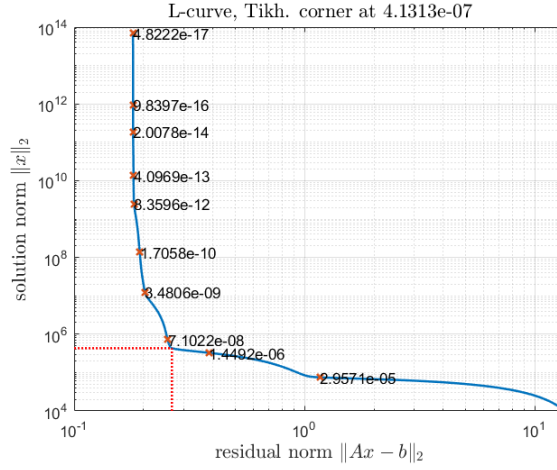
Figure 4.48: *Difficulty in choosing the regularization parameter for higher order polynomial interpolation.*

where now the matrices $\boldsymbol{T}_k$ contain the strain responses due to an external impulse. Furthermore, note that even though now we are directly using the strain responses, also the displacement is needed in order to limit the simulation on smaller intervals as done before. In the following, the displacement field will be computed using the Modal Method. The load distribution has been recovered directly from the pseudo-inverse since it has been observed that the choice of the regularization parameter from the L-curve was not clear. Two interpolation schemes were considered:

- Using the control point interpolation, the results obtained are not satisfactory as shows Figure 4.49a.

- Using a polynomial interpolation, there is an improvement but still, compared to before, the results obtained are worse as shown in Figure 4.49b.
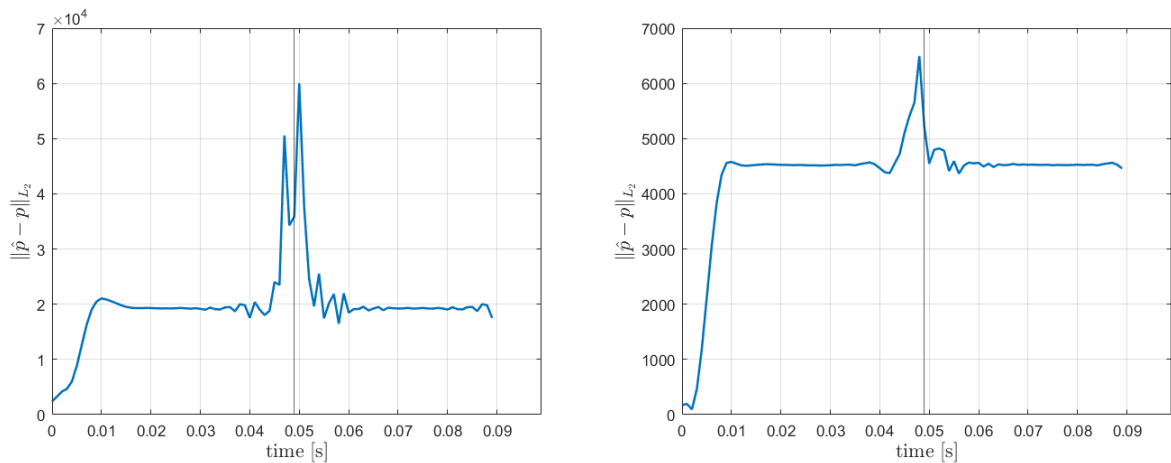
(a) *Pressure field error using inverse distance weighting interpolation.*

(b) *Pressure field error using polynomial interpolation.*

Figure 4.49: *Load reconstruction with deconvolution from strain measurements. Note that the error occurring at the ends of the intervals has not been corrected.*

4.3.3 Frequency domain method

The analysis carried out so far has been done exclusively in time domain. In this section the aim is to analyze how a frequency domain reconstruction would perform for our study cases. These types of methods have been extensively studied in literature. See for example [62].

The most common approach consists in realizing that, in the frequency domain, the measured displacement field (obtained from the shape sensing study) and the external forces can be related knowing the frequency response function matrix $\boldsymbol{H}(\omega)$ as:

$$\boldsymbol{X}(\omega) = \boldsymbol{H}(\omega)\boldsymbol{F}(\omega) \quad \Rightarrow \quad \boldsymbol{F}(\omega) = \big(\boldsymbol{H}(\omega)\big)^{-1}\boldsymbol{X}(\omega) \tag{4.50}$$

with $\boldsymbol{X}(\omega)$ the Discrete Fourier Transform of the displacement field, $\boldsymbol{F}(\omega)$ the one of the external loads and finally for MIMO systems (as the ones we will be analyzing) the frequency response function matrix given by:

$$\boldsymbol{H}(\omega) = \begin{bmatrix} H_{11}(\omega) & H_{12}(\omega) & \cdots & H_{1n}(\omega) \\ H_{21}(\omega) & H_{22}(\omega) & \cdots & H_{2n}(\omega \\ \vdots & \vdots & & \vdots \\ H_{n1}(\omega) & H_{m2}(\omega) & \cdots & H_{mn}(\omega) \end{bmatrix} \tag{4.51}$$

with n the number of external forces and m the number of measured responses.

At first sight, it might be possible to be tempted to express the inverse of $\boldsymbol{H}(\omega)$ as a function of the structural matrices, that is:

$$\boldsymbol{H}(\omega)^{-1} = -\omega^2 \boldsymbol{M} + i\omega \boldsymbol{C} + \boldsymbol{K} \tag{4.52}$$

in this way, the external forces could be computed directly from a simple matrix multiplication with no need to invert $\boldsymbol{H}(\omega)$ at every frequency step. However it has been seen that this approach does not allow to take into account the presence of errors in $\boldsymbol{X}(\omega)$ and in general a poor force estimation would be obtained also for negligible errors in the displacement field. Intuitively, this would correspond in statics to multiplying the stiffness matrix with the displacement field. And, as it has been pointed out before, this approach does not yield good results.

A better approach consists in expressing directly $\boldsymbol{H}(\omega)$. In this way, computing its inverse in order to retrieve the external loads, it is possible to apply the same framework of the Tikhonov regularization used before. This will allow to take into account errors in the displacement field and in finding a regularized solution.
In the following the frequency response function matrix $\boldsymbol{H}(\omega)$ has been computed from modal analysis. Expressing the modal coordinates as $\boldsymbol{r}(t) = \boldsymbol{R}(\omega)e^{i\omega t}$ and the modal forces in the same manner $\boldsymbol{f}_m(t) = \boldsymbol{F}_m(\omega)e^{i\omega t}$, then:

$$\boldsymbol{R}(\omega) = \underbrace{\begin{bmatrix} \dfrac{1}{-\omega^2 + 2\zeta_1 \omega \omega_n^{(1)} + (\omega_n^{(1)})^2} & & \\ & \ddots & \\ & & \dfrac{1}{-\omega^2 + 2\zeta_N \omega \omega_n^{(N)} + (\omega_n^{(N)})^2} \end{bmatrix}}_{\boldsymbol{\Sigma}} \boldsymbol{F}_m(\omega) \tag{4.53}$$

with ζ_i the modal damping of the ith mode and $\omega_n^{(i)}$ its natural frequency. Going back to physical coordinates:

$$\boldsymbol{X}(\omega) = \bar{\boldsymbol{\Phi}}\boldsymbol{R}(\omega) = \bar{\boldsymbol{\Phi}}\boldsymbol{\Sigma}\boldsymbol{F}_m(\omega) = \underbrace{\bar{\boldsymbol{\Phi}}\boldsymbol{\Sigma}\widetilde{\boldsymbol{\Phi}}^T}_{\boldsymbol{H}(\omega)} \widetilde{\boldsymbol{F}}(\omega) \tag{4.54}$$

where $\bar{\bullet}$ stands for the degrees of freedom related to the measured m responses, while $\widetilde{\bullet}$ for the n excited input degrees of freedom. In both cases, this implies just taking the specified rows of the correspondent matrix.

Now, it is possible to regularize the system:

$$X(\omega) = H(\omega)\widetilde{F}(\omega) \tag{4.55}$$

in order to compute $\widetilde{F}(\omega)$. Similarly as done before, it has been noticed that it is beneficial to interpolate the load vector. In the following, only a polynomial interpolation will be used and so Eq.(4.55) becomes:

$$X(\omega) = H(\omega)W a(\omega) \tag{4.56}$$

with $a(\omega)$ the vector containing the (unknown) polynomial coefficients.

A few observations can be done as follows:

- Eq.(4.56) is in general computationally cheaper compared to the convolution matrix.

- Differently from before, the quantity which can be retrieved now it directly the load vector $\widetilde{F}(\omega)$ and not the pressure on each element. Therefore, in order to retrieve the external pressure field, it is necessary to carry out a similar operation to the one illustrated in Section 4.3.1.

- The main difference consists in the fact that the system needs to be inverted for every frequency under consideration. Before, on the contrary, the solution on an entire time interval was obtained.

Once $a(\omega)$ has been retrieved, the load vector can be obtained as $\widetilde{F}(\omega) = W a(\omega)$ and the Inverse Fourier Transform can be exploited to obtain again the external forces as a function of time. The whole procedure is briefly summarized in Figure 4.50.
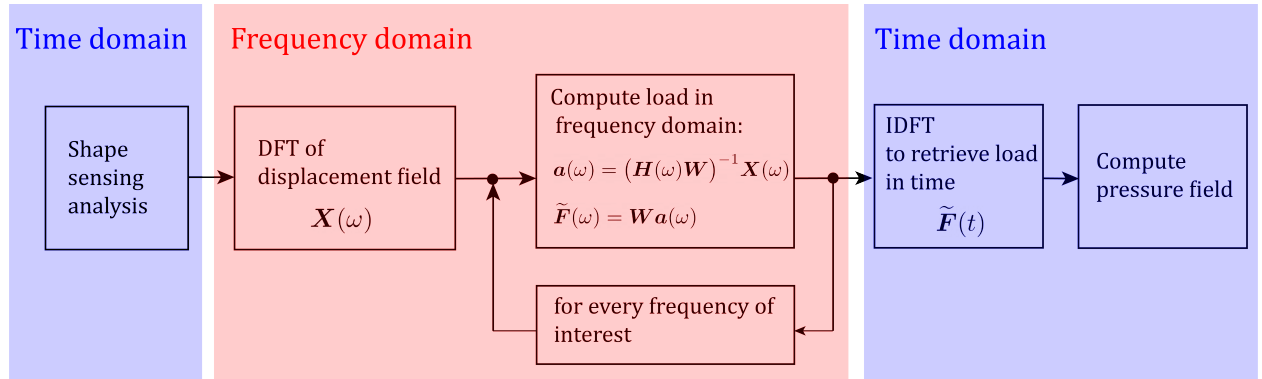
Figure 4.50: *Work-flow for load reconstruction in frequency domain.*

This method has been applied to recover the parabolic pressure distribution on the ISTAR wing. Similarly as done for the deconvolution approach, also here a cubic distribution is chosen along the span. However, now locating a suitable choice for the regularization parameter using the L-curve is much more challenging. The L-curve has to be computed for every frequency of interest and its shape changes significantly. Some results are reported below in Figure 4.51.
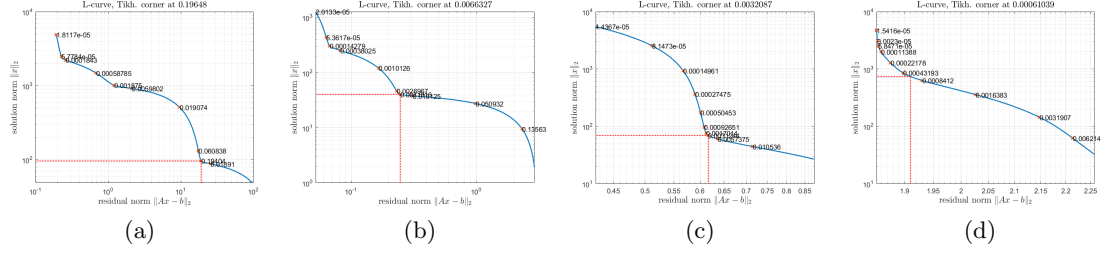
Figure 4.51: *Examples of L-curves for some frequencies.*

This renders the choice of a suitable regularization parameter relatively hard and difficult to automate. Also for this reason, the error of the resulting pressure field which has been obtained now is more noisy. Choosing the corner of the L-curve corresponding to the lowest regularization parameter, the error and the steady-state load distribution are shown in Figure 4.52.

(a) *Error pressure field.*

(b) *Distribution of nodal forces along z at steady state.*
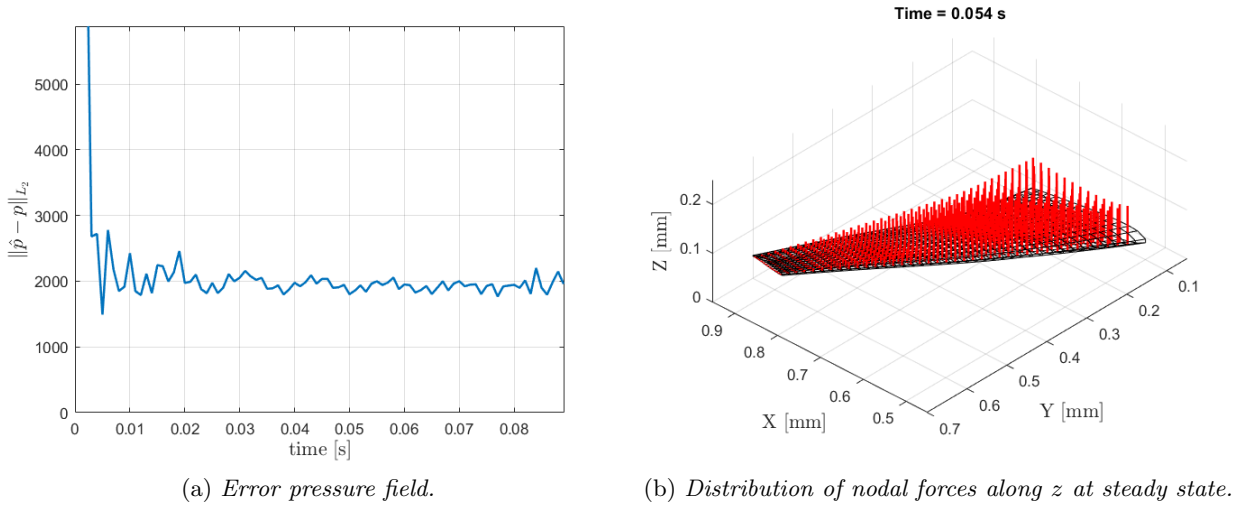
Figure 4.52: *Pressure field reconstruction for ISTAR demonstrator wing with frequency domain methods.*

A similar approach in frequency domain can also be carried out starting directly from the strain measurements. In this case it is possible to write:

$$\boldsymbol{\varepsilon}^{\varepsilon}(\omega) = \boldsymbol{\Psi}\boldsymbol{\Sigma}\widetilde{\boldsymbol{\Phi}}\widetilde{\boldsymbol{F}}(\omega) \qquad (4.57)$$

with $\boldsymbol{\varepsilon}^{\varepsilon}(\omega)$ the strain measurements in frequency domain and $\boldsymbol{\Psi}$ the corresponding strain mode shapes. In order to recover the load it has been simply computed the pseudo-inverse since, as before, a polynomial interpolation has been used, rendering the condition number of the system to invert relatively low. However, the results obtained turn out to be not satisfactory, with errors in general higher than the ones obtained from the displacement field as in Figure 4.53, where a quadratic polynomial interpolation was employed.
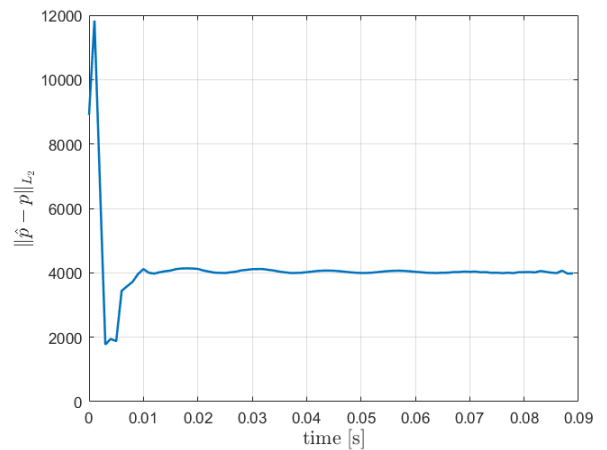
Figure 4.53: *Error pressure field for load reconstruction from strain measurements using the frequency domain method.*

4.4   Summary of the chapter

In this chapter the external load acting on the structure has been recovered under the form of a pressure field.

For static applications a technique based on the superposition of "primitive" loads has been chosen. The building block of the load reconstruction is represented by a constant pressure applied on the element domain to which it is associated a column of the so-called sensitivity matrix. In this context, using a preliminary interpolation of the pressure field it is possible to obtain better results compared to the ones available in literature. The method has been assessed using as input both the strain measurements and the full displacement field from the shape sensing study. The first approach gave the best results, even though it is quite sensitive to noise and uncertainties.

The reconstruction of time-varying loads has been carried out with three different methods. The first one, based on correcting the static solution, is able to give a reasonable estimate of the load only for relatively low dynamics. The other two are more consistent, but suffer from higher errors especially due to the difficulty encountered in the regularization of the system.

Chapter 5

Experimental validation

In this chapter some results regarding the experimental activity are presented. The primary aim has been to apply the methods studied numerically in the previous chapters and use them on a real study case. In doing that, a cantilever beam has been taken into consideration. Its simplicity has allowed to easily study different configurations and to monitor the main structural responses.

The chapter is structured as follows:

- In Section 5.1 the study case is presented together with the applied sensors.

- Section 5.2 applies the beam model to reconstruct simple bending deflections of the beam under concentrated loads.

- It has been observed that the flexibility of the beam root plays a major role in the deflection reconstruction and a clamped boundary condition might deliver unconservative results. Therefore, in Section 5.3 it is reviewed a method to estimate the rotational stiffness at the beam root and it is assessed for the study case.

- In Section 5.4 the beam has been subjected to a combined bending and torsional load case. The deflection will be retrieved with the beam model, with iFEM and with MM.

- Finally, in Section 5.5 some dynamic tests have been carried out with the aim to retrieve the external load both in space and in time with the methods presented in Chapter 4.

5.1 Geometry and sensors

The geometry of the structure used for the experimental set-up is shown in Figure 5.1: it consists of a simple prismatic aluminum beam, thin-walled with rectangular cross-section. The beam root is welded to a square aluminium plate as shown in Figure 5.2.

More details about the structure can be also found in another study [69].
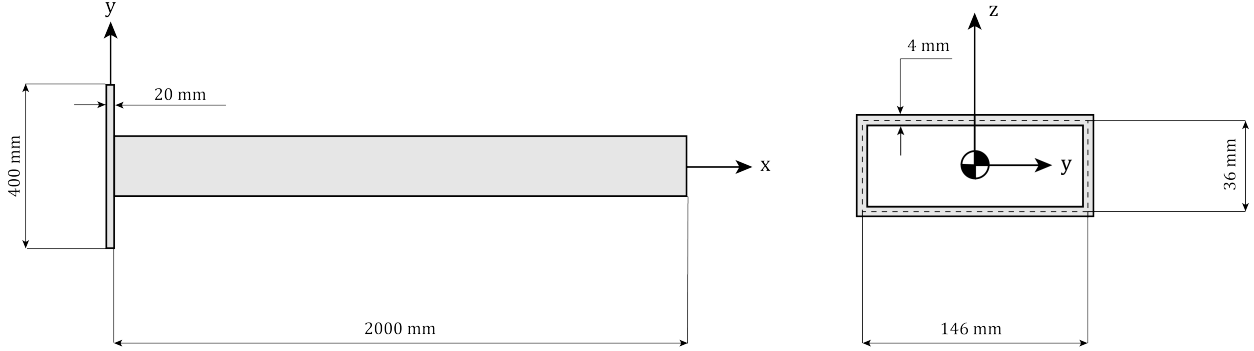
Figure 5.1: *Beam geometry and dimensions.*
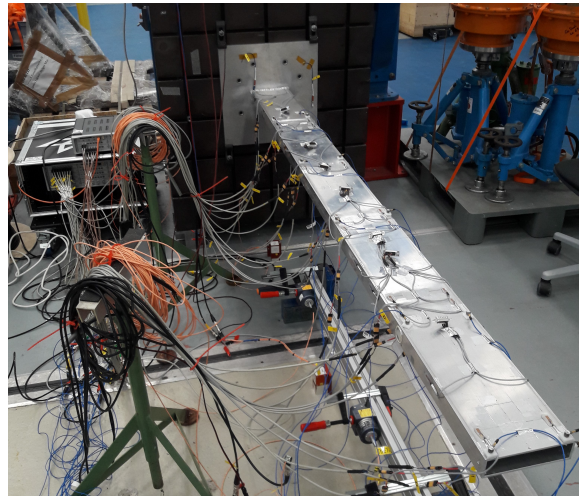
Figure 5.2: *Picture of experimental set-up.*

The beam has been instrumented with several sensors (Figure 5.3):

- 24 axial strain gauges.

- 3 strain gauges oriented with 45° w.r.t. the beam axis.

- 3 angle sensors, each one measures both bending and torsion angles.

- 3 wire sensors measuring the beam deflection.

- 1 load cell to measure the load applied.

The sensors (with the exception of the strain gauges, automatically calibrated by `Simcenter Testlab`) have been calibrated as reported in the Table 5.1. Some examples of the measurements carried out in order to estimate the sensors sensitivity is reported in Figure 5.4 and Figure 5.5 for respectively the wire sensors and the load cell.

All the measurements have been acquired with the help of `Simcenter Testlab`. The beam geometry given to the software is reported in Figure 5.6.

183
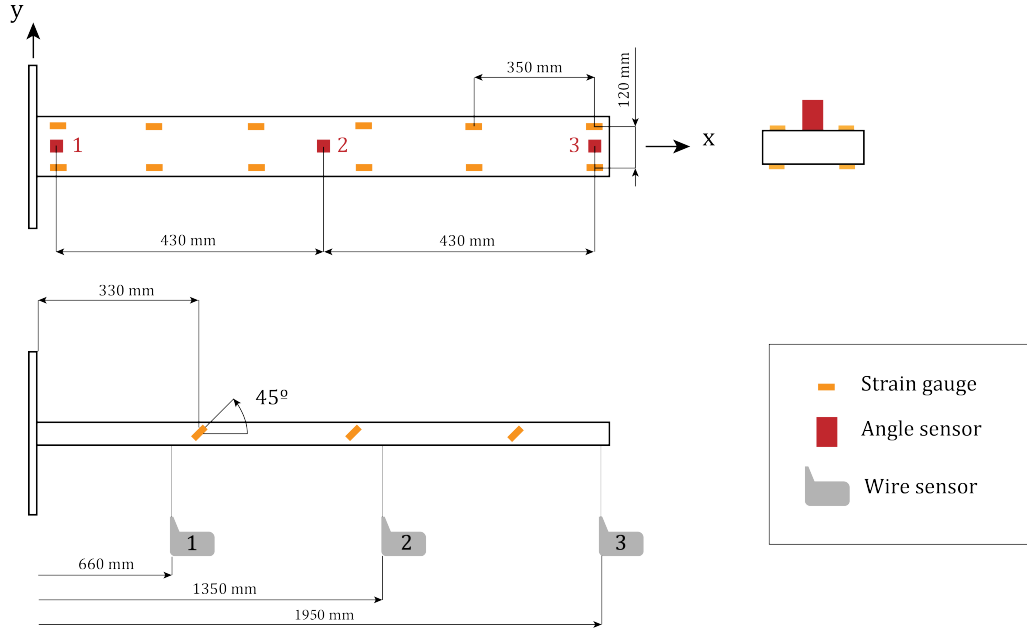
Figure 5.3: *Sensors installed on the beam.*
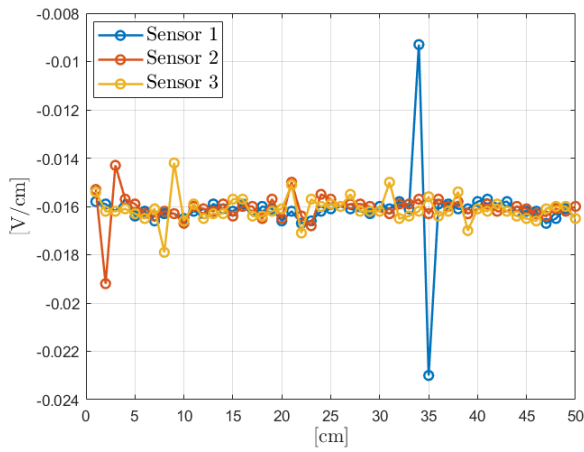
Figure 5.4: *Measurement of wire-sensor sensitivity.*
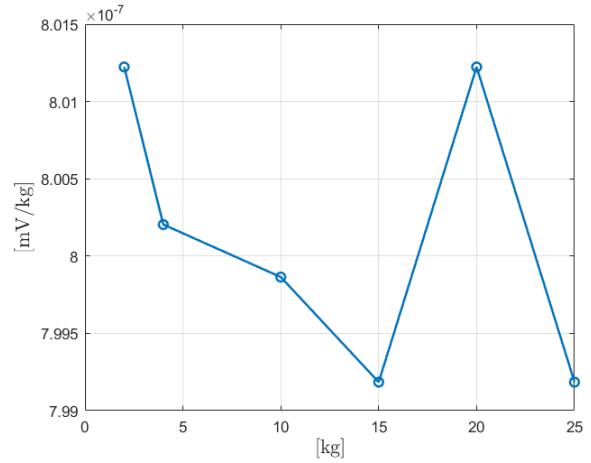
Figure 5.5: *Measurement of load cell sensitivity.*
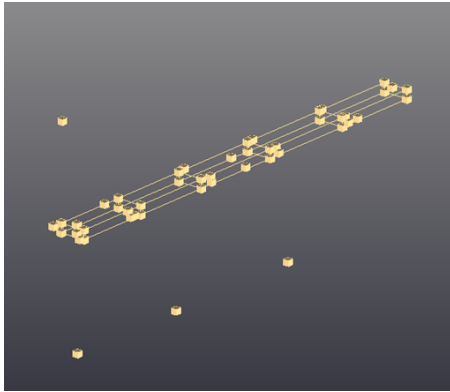
Figure 5.6: *Geometry of aluminum beam in* `Simcenter Testlab`.

Sensor		Sensitivity
Wire sensor	# 1	$-0.0162\,mV/cm$
	# 2	$-0.0161\,mV/cm$
	# 3	$-0.0161\,mV/cm$
Load cell		$8.0015e-07\,mV/kg$
Angle sensor	# 1 bending	$308.58\,mV/°$
	# 1 torsion	$-$
Angle sensor	# 2 bending	$307.81\,mV/°$
	# 2 torsion	$306.27\,mV/°$
Angle sensor	# 3 bending	$309.36\,mV/°$
	# 3 torsion	$310.9\,mV/°$

Table 5.1: *Sensor sensitivities.*

5.2 Pure bending tests with beam model

5.2.1 Tip load

The beam has been loaded with incrementally higher loads at the tip, pulling it upwards. The axial strain history and the extracted values are shown in Figure 5.7. Five different steps have been considered, with an increment of the tip load from the first to the last one.

(a) *Strain gauge history.*

(b) *Strain values along beam span for the identified 5 steps.*
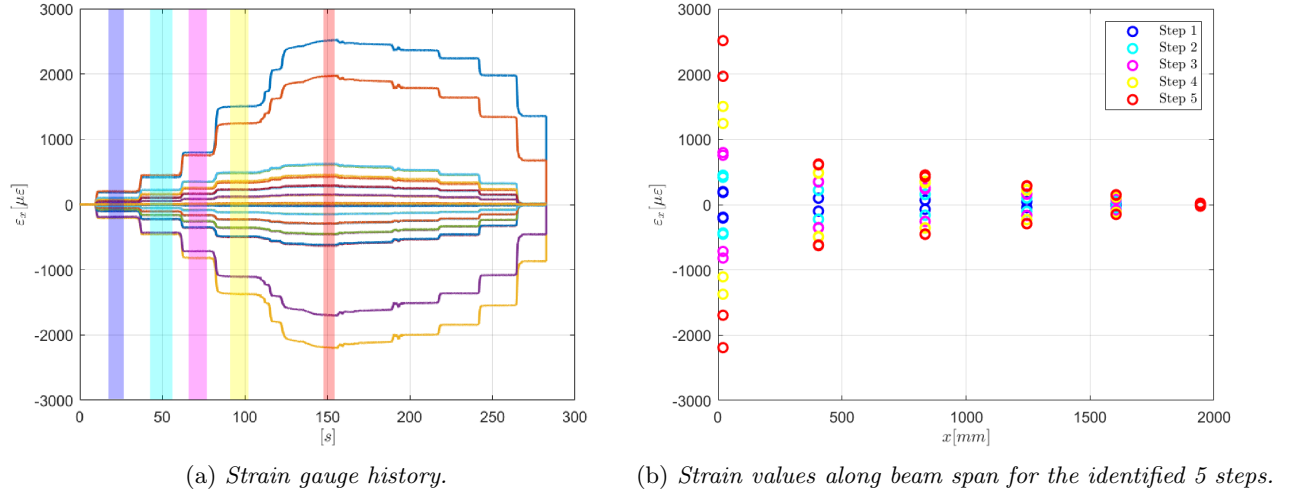
Figure 5.7: *Axial strain gauge values for tip load case.*

All the strain gauges show a linear behaviour along the beam span (Figure 5.7b), apart from the ones at the root where a much higher value is observed. This effect is closely related to the clamping of the beam, as it has also seen from the corresponding FE model (Figure 5.8).

(a) *Root of the beam.*

(b) *Axial strain from FE model.*
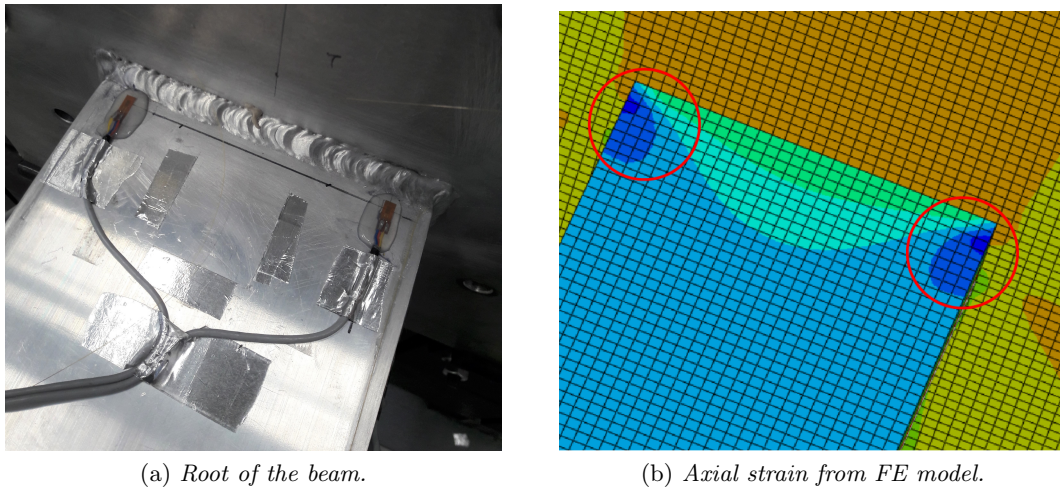
Figure 5.8: *Higher strains occurring at the beam root.*

Since this is a local effect, not related to the beam behaviour, it has been decided not to consider these values in the following shape sensing analysis. As a consequence, the beam has been discretized with two inverse elements. The results for the first step are shown in Figure 5.9, where the iFEM results, the direct FEM and the experimental ones are shown. For the other steps completely analogous results have been observed. The direct FEM results have been

obtained applying a tip load with magnitude equal to the corresponding value of the load cell. Furthermore, in the FE model the beam root has been completely clamped.

(a) *Vertical deflection.*

(b) *Rotation.*
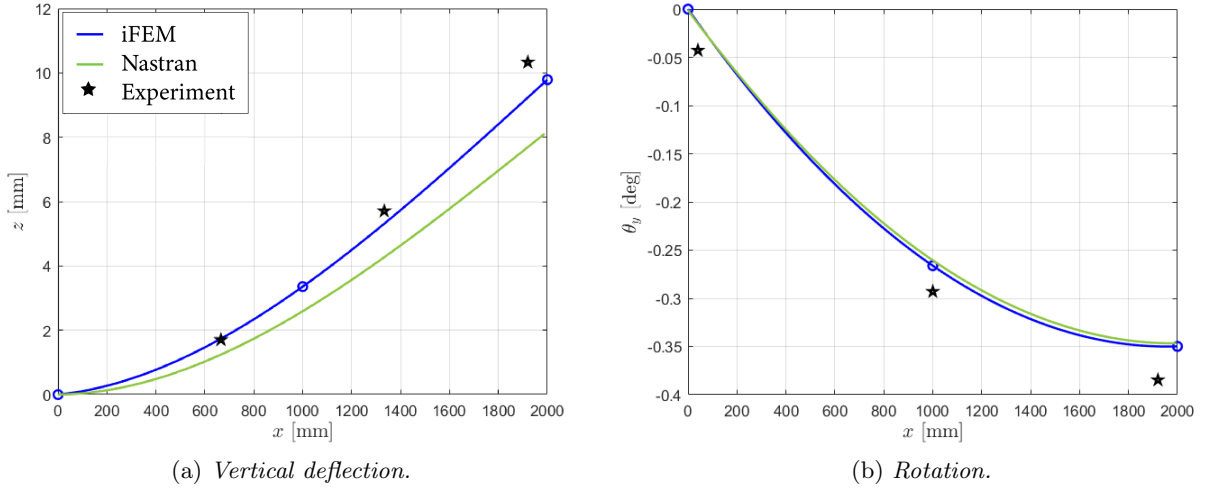
Figure 5.9: *Deflection for step 1.*

As it is possible to see, even though the iFEM results agree well with the `Nastran` ones, the experimental values show a discrepancy common to all the cases analysed. This is deemed to be due to the fact that the beam root is not exactly clamped, but shows some stiffness, also because of the attachment with the square aluminium plate. Simplifying this attachment with a rotational spring attached to the beam root, it is possible to estimate this stiffness from the experimental rotational angle measurements close to the root. Since the load applied is known, the rotational stiffness has been computed simply dividing the internal moment at the beam root by the measured angle and the graph of Figure 5.10b has been obtained. For low values of the load, the rotational stiffness seems to be relatively constant, but decreases significantly for higher loads.
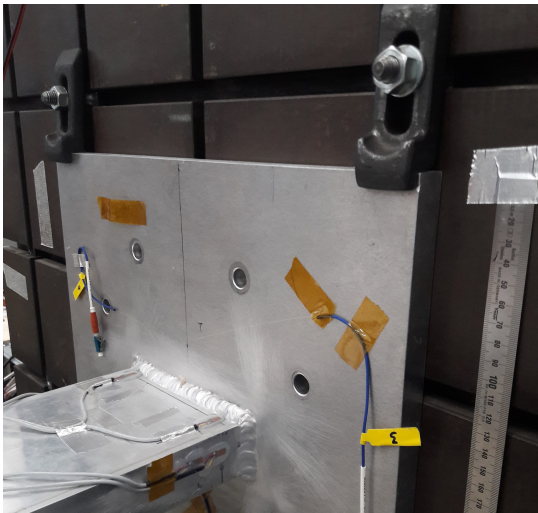
(a) *Clamping of the beam.*
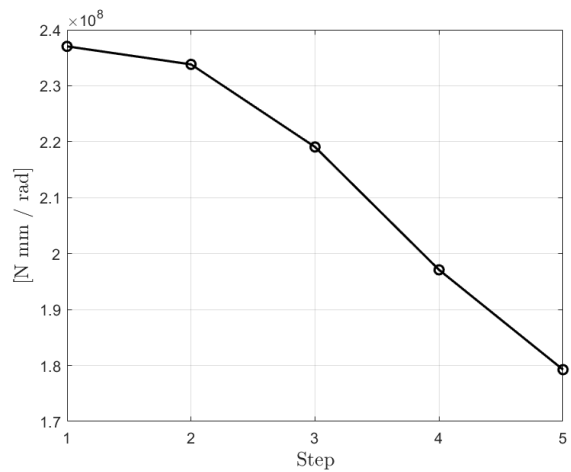
(b) *Estimated rotational stiffness.*

Figure 5.10: *Study of the rotational stiffness at the beam root.*

Using the experimental value of the rotational spring stiffness at the root, it is possible to correct the results given by iFEM. In particular, the following approach can be followed:

1. The internal moment can be written as:

$$M_y(x) = -x \sum_i P_{yi} + \sum_i P_{yi} r_i \tag{5.1}$$

So, interpolating the axial strain as:

$$\varepsilon_x(x, y, z) = \varepsilon_{10} + y(\varepsilon_{20} + \varepsilon_{21}x) + z(\varepsilon_{30} + \varepsilon_{31}x) \tag{5.2}$$

the loads can be obtained as:

$$\sum_i P_{zi} r_i = EI_{z0}\varepsilon_{20}$$
$$\sum P_{zi} = -EI_{z0}\varepsilon_{21} \tag{5.3}$$

2. Considering the element at the beam root, the initial angle θ_{y0} can be computed as:

$$\theta_{y0} = \frac{\sum_i P_{zi} r_i}{k_{rot}} \tag{5.4}$$

3. At this point, iFEM can be carried out where, however, it is important to set as boundary condition for θ_y the value of θ_{y0}. This can be done dividing the degrees of freedom in prescribed and not, as follows:

$$\begin{bmatrix} \boldsymbol{K}_{uu} & \boldsymbol{K}_{uk} \\ \boldsymbol{K}_{ku} & \boldsymbol{K}_{kk} \end{bmatrix} \begin{bmatrix} \boldsymbol{u}_u \\ \boldsymbol{u}_k \end{bmatrix} = \begin{bmatrix} \boldsymbol{f}_u \\ \boldsymbol{f}_k \end{bmatrix} \tag{5.5}$$

$$\Rightarrow \quad \boldsymbol{u}_u = \boldsymbol{K}_{uu}^{-1}(\boldsymbol{f}_u - \boldsymbol{K}_{uk}\boldsymbol{u}_k)$$

where, at the beam root:

$$\boldsymbol{u}_k = \begin{bmatrix} 0 & 0 & 0 & \theta_{y0} & 0 \end{bmatrix}^\top$$

(a) *Vertical deflection.*
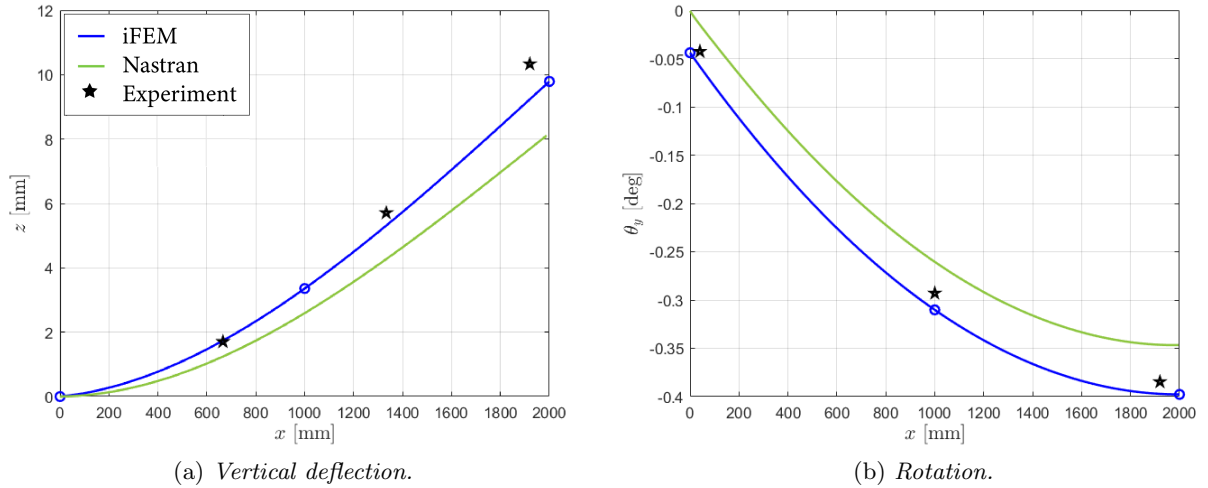
(b) *Rotation.*

Figure 5.11: *Corrected deflection for step 1.*

The results obtained with the beam model from iFEM can also be compared to the ones coming from the Modal Method, also using a beam model, together with a rotational spring at the beam root.

(a) *Mode shapes of beam with elastic root.*

(b) *Deflection with Modal Method.*
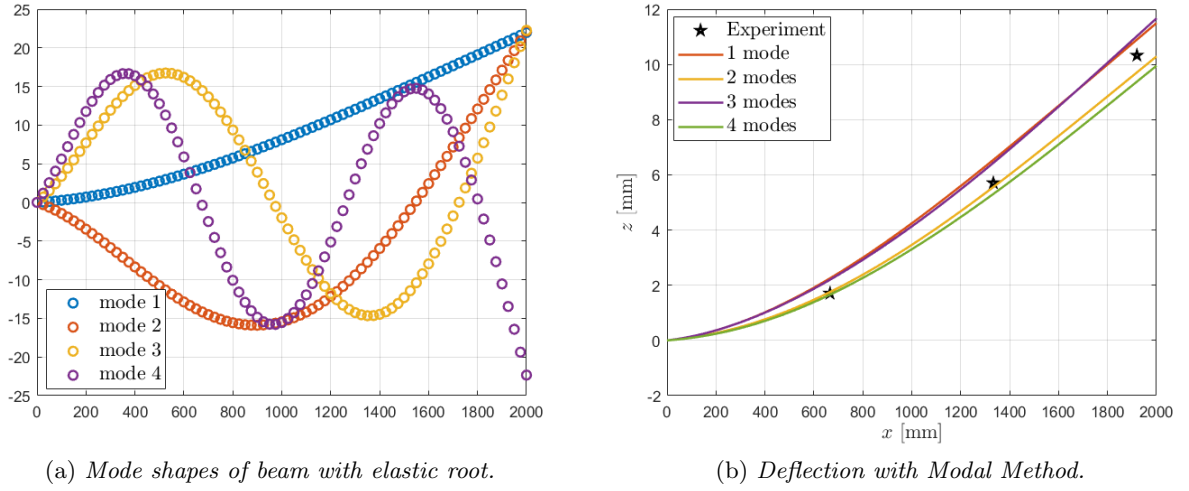
Figure 5.12: *Beam model for Modal Method.*

The obtained deflection, again for just for the first step, is shown in Figure 5.12. Overall, it is close to the measured values, even if increasing the number of mode shapes does not stabilize the deflection which keeps "oscillating" around the experimental measurements.

5.2.2 Two concentrated loads

The beam has been loaded by two concentrated loads, respectively at the tip and at the mid-span. The loading device used allows to equally distribute the load between the two points (Figure 5.13). Also in this case the beam has been loaded in different steps (Figure 5.14). Just the results for the first step will be shown, since for the others analogous observations hold.

The beam deflection has been recovered in two ways. First, two inverse beam elements have been used. Since the loads are applied at their nodes, this should be the optimal configuration. Then, a single element is used but taking advantage from the formulation based on distributed loads. That is, from the experimental measurements the axial strain is interpolated over the beam span as:

$$\varepsilon_x(x, z) = \varepsilon_{10} + z\big(\varepsilon_{20} + x\varepsilon_{21} + x^2\varepsilon_{22}\big) \quad (5.6)$$

and then is sampled at (x_1, x_2) as specified in Chapter 2. In particular, in this case it was considered $(x_1 = L/4, x_2 = L)$, with L the beam length. The results obtained have been corrected with the root rotational stiffness and are reported in Figure 5.15.
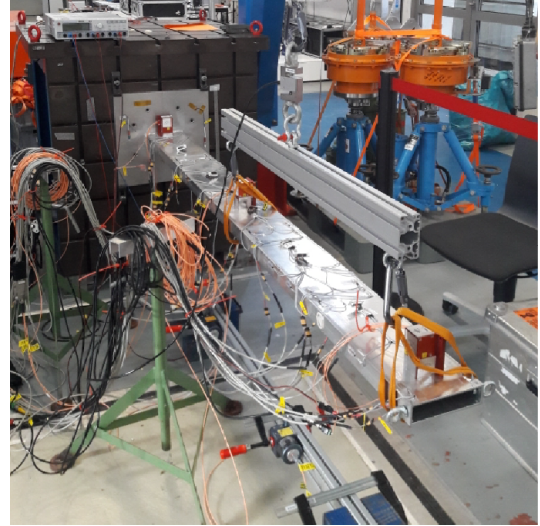
Figure 5.13: *Beam loaded at mid-span and tip.*

(a) *Strain gauge history.*

(b) *Strain values along beam span for the identified 5 steps.*
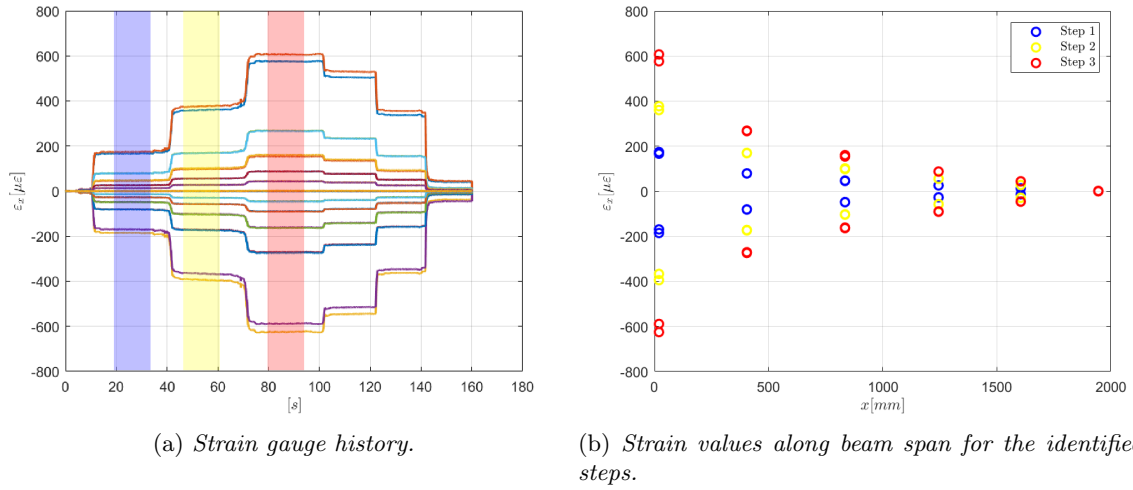
Figure 5.14: *Strain values along beam span for the identified 3 steps.*

In general there is a close correspondence between the deformations found with the two approaches, meaning that for an unknown loading condition it is safe to act following the method presented for distributed loads which, as a consequence, represents the most general case that can be used to model unknown loading conditions with good results.
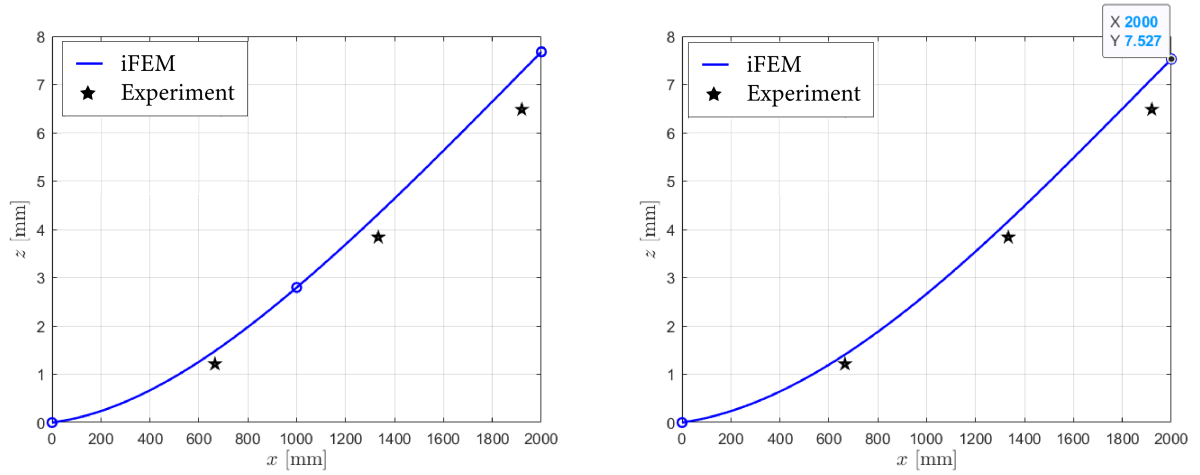
(a) *Vertical deflection obtain with 2 inverse elements.*

(b) *Vertical deflection obtained with a single inverse element.*

Figure 5.15: *Comparison between experimental and reconstructed deflections for the beam loaded by two concentrated forces.*

5.3 Assessment of root stiffness estimation

Since the root rotational stiffness plays an important role in the deflection reconstruction of a beam, it is important to obtain an estimate of it in case it is not possible to directly obtain the initial rotation angle as done before. A simple method has been proposed by [27] and in this section the aim is to apply it in order to gain confidence in its applications for shape sensing purposes.

Considering a freely vibrating mechanical system, the equation of motion can be written as:

$$-\omega^2 \boldsymbol{M}\boldsymbol{x} + \boldsymbol{K}\boldsymbol{x} = \boldsymbol{f} \tag{5.7}$$

The degrees of freedom of the structure can be divided in the ones at the boundary ($\boldsymbol{x}_b$, subjected to the reaction forces $\boldsymbol{f}_b$) and the ones within the structure ($\boldsymbol{x}_r$, where no external force is applied). Let $\boldsymbol{D} = \boldsymbol{K} - \omega^2 \boldsymbol{M}$, then the system can be rewritten as:

$$\begin{bmatrix} \boldsymbol{D}_{bb} & \boldsymbol{D}_{br} \\ \boldsymbol{D}_{br}^\top & \boldsymbol{D}_{rr} \end{bmatrix} \begin{bmatrix} \boldsymbol{x}_b \\ \boldsymbol{x}_r \end{bmatrix} = \begin{bmatrix} \boldsymbol{f}_b \\ \boldsymbol{0} \end{bmatrix} \tag{5.8}$$

And combining the two equations:

$$\left(\boldsymbol{D}_{bb} - \boldsymbol{D}_{br} \boldsymbol{D}_{rr}^{-1} \boldsymbol{D}_{br}^\top \right) \boldsymbol{x}_b = \boldsymbol{f}_b \tag{5.9}$$

At the same time the (unknown) reaction forces can be expressed from the boundary stiffness matrix $\boldsymbol{K}_b$:

$$\boldsymbol{K}_b \boldsymbol{x}_b = -\boldsymbol{f}_b \tag{5.10}$$

And so summing Eq.(5.10) and Eq.(5.9):

$$\left(\boldsymbol{K}_b + \boldsymbol{D}_{bb} - \boldsymbol{D}_{br} \boldsymbol{D}_{rr}^{-1} \boldsymbol{D}_{br}^\top \right) \boldsymbol{x}_b = \boldsymbol{0} \tag{5.11}$$

If the boundary is elastic, then $\boldsymbol{x}_b$ is a non-zero vector and therefore the coefficient matrix must be singular:

$$\left| \boldsymbol{K}_b + \boldsymbol{D}_{bb} - \boldsymbol{D}_{br} \boldsymbol{D}_{rr}^{-1} \boldsymbol{D}_{br}^\top \right| = 0 \tag{5.12}$$

This equation should hold for every mode and so gives to possibility to estimate the entries of $\boldsymbol{K}_b$.

In our case, the beam root can be modelled as in Figure 5.16 and so:
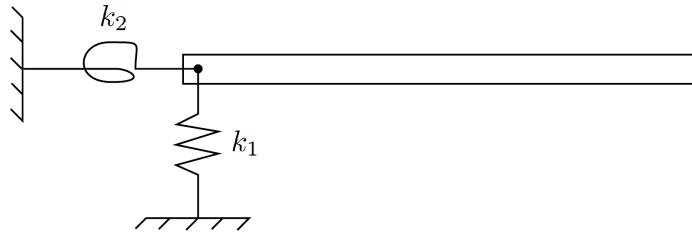
Figure 5.16: *Beam with elastic root.*

$$\boldsymbol{K}_b = \begin{bmatrix} k_1 & 0 \\ 0 & k_2 \end{bmatrix}$$

At this point, the values of (k_1, k_2) which satisfy Eq.(5.12) for every mode will represent the root stiffness.

It is therefore necessary to obtain experimentally the values of the natural frequencies of the system. This has been done with an impact hammer test. The beam has been instrumented with accelerometers sensors placed along three rows along the beam span. The obtained mode shapes and the corresponding frequencies are reported in Figure 5.18.
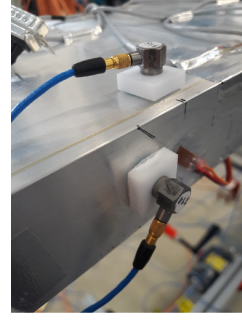
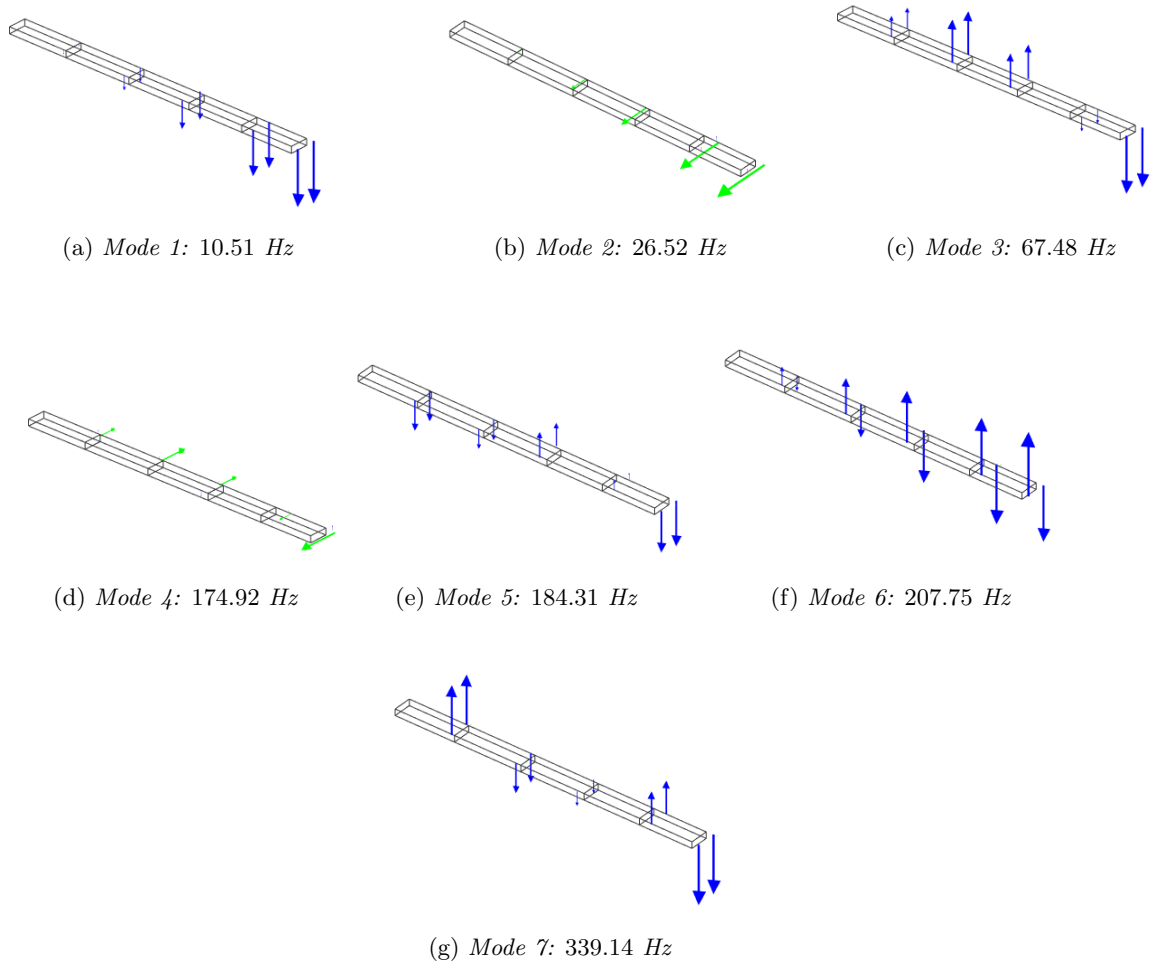

Figure 5.17: *Accelerometer sensor on aluminum beam.*

(a) *Mode 1:* 10.51 *Hz*

(b) *Mode 2:* 26.52 *Hz*

(c) *Mode 3:* 67.48 *Hz*

(d) *Mode 4:* 174.92 *Hz*

(e) *Mode 5:* 184.31 *Hz*

(f) *Mode 6:* 207.75 *Hz*

(g) *Mode 7:* 339.14 *Hz*

Figure 5.18: *Experimental mode shapes.*

Since the problem is in our case two-dimensional, we are interested only in the modes oscillating in the vertical plane, so modes 1, 3, 5, 7 (mode 6 is a torsional mode and will be neglected). The results are reported in Figure 5.19 showing that, due to experimental errors, the curves related to the different characteristic equations do not exactly intersect at the same point. However, all the intersection points seem to be reasonably close to $2.4\,10^8$ Nmm/rad, that is the measured value of the root stiffness for low moments applied. A possible approach could be to simply take

the average value among all the intersections which would bring to a stiffness estimation close to the measured one.
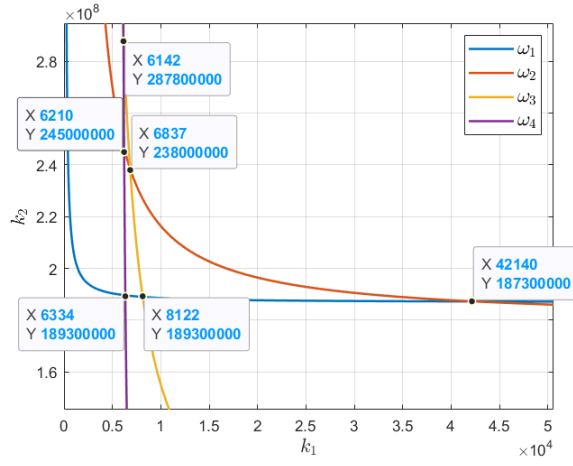
(a) *Curves from characteristic equation.*
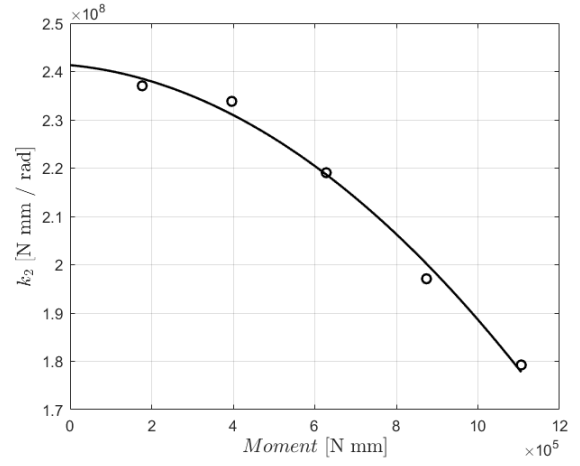
(b) *Experimental value of root stiffness in function of root internal moment.*

Figure 5.19: *Root stiffness estimation.*

5.4 Combined bending and torsion test

The beam has been subjected to both bending and torsion applying as in Figure 5.20b a concentrated force at the tip through a rod.
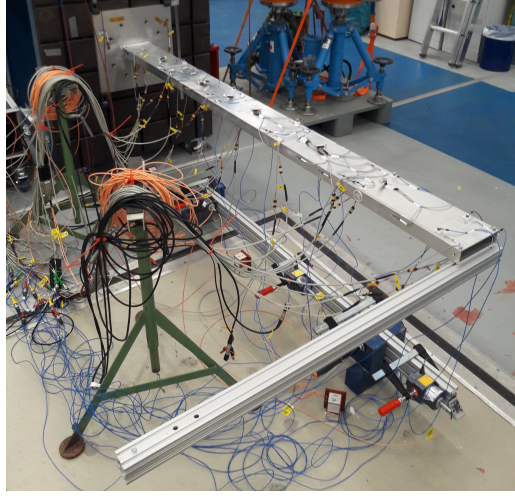
(a) *Experimental set-up.*
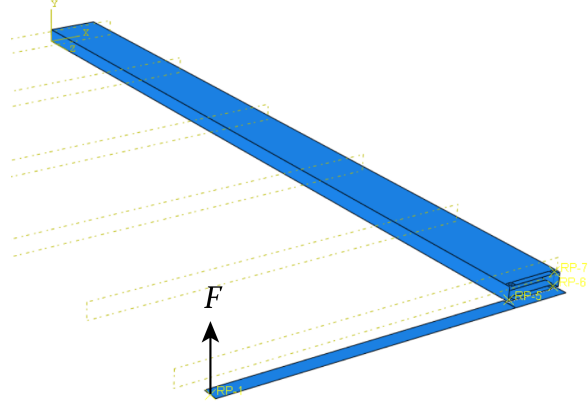
(b) *Geometry from FE model.*

Figure 5.20: *Aluminum beam under bending and torsion.*
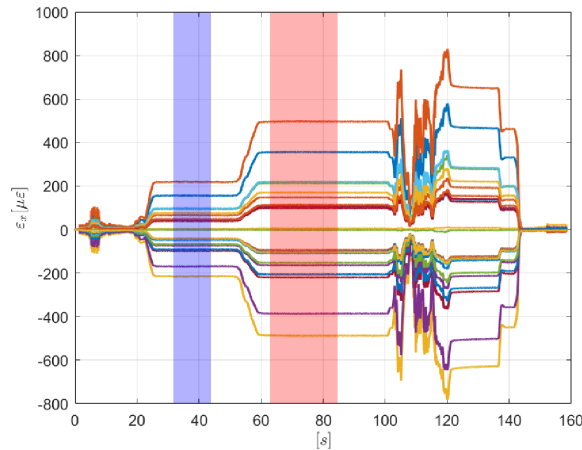
(a) *Strain gauge history.*
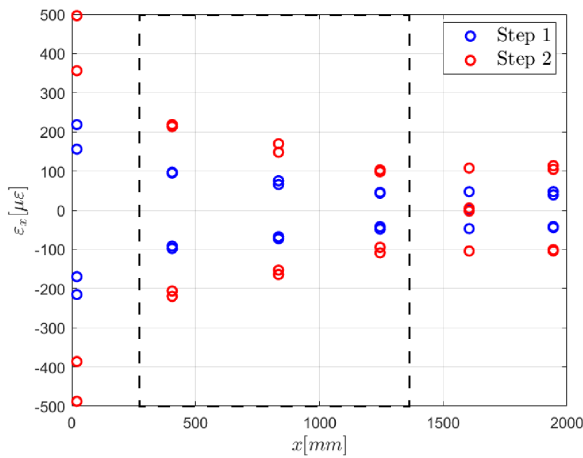
(b) *Axial strain values along beam span.*
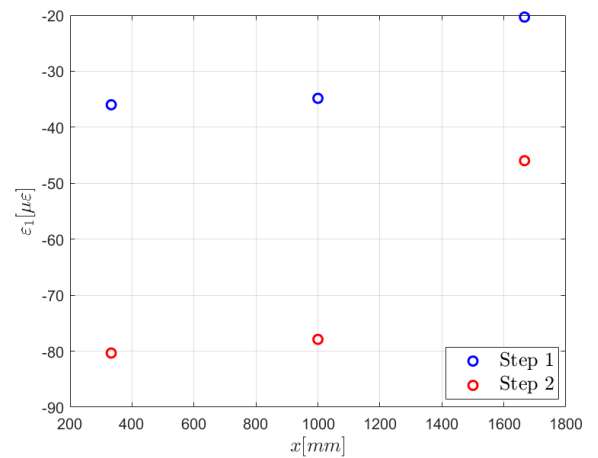
(c) *Strain values at 45° along beam span.*

Figure 5.21: *Axial strain gauge measured values.*

The deformed shape will be reconstructed in three different ways: with the beam model (Section 5.4.1), with iFEM (Section 5.4.2) and with the Modal Method (Section 5.4.3). The beam has been loaded in two steps. The history of the axial strain gauges output is shown in Figure 5.21. As it is possible to see, the strain measurements near the tip do not follow the expected linear behavior. This is mainly due to how the load has been introduced and it has been verified with FEM (Figure 5.22). Since these values are not representative of the beam behavior, they have been neglected in the bending deflection reconstruction for the beam model, considering for the axial strains just the values highlighted in Figure 5.21b.
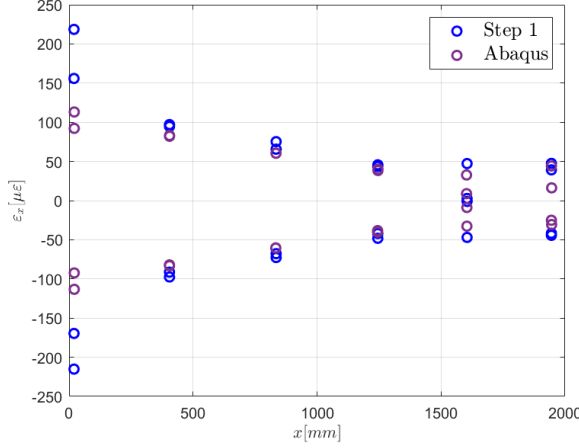
(a) *Axial strain values over beam span.*
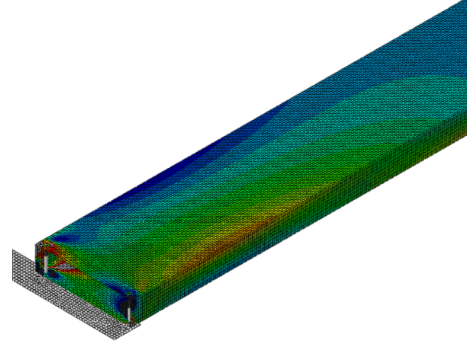
(b) *FEM model of the beam under combined bending and torsion.*

Figure 5.22: *Comparison between experimental and FE strains.*

5.4.1 Beam model

For the twist angle reconstruction part, the beam has been divided into three equi-length sections, each one containing one shear-sensitive strain gauge. The shear stresses due to unit shear forces and unit torsion moment applied on the section have been recovered directly from FEM giving the results reported in Table 5.2.

Shear stress	
τ_{12}^{z}	$-3.66\,10^{-3}$ MPa/N
τ_{12}^{t}	$-2.69\,10^{-5}$ MPa/Nmm

Table 5.2: *Shear stresses due to unit internal loads*
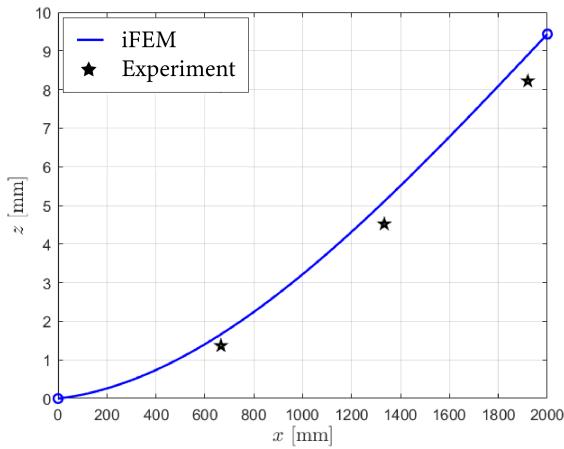
(a) *Bending reconstruction.*
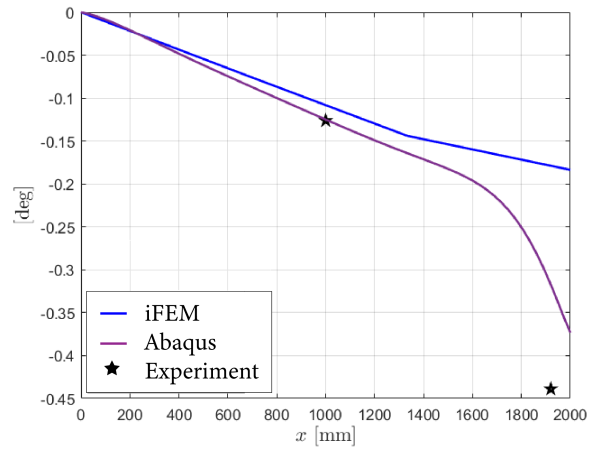
(b) *Twist reconstruction.*

Figure 5.23: *Shape sensing with beam model for step 1.*

The reconstructed deformations are shown in Figure 5.23. As it is possible to see, the shear-sensitive strain gauge near the tip is not representative of the torsional behaviour of the beam and is not able to recover the twist angle in that region.

5.4.2 iFEM

The beam deflection has also been recovered using inverse shell elements together with the help of a preliminary SEA pre-extrapolation of the strain field.

Given the measured strain, first SEA has been applied. In Figure 5.24 and Figure 5.25 the variations of the residuals Φ_α and Φ_ε are shown. While for the axial strain measures the graph shows a quite distinct corner (Figure 5.24a) from which the value of α has been chosen ($\alpha = 31.66$), for the strain measured at 45° the value of Φ_ε seems to be fairly independent on the choice of α (Figure 5.25a). This is certainly due to the fact that this strain measure has been sampled just on one side of the beam, not providing sufficiently measurements over the whole surface. In the following, the value of $\alpha = 0.1$ has been used for this strain field.

(a) *Residuals curve.*

(b) *Pre-extrapolated axial strain field ε_x.*
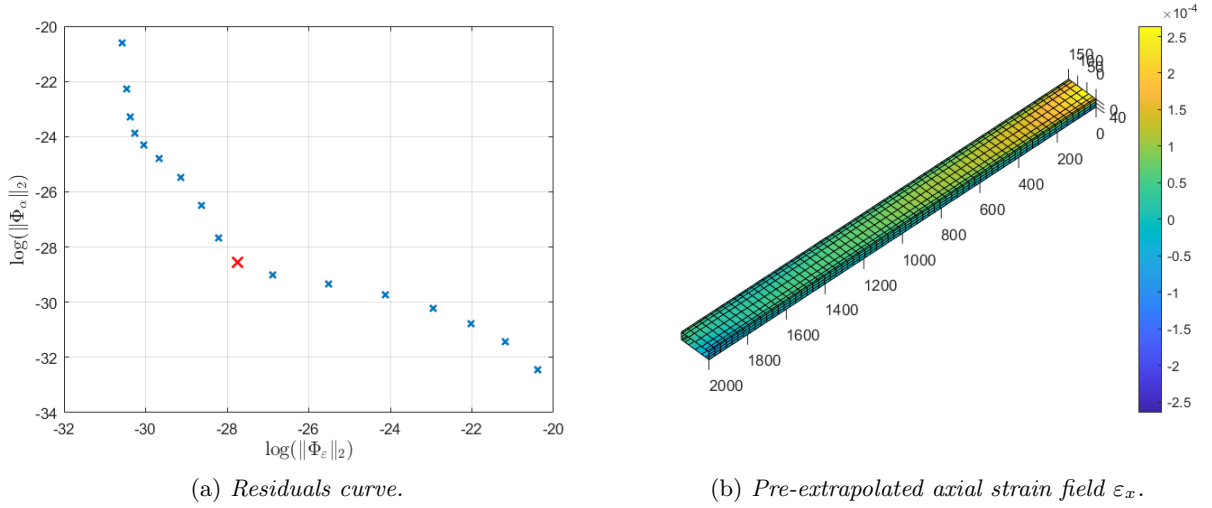
Figure 5.24: *SEA for axial strain field.*

(a) *Residuals curve.*

(b) *Pre-extrapolated strain field ε_1.*
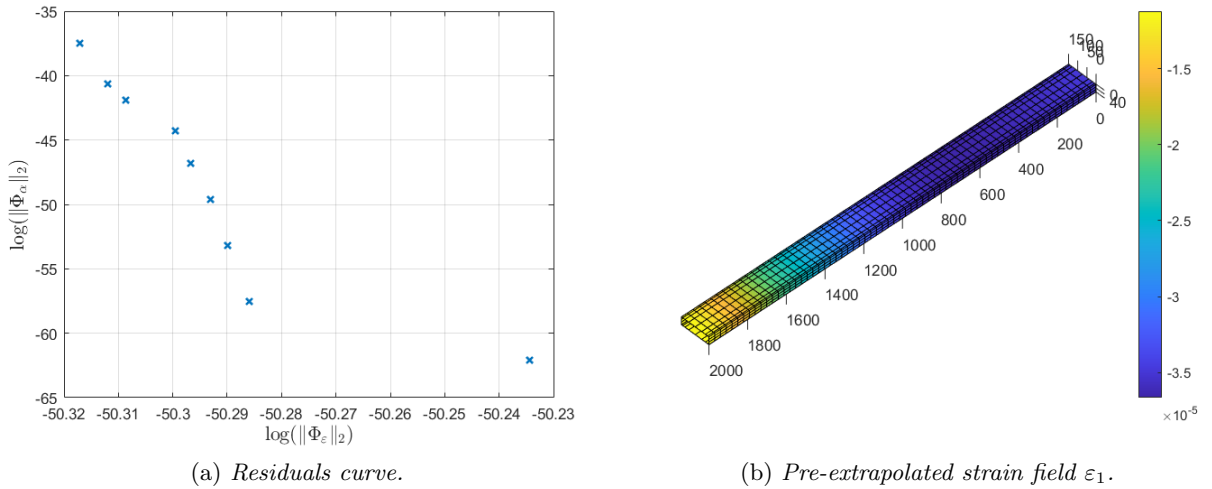
Figure 5.25: *SEA for strain field measured by strain gauges at 45°.*

Now that the strain field has been pre-extrapolated, iFEM can be applied. It is important to note that in this experiment no measurement of the transverse strain (ε_y) is done. This is necessary

because, in order to recover the shear strain, three measurements along three different directions are needed. Since the structure in this case behaves like a beam, it is therefore assumed that $\varepsilon_2 = -\nu\varepsilon_1$. However, the strain is not actually measured in three different directions in the same place, but generally there is a combinations of actual strain measurements and pre-extrapolated strain fields. This affects the choice of the weights which have to be given to the different strain measures. The following scheme has been used:

- For fully un-instrumented elements:

$$ \boldsymbol{w} = \begin{bmatrix} \underbrace{10^{-4}}_{\varepsilon_{x0}} & \underbrace{10^{-4}}_{\varepsilon_{y0}} & \underbrace{10^{-4}}_{\gamma_{x0}} & \underbrace{10^{-4}}_{\kappa_{x0}} & \underbrace{10^{-4}}_{\kappa_{y0}} & \underbrace{10^{-4}}_{\kappa_{xy0}} & \underbrace{10^{-5}}_{\gamma_{xz}} & \underbrace{10^{-5}}_{\gamma_{yz}} \end{bmatrix} $$

- For the elements in which the strain measurement at $45°$ lies, again the same weight $\boldsymbol{w}$ has been used. This because, even though there is a real strain measurement, the computation of the shear strain mixes the contributions of pre-extrapolated measurement and the actual one as:

$$ \gamma_{xy} = \frac{\varepsilon^\varepsilon - \varepsilon_x^{SEA}\cos^2\beta + \nu\varepsilon_x^{SEA}\sin^2\beta}{\cos\beta\sin\beta} $$

with ε^ε the value of the actual strain measurement.

- For elements in which the axial strain measurements lie:

$$ \boldsymbol{w} = \begin{bmatrix} \underbrace{1}_{\varepsilon_{x0}} & \underbrace{10^{-4}}_{\varepsilon_{y0}} & \underbrace{10^{-4}}_{\gamma_{x0}} & \underbrace{1}_{\kappa_{x0}} & \underbrace{10^{-4}}_{\kappa_{y0}} & \underbrace{10^{-4}}_{\kappa_{xy0}} & \underbrace{10^{-5}}_{\gamma_{xz}} & \underbrace{10^{-5}}_{\gamma_{yz}} \end{bmatrix} $$

it is assumed that the panels on which the strain is measured undergo mainly a membrane strain condition. For this reason the weight related to κ_{x0} has been set to unity.

For the first step, the reconstruction of the displacement is shown in Figure 5.26 (magnified by 50 times). The effect of the elastic root has been corrected simply adding the corresponding initial angle to the vertical deflection. In general it is possible to say that the results are completely analogous to the beam model (Figure 5.27). This is also due to the fact that the transverse strain was set equal to $-\nu\varepsilon_x$. The results for the second step are analogous and have not been reported here.
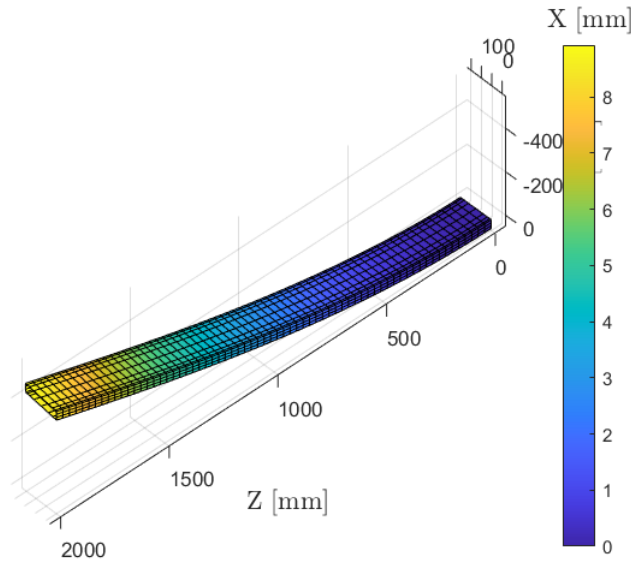

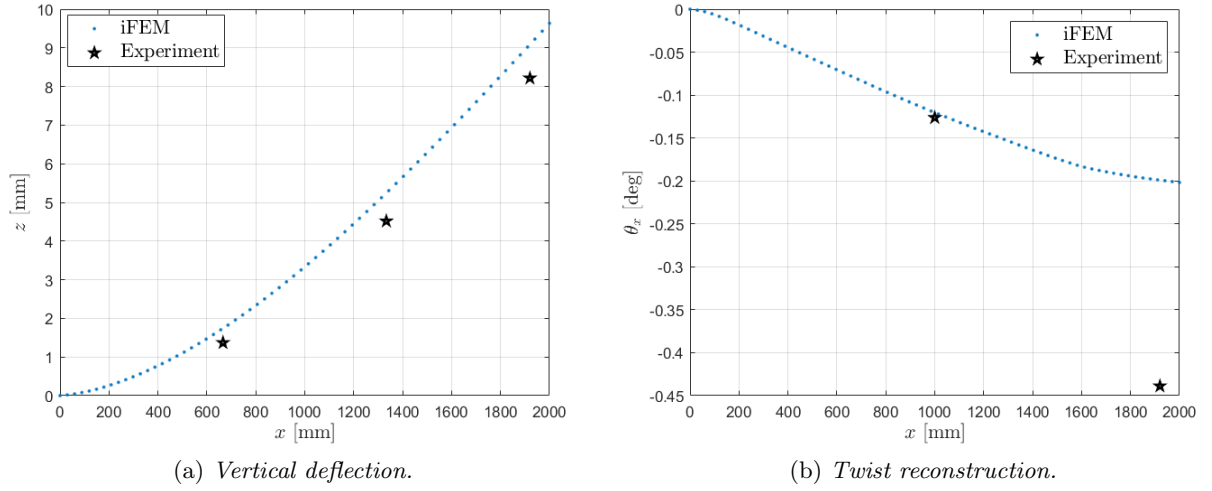Figure 5.26: *Deformed shape obtained from iFEM (magnified).*

(a) *Vertical deflection.*

(b) *Twist reconstruction.*

Figure 5.27: *Shape sensing with iFEM for step 1.*

5.4.3   MM

Finally, also the Modal Method has been used, obtaining the results of Figure 5.28 for the first step. While for the bending deflection similar results to the previous cases can been observed, for the twist one a different behaviour is reconstructed. Overall, now the twist is recovered also near the tip, even though there is a larger error w.r.t. the first measurement.
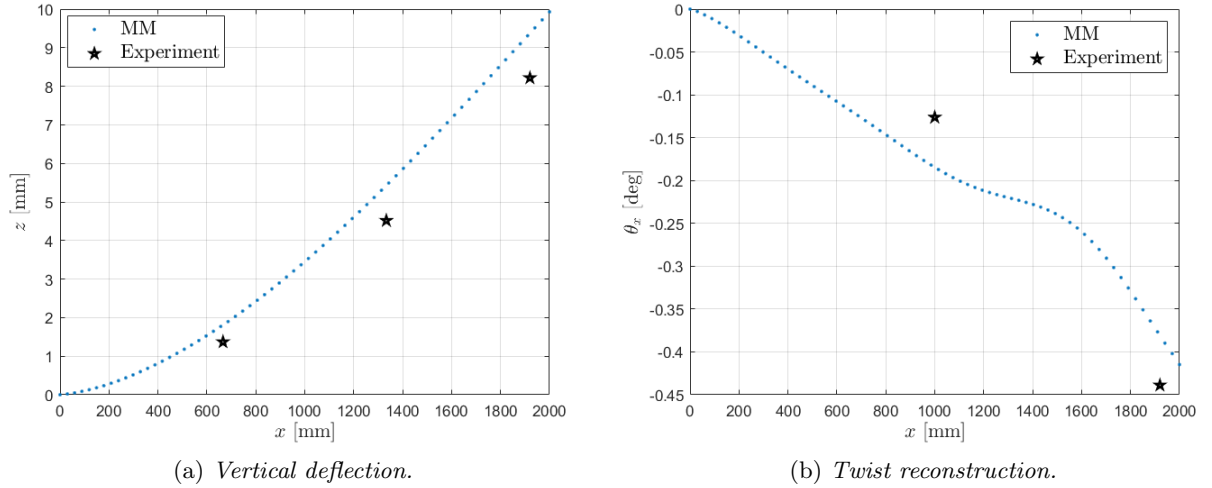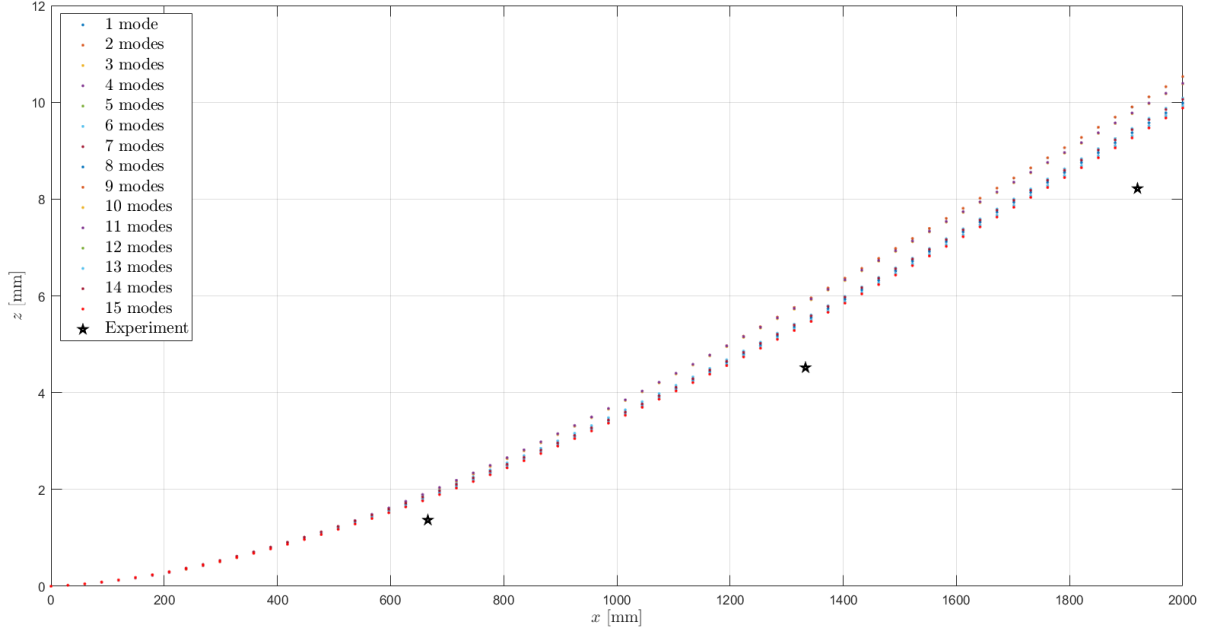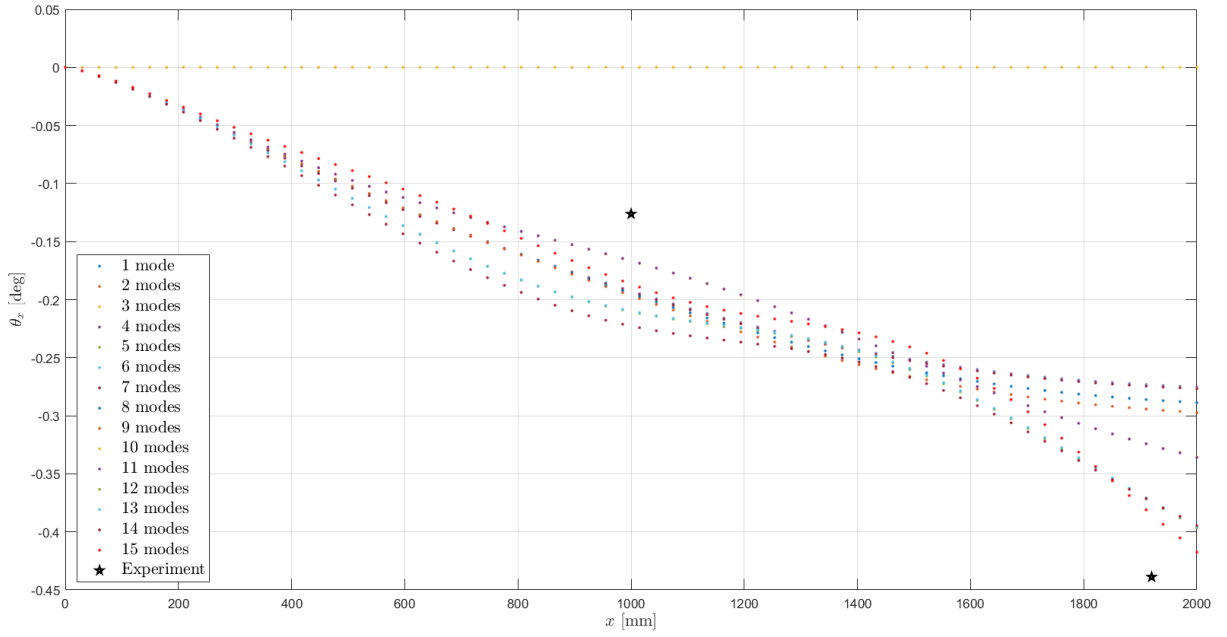

(a) *Vertical deflection.*

(b) *Twist reconstruction.*

Figure 5.28: *Shape sensing with MM for step 1.*

A total of 15 modes have been used for these analyses. The effect of the addition of the modes is shown in Figure 5.29 for the first step. For a larger number, basically no difference has been observed.

(a) *Vertical deflection.*

(b) *Twist reconstruction.*

Figure 5.29: *Effect of number of modes used for shape sensing with MM.*

5.5   Dynamic tests

A shaker has been mounted at the tip of the beam (Figure 5.30) and three different load cases
have been considered, with a sinusoidal tip force of frequency 1 Hz, 15 Hz and 20 Hz respectively.
The time histories of the measured tip force and deflections are reported in Figure 5.31.
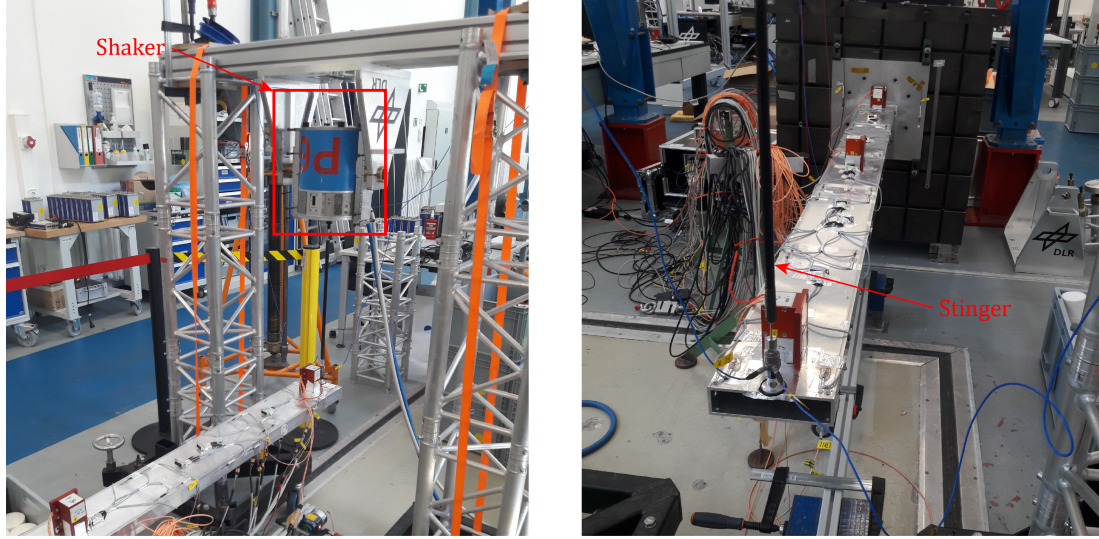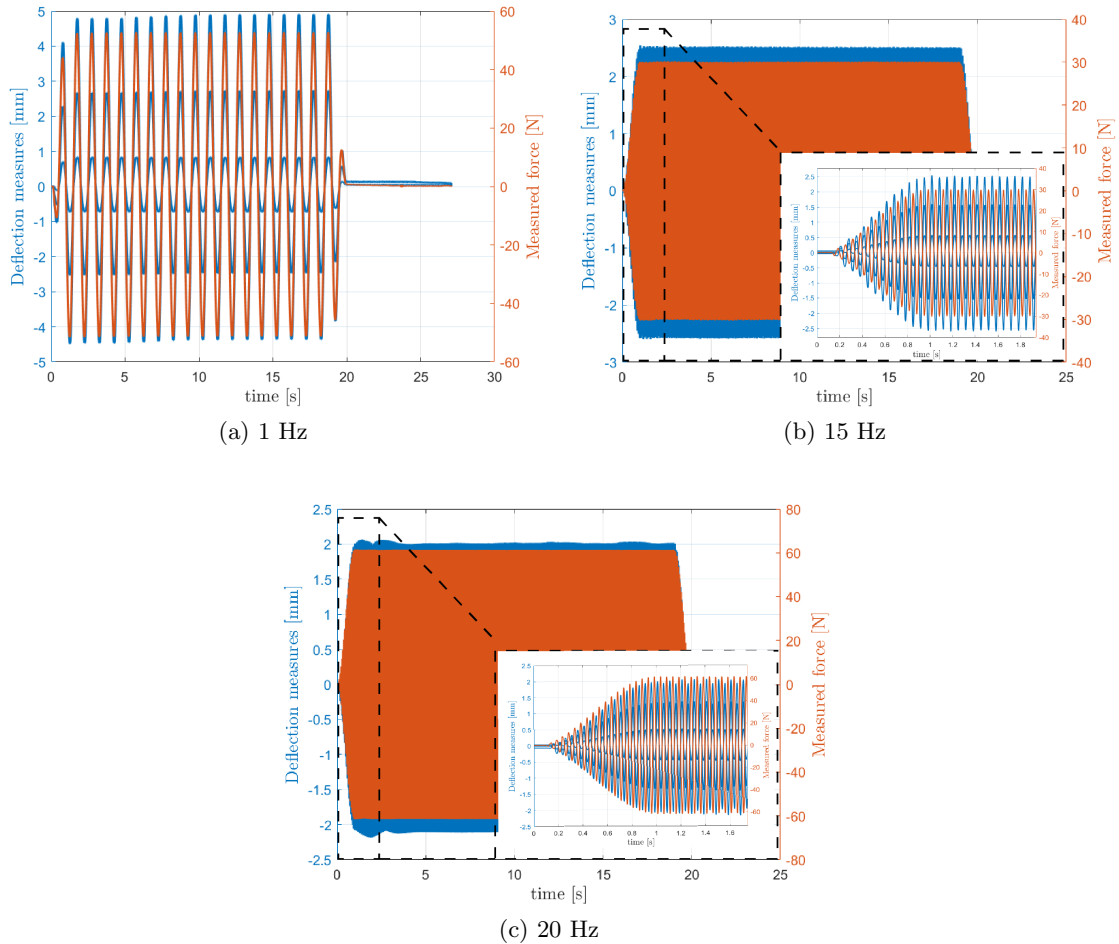

Figure 5.30: *Experimental set-up for dynamic tests.*

(a) 1 Hz

(b) 15 Hz

(c) 20 Hz

Figure 5.31: *Measured tip deflection and applied forces for the three different load cases.*

Considering first just the shape sensing part, it is possible to compare the results obtained by iFEM and by MM. Defining the displacement error as:

$$\text{Error} = \sqrt{\sum_{i=1}^{3} \left(v_i^{iFEM/MM} - v_i^{\varepsilon} \right)^2}$$

where $v^{iFEM/MM}$ is the vertical deflection reconstructed either by iFEM or MM at the ith positions where the displacement is measured by a wire sensor (for a total of 3 sensors), then for the 1 Hz load case the results of Figure 5.32 have been obtained. For the other load cases similar results have been observed. In general, iFEM seems to perform better. However, it is important to notice that the relative difference is actually relatively small.
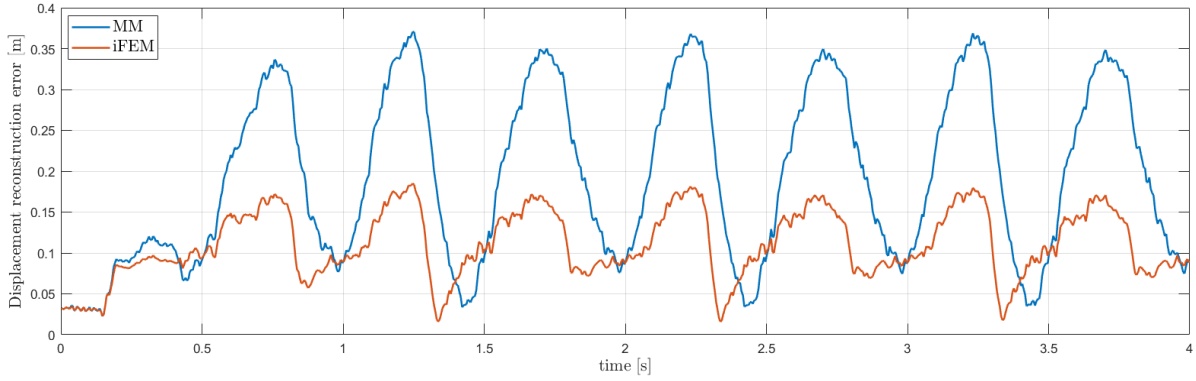
Figure 5.32: *Error of reconstructed displacement for iFEM and MM.*

Furthermore, a few comments have to be done over the possibility to have a real time displacement reconstruction with the methods used. The following situation has been observed:

- For MM, at each time step t_i a simple matrix multiplication is necessary. That is:

$$\boldsymbol{u}_i = \mathbf{DST}\ \boldsymbol{\varepsilon}_i^{\varepsilon}$$

For the current study case, this takes around $2.7193e-04\,s$.

- Using iFEM instead for each time step much more computations are required. In particular:

  - SEA: assembly of the input vector $\boldsymbol{f}_{\varepsilon_x}$ related to the axial strain measurements.
  - SEA: computation of the axial strain field as: $\boldsymbol{\varepsilon}_x = \boldsymbol{K}_{\varepsilon_x}^{-1} \boldsymbol{f}_{\varepsilon_x}$
  - SEA: assembly of the input vector $\boldsymbol{f}_{\varepsilon_{45}}$ related to the strain measurements at $45°$.
  - SEA: computation the corresponding strain field as: $\boldsymbol{\varepsilon}_{45} = \boldsymbol{K}_{\varepsilon_{45}}^{-1} \boldsymbol{f}_{\varepsilon_{45}}$
  - iFEM: assembly of the input vector $\boldsymbol{f}$ from real and interpolated strain measurements.
  - iFEM: computation of the displacements at time t_i as: $\boldsymbol{u}_i = \boldsymbol{K}_{iFEM}^{-1} \boldsymbol{f}$

For the current study this takes around $1.586\,s$.

In the current load recovery analysis therefore just the results coming from the MM will be used, since much quicker to obtain. No particular difference was observed using iFEM, also given the fact that a very simple load case is considered.

Since the primary goal is to correctly recover the force in terms of magnitude and phase, for the moment the point of application of the load will be considered as known. So, no interpolation needs to be defined and instead the external pressure has been located just on the elements at the tip where the force was actually present (Figure 5.33). In the next sections the methods introduced in Chapter 4 will be applied to this study case.
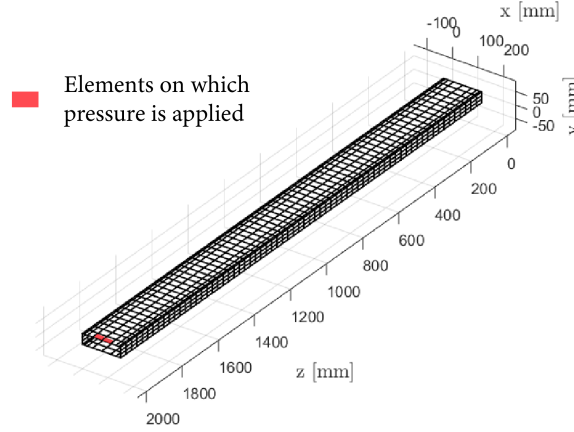

Figure 5.33: *Elements used for the reconstruction of the external pressure considering as known the point of application of the external force.*

5.5.1 Correction for the inertia forces

Using the approach outlined in Section 4.3.1, the results for the load case at 1 Hz and at 20 Hz are respectively reported in Figure 5.34.

(a) *Results for* 1 Hz *load case.*

(b) *Results for* 20 Hz *load case.*
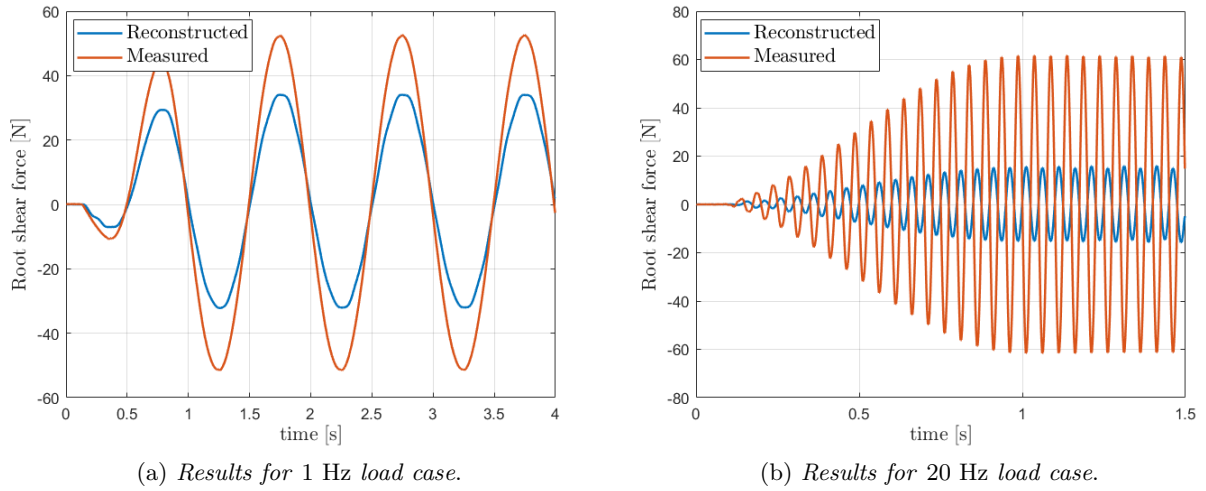
Figure 5.34: *Reconstructed total force applied correcting the static results for the inertia inertia forces.*

A few observations can be done as follows:

- In Figure 5.34a, the load seems to be approximately recovered. Even if the magnitude is not perfectly obtained, the measured and reconstructed forces are in-phase.

- For the 20 Hz load case however, not only the magnitude of the force is wrong, but even the phase shift (note that the frequency is higher than the first natural frequency) is not recovered.

From this small example it is therefore possible to see that when the inertia forces become significant, the approach used here does not seem to deliver satisfactory results.

5.5.2 Deconvolution

In order to get better results, the method based on deconvolution has been used. First the results obtained from the reconstructed displacement field with MM will be shown. Then, the ones from the strain measurements.

The impulse response functions of the beam have been computed from the FEM model with modal dynamics. For the three load cases the corresponding L-curves used to solve the regularized system and the root shear force versus time have been plotted in Figure 5.36. As it is possible to see, the load reconstruction works well for the cases at 1 Hz and 20 Hz, while for the 15 Hz case a significant error is present. In order to explain that, it is important to understand that the impulse response functions used to recover the load have been computed from the FEM model of the clamped beam, that is with the root completely clamped (see Figure 5.33 for the mesh representation). Comparing the model natural frequencies with the measured ones, it is possible to see that the values are not perfectly in accordance, as reported in Table 5.3. Since 15 Hz is relatively close to the first eigenfrequency of the beam, this is likely the cause of the error. It is possible to improve the model adding the presence of the plate at the beam root, as shown in Figure 5.35.
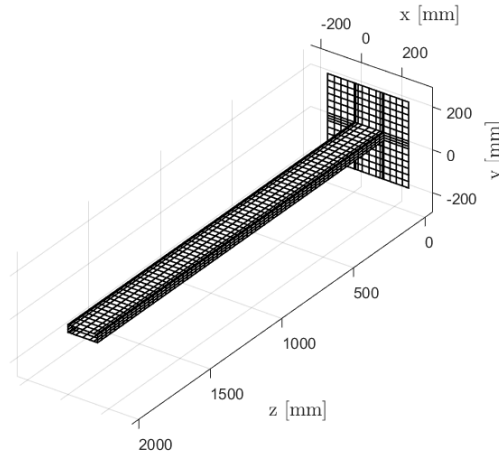

Figure 5.35: *Mesh giving a better representation of actual model.*
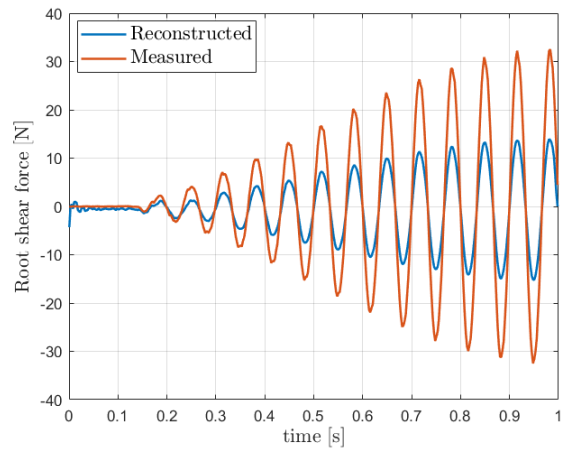
In this way, the new natural frequencies match a bit better with the experimental values (Table 5.3) and the new reconstructed load is shown in Figure 5.37. It is important to note that this correction is possible just with the MM since for iFEM no measured strain would be available on the root plate.

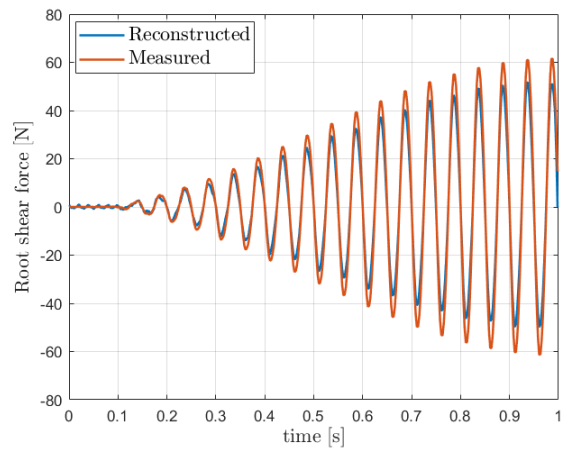|		mode 1	mode 2	mode 3	mode 4	mode 5	mode 6
Hammer test	f_n	10.51	26.52	67.48	174.92	184.31	207.75
	ζ	0.0167	0.0155	0.0106	0.0081	0.0056	0.0054
FEM clamped beam	f_n	12.0	36.0	73.197	192.12	195.20	217.56
FEM beam with plate	f_n	11.2	25.52	69.19	174.98	187.32	210.78

Table 5.3: *Comparison of the natural frequencies of the beam.*

(a) *1 Hz: L-curve.*

(b) *1 Hz: Load reconstruction.*

(c) *15 Hz: L-curve.*
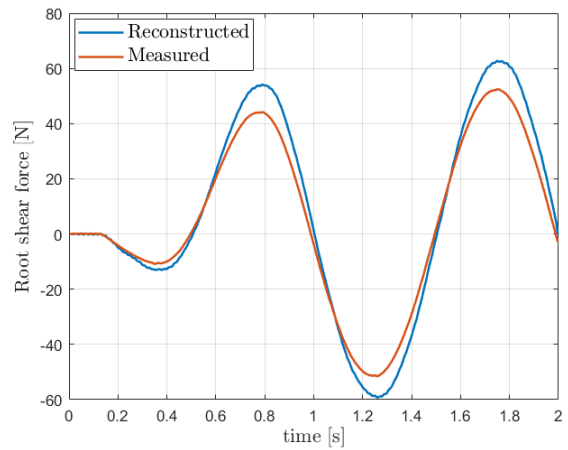
(d) *15 Hz: Load reconstruction.*

(e) *20 Hz: L-curve.*

(f) *20 Hz: Load reconstruction.*

Figure 5.36: *Load reconstruction using deconvolution.*

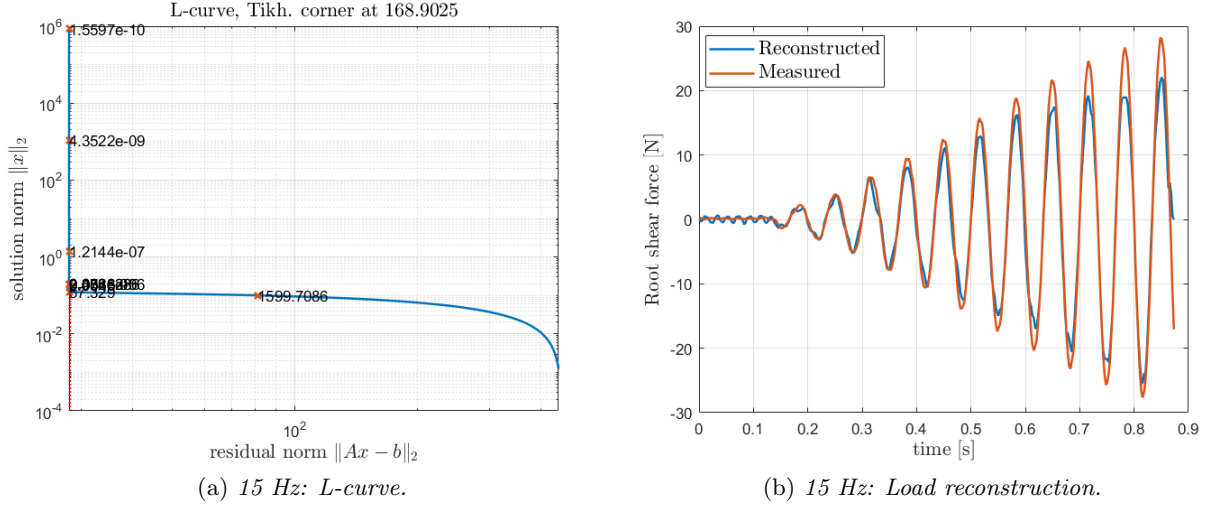(a) *15 Hz: L-curve.*

(b) *15 Hz: Load reconstruction.*

Figure 5.37: *Load reconstruction at 15 Hz using improved model.*

So far, the load reconstruction has been carried out performing the deconvolution on the whole time domain in a single step. This was feasible since the load was looked for just on two elements. If on the other hand it is desired to reconstruct the load on a larger surface, then it is necessary to follow the method developed in Chapter 4, that is dividing the simulation in smaller intervals and carrying out the deconvolution in each of them independently.

(a) *First window.*

(b) *Second window.*

(c) *Combination.*
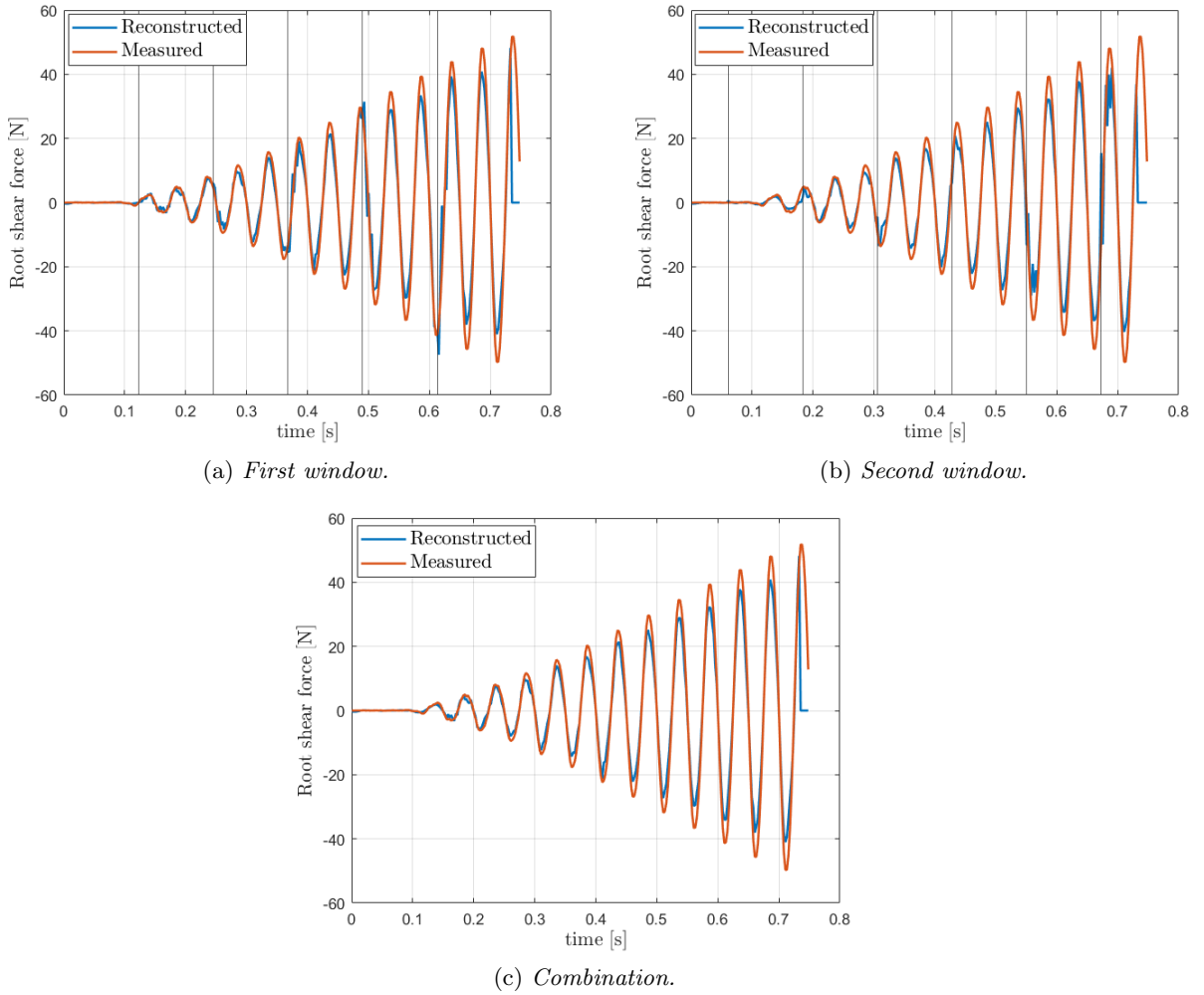
Figure 5.38: *Reconstructed total vertical force for 20 Hz load case.*

The deconvolution has been done in parallel using two windows shifted w.r.t. each other (see Figure 5.38a and Figure 5.38b). Combining the two results, the plot of Figure 5.38c was obtained which is in quite a good agreement with the actual measured force.

At this point, the information of the location of the applied force is dropped. That is, the load is looked for on the whole upper surface of the beam. In doing this, some control points have been introduced as shown in Figure 5.39.
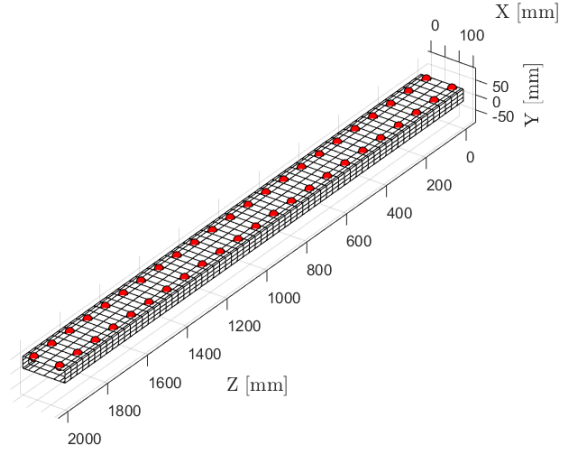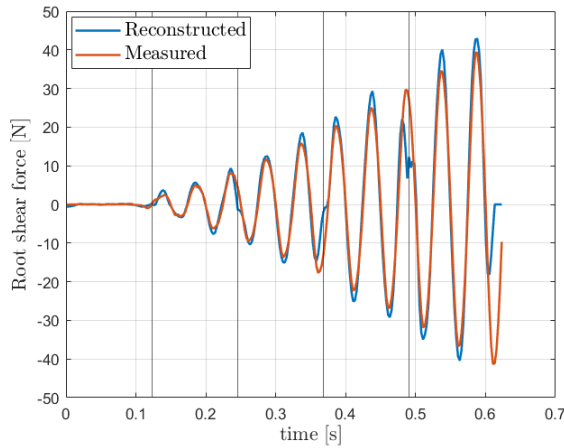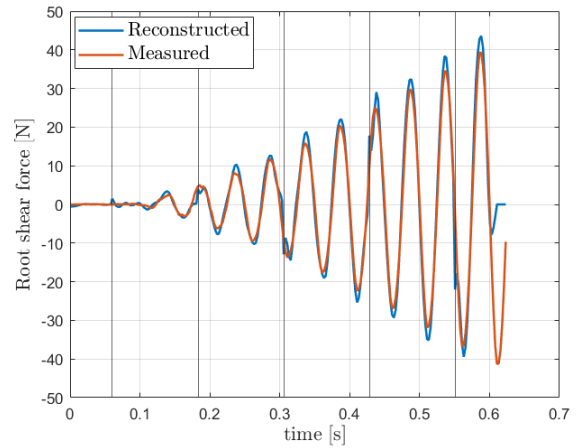
Repeating the analysis similarly as before, the results of Figure 5.40 have been obtained.

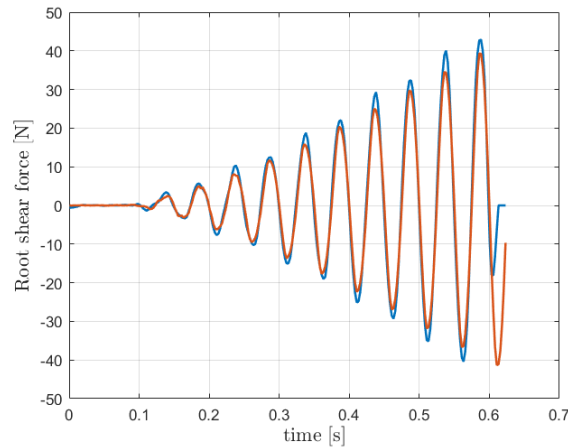Figure 5.39: *Control points for pressure interpolation over beam upper surface.*

(a) *First window.*

(b) *Second window.*

(c) *Combination.*

Figure 5.40: *Reconstructed total vertical force for 20 Hz load case with load application region the whole beam upper surface.*

The final results for the total vertical force are in good agreement with the actual applied load, however a few comments have to be done:

- The resulting pressure distribution, even though it is concentrated near the tip where the actual load is applied, it quite smeared over the whole upper surface as it is possible to see in Figure 5.41. This is also a consequence of the usage of the control points in the solution methodology which cause the load to be interpolated over a larger region. In order to limit this effect, a relatively low shape factor of $\lambda = 50$ mm has been used.
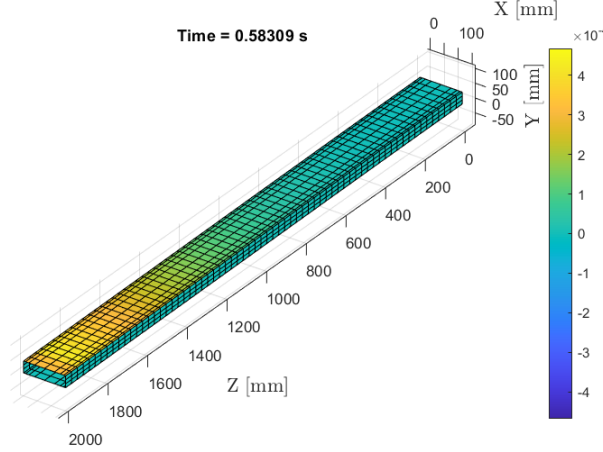

Figure 5.41: *Example of pressure distribution at particular time step.*

- The choice of the regularization parameter is quite ambiguous in this particular case since the resulting L-curve for each interval looks usually like the one reported in Figure 5.42.
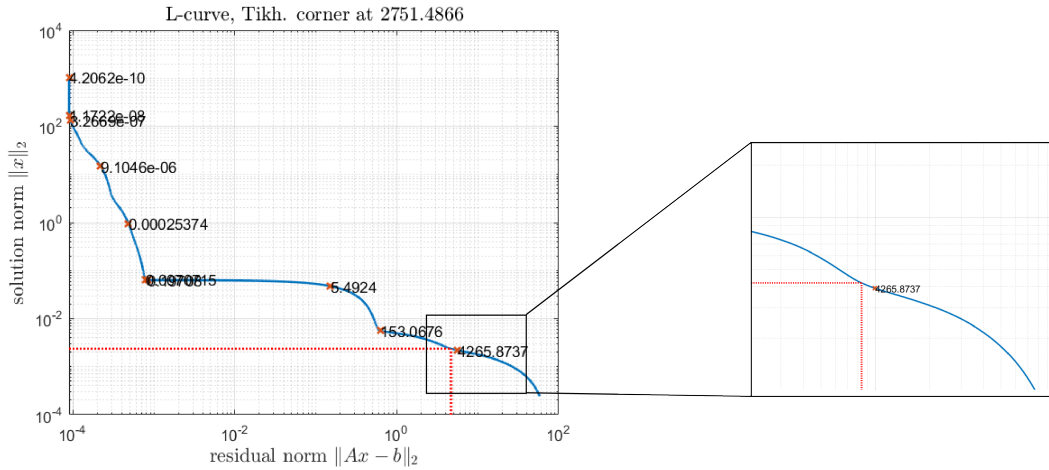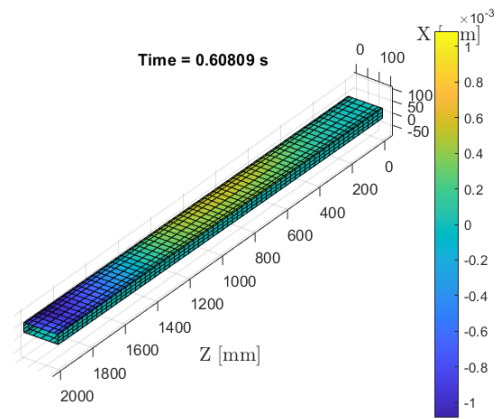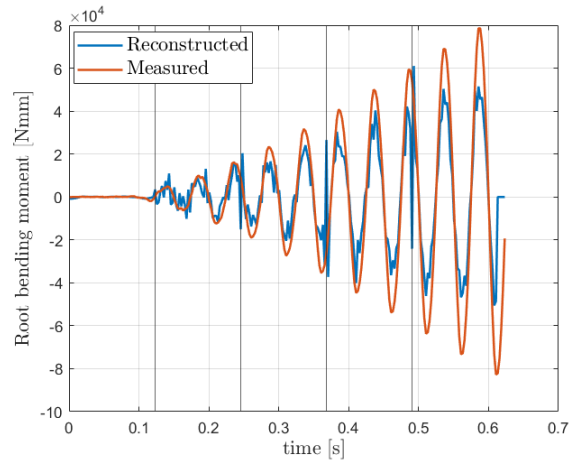

Figure 5.42: *Typical L-curve obtained from deconvolution.*

where the choice of the regularization parameter used corresponds to the last corner of the L-curve, even if it is far less pronounced compared to the others. If a less regularized solution is chosen (that is, with a lower regularization parameter α), the resulting pressure field diverges from the actual applied load. As an example, choosing the corner shown in Figure 5.43a, the pressure field obtained looks like the one in Figure 5.43b. This results in a total shear force at the root almost null (Figure 5.44a), while the moment still follows that actual applied one (Figure 5.44b).

(a) *Choice of the L-curve corner.*

(b) *Resulting pressure distribution at a particular time step.*

Figure 5.43: *Results for another choice of the regularization parameter.*

(a) *Total vertical force.*

(b) *Root bending moment.*

Figure 5.44: *Comparison with experimental values with wrong choice of the regularization parameter.*

- Other ways to compute the regularization parameter have been used, such the the so-called Generalized Cross Validation [51], but in all cases an under-regularized solution has been obtained, leading to a very poor load reconstruction.

It is possible to make easier the choice of the regularization using a low order polynomial interpolation as done in Chapter 4. Also here, the pressure field is expressed as a cubic polynomial, only function of the z coordinate. The limited number of degrees of freedom renders the L-curve corner very easy to identify, as already mentioned for the ISTAR wing. Furthermore, again similarly to what happened for the wing, also here two possible candidates occur and it is necessary that the user chooses the most suitable value (in this case, the one highlighted). The results obtained from the polynomial expansion are quite good, as shown in Figure 5.45a where the total vertical force is compared with the measured one (note that the error occurring at the edges of the intervals has not been corrected as explained before).
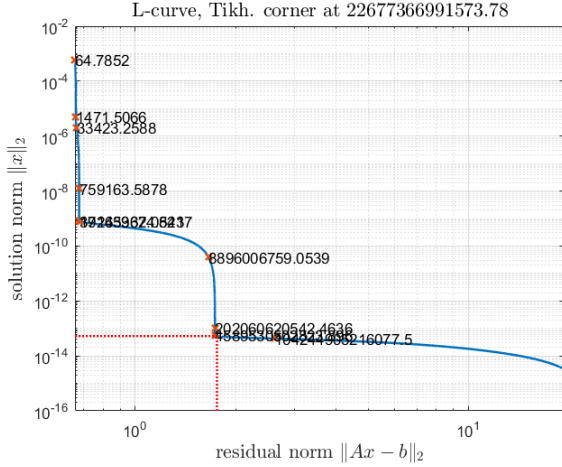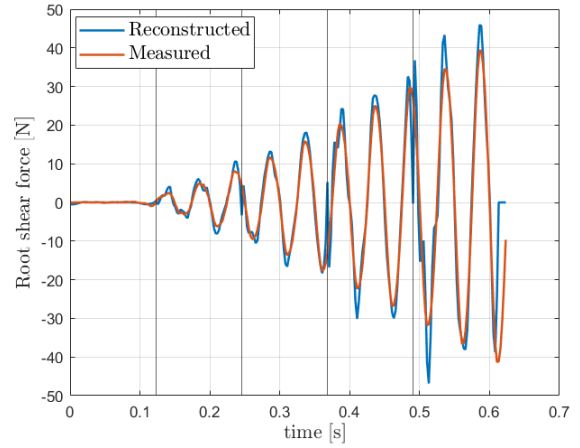
(a) *L-curve obtained with low order polynomial interplation.*

(b) *Total vertical force.*

Figure 5.45: *Load reconstruction using a low order polynomial interpolation.*

Finally, the deconvolution has been applied using as input directly the strain measurements instead of the recovered displacement field. Interpolating the pressure field using the control points, again a similar situation to the one encountered before has been obtained (Figure 5.46a), with an L-curve at each time interval which does not clearly show a single suitable choice for the regularization parameter. For example, choosing the corner highlighted in Figure 5.46a, the pressure field looks like in Figure 5.46b.
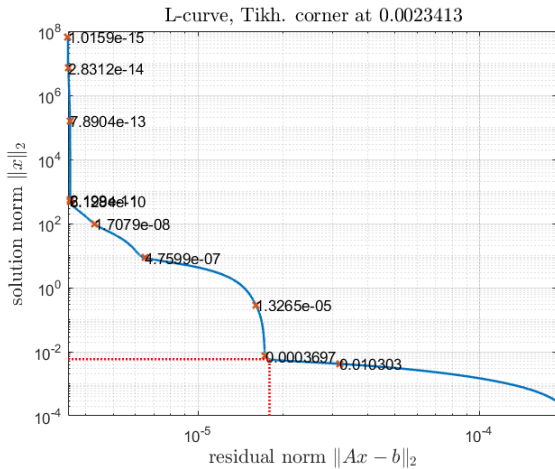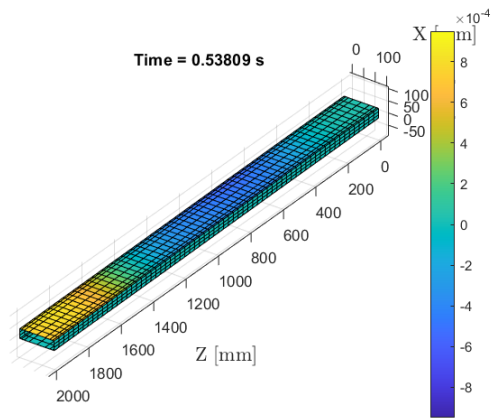

(a) *Wrong choice for regularization parameter.*

(b) *Corresponding pressure field at particular time step.*

Figure 5.46: *Load reconstruction using control point interpolation from strain measurements.*

In order to improve the results, a polynomial interpolation has been employed. Using a third order polynomial (to make a comparison with the previous case where the displacement field was used as input), the corresponding L-curve is shown in Figure 5.47. In general, the choice of a suitable regularization parameter is more ambiguous compared to before. This is likely due to the fact that in this case fewer inputs are given and therefore more load cases would give a good compromise between a low residual norm and a low norm of the regularized solution. The regularization parameter which would give the best results is the one at the corner highlighted, and the pressure field at a particular time instant in reported in Figure 5.47b as an example. The total vertical force is compared with the applied one in Figure 5.48a, showing in general a

relatively good match, even though the peaks are higher than the real ones. The root bending moment is shown in Figure 5.48b. Furthermore, note that the simulation has been divided into smaller temporal intervals, but the error at the edges has not been corrected with a second simulation.
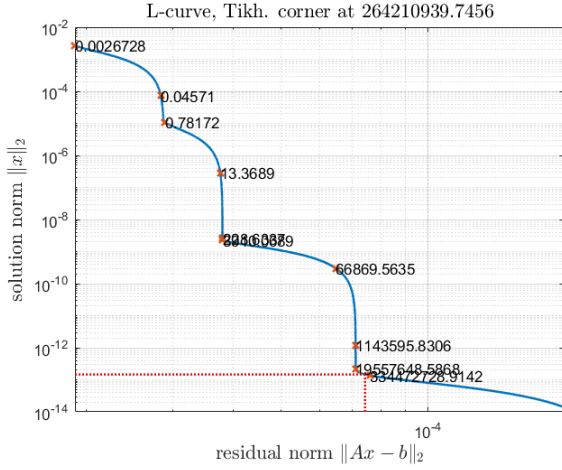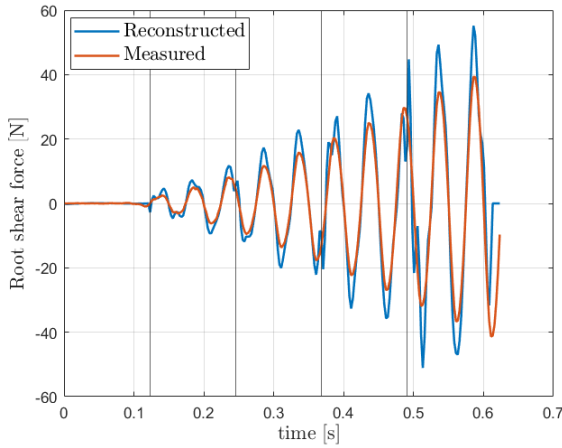
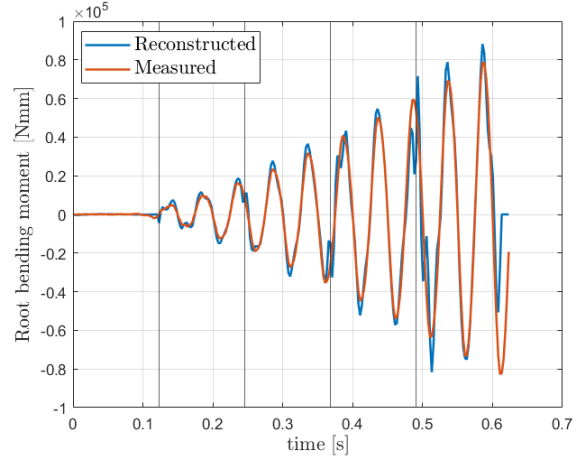

(a) *L-curve and corner chosen.*
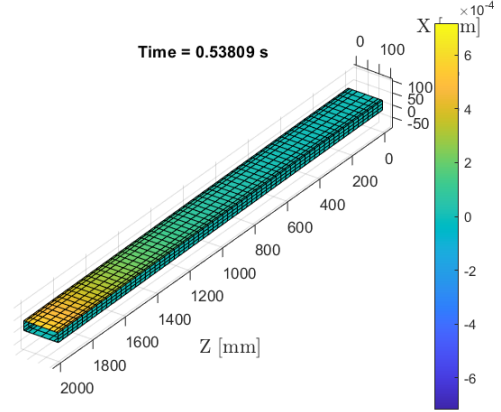
(b) *Pressure reconstruction at particular time step.*

Figure 5.47: *Load reconstruction using low order polynomial interpolation from strain measurements.*

(a) *Total vertical force.*

(b) *Root bending moment.*

Figure 5.48: *Comparison with experimental values of load reconstruction from strain measurements.*

5.5.3 Frequency domain

In this section, the dynamic load on the aluminum beam is reconstructed using the frequency domain method introduced in Chapter 4. In the following just the load case at 20 Hz will be considered and the load will be derived using both the displacement field from MM and the strain measurements.
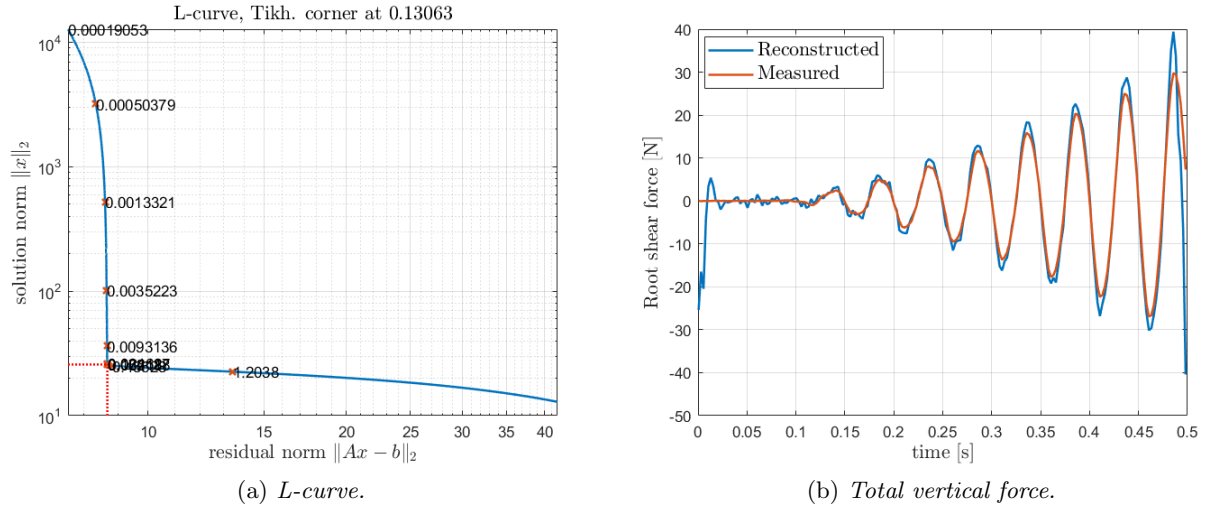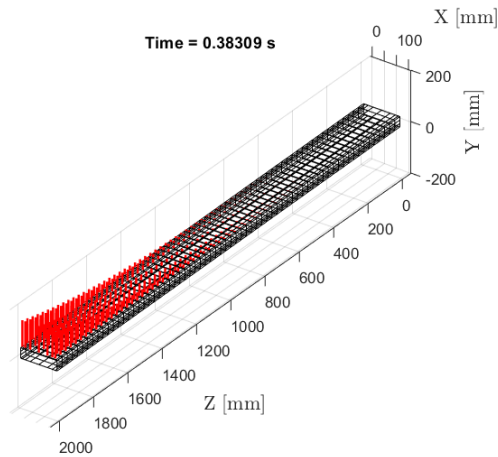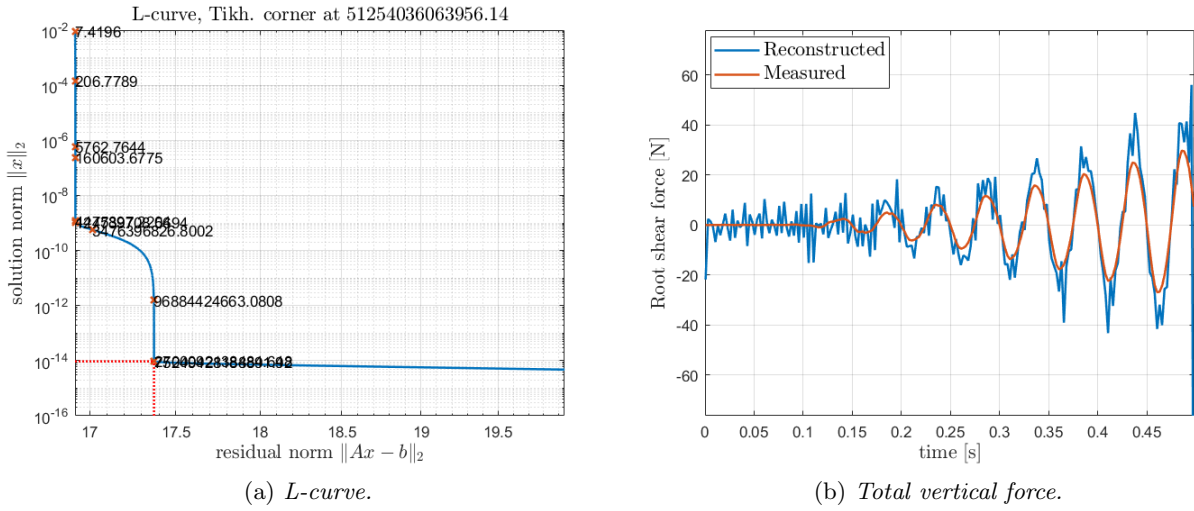
(a) *L-curve.*

(b) *Total vertical force.*

Figure 5.49: *Load reconstruction from displacement field with frequency domain method and load application region only the beam tip.*

(a) *L-curve.*

(b) *Total vertical force.*

(c) *Example of force distribution at a particular time step.*

Figure 5.50: *Load reconstruction from displacement field with frequency domain method and load application region the whole upper beam surface.*

If the load is looked for just at the tip, then the load reconstruction proceeds without any difficulty: the L-curve presents a sharp corner which makes it easy to identify a suitable regularization parameter (Figure 5.49a) and the results are in good agreement with the measurements (Figure 5.49b).

Next, the load is looked for on the entire upper surface similarly as done before. A fourth order polynomial has been used to build the weighting matrix $\boldsymbol{W}$. The L-curve presents two sharp corners and, even though it changes throughout the simulation, always the higher regularization parameter has been picked (Figure 5.50a) from which the load distribution can be obtained. The total vertical force is more noisy (Figure 5.50b) compared to the one obtained with deconvolution, probably due to the not optimal choice of the regularization parameter at each frequency. The load is still quite smeared over the surface, even though it concentrates towards the tip. As an example, the load distribution is reported in Figure 5.50c. Note that the magnitude of the nodal vertical forces has been drawn, not the pressure distribution. This just to highlight the difference w.r.t. the previous method: before the pressure distribution was directly retrieved, while now the load vector is the quantity which is actually computed.

So far, the input used for the load reconstruction has always been the reconstructed displacement. Now, the strain measurements will be used to directly recover the load in the frequency domain. Again, only the 20 Hz load case will be analyzed.

Starting as before concentrating the load just at the tip, the framework explained in Chapter 4 has been used. The L-curve shows a clear choice for the regularization parameter and correspondingly there is a relatively good load reconstruction in time (Figure 5.51).
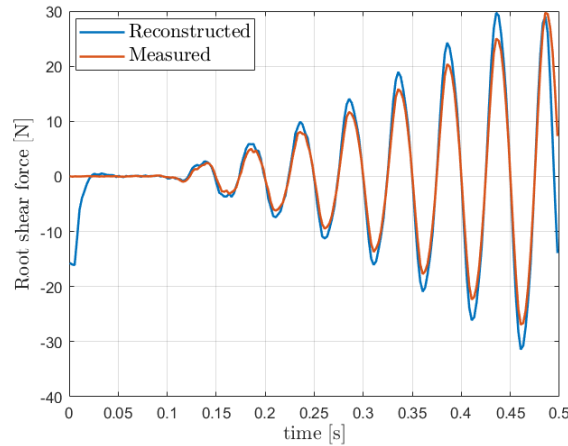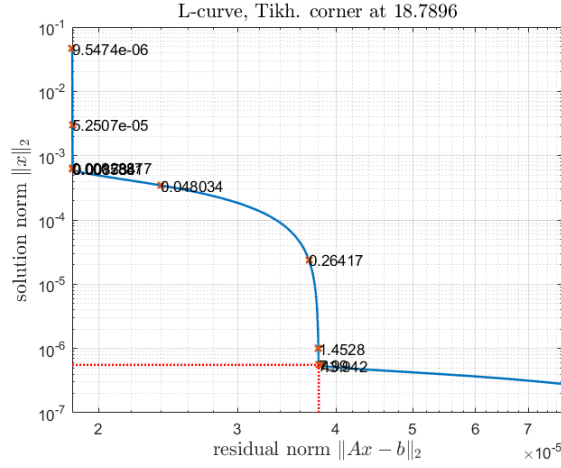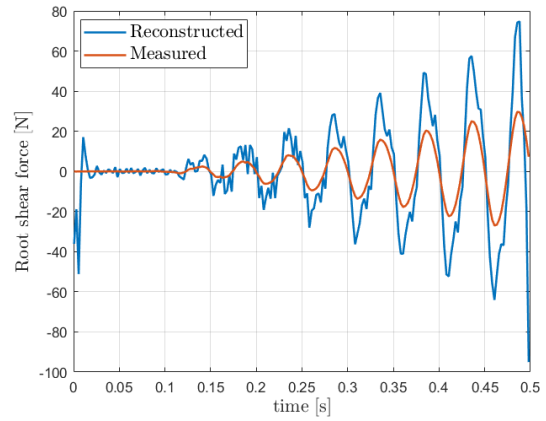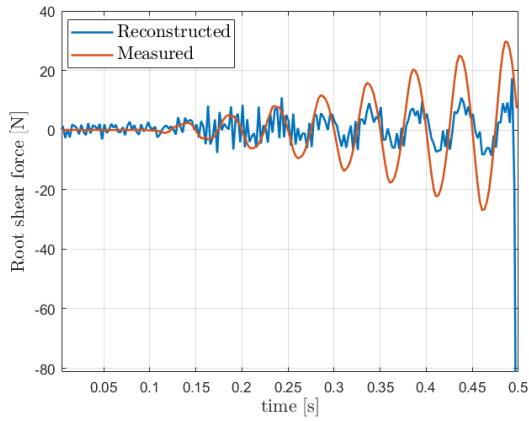

Figure 5.51: *Load reconstruction from strain measurements with load application region only the beam tip.*

A different situation occurs looking for the load on the whole upper surface. In general (and again similarly as before) the L-curve shows two possible candidates for the regularization parameter, as in Figure 5.52a. However, either choosing the smallest (Figure 5.52a) or the highest one (Figure 5.52b), the reconstructed load does not seem to be satisfactory. This is probably due to the fact that it is not clear which regularization parameter to pick at each frequency, and just restricting the choice on smaller / higher values as done here does not lead to good results.

(a) *Typical L-curve.*

(b) *Total vertical force using the lower regularization parameter.*

(c) *Total vertical force using the higher regularization parameter.*

Figure 5.52: *Load reconstruction from strain measurements with frequency domain method and as load application region the whole upper beam surface.*

5.6   Summary of the chapter

The aluminum beam used as case study has allowed to apply the methods described in the previous chapters on a relatively simple structure but which offers some interesting features. The most relevant for the shape sensing framework is the finite stiffness of the root. This parameter has been both measured experimentally and estimated theoretically with a method available in literature. Correcting for the root stiffness, simple static tests have been done. The bending deflection is in general well recovered, while the twist angle reconstruction is highly influenced by how the load is introduced. This affected particularly the beam model and iFEM with iQS4 elements.

In the last part of the chapter, some dynamic tests have been used to reconstruct time-varying loads. The correction of the static solution seems to work only for the low-frequency case, giving completely erroneous results for higher dynamics. The deconvolution and the frequency domain method on the other hand are able to give correct answers if the load is reconstructed only in time. However, if the spacial reconstruction is added, the situation is more challenging. This is mainly due to the difficulty in choosing a suitable regularization parameter. Similar cases have been observed either recovering the load from the measured strains and from the full displacement field.

Chapter 6

Conclusions

6.1   Main conclusions and answers to research questions

The work presented has been divided into three main parts, which correspond to the research questions that were initially posed. All the studies illustrated have contributed to the main research objective of the work, that is retrieving the deformed shape of the structure and in turn the external loads with a limited number of strain measurements.

Is it possible to develop a simple beam model which requires the minimum amount of input strain data, but which allows to obtain the deformations of relatively complex beam-like structures?

To answer this question, the framework of iFEM has been exploited and a simple beam model to recover both bending and torsional deformations has been discussed.
Regarding the reconstruction of the bending displacements, it is suggested the idea to sample the strain where it is more "convenient" such that the deflection is overall captured without the need to use additional gauges. In this way a very limited amount of input strain data is necessary. This method is extended to tapered beams, therefore making it suitable also for relatively complex geometries. The main disadvantage in this context is the necessity to estimate the external loads. Two methods have been proposed, either from the interpolation of the strain field or from a linear superposition of a step-wise constant distributed loads.
The reconstruction of the twist angle on the other hand is simply done piece-wise on each element domain. From the bending deflection, the shear stress due to just torsional forces is derived and this in turn allows to compute the twist rate.
Overall, in this framework for each element just 6 strain measurements are needed (5 axial for bending reconstruction and 1 with a certain angle w.r.t. the beam axis for the twist reconstruction). Relatively complex beam-like structures have been simulated, including the ISTAR demonstrator wing. In general the bending deflections were retrieved also for the most complex geometries, while the twist accuracy decreases for tapered beams.

How does iFEM perform in case of sparse strain measurements in comparison with the Modal Method? And which approach is advisable for the shape sensing monitoring of wing-like structures under real measurement conditions?

The iFEM capabilities have been significantly improved coupling it with a preliminary strain pre-extrapolation carried out with the help of SEA. This allows to apply iFEM also in case of sparse strain measurements, otherwise its results would be completely meaningless. In this context, for the SEA analysis a 4-node element has been used which appeared to perform better compared to the already available 3-node one. Comparing MM with iFEM using the ISTAR

demonstrator wing as study case however, shows that MM still is able to perform better giving the most accurate results. This has been assessed also through an uncertainty quantification study from which the error distribution with MM is lower compared to the one from iFEM. So, at least for the case study analyzed, it can be concluded that for sparse strain measurements MM gives a good estimate of the deformation and that, unless the material properties of the structure are completely unknown and untrustworthy, it can be considered to be a reliable shape sensing method.

Can the external loads be reconstructed from the deformed shape computed with the selected shape sensing scheme? And how do the results compare with the load reconstructed directly from the measured strains?

The external loads have been reconstructed under the form of a pressure field. The existing approaches based on a load superposition were considered the most promising and they have been improved introducing a preliminary interpolation of the pressure field followed by a regularization of the system. The procedure is basically the same either if it is carried out from the strain measurements or from the displacement field. Reconstructing the pressure field with the strain data has given the most accurate results, even if it showed to be quite sensitive because of the input noise in the strain measurements. In this context, the load reconstruction with iFEM was the most stable method, but not the best considering the absolute value of the error.

After having completed the study for static loads, also dynamic loads have been considered. Reconstructing time-varying loads has proved to be a much more challenging task. Among the methods used, the deconvolution seems to give the most consistent results. It has been improved to be able to simulate relatively long time intervals, but it generally suffers from the fact of choosing a suitable regularization parameter.

6.2 Recommendations for future work

Regarding the beam model, the main limitation consists in the poor twist reconstruction for the most complex geometries. A possible improvement which has not been studied in this work would consist in developing an analytical solution of the twist angle variation for tapered beams under constrained warping. This would give significantly better results for cases where the beam root can be considered to be completely restrained since, being the twist reconstructed sequentially, a small variation at the root has in general large effects for the twist angle at the tip.
Furthermore, an uncertainty quantification study in this context is still missing in order to determine the impact of measurement and system uncertainties.
Another important point to mention is that the beam model used should be assessed also for more conventional wings since the application studied has been just about a simple load-carrying composite skin wing filled with foam.

Similarly, for the shape sensing part using shell elements a future extension of the present work is certainy represented by the assessment of the results for more classical wings in case of sparse strain measurements.

Finally, the study which certainly requires the largest improvements is the load reconstruction of time-varying loads. Using the framework which has been used in this thesis, the main issue consists in finding a suitable regularization parameter. Therefore, further studies in this direction are necessary.

Appendix A

Hermite polynomials derivation

When both the function and its first derivative have to be assigned at each interpolation point, then the polynomial is called *Hermite* and is generally defined with the notation $H_{ki}^{(N)}$, with N the number of derivatives to be interpolated, k an index going from 0 to N and i the interpolation point.

As explained in [60], the Hermite polynomials have the following property:

$$\left. \frac{\mathrm{d}^r H_{ki}^{(N)}}{\mathrm{d}x^r} \right|_{x_p} = \delta_{ip}\delta_{kr}$$

where $i = \{1, 2\}$, $p = \{1, 2\}$, $k = \{0, ..., N\}$, $r = \{0, ..., N\}$ and x_p is the coordinate of the interpolation point. Considering a two point interpolation (as for the 0th order inverse Euler-Bernoulli beam element), then from the previous relation the explicit expression of the Hermite polynomials can be easily obtained:

- For the case $N = 0$ (that is only the function and not its derivatives are interpolated) the expression results to be the same of a Lagrange polynomial. It follows that:

$$H_{0i}^{(0)}(x_p) = \delta_{ip}\delta_{00} = \delta_{ip}$$

  For $i = 1$, then:

$$\begin{cases} H_{01}^{(0)}(x_1) = 1 \\ H_{01}^{(0)}(x_2) = 0 \end{cases}$$

  For $i = 2$, then:

$$\begin{cases} H_{02}^{(0)}(x_1) = 0 \\ H_{02}^{(0)}(x_2) = 1 \end{cases}$$

  Setting $x_1 = 0$ and $x_2 = L_e$ the usual Lagrange polynomial expressions can be derived.

- For the case $N = 1$ (both the function and its first derivative are interpolated) then:

$$\begin{cases} H_{ki}^{(1)}(x_p) = \delta_{ip}\delta_{k0} \\ \left. \dfrac{\mathrm{d}H_{ki}^{(1)}}{\mathrm{d}x} \right|_{x_p} = \delta_{ip}\delta_{k1} \end{cases}$$

For example, using $i = 1$ and $k = 0$, then:

$$
\begin{cases}
H_{01}^{(1)}(x_1) = 1 \\[6pt]
H_{01}^{(1)}(x_2) = 0 \\[6pt]
\dfrac{\mathrm{d}H_{01}^{(1)}}{\mathrm{d}x}(x_1) = 0 \\[10pt]
\dfrac{\mathrm{d}H_{01}^{(1)}}{\mathrm{d}x}(x_2) = 0
\end{cases}
$$

Since four conditions are given, the polynomial can be written with a cubic expression as:

$$
H_{01}^{(1)}(x) = a_1 + a_2 x + a_3 x^2 + a_4 x^3
$$

And using the previous equations the coefficients a_1, a_2, a_3 and a_4 can be easily determined. Analogously, the same procedure can be followed to obtain $H_{02}^{(1)}$, $H_{11}^{(1)}$ and $H_{12}^{(1)}$.

For the case of a three point interpolation, the situation remains similar. The Hermite polynomial becomes of fifth degree and so:

$$
H_{ki}^{(1)} = a_1 + a_2 x + a_3 x^2 + a_4 x^3 + a_5 x^4 + a_6 x^5
$$

and for example to obtain $H_{01}^{(1)}$ the following equations have to be satisfied:

$$
\begin{cases}
H_{01}^{(1)}(0) = 1 \\[6pt]
H_{01}^{(1)}(L^{(e)}/2) = 0 \\[6pt]
H_{01}^{(1)}(L^{(e)}) = 0 \\[6pt]
\left.\dfrac{\mathrm{d}H_{01}^{(1)}}{\mathrm{d}x}\right|_{x=0} = 0 \\[12pt]
\left.\dfrac{\mathrm{d}H_{01}^{(1)}}{\mathrm{d}x}\right|_{x=L^{(e)}/2} = 0 \\[12pt]
\left.\dfrac{\mathrm{d}H_{01}^{(1)}}{\mathrm{d}x}\right|_{x=L^{(e)}} = 0
\end{cases}
$$

The following expressions can be obtained:

$$
H_{01}^{(1)}(x) = 1 - \frac{23}{(L^{(e)})^2}x^2 + \frac{66}{(L^{(e)})^3}x^3 - \frac{68}{(L^{(e)})^4}x^4 + \frac{24}{(L^{(e)})^5}x^5
$$

$$
H_{0m}^{(1)}(x) = \frac{16}{(L^{(e)})^2}x^2 - \frac{32}{(L^{(e)})^3}x^3 + \frac{16}{(L^{(e)})^4}x^4
$$

$$
H_{02}^{(1)}(x) = \frac{7}{(L^{(e)})^2}x^2 - \frac{34}{(L^{(e)})^3}x^3 + \frac{52}{(L^{(e)})^4}x^4 - \frac{24}{(L^{(e)})^5}x^5
$$

$$
H_{11}^{(1)}(x) = x - \frac{6}{(L^{(e)})}x^2 + \frac{13}{(L^{(e)})^2}x^3 - \frac{12}{(L^{(e)})^3}x^4 + \frac{4}{(L^{(e)})^4}x^5
$$

$$
H_{1m}^{(1)}(x) = -\frac{8}{(L^{(e)})}x^2 + \frac{32}{(L^{(e)})^2}x^3 - \frac{40}{(L^{(e)})^3}x^4 + \frac{16}{(L^{(e)})^4}x^5
$$

$$
H_{12}^{(1)}(x) = -\frac{1}{(L^{(e)})}x^2 + \frac{5}{(L^{(e)})^2}x^3 - \frac{8}{(L^{(e)})^3}x^4 + \frac{4}{(L^{(e)})^4}x^5
$$

Appendix B

Analytical Euler - Bernoulli derivations

Considering a clamped beam under tip load as in Figure B.1, from the Euler-Bernoulli beam theory the following equation holds:

$$EI\frac{\mathrm{d}^4 w}{\mathrm{d}x^4} = q$$

with q the distributed load. In this case $q = 0$ and so, integrating four times it is possible to obtain:

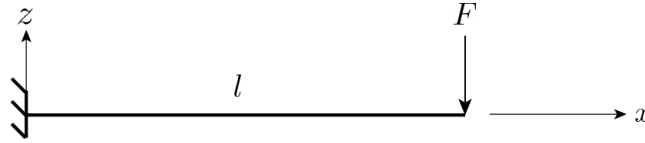$$w(x) = \frac{c_1}{6}x^3 + \frac{c_2}{2}x^2 + c_3 x + c_4$$

Figure B.1: *Cantilever beam under tip load using Euler-Bernoulli beam theory*

The coefficients c_1, c_2, c_3, c_4 can be determined from the boundary conditions. In particular, knowing that the curvature is given by:

$$\kappa(x) = -\frac{\mathrm{d}^2 w}{\mathrm{d}x^2} = \frac{M(x)}{EI}$$

It is possible to write:

$$\begin{cases} w(0) = 0 \\ \left.\dfrac{\mathrm{d}w}{\mathrm{d}x}\right|_{x=0} = 0 \\ M(0) = -Fl \\ M(l) = 0 \end{cases}$$

From which it is possible to obtain:

$$w(x) = \frac{F}{6EI}x^3 - \frac{Fl}{2EI}x^2$$

Then, knowing that $M(x) = F(x - l)$ and that:

$$\sigma_x(x, z) = \frac{M(x)}{I}z$$

it follows that:

$$\varepsilon_x(x, z) = \frac{M(x)}{EI} z = \frac{F(x - l)}{EI} z$$

Considering now a distributed load, the procedure is analogous:

$$EI \frac{\mathrm{d}^4 w}{\mathrm{d}x^4} = q \quad \Rightarrow \quad w(x) = \frac{q}{EI} \frac{x^4}{24} + c_1 \frac{x^3}{6} + c_2 \frac{x^2}{2} + c_3 x + c_4$$
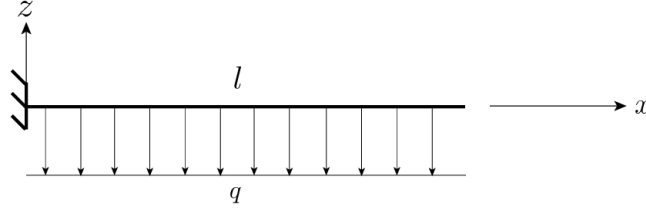

Figure B.2: *Cantilever beam under tip load using Euler-Bernoulli beam theory*

From the boundary conditions:

$$\begin{cases} w(0) = 0 \\ \dfrac{\mathrm{d}w}{\mathrm{d}x}\bigg|_{x=0} = 0 \\ V(l) = 0 \quad \Rightarrow \quad -EI \dfrac{\mathrm{d}^3 w}{\mathrm{d}x^3}\bigg|_{x=l} = 0 \\ M(l) = 0 \quad \Rightarrow \quad -EI \dfrac{\mathrm{d}^2 w}{\mathrm{d}x^2}\bigg|_{x=l} = 0 \end{cases}$$

From which it follows that:

$$w(x) = \frac{q}{EI} \left(\frac{x^4}{24} - \frac{l}{6} x^3 + \frac{l^2}{4} x^2 \right)$$

And knowing that the internal moment is given by:

$$M(x) = q \left(\frac{x^2}{2} - lx + \frac{l^2}{2} \right)$$

then:

$$\varepsilon_x(x) = \frac{M(x)}{EI} z = \frac{q}{EI} \left(\frac{x^2}{2} - lx + \frac{l^2}{2} \right) z$$

Appendix C

Analytical shear stress for thin-walled box beam

The shear flow $q = \tau t$ along the cross section shown in Figure C.1 can be obtained first "opening" the cross section (for example at 1) and computing the "basic" shear flow q_b. Then, the constant shear flow $q_{s,0}$ can be obtained. Since the section has double symmetry, it is possible to obtain the following general expression [63]

Figure C.1: *Rectangular thin-walled cross-section.*

$$q_b(\xi) = -\frac{V_z}{I_y} \int_0^\xi tz\,\mathrm{d}\xi + (\text{shear flow at } \xi = 0)$$

Then, for each panel starting from 1:

1-2)

$$q_b(\xi) = -\frac{V_z}{I_y} \int_0^\xi -t\frac{h}{2}\mathrm{d}\xi = \frac{V_z th}{2I_y}\xi$$

2-3)

$$q_b(\xi) = -\frac{V_z}{I_y} \int_0^\xi t\left(\xi - \frac{h}{2}\right)\mathrm{d}\xi + \frac{V_z thb}{4I_y} = \frac{V_z t}{I_y}\left(-\frac{\xi^2}{2} + \frac{h\xi}{2} + \frac{hb}{4}\right)$$

3-4)

$$q_b(\xi) = -\frac{V_z}{I_y} \int_0^\xi \frac{th}{2}\mathrm{d}\xi + \frac{V_z thb}{4I_y} = \frac{V_z t}{I_y}\left(-\frac{h}{2}\xi + \frac{h}{4}b\right)$$

4-5)

$$q_b(\xi) = -\frac{V_z}{I_y} \int_0^\xi t\left(\frac{h}{2} - \xi\right)\mathrm{d}\xi - \frac{V_z thb}{4I_y} = -\frac{V_z t}{I_y}\left(\frac{h}{2}\xi - \frac{\xi^2}{2}\right) - \frac{V_z thb}{4I_y}$$

5-1)

$$q_b(\xi) = -\frac{V_z}{I_y} \int_0^\xi -\frac{ht}{2}\mathrm{d}\xi - \frac{V_z thb}{4I_y} = \frac{V_z ht}{I_y}\left(\frac{\xi}{2} - \frac{b}{4}\right)$$

At this point, the constant shear flow $q_{s,0}$ can be computed as: $q_{s,0} = -\dfrac{\oint pq_b\,\mathrm{d}\xi}{2\Omega} = 0$ where p is the distance from then shear center and Ω the area enclosed by the section. Therefore: $q = t\tau = q_b$.

Appendix D

Deflection of tapered beam under constant load (single element)

The internal moment can be easily computed and is given by:

$$\overline{M}_y(x) = -\frac{q_z}{2}x^2 + q_z L^{(e)} x - \frac{q_z}{2}L^{(e)2} \tag{D.1}$$

And so using the Euler-Bernoulli assumptions the deflection can be computed as:

$$\overline{w}(x) = -\iint \frac{\overline{M}_y(x)}{EI_y(x)} \mathrm{d}x\mathrm{d}x = -\frac{1}{EI_{y0}} \iint \frac{1}{(1+cx)^3} \left(-\frac{q_z}{2}x^2 + q_z L^{(e)} x - \frac{q_z}{2}L^{(e)2}\right) \mathrm{d}x\mathrm{d}x \tag{D.2}$$
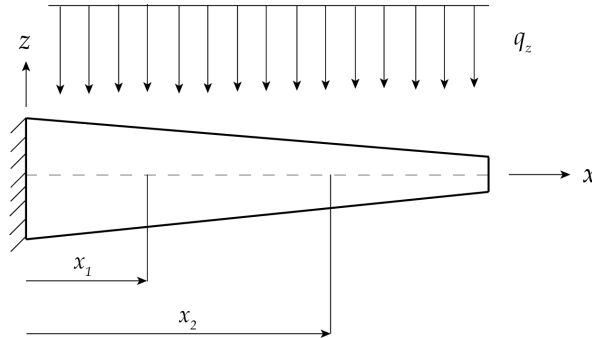
Figure D.1: *Tapered beam under constant distributed load.*

The linear moment which comes from the inverse element used can be expressed as (Figure D.1):

$$M_y(x) = \left(\frac{\overline{M}_{y2} - \overline{M}_{y1}}{x_2 - x_1}\right)(x - x_1) + \overline{M}_{y1} \tag{D.3}$$

and so its deflection is:

$$w(x) = -\iint \frac{M_y(x)}{EI_y(x)} \mathrm{d}x\mathrm{d}x \tag{D.4}$$

Integrating it is possible to obtain:

$$\frac{\mathrm{d}\overline{w}}{\mathrm{d}x} =$$

$$\frac{q_z}{4} \frac{-2\ln(cx+1)c^2x^2 + L^{(e)2}c^2 - 4L^{(e)}c^2x - 4\ln(cx+1)cx - 2L^{(e)}c - 4cx - 2\ln(cx+1) - 3}{c^3(cx+1)^2} + C_1 \tag{D.5}$$

221

$$\bar{w}(x) = q_z \left[\frac{-1}{4c^4(cx+1)} - \frac{1}{2}\frac{\ln(cx+1)x}{c^3} + \frac{1}{2}\frac{x}{c^3} - \frac{3}{2}\frac{\ln(cx+1)}{c^4} + \frac{1}{2c^4} - \frac{1}{2}\frac{L^{(e)}}{c^3(cx+1)} + \right.$$
$$\left. - \frac{L^{(e)}\ln(cx+1)}{c^3} - \frac{1}{4}\frac{L^{(e)2}}{c^2(cx+1)} \right] + C_1 x + C_2 \tag{D.6}$$

$$\frac{\mathrm{d}w}{\mathrm{d}x} = \frac{q_z}{4} \frac{L^{(e)2}c - 4L^{(e)}cx + 2cxx_1 + 2cxx_2 - cx_1x_2 - 2L^{(e)} + x_1 + x_2}{c^2(cx+1)^2} + C_3 \tag{D.7}$$

$$w(x) = -\frac{q_z}{4c^3(cx+1)} \left[4L^{(e)}\ln(cx+1)cx - 2\ln(cx+1)cxx_1 - 2\ln(cx+1)cxx_2 + L^{(e)2}c+ \right.$$
$$\left. - cx_1x_2 + 4L^{(e)}\ln(cx+1) - 2\ln(cx+1)x_2 + 2L^{(e)} - x_1 - x_2 \right] + C_3 x + C_4 \tag{D.8}$$

Applying the boundary conditions:

$$\left.\frac{\mathrm{d}w}{\mathrm{d}x}\right|_{x=0} = \left.\frac{\mathrm{d}\bar{w}}{\mathrm{d}x}\right|_{x=0}$$
$$\Rightarrow \quad C_3 = \frac{q_z}{4}\left[\frac{L^{(e)2}c^2 - 2L^{(e)}c - 3}{c^3} - \frac{L^{(e)}c - cx_1x_2 - 2L^{(e)} + x_1 + x_2}{c^2} \right] + C_1 \tag{D.9}$$

$$\bar{w}(0) = w(0)$$
$$\Rightarrow \quad C_4 = q_z\left[\frac{1}{4c^4} - \frac{L^{(e)}}{2c^3} - \frac{L^{(e)2}}{4c^2} + \frac{L^{(e)2}c - cx_1x_2 + 2L^{(e)} - x_1 - x_2}{4c^3} \right] + C_2 \tag{D.10}$$

And so now it can be obtained the equation which relates x_1 and x_2 from:

$$\bar{w}(x = L^{(e)}) = w(x = L^{(e)}) \tag{D.11}$$

and which can be solved numerically.

Appendix E

Deflection of tapered beam under constant load (multiple elements)

As reported in the text, the internal moment of the element is given by:

$$\overline{M}_y(x) = q_z \left(L^{(e)}x - \frac{x^2}{2} \right) + \left(\sum_{i+1} q_{zi}L_i^{(e)} \right) x - \sum_i q_{zi}L_i^{(e)} r_i \tag{E.1}$$

And so the equivalent moment is:

$$M_{eq}(x) = \frac{1}{(1+cx)^3} \left[q_z \left(L^{(e)}x - \frac{x^2}{2} \right) + \left(\sum_{i+1} q_{zi}L_i^{(e)} \right) x - \sum_i q_{zi}L_i^{(e)} r_i \right] \tag{E.2}$$

Integrating $\overline{M}_y$ and $M_y(x)$ it is possible to obtain the deflection:

$$\frac{\mathrm{d}\overline{w}}{\mathrm{d}x} = -\frac{1}{2} \frac{q_z \ln(cx+1)}{c^3} + \frac{1}{2} \frac{q_z L}{c^2 (cx+1)^2} + \frac{1}{2} \frac{\sum_i q_{zi}L_i^{(e)} r_i}{c(cx+1)^2} +$$
$$+ \frac{1}{2} \frac{\sum_{i+1} q_{zi}L_i^{(e)}}{c^2 (cx+1)^2} + \frac{1}{4} \frac{qz}{c^3 (cx+1)^2} - \frac{qz L}{c^2 (cx+1)} - \frac{\sum_{i+1} q_{zi}L_i^{(e)}}{c^2 (cx+1)} - \frac{qz}{c^3 (cx+1)} + C_1 \tag{E.3}$$

$$\overline{w}(x) = -\frac{q_z L \ln(cx+1)}{c^3} - \frac{\sum_{i+1} q_{zi}L_i^{(e)} \ln(cx+1)}{c^3} - \frac{3}{2} \frac{qz \ln(cx+1)}{c^4} +$$
$$- \frac{1}{2} \frac{qz L}{c^3 (cx+1)} - \frac{1}{2} \frac{\sum_i q_{zi}L_i^{(e)} r_i}{c^2 (cx+1)} - \frac{1}{2} \frac{\sum_{i+1} q_{zi}L_i^{(e)}}{c^3 (cx+1)} - \frac{1}{4} \frac{qz}{c^4 (cx+1)} +$$
$$- \frac{1}{2} \frac{q_z \ln(cx+1) x}{c^3} + 1/2 \frac{qz\, x}{c^3} + \frac{1}{2} \frac{qz}{c^4} + C_1 x + C_2 \tag{E.4}$$

$$\frac{\mathrm{d}w}{\mathrm{d}x} = \frac{1/2\, x^2 - x_1\, x}{x_2 - x_1} \cdot$$
$$\cdot \left(\frac{q_z \left(Lx_2 - 1/2\, x_2{}^2 \right) + \sum_{i+1} q_{zi}L_i^{(e)}\, x2 - \sum_i q_{zi}L_i^{(e)} r_i}{(cx2+1)^3} + \right.$$
$$- \frac{qz \left(Lx_1 - 1/2\, x_1{}^2 \right) + \sum_{i+1} q_{zi}L_i^{(e)}\, x_1 - \sum_i q_{zi}L_i^{(e)} r_i}{(cx_1+1)^3} \left. \right) +$$
$$+ \frac{\left(q_z \left(Lx_1 - 1/2\, x_1{}^2 \right) + \sum_{i+1} q_{zi}L_i^{(e)}\, x_1 - \sum_i q_{zi}L_i^{(e)} r_i \right) x}{(cx_1+1)^3} + C_3 \tag{E.5}$$

$$w(x) = \frac{1/6\,x^3 - 1/2\,x1\,x^2}{x_2 - x_1} \cdot$$

$$\cdot \left(\frac{q_z\left(Lx_2 - 1/2\,x_2{}^2\right) + \sum_{i+1} q_{zi} L_i^{(e)} x_2 - \sum_i q_{zi} L_i^{(e)} r_i}{(cx_2 + 1)^3} + \right.$$

$$\left. - \frac{q_z\left(Lx_1 - 1/2\,x_1{}^2\right) + \sum_{i+1} q_{zi} L_i^{(e)} x1 - \sum_i q_{zi} L_i^{(e)} r_i}{(cx_1 + 1)^3} \right) + \tag{E.6}$$

$$+ 1/2\,\frac{\left(q_z\left(Lx_1 - \tfrac{1}{2}\,x1{}^2\right) + \sum_{i+1} q_{zi} L_i^{(e)} x1 - \sum_i q_{zi} L_i^{(e)} r_i\right) x^2}{(cx_1 + 1)^3} +$$

$$+ C_3 x + C_4$$

The relations between the integration constants can be obtained from the boundary conditions:

$$\begin{cases} \left.\dfrac{\mathrm{d}\overline{w}}{\mathrm{d}x}\right|_{x=0} = \left.\dfrac{\mathrm{d}w}{\mathrm{d}x}\right|_{x=0} \\[2mm] \overline{w}(0) = w(0) \end{cases} \tag{E.7}$$

And so the equation $\overline{w}(L^{(e)}) = w(L^{(e)})$ delivers the sought for relation between x_1 and x_2 which can be solved numerically.

Appendix F

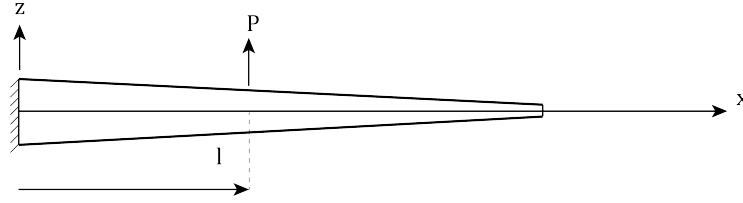# Analytical solution of tapered beam under concentrated load

Figure F.1: *Tapered beam under concentrated load P at $x = l$.*

The tapered beam shown in Figure F.1 is loaded by a concentrated force P at $x = l$. So the internal moment $M_y(x)$ is given by:

$$M_y(x) = \begin{cases} P(x-l) & ; \quad x \leq l \\ 0 & ; \quad x > l \end{cases} \tag{F.1}$$

And the deflection can be computed from:

$$w(x) = -\iint \frac{M_y(x)}{EI_y(x)} \mathrm{d}x\mathrm{d}x = -\frac{1}{EI_{y0}} \iint \frac{M_y(x)}{(1+cx)^3} \mathrm{d}x\mathrm{d}x \tag{F.2}$$

The results are reported below:

- $x < l$:
$$w(x) = -\frac{P}{EI_{y0}} \left(-\frac{1}{2} \frac{2\ln(1+cx)cx + lc + 2\ln(1+cx) + 1}{c^3(1+cx)} + C_1 x + C_2 \right) \tag{F.3}$$

  where from $w(0) = 0$ and $w'(0) = 0$ it follows that:
$$C_1 = -\frac{1}{2} \frac{cl-1}{c^2} \quad ; \quad C_2 = \frac{1}{2} \frac{lc+1}{c^3}$$

- $x \geq l$:
$$w(x) = C_3 x + C_4 \tag{F.4}$$

  where from the continuity of $w(x)$ and $w'(x)$ at $x = l$ with the previous case it follows that:
$$C_3 = -\frac{1}{2} \frac{cl+1}{c^2(1+cl)^2} + C_1$$

$$C_4 = -\frac{1}{2} \frac{2\ln(1+cl)cl + cl + 2\ln(1+cl) + 1}{c^3(1+cl)} + C_1 l + C_2 - C_3 l$$

225

Appendix G

Analytical solution of tapered beam under locally constant load
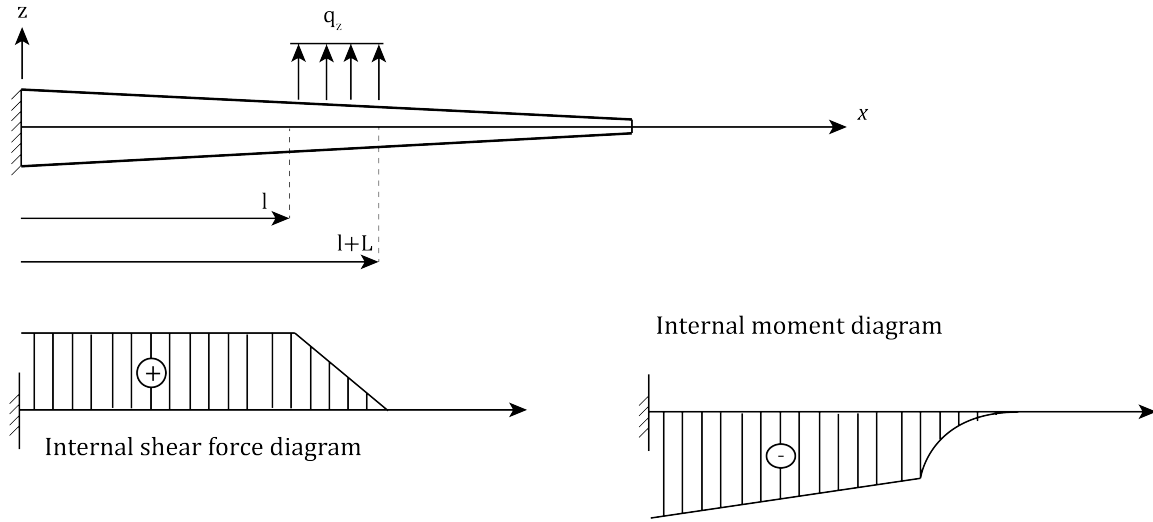

Figure G.1: *Tapered beam under locally constant load q_z.*

Consider a tapered beam subjected to a constant load q_z between $x = l$ and $x = l + L$ (Figure G.1). The internal moment along the beam span is given by:

$$M_y(x) = \begin{cases} q_z L x - q_z L \left(l + \dfrac{L}{2}\right) & ; \quad x < l \\ q_z L \left[x - \dfrac{1}{L}\left(\dfrac{x^2}{2} - lx\right)\right] - q_z \left(\dfrac{L^2}{2} + \dfrac{l^2}{2} + Ll\right) & ; \quad l \le x < l + L \\ 0 & ; \quad x \ge l + L \end{cases}$$

(G.1)

And so the deflection can be computed from:

$$w(x) = -\iint \frac{M_y(x)}{EI_y(x)}\mathrm{d}x\mathrm{d}x = -\frac{1}{EI_{y0}}\iint \frac{M_y(x)}{(1+cx)^3}\mathrm{d}x\mathrm{d}x$$

(G.2)

The results are reported below:

- $x < l$:

$$w(x) = -\frac{1}{4}\frac{qz\, L\left(4\ln\left(cx+1\right)cx + Lc + 2\,lc + 4\ln\left(cx+1\right)+2\right)}{c^3\left(cx+1\right)} + C_1 x + C_2$$

(G.3)

226

where:

$$C_1 = -\frac{1}{4}\frac{q_z L}{c^2}\left(Lc + 2cl - 2\right)$$

$$C_2 = \frac{1}{4}\frac{q_z L}{c^3}\left(Lc + 2lc + 2\right)$$

- $l \leq x < l + L$

$$
\begin{aligned}
w(x) = &-\frac{q_z\, L \ln\left(cx+1\right)}{c^3} - \frac{q_z\, l \ln\left(cx+1\right)}{c^3} - \frac{3}{2}\frac{q_z\, \ln\left(cx+1\right)}{c^4} \\
&-\frac{1}{4}\frac{q_z\, L^2}{c^2\left(cx+1\right)} - \frac{1}{2}\frac{q_z\, Ll}{c^2\left(cx+1\right)} - \frac{1}{4}\frac{q_z\, l^2}{c^2\left(cx+1\right)} \\
&-\frac{1}{2}\frac{q_z\, L}{c^3\left(cx+1\right)} - 1/2\frac{q_z\, l}{c^3\left(cx+1\right)} - \frac{1}{4}\frac{qz}{c^4\left(cx+1\right)} \\
&-\frac{1}{2}\frac{q_z\, \ln\left(cx+1\right)x}{c^3} + \frac{1}{2}\frac{q_z\, x}{c^3} + 1/2\frac{q_z}{c^4} + C_3 x + C_4
\end{aligned}
\tag{G.4}
$$

where:

$$
\begin{aligned}
C_3 = &\frac{q_z\left(2\,\ln\left(cl+1\right) + 2\,Lc + 6\,cl - L^2\,c^2 + 3\,c^2\,l^2\right)}{4\,c^3\left(cl+1\right)^2} + \\
&+\frac{q_z\left(4\,cl\,\ln\left(cl+1\right) + 2\,Lc^2\,l + 2\,c^2\,l^2\,\ln\left(cl+1\right) + 3\right)}{4\,c^3\left(cl+1\right)^2} + \\
&-\frac{Lq_z\left(Lc + 2\,cl - 2\right)}{4\,c^2} - \frac{Lq_z\left(2\,cl - Lc + 2\right)}{4\,c^2\left(cl+1\right)^2}
\end{aligned}
$$

$$
\begin{aligned}
C_4 = &\,l\left[\frac{Lq_z\left(Lc + 2\,cl - 2\right)}{4\,c^2} + \frac{Lq_z\left(2\,cl - Lc + 2\right)}{4\,c^2\left(cl+1\right)^2} + \right. \\
&-\frac{q_z\left(2\,\ln(cl+1) + 2\,Lc + 6\,cl - L^2\,c^2 + 3\,c^2\,l^2 + 4\,cl\,\ln(cl+1)\right)}{4\,c^3\left(cl+1\right)^2}\bigg] + \\
&\left.-\frac{q_z\left(2\,Lc^2\,l + 2\,c^2\,l^2\,\ln(cl+1) + 3\right)}{4\,c^3\left(cl+1\right)^2}\right] + \\
&+\frac{Lq_z\left(Lc + 2\,cl + 2\right)}{4\,c^3} - \frac{Llq_z\left(Lc + 2\,cl - 2\right)}{4\,c^2} + \\
&-\frac{Lq_z\left(4\,\ln(cl+1) + Lc + 2\,cl + 4\,cl\,\ln(cl+1) + 2\right)}{4\,c^3\left(cl+1\right)} \\
&+\frac{q_z\left(6\,\ln(cl+1) + 2\,Lc - 2\,cl + L^2\,c^2 - c^2\,l^2 + 4\,Lc\,\ln(cl+1)\right)}{4\,c^4\left(cl+1\right)(} + \\
&+\frac{q_z\left(12\,cl\,\ln(cl+1) + 2\,Lc^2\,l + 6\,c^2\,l^2\,\ln(cl+1) + 4\,Lc^2\,l\,\ln(cl+1) - 1\right)}{4\,c^4\left(cl+1\right)}
\end{aligned}
$$

- $x \geq l + L$:

$$w(x) = C_5 x + C_6 \tag{G.5}$$

$$
\begin{aligned}
C_6 = \; & l\,\frac{L\,q_z\,(L\,c + 2\,c\,l - 2)}{4\,c^2} \\
& - \frac{q_z\,(2\,\ln(c\,l+1) + 2\,L\,c + 6\,c\,l - L^2\,c^2 + 3\,c^2\,l^2 + 4\,c\,l\,\ln(c\,l+1) + 2\,L\,c^2\,l + 2\,c^2\,l^2\,\ln(c\,l+1) + 3)}{4\,c^3\,(c\,l+1)^2} + \\
& \frac{L\,q_z\,(2\,c\,l - L\,c + 2)}{4\,c^2\,(c\,l+1)^2}) - (L+l)\,(\frac{L\,q_z\,(L\,c + 2\,c\,l - 2)}{4\,c^2} + \\
& - \frac{q_z\,(2\,\ln(c\,l+1) + 2\,L\,c + 6\,c\,l - L^2\,c^2 + 3\,c^2\,l^2 + 4\,c\,l\,\ln(c\,l+1) + 2\,L\,c^2\,l + 2\,c^2\,l^2\,\ln(c\,l+1) + 3)}{4\,c^3\,(c\,l+1)^2} + \\
& + \frac{L\,q_z\,(2\,c\,l - L\,c + 2)}{4\,c^2\,(c\,l+1)^2}) + \\
& + (L+l)\,\frac{q_z\,(2\,\ln(c\,(L+l)+1) + 2\,L\,c + 2\,c\,l - L^2\,c^2 + 4\,c\,(L+l))}{4\,c^3\,(c\,(L+l)+1)^2} + \\
& + \frac{-c^2\,l^2 + 2\,c^2\,\ln(c\,(L+l)+1)\,(L+l)^2}{4\,c^3\,(c\,(L+l)+1)^2} + \\
& + (L+l)\,\frac{q_z(4\,c\,\ln(c\,(L+l)+1)\,(L+l) + 4\,L\,c^2\,(L+l) + 4\,c^2\,l\,(L+l) - 2\,L\,c^2\,l + 3)}{4\,c^3\,(c\,(L+l)+1)^2} + \\
& - \frac{q_z\,(2\,\ln(c\,l+1) + 2\,L\,c + 6\,c\,l - L^2\,c^2 + 3\,c^2\,l^2 + 4\,c\,l\,\ln(c\,l+1) + 2\,L\,c^2\,l + 2\,c^2\,l^2\,\ln(c\,l+1) + 3)}{4\,c^3\,(c\,l+1)^2} + \\
& + \frac{L\,q_z\,(L\,c + 2\,c\,l - 2)}{4\,c^2} + \frac{L\,q_z\,(2\,c\,l - L\,c + 2)}{4\,c^2\,(c\,l+1)^2}) + \\
& + \frac{L\,q_z\,(L\,c + 2\,c\,l + 2)}{4\,c^3} + \\
& - \frac{q_z\,(6\,\ln(c\,(L+l)+1) + 2\,L\,c + 2\,c\,l - 2\,c^2\,(L+l)^2}{4\,c^4\,(c\,(L+l)+1)} + \\
& + \frac{q_z(L^2\,c^2 - 4\,c\,(L+l) + c^2\,l^2 + 2\,c^2\,\ln(c\,(L+l)+1)\,(L+l)^2)}{4\,c^4\,(c\,(L+l)+1)} + \\
& - \frac{q_z(8\,c\,\ln(c\,(L+l)+1)\,(L+l) + 4\,L\,c\,\ln(c\,(L+l)+1)}{4\,c^4\,(c\,(L+l)+1)} + \\
& + \frac{q_z(4\,c\,l\,\ln(c\,(L+l)+1)}{4\,c^4\,(c\,(L+l)+1)} + \\
& + \frac{q_z(2\,L\,c^2\,l + 4\,L\,c^2\,\ln(c\,(L+l)+1)\,(L+l) + 4\,c^2\,l\,\ln(c\,(L+l)+1)\,(L+l) - 1)}{4\,c^4\,(c\,(L+l)+1)} + \\
& + \frac{q_z\,(6\,\ln(c\,l+1) + 2\,L\,c - 2\,c\,l + L^2\,c^2 - c^2\,l^2 + 4\,L\,c\,\ln(c\,l+1) + 12\,c\,l\,\ln(c\,l+1)}{4\,c^4\,(c\,l+1)} + \\
& + \frac{q_z(2\,L\,c^2\,l + 6\,c^2\,l^2\,\ln(c\,l+1) + 4\,L\,c^2\,l\,\ln(c\,l+1) - 1)}{4\,c^4\,(c\,l+1)} + \\
& - \frac{L\,l\,q_z\,(L\,c + 2\,c\,l - 2)}{4\,c^2} - \frac{L\,q_z\,(4\,\ln(c\,l+1) + L\,c + 2\,c\,l + 4\,c\,l\,\ln(c\,l+1) + 2)}{4\,c^3\,(c\,l+1)}
\end{aligned}
$$

$$C_5 = \frac{q_z \left[2 \ln\left(c\,l + 1\right) + 2\,L\,c + 6\,c\,l - L^2\,c^2 + 3\,c^2\,l^2\right]}{4\,c^3\left(c\,l + 1\right)^2} +$$

$$\frac{q_z \left[4\,c\,l \ln\left(c\,l + 1\right) + 2\,L\,c^2\,l + 2\,c^2\,l^2\,\ln\left(c\,l + 1\right) + 3\right]}{4\,c^3\left(c\,l + 1\right)^2} +$$

$$-\frac{q_z \left[2 \ln\left(c\,\left(L + l\right) + 1\right) + 2\,L\,c + 2\,c\,l - L^2\,c^2 + 4\,c\,\left(L + l\right) - c^2\,l^2 + 2\,c^2\,\ln\left(c\,\left(L + l\right) + 1\right)\left(L + l\right)^2\right]}{4\,c^3\left(c\,\left(L + l\right) + 1\right)^2} +$$

$$-\frac{q_z \left[4\,c\,\ln\left(c\,\left(L + l\right) + 1\right)\left(L + l\right) + 4\,L\,c^2\,\left(L + l\right) + 4\,c^2\,l\,\left(L + l\right) - 2\,L\,c^2\,l + 3\right]}{4\,c^3\left(c\,\left(L + l\right) + 1\right)^2} +$$

$$-\frac{L\,q_z\,\left(L\,c + 2\,c\,l - 2\right)}{4\,c^2} - \frac{L\,q_z\,\left(2\,c\,l - L\,c + 2\right)}{4\,c^2\left(c\,l + 1\right)^2}$$

where all the integration constant have been obtained setting that $w(0) = 0$, $w'(0) = 0$ and C^1 continuity at $x = \{l, l + L\}$.

Appendix H

Shear stress for tapered wing converging towards its shear center

In this example, the point at which the wing is converging has been set on the shear center of the tip cross-section (in Figure H.1).
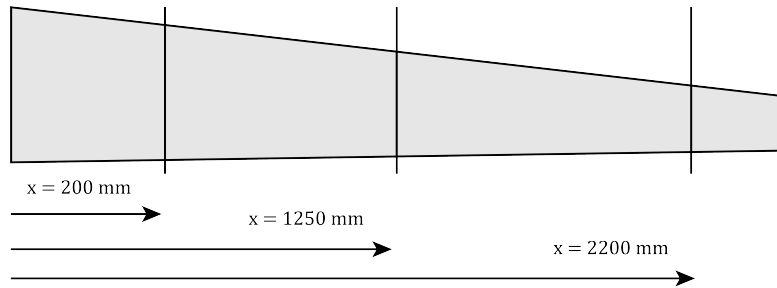
Figure H.1: *Tapered wing converging towards its shear center.*

A load of 1 N has been applied at the tip shear center and the shear stress has again been recovered at the three span locations of Figure H.1.

(a) $x = 2200$ mm   (b) $x = 1250$ mm   (c) $x = 200$ mm
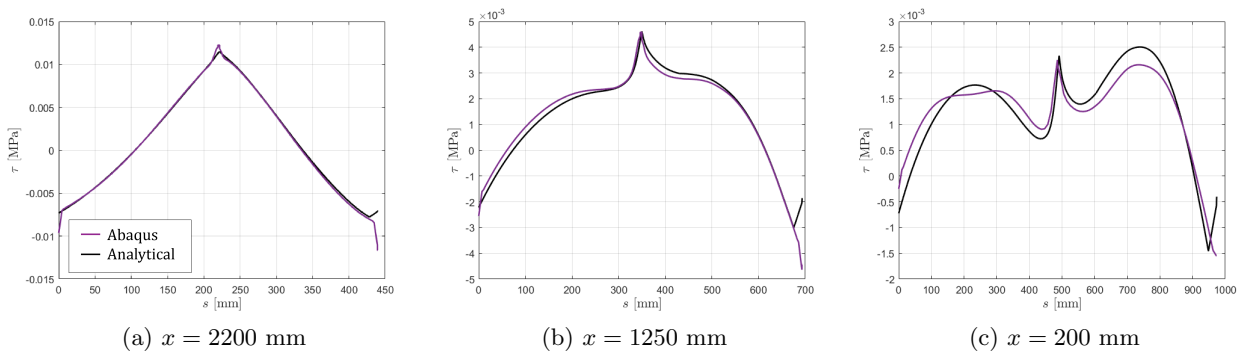
Figure H.2: *Shear stress distribution at three different cross-sections.*

As it is possible to see from Figure H.2, a small geometrical variation has led to significant differences on the behaviour of the shear stress, especially towards the leading edge where a high peak appears. With the method developed, these differences are well captured as it is possible to see comparing with the reference FEM solution.

Appendix I

Computation of laminate elastic properties

Considering a plane-stress configuration, for each ply k the stress and strain vectors can be related as:

$$\begin{bmatrix} \sigma_1 \\ \sigma_2 \\ \tau_{12} \end{bmatrix} = \underbrace{\begin{bmatrix} Q_{11} & Q_{12} & 0 \\ Q_{21} & Q_{22} & 0 \\ 0 & 0 & Q_{66} \end{bmatrix}}_{\boldsymbol{Q}^{(k)}} \begin{bmatrix} \varepsilon_1 \\ \varepsilon_2 \\ \gamma_{12} \end{bmatrix} \tag{I.1}$$

where:

$$Q_{11} = \frac{E_{11}}{1 - \nu_{12}\nu_{21}} \quad ; \quad Q_{22} = \frac{E_{22}}{1 - \nu_{12}\nu_{21}} \quad ; \quad Q_{12} = \frac{\nu_{12}E_{22}}{1 - \nu_{12}\nu_{21}} \quad ; \quad Q_{21} = Q_{12} \quad ; \quad Q_{66} = G_{12}$$

The ply stiffness matrix $\boldsymbol{Q}^{(k)}$ is expressed in the ply reference system. In order to express it in the laminate reference system, a transformation can be applied following the standard tensor rotations and so obtaining the stiffness matrix $\boldsymbol{Q}^{(k)}_{xy}$.
At this point the laminate $\boldsymbol{A}$, $\boldsymbol{B}$ and $\boldsymbol{D}$ matrices can be computed as:

$$\boldsymbol{A} = \sum_k \boldsymbol{Q}^{(k)}_{xy} \left(z_k - z_{k-1} \right)$$

$$\boldsymbol{B} = \sum_k \frac{1}{2} \boldsymbol{Q}^{(k)}_{xy} \left(z_k^2 - z_{k-1}^2 \right) \tag{I.2}$$

$$\boldsymbol{D} = \sum_k \frac{1}{3} \boldsymbol{Q}^{(k)}_{xy} \left(z_k^3 - z_{k-1}^3 \right)$$

with z_k the coordinate of the ply interfaces measured from the laminate mid-plane. So, the **ABD** matrix can be obtained as:

$$\boldsymbol{ABD} = \begin{bmatrix} \boldsymbol{A} & \boldsymbol{B} \\ \boldsymbol{B} & \boldsymbol{D} \end{bmatrix} \tag{I.3}$$

whose inverse is:

$$\boldsymbol{abd} = \begin{bmatrix} \boldsymbol{A} & \boldsymbol{B} \\ \boldsymbol{B} & \boldsymbol{D} \end{bmatrix}^{-1} \tag{I.4}$$

And now the laminate stiffness properties can be directly computed. For example, the membrane elastic modulus is given by [14]:

$$E_{xx} = \frac{1}{h\,\boldsymbol{abd}(1,1)} \tag{I.5}$$

with h the laminate thickness and $\boldsymbol{abd}(1,1)$ the corresponding component of the **abd** matrix (MATLAB notation).

Appendix J

Anisotropic interpolation

As pointed out in [64], an *enormous amount of effort has been devoted to the development of finite elements for the bending of plates.* In particular, the main problem consists in finding elements capable of giving good predictions over wide range of thicknesses without incurring in the so-called *shear locking.* This means that for thin beams (and correspondingly plates) overly stiff elements are obtained. An intuitive explanation of this phenomenon can be found in [64], but more insight is probably given in [9]. It is well known that the difference between the bending rotation θ and $\partial w/\partial x$ gives the shear angle β:

$$\beta = \frac{\partial w}{\partial x} - \theta \tag{J.1}$$

Now, if the shear is negligible it follows that:

$$\theta = \frac{\partial w}{\partial x} \tag{J.2}$$

Consider now that, for example, both w and θ are interpolated linearly along the element as:

$$
\begin{aligned}
w &= a_0 + a_1\xi \\
\theta &= b_0 + b_1\xi
\end{aligned} \tag{J.3}
$$

with $\xi = x/L^{(e)}$. That is, just for the purpose of illustration, the element in Figure J.1 in considered.
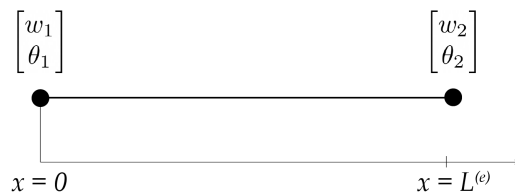
Figure J.1: *Two-node element for illustrating how an anisotropic interpolation works*

Now, computing the coefficients from $w(0) = w_1$ and $w(1) = w_2$ (and analogously for θ) it is possible to obtain:

$$
\begin{aligned}
w &= w_1 + (w_2 - w_1)\xi \\
\theta &= \theta_1 + (\theta_2 - \theta_1)\xi
\end{aligned} \tag{J.4}
$$

And imposing the condition for negligible shear:

$$\frac{\partial w}{\partial \xi} = \theta \quad \Rightarrow \quad (w_2 - w_1) = \theta_1 + (\theta_2 - \theta_1)\xi \tag{J.5}$$

Therefore, since there is no reason why the linear combination of θ_1 and θ_2 should be identically equal to zero, Eq.(J.2) cannot be enforced continuously over the element and this causes problems when the thickness is small compared to the other dimensions.

The solution proposed by [64] is probably the most widespread and well-known. It consists simply in using a one point Gauss quadrature for the transverse shear stiffness term. To exactly integrate the term, a two point quadrature should be required, and therefore using just one point this method is effectively under-integrating the shear energy term. This helps in preventing overly stiff behaviours resulting in shear locking. Another approach consists in using the same order of interpolation for $\partial w / \partial x$ and θ. In other words, w should be interpolated with a polynomial of one order higher than θ. This procedure is referred to as "interdependent variable interpolation" or more commonly as *anisotropic interpolation.*

Appendix K

Optimal SEA parameter

For the uniform pressure load case, the results from the SEA analysis are reported in Table K.1 and in Figure K.1. In general, the position found on the residual curve with the maximum curvature is very close to the configuration which gives the lowest error for every strain component.

		α	L2-norm error
ε_x	Sampled	0.0099	0.19
	Max curvature	0.0099	0.19
ε_y	Sampled	0.032	0.33
	Max curvature	0.01	0.33
γ_{xy}	Sampled	0.005	0.49
	Max curvature	0.01	0.487

Table K.1: *Error of interpolated strain field using optimal values for α, either from the sampled values and from the maximum curvature of the residual curve for uniform pressure load case.*

For the parabolic pressure load case, the corresponding results are reported in Table K.2 and in Figure K.2. Again, the position found on the residual curve with the maximum curvature seem to give a suitable interpolation for every component of the strain field. An exception is given this time by ε_y, whose minimum does not exactly correspond to the identified corner. However, the difference in the error is relatively small.

		α	L2-norm error
ε_x	Sampled	0.01	0.1942
	Max curvature	0.0062	0.1946
ε_y	Sampled	0.0001	0.3668
	Max curvature	0.0084	0.3896
γ_{xy}	Sampled	0.01	0.419
	Max curvature	0.0039	0.424

Table K.2: *Error of interpolated strain field using optimal values for α, either from the sampled values and from the maximum curvature of the residual curve for parabolic pressure load case.*
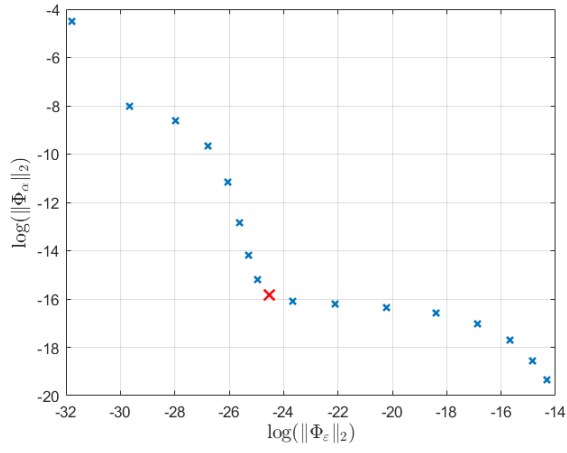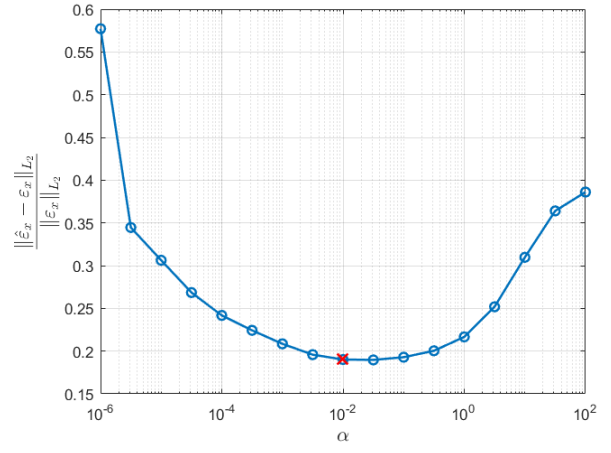
(a) *Residuals of ε_x for different values of α.*

(b) *Relative L2-norm error of ε_x strain field.*
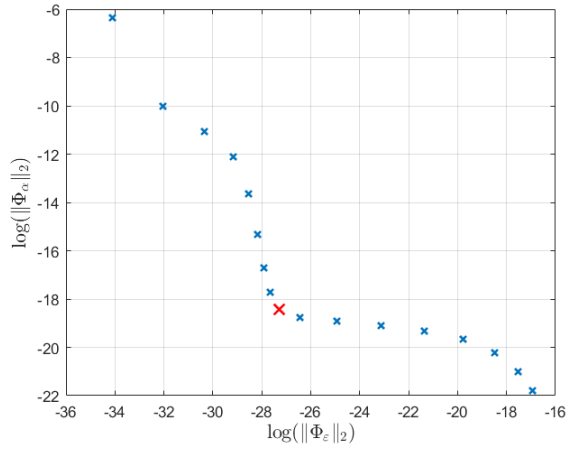
(c) *Residuals of ε_y for different values of α.*
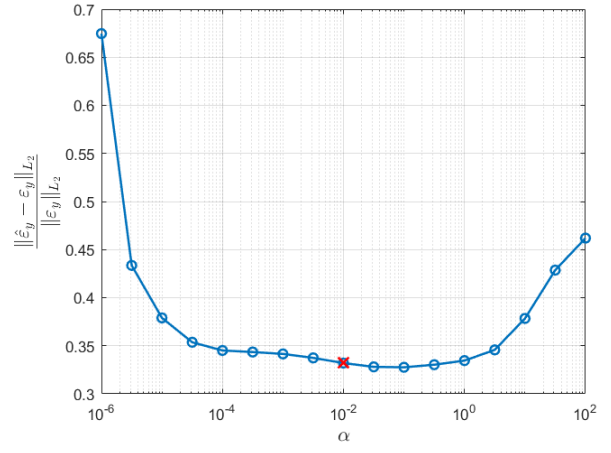
(d) *Relative L2-norm error of ε_y strain field.*
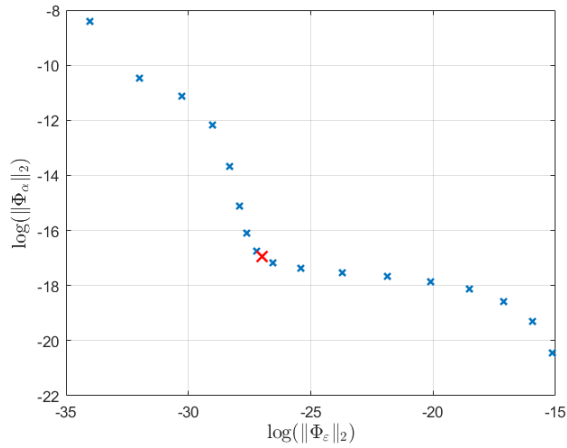
(e) *Residuals of γ_{xy} for different values of α.*
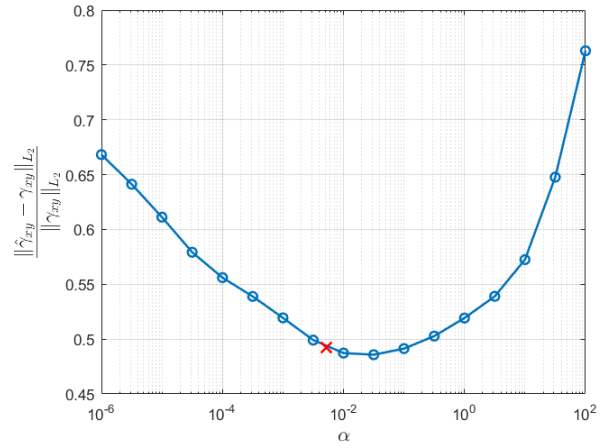
(f) *Relative L2-norm error of γ_{xy} strain field.*

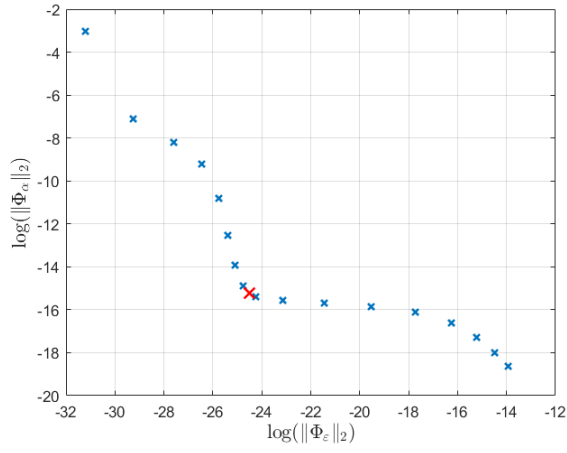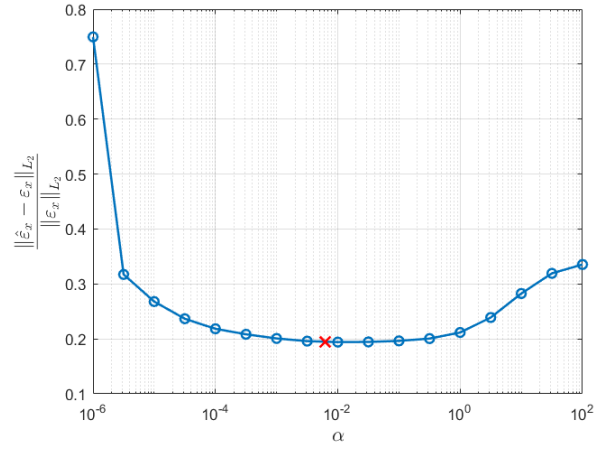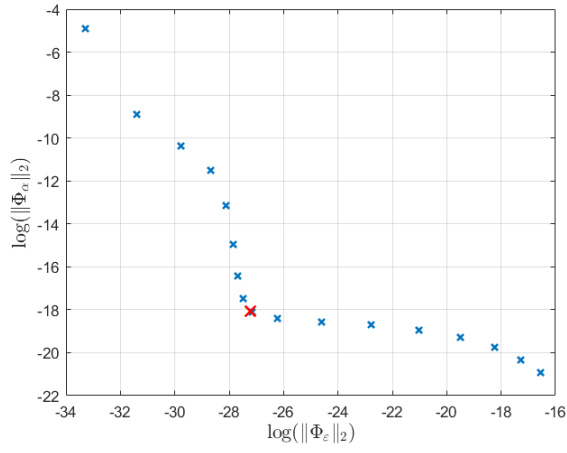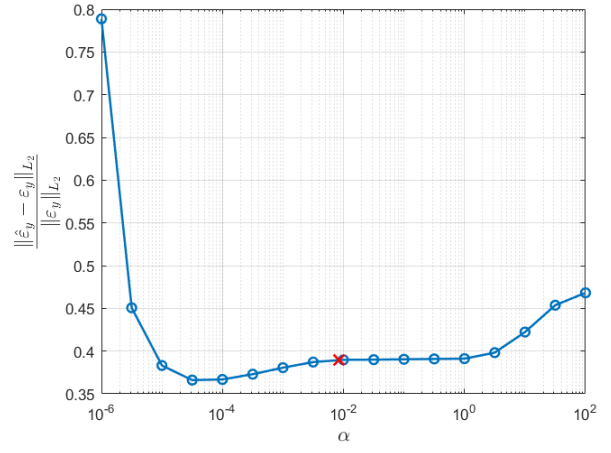Figure K.1: *Interpolation of strain field with SEA for the constant pressure load case.*

(a) *Residuals of ε_x for different values of α.*

(b) *Relative L2-norm error of ε_x strain field.*

(c) *Residuals of ε_y for different values of α.*

(d) *Relative L2-norm error of ε_y strain field.*
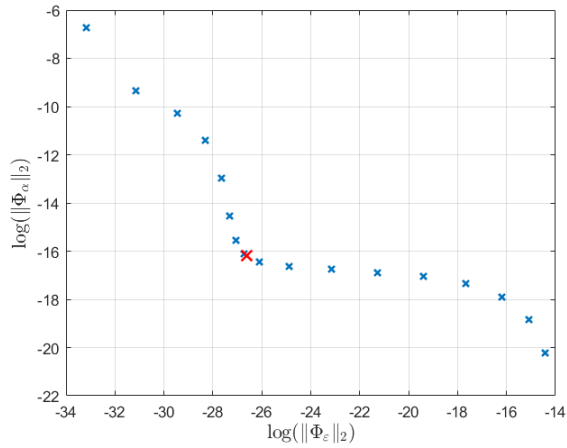
(e) *Residuals of γ_{xy} for different values of α.*
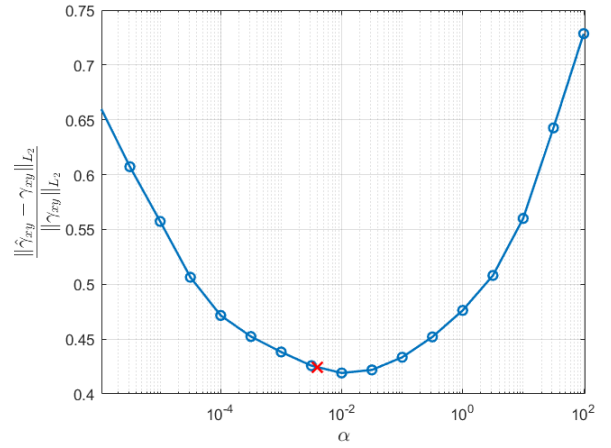
(f) *Relative L2-norm error of γ_{xy} strain field.*

Figure K.2: *Interpolation of strain field with SEA for the parabolic pressure load case.*

Appendix L

Computation of structural matrices from Abaqus

The stiffness and mass matrix can be easily extracted from the FEM software package without the need to built it yourself. In particular, `Abaqus` has been used and this can be obtained modifying the input file creating an additional step as:

```
* STEP, NAME = CreateMatrices
* MATRIX GENERATE, STIFFNESS, MPC = NO
* MATRIX OUTPUT, STIFFNESS, FORMAT = COORDINATE
* End Step
```

which returns, as `.mtx` files, the mass and the stiffness matrix of the model. It is important to note two points:

- `MPC=NO` suppresses the automatic elimination of independent degrees of freedom (in case in the model are present constraints). In this way the matrices which will be obtained will have as size the total number of degrees of freedom.

- `FORMAT = COORDINATE` renders the output files much easier to read, since they are written in the format (row)-(column)-(value), for each matrix entry.

The matrix obtained is ordered using the `Abaqus` numbering of the degrees of freedom:

$$\boldsymbol{u}^{(e)} = \begin{bmatrix} u\ v\ w\ \theta_x\ \theta_y\ \theta_z \end{bmatrix}^\top$$

Appendix M

Details of FEM models

Prismatic airfoil beam

Main geometric parameters (Figure M.1) and the FE model (Figure M.2) for the prismatic beam with thin-walled airfoil cross-section. The positions of the strain gauges from Table M.1 correspond to the discretization with a single inverse element. In general, when more elements have been used, just the axial positions has been changed.
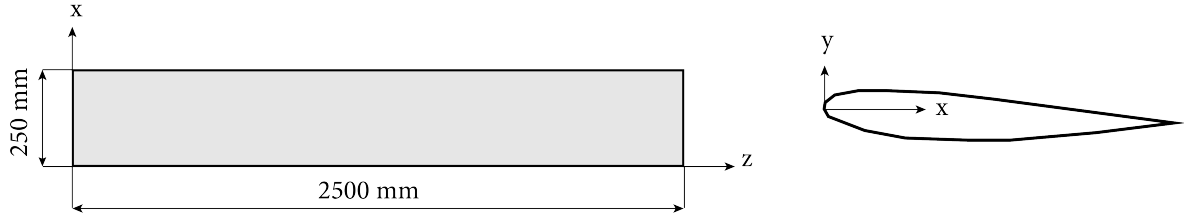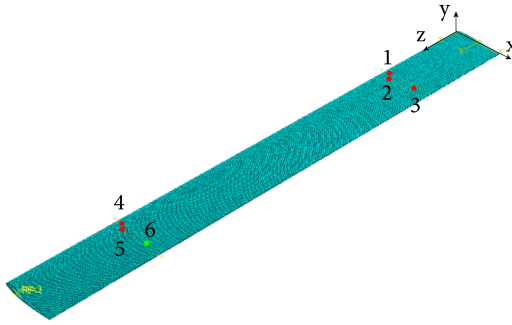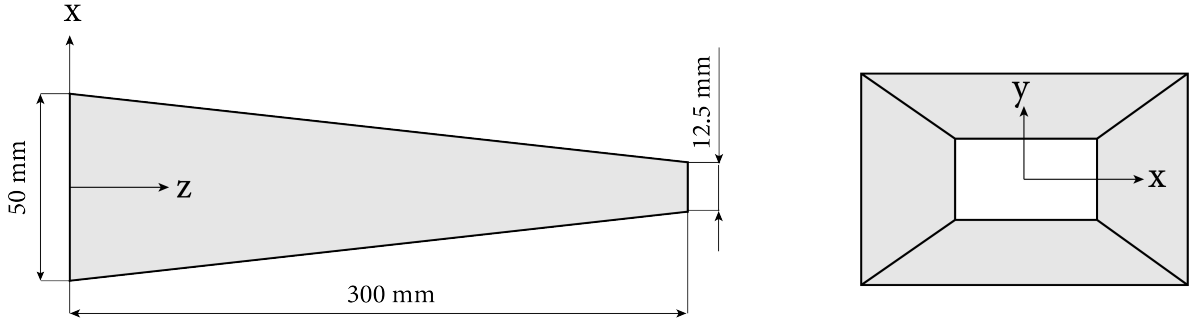

Figure M.1: *Geometry and reference system.*

Figure M.2: *FEM model of prismatic airfoil beam.*

# Elements	177707 (S4R)
Strain gauge	(X, Y, Z)
#1	$(33, 12, 501)$ mm
#2	$(33., -16, 501)$ mm
#3	$(175, 0, 501)$ mm
#4	$(34, 12, 2001)$ mm
#5	$(33, -16, 2001)$ mm
#6	$(175, 0, 2001)$ mm

Table M.1: *Strain gauge positions.*

Box tapered beam

Main geometric parameters (Figure M.3) and the FE model (Figure M.4) for the tapered box beam. The positions of the strain gauges from Table M.2 correspond to the discretization with a single inverse element. In general, when more elements have been used, just the axial positions have been changes and the strain gauges have been moved according to the taper ratio of the beam.
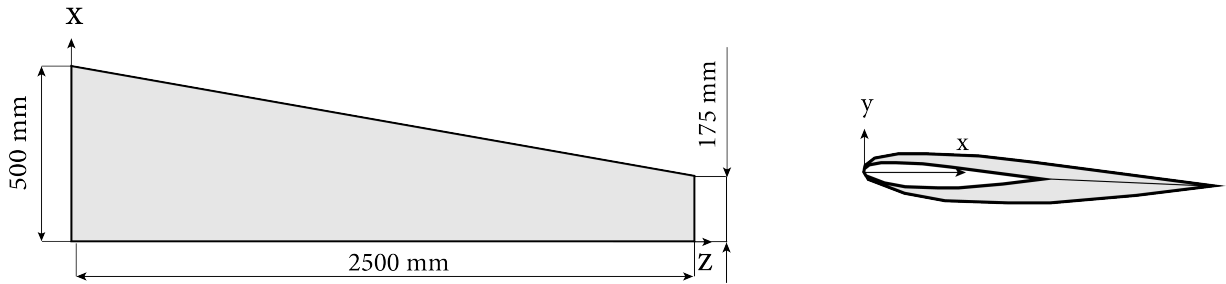
Figure M.3: *Geometry and reference system.*
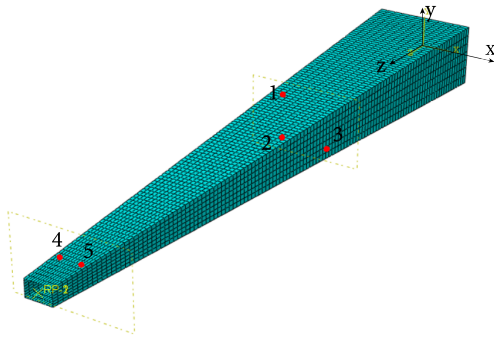
Figure M.4: *FEM model of box tapered beam.*

# Elements	4560 (S4R)
Strain gauge	(X, Y, Z)
#1	$(-12, 11, 120)$ mm
#2	$(-12, -11, 120)$ mm
#3	$(12, -11, 120)$ mm
#4	$(-5, 4, 283)$ mm
#5	$(5, 4, 283)$ mm

Table M.2: *Strain gauge positions.*

Tapered airfoil beam

Main geometric parameters (Figure M.5) and the FE model (Figure M.7) for the tapered beam with thin-walled airfoil cross-section. The positions of the strain gauges from Table M.3 correspond to the discretization with a single inverse element. In general, when more elements have been used, just the axial positions have been changes and the strain gauges have been moved according to the taper ratio of the beam.
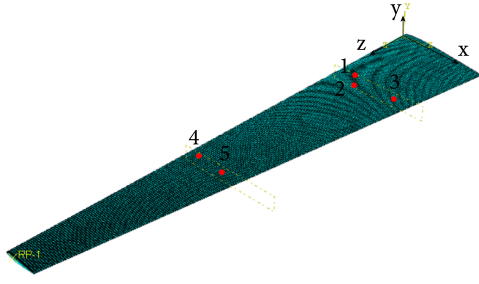

Figure M.5: *Geometry and reference system.*

Figure M.6: *FEM model of airfoil tapered beam.*

# Elements	49949 (S4R)
Strain gauge	(X, Y, Z)
#1	$(104, 21, 498)$ mm
#2	$(102, -37, 498)$ mm
#3	$(350, -7, 498)$ mm
#4	$(63, 15, 1500)$ mm
#5	$(211, 0, 1500)$ mm

Table M.3: *Strain gauge positions.*

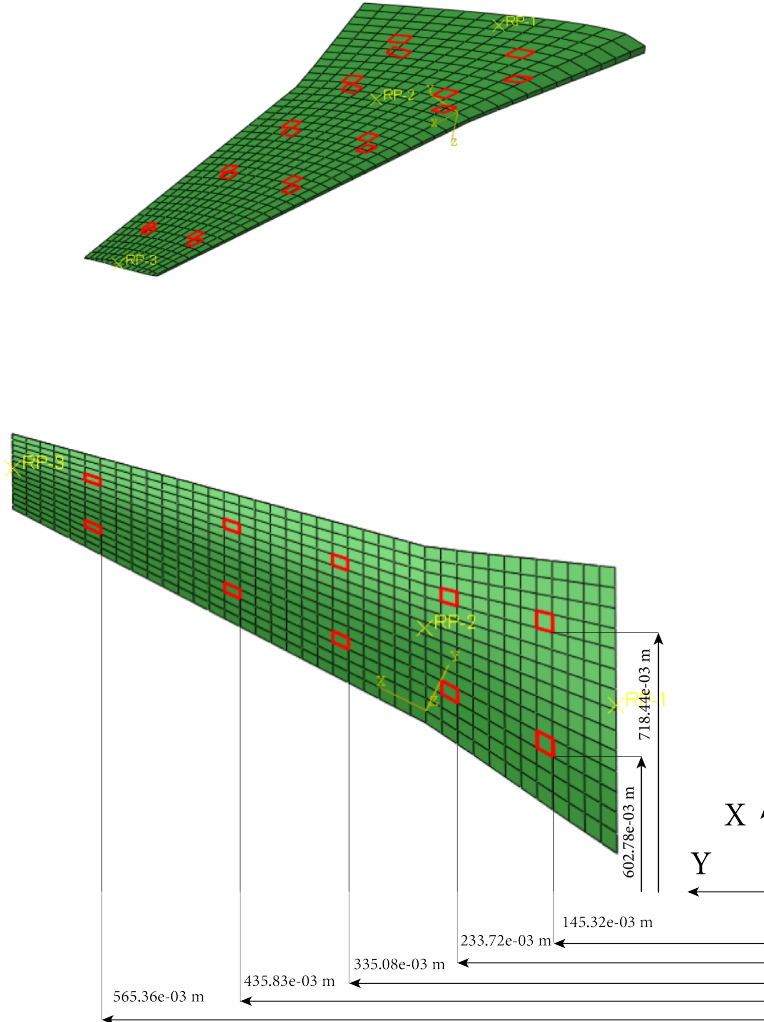## Strain rosettes on ISTAR demonstrator wing

Figure M.7: *FEM model of ISTAR demonstrator wing with highlighted the positions of the elements from which the strain field is sampled.*

References

[1] Airoldi A et al. "Load Monitoring by Means of Optical Fibres and Strain Gages". In: *Smart Intelligent Aircraft Structures (SARISTU)* June (2016), pp. 433–469. DOI: 10.1007/978-3-319-22413-8_20.

[2] Airoldi A et al. "Strain field reconstruction on composite spars based on the identification of equivalent load conditions". In: *Sensors and Smart Structures Technologies for Civil, Mechanical, and Aerospace Systems 2017* (2017), pp. 101–680. DOI: 10.1117/12.2260161.

[3] Kefal A. "An efficient curved inverse-shell element for shape sensing and structural health monitoring of cylindrical marine structures". In: *Ocean Engineering* 19.June (2019), pp. 1299–1313. DOI: 10.1016/j.oceaneng.2019.106262.

[4] Kefal A et al. "A quadrilateral inverse-shell element with drilling degrees of freedom for shape sensing and structural health monitoring". In: *Engineering Science and Technology, an International Journal* 19.3 (2016), pp. 1299–1313. DOI: 10.1016/j.jestch.2016.03.006.

[5] Tessler A, Riggs HR, and Dambach M. "A novel four-node quadrilateral smoothing element for stress enhancement and error estimation". In: *International Journal for Numerical Methods in Engineering* 44.10 (1999), pp. 1527–1543. DOI: 10.1002/(SICI)1097-0207(19990410)44:10<1527::AID-NME497>3.0.CO;2-1.

[6] Tessler A, Riggs HR, and Macy SC. "A variational method for finite element stress recovery and error estimation". In: *Computer Methods in Applied Mechanics and Engineering* 111.3-4 (1994), pp. 369–382. DOI: 10.1016/0045-7825(94)90140-6.

[7] Tessler A and Spangler J. "Inverse FEM for Full-Field Reconstruction of Elastic Deformations in Shear Deformable Plates and Shells". In: *Proceedings of Second European Workshop on Structural Health Monitoring* (2004), pp. 83–90.

[8] Tessler A and Spangler JL. *An Inverse Finite Element Method for Application to Structural Health Monitoring*. https://ifem.larc.nasa.gov/publications.html. 2002.

[9] Tessler A and Dong SB. "On a hierarchy of conforming timoshenko beam elements". In: *Computers and Structures* 14.3 (1981), pp. 335–344. DOI: 10.1016/0045-7949(81)90017-1.

[10] Tessler A and Hughes TJR. "An improved treatment of transverse shear in the mindlin-type four-node quadrilateral element". In: *Computer Methods in Applied Mechanics and Engineering* 39.3 (1983), pp. 311–335. DOI: 10.1016/0045-7825(83)90096-8.

[11] Tessler A et al. "An improved variational method for finite element stress recovery and a posteriori error estimation". In: *Computer Methods in Applied Mechanics and Engineering* 155.1-2 (1998), pp. 15–30. DOI: 10.1016/S0045-7825(97)00135-7.

[12] Pisoni AC et al. "Displacements in a vibrating body by strain gauge measurements". In: *Proceedings of the 13th international modal analysis conference* (1995), pp. 119–125.

[13]   Garda B and Galias Z. "Non-negative least squares and the Tikhonov regularization methods for coil design proglems". In: *Conference: Signals and Electronic Systems* (2012).

[14]   Kassapoglou C. *Design and Analysis of Composite Structures*. Wiley, 2010.

[15]   Pak CG. "Wing shape sensing from measured strain". In: *AIAA Journal* 54.3 (2016), pp. 1064–1073. ISSN: 00011452. DOI: 10.2514/1.J053986.

[16]   Lawson CL and Hanson RJ. *Solving Least Squares Problems*. Society for Industrial and Applied Mathematics, 1995.

[17]   Chen CS, Hon YC, and Schaback RA. *Scientific Computing with Radial Basis Functions*. 2007.

[18]   Jutte CV et al. "Deformed Shape Calculation of a Full-Scale Wing Using Fiber Optic Strain Data from a Ground Loads Test". In: *NASA/TP—2011–215975* (2011).

[19]   Oboe D et al. "Comparison of strain pre-extrapolation techniques for shape and strain sensing by iFEM of a composite plate subjected to compression buckling". In: *Composite Structures* 262.November (2021). DOI: 10.1016/j.compstruct.2021.113587.

[20]   Xiu D. *Numerical Merthods for Stochastic Computations*. Princeton University Press, 2010.

[21]   Fertis DG and Keene ME. "Elastic and Inelastic Analysis of Nonprismatyic Members". In: *Journal of Structural Engineering* 116 (1990).

[22]   Jacquelin E, Bennani A, and Hamelin P. "Force reconstruction: analysis and regularizaion of a deconvolutoin problem". In: *Journal of Sound and Vibration* (2003).

[23]   Torre E, Marelli S, and Sudret B. *UQLab user manual – Statistical inference*. Tech. rep. Report UQLab-V2.0-114. Chair of Risk, Safety and Uncertainty Quantification, ETH Zurich, Switzerland, 2022.

[24]   Russo EP and Garic G. "Shear-Stress Distribution in Symetrically Tapered Cantilever Beam". In: *Journal of Structural Engineering* 118 (1992).

[25]   Zhao F et al. "Shape sensing of variable cross-section beam using the inverse finite element method and isogeometric analysis". In: *Measurement: Journal of the International Measurement Confederation* 158 (2020). DOI: 10.1016/j.measurement.2020.107656.

[26]   Genaro G and Rade DA. "Input Force Identification in the Time Domain". In: *Proceedings of the 16th International Modal Analysis Conference* (1998), p. 124.

[27]   Ahmadian H, Mottershead JE, and Friswell MI. "Boundary Condition Identification by Solving Characteristic Equations". In: *Journal of Sound and Vibration* 247 (2001).

[28]   Kim HI, Kang LH, and Han JH. "Shape estimation with distributed fiber Bragg grating sensors for rotating structures". In: *Smart Materials and Structures* 20.3 (2011). DOI: 10.1088/0964-1726/20/3/035011.

[29]   Bang HJ et al. "Shape estimation and health monitoring of wind turbine tower using a FBG sensor array". In: *2012 IEEE I2MTC - International Instrumentation and Measurement Technology Conference, Proceedings* 3 (2012), pp. 496–500. DOI: 10.1109/I2MTC.2012.6229407.

[30]   Riggs HR, Tessler A, and Chu H. "C1-continuous stress recovery in finite element analysis". In: *Computer Methods in Applied Mechanics and Engineering* 143.3-4 (1997), pp. 299–316. DOI: 10.1016/S0045-7825(96)01151-6.

[31]   Bakalyar J and Jutte C. "Validation tests of fiber optic strain-based operational shape and load measurements". In: *Collection of Technical Papers - AIAA/ASME/ASCE/AHS/ASC Structures, Structural Dynamics and Materials Conference* April (2012), pp. 1–81. DOI: 10.2514/6.2012-1904.

[32] Colombo L, Sbarufatti C, and Giglio M. "Definition of a load adaptive baseline by inverse finite element method for structural damage identification". In: *Mechanical Systems and Signal Processing* 120 (2019), pp. 584–607. DOI: `10.1016/j.ymssp.2018.10.041`.

[33] Li L et al. "Structural shape reconstruction through modal approach using strain gages". In: *Communications in Computer and Information Science* 462 (2014), pp. 273–281.

[34] Taglialegne L. "Analytical study of stress fields in wind turbine blades". PhD thesis. University of Braunschweig and University of Florence, 2019.

[35] Silva LA and Rade DA. "Time domain-based identification of mechanical characteristics of supporting elements". In: *Proceedings of the 17th International Modal Analysis Conference* (1999).

[36] Esposito M. "Shape sensing and load reconstruction for aerospace structures". PhD thesis. Politecnico di Torino, 2021.

[37] Esposito M and Gherlone M. "Composite wing box deformed-shape reconstruction based on measured strains: Optimization and comparison of existing approaches". In: *Aerospace Science and Technology* 99 (2020). DOI: `10.1016/j.ast.2020.105758`.

[38] Esposito M and Gherlone M. "Material and strain sensing uncertainties quantification for the shape sensing of a composite wing box". In: *Mechanical Systems and Signal Processing* 160 (2021). DOI: `10.1016/j.ymssp.2021.107875`.

[39] Esposito M, Gherlone M, and Marzocca P. "External loads identification and shape sensing on an aluminum wing box: An integrated approach". In: *Aerospace Science and Technology* 114 (2021). DOI: `10.1016/j.ast.2021.106743`.

[40] Gherlone M et al. "Dynamic shape reconstruction of three-dimensional frame structures using the inverse finite element method". In: *ECCOMAS Thematic Conference - COMPDYN 2011: 3rd International Conference on Computational Methods in Structural Dynamics and Earthquake Engineering: An IACM Special Interest Conference, Programme* February (2011).

[41] Gherlone M et al. "Shape sensing of 3D frame structures using an inverse Finite Element Method". In: *International Journal of Solids and Structures* 49.22 (2012), pp. 3100–3112. DOI: `10.1016/j.ijsolstr.2012.06.009`.

[42] S. Marelli, N. Lüthen, and B. Sudret. *UQLab user manual – Polynomial Chaos Expansion*. Tech. rep. Report UQLab-V2.0-104. Chair of Risk, Safety and Uncertainty Quantification, ETH Zurich, Switzerland, 2022.

[43] Murray NW. *Introduction to the Theory of Thin-Walled Elastic Structures*. Clarendon Press, 1984.

[44] Zienkiewicz OC and Taylor RL. *Finite Element Method: Volume 2*. Butterworth Heinemann, 2005.

[45] Cerracchio P, Gherlone M, and Tessler A. "Real-time displacement monitoring of a composite stiffened panel subjected to mechanical and thermal loads". In: *Meccanica* 50.10 (2015), pp. 2487–2496. DOI: `10.1007/s11012-015-0146-8`.

[46] Dumitrache P. "Shear Stresses in Beams with Variable Cross Section Subjected to non-uniuniform Bending". In: *Annals of Dunarea de Jos University of Galati* (2012).

[47] Lancaster P and Salkauskas K. *Curve and Surface Fitting - An Introduction*. 1986.

[48] Savino P, Gherlone M, and Tondolo F. "Shape sensing with inverse finite element method for slender structures". In: *Structural Engineering and Mechanics* 72 (2019), pp. 217–227.

REFERENCES

[49] Bogert PB, Haugse E, and Gehrki RE. "Structural shape identification from experimental strains using a modal transformation technique". In: *Collection of Technical Papers - AIAA/ASME/ASCE/AHS/ASC Structures, Structural Dynamics and Materials Conference* 3.April (2003), pp. 2026–2043. DOI: 10.2514/6.2003-1626.

[50] Hansen PC. "Analysis of discrete ill-posed problems by means of the L-curve". In: 34.4 (1992), pp. 561–580.

[51] Hansen PC. *Discrete Inverse Problems.* SIAM Society for Industrial and Applied Mathemetics, 2010.

[52] Hansen PC. "Regularization Tools: a Matlab package for analysis and solution of discrete ill-posed problems". In: *Numerical Algorithms* 6 (1994), pp. 1–35.

[53] Hansen PC and O'Leary DP. "The Use of the L-Curve in the Regularization of Discrete Ill-Posed Problems". In: *SIAM Journal on Scientific Computing* 14.6 (1993), pp. 1487–1503. DOI: 10.1137/0914086.

[54] Roy R et al. "Shape sensing of plate structures using the inverse finite element method: Investigation of efficient strain–sensor patterns". In: *Sensors (Switzerland)* 20.24 (2020), pp. 1–24. DOI: 10.3390/s20247049.

[55] Cook RD. "Four-node 'flat' shell element: Drilling degrees of freedom, membrane-bending coupling, warped geometry, and behavior". In: *Computers and Structures* 50.4 (1994), pp. 549–555. DOI: 10.1016/0045-7949(94)90025-6.

[56] Jones RT et al. "Determination of cantilever plate shapes using wavelength division multiplexed fiber Bragg grating sensors and a least-squares strain-fitting algorithm". In: *Smart Materials and Structures* 7.2 (1998), pp. 178–188. DOI: 10.1088/0964-1726/7/2/005.

[57] Marelli S and Sudret B. "UQLab: A Framework for Uncertainty Quantification in MATLAB". In: *The 2nd International Conference on Vulnerability and Risk Analysis and Management* (2014).

[58] Rapp S et al. "Displacement field estimation for a two-dimensional structure using fiber Bragg grating sensors". In: *Smart Materials and Structures* 18.2 (Feb. 2009). DOI: 10.1088/0964-1726/18/2/025006.

[59] Shkarayev S, Krashantisa R, and Tessler A. "An Inverse Interpolation Method Utilizing In-Flight Strain Measurements for Determining Loads and Structural Response of Aerospace Vehicles". In: *Third Int. Workshop on Structural Health Monitoring* November (2001), pp. 336–343.

[60] Rao SS. *The Finite Element Method in Engineering.* Butterworth-Heinemann, 2017.

[61] Nakamura T, Igawa H, and Kanda A. "Inverse identification of continuously distributed loads using strain data". In: *Aerospace Science and Technology* 23.1 (2012), pp. 75–84. DOI: 10.1016/j.ast.2011.06.012.

[62] Kriel TES. "Assessment of Frequency Domain Force Identification Proceudres". MA thesis. University of Pretoria, 2000.

[63] Megson THG. *Aircraft Structures for Engineering Students, Fourth Edition.* Butterworth-Heinemann, 2007.

[64] Hughes TJR. "A simple and efficient triangular finite element for plate bending". In: *International Journal for Numerical Methods in Engineering* 11 (1977), pp. 1529–1543. DOI: 10.1007/BF02485859.

[65] Capacia VN. "Wing Panel Optimization using Lamination Parameters and Inverse Distance Weighting Interpolation". MSc thesis. Istituto Tecnologico de Aeronautica, 2018.

[66] Pilkey WD. *Analysis and design of elastic beams: computational methods.* Wiley, 2002. ISBN: 0471381527.

[67] Ko WL, Richards WL, and Fleischer VT. "Applications of Ko Displacement Theory to the Deformed Shape Predictions of the Doubly-tapered Ikhana Wing". In: *NASA/TP-2009-214652.* October (2009).

[68] Ko WL, Richards WL, and Tran VT. "Displacement Theories for In-Flight Deformed Shape Predictions of Aerospace Structures". In: *NASA/TP-2007-214612* October (2007).

[69] Govers Y, Jelicic G, and Akbay T. "The use of strain sensors for modal identification of aeroelastic structures". In: *International Conference on Noise and Vibration Engineering* (2016), pp. 2207–2216.

[70] Luo Y. "An efficient 3D Timoshenko beam element with consistent shape functions". In: *Adv. Theor. Appl. Mech* 1 (2008), pp. 95–106. URL: https://www.researchgate.net/publication/259345543.